Mechanics of Microelectromechanical Systems

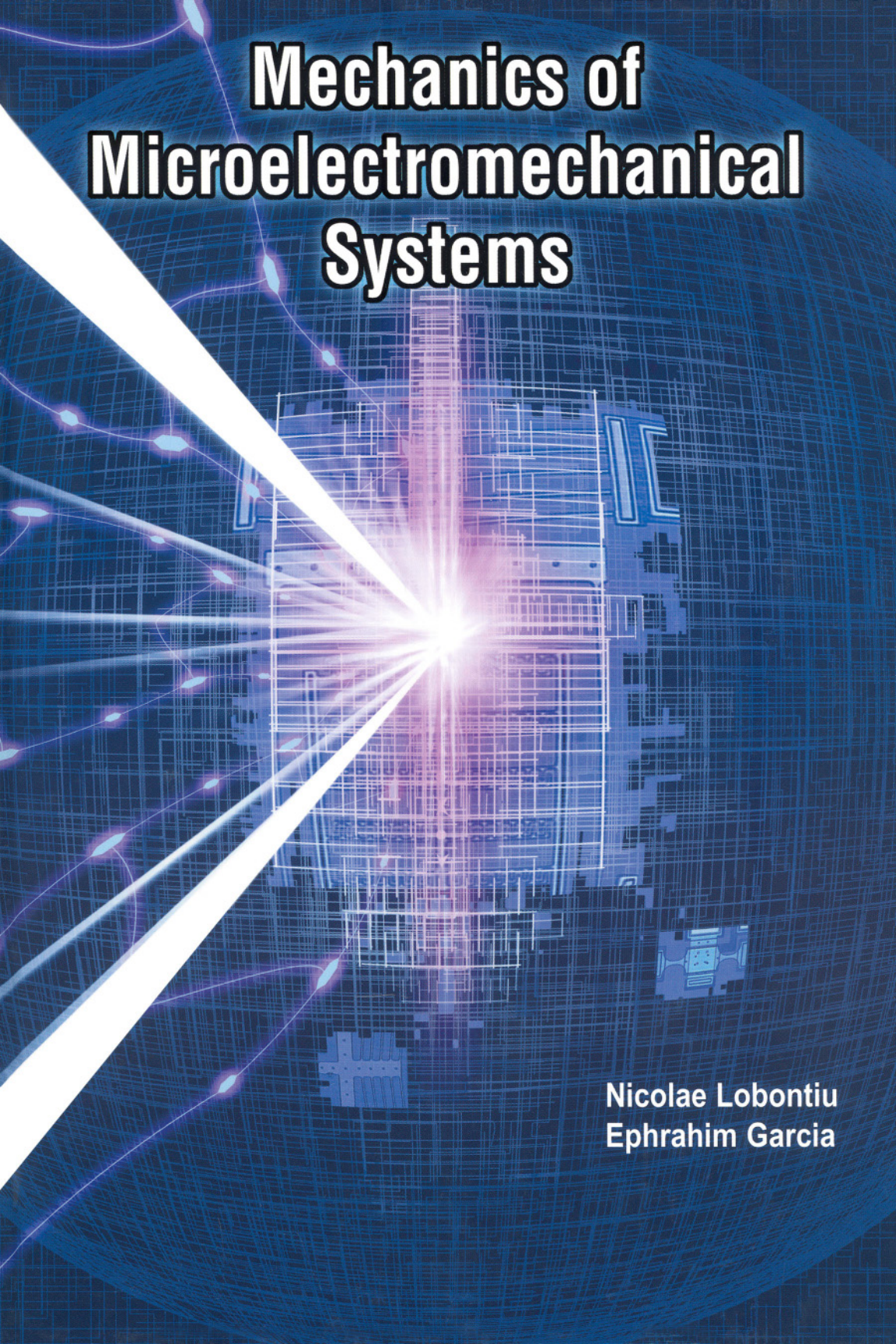

Nicolae Lobontiu
Ephrahim Garcia

VISIT…

Mechanics of Microelectro-mechanical Systems

This page intentionally left blank

Nicolae Lobontiu
Ephrahim Garcia

Mechanics of Microelectromechanical Systems

KLUWER ACADEMIC PUBLISHERS
NEW YORK, BOSTON, DORDRECHT, LONDON, MOSCOW

eBook ISBN: 0-387-23037-8
Print ISBN: 1-4020-8013-1

©2005 Springer Science + Business Media, Inc.

Print ©2005 Kluwer Academic Publishers
Boston

All rights reserved

No part of this eBook may be reproduced or transmitted in any form or by any means, electronic, mechanical, recording, or otherwise, without written consent from the Publisher

Created in the United States of America

Visit Springer's eBookstore at: http://ebooks.kluweronline.com
and the Springer Global Website Online at: http://www.springeronline.com

To our families

This page intentionally left blank

TABLE OF CONTENTS

Preface ix

1 STIFFNESS BASICS 1
1 INTRODUCTION 1
2 STIFFNESS DEFINITION 1
3 DEFORMATIONS, STRAINS AND STRESSES 6
4 MEMBERS, LOADS AND BOUNDARY CONDITIONS ... 14
5 LOAD-DISPLACEMENT CALCULATION METHODS: CASTIGLIANO'S THEOREMS 21
6 COMPOSITE MEMBERS 43
7 PLATES AND SHELLS 58
Problems 60

2 MICROCANTILEVERS, MICROHINGES, MICROBRIDGES 65
1 INTRODUCTION 65
2 MICROCANTILEVERS 66
3 MICROHINGES 97
4 COMPOUND MICROCANTILEVERS 103
5 MICROBRIDGES 114
Problems 126

3 MICROSUSPENSIONS 131
1 INTRODUCTION 131
2 MICROSUSPENSIONS FOR LINEAR MOTION 131
3 MICROSUSPENSIONS FOR ROTARY MOTION 170
Problems 179

4 MICROTRANSDUCTION: ACTUATION AND SENSING .. 183
1 INTRODUCTION 183
2 THERMAL TRANSDUCTION 184
3 ELECTROSTATIC TRANSDUCTION 195
4 ELECTROMAGNETIC/MAGNETIC TRANSDUCTION ... 212
5 PIEZOELECTRIC (PZT) TRANSDUCTION 223
6 PIEZOMAGNETIC TRANSDUCTION 230
7 SHAPE MEMORY ALLOY (SMA) TRANSDUCTION 232
8 BIMORPH TRANSDUCTION 238
9 MULTIMORPH TRANSDUCTION 249
10 OTHER FORMS OF TRANSDUCTION 256
Problems 257

5 STATIC RESPONSE OF MEMS 263
1 INTRODUCTION 263
2 SINGLE-SPRING MEMS 263
3 TWO-SPRING MEMS 271
4 MULTI-SPRING MEMS 285
5 DISPLACEMENT-AMPLIFICATION MICRODEVICES ... 286
6 LARGE DEFORMATIONS 307
7 BUCKLING 315
8 COMPOUND STRESSES AND YIELDING 330
Problems 335

6 MICROFABRICATION, MATERIALS, PRECISION AND SCALING 343
1 INTRODUCTION 343
2 MICROFABRICATION 343
3 MATERIALS 363
4 PRECISION ISSUES IN MEMS 365
5 SCALING 381
Problems 390

Index 395

PREFACE

This book offers a comprehensive coverage to the mechanics of microelectromechanical systems (MEMS), which are analyzed from a mechanical engineer's viewpoint as devices that transform an input form of energy, such as thermal, electrostatic, electromagnetic or optical, into output mechanical motion (in the case of actuation) or that can operate with the reversed functionality (as in sensors) and convert an external stimulus, such as mechanical motion, into (generally) electric energy. The impetus of this proposal stems from the perception that such an approach might contribute to a more solid understanding of the principles governing the mechanics of MEMS, and would hopefully enhance the efficiency of modeling and designing reliable and desirably-optimized microsystems. The work represents an attempt at both extending and deepening the mechanical-based approach to MEMS in the static domain by providing simple, yet reliable tools that are applicable to micromechanism design through current fabrication technologies.

Lumped-parameter stiffness and compliance properties of flexible components are derived both analytically (as closed-form solutions) and as simplified (engineering) formulas. Also studied are the principal means of actuation/sensing and their integration into the overall microsystem. Various examples of MEMS are studied in order to better illustrate the presentation of the different modeling principles and algorithms.

Through its objective, approach and scope, this book offers a novel and systematic insight into the MEMS domain and complements existing work in the literature addressing part of the material developed herein. Essentially, this book provides a database of stiffness/compliance models for various spring-type flexible connectors that transmit the mechanical motion in MEMS, as well as of the various forces/moments that are involved in microtransduction. In order to predict their final state, the microsystems are characterized by formulating, solving and analyzing the static equilibrium equations, which incorporate spring, actuation and sensing effects.

Chapter 1 gives a succinct, yet comprehensive review of the main tools enabling stiffness/compliance characterization of MEMS as it lays the foundation of further developments in this book. Included are basic topics from mechanics of materials and statics such as load-deformation, stress-strain or structural members. Presented are the Castigliano's theorems as basic tools in stiffness/compliance calculation. Straight and curved line elements are studied by explicitly formulating their compliance/stiffness characteristics. Composite micromembers, such as sandwiched, serial, parallel, and hybrid (serial-parallel) are also treated in detail, as well as thin plates and shells. All the theoretical apparatus presented in this chapter is illustrated with examples of MEMS designs.

Chapter 2 is dedicated to characterizing the main flexible components that are encountered in MEMS and which enable mechanical mobility through

their elastic deformation. Studied are flexible members such as microhinges (several configurations are presented including constant cross-section, circular, corner-filleted and elliptic configurations), microcantilevers (which can be either solid or hollow) and microbridges (fixed-fixed mechanical components). Each compliant member presented in this chapter is defined by either exact or simplified (engineering) stiffness or compliance equations that are derived by means of lumped-parameter models. Solved examples and proposed problems accompany again the basic text.

Chapter 3 derives the stiffnesses of various microsuspensions (microsprings) that are largely utilized in the MEMS design. Included are beam-type structures (straight, bent or curved), U-springs, serpentine springs, sagittal springs, folded beams, and spiral springs (with either small or large number of turns). All these flexible components are treated in a systematic manner by offering equations for both the main (active) stiffnesses and the secondary (parasitic) ones.

Chapter 4 analyzes the micro actuation and sensing techniques (collectively known as transduction methods) that are currently implemented in MEMS. Details are presented for microtransduction procedures such as electrostatic, thermal, magnetic, electromagnetic, piezoelectric, with shape memory alloys (SMA), bimorph- and multimorph-based. Examples are provided for each type of actuation as they relate to particular types of MEMS.

Chapter 5 is a blend of all the material comprised in the book thus far, as it attempts to combine elements of transduction (actuation/sensing) with flexible connectors in examples of real-life microdevices that are studied in the static domain. Concrete MEMS examples are analyzed from the standpoint of their structure and motion traits. Single-spring and multiple-spring micromechanisms are addressed, together with displacement-amplification microdevices and large-displacement MEMS components. The important aspects of buckling, postbuckling (evaluation of large displacements following buckling), compound stresses and yield criteria are also discussed in detail. Fully-solved examples and problems add to this chapter's material.

The final chapter, Chapter 6, includes a presentation of the main microfabrication procedures that are currently being used to produce the microdevices presented in this book. MEMS materials are also mentioned together with their mechanical properties. Precision issues in MEMS design and fabrication, which include material properties variability, microfabrication limitations in producing ideal geometric shapes, as well as simplifying assumptions in modeling, are addressed comprehensively. The chapter concludes with aspects regarding scaling laws that apply to MEMS and their impact on modeling and design.

This book is mainly intended to be a textbook for upper-undergraduate/graduate level students. The numerous solved examples together with the proposed problems are hoped to be useful for both the student and the instructor. These applications supplement the material which

is offered in this book, and which attempts to be self-contained such that extended reference to other sources be not an absolute pre-requisite. It is also hoped that the book will be of interest to a larger segment of readers involved with MEMS development at different levels of background and proficiency/skills. The researcher with a non-mechanical background should find topics in this book that could enrich her/his customary modeling/design arsenal, while the professional of mechanical formation would hopefully encounter familiar principles that are applied to microsystem modeling and design.

Although considerable effort has been spent to ensure that all the mathematical models and corresponding numerical results are correct, this book is probably not error-free. In this respect, any suggestion would gratefully be acknowledged and considered.

The authors would like to thank Dr. Yoonsu Nam of Kangwon National University, Korea, for his design help with the microdevices that are illustrated in this book, as well as to Mr. Timothy Reissman of Cornell University for proof-reading part of the manuscript and for taking the pictures of the prototype microdevices that have been included in this book.

Ithaca, New York
June 2004

This page intentionally left blank

Chapter 1

STIFFNESS BASICS

1. INTRODUCTION

Stiffness is a fundamental qualifier of elastically-deformable mechanical microcomponents and micromechanisms whose static, modal or dynamic response need to be evaluated. This chapter gives a brief introduction to the stiffness of microeletromechanical structural components by outlining the corresponding linear, small-deformation theory, as well as by studying several concrete examples. The fundamental notions of elastic deformation, strain, stress and strain energy, which are all related to stiffness, are briefly outlined. Energy methods are further presented, specifically the Castigliano's theorems, which are utilized herein to derive stiffness or compliance equations.

A six degree-of-freedom lumped-parameter stiffness model is proposed for the constant cross-section fixed-free straight members that are sensitive to bending, axial and torsion loading. A similar model is developed for curved members, both thick and thin, by explicitly deriving the compliance equations. Composite beams, either sandwiched or in serial/parallel configurations, are also presented in terms of their stiffnesses. Later, the stiffness of thin plates and membranes is approached and equations are formulated for circular and rectangular members. Problems that are proposed to be solved conclude this chapter.

2. STIFFNESS DEFINITION

MEMS mainly move by elastic deformation of their flexible components. One way of characterizing the static response of elastic members is by defining their relevant stiffnesses. The simple example of a linear spring is shown in Fig. 1.1, where a force is applied by slowly increasing its magnitude from zero to a final value F_1 over a period of time t_1 such that the force is in static equilibrium with the spring force at any moment in time.

The force necessary to extend the spring by the quantity Δl is calculated as:

$$F_l = K_l \Delta l \tag{1.1}$$

where K_l is the spring's *linear stiffness,* which depends on the material and geometrical properties of the spring. This simple linear-spring model can be used to evaluate axial deformations and forced-produced beam deflections of mechanical microcomponents. For materials with linear elastic behavior and in the small-deformation range, the stiffness is constant. Chapter 5 will introduce the large-deformation theory which involves non-linear relationships between load and the corresponding deformation. Another way of expressing the load-deformation relationship for the spring in Fig. 1.1 is by reversing the causality of the problem, and relating the deformation to the force as:

$$\Delta l = C_l F_l \tag{1.2}$$

where C_l is the spring's *linear compliance,* and is the inverse of the stiffness, as can be seen by comparing Eqs. (1.1) and (1.2).

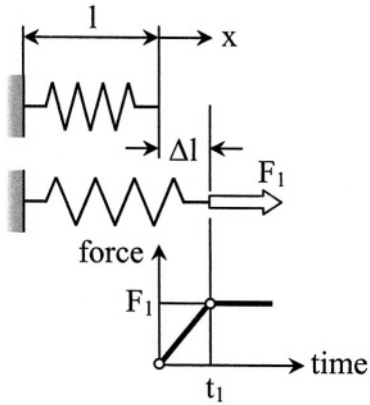

Figure 1.1 Load and deformation for a linear spring

Similar relationships do also apply for rotary (or torsion) springs, as the one sketched in Fig. 1.2 (a). In this case, a torque M_l is applied to a central shaft. The applied torque has to overcome the torsion spring elastic resistance, and the relationship between the torque and the shaft's angular deflection can be written as:

$$M_l = K_r \Delta\theta \tag{1.3}$$

The compliance-based equation is of the form:

$$\Delta\theta = C_r M_1 \tag{1.4}$$

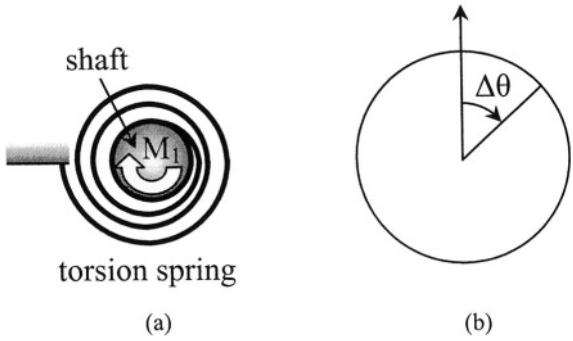

Figure 1.2 Rotary/spiral spring: (a) Load; (b) Deformation

Again, Eqs. (1.3) and (1.4) show that the *rotary compliance* is the inverse of the *rotary stiffness.* The rotary spring is the model for torsional bar deformations and moment-produced bending slopes (rotations) of beams.

Both situations presented here, the linear spring under axial load and the rotary spring under a torque, define the stiffness as being the inverse to the corresponding compliance. There is however the case of a beam in bending where a force that is applied at the free end of a fixed-free beam for instance produces both a linear deformation (the deflection) and a rotary one (the slope), as indicated in Fig. 1.3 (a).

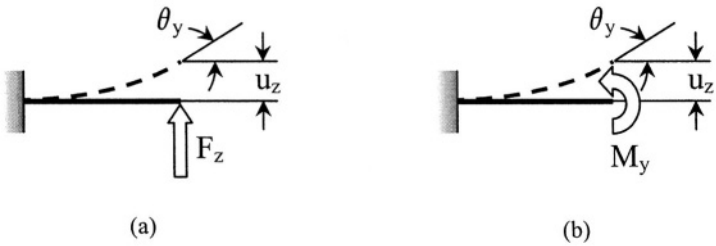

Figure 1.3 Load and deformations in a beam under the action of a: (a) force; (b) moment

In this case, the stiffness-based equation is:

$$F_z = K_l u_z + K_c \theta_y \tag{1.5}$$

The stiffness $\mathbf{K_l}$ connects the force to its direct effect, the deflection about the force's direction (the subscript l indicates its linear/translatory character). The other stiffness, $\mathbf{K_c}$, which is called *cross-stiffness* (indicated by the

subscript *c*), relates a cause (the force) to an effect (the slope/rotation) that is not a direct result of the cause, in the sense discussed thus far. A similar causal relationship is produced when applying a moment at the free end of the cantilever, as sketched in Fig. 1.3 (b). The moment generates a slope/rotation, as well as a deflection at the beam's tip, and the following equation can be formulated:

$$M_y = K_c u_z + K_r \theta_y \tag{1.6}$$

Formally, Eqs. (1.5) and (1.6) can be written in the form:

$$\begin{Bmatrix} F_z \\ M_y \end{Bmatrix} = \begin{bmatrix} K_l & K_c \\ K_c & K_r \end{bmatrix} \begin{Bmatrix} u_z \\ \theta_y \end{Bmatrix} \tag{1.7}$$

where the matrix connecting the load vector on the left hand side to the deformation vector in the right hand side is called bending-related *stiffness matrix.*

Elastic systems where load and deformation are linearly proportional are called linear, and a feature of *linear systems* is exemplified in Eq. (1.5), which shows that part of the force F_z is spent to produce the deflection u_z and the other part generates the rotation (slope) θ_y. Equation (1.6) illustrates the same feature. The cross-compliance K_c connects a moment to a deflection, whereas K_r (the rotary stiffness, signaled by the subscript *r)* relates two causally-consistent amounts: the moment to the slope/rotation. The stiffnesses K_l and K_r can be called *direct stiffnesses,* to indicate a force-deflection or moment-rotation relationship. Equations that are similar to Eqs. (1.5) and (1.6) can be written in terms of compliances, namely:

$$u_z = C_l F_z + C_c M_y \tag{1.8}$$

and

$$\theta_y = C_c F_z + C_r M_y \tag{1.9}$$

where the significance of compliances is highlighted by the subscripts which have already been introduced when discussing the corresponding stiffnesses. Equations (1.8) and (1.9) can be collected into the matrix form:

$$\begin{Bmatrix} u_z \\ \theta_y \end{Bmatrix} = \begin{bmatrix} C_l & C_c \\ C_c & C_r \end{bmatrix} \begin{Bmatrix} F_z \\ M_y \end{Bmatrix} \tag{1.10}$$

where the *compliance matrix* links the deformations to the loads. Equations (1.8) and (1.9) indicate that the end deflection u_z can be produced by *linearly superimposing* (adding) the separate effects of F_z and M_y. As shown later on, Equations (1.5) and (1.6), as well as Eqs. (1.8) and (1.9) indicate that three different stiffnesses or compliances, namely: two direct (linear and rotary) and one crossed, define the elastic response at the free end of a cantilever. More details on the spring characterization of fixed-free microcantilevers that are subject to forces and moments producing bending will be provided in this chapter, as well as in Chapter 2, by defining the associated stiffnesses or compliances for various geometric configurations

Example 1.1

Knowing that $C_l = l^3/(3EI_y)$, $C_c = l^2/(2EI_y)$, $C_r = l/(EI_y)$ for the constant cross-section cantilever loaded as shown in Fig. 1.4, demonstrate that $[C]^{-1} = [K]$, where [K] is the symmetric stiffness matrix defined by: $K_l = 12EI_y/l^3$, $K_c = -6EI_y/l^2$, $K_r = 4EI_y/l$.

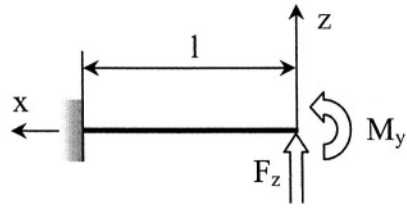

Figure 1.4 Cantilever with tip force and moment

Solution:

Equation (1.10) can be written in the generic form:

$$\{u\} = [C]\{F\} \tag{1.11}$$

When left-multiplying Eq. (1.11) by $[C]^{-1}$, the following equation is obtained:

$$[C]^{-1}\{u\} = \{F\} \tag{1.12}$$

Equation (1.7) can also be written in the compact form:

$$\{F\} = [K]\{u\} \tag{1.13}$$

By comparing Eqs. (1.12) and (1.13) it follows that:

$$[C]^{-1} = [K] \tag{1.14}$$

The compliance matrix:

$$[C] = \begin{bmatrix} l^3/(3EI_y) & l^2/(2EI_y) \\ l^2/(2EI_y) & l/(EI_y) \end{bmatrix} \tag{1.15}$$

is now inverted and the resulting stiffness matrix is:

$$[K] = \begin{bmatrix} 12EI_y/l^3 & -6EI_y/l^2 \\ -6EI_y/l^2 & 4EI_y/l \end{bmatrix} \tag{1.16}$$

An explanation of the minus sign in front of the cross-stiffness in Eq. (1.16) will be provided in Example 1.15 of this chapter.

The direct stiffnesses can physically be represented by a linear spring (in the case of a force-deflection relationship) – as pictured in Fig 1.1, or a rotary one (for a moment-rotation relationship) – as indicated in Fig. 1.2. These two cases are sketched for a cantilever beam in Figs. 1.5 (a) and (b) by the two springs, one linear of stiffness K_l, and one rotary of stiffness K_r. The cross-stiffness K_c is represented in Fig. 1.5 (c), which attempts to give a physical, spring-based representation of the situation where the moment M_y creates a linear deformation (the deflection u_z), by means of the eccentric disk which rotates around a fixed shaft and thus moves vertically the tip of the beam.

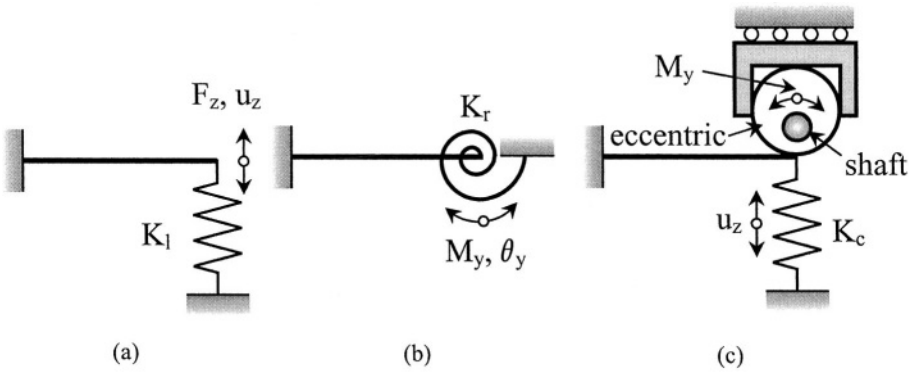

Figure 1.5 Spring-based representation of the bending stiffnesses: (a) direct linear stiffness; (b) direct rotary stiffness; (c) cross-stiffness

3. DEFORMATIONS, STRAINS AND STRESSES

The stiffness of a deformable MEMS component can generally be found by prior knowledge of the corresponding deformations, strains and/or stresses. The deformations of elastic bodies under load can be linear (extension or compression) or angular, and Fig. 1.6 contains the sketches that illustrate these two situations. When a constant pressure is applied normally

on the right face of the element shown in Fig. 1.6 (a), while the opposite face is fixed, the elastic body will deform linearly by a quantity Δl_1, such that the final length about the direction of deformation will be $l_1 + \Delta l_1$. The ratio of the change in length to the initial length is the *linear strain:*

$$\varepsilon = \Delta l_1 / l_1 \tag{1.17}$$

If an elementary area dA is isolated from the face that has translated, one can define the normal stress on that surface as the ratio:

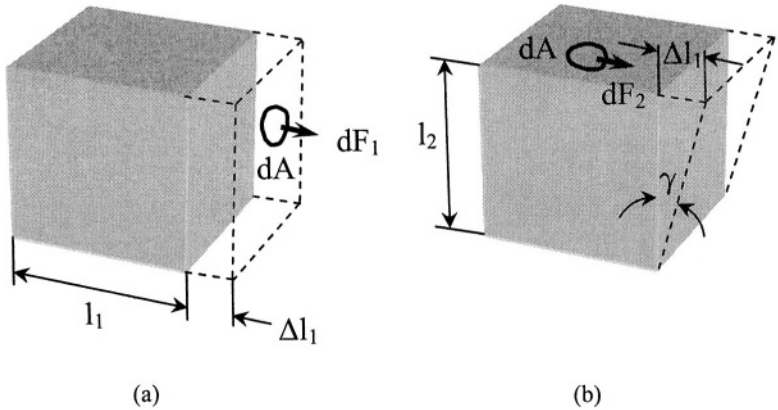

Figure 1.6 Element stresses: (a) normal; (b) shearing

$$\sigma = dF_1 / dA \tag{1.18}$$

where dF_1 is the elementary force acting perpendicularly on dA. For small deformations and elastic materials, the stress-strain relationship is linear, and in the case of Fig. 1.6 (a) the normal stress and strain are connected by means of *Hooke's law:*

$$\sigma = E\varepsilon \tag{1.19}$$

where E is *Young's modulus,* a constant that depends on the material under investigation.

When the distributed load acts on the upper face of the volume element and is contained in that face, as sketched in Fig. 1.6 (b), while the opposite face is fixed, the upper face will shear (rotate) with respect to the fixed surface. The relevant deformation here is angular, and the change in angle γ is defined as the *shear strain* in the form:

$$\gamma \approx \tan\gamma = \Delta l_1 / l_2 \tag{1.20}$$

Similarly to the normal strain, the shear strain is defined as:

$$\tau = dF_2 / dA \tag{1.21}$$

A linear relationship also exists between shear stress and strain, namely:

$$\tau = G\gamma \tag{1.22}$$

where G is the *shear modulus* and, for a given material, is a constant amount. Young's modulus and the shear modulus are connected by means of the equation:

$$G = \frac{E}{2(1+\mu)} \tag{1.23}$$

where μ is *Poisson's ratio.*

For a three-dimensional elastic body that is subject to external loading the state of strain and stress is generally three-dimensional. Figure 1.7 shows an elastic body that is subject to the external loading system generically represented by the forces F_1 through F_n. In the case of static equilibrium, with thermal effects neglected, an elementary volume can be isolated, which is also in equilibrium under the action of the stresses that act on each of its eight different faces.

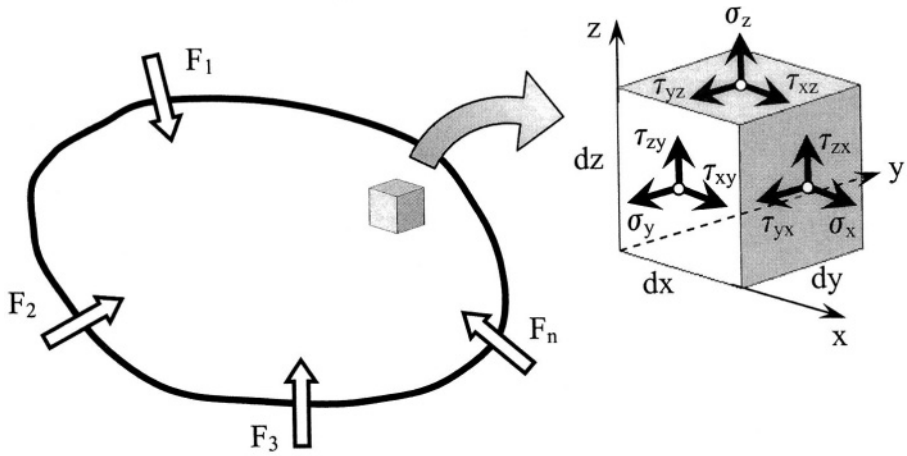

Figure 1.7 Stresses on an element removed from an elastic body in static equilibrium

As Fig. 1.7 indicates, there are 9 stresses acting on the element's faces, but the following equalities, which connect the stresses, do apply:

$$\begin{cases} \tau_{xy} = \tau_{yx} \\ \tau_{yz} = \tau_{zy} \\ \tau_{zx} = \tau_{xz} \end{cases} \tag{1.24}$$

Because of the three Eqs. (1.24), which enforce the rotation equilibrium, only 6 stresses are independent. The *equilibrium* (or *Navier's*) *equations* are:

$$\begin{cases} \partial\sigma_x / \partial x + \partial\tau_{xy} / \partial y + \partial\tau_{xz} / \partial z + X = 0 \\ \partial\tau_{yx} / \partial x + \partial\sigma_y / \partial y + \partial\tau_{yz} / \partial z + Y = 0 \\ \partial\tau_{zx} / \partial x + \partial\tau_{zy} / \partial y + \partial\sigma_z / \partial z + Z = 0 \end{cases} \tag{1.25}$$

where X, Y and Z are body force components acting at the center of the isolated element.

Six strains correspond to the six stress components, as expressed by the generalized *Hooke's law*:

$$\begin{cases} \sigma_x = E[(1-\mu)\varepsilon_x + \mu\varepsilon_y + \mu\varepsilon_z] / [(1+\mu)(1-2\mu)] \\ \sigma_y = E[\mu\varepsilon_x + (1-\mu)\varepsilon_y + \mu\varepsilon_z] / [(1+\mu)(1-2\mu)] \\ \sigma_z = E[\mu\varepsilon_x + \mu\varepsilon_y + (1-\mu)\varepsilon_z] / [(1+\mu)(1-2\mu)] \\ \tau_{xy} = G\gamma_{xy} \\ \tau_{yz} = G\gamma_{yz} \\ \tau_{zx} = G\gamma_{zx} \end{cases} \tag{1.26}$$

The *strain-displacement* (or *Cauchy's*) *equations* relate the strains to the displacements as:

$$\begin{cases} \varepsilon_x = \partial u_x / \partial x \\ \varepsilon_y = \partial u_y / \partial y \\ \varepsilon_z = \partial u_z / \partial z \\ \gamma_{xy} = \partial u_x / \partial y + \partial u_y / \partial x \\ \gamma_{yz} = \partial u_y / \partial z + \partial u_z / \partial y \\ \gamma_{zx} = \partial u_z / \partial x + \partial u_x / \partial z \end{cases} \tag{1.27}$$

It should be noted that for normal strains (and stresses), the subscript indicates the axis the stress is parallel to, whereas for shear strains (and stresses), the first subscript indicates the axis which is parallel to the strain,

while the second one denotes the axis which is perpendicular to the plane of the respective strain.

By combining Eqs. (1.25), (1.26) and (1.27), the following equations are obtained, which are known as *Lamé's equations:*

$$\begin{cases} G(\partial^2 u_x/\partial x^2 + \partial^2 u_x/\partial y^2 + \partial^2 u_x/\partial z^2) + (\lambda + G)[\partial^2 u_x/\partial x^2 \\ + \partial^2 u_y/(\partial x \partial y) + \partial^2 u_z/(\partial z \partial x)] + X = 0 \\ G(\partial^2 u_y/\partial x^2 + \partial^2 u_y/\partial y^2 + \partial^2 u_y/\partial z^2) + (\lambda + G)[\partial^2 u_x/(\partial x \partial y) \\ + \partial^2 u_y/\partial y^2 + \partial^2 u_z/(\partial y \partial z)] + Y = 0 \\ G(\partial^2 u_z/\partial x^2 + \partial^2 u_z/\partial y^2 + \partial^2 u_z/\partial z^2) + (\lambda + G)[\partial^2 u_x/(\partial z \partial x) \\ + \partial^2 u_y/(\partial y \partial z) + \partial^2 u_z/\partial z^2] + Z = 0 \end{cases} \tag{1.28}$$

Equations (1.28) contain as unknowns only the three displacements u_x, u_y and u_z. In Eqs. (1.28), λ is *Lamé's constant,* which is defined as:

$$\lambda = \mu E/[(1+\mu)(1-2\mu)] \tag{1.29}$$

In order for the equation system (1.28) to yield valid solutions, it is necessary that the *compatibility* (or *Saint Venant's*) *equations* be complied with:

$$\begin{cases} \partial^2 \varepsilon_x/\partial y^2 + \partial^2 \varepsilon_y/\partial x^2 - \partial^2 \gamma_{xy}/(\partial x \partial y) = 0 \\ \partial^2 \varepsilon_y/\partial z^2 + \partial^2 \varepsilon_z/\partial y^2 - \partial^2 \gamma_{yz}/\partial y \partial z = 0 \\ \partial^2 \varepsilon_z/\partial x^2 + \partial^2 \varepsilon_x/\partial z^2 - \partial^2 \gamma_{zx}/(\partial z \partial x) = 0 \\ 2\partial^2 \varepsilon_x/(\partial y \partial z) + \dfrac{\partial}{\partial x}(\partial \gamma_{yz}/\partial x - \partial \gamma_{zx}/\partial y - \partial \gamma_{xy}/\partial z) = 0 \\ 2\partial^2 \varepsilon_y/(\partial z \partial x) + \dfrac{\partial}{\partial y}(\partial \gamma_{zx}/\partial y - \partial \gamma_{xy}/\partial z - \partial \gamma_{yz}/\partial x) = 0 \\ 2\partial^2 \varepsilon_z/(\partial x \partial y) + \dfrac{\partial}{\partial z}(\partial \gamma_{xy}/\partial z - \partial \gamma_{yz}/\partial x - \partial \gamma_{zx}/\partial y) = 0 \end{cases} \tag{1.30}$$

Equations (1.24) through (1.30) are the core mathematical model of the *theory of elasticity.* More details on this subject can be found in advanced mechanics of materials textbooks, such as the works of Boresi, Schmidt and Sidebottom [1], Ugural and Fenster [2] or Cook and Young [3].

Many MEMS components and devices are built as thin structures, and therefore the corresponding stresses and strains are defined with respect to a

plane. Two particular cases of the general state of deformations described above are the state of plane stress and the state of plane strain. In a *state of plane stress,* as the name suggests, the stresses are located in a plane (such as the middle plane that is parallel to the xy plane in Fig. 1.7). The following stresses are zero:

$$\begin{cases} \sigma_z = 0 \\ \tau_{zx} = 0 \\ \tau_{yz} = 0 \end{cases} \tag{1.31}$$

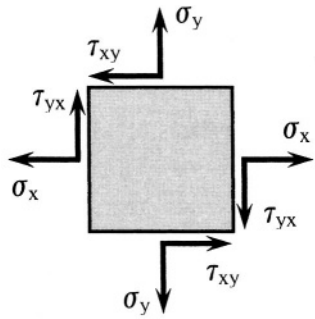

Figure 1.8 Plane state of stress/strain

Thin plates, thin bars and thin beams that are acted upon by forces in their plane, are examples of MEMS components that are in a plane state of stress. For thicker components, the cross-sections of shafts in torsion are also in a state of plane stress. In a *state of plane strain,* the stress perpendicular to the plane of interest does not vanish, $\sigma_z \neq 0$, but all other stresses in Eqs. (1.31) are zero. Microbeams that are acted upon by forces perpendicular to the larger cross-sectional dimension are in a state of plane strain for instance. Figure 1.8 illustrates both the state of plane stress and the state of plane strain.

Example 1.2

A thin microcantilever, for which t << w, can be subject to a force as shown in Fig. 1.9 (a) or to a force as pictured in Fig. 1.9 (b). Decide on the state of stress/strain that is setup in each of the two cases.

Solution:

The loading and geometry of Fig. 1.9 (a) show that the stresses and strains will be planar because of the thin condition of the microcantilever (t << w). However, because the load is perpendicular to the plane xy, the stress about the z-direction does not vanish, $\sigma_z \neq 0$, and therefore, according to the definition introduced previously, the microcantilever is in a state of plane strain. In the case pictured in Fig. 1.9 (b), the force F_y is located in the xy

plane of the thin microcantilever, and there is no stress acting about the z-direction. As a consequence, and according to its definition, a state of plane stress is setup in the microcantilever under this particular load.

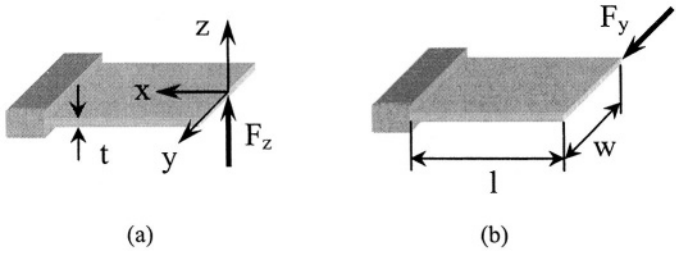

Figure 1.9 Thin microbeams under the action of a tip force: (a) perpendicular to the plane; (b) in-the-plane

Example 1.3

A thin-film microbar, having the configuration and dimensions of Fig. 1.10 is subject to a state of extensional residual stresses (this condition will be detailed in Chapter 6) after microfabrication. The state of residual stress will generate an axial deformation of the bar, which can be monitored experimentally, as sketched in Fig. 1.10. By using the theory of elasticity equations, determine the residual stress in the film. Known are: $u_x = 0.1\ \mu m$, $l = 240\ \mu m$ and E=120GPa.

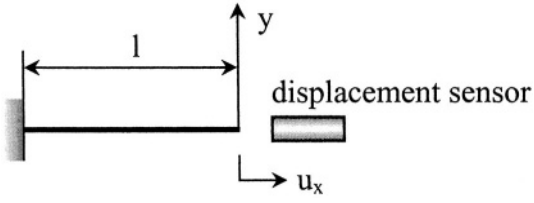

Figure 1.10 Displacement sensing for residual stress measurement in a microbar

Solution:

This particular state of stress, where only the normal stresses about the x-direction are non-zero, is called *state of uniaxial stresses.* Hooke's law Eqs. (1.26) simplify to the following form:

$$\begin{cases} \sigma_x = E[(1-\mu)\varepsilon_x + \mu\varepsilon_y + \mu\varepsilon_z]/[(1+\mu)(1-2\mu)] \\ 0 = E[\mu\varepsilon_x + (1-\mu)\varepsilon_y + \mu\varepsilon_z]/[(1+\mu)(1-2\mu)] \\ 0 = E[\mu\varepsilon_x + \mu\varepsilon_y + (1-\mu)\varepsilon_z]/[(1+\mu)(1-2\mu)] \end{cases} \tag{1.32}$$

Equations (1.32) are solved for the strains ϵ_x, ϵ_y and ϵ_z:

$$\begin{cases} \varepsilon_x = \sigma_x / E \\ \varepsilon_y = \varepsilon_z = -\mu\sigma_x / E \end{cases} \tag{1.33}$$

Because this is a state of uniaxial stress, the only variable is x, and therefore the displacement about this direction can be calculated as:

$$u_x = \int_0^l \varepsilon_x dx = \varepsilon_x l \tag{1.34}$$

under the assumption that the strain is constant about the microbar's length. By combining now the first of Eqs. (1.33) with Eq. (1.34) results in the following stress about the x-direction (which is also the tensile residual stress):

$$\sigma_x = \sigma_r = E u_x / l \tag{1.35}$$

where the subscript *r* indicates residual. The numerical value of the residual stress is: $\sigma_r = 50$ MPa.

The work done quasi-statically by the normal stress σ on the volume element of Fig. 1.6 (a) is equal to $1/2\ \sigma\epsilon$, because the intensity of the stress increases gradually from zero to its actual value σ. Similarly, the work performed by the shear stress τ on the element of Fig. 1.6 (b) is $1/2\ \tau\gamma$. Since the two elements are in static equilibrium, the external work fully converts into strain (elastic) energy under ideal conditions. The potential strain energy which is stored in a body that deforms elastically, such as the element in Fig. 1.7, comprises contributions from all the stresses and strains, namely:

$$dU = 1/2(\sigma_x\varepsilon_x + \sigma_y\varepsilon_y + \sigma_z\varepsilon_z + \tau_{xy}\gamma_{xy} + \tau_{yz}\gamma_{yz} + \tau_{zx}\gamma_{zx}) \tag{1.36}$$

The total strain energy can be expressed either in terms of stresses as:

$$\begin{aligned} U = (1+\mu)\int_V [\sigma_x^2 + \sigma_y^2 + \sigma_z^2 - \mu(\sigma_x + \sigma_y + \sigma_z)^2 /(1+\mu) \\ + 2(\tau_{xy}^2 + \tau_{yz}^2 + \tau_{zx}^2)]dV /(2E) \end{aligned} \tag{1.37}$$

or in terms of strains as:

$$U = G\int_V [\varepsilon_x^2 + \varepsilon_y^2 + \varepsilon_z^2 + \mu(\varepsilon_x + \varepsilon_y + \varepsilon_z)^2/(1-2\mu) + (\gamma_{xy}^2 + \gamma_{yz}^2 + \gamma_{zx}^2)/2]dV \quad (1.38)$$

The stress-strain Eqs. (1.26) have been utilized to derive Eqs. (1.37) and (1.38).

4. MEMBERS, LOADS AND BOUNDARY CONDITIONS

MEMS components are designed in various geometric configurations, and the states of external load, together with the constraining boundary conditions, can be diverse as well. These factors affect the stiffness/compliance properties of flexible mechanical microcomponents.

The elastic members can be one-dimensional (such as bars, rods, beams or columns), two-dimensional (such as membranes or plates) and three-dimensional (such as blocks). For each of them, specific equations that describe the state of deformation or stress apply. There are four different types of loading/deformations, namely: normal, torsion, shearing and bending. They are briefly characterized here in terms of stresses, deformations and strain energy for one-dimensional members.

4.1 Normal Loading

In the case of normal loading, the stresses and strains (deformations) are perpendicular to the surface where the axial (normal) force is applied. Figure 1.1 is the physical model of a fixed-free bar of constant cross-section that is acted upon by an axial force at its free end. The constant normal stress that is generated by an axial load N over an area A is:

$$\sigma = N/A \quad (1.39)$$

The total axial deformation which is registered at the free end (where the axial force is being applied) with respect to the fixed end, spaced at a distance l, is:

$$\Delta l = Nl/(EA) \quad (1.40)$$

and the strain is:

$$\varepsilon = \Delta l/l = N/(EA) \quad (1.41)$$

Because only normal stresses and strains are produced in this particular case, the strain energy of the generic Eq. (1.37), in combination with Eq. (1.39), simplifies, for the more generic case where the area is variable, to:

$$U_a = (\int_l N^2 / A\, dx)/(2E) \tag{1.42}$$

where it has been taken into account that the elementary volume can be expressed in terms of the cross-sectional area A and the elementary length dx as:

$$dV = Adx \tag{1.43}$$

4.2 Torsion Loading

MEMS deformable components are vastly conceived to have rectangular cross-sections because of either microfabrication constraints or design purposes. Torsion loading produces shearing, and the maximum shear stress, which is generated by a torque M_t acting on a fixed-free bar of rectangular cross-section, occurs at the middle of the longer side (w) and is expressed as:

$$\tau = M_t /(k_t w t^2) \tag{1.44}$$

where w and t are the cross-sectional dimensions (w > t) and k_t is a torsional constant depending on the w/t ratio, as mentioned by Boresi, Schmidt and Sidebottom [1]. For very thin cross-sections, where w/t > 10, $k_t \approx 0.333$, as indicated by the same source. The rotation angle at the free end of Fig. 1.9 (a) – where a torque can be applied about the x-axis – with respect to the fixed end, spaced at a distance l, is:

$$\theta = M_t l /(GI_t) \tag{1.45}$$

and the corresponding shear strain is:

$$\gamma = \theta / l = M_t /(GI_t) \tag{1.46}$$

In Eqs. (1.45) and (1.46), I_t is the torsion moment of inertia, which will be defined later in this chapter.

The total strain energy stored in the bar that is subject to torsion is:

$$U_t = (\int_l M_t^2 / I_t dx)/(2G) \tag{1.47}$$

4.3 Shearing

For shear loading, the maximum stress which is generated by a shear force S – consider it be the force F_z in Fig. 1.9 (a) – is:

$$\tau_{max} = \alpha S / A \tag{1.48}$$

where α is a coefficient depending on the cross-section shape and which is equal to 3/2 for rectangular cross-sections – see Young and Budynas [4]. The corresponding maximum shear strain is:

$$\gamma_{max} = \alpha S /(GA) \tag{1.49}$$

The strain energy stored in the elastic body through shearing is:

$$U_s = \kappa(\int_l S^2 / A\, dx)/(2G) \tag{1.50}$$

where $\kappa = 6/5$ for rectangular cross-sections – Young and Budynas [4].

4.4 Bending

The bending of a beam mainly produces normal stresses. The stress varies linearly over the cross-section going from tension to compression through zero in the so-called neutral axis, which coincides with a symmetry axis for a symmetric cross-section. The maximum stress values are found on the outer fibers as:

$$\sigma = M_b c / I \tag{1.51}$$

where c is half the cross-sectional dimension which is perpendicular to the bending axis, M_b is the bending moment, and I is the cross-sectional moment of inertia about the bending axis.

When a beam is subject to the action of distributed load, point forces perpendicular to its longitudinal axis and point bending moments, an element can be isolated from the full beam, as sketched in Fig. 1.11, and the following equilibrium equations can be written:

$$q = dS / dx = d^2 M_b / dx^2 \tag{1.52}$$

The deformations in bending consist of deflection and slope, as sketched in Fig. 1.3. These deformations are described by the following differential equations:

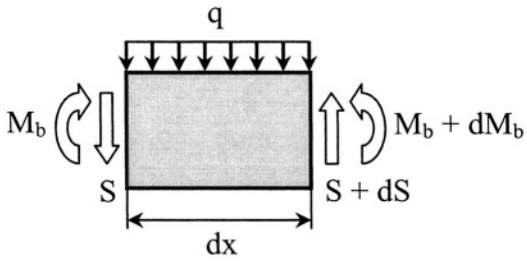

Figure 1.11 Beam element under the action of distributed load, shear force and bending moment

$$\begin{cases} d^2u/dx^2 = -M_b/EI \\ \theta = du/dx \end{cases} \tag{1.53}$$

Equations (1.53) are valid for small-deformations only and under the assumptions that plane cross-sections remain plane after deformations, and that cross-sections remain perpendicular to the neutral axis (as mentioned, the normal stresses are zero at the neutral axis). The latter two assumptions define what is known as the *Euler-Bernoulli beam model,* which is recognized to be valid for *long beams* where the length is at least 5-7 times larger than the largest cross-sectional dimension. For relatively-short beams, shearing effects become important, and the regular bending deformations are augmented by the addition of shearing deformations, according to a model known as *Timoshenko's beam model.* In this case, the cross-sections are no longer perpendicular to the neutral axis in the deformed state, and the deformations are described by the following equations:

$$\begin{cases} \dfrac{d}{dx}[\kappa GA(\theta - \dfrac{du}{dx})] = q \\ E\dfrac{d}{dx}(I\dfrac{du}{dx}) = \kappa GA(\theta - \dfrac{du}{dx}) \end{cases} \tag{1.54}$$

as shown, for instance, by Reddy [5] or Pilkey [6].

The strain energy stored in a beam that is acted upon by a bending moment over its length is:

$$U_b = (\int_l M_b^2/I\,dx)/(2E) \tag{1.55}$$

For relatively short beams, as already mentioned, the shearing effects are important, and the shearing stresses are given by the equation:

$$\tau = S \int_{A(z)} z dA / (wI) \tag{1.56}$$

where S is the shear force and the integral (the statical moment of area) is taken for the area enclosed by an arbitrary line, parallel to the y-axis, situated at a distance z measured from the cross-section center and one of the external fibers. The shear strain is:

$$\gamma = \tau / G \tag{1.57}$$

In this case, the total strain energy is:

$$U_b = \left(\int_l M_b^2 / I \, dx \right) / (2E) + \kappa \left(\int_l S^2 / A dx \right) / (2G) \tag{1.58}$$

4.5 Load Sign Conventions

Because the loads acting on an elastic body might be directed one way or the other about a specified direction, it is customary to follow some simple rules that define the *positive* direction for a particular load. For axial loading, the normal force is considered positive when its action tends to extend the portion of the body under consideration. In the case of torsion, selecting a positive direction is entirely arbitrary.

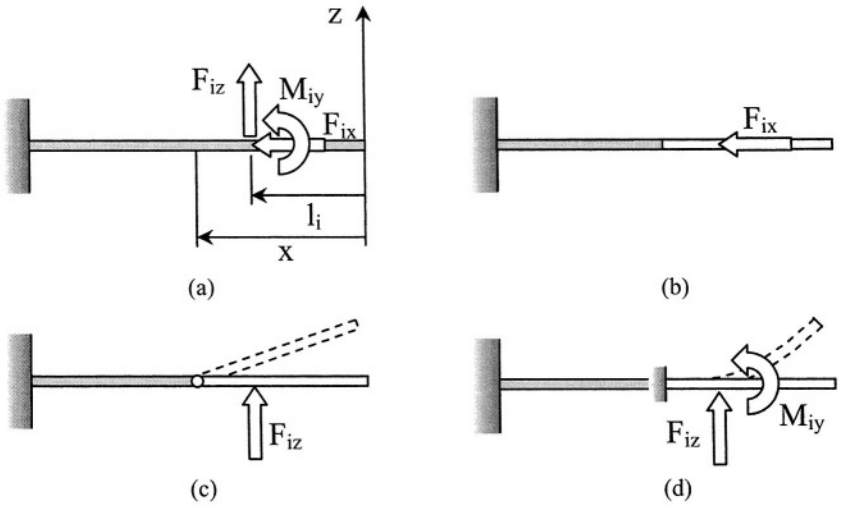

Figure 1.12 Load sign convention: (a) generic fixed-free member under planar loading; (b) axial force; (c) shearing force; (d) bending moment

In shearing, the variant generally accepted is that the shear force is positive when it tends to rotate the portion of the structure in a clockwise direction, whereas in bending, a component of the bending moment (either force or moment) produces a positive bending moment if the analyzed structural segment deforms in a *sagging* manner (by compressing the upper fiber). All these situations are sketched in Fig. 1.12.

The normal force N, shearing force S, torsion moment $\mathbf{M_t}$ and bending moment $\mathbf{M_b}$ are defined at a specific point on the linear member by calculating the sum of all relevant components that are applied between one end point of the member (the free end of Fig. 1.12 is a convenient choice because it does not introduce any reactions, which are usually unknown amounts) and the specific point, as given in the equations:

$$\begin{cases} N = \sum_{l_i=0}^{l_i=x} F_{ix} \\ S = \sum_{l_i=0}^{l_i=x} F_{iy} \\ M_t = \sum_{l_i=0}^{l_i=x} M_{ix} \\ M_b = \sum_{l_i=0}^{l_i=x} [M_{iz} + F_{iy}(x - l_i)] \end{cases} \tag{1.59}$$

Example 1.4

Determine the axial, shearing and bending moment equations for the fixed-free microcantilever, which is loaded with the tip forces $\mathbf{F_{1x}}$ and $\mathbf{F_{1y}}$, as shown in Fig. 1.13.

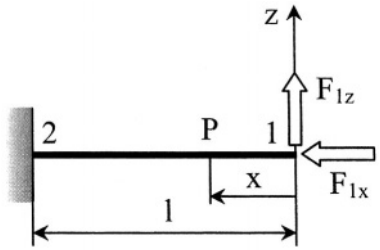

Figure 1.13 Cantilever under tip axial force and shearing force

Solution

The axial force, as generally defined in the first Eq. (1.59), is in this case:

$$N = -F_{1x} \tag{1.60}$$

and the minus sign indicates that F_{1x} produces compression of the segment limited by the point of abscissa x and the end 1. There is obviously no torsion acting on the microcantilever, but the shear force is:

$$S_z = F_{1z} \tag{1.61}$$

where the plus sign shows compliance with the rule mentioned above, because this component tends to rotate the considered segment in a clockwise direction when this segment is allowed to rotate about point P. Similarly, the bending moment at point x is:

$$M_{by} = F_{1z}x \tag{1.62}$$

and it is positive because F_{1z} tends to sagg the portion 1-P with respect to point P which is considered fixed.

4.6 Boundary Conditions, Determinate/Indeterminate Systems

Figure 1.14 shows the most frequently encountered boundary conditions in one-dimensional members. In a given member under load, each boundary condition introduces a number of reactions, which are unknown initially. A pinned end, such as the one shown in Fig. 1.14 (a) introduces one reaction force, which is normal to the support direction, a guided end – pictured in Fig. 1.14 (b) – has two unknown reactions: one force normal to the support direction and one moment perpendicular to the plane of the structure.

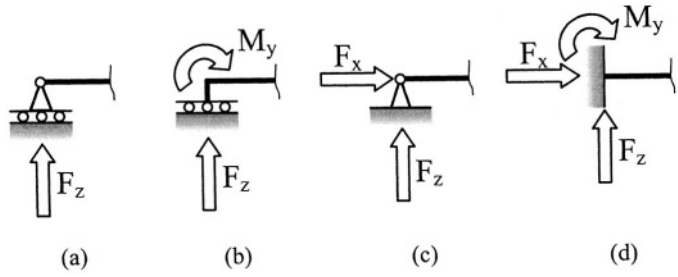

Figure 1.14 Main boundary conditions: (a) pinned; (b) guided; (c) simply-supported; (d) fixed

Two reaction forces correspond to the simply-supported boundary condition of Fig 1.14 (c), whereas the fixed end of Fig. 1.14 (d) adds a reaction moment to the forces of the previous case. It should be noted that for a line member, three equilibrium equations can be written, and therefore the boundary conditions should introduce three unknown reactions only, in order for the system to be *statically determinate.* When less than three reactions are present, the respective system is *statically unstable* (it is actually a mechanism). For more than three unknown reactions, the system is *statically indeterminate,* and additional equations need to be added to the equilibrium ones, in order to determine the reaction loads.

5. LOAD-DISPLACEMENT CALCULATION METHODS: CASTIGLIANO'S THEOREMS

5.1 Castigliano's Theorems

There are several methods that can be utilized to determine the deformations in an elastic body. In the case of bending for instance, procedures exist to find the slope and deflection, such as the direct integration method of the differential equation of beam flexure – Eq. (1.53), the area-moment method or the Myosotis method. More generic methods that allow calculation of elastic deformations for any type of load are the energy methods (such as the principle of virtual work or Castigliano's theorems), the variational methods (the methods of Euler, Rayleigh-Ritz, Galerkin or Trefftz), and the finite element method. Castigliano's methods are particularly useful when attempting to determine the stiffness of various elastic members, and they will be utilized in this work quite extensively. Figure 1.15 shows a bar that is acted upon axially and quasi-statically by a force F, which produces a deformation Δu.

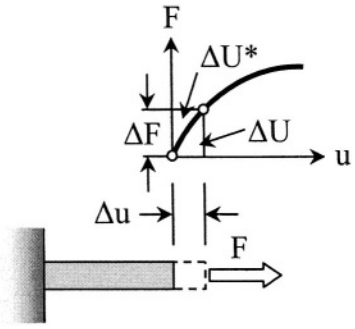

Figure 1.15 Strain energy and complementary energy in axial loading

In the general case where the material properties are non-linear (as indicated by the force-displacement curve of Fig. 1.15), two energy types can be defined, namely: the regular *strain energy,* which is:

$$\Delta U = F\Delta u \tag{1.63}$$

and the *complementary energy:*

$$\Delta U^* = u\Delta F \tag{1.64}$$

If the strain energy can be expressed as a function of solely the displacement function, as:

$$U = f(u) \tag{1.65}$$

then the variation in the strain energy can be written as:

$$\Delta U = \partial U / \partial u \Delta u \tag{1.66}$$

which, by comparison to Eq. (1.63) yields:

$$F = \partial U / \partial u \tag{1.67}$$

Equation (1.67) is actually the mathematical expression of *Castigliano's first theorem,* stating that the load which is applied to an elastic body can be calculated as the partial derivative of the strain energy stored in that body taken with respect to the deformation set at the considered point about the load's direction.

When the complementary energy is a function of simply the loads acting on the elastic body in the form:

$$U^* = f^*(F) \tag{1.68}$$

the variation of this energy is:

$$\Delta U^* = \partial U^* / \partial F \Delta F \tag{1.69}$$

By comparing Eqs. (1.69) and (1.64) results in:

$$u = \partial U^* / \partial F \tag{1.70}$$

which is the *Castigliano's second theorem ,* also known as the *displacement theorem,* stating that an elastic deformation can be found by taking the partial derivative of the complementary energy in terms of the load that is applied at that point and about the considered direction.

The first theorem of Castigliano can easily be applied when the deformation field is known in advance, but this proves to be difficult in situations where the cross-section of the line element is variable. Instead, the loads acting on a body can be known amounts, and the application of Castigliano's second (displacement) theorem is more feasible, especially in cases where the material is linear, and therefore the strain and complementary energies are equal (the force-displacement characteristic of Fig. 1.15 is a line). The strain energy for a relatively-long line member that is subject to complex load formed of axial force, torsion moment, shearing force and bending moment can be written –see Den Hartog [7] or Cook and Young [3] – in the form:

$$U = 1/2 \int_l \{ EA(du_x/dx)^2 + GI_t(d\theta_x/dx)^2 + \kappa GA[(du_z/dx)^2 + (du_y/dx)^2] + E[I_y(d^2u_z/dx^2)^2 + I_z(d^2u_y/dx^2)^2]\}dx \tag{1.71}$$

Equation (1.71) considered that the member's cross-section has two principal directions (it possesses two symmetry axes, and therefore a symmetry center) and that bending moments and shearing forces act about these axes. Similarly, the complementary energy can be expressed in terms of loading, and in the case of a linear material this energy is:

$$U = 1/2 \int_l [N^2/EA + M_t^2/GI_t + \kappa(S_z^2 + S_y^2)/(GA) + (M_{by}^2/I_y + M_{bz}^2/I_z)/E]dx \tag{1.72}$$

which has been obtained by collecting individual strain energy terms from axial, torsion, two-direction shearing and two-directional bending loads.

Example 1.5

Find the slope at the midspan of the beam shown in Fig. 1.16 by considering that the beam is relatively long and is constructed of a material with linear properties. An external moment M_{1y} loads the beam.

Solution

The beam is statically-indeterminate because there are four unknown reactions (one at point 1, F_{1z}, and 3 at point 3), and therefore an additional equation needs to be written in order to complement the regular three equations of static equilibrium. It can be seen that the specific boundary condition at point 1 prevents the vertical (z) motion at that point, and therefore:

$$u_{1z} = 0 \tag{1.73}$$

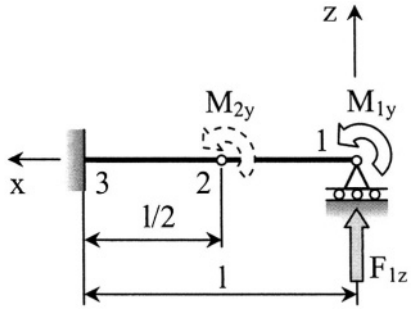

Figure 1.16 Fixed-guided beam

At the same time, the deflection u_{1z} can be expressed by means of Castigliano's displacement theorem, Eq. (1.70), as:

$$u_{1z} = \partial U / \partial F_{1z} = [\int_0^l M_{by}(\partial M_{by} / \partial F_{1z})dx] / (EI_y) \tag{1.74}$$

The bending moment at the generic position of abscissa x is:

$$M_{by} = M_{1y} + F_{1z}x \tag{1.75}$$

It can be seen in Eq, (1.75) that the partial derivative of M_{by} in terms of F_{1z} is x. As a consequence, Eq. (1.74) permits solving for the unknown F_{1z}, namely:

$$F_{1z} = -3M_{1y} / (2l) \tag{1.76}$$

In order to find the slope at midspan, a *dummy* moment M_{2y} is artificially applied at point 2 in order to enable performing calculations by means of Castigliano's displacement theorem in the form:

$$\theta_{2y} = \partial U / \partial M_{2y} = [\int_0^l M_{by}\partial M_{by} / \partial M_{2y}dx] / (EI_y) \tag{1.77}$$

The bending moment will have two different equations one for each of the intervals 1-2 and 2-3, namely:

$$M_{by} = \begin{cases} M_{1y} + F_{1z}x, 0 \le x \le l/2 \\ M_{1y} + F_{1z}x + M_{2y}, l/2 \le x \le l \end{cases} \tag{1.78}$$

After performing the needed calculations, the sought slope is:

$$\theta_{2y} = 1/(EI_y)\int_{l/2}^{l}(M_{1y} + F_{1z}x)dx = -l/(16EI_y)M_{1y} \tag{1.79}$$

Equation (1.79) took into account that the dummy moment is actually zero in the bending moment expression, and that the reaction F_{1z} is given in Eq. (1.76).

Example 1.6

Solve the problem of Example 1.5 by considering that the beam is relatively short, and compare the results with the results of the previous example.

Solution:

The shearing force needs to be taken into account in the strain energy equation, and therefore the deflection u_{1z} can be written as:

$$\begin{aligned} u_{1z} &= \partial U/\partial F_{1z} = [\int_0^l M_{by}(\partial M_{by}/\partial F_{1z})dx]/(EI_y) \\ &+ \kappa[\int_0^l S_z(\partial S_z/\partial F_{1z})dx]/(GA) \end{aligned} \tag{1.80}$$

where the shear force is simply F_{1z}. Solving Eq. (1.73) with the particular expression of Eq. (1.80) gives:

$$F_{1z}^{(sh)} = -3lM_{1y}/[2(3\kappa c + l^2)] \tag{1.81}$$

with:

$$c = EI_y/(GA) \tag{1.82}$$

The slope at midspan is calculated by means of Eq. (1.79) and its equation is:

$$\theta_{2y}^{sh} = l\{1 - 9l^2/[8(3\kappa c + l^2)]\}M_{1y}/(2EI_y) \tag{1.83}$$

A comparison is made now between Eqs. (1.79) and (1.83) by means of the following ratio:

$$r_\theta = \theta_{2y}^{(sh)}/\theta_{2y} \tag{1.84}$$

By considering the following equations that define the cross-sectional amounts of interest:

$$\begin{cases} A = wt \\ I_y = wt^3/12 \end{cases} \tag{1.85}$$

it can be shown that the ratio of Eq. (1.84) only depends on the length 1 and thickness t, and for a Poisson ratio of $\mu = 0.25$ (for a polysilicon material) and a value of $\kappa = 6/5$ (Young and Budynas [4]), the slope calculated with shearing effects taken into account is up to 30% smaller than the slope determined without considering shearing, as shown in Fig. 1.17.

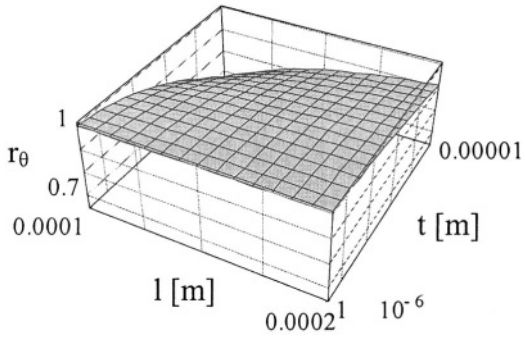

Figure 1.17 Plot of the ratio of slopes at midspan – according to Eq. (1.84)

5.2 Stiffnesses of Constant Cross-Section Straight Beam Using Castigliano's First Theorem

Castigliano's first theorem, as introduced in this chapter, enables calculation of the stiffnesses that connect a force/moment to the corresponding linear/angular displacement. A fixed-free straight beam of constant cross-section is considered here, loaded as shown in Fig. 1.18. Bending about the y-axis is produced by F_{1z} and M_{1y}. Bending about the z-direction is generated by F_{1y} and M_{1z}. Axial deformation is created by the force F_{1x} and torsion is caused by the moment M_{1x}.

5.2.1 Bending About the y-Axis

We shall assume here that the beam is relatively long (length is at least 5 times larger than the maximum cross-sectional dimension), and that plane sections that are perpendicular to the beam's midsurface (neutral fiber)

remain plane and perpendicular on this surface after the load has been applied. These assumptions are at the basis of the Euler-Bernoulli model, as mentioned previously.

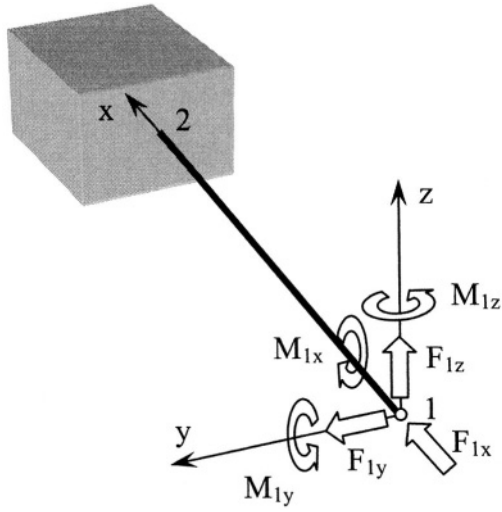

Figure 1.18 Cantilever with full three-dimensional loading

According to Castigliano's first theorem, the force or moment producing bending at a point on a beam can be found by evaluating the partial derivatives of the strain energy generated through bending in terms of the corresponding deflection or rotation (slope) at that point in the form:

$$F_{1z} = \frac{\partial U_{b,y}}{\partial u_{1z}} \tag{1.86}$$

$$M_{1y} = \frac{\partial U_{b,y}}{\partial \theta_{1y}} \tag{1.87}$$

where the subscript *b,y* indicates bending about the y-axis. Within the small-displacement (engineering) beam theory, the strain energy which is produced through bending about the y-axis is expressed as:

$$U_{b,y} = \frac{EI_y}{2} \int_0^l \left(\frac{d^2 u_z}{dx^2} \right)^2 dx \tag{1.88}$$

The following boundary conditions apply for the fixed-free beam:

$$\begin{cases} u_z(0) = u_{1z} \\ \left.\dfrac{du_z(x)}{dx}\right|_{x=0} = \theta_{1y} \\ u_z(l) = 0 \\ \left.\dfrac{du_z(x)}{dx}\right|_{x=l} = 0 \end{cases} \tag{1.89}$$

The differential equation for the equilibrium position of the analyzed cantilever can be written by combining Eqs. (1.52) and (1.53) as:

$$EI_y\left[\frac{d^4u_z(x)}{dx^4}\right] = 0 \tag{1.90}$$

The solution to Eq. (1.90) is a third degree polynomial in x whose 4 unknown coefficients can be found by applying the boundary conditions of Eq. (1.89). This solution can be put into the following form:

$$u_z(x) = f_{bd}(x)u_{1z} + f_{bs}(x)\theta_{1y} \tag{1.91}$$

where the distribution functions f_{bd} and f_{bs} (*b* stands for bending, *d* for deflection and *s* for slope, respectively) are dependent on the geometry of the analyzed microcantilever. For the specific case being analyzed here, the distribution functions are:

$$\begin{cases} f_{bd}(x) = 1 - 3x^2/l^2 + 2x^3/l^3 \\ f_{bs}(x) = x - 2x^2/l + x^3/l^2 \end{cases} \tag{1.92}$$

The slope function is the derivative of the deflection function in terms of the space variable x, and therefore its equation derives from Eq. (1.91):

$$\theta_y(x) = \frac{df_{bd}(x)}{dx}u_{1z} + \frac{df_{bs}(x)}{dx}\theta_{1y} \tag{1.93}$$

The tip force F_{1z} can be expressed by using Eqs. (1.86), (1.88), (1.91) and (1.93) as:

$$F_{1z} = K_{1,Fz-uz}u_{1z} + K_{1,Fz-\theta y}\theta_{1y} \tag{1.94}$$

where the stiffness terms are:

$$K_{1,Fz-uz} = EI_y \int_0^l \left[\frac{d^2 f_{bd}(x)}{dx^2} \right]^2 dx = 12 \frac{EI_y}{l^3} \tag{1.95}$$

and

$$K_{1,Fz-\theta y} = EI_y \int_0^l \frac{d^2 f_{bd}(x)}{dx^2} \frac{d^2 f_{bs}(x)}{dx^2} dx = 6 \frac{EI_y}{l^2} \tag{1.96}$$

Note:

In Example 1.1, the cross-stiffness of Eq. (1.96) has been derived by inversion of a compliance matrix. The minus sign in front of $\mathbf{K_c}$ (and which is denoted by $\mathbf{K_{1,Fz-\theta y}}$ in Eq. (1.96)) in Eq. (1.16) will be explained in Example 1.15.

In a similar fashion, $\mathbf{M_{1z}}$ is calculated by means of Eqs. (1.87), (1.88), (1.91) and (1.93), as:

$$M_{1y} = K_{1,Fz-\theta y} u_{1z} + K_{1,My-\theta y} \theta_{1y} \tag{1.97}$$

where the new stiffness term is:

$$K_{1,My-\theta y} = EI_y \int_0^l \left[\frac{d^2 f_{bs}(x)}{dx^2} \right]^2 dx = 4 \frac{EI_y}{l} \tag{1.98}$$

It should be remarked that $\mathbf{K_{1,Fz\text{-}uz}}$ and $\mathbf{K_{1,My\text{-}\theta y}}$ are direct-bending stiffnesses, and this particular subscript notation is utilized instead of using the already-introduced subscripts *l* and *r* of Eqs. (1.7) in order to emphasize the point where these stiffnesses are calculated (point 1 here), as well as the acting load (force $\mathbf{F_z}$ or moment $\mathbf{M_y}$) and the resulting elastic deformation (deflection $\mathbf{u_z}$ or slope/rotation $\boldsymbol{\theta_y}$). A similar rationale has been applied in the notation used for the cross-bending stiffness $\mathbf{K_{1,Fz\text{-}\theta y}}$ which has been symbolized by the subscript *c* in Eqs. (1.7).

Note:

The stiffnesses corresponding to bending about the z-axis are similar to the ones corresponding to bending about the y-axis, and they are not derived here. They can easily be obtained from the stiffnesses already formulated by switching the y and z subscripts, or by using z instead of y, when applicable.

5.2.2 Axial Loading

The axial force at the beam's free end can be expressed by means of Castigliano's first theorem as:

$$F_{1x} = \frac{\partial U_a}{\partial u_{1x}} \tag{1.99}$$

where U_a is the strain energy stored in the component of Fig. 1.18 under the action of F_{1x}. The strain energy produced in axial loading can be expressed from Eq. (1.71) in the form:

$$U_a = \frac{EA}{2}\int_0^l \left[\frac{du_x(x)}{dx}\right]^2 dx \tag{1.100}$$

The equilibrium equation in terms of axial loading is:

$$EA\frac{d^2u_x(x)}{dx^2} = 0 \tag{1.101}$$

The solution to the differential Eq. (1.101) is a second degree polynomial, which can be expressed as:

$$u_x(x) = f_a(x)u_{1x} \tag{1.102}$$

By applying the boundary conditions:

$$\begin{cases} u_x(0) = u_{1x} \\ u_x(l) = 0 \end{cases} \tag{1.103}$$

the distribution function $f_a(x)$ is found to be:

$$f_a(x) = 1 - x/l \tag{1.104}$$

The tip axial force F_{1x} can be determined by using Eqs. (1.99) through (1.104) as:

$$F_{1x} = K_{1,Fx-ux}u_{1x} \tag{1.105}$$

where the axial stiffness is:

$$K_{1,Fx-ux} = EA\int_0^l \left[\frac{df_a(x)}{dx}\right]^2 dx = EA/l \tag{1.106}$$

which is the known equation for the axial stiffness of a constant cross-section bar.

Example 1.7

Design a microcantilever of constant rectangular cross-section which needs to have a minimum stiffness $\mathbf{K}_{1,Fz\text{-}uz}$ while having maximum stiffnesses $\mathbf{K}_{1,Fy\text{-}uy}$ and $\mathbf{K}_{1,Fx\text{-}ux}$.

Solution:

The following objective function can be constructed:

$$f = K_{1,Fz-uz} / K_{1,Fy-uy} + K_{1,Fz-uz} / K_{1,Fx-ux} \tag{1.107}$$

which has to be minimized in order to satisfy the requirements of the example. By using Eqs. (1.95) and (1.106), the function of Eq. (1.107) becomes:

$$f = t^2(1/w^2 + 12/l^2) \tag{1.108}$$

It is assumed that the length l and width w can be expressed as fractions of the thickness t as:

$$\begin{cases} l = c_l t \\ w = c_w t \end{cases} \tag{1.109}$$

By substituting Eqs. (1.109) into Eq. (1.108), the objective function changes into:

$$f = 1/c_w^2 + 12/c_l^2 \tag{1.110}$$

In order to minimize f, $\mathbf{c}_w$ and $\mathbf{c}_l$ have to be maximum, which means that w and l have to be maximum.

5.2.3 Torsion

The tip moment that produces torsion is expressed in terms of the rotation angle by means of Castigliano's first theorem as:

$$M_{1x} = \frac{\partial U_t}{\partial \theta_{1x}} \tag{1.111}$$

where the torsion-related strain energy is formulated from Eq. (1.71) as:

$$U_t = \frac{GI_t}{2}\int_0^l \left[\frac{d\theta_x(x)}{dx}\right]^2 dx \tag{1.112}$$

The torsion equilibrium equation is:

$$EI_t \frac{d^2\theta_x(x)}{dx^2} = 0 \tag{1.113}$$

By applying the boundary conditions:

$$\begin{cases} \theta_x(0) = \theta_{1x} \\ \theta_x(l) = 0 \end{cases} \tag{1.114}$$

the angular deformation can be written as:

$$\theta_x(x) = f_a(x)\theta_{1x} \tag{1.115}$$

Similar to the case of axial loading, the torsion moment of Eq. (1.111) is determined as:

$$M_{1x} = K_{1,Mx-\theta x}\theta_{1x} \tag{1.116}$$

where the torsion stiffness is:

$$K_{1,Mx-\theta x} = GI_t \int_0^l \left[\frac{df_a(x)}{dx}\right]^2 dx = GI_t / l \tag{1.117}$$

The torsion moment of inertia of Eq. (1.117) can be calculated according to two different models, depending on the relationship between the thickness t and the width w. For very thin members (t << w), Boresi, Schmidt and Sidebottom [1] suggest:

$$I_t = wt^3 / 3 \tag{1.118}$$

whereas for members where t < w, simply, the moment of inertia can be approximated to:

$$I_t = wt^3(16/3 - 3.36t/w)/16 \tag{1.119}$$

as shown in Young and Budynas [4] or Lobontiu [8].

Example 1.8

Evaluate the relative difference (error) between the torsional stiffness of a fixed-free, constant rectangular cross-section microbar when considered very thin (t << w) versus the same stiffness when the cross-sectional dimensions are simply related as t < w.

Solution:

As previously indicated, the torsion stiffness is proportional to the torsion moment of inertia. As a consequence, differences between the stiffness produced by the two models only arise from differences in the respective moments of inertia. If the inertia moment of Eq. (1.118), which corresponds to very thin bars, is denoted by I_{t1} and the one corresponding to thin bars, Eq. (1.119), is I_{t2}, the relative difference between the two moments of inertia is:

$$error = (I_{t1} - I_{t2}) / I_{t1} \tag{1.120}$$

Figure 1.19 is the plot corresponding to Eq. (1.120) and has been drawn for t ranging from $0.5\ \mu m$ to $5\ \mu m$ and w varying from $10\ \mu m$ to $100\ \mu m$. The relative difference between the two models' compliances is largest for small values of the width w and large values of the thickness t.

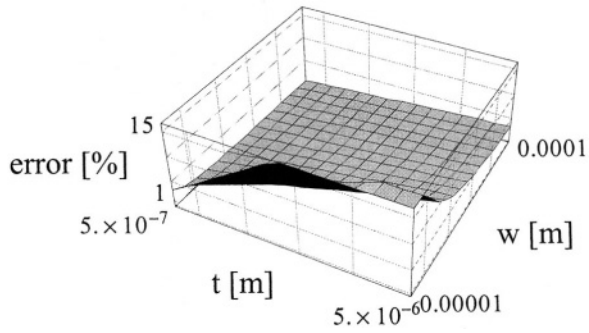

Figure 1.19 Relative stiffness differences between very thin and thin cross-section microbars in torsion

5.3 Compliances of Constant Cross-Section Curved Beam Using Castigliano's Second Theorem

Curved beams can be divided in two main categories, namely: thick beams, also named beams of relatively large curvature, and thin beams, or

beams of small curvature. Thin curved beams have their width w (the cross-sectional dimension which is in the plane of the curved beam) generally less than 10% of the radius R, as mentioned by Den Hartog [9] for instance. During planar deformation of thin beams, the loading mainly consists of the bending moment that acts perpendicularly to the beam's plane, whereas for thick beams, the effects of normal loading and shearing forces have to also be taken into account.

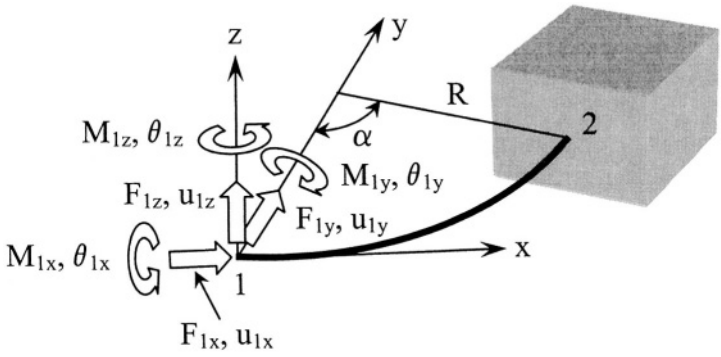

Figure 1.20 Loads and displacements for a curved beam of relatively-small curvature

The aim here is to define the six displacement components (three translations and three rotations) of the free-fixed curved beam of Fig. 1.20 in terms of the six load components, the geometry of the beam, namely its radius R, angle α, constant cross-section (the eccentricity e included), and the material parameters. Various compliances will be defined by this approach, similar to the stiffnesses which have been obtained previously for a straight beam. Formally, the load and displacement components are separated into in-plane and out-of-the-plane.

5.3.1 Thick Curved Beams

For a thick curved beam, the neutral axis (the axis where the stresses normal to the cross-section are zero) is offset from the geometric symmetry axis, by the quantity e – the *eccentricity,* as shown in Fig. 1.21. The eccentricity is dependent on the shape of the cross-section, and it can generally be calculated (see Young and Budynas [4], for instance) by means of the equation:

$$e = R - A / \int_A (dA / r) \tag{1.121}$$

For a rectangular cross-section, as the one sketched in Fig. 1.21, the eccentricity is:

$$e = R - w / ln[(2R + w)/(2R - w)] \tag{1.122}$$

when 0.6 < R/w < 8 – Young and Budynas [4], whereas for 8 <R/w < 10, the eccentricity can be approximated to:

$$e = I_c / (RA) \tag{1.123}$$

where I_C is the moment of inertia about the centroidal axis and A is the cross-sectional area, as indicated by Young and Budynas [4].

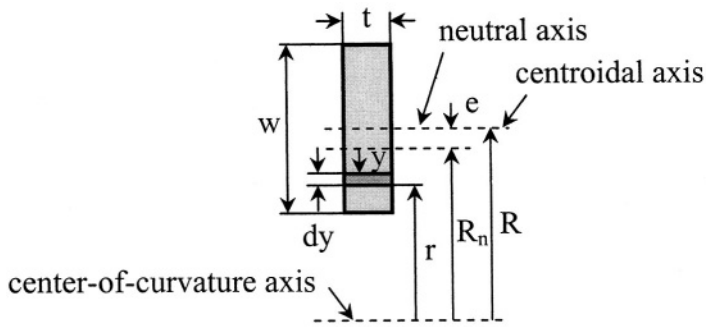

Figure 1.21 Cross-secion geometry and eccentricity position for a thick curved beam

5.3.1.1 In-Plane Compliances

The circular segment of Fig. 1.20 undergoes deformations within its own plane under the action of F_{1x}, F_{1y} and M_{1z} which are located at its free end 1. Unlike the case of the straight beam, where the action of F_{1x}, for instance, is strictly axial, all three loads combine in the present case to produce axial, shearing and bending deformations. The strain energy U contains contributions from the bending moment, the normal force, and the shearing force, in the form:

$$U = \int_0^{\alpha} M_{bz}^2 / (2AEe)d\beta + \int_0^{\alpha} RN^2 / (2AE)d\beta + \int_0^{\alpha} \kappa RS^2 / (2AG)d\beta - \int_0^{\alpha} M_{bz} N / (AE)d\beta \tag{1.124}$$

where β is a generic angle ranging between 0 and α. The displacements at point 1 are calculated by means of Castigliano's displacement theorem as:

$$\begin{cases} u_{1x} = \dfrac{\partial U}{\partial F_{1x}} = \dfrac{1}{AEe}\int_0^\alpha M_{bz}\dfrac{\partial M_{bz}}{\partial F_{1x}}d\beta + \dfrac{R}{AE}\int_0^\alpha N\dfrac{\partial N}{\partial F_{1x}}d\beta + \dfrac{\kappa R}{AG} \\ \int_0^\alpha S\dfrac{\partial S}{\partial F_{1x}}d\beta - \dfrac{1}{AE}\int_0^\alpha (M_{bz}\dfrac{\partial N}{\partial F_{1x}} + N\dfrac{\partial M_{bz}}{\partial F_{1x}})d\beta \\ u_{1y} = \dfrac{\partial U}{\partial F_{1y}} = \dfrac{1}{AEe}\int_0^\alpha M_{bz}\dfrac{\partial M_{bz}}{\partial F_{1y}}d\beta + \dfrac{R}{AE}\int_0^\alpha N\dfrac{\partial N}{\partial F_{1y}}d\beta + \dfrac{\kappa R}{AG} \\ \int_0^\alpha S\dfrac{\partial S}{\partial F_{1y}}d\beta - \dfrac{1}{AE}\int_0^\alpha (M_{bz}\dfrac{\partial N}{\partial F_{1y}} + N\dfrac{\partial M_{bz}}{\partial F_{1y}})d\beta \\ \theta_{1z} = \dfrac{\partial U}{\partial M_{1z}} = \dfrac{1}{AEe}\int_0^\alpha M_{bz}\dfrac{\partial M_{bz}}{\partial M_{1z}}d\beta + \dfrac{R}{AE}\int_0^\alpha N\dfrac{\partial N}{\partial M_{1z}}d\beta + \dfrac{\kappa R}{AG} \\ \int_0^\alpha S\dfrac{\partial S}{\partial M_{1z}}d\beta - \dfrac{1}{AE}\int_0^\alpha (M_{bz}\dfrac{\partial N}{\partial M_{1z}} + N\dfrac{\partial M_{bz}}{\partial M_{1z}})d\beta \end{cases} \tag{1.125}$$

The bending moment, axial force and shearing force are defined for a given point P on the curved beam, positioned at an angle β measured radially from point 1, as shown in Fig. 1.22, namely:

$$\begin{cases} M_{bz} = F_{1x}(R - R\cos\beta) - F_{1y}R\sin\beta - M_{1z} \\ N = -F_{1x}\cos\beta - F_{1y}\sin\beta \\ S = -F_{1x}\sin\beta + F_{1y}\cos\beta \end{cases} \tag{1.126}$$

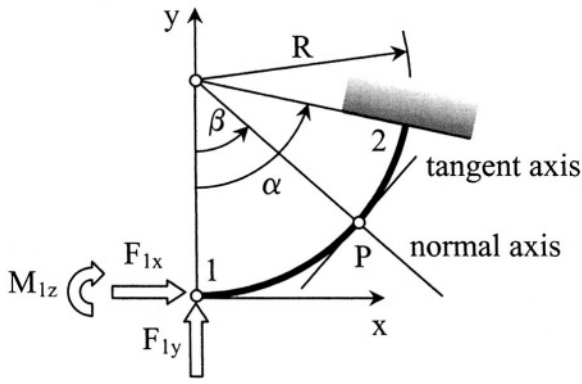

Figure 1.22 Geometry and loading for in-plane compliance derivation

The direction of the axial force N is the tangent axis at P, whereas the direction of the shearing force S is the normal (radial) axis in Fig. 1.22. Equations (1.124), (1.125) and (1.126), combine into:

$$\begin{Bmatrix} u_{1x} \\ u_{1y} \\ \theta_{1z} \end{Bmatrix} = \begin{bmatrix} C_{1,ux-Fx} & C_{1,ux-Fy} & C_{1,ux-Mz} \\ C_{1,ux-Fy} & C_{1,uy-Fy} & C_{1,uy-Mz} \\ C_{1,ux-Mz} & C_{1,uy-Mz} & C_{1,\theta z-Mz} \end{bmatrix} \begin{Bmatrix} F_{1x} \\ F_{1y} \\ M_{1z} \end{Bmatrix} \tag{1.127}$$

The terms of the symmetric compliance matrix of Eq. (1.127) are:

$$C_{1,ux-Fx} = \frac{R}{4AEGe}\{2\alpha[\kappa Ee + G(3R-e)] - 8G(R-e)\sin\alpha + [G(R-e) - \kappa Ee]\sin 2\alpha\} \tag{1.128}$$

$$C_{1,ux-Fy} = \frac{R}{4AEGe}\{3G(e-R) - \kappa Ee + 4G(R-e)\cos\alpha + [\kappa Ee - G(R-e)]\cos 2\alpha\} \tag{1.129}$$

$$C_{1,ux-Mz} = -\frac{\alpha R - (R-e)\sin\alpha}{AEe} \tag{1.130}$$

$$C_{1,uy-Fy} = \frac{R}{4AEGe}\{2\alpha[\kappa Ee + G(R-e)] + [\kappa Ee - G(R-e)]\sin 2\alpha\} \tag{1.131}$$

$$C_{1,uy-Mz} = \frac{(R-e)(1-\cos\alpha)}{AEe} \tag{1.132}$$

$$C_{1,\theta z-Mz} = \frac{\alpha}{AEe} \tag{1.133}$$

5.3.1.2 Out-of-the-Plane Compliances

The out-of-the-plane action is generated by the loads F_{1z}, M_{1x} and M_{1y}, which produce local bending about the tangent to the current point, torsion about the normal (radial) direction to the current point and shearing by the force F_{1z} in the case where the curved beam is relatively short, as shown in Fig. 1.23. The bending moment, torsion moment and shearing force are:

$$\begin{cases} M_b = F_{1z}R\sin\beta + M_{1x}\sin\beta - M_{1y}\cos\beta \\ M_t = F_{1z}(R - R\cos\beta) - M_{1x}\cos\beta - M_{1y}\sin\beta \\ S_z = F_{1z} \end{cases} \tag{1.134}$$

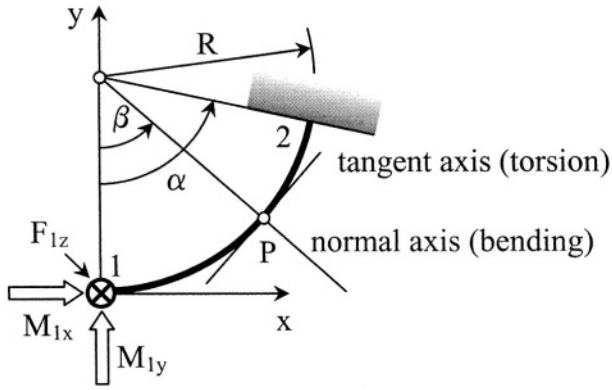

Figure 1.23 Geometry and loading for out-of-the-plane compliance derivation

The out-of-the-plane displacements at point 1 can be again calculated by means of Castigliano's second theorem as:

$$\begin{cases} u_{1z} = \dfrac{\partial U}{\partial F_{1z}} = \dfrac{R}{I_y E}\displaystyle\int_0^{\alpha} M_b \frac{\partial M_b}{\partial F_{1z}} d\beta + \frac{R}{I_t G}\int_0^{\alpha} M_t \frac{\partial M_t}{\partial F_{1z}} d\beta \\ \quad + \dfrac{\kappa R}{AG}\displaystyle\int_0^{\alpha} S_z \frac{\partial S_z}{\partial F_{1z}} d\beta \\ \theta_{1x} = \dfrac{\partial U}{\partial M_{1x}} = \dfrac{R}{I_y E}\displaystyle\int_0^{\alpha} M_b \frac{\partial M_b}{\partial M_{1x}} d\beta + \frac{R}{I_t G}\int_0^{\alpha} M_t \frac{\partial M_t}{\partial M_{1x}} d\beta \\ \theta_{1y} = \dfrac{\partial U}{\partial M_{1x}} = \dfrac{R}{I_y E}\displaystyle\int_0^{\alpha} M_b \frac{\partial M_b}{\partial M_{1y}} d\beta + \frac{R}{I_t G}\int_0^{\alpha} M_t \frac{\partial M_t}{\partial M_{1y}} d\beta \end{cases} \tag{1.135}$$

where the strain energy is:

$$U = \int_0^l \frac{M_b^2}{2EI_y} ds + \int_0^l \frac{M_t^2}{2GI_t} ds + \kappa \int_0^l \frac{S_z^2}{2GA} ds \tag{1.136}$$

After performing the calculations of Eqs. (1.134), (1.135) and (1.136), the out-of-the-plane displacements and loads can be connected as:

$$\begin{Bmatrix} u_{1z} \\ \theta_{1x} \\ \theta_{1y} \end{Bmatrix} = \begin{bmatrix} C_{1,uz-Fz} & C_{1,uz-Mx} & C_{1,uz-My} \\ C_{1,uz-Mx} & C_{1,\theta x-Mx} & C_{1,\theta x-My} \\ C_{1,uz-My} & C_{1,\theta x-My} & C_{1,\theta y-My} \end{bmatrix} \begin{Bmatrix} F_{1z} \\ M_{1x} \\ M_{1y} \end{Bmatrix} \tag{1.137}$$

where the terms of the symmetric compliance matrix are:

$$C_{1,uz-Fz} = \frac{R}{4}\left[\frac{4\kappa\alpha}{AG} + \frac{2R^2(\alpha - \sin\alpha\cos\alpha)}{I_t G} + \frac{R^2}{I_y E}(6\alpha - 8\sin\alpha + \sin 2\alpha)\right] \quad (1.138)$$

$$C_{1,uz-Mx} = \frac{R^2}{4}\left(\frac{2\alpha - \sin 2\alpha}{I_t G} + \frac{2\alpha - 4\sin\alpha + \sin 2\alpha}{I_y E}\right) \quad (1.139)$$

$$C_{1,uz-My} = -\frac{R^2}{4}\left(\frac{1 - \cos 2\alpha}{I_t G} + \frac{3 - 4\cos\alpha + \cos 2\alpha}{I_y E}\right) \quad (1.140)$$

$$C_{1,\theta x-Mx} = \frac{R}{4}\left(\frac{2\alpha - \sin 2\alpha}{I_t G} + \frac{2\alpha + \sin 2\alpha}{I_y E}\right) \quad (1.141)$$

$$C_{1,\theta x-My} = \frac{(1 - \cos 2\alpha)R}{4}\left(\frac{1}{I_y E} - \frac{1}{I_t G}\right) \quad (1.142)$$

$$C_{1,\theta y-My} = \frac{R}{4}\left(\frac{2\alpha - \sin 2\alpha}{I_y E} + \frac{2\alpha + \sin 2\alpha}{I_t G}\right) \quad (1.143)$$

Example 1.9

Determine the in-plane and out-of-the-plane compliances for a free-fixed curved beam, as the one of Fig. 1.20, in the case where $\alpha = \pi/2$.

Solution:

The in-plane compliances are:

$$C_{1,ux-Fx} = \frac{R}{4AEGe}\{\pi[\kappa Ee + G(3R - e)] - 8G(R - e)\} \quad (1.144)$$

$$C_{1,ux-Fy} = -\frac{R}{2AEGe}[\kappa Ee + G(R - e)] \quad (1.145)$$

$$C_{1,ux-Mz} = -\frac{(\pi/2 - 1)R + e}{AEe} \quad (1.146)$$

$$C_{1,uy-Fy} = \frac{\pi R}{4AEGe}[\kappa Ee + G(R - e)] \quad (1.147)$$

$$C_{1,uy-Mz} = \frac{R-e}{AEe} \tag{1.148}$$

$$C_{1,\theta z-Mz} = \frac{\pi}{2AEe} \tag{1.149}$$

The out-of-the-plane compliances are:

$$C_{1,uz-Fz} = \frac{R}{4}\left[\frac{2\kappa\pi}{AG} + \frac{\pi R^2}{I_t G} + \frac{(3\pi-8)R^2}{I_y E}\right] \tag{1.150}$$

$$C_{1,uz-Mx} = \frac{R^2}{4}\left(\frac{\pi}{I_t G} + \frac{\pi-4}{I_y E}\right) \tag{1.151}$$

$$C_{1,uz-My} = -\frac{R^2}{2}\left(\frac{1}{I_t G} + \frac{1}{I_y E}\right) \tag{1.152}$$

$$C_{1,\theta x-Mx} = C_{\theta y-My} = \frac{\pi R}{4}\left(\frac{1}{I_t G} + \frac{1}{I_y E}\right) \tag{1.153}$$

$$C_{1,\theta x-My} = \frac{R}{2}\left(\frac{1}{I_y E} - \frac{1}{I_t G}\right) \tag{1.154}$$

5.3.2 Thin Curved Beams

The in-plane and out-of-the-plane compliances are now derived for a thin beam (R/w > 10), according to Fig. 1.20. The beam is also considered long, which enables ignoring the shearing effects.

5.3.2.1 In-Plane Compliances

The two linear displacements about the x- and y-directions, together with the rotation about the z-axis, are again calculated by means of the generic formulation of Eqs. (1.125). The strain energy, as mentioned, includes only the bending moment, and therefore is of the form:

$$U = R\int_0^{\alpha} M_{bz}^2/(2EI_z)\,d\beta \tag{1.155}$$

where M_{bz} is given in the first Eq. (1.126). By taking the partial derivatives of the strain energy, Eq. (1.155), in terms of F_{1x}, F_{1y} and M_{1z} respectively, the compliances of Eq. (1.127) become:

$$C_{1,ux-Fx} = R^3/(4EI_z)[6\alpha - 8\sin\alpha + \sin(2\alpha)] \tag{1.156}$$

$$C_{1,ux-Fy} = R^3/(4EI_z)[4\cos\alpha - \cos(2\alpha) - 3] \tag{1.157}$$

$$C_{1,ux-Mz} = R^2/(EI_z)(\sin\alpha - \alpha) \tag{1.158}$$

$$C_{1,uy-Fy} = R^3/(4EI_z)[2\alpha - \sin(2\alpha)] \tag{1.159}$$

$$C_{1,uy-Mz} = R^2/(EI_z)(1 - \cos\alpha) \tag{1.160}$$

$$C_{1,\theta z-Mz} = \alpha R/(EI_z) \tag{1.161}$$

5.3.2.2 Out-of-the-Plane Compliances

Similar to the case of a thick curved beam, the out-of-the-plane compliances can be formulated as arranged in Eq. (1.137). The strain energy for a thin (relatively-long) curved beam is formed by contributions from the bending moment and the torsion moment only, namely:

$$U = R\left[\int_0^\alpha M_b^2/(2EI_y)d\beta + \int_0^\alpha M_t^2/(2GI_t)d\beta\right] \tag{1.162}$$

with M_b and M_t being defined in Eqs. (1.134). By performing the partial derivatives of the strain energy given in Eq. (1.162) in terms of F_{1z}, M_{1x} and M_{1y}, respectively (according to the first two sides of Eqs. 91.135)), the only compliance that is different from the ones already derived for a thick curved beam is:

$$C_{1,uz-Fz} = R^3/4\{[2\alpha - \sin(2\alpha)]/(GI_t) + [6\alpha - 8\sin\alpha + \sin(2\alpha)]/(EI_y)\} \tag{1.163}$$

It can be seen that Eq. (1.163) can be obtained from Eq. (1.138) by considering that the shearing effects are negligible ($\kappa = 0$).

Example 1.10

Consider a quarter-circle fixed-free curved bar for which w = 0.1 R. Calculate the compliance $C_{1,uy\text{-}Fy}$ by considering that the beam is thick and then compare the result with the one produced when considering that the beam is thin.

Solution

For a thin curved beam, the compliance of interest is in this particular case ($\alpha = \pi/2$):

$$C_{1,uy-Fy} = \pi R^3 /(4EI_z) \tag{1.164}$$

For a thick beam, the same compliance is given in Eq (1.131). After carrying out the required numerical calculations, the ratio between the compliance $C_{1,uy\text{-}Fy}$ calculated according to the thin beam theory and the same compliance computed by means of the thick beam assumption is 0.999, which proves that for the limit value w = 0.1 R, both theories provide similar predictions.

Example 1.11

Find the out-of-the-plane (z-direction) deflection of the free end 1 produced by the force F_{1z} = 30 μN acting about a direction perpendicular to the plane of the free-fixed quarter-circle microbeam of Fig. 1.24. The radius of the circle is R = 150 μm and the cross-section is rectangular with w = 20 μm and t = 2 μm. The material is homogeneous with E = 150 GPa and μ = 0.21.

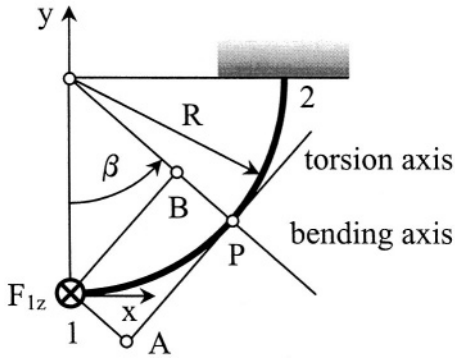

Figure 1.24 Out-of-the-plane loading of a curved beam

Solution

The deflection about the z-direction of point 1 can be found by using Eq. (1.137) in the form:

$$u_{1z} = C_{1,uz-Fz} F_{1z} \tag{1.165}$$

because the only load is F_{1z}.

The compliance of Eq. (1.165) can be determined from Eq. (1.163) in the following form:

$$C_{1,uz-Fz} = \frac{R^3}{4}\left(\frac{\pi}{GI_t} + \frac{3\pi - 8}{EI_y}\right) F_{1z} \tag{1.166}$$

The moments of inertia are:

$$\begin{cases} I_y = wt^3/12 \\ I_t = wt^3/3 \end{cases} \tag{1.167}$$

and E and G are related according to Eq. (1.23). By using the numerical values given in this example, it is found that the out-of-the-plane deflection is $u_{1z} = 42\ \mu m$.

6. COMPOSITE MEMBERS

Many structural microcomponents are built in a composite manner by depositing layers of different materials on a structural component. A thin piezoelectric layer might be attached to the structural layer of a microcantilever, in order to achieve actuation or sensing purposes for instance. There are also cases where members of different cross-sectional and/or material properties are fabricated in a serial manner in beam-type microcomponents that are designed for various transduction purposes. Both cases will be analyzed next by focusing on one-dimension (line) members.

6.1 Sandwiched Members

Figure 1.25 (a) shows the cross-section of a sandwich beam consisting of two different materials, having the elastic modulii E_1 and E_2 for instance. Figures 1.25 (b) and (c) picture the strain and stress variations over the height of the compound cross-section as produced through bending. The two layers have different thickness, t_1 and t_2, and identical widths w – but this is not a necessary condition. In such instances, stiffness properties can be formulated that are equivalent to the real situation, by utilizing the stiffness or compliance equations that have been derived for homogeneous cross-sections. The response to bending, axial loading and torsion will be addressed next.

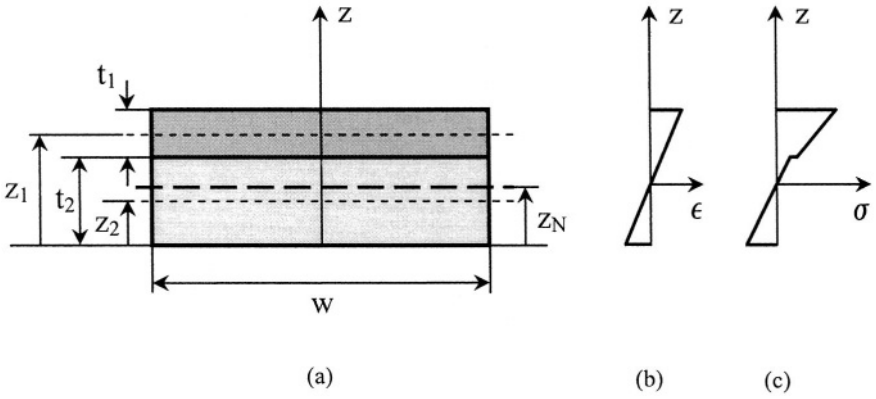

Figure 1.25 Beam of composite cross-section: (a) cross-section geometry; (b) bending strains; (c) bending stresses

6.1.1 Bending

Bending about the y-axis, which is assumed the most sensitive axis, will be thoroughly analyzed. Assume that a homogeneous cross-section is being studied first. The strain varies linearly about the z-axis, as sketched in Fig. 6.25 (b), and if the horizontal line that passes through the bottom of the cross-section is chosen as a datum line, the strain can be expressed as:

$$\varepsilon = a + bz \tag{1.168}$$

The normal stress is:

$$\sigma = E\varepsilon = E(a + bz) \tag{1.169}$$

The stress and strain are zero in the *neutral axis,* and therefore:

$$a = -bz_N \tag{1.170}$$

where z_N gives the position of the neutral axis, and in the case of a homogeneous cross-section this coordinate is half the beam's thickness. The bending moment that acts on the cross-section can be expressed as:

$$M_{by} = \int_A z\sigma dA = bE\left(\int_A z^2 dA - z_N^2 A\right) \tag{1.171}$$

This equation has been obtained by using Eqs. (1.169) and (1.170) and by considering that:

$$\int_A z dA = z_N A \tag{1.172}$$

Equation (1.171) can further be put in the standard form:

$$M_{by} = bEI_y \tag{1.173}$$

where, according to the parallel axis theorem, the moment of inertia is:

$$I_y = \int_A z^2 dA - z_N^2 A \tag{1.174}$$

A similar approach is now followed for the composite beam of Fig. 1.25 (a). In this case, the position of the neutral axis is unknown. Because the state of stress is of pure bending, the axial force that acts on the cross-section is zero, which leads to:

$$\int_A \sigma dA = \int_{A_1} \sigma_1 dA + \int_{A_2} \sigma_2 dA = 0 \tag{1.175}$$

where A_1 and A_2 are the cross-sectional areas of the two components. The strain will however follow the linear distribution of Eq. (1.168), and therefore Eq. (1.170) is still valid. The stresses in the two components are:

$$\begin{cases} \sigma_1 = E_1 b(z - z_N) \\ \sigma_2 = E_2 b(z - z_N) \end{cases} \tag{1.176}$$

By substituting Eqs. (1.176) into Eq. (1.175), the position of the neutral axis becomes:

$$z_N = (z_1 E_1 A_1 + z_2 E_2 A_2)/(E_1 A_1 + E_2 A_2) \tag{1.177}$$

When more than two layers form the composite cross-section, Eq. (1.177) generalizes to:

$$z_N = \sum_i (z_i E_i A_i) / \sum_i (E_i A_i) \tag{1.178}$$

The bending moment can be found by following the path detailed for the homogeneous cross-section, and it becomes simple to show that the bending moment is given by.

$$M_{by} = b\{E_1[I_{y1} + z_1 A_1(z_1 - z_N)] + E_2[I_{y2} + z_2 A_2(z_2 - z_N)]\} \quad (1.179)$$

where I_{y1} and I_{y2} are the moments of inertia of the two segments, each taken with respect to its own principal axis (passing through its center of symmetry). By comparing Eq. (1.179) to Eq. (1.173), it can be concluded that the bending rigidity of the composite beam is:

$$(EI_y)_e = E_1[I_{y1} + z_1 A_1(z_1 - z_N)] + E_2[I_{y2} + z_2 A_2(z_2 - z_N)] \quad (1.180)$$

where the subscript e denotes equivalent and z_N is given in Eq. (1.177). When more than two layers are included into the composite cross-section, the equivalent bending rigidity can be expressed as:

$$(EI_y)_e = \sum_i \{E_i[I_{yi} + z_i A_i(z_i - z_N)]\} \quad (1.181)$$

where z_N is calculated by means of Eq. (1.178). This formulation is quite convenient as any of the bending-related stiffnesses/compliances that can be formulated for various geometries in the case of homogeneous materials are able to be utilized by simply using the bending rigidity provided by Eq. (1.181).

Bending about the z-axis, which for classical MEMS devices where $w > t$ is not a very frequent occurrence, can be treated in a similar fashion, and the generic Eqs. (1.178) and (1.181) just need to use the subscript z instead of the subscript y.

6.1.2 Axial Loading and Torsion

For a homogeneous cross-section bar that is loaded axially by a force F_x, this force can be expressed as:

$$F_x = EA/\varepsilon \quad (1.182)$$

Consider now that the composite cross-section of Fig. 1.25 (a) belongs to a fixed-free bar subjected to an axial force F_x. This force will divide into two components, F_{1x} and F_{2x}, each of them acting on one of the two distinct portions. By assuming that the two segments are of equal length, they will also deform axially by the same quantity, and therefore their strains will be identical. In this case, the total axial force is:

$$F_x = (E_1 A_1 + E_2 A_2)/\varepsilon \tag{1.183}$$

By comparing Eqs. (1.182) and (1.183), it follows that the equivalent axial rigidity of the composite bar can be calculated as:

$$(EA)_e = E_1 A_1 + E_2 A_2 \tag{1.184}$$

or, in the case where more than two components make up the bar, in the form:

$$(EA)_e = \sum_i (E_i A_i) \tag{1.185}$$

This result is predictable, as the two portions have identical lengths and act as springs in parallel whose resultant stiffness is therefore the sum of the individual stiffnesses.

Torsion of composite cross-section bars is very similar to axial loading, and therefore the torsional rigidity of a composite bar is given by an equation similar to Eq. (1.184), namely:

$$(GI_t)_e = G_1 I_{t1} + G_2 I_{t2} \tag{1.186}$$

or, if the cross-section is composed of more than two different members, the equivalent rigidity in torsion is:

$$(GI_t)_e = \sum_i (G_i I_{ti}) \tag{1.187}$$

Note:

Caution should be exercised when a sandwiched member is subject to mixed loading, such as bending and axial, for instance, because the material or geometric properties that result from the different rigidity equivalence operations might be non-consistent. An example will be studied next where the thickness resulting from bending-related equivalence is not always equal to the thickness generated through axial-related equivalence.

Example 1.12

A sandwiched cantilever of the type shown in Fig. 1.25 (a) is formed of two different members that have equal widths ($w_1 = w_2$) and completely overlap over their length. Apply the bending-related equivalence, as well as the axial-related one, and find the two corresponding equivalent thicknesses by considering that E_1 is Young's modulus of the equivalent material. Also consider that $t_2 = c_t\, t_1$ and $E_2 = c_E\, E_1$.

Solution:

The position of the neutral axis is given by Eq. (1.177). It can be shown that this equation reduces to:

$$z_N = [1 + c_E c_t (2 + c_t)] / [2(1 + c_E c_t)] t_1 \tag{1.188}$$

The equivalent rigidity in bending is calculated by means of Eq. (1.180), and an equivalent homogeneous cross-section beam can be found whose bending rigidity is:

$$(EI_y)_e = E_1 w (t_e^{(b)})^3 / 12 \tag{1.189}$$

By equating Eqs. (1.180) and (1.189), the equivalent thickness is:

$$t_e^{(b)} = \sqrt[3]{2/7 [2 + c_E (21 + 23c_t + 2c_t^3 + 2c_E c_t^4]} / (1 + c_E c_t) \tag{1.190}$$

The rigidity that corresponds to axial equivalence is determined by using Eq. (1.184) and by considering that the same axial rigidity should be produced by an equivalent homogeneous bar, namely:

$$(EA)_e = E w t_e^{(a)} \tag{1.191}$$

and the axial-related thickness for this problem is:

$$t_e^{(a)} = (1 + c_E c_t) t_1 \tag{1.192}$$

which results from equating Eqs. (1.184) and (1.191).

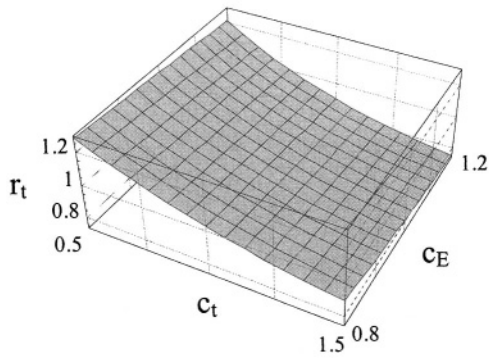

Figure 1.26 Thickness ratio r_t in terms of thickness factor c_t and elastic factor c_E

It is clear that the thicknesses produced by Eqs. (1.190) and (1.192) are equal only for one relationship between the two factors, c_t and c_E. Expressing one of the factors in terms of the other implies solving a third degree equation (resulting from equating the right hand sides of Eqs. (1.190)) and (1.192)), which will have one real solution. Figure 1.26 is the plot of the thickness ratio:

$$r_t = t_e^{(b)} / t_e^{(a)} \tag{1.193}$$

and it can be seen that this ratio spans the (0.8 → 1.2) range. It can also be seen that due to its monotonic variation, the ratio can only be equal to 1 for one (c_t, c_E) pair, and the two thicknesses are identical solely for that unique combination.

6.2 Serially-Connected Members

A problem directly resulting from the previous one addresses the case where two or more different structural members are connected serially, as depicted in the structure sketched in Fig. 1.27. The case studied in the previous subsection 6.1 offers the explanation with respect to the necessity of approaching the topic of serially-connected components. When the two different components that are sandwiched together do not have identical lengths, the equivalent rigidities can be calculated as shown in paragraph 6.1 for the overlapping length. This equivalent member will behave as a new portion that is serially connected to the remaining segments that are homogeneous.

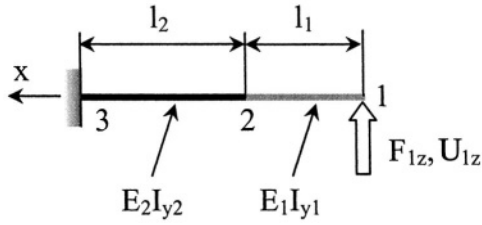

Figure 1.27 Two serially-connected members in a fixed-free configuration

The aim here is again to determine the equivalent rigidity/stiffness properties of the compound cantilever shown in Fig. 1.27, as produced through bending, axial loading, and torsion.

6.2.1 Bending

The stiffness of each of the two series-connected beams of Fig. 1.27 is given by:

$$K_{i,uz-Fz}^{(i)} = \frac{12E_i I_{yi}}{l_i^3} \tag{1.194}$$

where i = 1, 2. If the stiffness of the compound beam 1-3 were to be calculated by the rule that applies to serially-connected springs (this aspect will be treated in more detail in Chapter 5), then it would be found by means of the equation:

$$\frac{1}{K_{1,uz-Fz}} = \frac{1}{K_{1,uz-Fz}^{(1)}} + \frac{1}{K_{2,uz-Fz}^{(2)}} \tag{1.195}$$

and its value would be:

$$K_{1,uz-Fz} = 12/[l_1^3/(E_1 I_{y1}) + l_2^3/(E_2 I_{y2})] \tag{1.196}$$

However, if one calculates the free end's deflection by means of Castigliano's displacement theorem, the real stiffness is:

$$K_{1,Fz-uz} = [l_1/(E_1 I_{y1}) + l_2/(E_2 I_{y2})]/D_k \tag{1.197}$$

where the denominator D_k is:

$$D_k = 1/12[l_1^4/(E_1 I_{y1})^2 + l_2^4/(E_2 I_{y2})^2] + l_1 l_2[2(l_1^2 + l_2^2) + 3l_1 l_2]/(6E_1 E_2 I_{y1} I_{y2}) \tag{1.198}$$

It can be seen that the combined Eqs. (1.197) and (1.198) are not identical to Eq. (1.196), and therefore the stiffness of the compound beam of Fig. 1.27 cannot be solved by following the simple rule that applies to springs. Similarly, the other two bending-related compliances cannot be calculated by the serial rule for spring stiffnesses. By applying again Castigliano's displacement theorem it can be shown that the other direct-bending stiffness is given by the equation:

$$K_{1,My-\theta y} = [l_1^3/(E_1 I_{y1}) + l_2(3l_1^2 + 3l_1 l_2 + l_2^2)/(E_2 I_{y2})]/(3D_k) \tag{1.199}$$

whereas the cross-bending compliance is:

$$K_{1,Fz-\theta y} = [l_1^3/(E_1 I_{y1}) + l_2(2l_1 + l_2)/(E_2 I_{y2})]/(2D_k) \tag{1.200}$$

Example 1.13

Two microcantilevers are fabricated as shown in Fig. 1.28 (a) and (b) from the same material and they also have the same thickness t. Which of the two designs is the most compliant (in terms of the direct linear compliance about the z-axis, which is perpendicular to the planar microcantilevers at their free ends) when $w_1 = 2w_2$?

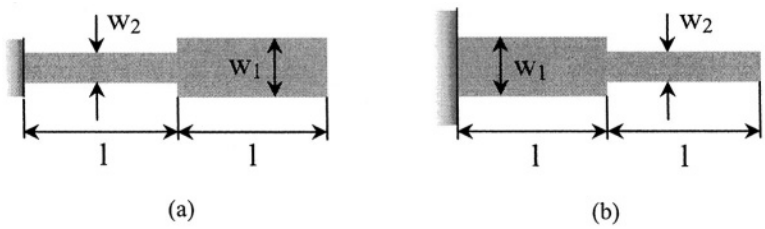

Figure 1.28 Two microcantilevers formed by serial connection of rectangular segments

Solution:

The linear direct compliance of the microcantilever sketched in Fig. 1.28 (a) can be obtained by applying Castigliano's displacement theorem in the presence of a force acting at the free end about a direction perpendicular to the microcantilever's plane. Its equation is:

$$C_{uz-Fz}^{(a)} = (7I_{y2} + I_{y1})l^3 / (3EI_{y1}I_{y2}) \tag{1.201}$$

Similarly, the compliance of the microcantilever of Fig. 1.28 (b) is:

$$C_{uz-Fz}^{(b)} = (7I_{y1} + I_{y2})l^3 / (3EI_{y1}I_{y2}) \tag{1.202}$$

By taking into account that:

$$\begin{cases} I_{y1} = w_1 t^3 / 12 \\ I_{y2} = w_2 t^3 / 12 \end{cases} \tag{1.203}$$

the ratio of the two compliances of Eqs. (1.201) and (1.202) is:

$$C_{uz-Fz}^{(a)} / C_{uz-Fz}^{(b)} = 5/3 \tag{1.204}$$

As a conclusion, the configuration of Fig. 1.28 (a) is approximately 1.66 times more compliant than the design of Fig. 1.28 (b).

6.2.2 Axial Loading and Torsion

The equivalence operation in the case where axial forces or torsion moments act on the serially-connected member of Fig. 1.27 is quite straightforward because in either of the situations the two components do behave as springs that are connected in series, and therefore the equivalent stiffness will be given by:

$$1/K_e = 1/K_1 + 1/K_2 \tag{1.205}$$

Specifically, in the case of axial loading, Eq. (1.205) gives:

$$1/K_e^{(a)} = l_1/(E_1A_1) + l_2/(E_2A_2) \tag{1.206}$$

whereas for torsion, the equivalent stiffness is:

$$1/K_e^{(t)} = l_1/(G_1I_{t1}) + l_2/(G_2I_{t2}) \tag{1.207}$$

Example 1.14

A microcantilever is formed of a structural layer of thickness t_1 on top of which another layer of thickness t_2 is deposited, as shown in Fig. 1.29 (a). Determine the deflection u_{1z} that is produced by a given tip force $F_{1z} = 10\ \mu$N when: $l_1 = l_2 = l_3 = 50\ \mu$m, t_1,= 1 μm, $t_2 = 0.8\ \mu$m, w = 15 μm, $E_1 = 150$ GPa, $E_2 = 130$ GPa.

Solution:

The two components overlap over the length l_2 and therefore the rigidity of that portion can be determined by means of the substitutions used in Example 1.12, namely:

$$(EI_y)_{2,e} = E_1[2 + c_E(21 + 23c_t + 2c_t^3 + 2c_ec_t^4)]wt_1^3/[42(1 + c_Ec_t)] \tag{1.208}$$

Now, the three portions shown in Fig. 1.29 (b) are serially connected, and therefore the direct stiffness about the z-direction can be calculated by means of Castigliano's displacement theorem, such that the required deflection is:

$$u_{1z} = \{7l_1[(8l_1^2 + 9l_1l_2 + 3l_2^2]/(E_1t_1^3w) + l_2(3l_1^2 + 3l_1l_2 + l_2^2)/(EI_y)_{2,e}\}F_{1z} \tag{1.209}$$

and the numerical value is $u_{1z} = 47.3\ \mu$m.

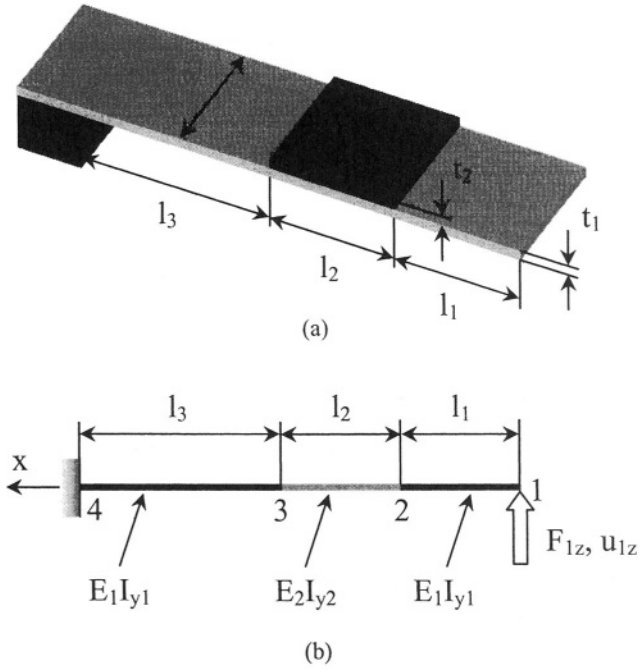

Figure 1.29 Hybrid microcantilever: (a) geometry of real design; (b) equivalent serial model

6.3 Beams in Parallel

The situation will be analyzed here where two beams are connected in parallel by means of a rigid link, and the direct-bending stiffness will be evaluated. However, in order to solve this particular problem an additional example is discussed that highlights the influence of boundary conditions on the stiffness of a beam in bending.

Example 1.15

Find the spring constant corresponding to the elastic interaction between the force F_{1z} and the resulting deflection u_{1z} for the beams shown in Fig. 1.30 by using Castigliano's displacement theorem. Compare the two results.

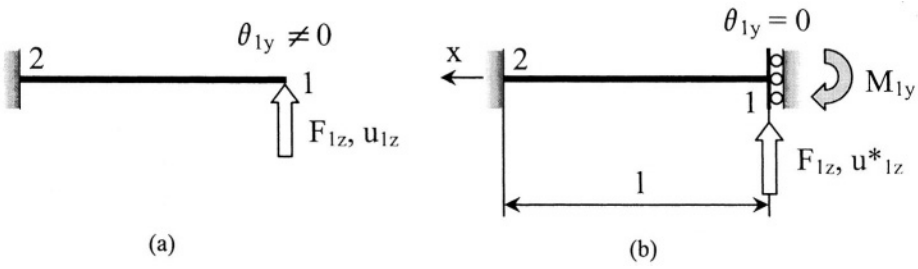

Figure 1.30 Boundary conditions in bending: (a) fixed-free beam; (b) fixed-guided beam

Solution:

For the fixed-free beam of Fig. 1.30 (a), the linear stiffness that corresponds to the free end's deflection was shown to be:

$$K_{1,Fz-uz} = 12EI_y / l^3 \tag{1.210}$$

in Example 1.1, or in the direct stiffness derivation of subsection 5.2.1. For the second configuration, the one sketched in Fig. 1.30 (b), where the end point 1 is confined to move vertically by always having zero slope, this point's deflection and slope can be expressed in terms of loading and of the compliances corresponding to a fixed-free beam as:

$$\begin{cases} u_{1z} = C_{1,uz-Fz} F_{1z} + C_{1,uz-My} M_{1y} \\ \theta_{1y} = C_{1,uz-My} F_{1z} + C_{1,\theta y-My} M_{1y} \end{cases} \tag{1.211}$$

Because the slope at that point is zero, it follows from the second Eq. (1.211) that:

$$M_{1y} = -\frac{C_{1,uz-My}}{C_{1,\theta y-My}} F_{1z} \tag{1.212}$$

and, as a consequence, by substituting Eq. (1.212) into the first Eq. (1.211), the sought stiffness is:

$$K^*_{1,Fz-uz} = \frac{F_{1z}}{u^*_{1z}} = 1/(C_{1,uz-Fz} - C^2_{1,uz-My} / C_{1,\theta y-My}) \tag{1.213}$$

For a constant cross-section fixed-free beam, the compliances of Eq. (1.213) are simply:

$$\begin{cases} C_{1,uz-Fz} = l^3/(3EI_y) \\ C_{1,uz-My} = l^2/(2EI_y) \\ C_{1,\theta y-My} = l/(EI_y) \end{cases} \tag{1.214}$$

By substituting now Eqs. (1.214) into Eq. (1.213), the stiffness of the beam sketched in Fig. 1.30 (b) becomes:

$$K^*_{1,Fz-uz} = \frac{12EI_y}{l^3} \tag{1.215}$$

It can be seen that the stiffness for this particular boundary conditions is equal to the stiffness of an identical beam whose boundary conditions are fixed-free, as illustrated in Fig. 1.30 (a).

This conclusion should not be very surprising within the context of the stiffness $K_{1,Fz\text{-}uz}$ that has been derived in Example 1.1, namely by means of inversion of the compliance matrix. The first equation of Eqs. (1.7) can be written with the aid of Eq. (1.16) as:

$$F_{1z} = 12EI_y / l^3 u_{1z} - 6EI_y / l^2 \theta_{1y} \tag{1.216}$$

This equation, again, reflects the principle of superposition which indicates that the total force being applied at the free end of a microcantilever is equal to the algebraic sum of a force that needs to purely translate the free end by u_{1z} with zero slope ($\theta_{1y} = 0$) – the first term of Eq. (1.216) – and a force that would simply rotate the free end by θ_{1y} with zero deflection ($u_{1z} = 0$) – the second term in Eq. (1.216). This latter term has to be negative because the real force that has to produce both u_{1z} and θ_{1y} for a free end cantilever is smaller than the force needed to only generate the same u_{1z} deflection, as in Fig. 1.30 (b). This is the reason why the bending-related stiffness has to be negative, as Example 1.1 has demonstrated.

However, individual springs, either linear or rotary, as the ones pictured in Fig. 1.5 and utilized as equivalent lumped-parameter models of real, distributed-parameter beams, have to be uniquely defined in terms of their stiffnesses. Because stiffness depends on boundary conditions, it is expected that two different sets of boundary conditions will generate two different stiffnesses for the same physical spring. Conversely, one stiffness could not possibly describe two different boundary conditions applied to the same spring. It has been shown at the beginning of this chapter that axial and torsional stiffnesses are simply calculated as algebraic inverses of their corresponding compliances, and this relationship should also hold true for bending-related stiffnesses as they define unique linear or rotary springs. Indeed, the direct and cross stiffnesses of springs that model bending of cantilevers are calculated as:

$$\begin{cases} \overline{K}_{1,Fz-uz} = 3EI_y / l^3 = 1/C_{1,uz-Fz} \\ \overline{K}_{1,Fz-\theta y} = 2EI_y / l^2 = 1/C_{1,uz-My} \\ \overline{K}_{1,My-\theta y} = EI_y / l = 1/C_{1,\theta y-My} \end{cases} \tag{1.217}$$

These expressions are clearly different from those of the stiffnesses $K_{1,Fz\text{-}uz}$, $K_{1,Fz\text{-}\theta y}$ and $K_{1,\ My\text{-}\theta y}$ that have been obtained in Example 1.1, Eq. (1.16), through inversion of the compliance matrix, for the same fixed-free boundary conditions. While the stiffness set of Eqs. (1.217) is utilized to individually

define the three springs that characterize the lumped-parameter elastic model of a cantilever, and is further employed in calculating the natural frequencies of such a structure, the stiffnesses of Eq. (1.16) are the ones to be used when calculating forces and moments that correspond to known tip deflections and slopes. The difference between individual (definition) stiffnesses (denoted with an upper bar, as shown in Eqs. (1.217) – this notation will be used from this point on) and stiffnesses resulting from inversion of the compliance matrix (which is unique for a given beam configuration) will become more evident in Chapter 2 when studying microcantilever applications.

Having solved this example, the particular case mentioned at the beginning of this subsection is studied now with the two beams connected in parallel by means of a rigid link, as shown in Fig. 1.31. The aim is to verify whether the two beams really do behave as two springs in parallel in terms of their direct-bending linear stiffnesses. For a beam that has one fixed end and the other end is constrained to strictly move on a direction perpendicular to the beam's axis, (the slope at that point is zero), the stiffness, as shown in Example 1.15, is given in Eq. (1.215).

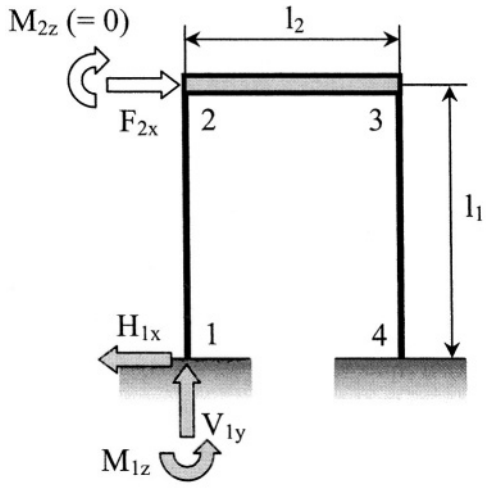

Figure 1.31 Identical beams connected in parallel

It is known that the stiffness of two identical springs in parallel can be calculated as:

$$K = 2K_1 \tag{1.218}$$

where K_1 is the stiffness of one spring. In order to check the validity of Eq. (1.218), the horizontal displacement at point 2 is calculated by means of Castigliano's displacement theorem as:

$$u_{2x} = \frac{\partial U}{\partial F_{2x}} \tag{1.219}$$

Since the system of Fig. 1.31 is three-times indeterminate, the reactions H_{1x}, V_{1y} and M_{1z} need to be first determined, by using the corresponding boundary conditions:

$$\begin{cases} u_{1x} = 0 \\ u_{1y} = 0 \\ \theta_{1z} = 0 \end{cases} \tag{1.220}$$

which can be expressed as:

$$\begin{cases} u_{1x} = \dfrac{\partial U}{\partial H_{1x}} = \dfrac{1}{EI_z}\displaystyle\int_0^{l_1}[M_{bz}^{(1)}\frac{\partial M_{bz}^{(1)}}{\partial H_{1x}} + M_{bz}^{(2)}\frac{\partial M_{bz}^{(2)}}{\partial H_{1x}}]dx = 0 \\ u_{1y} = \dfrac{\partial U}{\partial V_{1y}} = \dfrac{1}{EI_z}\displaystyle\int_0^{l_1}[M_{bz}^{(1)}\frac{\partial M_{bz}^{(1)}}{\partial V_{1y}} + M_{bz}^{(2)}\frac{\partial M_{bz}^{(2)}}{\partial V_{1y}}]dx = 0 \\ \theta_{1z} = \dfrac{\partial U}{\partial M_{1z}} = \dfrac{1}{EI_z}\displaystyle\int_0^{l_1}[M_{bz}^{(1)}\frac{\partial M_{bz}^{(1)}}{\partial M_{1z}} + M_{bz}^{(2)}\frac{\partial M_{bz}^{(2)}}{\partial M_{1z}}]dx = 0 \end{cases} \tag{1.221}$$

The bending moment is:

$$\begin{cases} M_{bz}^{(1)} = -M_{1z} + H_{1x}x \\ M_{bz}^{(2)} = -M_{1z} + H_{1x}(l_1 - x) + V_{1y}l_2 + F_{2x}x \end{cases} \tag{1.222}$$

The unknown reactions are:

$$\begin{cases} H_{1x} = F_{2x}/2 \\ V_{1y} = -F_{2x}l_1/(2l_2) \\ M_{1z} = F_{2x}l_1/4 \end{cases} \tag{1.223}$$

The horizontal displacement at point 2 can now be found by means of Eqs. (1.219), (1.221), (1.222) and (1.223), which give the stiffness about the x-direction as:

$$K = 24EI_z/l_1^3 \tag{1.224}$$

Equation (1.224) shows that the stiffness of the two-beam structure can be found by summing up the stiffnesses given in Eq. (1.215), and therefore it can be considered that the two beams act as two springs in parallel.

In addition, the slope at point 2 is calculated here. This slope can be found in a similar fashion, by following the two-step procedure outlined previously. The new reactions have to be determined by applying Eqs. (1.220) and (1.221). The only difference is that a M_{2z} dummy moment has to be added in the bending moment of the second Eq. (1.222). It can be shown that the two reactions of Eq. (1.223) are the same, whereas the bending moment reaction becomes:

$$M_{1z} = M_{2z} / l_1 - F_{2x} l_1 / (2 l_2) \tag{1.225}$$

With this addition, the slope at point 2 is calculated as:

$$\theta_{2z} = \frac{\partial U}{\partial M_{2z}} \tag{1.226}$$

and its value is zero since the dummy moment is also zero. This result confirms the physical intuition that the system should deform under the action of the horizontal force F_{2x} such that the rigid segment 2-3 translates horizontally.

7. PLATES AND SHELLS

Plates and shells are structural components that can use their elastic deformation in MEMS applications for devices such as valves, pumps, switches etc. By design, plates and shells have their thickness much smaller than the in-plane dimensions. Den Hartog [7] and Reddy [5], among others, mention that the thickness in these members is less than 1/10 of the smallest in-plane dimension, and moreover, if the thickness is less than 1/20 of the smallest planar dimension, the member is considered thin.

The plate is generally a flat member and it is the two-dimensional correspondent of the straight beam, whereas the shell is curved and is similar to a curved beam. In their thin variant, both members can accommodate bending and axial (stretching) loads. For small deformations, where the deflections are less than the thickness, the bending is preponderant, and the load-deformation relationship is linear. For large deformations, 5 times larger than the thickness or more, the membrane behavior becomes paramount, and the bending effects can be neglected. In such cases, the load-deformation law is non-linear. The transition cases, where the maximum deformation is comparable to the thickness, approximate equations can be formulated to accommodate both the bending and the membrane effects. For a circular thin plate of radius R and thickness t, clamped on its edge and acted upon by a

uniform pressure p, the maximum displacement is registered at its center, and it can be calculated by solving the following third degree equation – see den Hartog [7] for instance:

$$p = 64D / R^4 u_{1z} + 8/3E/(1-\mu)t / R^4 u_{1z}^3 \qquad (1.227)$$

where u_{1z} is the center deflection and D is the rigidity which is defined as:

$$D = Et^3 /[12(1-\mu^2)] \qquad (1.228)$$

It can be seen that Eq. (1.227) incorporates both the small-deformation bending effects through the linear term in u_{1z} and the membrane (stretching) effects through the non-linear term in the same u_{1z}.

For bending-dominated cases, where the membrane effects can be ignored, the differential equation of deflection is:

$$(\partial^2/\partial x^2 + \partial^2/\partial y^2)(\partial^2 u_z/\partial x^2 + \partial^2 u_z/\partial y^2) = p/D \qquad (1.229)$$

The maximum deflection for the circumferentially-clamped circular plate under uniform pressure is:

$$u_{1z} = pR^4/(64D) \qquad (1.230)$$

The maximum deflection of the same plate under a concentrated load acting normally at the disc's center is:

$$u_{1z} = F_{1z}R^2/(16\pi D) \qquad (1.231)$$

For rectangular plates, the solution to Eq. (1.229) is found by using the Fourier series expansion, and thus the solution is only approximate. For a rectangular plate of dimensions l_1 and l_2, which is fixed on its edges and is acted upon by a pressure p, the maximum center deflection is:

$$u_{1z} = 16p/(\pi^6 D)\sum_{i,j=1}^{\infty} 1/[ij(i^2/l_1^2 + j^2/l_2^2)^2] \qquad (1.232)$$

where the summation only retains the odd counters i and j. The maximum deflection of this plate when acted upon by a force, perpendicularly to the plate's plane, is similarly calculated as:

$$u_{1z} = 4F_{1z}/(\pi^4 D l_1 l_2)\sum_{i,j=1}^{\infty}[1/(i^2/l_1^2 + j^2/l_2^2)^2] \qquad (1.233)$$

Problems

Problem 1.1

In a plane stress problem, the non-zero stresses are located in the xy plane, as shown in Fig. 1.8. Express the strain energy when the shear modulus and Lamé's constant are known.

Answer:

$$U = 1/2 \int_V [(\lambda + 2G)(\varepsilon_x^2 + \varepsilon_y^2) + \lambda(2\varepsilon_x\varepsilon_y + \varepsilon_y\varepsilon_z + \varepsilon_z\varepsilon_x) + G\gamma_{xy}^2]dV$$

Problem 1.2

A fixed-free beam is acted upon by a force at its free end as shown in Fig. 1.9 (a). Determine the length of the beam 1 as well and its cross-sectional thickness t in such a way that the maximum tip deformations are u_{1z} and θ_{1y} without exceeding a bending stress limit σ_{max} when Young's modulus is E.

Answer:

$$\begin{cases} l = 3u_{1z}/(2\theta_{1y}) \\ t = 3u_{1z}\sigma_{max}/(2E\theta_{1y}^2) \end{cases}$$

Problem 1.3

Calculate the ratio of the tip deflection when shearing forces are accounted for to the tip deflection when shearing effects are negligible for a microcantilever acted upon by a tip force which is perpendicular to the longitudinal axis. Known are Poisson's ratio μ, beam thickness t and length l.

Answer:

$$u_{1z}^{(sh)}/u_{1z} = 1 + \kappa(1+\mu)/2(t/l)^2$$

Problem 1.4

Find the stiffness of the pinned-guided microbeam shown in Fig. 1.32 at its midspan about the z-direction (Hint: assume a force is applied at midspan about the z-direction).

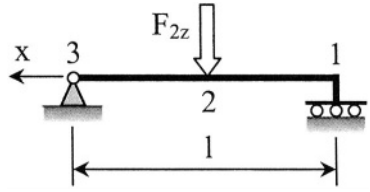

Figure 1.32 Simply supported – guided microbeam

Answer:

$$K_{2,Fz-uz} = F_{2z} / u_{2z} = 768EI_y /(7l^3)$$

Problem 1.5

Find the relationship between the thickness t and the length l for a microcantilever such that the stiffness ratio $K_{1,Fy-uy}/ K_{1,Fz-uz}$ at the free end 1 is equal to n (n > 1), and that the axial stiffness at the same point is less than a fixed value of K_a.

Answer:

$$l = E\sqrt{n} / K_a t^2$$

Problem 1.6

A curved beam of rectangular cross-section defined by w = 10 μm and t = 1 μm, has a radius of R = 80 μm. Determine the position of the neutral axis by calculating the eccentricity e.

Answer:

e = 0.10416 μm, for 0.6 < R/w < 8

e = 0.10427 μm, for R/w > 8

relative error between the first and second predictions: 0.1%

Problem 1.7

Find the z-direction deflection at point 1 for the free-fixed structure of Fig. 1.33. Known are l, R and F_{1z}. The constant cross-section is square and the material is homogeneous with known E and G.

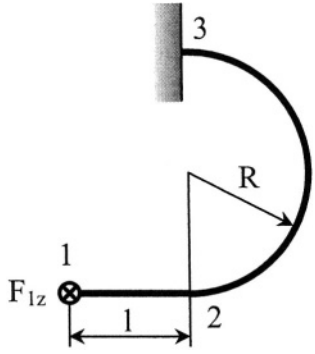

Figure 1.33 Out-of-the-plane deformation of a straight-circular beam

Answer:

$$u_{1z} = \{\frac{2l^3 + 3\pi R(l^2 + R^2)}{3EI_y} + \frac{R[\pi(l^2 + 3R^2) + 8lR]}{GI_t}\}F_{1z}$$

Problem 1.8

Compare the compliance $C_{1,uz\text{-}Fz}$ of a fixed-free straight beam with the same compliance of a fixed-free curved beam that subtends an arc of $\pi/2$. The two beams have identical lengths and rectangular cross-sections. Consider both the case where torsion is and is not taken into account.

Answer:

When torsion is ignored, the compliance ratio is:

$$C^{(s)}_{1,uz-Fz} / C^{(c)}_{1,uz-Fz} = 6(3\pi - 8)/\pi^3 \approx 3.627$$

When the torsion is taken into account, the compliance ratio becomes:

$$C^{(s)}_{1,uz-Fz} / C^{(c)}_{1,uz-Fz} = \pi^3 /\{3[(7+\mu)\pi - 16] \approx 1.52$$

Problem 1.9

Compare the bending rigidity of the sandwich beam in Fig. 1.34 for the particular case where $t_1 = t_2$, $w_1 = w_2$, $l_1 = 2l_2$, $E_2 = 1.1\ E_1$ to the bending rigidity of the homogeneous microcantilever of length l_1 and thickness t_1.

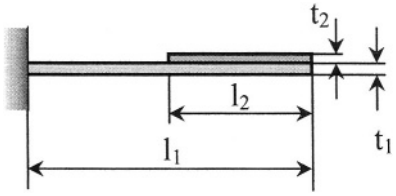

Figure 1.34 Sandwich beam

Answer:

$$(EI_y)_e /(E_1 I_{y1}) = 8.38$$

Problem 1.10

Calculate the stiffness about the x-direction (horizontal) at point 2 for the parallel beam structure of Fig. 1.35. The two side beams are identical and parallel to the center beam whose length is twice the length of the side beams. Consider that the three beams have identical cross-sections and are built of the same material.

Answer:

$$K_{2,Fx-ux} = 51/2EI_z / l^3$$

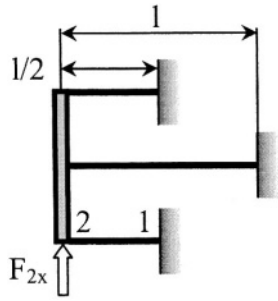

Figure 1.35 Three beams in parallel

Problem 1.11

Compare the maximum deflection of a thin circular plate with that of a thin square plate when the two structures are acted upon by the same uniform pressure, and when they have identical mid-plane areas and thicknesses. Consider that both members are clamped on their edges.

Answer:

The deflection ratio is:

$u_z^{sq} / u_z^c = 256 / \pi^4 \approx 2.628$

Problem 1.12

Design a constant rectangular cross-section microcantilever which is acted upon by a tip transverse force F_z in such a manner that the allowable bending stress σ_a is not exceeded, while producing a tip deflection u_z and tip slope θ_y. The material's Young's modulus is E.

Answer:

$$l = 3u_z /(2\theta_y);\ w = 4E^2\theta_y^2 /(\sigma_a^2 u_z);\ t = 3\sigma_a u_z /(2E\theta_y^2)$$

Problem 1.13

Find the value of the force F_z which needs to be applied at the midspan of a fixed-fixed beam (microbridge) of length $l = 100\ \mu m$, and cross-sectional dimensions of $w = 20\ \mu m$ and $t = 1\ \mu m$ in order to generate a deflection of $u_z = 1\ \mu m$ at the midspan. The material Young's modulus is E = 130 GPa.

Answer:

$F_z = 41.6\ \mu N$

Problem 1.14

Compare the bending rigidity of the two sandwiched-beam cross-sections shown in Fig. 1.36. The top layer's material has a Young's modulus of E_1, whereas the Young's modulus of the bottom layer is $E_2 = 0.8\ E_1$. Also $t_2 = 2t_1$.

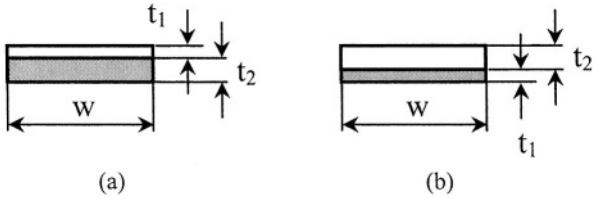

Figure 1.36 Cross-sections of two composite bending members

Answer:

$(EI_y)_a / (EI_y)_b = 1.439$

Problem 1.15

Compare the torsional stiffnesses of the two microcomponents pictured in Fig. 1.28. The shearing modulus is G and the cross-section is very thin ($t << w$).

Answer:

$K_{t,a} = K_{t,b}$

References

1. A.P. Boresi, R.J. Schmidt, O.M. Sidebottom, *Advanced Mechanics of Materials,* Fifth Edition, John Wiley & Sons, New York, 1993.
2. A.C. Ugural, S.K. Fenster, *Advanced Strength and Applied Elasticity,* Third Edition, Prentice Hall, Englewood Cliffs, 1995.
3. R.D. Cook, W.C. Young, *Advanced Mechanics of Materials,* MacMillan Publishing Company, New York, 1985.
4. W.C. Young, R.G. Budynas, *Roark's Formulas for Stress and Strain,* Seventh Edition, McGraw Hill, New York, 2002.
5. J.N. Reddy, *Energy Principles and Variational Methods in Applied Mechanics,* Second Edition, John Wiley & Sons, New York, 2002.
6. W.D. Pilkey, *Analysis and Design of Elastic Beams. Computational Methods,* John Wiley & Sons, New York, 2002.
7. J.P. Den Hartog, *Advanced Strength of Materials,* Dover Publications, New York, 1987.
8. N. Lobontiu, *Compliant Mechanisms: Design of Flexure Hinges,* CRC Press, Boca Raton, 2002.
9. J.P. Den Hartog, *Strength of Materials,* Dover Publications, New York, 1977.

Chapter 2

MICROCANTILEVERS, MICROHINGES, MICROBRIDGES

1. INTRODUCTION

This chapter studies the *microcantilevers,* the *microhinges* and the *microbridges,* which are MEMS components that can operate either individually – with no other accompanying structural component – or can be incorporated into more complex configurations. Essentially, all three components are designed to deform either in *bending* or *torsion* about a sensitive axis, but in actuality they are also subject to other deformations (called *parasitic* because they alter the intended functionality) such as those produced by axial forces, shearing forces or bending moments about directions other than the main sensitive axis. These microcomponents are one-dimensional members with either fixed-free boundary conditions (such as the microcantilevers and microhinges) or fixed-fixed boundary conditions (such as the microbridges). In other words, the very same geometrical configuration can function in either one of the three categories mentioned here, subject to different boundary conditions and overall structure of a specific mechanism. They can operate as sensors (the microcantilevers particularly), actuators (both the microcantilevers and microbridges) or as simple flexible joints in compliant microdevices (such as the case is with the microhinges).

The three categories are defined here in terms of their relevant stiffnesses and/or compliances according to the generic procedure outlined in the previous chapter. Designs from each category are specifically analyzed and discussed based on concrete and fully-solved examples. A section with problems to be solved completes this chapter. Although the prefix *micro* might seem redundant (and sometimes the structural dimensions can reduce to the nanometer level, case where *nano* would work better), the *micro* denomination will be kept here as in microcantilevers, microhinges and microbridges, which is also the terminology used in the specialty literature.

2. MICROCANTILEVERS

2.1 Introduction

The microcantilevers are used as sensing/actuation devices in a vast range of applications that include nanoindentation, high-resolution optical position detection, surface topology imaging, measurement/probing of material elastic and strength properties, writing on surface topologies, high-aspect ratio metrology, metallography, chemical/electrochemical characterization, micro-lubrication/tribology, corrosion processes, cellular engineering or grain growth and surface adhesion phenomena, as indicated by Morita et al. [1], Chui [2], Lange et al. [3], as well as Gad-El-Hak [4], Pelesko and Bernstein [5] or Madou [6], to name just a few works related to this area. Figure 2.1 is the photograph of a circularly-filleted microcantilever which is realized by the MUMPs (Multi User Multi Processes) technology, a surface micromachining procedure that builds three structural polysilicon layers on top of a pre-existing substrate. This prototype design can operate as a force-sensing device and will be more thoroughly discussed later in this chapter.

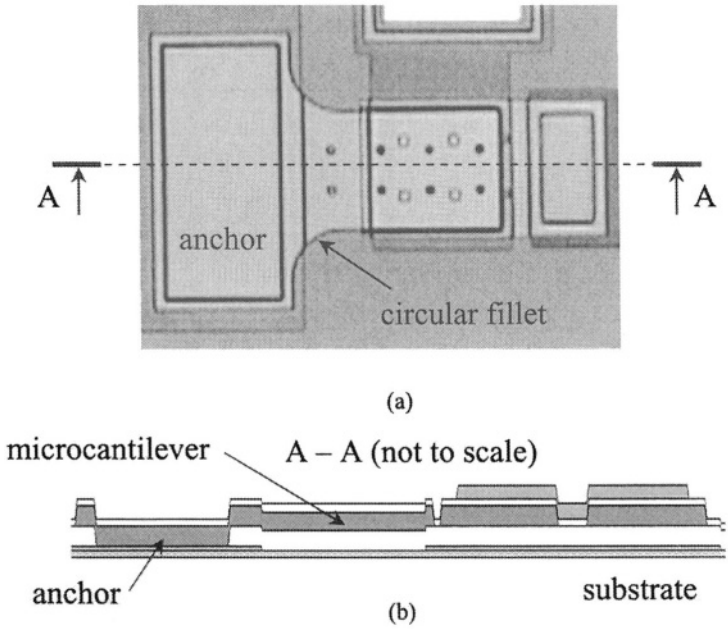

Figure 2.1 Circularly-filleted microcantilever prototype: (a) Top view; (b) Cross-section

The microcantilevers can be utilized either in the static/quasi-static regime – in order to generate/measure deflections and/or rotation angles – or

in the oscillating mode – when the modal frequencies are actually monitored and determined. They can operate in a contact mode or in a non-contact mode (when a pre-designed distance is kept between the microcantilever and the monitored three-dimensional topography, for instance). Functionally and constructively there are two main microcantilever categories. The first category includes configurations that are designed for *atomic force microscopy* (AFM) applications, where the out-of-the-plane bending of the microcantilever is superimposed to a planar motion of either the microcantilever or the target surface, such that a three-dimensional surface topology can be either *read* or *written* by means of a tip that is located at the microcantilever's free end, as sketched in Fig. 2.2. In such applications, the microcantilever needs to be compliant about one bending axis (also called the *sensitive axis*) and as stiff as possible in terms of other motions/deformations, such as torsion or in-plane bending about the other bending axis.

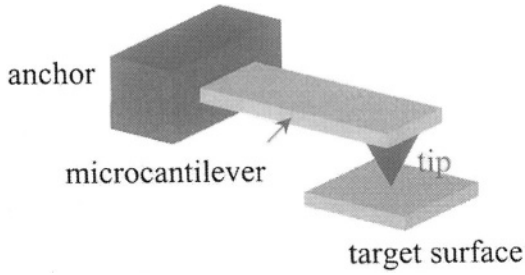

Figure 2.2 Schematic representation of a microcantilever for AFM applications

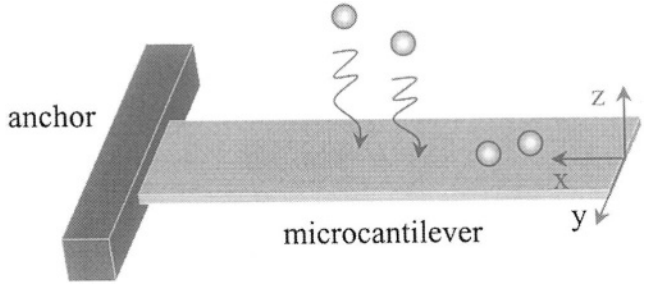

Figure 2.3 Schematic representation of a microcantilever for mass detection applications

The other category contains microcantilevers that are designed as sensing devices in applications such as detection of very small amounts of added substance, and Fig. 2.3 illustrates this principle.

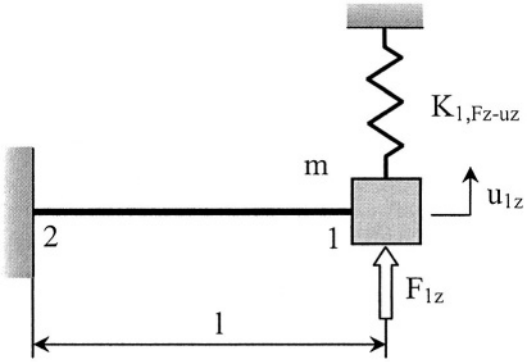

Figure 2.4 Lumped-parameter mass-spring model of a microcantilever

In either actuation or sensing, the microcantilever will deflect from its original straight shape/position. This alteration can be quantified by either measuring the deflection or the slope (generally at the tip of the microcantilever) through optical means, or by monitoring the change in the natural frequency. In both methods, knowledge of the stiffness properties is paramount. As shown in Fig. 2.4, a simplified representation of the distributed-parameter beam can be the equivalent lumped-parameter mass-spring model. For such a model, the linear direct stiffness about the z-axis has to be calculated either directly or based on previously-determined compliances.

This section focuses on the static response of microcantilevers by introducing and discussing the relevant stiffnesses/compliances of various designs. Microcantilevers of either solid or hollow geometries will be presented here.

2.2 Solid Microcantilevers

Solid microcantilever configurations such as rectangular, trapezoid and filleted (the fillet area is either circular or elliptic) are studied in this subsection. Two main applications are specifically addressed, namely the mass addition detection and the AFM reading/writing by defining the minimum set of compliances or stiffnesses that are necessary to solve either of the two problems in the static/quasi-static domain when experimental data is available.

2.2.1 Generic Formulation

The microcantilever is a fixed-free line member whose cross-section, mostly rectangular in MEMS, can be variable and whose compliance/stiffness characteristics are defined here by lumping the elastic properties at the free end. Chapter 1 described the procedure of calculating

the lumped-parameter axial, torsion and bending compliances/stiffnesses of fixed-free, constant rectangular cross-section straight and curved micromembers. The procedure followed in Chapter 1 – based on Fig. 1.18 – also applies here, where the straight member is of variable cross-section. The six degrees of freedom at the free end, as shown in Fig. 1.18, can formally be grouped into the ones generated by bending about the sensitive axis (the y-axis), namely: u_{1z} and θ_{1y}, bending about the other symmetry axis: u_{1y} and θ_{1z}, axial deformation, u_{1x}, and torsion, θ_{1x}. It has also been shown in Chapter 1 that the static response of a microcantilever can be formulated based on the lumped-parameter model, in one of the two equivalent forms:

$$\{u\} = [C]\{F\} \tag{2.1}$$

$$\{F\} = [K]\{u\} \tag{2.2}$$

where:

$$\{u\}^T = \{u_{1z}\ \theta_{1y}\ u_{1y}\ \theta_{1z}\ u_{1x}\ \theta_{1x}\} \tag{2.3}$$

is the displacement/deformation vector at the free end,

$$\{F\}^T = \{F_{1z}\ M_{1y}\ F_{1y}\ M_{1z}\ F_{1x}\ M_{1x}\} \tag{2.4}$$

is the forcing vector at the same end, and:

$$[C] = \begin{bmatrix} [C_{b,y}] & 0 & 0 & 0 \\ 0 & [C_{b,z}] & 0 & 0 \\ 0 & 0 & C_{1,ux-Fx} & 0 \\ 0 & 0 & 0 & C_{1,\theta x-Mx} \end{bmatrix} \tag{2.5}$$

is the compliance matrix whose bending-related sub-matrices are:

$$[C_{b,y}] = \begin{bmatrix} C_{1,uz-Fz} & C_{1,uz-My} \\ C_{1,uz-My} & C_{1,\theta y-My} \end{bmatrix} \tag{2.6}$$

and

$$[C_{b,z}] = \begin{bmatrix} C_{1,uy-Fy} & C_{1,uy-Mz} \\ C_{1,uy-Mz} & C_{1,\theta z-Mz} \end{bmatrix} \tag{2.7}$$

The compliance terms of Eqs. (2.6) and (2.7) have been calculated in Chapter 1 for a constant cross-section straight member. In the case of a variable cross-section member, the compliances of Eq. (2.6) are calculated (see Lobontiu [7] for instance) as:

$$C_{1,uz-Fz} = 1/E\int_0^l x^2 dx / I_y(x) \tag{2.8}$$

$$C_{1,uz-My} = 1/E\int_0^l x dx / I_y(x) \tag{2.9}$$

$$C_{1,\theta y-My} = 1/E\int_0^l dx / I_y(x) \tag{2.10}$$

The compliances of Eq. (2.7) are found by switching the subscripts y and z in Eqs. (2.8) through (2.10).

The axial-related compliance of Eq. (2.5) is calculated as:

$$C_{1,ux-Fx} = 1/E\int_0^l dx / A(x) \tag{2.11}$$

whereas the torsional compliance of Eq. (2.5) is:

$$C_{1,\theta x-Mx} = 1/G\int_0^l dx / I_t(x) \tag{2.12}$$

The variable rectangular cross-section amounts in the equations above are:

$$\begin{cases} I_y(x) = w(x)t^3/12 \\ I_z(x) = w(x)^3 t/12 \\ A(x) = w(x)t \\ I_t(x) = \begin{cases} w(x)t^3/3, t << w(x) \\ w(x)t^3[16/3 - 3.36t/w(x)]/16, t < w(x) \end{cases} \end{cases} \tag{2.13}$$

The equations for the torsion moment of inertia I_t are similar to Eqs. (1.118) and (1.119) that correspond to a constant rectangular cross-section. All cross-

sectional amounts in Eq. (2.13) take into account that the thickness t of the microcantilever is constant, whereas the width w(x) varies along the length.

The stiffness matrix [K] of Eq. (2.2) can be calculated either as:

$$[K] = [C]^{-1} \tag{2.14}$$

or by applying Castigliano's first theorem, as presented in Chapter 1. The compliance-based approach is computationally simpler, compared to the direct evaluation of stiffness properties, especially in the case of variable cross-section micromembers. In addition, the compliance expressions can be used to formulate/solve problems where the loads/deformations are required at locations other than the free end of the microcantilever. The stiffness matrix is expressed as:

$$[K] = \begin{bmatrix} [K_{b,y}] & 0 & 0 & 0 \\ 0 & [K_{b,z}] & 0 & 0 \\ 0 & 0 & K_{1,Fx-ux} & 0 \\ 0 & 0 & 0 & K_{1,Mx-\theta x} \end{bmatrix} \tag{2.15}$$

where:

$$[K_{b,y}] = \begin{bmatrix} K_{1,Fz-uz} & K_{1,Fz-\theta y} \\ K_{1,Fz-\theta y} & K_{1,My-\theta y} \end{bmatrix} \tag{2.16}$$

and

$$[K_{b,z}] = \begin{bmatrix} K_{1,Fy-uy} & K_{1,Fy-\theta z} \\ K_{1,Fy-\theta z} & K_{1,Mz-\theta z} \end{bmatrix} \tag{2.17}$$

Evidently, the stiffness submatrices of Eqs. (2.16) and (2.17) are the inverses of the compliance submatrices of Eqs. (2.6) and (2.7), respectively. Also:

$$K_{1,Fx-ux} = 1 / C_{1,ux-Fx} \tag{2.18}$$

and:

$$K_{1,Mx-\theta x} = 1 / C_{1,\theta x-Mx} \tag{2.19}$$

It has been shown in Chapter 1 that by inverting the bending-related compliance matrix of a constant rectangular cross-section microcantilever, a stiffness matrix is obtained whose components are not the direct inverses of their corresponding compliances. It has also been mentioned that although the three springs characterizing the lumped-parameter model of a microcantilever are defined by the stiffnesses $\overline{K}_{1,Fz-uz}$, $\overline{K}_{1,Fz-\theta y}$, $\overline{K}_{1,My-\theta y}$ (the algebraic inverses of $C_{1,uz\text{-}Fz}$, $C_{1,uz\text{-}My}$, $C_{1,\theta y\text{-}My}$), the stiffnesses $K_{1,Fz\text{-}uz}$, $K_{1,Fz\text{-}\theta y}$, $K_{1,My\text{-}\theta y}$ of Eqs. (1.16) – which are the components obtained by inverting the compliance matrix of Eq. (1.15) – should be used when calculating the force and moment at the free tip in terms of the deflection and slope at the same point.

All these conclusions are also valid for a variable cross-section microcantilever as demonstrated next. The compliance equation describing the bending about the y-axis is:

$$\begin{Bmatrix} u_{1z} \\ \theta_{1y} \end{Bmatrix} = \begin{bmatrix} C_{1,uz-Fz} & C_{1,uz-My} \\ C_{1,uz-My} & C_{1,\theta y-My} \end{bmatrix} \begin{Bmatrix} F_{1z} \\ M_{1y} \end{Bmatrix} \tag{2.20}$$

where the matrix of the right-hand side is $[C_{b,y}]$ of Eq. (2.6). Equation (2.20) can be rewritten by expressing the loads in terms of displacements in the form:

$$\begin{Bmatrix} F_{1z} \\ M_{1y} \end{Bmatrix} = \begin{bmatrix} K_{1,Fz-uz} & K_{1,Fz-\theta y} \\ K_{1,Fz-\theta y} & K_{1,My-\theta y} \end{bmatrix} \begin{Bmatrix} u_{1z} \\ \theta_{1y} \end{Bmatrix} \tag{2.21}$$

where the matrix of the right-hand side is the $[K_{b,y}]$ submatrix of Eq. (2.16). It is clear that:

$$[K_{b,y}] = [C_{b,y}]^{-1} \tag{2.22}$$

and the components of $[K_{b,y}]$ are related to the components of $[C_{b,y}]$ as:

$$\begin{cases} K_{1,Fz-uz} = C_{1,\theta y-My} / (C_{1,\theta y-My} C_{1,uz-Fz} - C_{1,uz-My}^2) \neq 1 / C_{1,uz-Fz} \\ = \overline{K}_{1,Fz-uz} \\ K_{1,Fz-\theta y} = C_{1,uz-My} / (C_{1,uz-My}^2 - C_{1,\theta y-My} C_{1,uz-Fz}) \neq 1 / C_{1,uz-My} \\ = \overline{K}_{1,Fz-\theta y} \\ K_{1,My-\theta y} = C_{1,uz-Fz} / (C_{1,\theta y-My} C_{1,uz-Fz} - C_{1,uz-My}^2) \neq 1 / C_{1,\theta y-My} \\ = \overline{K}_{1,My-\theta y} \end{cases} \tag{2.23}$$

Equations (2.23) prove that the stiffnesses obtained by inverting the bending-related compliance matrix are different from the stiffnesses that define the three different springs and that are calculated as the algebraic inverses of the corresponding compliances. It is useful to express one set of stiffnesses in terms of the other set as:

$$\begin{cases} K_{1,Fz-uz} = \overline{K}^2_{1,Fz-\theta y}\overline{K}_{1,Fz-uz}/(\overline{K}^2_{1,Fz-\theta y} - \overline{K}_{1,Fz-uz}\overline{K}_{1,My-\theta y}) \\ K_{1,Fz-\theta y} = -\overline{K}_{1,Fz-uz}\overline{K}_{1,Fz-\theta y}\overline{K}_{1,My-\theta y}/(\overline{K}^2_{1,Fz-\theta y} - \overline{K}_{1,Fz-uz}\overline{K}_{1,My-\theta y}) \\ K_{1,My-\theta y} = \overline{K}^2_{1,Fz-\theta y}\overline{K}_{1,My-\theta y}/(\overline{K}^2_{1,Fz-\theta y} - \overline{K}_{1,Fz-uz}\overline{K}_{1,My-\theta y}) \end{cases} \quad (2.24)$$

or as:

$$\begin{cases} \overline{K}_{1,Fz-uz} = 1/C_{1,uz-Fz} = (K_{1,Fz-uz}K_{1,My-\theta y} - K^2_{1,Fz-\theta y})/K_{1,My-\theta y} \\ \overline{K}_{1,Fz-\theta y} = 1/C_{1,uz-My} = -(K_{1,Fz-uz}K_{1,My-\theta y} - K^2_{1,Fz-\theta y})/K_{1,Fz-\theta y} \\ \overline{K}_{1,My-\theta y} = 1/C_{1,\theta y-My} = (K_{1,Fz-uz}K_{1,My-\theta y} - K^2_{1,Fz-\theta y})/K_{1,Fz-uz} \end{cases} \quad (2.25)$$

Example 2.1

The tip deflection u_{1z} and slope θ_{1y} are available for a constant cross-section rectangular microcantilever. Find the errors of calculating the tip force F_{1z} according to the approximate equation: $F_{1z} = 3EI_y/l^3\, u_{1z} + 2EI_y/l^2\, \theta_{1y}$ with respect to the force calculated by means of the exact equation: $F_{1z} = 12EI_y/l^3\, u_{1z} - 6EI_y/l^2\, \theta_{1y}$.

Solution:

The relative error is:

$$e_{Fz} = 100(F_{1z} - \overline{F}_{1z})/F_{1z} \quad (2.26)$$

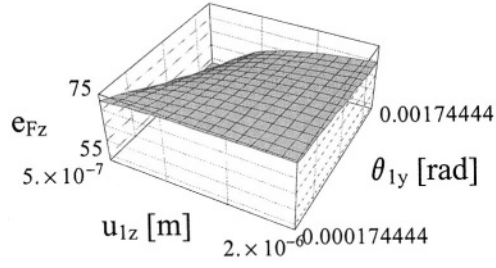

Figure 2.5 Errors in evaluating the tip force F_{1z} by approximate versus exact equations

Figure 2.5 is the plot of this error function in terms of the tip deflection u_{1z} and slope θ_{1y} when $u_{1z} \rightarrow [0.5\ \mu m; 2\ \mu m]$ and $\theta_{1y} \rightarrow [0.01^{\circ}; 0.1^{\circ}]$. It can be seen that the errors can be as high as 75% for large tip deflections and small slopes.

2.2.2 Constant Rectangular Cross-Section Design

The absolute values of the stiffnesses that define the out-of-the-plane bending about the sensitive axis (the y-axis in Fig. 2.3) have been given in Chapter 1 and are written here as:

$$\begin{cases} K_{1,Fz-uz} = Ewt^3 / l^3 \\ K_{1,Fz-\theta y} = Ewt^3 /(2l^2) \\ K_{1,My-\theta y} = Ewt^3 /(3l) \end{cases} \tag{2.27}$$

Similarly, the magnitudes of the stiffnesses that define the bending about the z-axis are:

$$\begin{cases} K_{1,Fy-uy} = Ew^3t / l^3 \\ K_{1,Fy-\theta z} = Ew^3t /(2l^2) \\ K_{1,Mz-\theta z} = Ew^3t /(3l) \end{cases} \tag{2.28}$$

The axial stiffness is:

$$K_{1,Fx-ux} = Ewt / l \tag{2.29}$$

The torsion stiffness in the case where the thickness is considerably smaller than the width (t << w) is:

$$K_{1,Mx-\theta x} = Gwt^3 /(3l) \tag{2.30}$$

Example 2.2

Compare the stiffnesses that characterize the bending about the sensitive axis (the y-axis) to the other pertinent stiffnesses of a constant rectangular cross-section microcantilever.

Solution:

The length l and width w of a microcantilever are expressed in terms of the thickness t as:

$$\begin{cases} l = c_1 t \\ w = c_2 t \end{cases} \tag{2.31}$$

The stiffnesses of Eqs. (2,27) to (2.30) can be written as functions of c_1, c_2 and t only, where t enters to its first, second or third power in the respective stiffnesses. In order to compare the stiffnesses containing t to its first power, the following ratios are introduced:

$$\begin{cases} K_{1,Fy-uy} / K_{1,Fz-uz} = c_2^2 \\ K_{1,Fx-ux} / K_{1,Fz-uz} = c_1^2 \end{cases} \tag{2.32}$$

According to their definitions given in Eq. (2.31), both c_1 and c_2 are larger than 1, and also $c_1 > c_2$ because the length is at least a few times larger than the width. It is then clear that $K_{1,Fz\text{-}uz} < K_{1,Fy\text{-}uy} < K_{1,Fx\text{-}ux}$. In other words, the smallest is the linear direct-bending stiffness $K_{1,Fz\text{-}uz}$ whereas the largest is the axial stiffness $K_{1,Fx\text{-}x}$. If c_1 and c_2 range within the intervals $[c_{i,min}, c_{i,max}]$, with i= 1, 2 , then $K_{1,Fy\text{-}uy}$ can be up to $c_{2,max}^2$ larger than $K_{1,Fz\text{-}uz}$, which, for $c_{2,max}$ = 10, means 100 times larger. $K_{1,Fx\text{-}ux}$ can be up to $c_{1,max}^2$ larger than $K_{1,Fz\text{-}uz}$, which for a value of $c_{1,max}$ = 100, for instance, signifies 10000 times larger.

The cross-stiffnesses can be related as:

$$K_{1,Fy-\theta z} / K_{1,Fz-\theta y} = c_2^2 \tag{2.33}$$

and the interpretation given to the first Eq. (2.32) remains valid. The rotary stiffnesses can be connected according to:

$$\begin{cases} K_{1,Mz-\theta z} / K_{1,My-\theta y} = c_2^2 \\ K_{1,Mx-\theta x} / K_{1,My-\theta y} = G / E = 1/[2(1+\mu)] \end{cases} \tag{2.34}$$

The second Eq. (2.34) indicates that the ratio of the torsion stiffness to the direct-bending rotation stiffness is a fixed amount in terms of geometry. Moreover, the second Eq. (2.34) indicates that for very thin cross-sections, the torsional stiffness is smaller than the bending-related one.

2.2.2.1 Sensitivity to Position of Applied Load in Mass Deposition Applications

As previously mentioned, the microcantilevers can be utilized to detect minute amounts of substances that attach to them, either chemically or physically (through adsorbtion mainly). The addition of new substances alters the elastic and inertia properties of the microcantilevers, and these

changes can be monitored quasi-statically or dynamically. The amount of mass, as well as its position on the microcantilever's plane, can be determined by combining experimental data with modeling as shown in the following examples.

Example 2.3

Calculate the amount of deposited mass, as well as its position on a constant rectangular cross-section microcantilever, as the one sketched in Fig. 2.6 when the following amounts are known: E = 180 GPa, w = 10 μm, t = 1 μm, $\theta_{1y} = 0.2^{o}$, l = 100 μm.

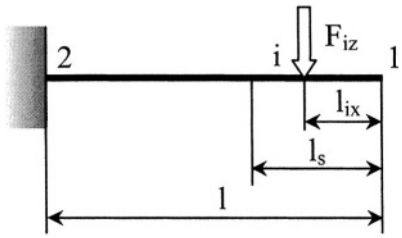

Figure 2.6 Mass added to a microcantilever as a gravitational force

Solution:

Assume that a certain amount of mass attaches locally on the microcantilever such that it can be treated as a point load. If a sensitive layer is set over the length l_s measured from the free end, the attached mass (positioned at length l_{ix}, which is measured as shown in Fig. 2.6) will deflect the microcantilever a tip slope θ_{1y} that can be determined experimentally for instance. The tip rotation is related to the force owing to the deposited mass as:

$$\theta_{1y} = F_{iz}(l - l_{ix})^2 / (2EI_y) \tag{2.35}$$

The gravitational force F_{iz} is equal to mass times the gravity constant, and therefore Eq. (2.35) changes to:

$$\Delta m = 2EI_y\theta_{1y} / [g(l - l_{ix})^2] \tag{2.36}$$

As Eq. (2.36) indicates it, a given tip rotation can be produced by different mass quantities because they can attach at different locations l_{ix} over the sensitive length l_s. Figure 2.7 shows the plot of mass in terms of the deposition location, and it can be seen that all the points located on the curve satisfy the condition of Eq. (2.36).

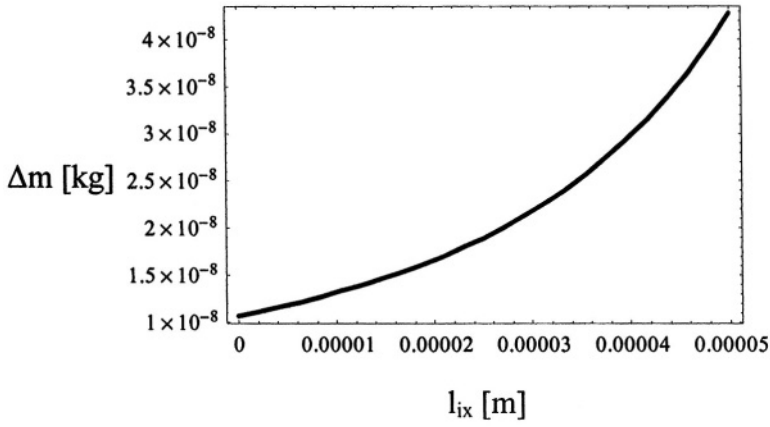

Figure 2.7 Plot of added mass as a function of position on microcantilever

In order to unequivocally determine the quantity of deposited mass, together with its position, another experimental measurement needs to be available, such as knowledge of the tip deflection. In this case, the tip displacement about the z-axis, which is caused by the mass added at point i, is calculated as:

$$u_{1z} = \Delta mg(l - l_{ix})^2(2l + l_{ix})/(6EI_y) \tag{2.37}$$

Equations (2.36) and (2.37) can now be used to solve for the unknown quantities Δm and l_{ix}.

Another possible situation occurs in the case of microcantilevers of relatively-large widths, where the mass might attach in a position that is offset from the longitudinal symmetry axis by a quantity l_{iy}. The tip slope can be determined experimentally by monitoring the position of a laser beam which is reflected by the deformed microcantilever, as sketched in Fig. 2.8. In such cases, the torsion of the microcantilever as produced by the deposited mass will shift the light reflected by the tip of the beam not only along the x-axis, by a quantity Δx, but also along the y-axis, by a quantity Δy, (as sketched in Fig. 2.8). Both amounts can be determined experimentally by specialized detection devices. The tip angles can be calculated as:

$$\begin{cases} tan\theta_{1y} = \Delta x / h \\ tan\theta_{1x} = \Delta y / h \end{cases} \tag{2.38}$$

where h is the distance measured about the z-direction between the microcantilever and the xy detection plane.

Figure 2.9 indicates the in-plane position of the attached mass. The torsion moment produced by the added mass is:

$$M_{1x} = F_{iz} l_{iy} = \Delta m g l_{iy} \tag{2.39}$$

such that the tip torsion angle is:

$$\theta_{1x} = \Delta m g l_{iy} (l - l_{ix}) / (G I_t) \tag{2.40}$$

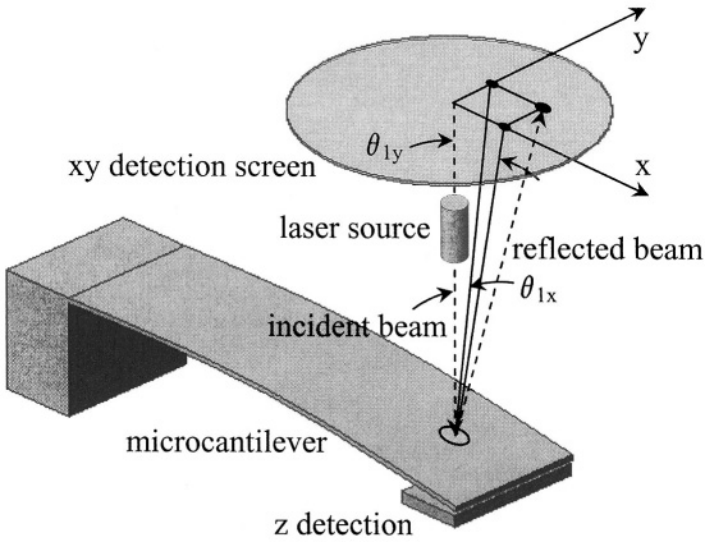

Figure 2.8 Experimental system for in-plane mass detection

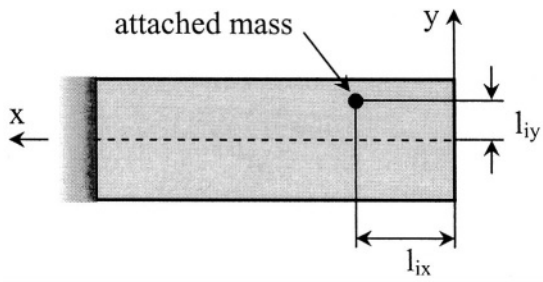

Figure 2.9 In-plane position of added mass

By coupling Eqs. (2.36) through (2.40) it is possible to determine the amount of deposited mass Δm, as well as its in-plane position defined by l_{ix} and l_{iy}.

Example 2.4

Determine the added mass Δm, as well as its position (l_{ix} and l_{iy}) on a variable cross-section microcantilever when the tip slopes θ_{1x} and θ_{1y} and the deflection u_{1z} are known.

Solution:

When the cross-section of the microcantilever is variable, the tip slope θ_{1y} (which is given in Eq. (2.35) for a constant cross-section) can be found by means of Castigliano's displacement theorem as:

$$\theta_{1y} = \Delta m g C_{i,uz-My} \tag{2.41}$$

where:

$$C_{i,uz-My} = \int_{l_{ix}}^{l} x/[EI_y(x)]dx \tag{2.42}$$

is the compliance of the microcantilever portion which is comprised between the point of application of the deposited mass and the fixed root. In a similar manner, the tip deflection can be expressed as:

$$u_{1z} = \Delta m g(C_{i,uz-Fz} - l_{ix}C_{i,uz-My}) \tag{2.43}$$

where the new partial compliance is:

$$C_{i,uz-Fz} = \int_{l_{ix}}^{l} x^2/[EI_y(x)]dx \tag{2.44}$$

The torsion-related tip slope is expressed as:

$$\theta_{1x} = \Delta m g l_{iy} C_{i,\theta x-Mx} \tag{2.45}$$

with the partial torsional compliance being:

$$C_{i,\theta x-Mx} = \int_{l_{ix}}^{l} dx/[GI_t(x)] \tag{2.46}$$

Equations (2.41), (2.43) and (2.45) can be solved for the unknown amounts Δm, l_{ix} and l_{iy} by also employing Eqs. (2.42), (2.44) and (2.46).

2.2.2.2 Three Dimensional Force Detection in Atomic Force Microscopy Applications

In atomic force microscopy (AFM) reading applications, a microcantilever such as the one sketched in Fig. 2.10 is designed to determine the amounts of force that are applied on its tip about the x-, y- and z-directions, and thus describe (*read*) a three-dimensional variable geometry. The experimental setup pictured in Fig. 2.8 can again be utilized to evaluate the tip rotations θ_{1y} and θ_{1x}.

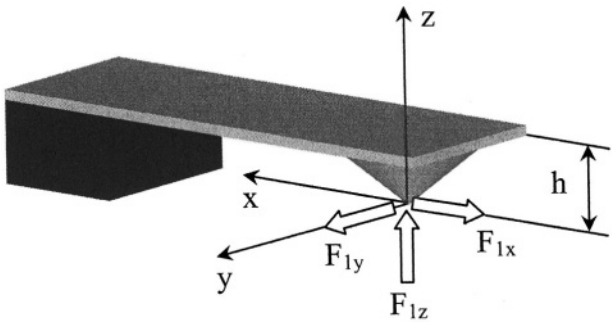

Figure 2.10 Tip forces detected by a microcantilever in atomic force microscopy

Example 2.5

Evaluate the forces F_{1x}, F_{1y} and F_{1z} that act on the tip of the constant rectangular cross-section microcantilever of Fig. 2.10 by using the available experimental data.

Solution:

It can simply be shown that the tip slope θ_{1y}, which is produced through bending by the combined action of F_{1x} and F_{1z}, as well as the slope θ_{1x}, which is generated by torsion due to F_{1y}, can be calculated as:

$$\begin{cases} \theta_{1y} = (F_{1z}l + 2F_{1x}h)l/(2EI_y) \\ \theta_{1x} = F_{1y}hl/(GI_t) \end{cases} \tag{2.47}$$

If the only experimental information consisted of the tip slopes θ_{1y} and θ_{1x}, the bending-produced deformation can globally be interpreted as generated by an *apparent* tip force, such that:

$$\theta_{1y} = F_{1z}^{app} l^2 /(2EI_y) \tag{2.48}$$

By equating the first Eq. (2.47) to Eq. (2.48) results in:

$$F_{1z}^{app} = F_{1z} + 2h/lF_{1x} \tag{2.49}$$

which indicates that by approximating the force F_{1z} according to this equation will always result in either an overestimation, when F_{1x} acts in unison with F_{1z}, or in an underestimation, when F_{1x} is directed in the opposite direction. Assuming that the force F_{1x} can be expressed as a fraction of the real F_{1z}, namely:

$$F_{1x} = cF_{1z} \tag{2.50}$$

the apparent force of Eq. (2.49) can be written as:

$$F_{1z}^{app} = (1 + 2hc/l)F_{1z} \tag{2.51}$$

The relative error between the force calculated by Eq. (2.51) and the real force is:

$$err = (F_{1z}^{app} - F_{1z})/F_{1z} = 2hc/l \tag{2.52}$$

and Fig. 2.11 is a plot giving the relative errors for the case where c = 0.5.

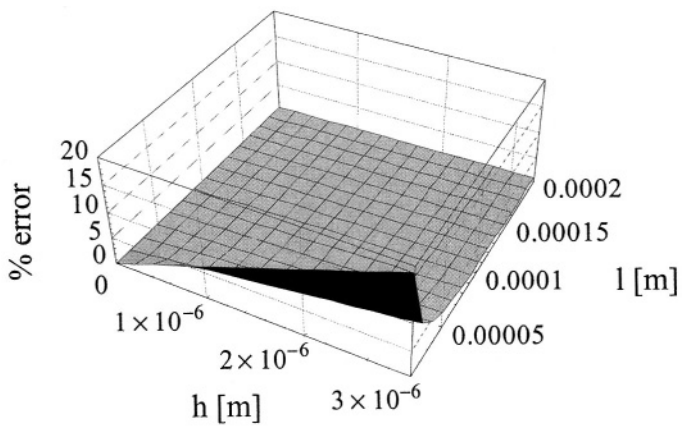

Figure 2.11 Errors between the real force and the apparent one in AFM measurements

In order to render this problem determinate, another set of experimental measurements, for instance the deflection u_{2z} at a point placed at a distance l_1 from the free end, is needed. In this case, the deflection at the experimental point of detection is:

$$u_{2z} = \{F_{1z}[2(l^3 - l_1^3) - 3l_1(l^2 - l_1^2)] + F_{1x}[3h(l^2 - l_1^2) - 6l_1h(l - l_1)]\}/(6EI_y) \tag{2.53}$$

Equations (2.47) and (2.53), together with Eqs. (2.38), enable solving for F_{1x}, F_{1y} and F_{1z}, from experimental measurements.

All these calculations are valid for and have been applied thus far to a constant cross-section microcantilever. The following example will solve this problem for the cases where the cross-section of the microcantilever is variable.

Example 2.6

Determine the force components F_{1x}, F_{1y} and F_{1z} that are applied at a microcantilever's tip when contacting a three-dimensional surface. The tip slopes θ_{1x}, θ_{1y} and tip deflection u_{1z} are experimentally available. Assume that the microcantilever's cross-section is variable and neglect the axial deformation.

Solution:

The Castigliano's displacement theorem is utilized again to express the tip displacements. The torsion, for instance, is produced by the force F_{1y} which is offset by the quantity h and the corresponding tip slope is given by the equation:

$$\theta_{1x} = C_{1,\theta x - Mx} F_{1y} h \tag{2.54}$$

where the torsional compliance has been defined in Eq. (2.12). The tip slope in bending is produced by the combined action of the forces F_{1x} and F_{1z} and is:

$$\theta_{1y} = C_{1,uz - My} F_{1z} + C_{1,\theta y - My} F_{1x} h \tag{2.55}$$

whereas the tip deflection is:

$$u_{1z} = C_{1,uz - Fz} F_{1z} + C_{1,uz - My} F_{1x} h \tag{2.56}$$

Equations (2.54), (2.55) and (2.56) enable finding the tip force components when θ_{1x}, θ_{1x} and u_{1z} are available experimentally.

2.2.3 Solid Trapezoid Design

The geometry of a trapezoid microcantilever is sketched in Fig. 2.12.

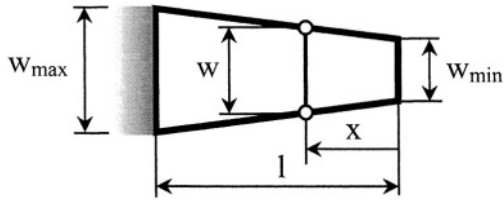

Figure 2.12 Geometry of solid trapezoid microcantilever

The variable width depends linearly on the abscissa x, namely:

$$w = w_{min} + (w_{max} - w_{min})x/l \tag{2.57}$$

By utilizing this equation in the generic compliance formulation, the stiffnesses of a solid trapezoidal microcantilever can be computed by inverting the compliance submatrices or terms. The bending-related stiffnesses corresponding to the sensitive axis are:

$$K_{1,Fz-uz} = Et^3(w_{max} - w_{min})^2 ln(w_{max}/w_{min})/\{6l^3[(w_{max} + w_{min})ln(w_{max}/w_{min}) - 2(w_{max} - w_{min})]\} \tag{2.58}$$

$$K_{1,Fz-\theta y} = Et^3(w_{max} - w_{min})\{w_{max} - w_{min}[1 + ln(w_{max}/w_{min})]\}/\{6l^2[(w_{max} + w_{min})ln(w_{max}/w_{min}) - 2(w_{max} - w_{min})]\} \tag{2.59}$$

$$K_{1,My-\theta y} = Et^3[(w_{max} - 3w_{min})(w_{max} - w_{min}) + 2w_{min}^2 ln(w_{max}/w_{min})]/\{12l[(w_{max} + w_{min})ln(w_{max}/w_{min}) - 2(w_{max} - w_{min})]\} \tag{2.60}$$

The stiffnesses that describe bending about the other bending axis (the z-axis) are:

$$K_{1,Fy-uy} = Et(w_{max} - w_{min})^3(w_{max} + w_{min})/\{12l^3[(w_{max} + w_{min}) ln(w_{max}/w_{min}) - 2(w_{max} - w_{min})]\} \tag{2.61}$$

$$K_{1,Fy-\theta z} = Et(w_{max} - w_{min})^3 w_{min} / \{12l^2 [(w_{max} + w_{min}) \ln(w_{max} / w_{min}) - 2(w_{max} - w_{min})]\} \quad (2.62)$$

$$K_{1,Mz-\theta z} = Etw_{min}^2 \{w_{max}^2 [3 - 2\ln(w_{max} / w_{min})] - 4w_{max} w_{min} + w_{min}^2\} / \{12l[(w_{max} + w_{min}) \ln(w_{max} / w_{min}) - 2(w_{max} - w_{min})]\} \quad (2.63)$$

The axial stiffness and torsional stiffness are:

$$K_{1,Fx-ux} = Et(w_{max} - w_{min}) / [l \ln(w_{max} / w_{min})] \quad (2.64)$$

$$K_{1,Mx-\theta x} = Gt^3 (w_{max} - w_{min}) / [3l \ln(w_{max} / w_{min})] \quad (2.65)$$

For the particular condition where $w_{max} = w_{min}$, the trapezoid becomes a rectangle, and consequently by taking the limit $w_{max} \rightarrow w_{min}$ in Eqs. (2.58) through (2.65), the stiffness equations for a constant, rectangular cross-section cantilever – Eqs. (2.27), (2.28), (2.29) and (2.30) – should be retrieved, which indeed occurs, as it can easily e checked.

Example 2.7

Compare a constant cross-section, rectangular microcantilever to one of trapezoid configuration, which has the same length and $w_{min} = w$ by analyzing the K_{Fz-uz} and $K_{Mx-\theta x}$ stiffnesses. Consider that $w_{max} = cw_{min}$ and c spans the [1, 5] range. Also consider that the microcantilever's cross-section is very thin ($t << w$).

Solution:

The following stiffness ratios can be formulated:

$$\begin{cases} rK_{Fz-uz} = K_{1,Fz-uz} / K_{1,Fz-uz}^* \\ rK_{Mx-\theta x} = K_{1,Mx-\theta x} / K_{1,Mx-\theta x}^* \end{cases} \quad (2.66)$$

where the * superscript indicates the constant rectangular cross-section microcantilever. By utilizing Eqs. (2.27), (2.30), (2.58) and (2.65), together with the given width relationship, Eqs. (2.66) transform into:

$$\begin{cases} rK_{Fz-uz} = (c-1)^2 \ln(1/c) / \{6[(c+1)\ln(1/c) + 2(c-1)]\} \\ rK_{Mx-\theta x} = (c-1) / \ln c \end{cases} \quad (2.67)$$

which are functions of only one variable, the parameter c. Figure 2.13 shows the variation of these stiffness ratios, and it can be seen that, as expected, the trapezoid design becomes stiffer in both bending about the sensitive axis and torsion as the ratio of the maximum width to the minimum width increases.

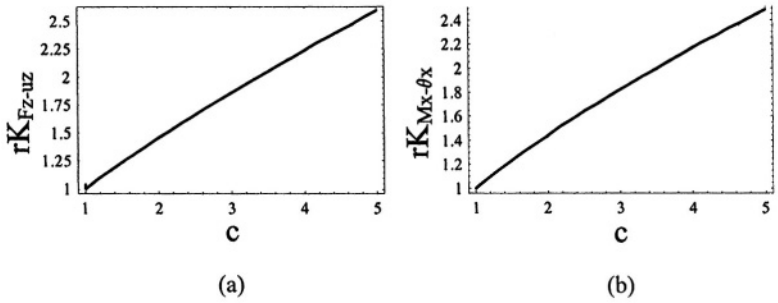

Figure 2.13 Stiffness comparison between constant rectangular and trapezoid microcantilevers: (a) bending about the sensitive axis; (b) torsion

Example 2.8

Determine the deformations at the tip of a trapezoid microcantilever that is acted upon by the forces $F_{1z} = 10\ \mu N$ and $F_{1y} = 100\ \mu N$, as indicated in Fig. 2.10. Consider that the member is constructed of a material with E = 160 GPa and $\mu = 0.25$, and that its geometry is defined by: $l = 120\ \mu m$, $w_{max} = 30\ \mu m$, $w_{min} = 5\ \mu m$, $t = 2\ \mu m$.

Solution:

The displacements that are related to y-axis bending can be expressed in terms of compliances as:

$$\begin{cases} u_{1z} = C_{1,uz-Fz} F_{1z} \\ \theta_{1y} = C_{1,uz-My} F_{1z} \end{cases} \tag{2.68}$$

It has been shown that the compliance matrix corresponding to bending about the y-axis is the inverse of the related stiffness matrix, which is given in Eq. (2.16). The terms entering the stiffness matrix of Eq. (2.16) are calculated by means of Eqs. (2.58), (2.59) and (2.60). They have the following values: $K_{1,Fz-uz} = 10.876$ N/m , $K_{1,Fz-\theta y} = 0.00047$ N , $K_{1,My-\theta y} = 3.25 \times 10^{-8}$ Nm. It follows that the stiffness matrix of Eq.(2.16) is:

$$[K_{b,y}] = \begin{bmatrix} 10.876 & -0.00047 \\ -0.00047 & 3.25/10^8 \end{bmatrix} \tag{2.69}$$

By inverting Eq. (2.69) it is found that the related compliance matrix is:

$$[C_{b,y}] = \begin{bmatrix} 0.24 & 3464.9 \\ 3464.9 & 8.06/10^{-7} \end{bmatrix} \tag{2.70}$$

and therefore $C_{1,uz\text{-}Fz} = 0.24$ m/N and $C_{1,uz\text{-}my} = 3464.9$ 1/N, such that, according to Eqs. (2.68), $u_{1z} = 2.4$ μm and $\theta_{1y} = 1.98°$.

By applying a similar procedure for the bending about the z-axis, which is produced by the force F_{1y}, the corresponding tip displacements are: $u_{1y} = 0.25$ μm and $\theta_{1z} = 0.34°$. It can be seen that although the force F_{1y} is 10 times larger than the force F_{1z}, the displacements produced by F_{1y} are approximately one order of magnitude smaller than those generated by F_{1z}.

2.2.4 Filleted Microcantilevers

Microcantilevers that are filleted at their root by means of two circular portions are customary designs, particularly in mass detection applications. The circularly-filleted area is a way of reducing the stress concentrations, but sometimes is a technological by-product, as sharp corners at a microcantilever's root are difficult to obtain through certain microfabrication procedures. However, when the fillet radius is small compared to the length and width, the fillet area is usually neglected in analytical calculations.

On occasion, the fillet radius can be relatively large, as a means of increasing the root area, and therefore increasing the torsional stiffness for instance. In such situations, neglecting the contribution of the fillet zone to the various stiffnesses defining the microcantilever would amount to unacceptable error levels. Closed form compliance equations will be provided here (as also given in Lobontiu and Garcia [8], where a more generic model has been proposed) for two filleted designs, namely: one with circular areas, and the other with elliptical areas.

2.2.4.1 Circularly-Filleted Design

A circularly-filleted microcantilever is shown in Fig. 2.14, together with the defining geometry. The filleted area extends over the entire length of the microcantilever and the length is equal to the radius of the circular fillet. The circular fillet is tangent to both the horizontal and vertical lines that meet at the root, and therefore this particular configuration is called *right circularly-filleted* microcantilever. The variable width of this configuration is:

$$w(x) = w + 2\left(r - \sqrt{r^2 - x^2}\right) \tag{2.71}$$

The eight compliances that characterize the elastic behavior of this design can be calculated according to their definitions, as defined in Eqs. (2.8) through (2.12), by using the variable width of Eq. (2.71). The bending about the sensitive axis (the y-axis, which is contained in the plane of the figure) is defined by the following compliances, which are calculated based on their definition of Eqs. (2.8) through (2.10):

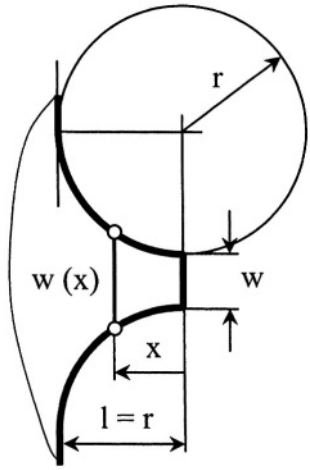

Figure 2.14 Geometry of a right circularly-filleted microcantilever

$$C_{1,uz-Fz} = 3[\,2(4+\pi)r^2 + 4(1+\pi)rw + \pi w^2 + 4(2r+w)\sqrt{w(4r+w)}\,\arctan\sqrt{1+4r/w}\,]/(4Et^3) \tag{2.72}$$

$$C_{1,uz-My} = 3[(2r+w)\ln(1+2r/w) - 2r]/(Et^3) \tag{2.73}$$

$$C_{1,\theta y-My} = 3[\,4(2r+w)/\sqrt{w(4r+w)}\,\arctan\sqrt{1+4r/w} - \pi\,]/(Et^3) \tag{2.74}$$

The corresponding stiffnesses, $K_{1,Fz\text{-}uz}$, $K_{1,Fz\text{-}\theta y}$ and $K_{1,My\text{-}\theta y}$, can be determined through inversion of the compliance matrix, which comprises, according to Eq. (2.6), the individual compliances of Eqs. (2.72), (2.73) and (2.74). The compliances that are connected to bending about the z-axis can similarly be calculated and they are:

$$C_{1,uy-Fy} = 3\{[8r^3 + 8(2+\pi)r^2 w + 2(2+3\pi)rw^2 + \pi w^3]/ [w(4r+w)] + 4(2r+w)^2[2r^2 - w(4r+w]/ \sqrt{w^3(2r+w)^3}\ arctan\sqrt{1+4r/w}\}/[4Et(2r+w)] \quad (2.75)$$

$$C_{1,uy-Mz} = 6r^2/[Etw^2(2r+w)] \quad (2.76)$$

$$C_{1,\theta z-Mz} = 12r\{(6r^2 + 4rw + w^2)/[w^2(2r+w)(4r+w)^2] + 6(2r+w)/\sqrt{w^5(4r+w)^5}\ arctan\sqrt{1+4r/w}\}/(Et) \quad (2.77)$$

Again, the stiffnesses corresponding to bending about the z-axis can be determined by inverting the compliance submatrix, Eq. (2.6), containing the terms of Eqs. (2.75), (2.76) and (2.77).

The axial compliance is:

$$C_{1,ux-Fx} = [\sqrt{1+2r/w}\ arctan\sqrt{1+4r/w} - \pi/4]/(Et) \quad (2.78)$$

and the torsional compliance for a very thin cross-section (t << w) is:

$$C_{1,\theta x-Mx} = 3EC_{1,ux-Fx}/(Gt^2) \quad (2.79)$$

The axial- and torsional-related stiffnesses are the algebraic inverses of the corresponding compliances of Eqs. (2.78) and (2.79), respectively.

2.2.4.2 Elliptically-Filleted Design

The right elliptically-filleted microcantilever and the defining geometric parameters are sketched in Fig. 2.15. The length of the microcantilever is equal to the longer semi-axis a, whereas the height of the two filleted areas is equal to the length of the other semi-axis b, but the design with the reversed axes is also possible.

The variable width for this design is:

$$w(x) = w + 2b(1 - \sqrt{1 - x^2/a^2} \quad (2.80)$$

The compliances corresponding to bending about the sensitive axis are:

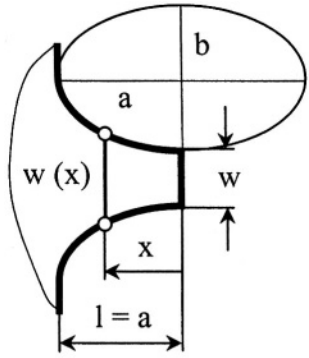

Figure 2.15 Geometry of a right elliptically-filleted microcantilever

$$C_{1,uz-Fz} = 3a^3[2(4+\pi)b^2 + 4(1+\pi)bw + \pi w^2 - 4(2b+w)\sqrt{w(4b+w)}\arctan\sqrt{1+4b/w}]/(4Eb^3t^3) \quad (2.81)$$

$$C_{1,uz-My} = 3a^2[(2b+w)\ln(1+2b/w) - 2b]/(Eb^2t^3) \quad (2.82)$$

$$C_{1,\theta y-My} = 3a[4(2b+w)/\sqrt{w(4b+w)}\arctan\sqrt{1+4b/w} - \pi]/(Ebt^3) \quad (2.83)$$

and the corresponding stiffnesses can be found by inverting the compliance submatrix of Eq. (2.6).

The compliances characterizing the bending about the z-axis are:

$$C_{1,uy-Fy} = 3a^3\{\sqrt{w}[2(2+\pi)bw + \pi w^2 + 8b^3/(4b+w)] - 4(2b+w)^2(w2+4wb-2b^2)/\sqrt{(4b+w)^3}\arctan\sqrt{1+4b/w}\}/[4Eb^3\sqrt{w^3}(2b+w)t] \quad (2.84)$$

$$C_{1,uy-Mz} = 6a^2/[E(2b+w)w^2t] \quad (2.85)$$

$$C_{1,\theta z-Mz} = 12a[(w^2+4wb+6b^2)\sqrt{w(4b+w)} + 6b(2b+w)^2\arctan\sqrt{1+4b/w}]/[E(2b+w)\sqrt{w^5(4b+w)^5}t] \quad (2.86)$$

The axial compliance is:

$$C_{1,ux-Fx} = a[(2b+w)/\sqrt{w(4b+w)} \\ arctan\sqrt{1+4b/w} - \pi/4]/(Ebt) \tag{2.87}$$

The torsional stiffness for a very thin cross-section is given in Eq. (2.79).

Example 2.9

Compare the performance of a right circularly-filleted microcantilever to the performance of a right elliptically-filleted one when $F_{1y} = 0$ and F_{1x} is the friction force between the microcantilever tip and the investigated three-dimensional surface. The microcantilevers have the same length ($l = r = a = 100\ \mu m$), thickness $t = 1\ \mu m$, width w = 1/4 and the other semi-axis of the elliptical configuration is b = 2a.

Solution:

The friction force is related to the normal force as:

$$F_{1x} = \mu F_{1z} \tag{2.88}$$

and therefore the tip slope is:

$$\theta_{1y} = (C_{1,uz-My} + \mu h C_{1,\theta y-My}) F_{1z} \tag{2.89}$$

The ratio of the θ_{1y} slopes can therefore be written as:

$$r_{\theta y} = \theta_{1y}^{(c)} / \theta_{1y}^{(e)} = (C_{1,uz-My}^{(c)} + \mu h C_{1,\theta y-My}^{(c)}) / (C_{1,uz-My}^{(e)} \\ + \mu h C_{1,\theta y-My}^{(e)}) \tag{2.90}$$

where c denotes circular and e indicates the elliptical.

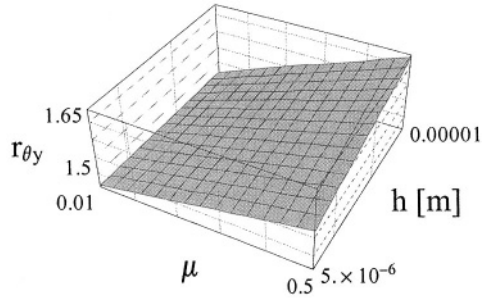

Figure 2.16 Tip slope ratio as a function of the friction coefficient and height of the microcantilever's tip

Figure 2.16 is the plot of the ratio formulated in Eq. (2.90) in terms of the friction coefficient μ and the height h of the microcantilever's tip. It can be seen that the circularly-filleted microcantilever can rotate up to 65 % more at its tip than the elliptical design, and that the ratio between the tip slopes of the two designs increases quasi-linearly when both μ and h are increasing.

2.3 Hollow Microcantilevers

Several hollow microcantilever configurations are now analyzed, and the trapezoid design sketched in Fig. 2.17 is one example. These microcantilevers can be used in AFM applications where the bending stiffness about the sensitivity axis needs to be relatively low, because this motion is the most important one.

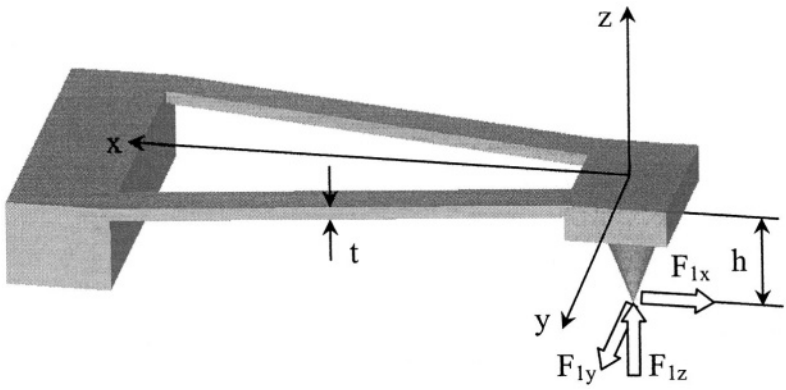

Figure 2.17 Hollow microcantilever for AFM applications

As mentioned previously, the tip of the microcantilever might interact with a non-smooth three-dimensional surface (either directly, through contact, or by preserving a specified distance to the sample), such that three force components, F_{1x}, F_{1y} and F_{1z}, act on the microcantilever's tip. The main motion is the bending produced by the F_{1z} component as the microcantilever is designed to be sensitive in bending about the y-axis. It is therefore important to define the stiffness of the member about this direction. The other two forces might also be sizeable such that the stiffnesses about the z-axis and the x-axis can also be important. In addition, the force F_{1y} produces torsion due to its offset by the quantity h, whereas the force F_{1x} is producing both axial deformation and bending of the microcantilever. Compliances will be determined for a few hollow microcantilever configurations with respect to the six degrees of freedom that can be set to define the elastic deformations at the free tip.

As shown previously, the tip slopes θ_{1y} and θ_{1x}, as well as the tip deflection u_{1z}, might be available experimentally, which can aid in determining the forces on the microcantilevers via compliances/stiffnesses.

2.3.1 Rectangular Design

Figure 2.18 is the simplified model of a hollow rectangular microcantilever with its defining geometry. The transverse portion of length l_2 is usually designed to be stiffer than the two parallel segments, and therefore this component can be considered rigid.

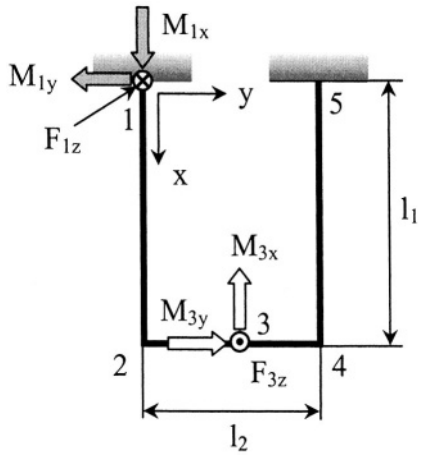

Figure 2.18 Hollow rectangular microcantilever

The point of interest in defining the elastic properties of this microcantilever is point 3, where the loads do apply in AFM applications. The loads and the resulting compliances can be separated into two subcategories, namely *out-of-the-plane* and *in-plane*. The force F_{3z} and moments M_{3x} and M_{3y} generate deformations that are out of the xy plane, as sketched in Fig. 2.18. Application of these loads will generate 6 reactions at the fixed points 1 and 5. In order to find the unknown reactions F_{1z}, M_{1x} and M_{1y} (shown in Fig. 2.18), the equations of zero displacements at point 1 have to be used in conjunction with the Castigliano's displacement theorem. By considering bending and torsion of the parallel segments, the three unknown reactions can be expressed in terms of the loads at point 3. It is thus possible to determine the displacements at 3 by using the same theorem. The deflection u_{3z} and rotation θ_{3y} are bending-coupled and their equations are:

$$\begin{Bmatrix} u_{3z} \\ \theta_{3y} \end{Bmatrix} = \begin{bmatrix} C_{3,uz-Fz} & C_{3,uz-My} \\ C_{3,uz-My} & C_{3,\theta y-My} \end{bmatrix} \begin{Bmatrix} F_{3z} \\ M_{3y} \end{Bmatrix} \tag{2.91}$$

with:

$$\begin{cases} C_{3,uz-Fz} = l_1^3/(6EI_y) \\ C_{3,uz-My} = l_1^2/(4EI_y) \\ C_{3,\theta y-My} = l_1/(2EI_y) \end{cases} \tag{2.92}$$

Equations (2.92) indicate that the compliances of the hollow rectangular design are half the ones corresponding to a single cantilever of length 1. The two segments, 1-2 and 4-5, are actually combined in parallel by means of the rigid coupler 2-4, and therefore the compliances of the parallel combination are always half the compliances of one single member. The moment M_{3x} produces a torsion angle, according to:

$$\theta_{3x} = C_{3,\theta x-Mx} M_{3x} \tag{2.93}$$

where the torsion stiffness is:

$$C_{3,\theta x-Mx} = l_1^3/[2(GI_t l_1^2 + 3EI_y l_2^2)] \tag{2.94}$$

The in-plane compliances can be determined by applying two forces, F_{3x} and F_{3y}, and a moment M_{3z} (none of them are shown in Fig. 2.18). By applying the same procedure as above, the in-plane displacements and loads that correspond to bending and axial loading are related as:

$$\begin{Bmatrix} u_{3y} \\ \theta_{3z} \end{Bmatrix} = \begin{bmatrix} C_{3,uy-Fy} & C_{3,uy-Mz} \\ C_{3,uy-Mz} & C_{3,\theta z-Mz} \end{bmatrix} \begin{Bmatrix} F_{3y} \\ M_{3z} \end{Bmatrix} \tag{2.95}$$

where:

$$\begin{cases} C_{3,uy-Fy} = l_1^3(16I_z + Al_2^2)/[24EI_z(4I_z + Al_2^2)] \\ C_{3,uy-Mz} = -l_1^2/[E(4I_z + Al_2^2)] \\ C_{3,\theta z-Mz} = 2l_1/[E(4I_z + Al_2^2)] \end{cases} \tag{2.96}$$

The axial load and deformation are decoupled from bending and they are related by the equation:

$$u_{3x} = C_{3,ux-Fx} F_{3x} \tag{2.97}$$

where the axial compliance is:

$$C_{3,ux-Fx} = l_1 /(2EA) \tag{2.98}$$

Equation (2.98) indicates that, being composed of two bars in parallel, the axial compliance of the hollow rectangular microcantilever is half the axial compliance of one component.

2.3.2 Triangular Design

A triangular hollow microcantilever is now analyzed according to the geometry shown in Fig. 2.19 (a). The out-of-the plane compliances only will be derived here, as they are the ones of main importance. The conclusions drawn with respect to the compliances of microstructures that are formed as parallel combinations of identical components can also be applied here, as the two inclined legs are identical and are coupled in parallel. It will therefore suffice finding the compliances of one leg as sketched in Fig. 2.19 (b).

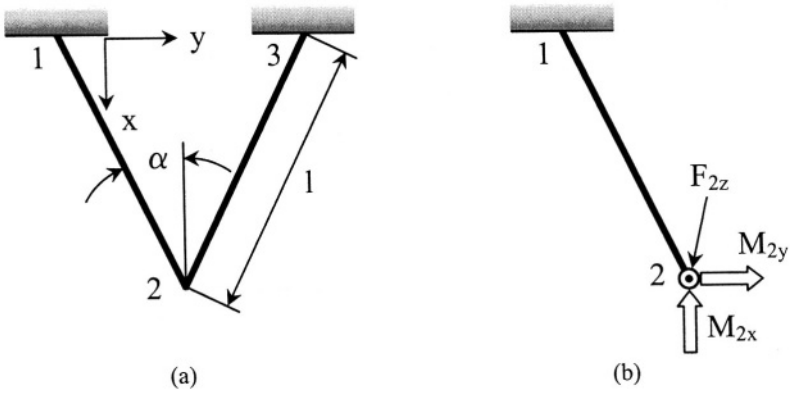

Figure 2.19 Hollow triangular microcantilever: (a) full model; (b) half model

The calculation procedure follows the one detailed previously, and therefore application of the loads F_{2z}, M_{2x} and M_{2y} will produce the elastic deformations u_{2z}, θ_{2x} and θ_{2y}. The deformations and loads are formally connected as:

$$\begin{Bmatrix} u_{2z} \\ \theta_{2x} \\ \theta_{2y} \end{Bmatrix} = \begin{bmatrix} C_{2,uz-Fz} & C_{2,uz-Mx} & C_{2,uz-My} \\ C_{2,uz-Mx} & C_{2,\theta x-Mx} & C_{2,\theta x-My} \\ C_{2,uz-My} & C_{2,\theta x-My} & C_{2,\theta y-My} \end{bmatrix} \begin{Bmatrix} F_{2z} \\ M_{2x} \\ M_{2y} \end{Bmatrix} \tag{2.99}$$

where the components of the symmetric matrix are:

$$C_{2,uz-Fz} = l^3/(3EI_y) \tag{2.100}$$

$$C_{2,uz-Mx} = -l^2 \sin\alpha/(2EI_y) \tag{2.101}$$

$$C_{2,uz-My} = l^2 \cos\alpha/(2EI_y) \tag{2.102}$$

$$C_{2,\theta x-Mx} = l[\sin^2\alpha/(EI_y) + \cos^2\alpha/(GI_t)] \tag{2.103}$$

$$C_{2,\theta x-My} = l[1/(GI_t) - 1/(EI_y)]\sin\alpha\cos\alpha \tag{2.104}$$

$$C_{2,\theta y-My} = l[\cos^2\alpha/(EI_y) + \sin^2\alpha/(GI_t)] \tag{2.105}$$

As Eq. (2.99) indicates it, bending and torsional are coupled this time, unlike the case of the hollow rectangular design.

2.3.3 Trapezoid Design

Figure 2.20 (a) is the simplified model of a hollow trapezoid microcantilever's. The stiffnesses which are of interest are found in a similar fashion to the ones determined for the triangular configuration. The coupler 2-4 is considered rigid.

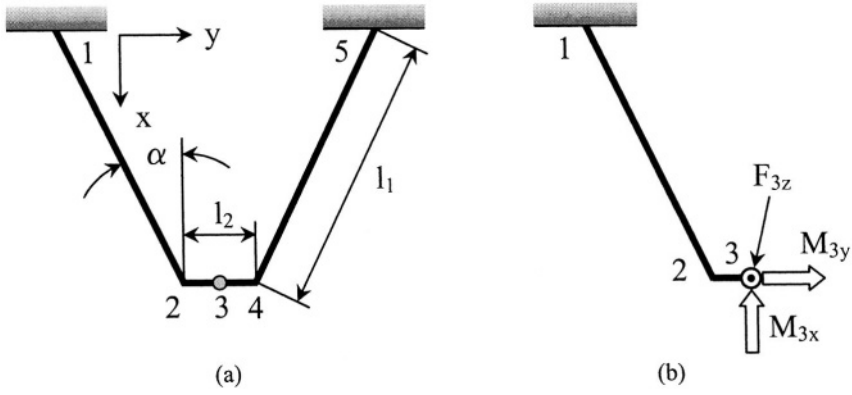

Figure 2.20 Hollow trapezoid microcantilever: (a) full model; (b) half model

By applying a procedure similar to the one used to find the out-of-the-plane compliances for half the triangular microcantilever, the displacements at the mid-point 3 in Fig. 2.20 (b) can be expressed as:

$$\begin{Bmatrix} u_{3z} \\ \theta_{3x} \\ \theta_{3y} \end{Bmatrix} = \begin{bmatrix} C_{3,uz-Fz} & C_{3,uz-Mx} & C_{3,uz-My} \\ C_{3,uz-Mx} & C_{3,\theta x-Mx} & C_{3,\theta x-My} \\ C_{3,uz-My} & C_{3,\theta x-My} & C_{3,\theta y-My} \end{bmatrix} \begin{Bmatrix} F_{3z} \\ M_{3x} \\ M_{3y} \end{Bmatrix} \tag{2.106}$$

The compliances of Eq. (2.106) are:

$$C_{3,uz-Fz} = l_1[3EI_y l_2^2 \cos^2\alpha + (4l_1^2 + 6l_1 l_2 \sin\alpha + 3l_2^2 \sin^2\alpha)GI_t] / (12EGI_y I_t) \tag{2.107}$$

$$C_{3,uz-Mx} = l_1[EI_y l_2 \cos^2\alpha - GI_t(l_1 + l_2 \sin\alpha)\sin\alpha] / (2EGI_y I_t) \tag{2.108}$$

$$C_{3,uz-My} = l_1[GI_t l_1 + (EI_y + GI_t) l_2 \sin\alpha)] \cos\alpha / (2EGI_y I_t) \tag{2.109}$$

$$C_{3,\theta x-Mx} = l_1[\sin^2\alpha / (EI_y) + \cos^2\alpha / (GI_t)] \tag{2.110}$$

$$C_{3,\theta x-My} = l_1 \sin\alpha \cos\alpha [1/(GI_t) - 1/(EI_y)] \tag{2.111}$$

$$C_{3,\theta y-My} = l_1[\cos^2\alpha / (EI_y) + \sin^2\alpha / (GI_t)] \tag{2.112}$$

Example 2.10

A rectangular microcantilever and a triangular one, both hollow, provide identical tip experimental data for u_z and θ_y. Assuming the two designs have identical geometries and material properties, determine the force F_{1z} which is sensed by each configuration. Consider the following numerical values: u_z = 0.5 μm, $\theta_y = 0.001^o$, l_1 = 100 μm, w = 3 μm, t = 1 μm, E= 130 GPa, G = 0.8 E.

Solution:

The force detected by a hollow rectangular microcantilever is calculated by means of Eqs. (2.91) and (2.92) which enable solving for the unknowns F_{3z} and M_{3y}. The tip force is $F_{3z} = 3.89 \times 10^{-7}$ N.

The force corresponding to the hollow triangular microcantilever is calculated by using Eqs. (2.99) through (2.102). These compliances have been divided by 2 in order to account for the two members that compose the triangular design. The force depends on the tip semi-angle α for the hollow design. Figure 2.21 plots the tip force in terms of the semi-angle.

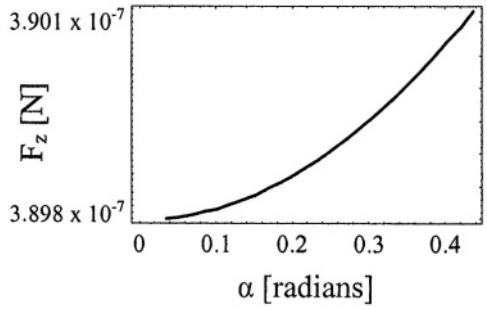

Figure 2.21 Tip force F_z as a function of the triangular microcantilever semi-angle

3. MICROHINGES

3.1 Introduction

Flexure or torsion hinges, or simply called hinges, are utilized as joints in MEMS that provide the relative motion between two adjacent rigid links through elastic deformation. In small-scale applications the microhinges mainly deform in bending or torsion. Figure 2.22 (a) shows an accelerometer whose out-of-the-plane motion is supported by four flexure hinges, which bend and enable the z-motion of the central mass.

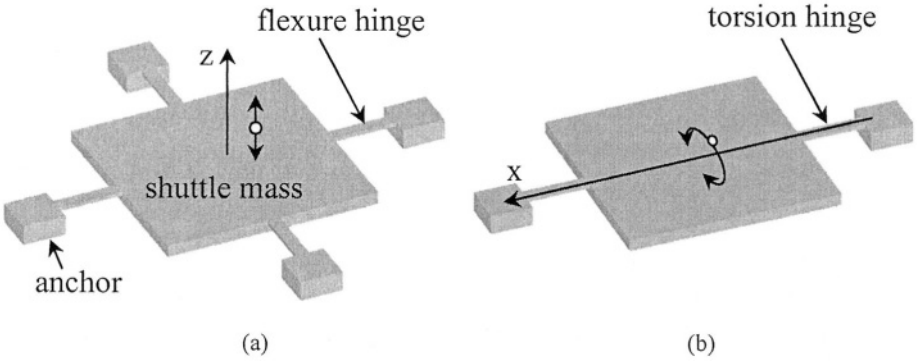

Figure 2.22 Two applications of monolithic microhinges: (a) accelerometer with four flexure hinges; (b) micromirror with two torsion hinges

Figure 22 (b) is the sketch of a micromirror whereby the rotational motion about the x-axis is enabled by the torsion of the aligned hinges. Constructively, the hinges of these two examples can be identical, only their deformations and resulting operational roles are different. Figure 2.23 shows the picture of a double-symmetry circular corner-filleted microhinge which is realized by means of the MUMPs technology. The microhinge is fixed at one end on the substrate and connects to a rectangular plate (which is used in this application for electrostatic actuation/sensing) at the other end. The main motion of this device is an out-of-the-plane bending about an axis contained in the plane of the microflexure.

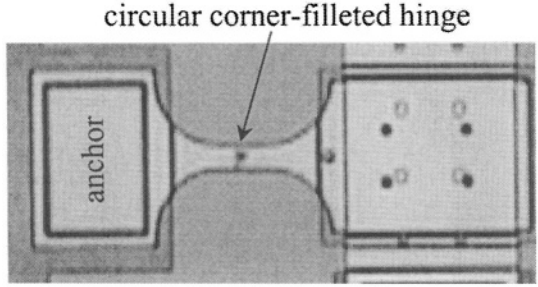

Figure 2.23 Double-symmetry circular corner-filleted microflexure

The microhinges are generally slender portions (notches) that can sustain axial and shearing deformations in addition to bending and torsion. A microhinge is modeled as a fixed-free member, exactly as the microcantilever was, and therefore all the derivations that have been developed so far in terms of stiffnesses/compliances are valid. The simplest hinge is a constant rectangular cross-section member defined by a length 1, width w and thickness t. The lumped stiffnesses and, conversely, the related compliances have been given at the beginning of this chapter when treating the microcantilevers. Other designs will be introduced here in terms of their stiffnesses in bending about the sensitive axis, torsion and axial loading. Figure 2.24 pictures three configurations that have fillets at their root areas. The fillet area is a circle of radius r– Fig. 2.24 (a) and an ellipse of semi-axes a and b – Figs. 2.24 (b) and (c). It can be seen that for all these configurations, the total length is larger than two times the circle radius r or two times the corresponding ellipse semi-axis.

The microhinge configurations that are pictured in Fig. 2.25 (again the fillet area is a circle, as in Fig. 2.25 (a) or an ellipse as in Figs. 2.25 (b) and (c)) share the feature that the total length of these designs is twice the length of the corresponding fillet feature (either the radius r – Fig. 2.25 (a) or the corresponding semi-axes – Figs. 2.25 (a) and (b)), and such designs are called *right microhinges.* The stiffnesses characterizing the bending about the

sensitive axis (the y-axis), the torsion and the axial loading will be given next for a corner-filleted microhinge, such as the one pictured in Fig. 2.24 (a), for a right circular design as sketched in Fig. 2.25 (a) and a right elliptic one – Fig. 2.25 (b).

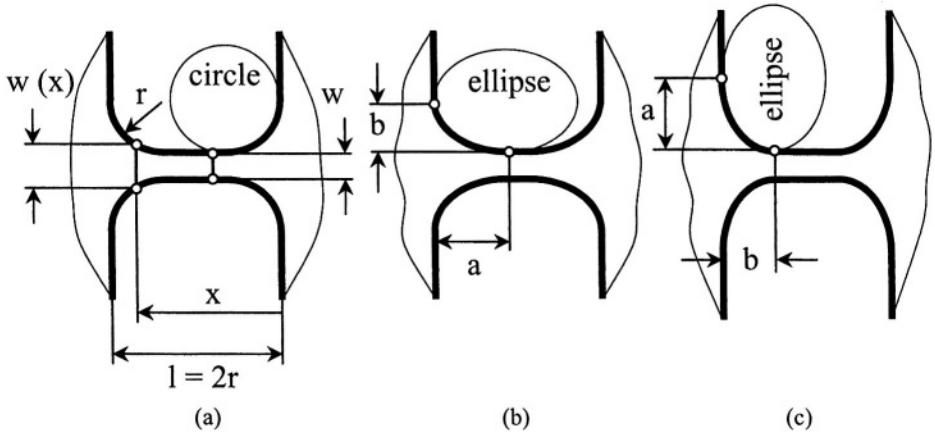

Figure 2.24 Filleted microhinges: (a) circular; (b) elliptic – large semi-axis is aligned with length; (c) elliptic – small semi-axis is aligned with length

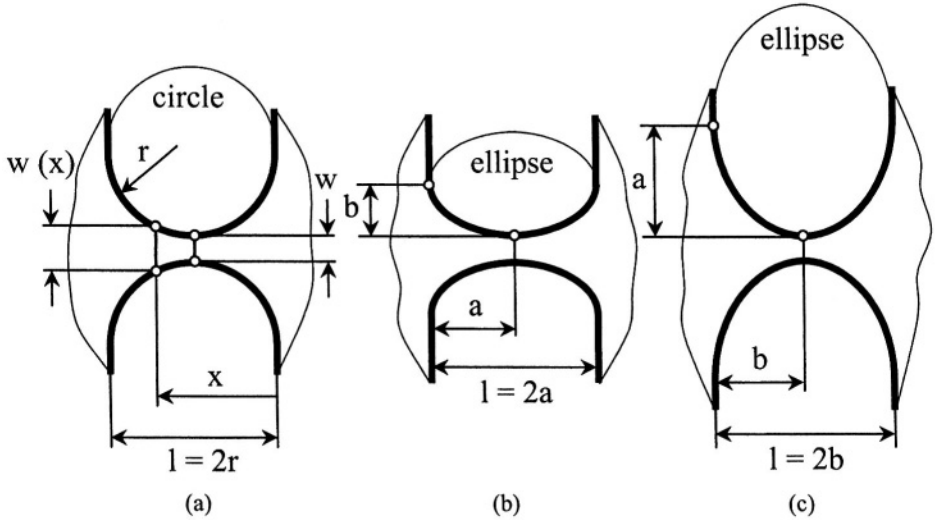

Figure 2.25 Right filleted microhinges: (a) circular; (b) elliptic – large semi-axis aligned with length; (c) elliptic – small semi-axis aligned with length

3.2 Designs

The stiffnesses and/or compliances of the above-mentioned microhinge configurations will be calculated for one end of the microhinge (for instance, the right end point from where the abscissa x is measured in Figs. 2.24 (a) and 2.25 (a)) – this end point is free and is formally denoted by 1 – with respect to the other end which is considered fixed. Of special interest will be the stiffnesses describing the bending about the sensitive y-axis, namely: $K_{1,Fz\text{-}uz}$, $K_{1,Fz\text{-}\theta y}$, $K_{1,My\text{-}\theta y}$, as well as the axial stiffness $K_{1,Fx\text{-}ux}$ and the torsional stiffness $K_{1,Mx\text{-}\theta x}$.

3.2.1 Circular Corner-Filleted Microhinge

For the circularly corner-filleted microhinge of Fig. 2.24 (a), the variable width can be expressed as:

$$w(x)=\begin{cases} w+2[r-\sqrt{x(2r-x)}\,], x\in[0,r] \\ w, x\in[r,l-r] \\ w+2[r-\sqrt{(l-x)(2r+x-l)}\,], x\in[l-r,r] \end{cases} \tag{2.113}$$

The stiffnesses that are related to bending about the sensitive axis are:

$$K_{1,Fz-uz}=Et^3wA/[6(2wAB-C^2)] \tag{2.114}$$

$$K_{1,Fz-\theta y}=Et^3wC/[6(C^2-2wAB)] \tag{2.115}$$

$$K_{1,My-\theta y}=Et^3wB/[3(2wAB-C^2)] \tag{2.116}$$

where A, B and C are functions depending on w, r and l in the form:

$$A=2[l-2r+2(2r+w)\sqrt{w/(4r+w)}\,\arctan\sqrt{w/(4r+w)}\,]-\pi w \tag{2.117}$$

$$B=(l-2r)(l^2-lr+r^2)/(3w)+lr\{\ln[w/(2r+w)]-2(l-2r)/\sqrt{w(4r+w)}\,\arctan\sqrt{1+4r/w}\,\} \tag{2.118}$$

$$C=(l-2r)[l-4r\sqrt{w/(4r+w)}\,\arctan\sqrt{1+4r/w}\,]+2rwln[w/(2r+w)] \tag{2.119}$$

The torsional stiffness for the case where t<<w is:

$$K_{1,Mx-\theta x} = Gt^3 w\{1/(l-2r) - 8\pi(2r+w)/[\pi^2 w(2r+w) - 16(r+w)^2 \arctan^2\sqrt{1+2r/w}]\}/3 \quad (2.120)$$

The axial stiffness is:

$$K_{1,Fx-ux} = Et/[(l-2r)/w + 2(2r+w)/\sqrt{w(4r+w)}\ \arctan\sqrt{1+4r/v} - \pi/2] \quad (2.121)$$

3.2.2 Right Circular Microhinge

The variable width of the right circular microhinge with the dimensions indicated in Fig. 2.25 (a) is:

$$w(x) = w + 2[r - \sqrt{x(2r-x)}] \quad (2.122)$$

The stiffnesses that define bending about the sensitive axis (the y-axis) are:

$$K_{1,Fz-uz} = Et^3[\pi\sqrt{w(4r+w)} - 4(2r+w)\arctan\sqrt{1+4r/w}]/\{24r^2 \ln[w/(2r+w)]A\} \quad (2.123)$$

$$K_{1,Fz-\theta y} = Et^3\sqrt{w(4r+w)}/(12rA) \quad (2.124)$$

$$K_{1,My-\theta y} = 2rK_{1,Fz-\theta y} \quad (2.125)$$

where the function A is:

$$A = \{\pi + \ln[w/(2r+w)]\}\sqrt{w(4r+w)} - 4(2r+w)\arctan\sqrt{1+4r/w} \quad (2.126)$$

The torsion-related stiffness is:

$$K_{1,Mx-\theta x} = 8Gt^3\sqrt{w(2r+w)}/\{3[\pi\sqrt{w(2r+w)} - 4(r+w)\arctan\sqrt{1+2r/w}]\} \quad (2.127)$$

The axial stiffness is:

$$K_{1,Fx-ux} = Et/[2(2r+w)/\sqrt{w(4r+w)}\arctan\sqrt{1+4r/w}] \quad (2.128)$$

3.2.3 Right Elliptic Microhinge

For a right elliptic microhinge, as the one pictured in Fig. 2.25 (b), the variable width is defined as:

$$w(x) = w + 2b[1-\sqrt{1-(1-2x/b)^2}] \quad (2.129)$$

The stiffness equations related to the main bending axis are quite complex, and therefore the compliance equations that describe the same bending are given here, after being calculated by means of Castigliano's displacement theorem. They are:

$$\begin{aligned} C_{1,uz-Fz} &= 3l^3\{\sqrt{w(4b+w)}[2(4-\pi)b^2+4(1+\pi)bw+\pi w^2] \\ &-(2b+w)(-4b^2+4bw+w^2)[2\arctan(2b/\sqrt{w(4b+w)} \\ &-\pi]\}/(16Eb^3t^3\sqrt{w(4b+w)}) \end{aligned} \quad (2.130)$$

$$\begin{aligned} C_{1,uz-My} &= 3l^2\{(2b+w)/\sqrt{w(4b+w)} \\ &[2\arctan(2b/\sqrt{w(4b+w)})+\pi]-\pi\}/(2Ebt^3) \end{aligned} \quad (2.131)$$

$$C_{1,\theta y-My} = 12/t^2 C_{1,ux-Fx} \quad (2.132)$$

The torsional stiffness is:

$$\begin{aligned} K_{1,Mx-\theta x} &= 4Gbt^3/\{3l[\pi+(2b+w)/\sqrt{w(4b+w)} \\ &(\pi+2\arctan(2b/\sqrt{w(4b+w)})]\} \end{aligned} \quad (2.133)$$

The axial stiffness is:

$$\begin{aligned} K_{1,Fx-ux} &= 4Ebt/\{l[4(2b+w)/\sqrt{w(4b+w)} \\ &\arctan\sqrt{1+4b/w}-\pi]\}/ \end{aligned} \quad (2.134)$$

The length l is equal to 2a in Eqs. (2.130) to (2.134), as shown in Fig. 2.25 (b).

Equation (2.134) also serves at determining the corresponding axial compliance $C_{1,ux\text{-}Fx}$ by simple inversion, so that the compliance of Eq. (2.132)

can be determined. The bending-related stiffnesses can be found by inversion of the compliance sub-matrix, namely:

$$\begin{bmatrix} K_{1,Fz-uz} & K_{1,Fz-\theta y} \\ K_{1,Fz-\theta y} & K_{1,My-\theta y} \end{bmatrix} = \begin{bmatrix} C_{1,uz-Fz} & C_{1,uz-My} \\ C_{1,uz-My} & C_{1,\theta y-My} \end{bmatrix}^{-1} \tag{2.135}$$

Example 2.11

A right circular microhinge is designed to produce a tip slope of θ_{1y} = 0.1° under a force F_{1z} = 5 μN. Determine the thickness t when l = 150 μm, w_{min} = 10 μm and E = 135 GPa and when the tip deflection is not taken into account.

Solution:

The tip force can be approximated to:

$$F_{1z} = K_{1,Fz-\theta y}\theta_{1y} \tag{2.136}$$

in the case where no other experimental data, such as the tip deflection u_{1z} is available. The cross-bending stiffness is given in Eq. (2.124). By substituting it into Eq. (2.136), the thickness can be determined as:

$$t = \sqrt[3]{12rAF_{1z}/[E\sqrt{w(4r+w)}]} \tag{2.137}$$

and its numerical value is t = 6.7 μm.

4. COMPOUND MICROCANTILEVERS

The solid microcantilevers that have been analyzed thus far were constructed as single members, but designs do also exist with several compliant members of different geometries making up together compound devices that overall function as regular microcantilevers. Two cases will be analyzed here, namely the notched microcantilever and the folded one.

4.1 Notched Microcantilevers

Applications such as mass addition detection by means of monitoring the tip slope of a microcantilever might require stiffnesses that have specific values, enabling thus capturing of discrete environmental changes such as mass deposition. For a pre-specified geometric envelope of the microcantilever (such as a rectangle), the only way of altering the stiffness is

by changing the geometry of the member, which can be done for instance by cutting notches in the original rectangular profile. The design of a microcantilever having two circular notches is pictured in Fig. 2.26 (a). This configuration is formed of a constant rectangular cross-section portion of length l_1 that is connected in series to the circularly-notched segment whose length l_2 is twice the notch radius r. The serial connection of the two distinct portions is schematically illustrated in Fig. 2.26 (b).

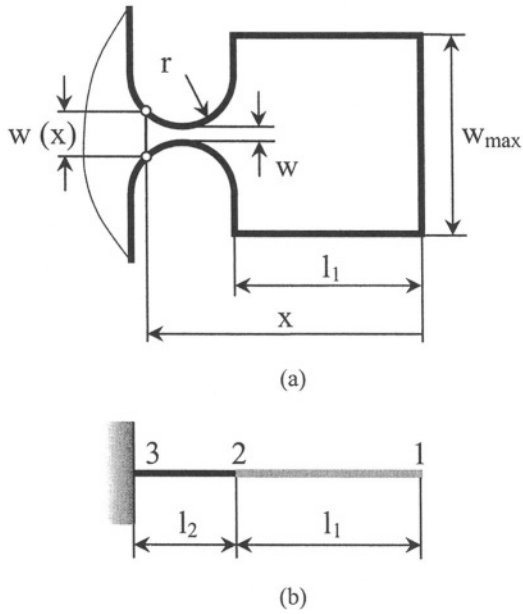

Figure 2.26 Circularly-notched microcantilever: (a) geometry; (b) equivalent series connection

The overall stiffness properties of this compound cantilever can be determined by applying a serial-connection calculation procedure, based on Castigliano's displacement theorem, as outlined in the previous chapter for two constant cross-section members. A generic formulation will be first derived here, enabling stiffness computation for any constant-thickness flexible components that are serially connected in a compound microcantilever design. The only required condition is that the compliances of any of the microcantilever's components be known. Two examples will then be solved, based on the generic formulation.

When considering that the compound microcantilever of Fig. 2.26 (b) is loaded by a transverse force F_{1z} and a moment M_{1y} at the free end, the Castigliano's displacement theorem can be applied to determine the tip deflection and slope in the following manner:

$$\begin{cases} u_{1z} = C_{1,uz-Fz} F_{1z} + C_{1,uz-My} M_{1y} \\ \theta_{1y} = C_{1,uz-My} F_{1z} + C_{1,\theta y-My} M_{1y} \end{cases} \tag{2.138}$$

where the compliances of Eqs. (2.138) are calculated as:

$$C_{1,uz-Fz} = C^{(1)}_{1,uz-Fz} + C^{(2)}_{2,uz-Fz} + 2l_1 C^{(2)}_{2,uz-My} + l_1^2 C^{(2)}_{2,\theta y-My} \tag{2.139}$$

$$C_{1,uz-My} = C^{(1)}_{1,uz-My} + C^{(2)}_{2,uz-My} + l_1 C^{(2)}_{2,\theta y-My} \tag{2.140}$$

$$C_{1,\theta y-My} = C^{(1)}_{1,\theta y-My} + C^{(2)}_{2,\theta y-My} \tag{2.141}$$

The superscripts (1) and (2) in Eqs. (2.139), (2.140) and (2.141) indicate the first component and the second component, respectively, whereas the same numbers in the subscripts indicate the point where the respective compliance has been calculated. In other words, $C^{(1)}_{1,uz\text{-}Fz}$ indicates the linear compliance of the component at the tip (the first component), calculated at point 1 and considering that the member 1-2 is fixed at 2. Similarly, $C^{(2)}_{2,uz\text{-}Fz}$ represents the linear compliance of the component at the root of the compound microcantilever (component number 2), calculated at point 2 with respect to the fixed point 3. Having found the overall compliances of the compound microcantilever, the corresponding stiffnesses are simply determined by inversion of the symmetric compliance matrix, which consists of $C_{1,uz\text{-}Fz}$, $C_{1,uz\text{-}My}$ and $C_{1,\theta y\text{-}My}$, as shown in Eq. (2.127), for instance.

It is also simple to demonstrate that the overall axial and torsional compliances are the sums of the corresponding individual compliances, namely:

$$C_{1,ux-Fx} = C^{(1)}_{1,ux-Fx} + C^{(2)}_{2,ux-Fx} \tag{2.142}$$

and

$$C_{1,\theta x-Mx} = C^{(1)}_{1,\theta x-Mx} + C^{(2)}_{2,\theta x-Mx} \tag{2.143}$$

One of the simplest two-component microcantilevers is shown in Fig. 2.27, where two rectangular cutouts have been removed symmetrically from a rectangular microcantilever.

Example 2.12

Determine the stiffness that are related to bending about the sensitive axis (which passes through the anchor) to axial deformation and torsion for a microcantilever which if formed of two constant rectangular cross-section segments, as sketched in Fig. 2.27. It is known that $l_1 = l_2 = l$, $w_1 = 2w_2 = w$, $t_1 = t_2 = t$ and $E_1 = E_2 = E$ (the sensitive plate is denoted by 1 and the thinner microcantilever by 2).

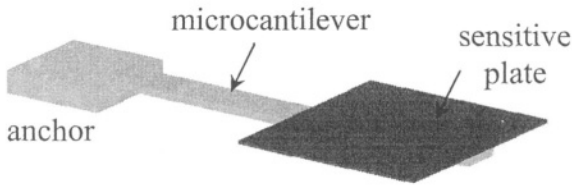

Figure 2.27 Microcantilever formed of two rectangular components

Solution:

The individual compliances of the two portions are:

$$\begin{cases} C^{(1)}_{1,uz-Fz} = 2l^3/(Ewt^3) \\ C^{(1)}_{1,uz-My} = 3l^2/(Ewt^3) \\ C^{(1)}_{1,\theta y-My} = 6l/(Ewt^3) \end{cases} \tag{2.144}$$

for the free end segment and:

$$\begin{cases} C^{(2)}_{2,uz-Fz} = 4l^3/(Ewt^3) \\ C^{(2)}_{2,uz-My} = 6l^2/(Ewt^3) \\ C^{(2)}_{2,\theta y-My} = 12l/(Ewt^3) \end{cases} \tag{2.145}$$

for the root segment. The overall compliances are found by using Eqs. (2.139) through (2.143), which enables formulation of the 2 x 2 compliance matrix. The stiffness matrix is determined by inversion of the compliance matrix and its terms are:

$$\begin{cases} K_{1,Fz-uz} = 2Ewt^3/(11l^3) \\ K_{1,Fz-\theta y} = -7Ewt^3/(33l^2) \\ K_{1,My-\theta y} = 10Ewt^3/(33l) \end{cases} \quad (2.146)$$

The overall axial stiffness is:

$$K_{1,Fx-ux} = 1/C_{ux-Fx} = 1/[l/(2Ewt) + l/(Ewt)] = 2Ewt/(3l) \quad (2.147)$$

an the overall torsion stiffness is:

$$K_{1,Mx-\theta x} = 1/C_{1,\theta x-Mx} = 1/[3l/(2Gwt^3) + 3l/(Gwt^3)] = 2Gwt^3/(9l) \quad (2.148)$$

Example 2.13

Determine the mass that attaches to the microcantilever sketched in Fig. 2.26 (a), assuming that the deposition takes place at the free end on the longitudinal (symmetry) axis. The tip slope θ_{1y} is 0.02° and known are also the following material and geometry parameters: E = 140 GPA, l_1 = 100 μm, r = 12 μm, w_{max} = 26 μm, w = 2 μm, t = 1 μm.

Solution:

The free end slope can be expressed in this case as:

$$\theta_{1y} = C_{1,uz-My} F_{1z} \quad (2.149)$$

where $C_{1,uz-My}$ is calculated by means of Eq. (2.140). The component compliances are calculated as:

$$C^{(1)}_{1,uz-My} = 6l^2/(Ew_{max}t^3) \quad (2.150)$$

$$C^{(2)}_{2,uz-My} = 12r^2[2\arctan(2r/\sqrt{w(w+4r)}) - \pi]/[\sqrt{w(w+4r)}Et^3] \quad (2.151)$$

$$C^{(2)}_{2,\theta y-My} = C^{(2)}_{2,uz-My}/r \quad (2.152)$$

Because the gravity force is equal to mass times gravitational acceleration, Eq. (2.149) gives the unknown mass as:

$$\Delta m = \theta_{1y} / (g C_{1,uz-My}) \qquad (2.153)$$

By using the data of this example, the numerical value of the attached mass is 1.57×10^{-9} kg.

4.2 Folded Microcantilevers

Figure 2.28 shows a design which utilizes a folded series/parallel configuration consisting of one microcantilever that is attached serially to another microcantilever pair. This particular design is also known as *microcantilever-in- microcantilever* – Spacek et al. [9]. The primary out-of-the-plane bending is realized by the two side microcantilevers, such that the deformation of the center (inner) microcantilever, which is serially connected to the outer pair, is augmented.

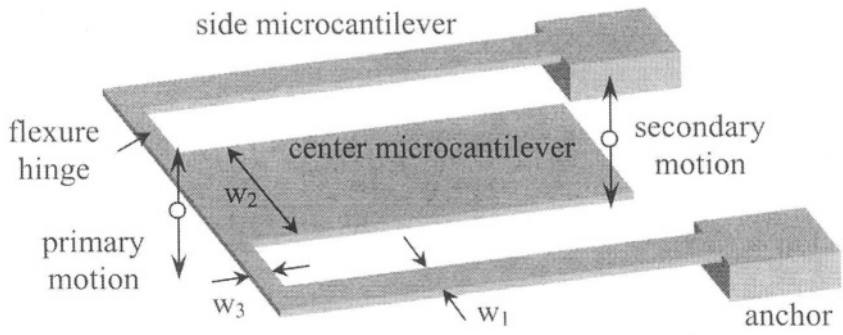

Figure 2.28 Folded microcantilever

Figure 2.29 (a) is the simplified model of a planar folded microcantilever as the one shown three-dimensionally in Fig. 2.28, and it is considered first that the two cross microhinges 2-3 and 3-5 of Fig. 2.29 (a) are rigid.

One advantage of the folded microcantilever design is space saving, because the compliant member 3-4 is placed inside the space enclosed by the two root compliant members 1-2 and 5-6, as shown in Fig. 2.29 (a). Figure 2.29 (b) indicates that in reality, the member 3-4 can be mirrored with respect to the 2-5 line and placed outside the space formed by the links 1-2, 2-5 and 5-6. On the other hand, the two identical components, 1-2 and 5-6, can be reduced to one single component, as demonstrated for hollow rectangular microcantilevers in this chapter. As a consequence, the equivalent simplified model of a folded microcantilever is sketched in Fig. 2.29 (c), and consists of two compliant members connected serially.

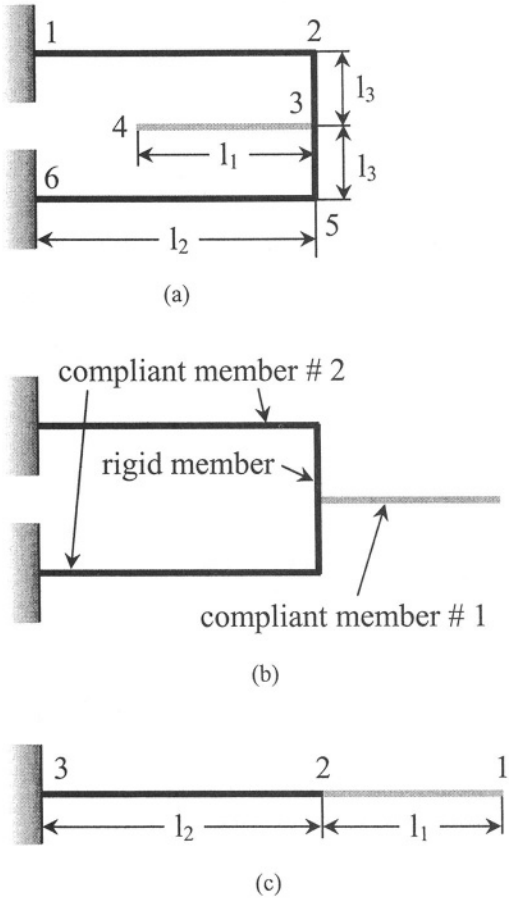

Figure 2.29 Geometry and loading for a folded microcantilever. (a) beam model; (b) simplified parallel/series model; (c) simplified equivalent series model

This last configuration was studied in the previous sub-section, and the out-of-the-plane, bending-related compliances are:

$$C_{1,uz-Fz} = C^{(1)}_{1,uz-Fz} + (C^{(2)}_{2,uz-Fz} + 2l_1 C^{(2)}_{2,uz-My} + l_1^2 C^{(2)}_{2,\theta y-My})/2 \quad (2.154)$$

$$C_{1,uz-My} = C^{(1)}_{1,uz-My} + (C^{(2)}_{2,uz-My} + l_1 C^{(2)}_{2,\theta y-My})/2 \quad (2.155)$$

$$C_{1,\theta y-My} = C^{(1)}_{1,\theta y-My} + C^{(2)}_{2,\theta y-My}/2 \quad (2.156)$$

Compared to the original equations of a two-member serial microcantilever – Eqs. (2.139), (2.140) and (2.141) –, all compliances of the root member 2 in

Fig. 2.29 (c) are divided by 2 because in actuality there are two such segments – see Fig. 2.29 (b) – which are connected in parallel, and, as demonstrated for hollow rectangular microcantilevers, the resulting compliances of the equivalent member are half the ones of a single component member.

Example 2.14

Compare the linear bending stiffness of a folded microcantilever having constant rectangular cross-section compliant members with $I_{y1} = 2I_{y2}$ to the linear bending stiffness of a similar folded microcantilever where $I_{y1} = I_{y2}$. Consider the two designs have lengths that are correspondingly identical.

Solution:

For constant rectangular cross-section compliant members, the generic Eqs. (2.154), (2.155) and (2.156) reduce to:

$$C_{1,uz-Fz} = [\,l_2(6l_1^2 + 3l_1l_2 + 2l_2^2)I_{y1} + 4l_1^3 I_{y2}\,] / (12EI_{y1}I_{y2}) \quad (2.157)$$

$$C_{1,uz-My} = [\,l_2(2l_1 + l_2)I_{y1} + 2l_1^2 I_{y2}\,] / (4EI_{y1}I_{y2}) \quad (2.158)$$

$$C_{1,\theta y-My} = (l_2 I_{y1} + 2l_1 I_{y2}) / (2EI_{y1}I_{y2}) \quad (2.159)$$

The stiffness matrix can be obtained by inverting the corresponding compliance matrix, as has been previously explained in Eq. (2.135). The generic stiffness $K_{1,Fz\text{-}uz}$ is located in the first row and first column of the generic stiffness matrix, and its equation is:

$$K_{1,Fz-uz} = 24EI_{y1}I_{y2}(l_2 I_{y1} + 2l_1 I_{y2}) / [\,l_2^3(l_2 - 6l_1)I_{y1}^2 + 8l_1l_2(l_1^2 + l_2^2)I_{y1}I_{y2} + 4l_1^4 I_{y2}^2\,] \quad (2.160)$$

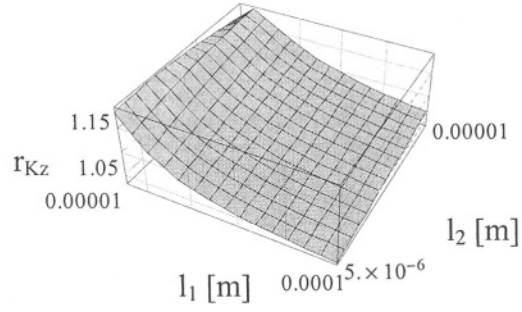

Figure 2.30 Ratio of K_z stiffnesses

The stiffness of the first design can be found by taking $I_{y2} = 2I_{y1}$ in Eq. (2.160) and the stiffness of the second design also results from Eq. (2.160) when taking $I_{y2} = I_{y1}$. The ratio of the two stiffnesses is plotted in Fig. 2.30. It can be seen that the stiffness of the microcantilever with $I_{y2} = 2I_{y1}$ can be up to 15 % higher than the stiffness of the design with $I_{y2} = I_{y1}$.

Example 2.15

Find the linear bending stiffness $K_{1,uz\text{-}Fz}$ of the folded microcantilever drawn in Fig. 2.31 by only considering the bending deformations in the five parallel legs. Known are the lengths l_1, l_2 and l_3 (assume that $l_3 = 2l_1$) of the three bending-compliant legs, as well as the cross-sectional moment of inertia, I_y (identical for all compliant legs), and the material Young's modulus E. Compare this stiffness with the one corresponding to a regular folded microcantilever with legs of length l_1 and l_2, as the one shown in Fig. 2.29 (a).

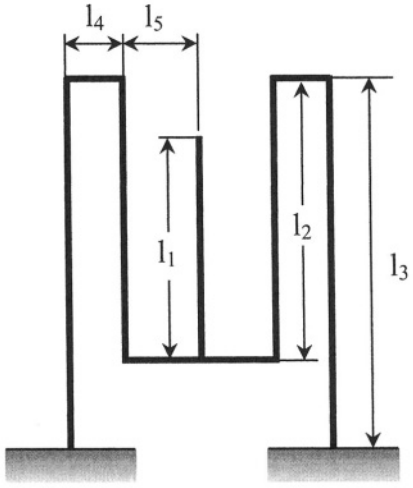

Figure 2.31 Folded microcantilever with two pairs of side long segments and a middle shorter segment

Solution:

When only bending of the relatively-long beams is considered, the folded microcantilever of Fig. 2.31 behaves as a serial-parallel combination of the three different beams. Similar to the algorithm presented for a folded microcantilever with two different beams, the present case has the following compliances that are associated with the free end of the middle microbeam:

$$C_{1,uz-Fz} = C^{(1)}_{1,uz-Fz} + [\,C^{(2)}_{2,uz-Fz} + 2l_1 C^{(2)}_{2,uz-My} + l_1^2 C^{(2)}_{2,\theta y-My} + C^{(3)}_{3,uz-Fz} + 2(l_1+l_2)C^{(3)}_{3,uz-My} + (l_1+l_2)^2 C^{(3)}_{3,\theta y-My}\,]/2 \qquad (2.161)$$

$$C_{1,uz-My} = C^{(1)}_{1,uz-My} + [\,C^{(2)}_{2,uz-My} + l_1 C^{(2)}_{2,\theta y-My} + C^{(3)}_{3,uz-My} + (l_1 + l_2)C^{(3)}_{3,\theta y-My}\,]/2 \tag{2.162}$$

$$C_{1,\theta y-My} = C^{(1)}_{1,\theta y-My} + [\,C^{(2)}_{2,\theta y-My} + C^{(3)}_{3,\theta y-My}\,]/2 \tag{2.163}$$

where the individual compliances of the three microbeams are indicated by the superscripts 1,2 and 3.

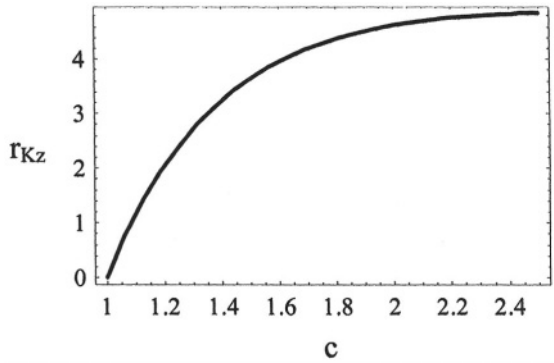

Figure 2.32 Stiffness ratio: two- versus three-leg folded microcantilevers

Because there are two beams number 2 and also two beams number 3, each pair being a parallel combination of two identical beams, the respective compliances have been divided by two, as shown in Eqs. (2.161), (2.162) and (2.163). The stiffness $K_{1,Fz\text{-}uz}$ can be found by inverting the symmetric compliance matrix formed with the three compliances defined here, as the term in the first row and first column. Its equation is:

$$K_{1,Fz-uz} = 12(l_1 + 2l_2)EI_y/[5(l_2 - l_1)(3l_1 + l_2)^3] \tag{2.164}$$

For a two-leg folded microcantilever, the z-stiffness was determined in the previous example.

Figure 2.32 plots the ratio of the $K_{1,Fz\text{-}uz}$ stiffness for a regular two-leg folded microcantilever to the similar stiffness of this three-leg configuration for the particular case where $l_3 = 2l_1$ and when considering that $l_2 = cl_1$, where the fraction c ranges within the [1, 2.5] interval. As it can be seen, the stiffness of the regular folded microcantilever can be up to 4 times higher than the stiffness of the design analyzed herein.

A more complete model of the folded microcantilever would be one accounting for torsion of the cross microhinges (which have been considered

rigid thus far), in addition to the bending of the relatively-long beams. By applying a force F_{4z} perpendicularly to the plane of the microhinge, as well as a moment M_{4y}, as sketched in Fig. 2.33, the out-of-the-plane bending (which is the operational deformation of the system) can be studied.

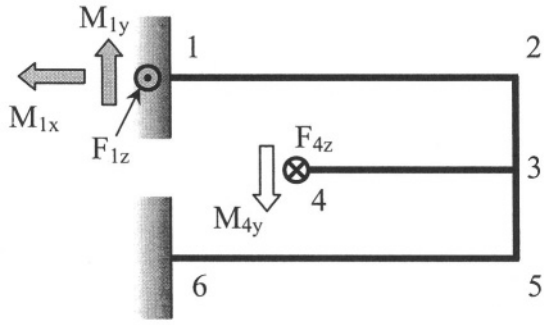

Figure 2.33 Folded microcantilever with torsional hinges included in the model

The system is three times indeterminate because three equations of static equilibrium can only solve for three unknown reactions out of the six unknowns introduced by the two fixed supports 1 and 6. By applying again Castigliano's displacement theorem, the three reactions at point 1, M_{1x}, M_{1y} and F_{1z}, can be determined by using the following boundary conditions:

$$\begin{cases} \theta_{1x} = 0 \\ \theta_{1y} = 0 \\ u_{1z} = 0 \end{cases} \tag{2.165}$$

Having found these unknown reactions, the free end deflection u_{4z} and slope θ_{4y} can be found and expressed in the known manner:

$$\begin{cases} u_{4z} = C_{4,uz-Fz} F_{4z} + C_{4,uz-My} M_{4y} \\ \theta_{4y} = C_{4,uz-My} F_{4z} + C_{4,\theta y-My} M_{4y} \end{cases} \tag{2.166}$$

The equations of the three global compliances entering Eqs. (2.166) are quite complex and are not given explicitly here. The following example will however express these compliances for a particular case.

Example 2.16

Calculate the three compliances of Eqs. (2.166) for a two-leg folded microcantilever defined by: $I_{y1} = I_{y2} = I_{y3} = I_y$, $l_1 = l_3 = l$, $l_2 = 2l_1$. Also consider that Poisson's ratio of the material is $\mu = 0.25$, and that the microcantilever is very thin.

Solution:

Young's modulus and the shear modulus are connected as:

$$G = E/[2(1+\mu)] = E/2.5 \tag{2.167}$$

when Poisson's ratio is equal to 0.25. In the case of very thin cross-sections, the relationship between the torsional moment of inertia and the regular (bending) moment of inertia is:

$$I_t = 4I_y \tag{2.168}$$

By using Eqs. (2.167) and (2.168), together with the relationships known in this example, the following compliances are obtained:

$$\begin{cases} C_{4,uz-Fz} = 5.864l^3/(EI_y) \\ C_{4,uz-My} = 1.75l^2/(EI_y) \\ C_{4,\theta y-My} = 3.25l/(EI_y) \end{cases} \tag{2.169}$$

5. MICROBRIDGES

5.1 Introduction

Microbridges are essentially microcantilevers (or microhinges) that are fixed at both ends. They are mainly used in MEMS applications such as filters and switches. Actuation is usually applied over a region located about the member's center line, such that out-of-the-plane bending motion is achieved. The main stiffness of a fixed-fixed constant rectangular cross-section member is the one relating to z-translation (bending about the y-axis) and is formulated at the midpoint of the bridge, as sketched in Fig. 2.34.

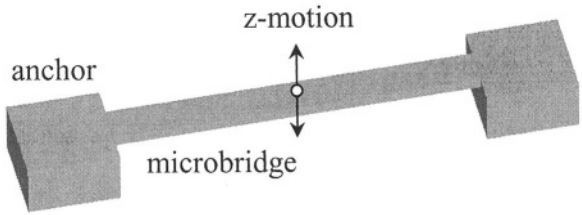

Figure 2.34 Microbridge as a fixed-fixed beam

Figure 2.35 is the photograph of a microbridge built by means of the MUMPs technology and which consists of two notched areas that border a central plate where electrostatic actuation/sensing can be applied. The advantage of this particular configuration is that bending is localized at the two notch regions such that the central portion can perform an out-of-the-plane motion, which more closely resembles the translation of a rigid body.

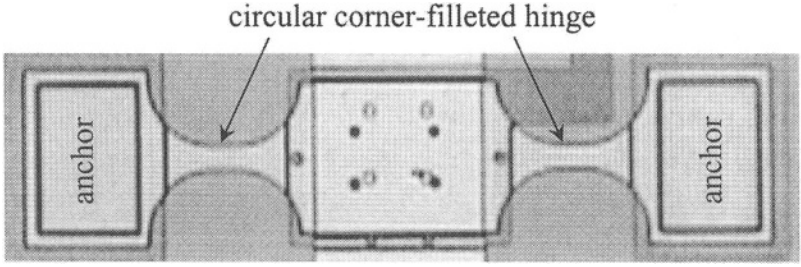

Figure 2.35 Prototype microbridge with two circular corner-filleted hinges

5.2 Single-Profile Designs

The main motions that are of interest here are the out-of-the-plane bending and the torsion about an axis passing longitudinally through the microbridge and its two anchors. As a consequence, two stiffnesses, $K_{Fz\text{-}uz}$ and $K_{Mx\text{-}\theta x}$, both evaluated at the symmetry center of the microbridge (see Fig. 2.36) will be calculated next. Examples of this generic design include the constant rectangular cross-section, the circularly-filleted, the right-circular and right-elliptic configurations that have been analyzed in this chapter's section dedicated to microhinges.

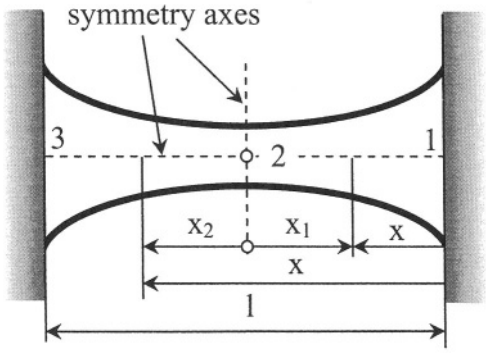

Figure 2.36 Microbridge of double symmetry

For all these designs, stiffnesses or compliances have been derived at the free end with respect to the opposite fixed one. It is considered that the microbridge has a variable cross-section and is symmetric about both the longitudinal and transverse axes in its front section, as indicated in Fig. 2.36. These features will enable expressing the sought stiffnesses of the whole microstructure in terms of the compliances that have already been defined for half the structure.

5.2.1 Bending

The z-direction stiffness at the midspan of a microbridge can be determined by considering that a force F_{2z} loads the fixed-fixed beam (microbridge) shown in Fig. 2.37. The stiffness of this beam about the z-direction at the midpoint can be calculated as:

$$K_{2,Fz-uz} = F_{2z} / u_{2z} \tag{2.170}$$

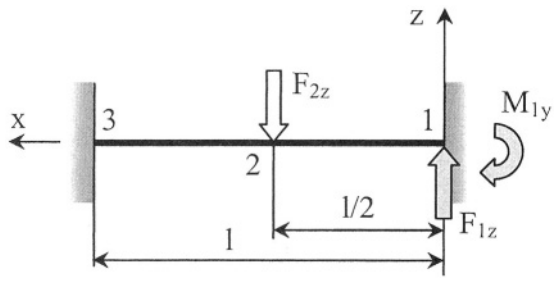

Figure 2.37 Microbridge loaded with a force at its midpoint

The two unknown reactions F_{1z} and M_{1y} need to be first determined in order to enable subsequent calculation of the deflection u_{2z}. The slope and deflection are zero at point 1, and therefore Castigliano's displacement theorem can be applied in the form:

$$\begin{cases} \theta_{1y} = \dfrac{\partial U}{\partial M_{1y}} = \displaystyle\int_0^l \frac{M_b}{EI_y(x)} \frac{\partial M_b}{\partial M_{1y}} dx = 0 \\ u_{1z} = \dfrac{\partial U}{\partial F_{1z}} = \displaystyle\int_0^l \frac{M_b}{EI_y(x)} \frac{\partial M_b}{\partial F_{1z}} dx = 0 \end{cases} \tag{2.171}$$

After expressing the bending moments on the two intervals, 1-2 and 2-3, Eqs. (2.171) can be written in the form:

$$\begin{cases} M_{1y}\int_0^{l/2}\frac{dx}{EI_y(x)} - F_{1z}\int_0^{l/2}\frac{xdx}{EI_y(x)} + (M_{1y} - F_{2z}l/2) \\ \int_{l/2}^{l}\frac{dx}{EI_y(x)} + (F_{2z} - F_{1z})\int_0^{l/2}\frac{xdx}{EI_y(x)} = 0 \\ -M_{1y}\int_0^{l/2}\frac{xdx}{EI_y(x)} + F_{1z}\int_0^{l/2}\frac{x^2dx}{EI_y(x)} - (M_{1y} - F_{2z}l/2) \\ \int_{l/2}^{l}\frac{xdx}{EI_y(x)} + (F_{1z} - F_{2z})\int_0^{l/2}\frac{x^2dx}{EI_y(x)} = 0 \end{cases} \quad (2.172)$$

By using the following variable change (as indicated in Fig. 2.36):

$$x = l/2 - x_1 \quad (2.173)$$

it is possible to express the integrals taken between 0 and l/2 in Eqs. (2.172) as:

$$\int_0^{l/2}\frac{x^2dx}{EI_y(x)} = \int_0^{l/2}\frac{(l/2 - x_1)^2dx_1}{EI_y(x_1)} = C^{(1)}_{2,uz-Fz} - lC^{(1)}_{2,uz-My} + l^2C^{(1)}_{2,\theta y-My}/4 \quad (2.174)$$

$$\int_0^{l/2}\frac{xdx}{EI_y(x)} = \int_0^{l/2}\frac{(l/2 - x_1)dx_1}{EI_y(x_1)} = -C^{(1)}_{2,uz-My} + lC^{(1)}_{2,\theta y-My}/2 \quad (2.175)$$

$$\int_0^{l/2}\frac{dx}{EI_y(x)} = \int_0^{l/2}\frac{dx_1}{EI_y(x_1)} = C^{(1)}_{2,\theta y-My} \quad (2.176)$$

where the superscript 1 indicates the first (1-2) symmetric part of the microbridge of Fig. 2.36. All the compliances in Eqs. (2.174), (2.175) and (2.176) are calculated at point 2 (assumed free) with respect to the fixed point 1. Such compliances have been provided for various microhinge configurations in this chapter.

The integrals that are taken between the limits of l/2 and l in Eqs. (2.172) can be expressed in a more convenient manner by using the following change of variable:

$$x = x_2 + l/2 \quad (2.177)$$

and this enables formulating the integrals in terms of the compliances of the second interval, 2-3 (where 2 is considered free and 3 fixed) as:

$$\int_{l/2}^{l} \frac{x^2 dx}{EI_y(x)} = \int_{0}^{l/2} \frac{(x_2 + l/2)^2}{EI_y(x_1)} / dx_1 = C^{(2)}_{2,uz-Fz} + lC^{(2)}_{2,uz-My} + l^2 C^{(2)}_{2,\theta y-My} / 4 \tag{2.178}$$

$$\int_{l/2}^{l} \frac{x dx}{EI_y(x)} = \int_{0}^{l/2} \frac{x_1 + l/2}{EI_y(x_1)} dx_1 = C^{(2)}_{2,uz-My} + lC^{(2)}_{2,\theta y-My} / 2 \tag{2.179}$$

$$\int_{l/2}^{l} \frac{dx}{EI_y(x)} = \int_{0}^{l/2} \frac{dx_1}{EI_y(x_1)} = C^{(2)}_{2,\theta y-My} \tag{2.180}$$

The superscript 2 in Eqs. (2.178) through (2.180) indicates the second (2-3) symmetric segment of the microbridge of Fig. 2.36, and the compliances of the same equations are calculated at point 2 (considered free) with respect to the fixed point 3. Because the way in which the variables x_1 and x_2 have been chosen, and because the two segments, 2-1 and 2-3, are identical, it follows that any compliance denoted by the superscript 1 in Eqs. (2.175) through (2.177) is identical to the corresponding compliance bearing the superscript 2 in Eqs. (2.178) through (2.180). As a consequence, Eqs. (2.172) permit solving for the unknowns F_{1z} and M_{1y} in the form:

$$\begin{cases} F_{1z} = F_{2z} / 2 \\ M_{1y} = F_{2z}(lC^{(2)}_{2,\theta y-My} - 2C^{(2)}_{2,uz-My}) / (4C^{(2)}_{2,\theta y-My}) \end{cases} \tag{2.181}$$

The superscript 2 indicates again that the compliances in Eqs. (2.181) correspond to one symmetric half of the microbridge sketched in Fig. 2.36. The deflection at midpoint 2 can now be found by using a procedure similar to the one that gave the reactions at point 1, namely:

$$u_{2z} = \frac{\partial U}{\partial F_{2z}} \tag{2.182}$$

After performing the necessary calculations, it is found that the bending stiffness is:

$$K_{2,uz-Fz} = F_{2z} / u_{2z} = 2C^{(2)}_{2,\theta y-My} / [C^{(2)}_{2,\theta y-My} C^{(2)}_{2,uz-Fz} - (C^{(2)}_{2,uz-Fz})^2] \tag{2.183}$$

A check was performed by considering that the cross-section is constant, and the compliances of Eq. (2.183) reduced to the simpler form:

$$\begin{cases} C^*_{2,uz-Fz} = (l/2)^3/(3EI_y) \\ C^*_{2,uz-My} = (l/2)^2/(2EI_y) \\ C^*_{2,\theta y-My} = (l/2)/(EI_y) \end{cases} \tag{2.184}$$

By substituting Eqs. (2.184) into Eq. (2.183), the stiffness becomes:

$$K^*_{2,uz-Fz} = 192EI_y / l_3 \tag{2.185}$$

which is indeed the stiffness of a constant cross-section fixed-fixed beam of length l.

Example 2.17

Compare the bending stiffness of a right elliptic microbridge, as the one sketched in Fig. 2.25 (b), to the bending stiffness of a constant rectangular cross-section microbridge. The two microstructures have the same length, thickness, minimum width and material properties.

Solution:

The right elliptic microbridge is formed of two identical right elliptically-filleted microhinges (as the one sketched in Fig. 2.14). As a consequence, by using the compliances of Eqs. (2.81), (2.82) and (2.83), the stiffness of Eq. (2.183) can be found for the right elliptic microbridge.

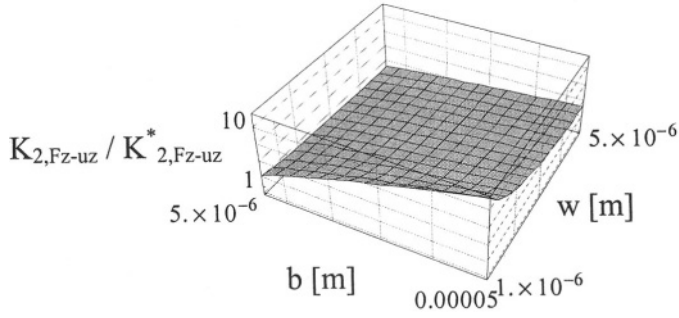

Figure 2.38 Bending stiffness comparison between right elliptic microbridge and constant rectangular cross-section microbridge

The bending stiffness of a constant rectangular cross-section microbridge is given in Eq. (2.185), and consequently, the ratio of the two microbridges, $K_{2,Fz\text{-}uz} / K^{*}_{2,Fz\text{-}uz}$ can be expressed just in terms of the parameters b and w, as plotted in Fig. 2.38. The bending stiffness of the right elliptic microbridge can be 10 times larger than the stiffness of the constant cross-section design, as illustrated in Fig. 2.38.

5.2.2 Torsion

A torque M_{2x} is applied at point 2 of the microbridge sketched in Fig 2.37 in order to determine the torsion-related stiffness at that point. The two end-point torque reactions are equal to half the torque that is applied at midpoint 2. The torsional stiffness is defined as:

$$K_{2,Mx-\theta x} = M_{2x} / \theta_{2x} \tag{2.186}$$

The angular displacement at point 2 is found by means of Castigliano's displacement theorem as:

$$\theta_{2x} = \frac{\partial U}{\partial M_{2x}} = \int_0^l \frac{M_t}{GI_t(x)} \frac{\partial M_t}{\partial M_{2x}} dx \tag{2.187}$$

By applying considerations similar to the ones presented for bending, the torsional stiffness can be expressed as:

$$K_{2,Mx-\theta x} = 2 / C^{(2)}_{2,\theta x-Mx} \tag{2.188}$$

where the compliance of Eq. (2.188) corresponds to the 2-3 interval of the microbridge.

For a thin, constant cross-section configuration, the torsional stiffness of Eq. (2.170) simplifies to:

$$K^{*}_{2,Mx-\theta x} = 4GI_t / l \tag{2.189}$$

which is indeed the known relationship.

5.3 Compound Designs

Microbridges can be formed of different compliant segments that are connected serially and are fixed at the extremities of the chain, as pictured in Fig. 2.39 for instance. Figure 2.39 gives the geometric dimensions of a

microbridge which is composed of two identical segments, 1-2 and 4-5, which are adjacent to the middle segment 2-4.

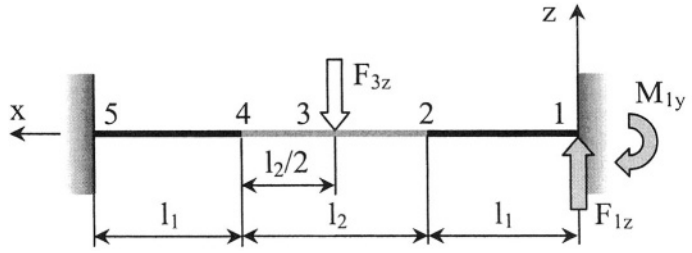

Figure 2.39 Microbridge formed of three compliant segments

Such a design can use microhinges for the identical parts 1-2 and 4-5, enabling thus the mid-segment to either translate about the z-axis (as in the case where a transverse force acts on it, as shown in Fig. 2.39), or to rotate about the longitudinal x-axis, under the action of a torque. As a consequence, the bending stiffness and the torsion stiffness that are connected to the mid-point 3 might present interest and will be derived in the following.

5.3.1 Bending

Bending of the compound microbridge of Fig. 2.39 will be analyzed first under the assumption that a transverse force F_{3z} acts at the midpoint 3. The aim is to find the linear direct bending $K_{3,Fz\text{-}uz}$ by following a derivation similar to the one detailed for single-profile microbridges. Before determining the sought stiffness, an example will be solved in order to establish connections between the compliances calculated at the midpoint of a microcantilever and the corresponding ones determined with respect to the free end.

Example 2.18

Find the bending-related compliances connected to the midpoint of a microcantilever of length l and of constant cross-section in terms of the compliances determined with respect to the free end, according to Fig. 2.40.

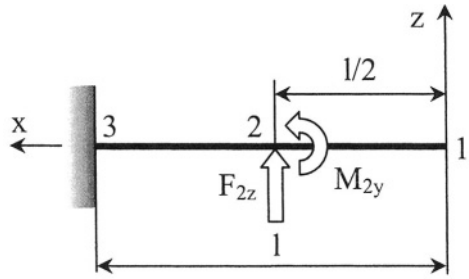

Figure 2.40 Model for mid-point compliances of a microcantilever

Solution:

By applying Castigliano's displacement theorem, the deflection and slope at point 2 can be calculated as:

$$\begin{cases} u_{2z} = l^3/(24EI_y)F_{2z} + l^2/(8EI_y)M_{2y} \\ \theta_{2y} = l^2/(8EI_y)F_{2z} + l/(2EI_y)M_{2y} \end{cases} \tag{2.190}$$

which indicates that the compliances are:

$$\begin{cases} C_{2,uz-Fz} = l^3/(24EI_y) \\ C_{2,uz-My} = l^2/(8EI_y) \\ C_{2,\theta y-My} = l/(2EI_y) \end{cases} \tag{2.191}$$

and therefore, each of these compliances has the general form of the full-length compliances given in Chapter 1, but they are calculated for half the length. They can be expressed in terms of the compliances corresponding to a microcantilever of length l as:

$$\begin{cases} C_{2,uz-Fz} = C_{1,uz-Fz}/8 \\ C_{2,uz-My} = C_{1,uz-My}/4 \\ C_{2,\theta y-My} = C_{1,\theta y-My}/2 \end{cases} \tag{2.192}$$

Returning to the generic microbridge of Fig. 2.39, the unknown reactions F_{1z} and M_{1y} are first determined by applying Castigliano's displacement theorem and the zero deflection and zero slope boundary conditions at point 1. The reactions are of the form:

$$\begin{cases} F_{1z} = c_1 F_{3z} \\ M_{1y} = c_2 F_{3z} \end{cases} \tag{2.193}$$

where the constants c_1 and c_2 are calculated as:

$$\begin{cases} c_1 = (b_1 a_{22} + b_2 a_{12})/(a_{11}a_{22} - a_{12}^2) \\ c_2 = (b_1 a_{12} + b_2 a_{11})/(a_{11}a_{22} - a_{12}^2) \end{cases} \tag{2.194}$$

The coefficients of Eqs. (2.194) depend on the compliances of the individual portions 1-2, 2-4 and 4-5 in the form:

$$a_{11} = 2C^{(1)}_{1,uz-Fz} + C^{(2)}_{2,uz-Fz}/4 + 2(l_1 + l_2)C^{(1)}_{1,uz-My} + (2l_1 + l_2/2)C^{(2)}_{2,uz-My}/2 + (l_1 + l_2)^2 C^{(1)}_{1,\theta y-My} + [l_1^2 + (l_1 + l_2/2)^2] C^{(3)}_{2,\theta y-My}/2 \quad (2.195)$$

$$a_{12} = 2C^{(1)}_{1,uz-My} + C^{(2)}_{2,uz-My}/2 + (l_1 + l_2)C^{(1)}_{1,\theta y-My} + (2l_1 + l_2/2)C^{(2)}_{2,\theta y-My}/2 \quad (2.196)$$

$$a_{22} = 2C^{(1)}_{1,\theta y-My} + C^{(2)}_{2,\theta y-My} \quad (2.197)$$

$$b_1 = C^{(1)}_{1,uz-Fz} + C^{(2)}_{2,uz-Fz}/8 + (l_1 + 3l_2/2)C^{(1)}_{1,uz-My} + (l_1 + l_2/2)C^{(2)}_{2,uz-My}/4 + l_2(l_1 + l_2)C^{(1)}_{1,\theta y-My}/2 \quad (2.198)$$

$$b_2 = -C^{(1)}_{1,uz-My} - C^{(2)}_{2,uz-My}/4 - l_2/2C^{(1)}_{1,\theta y-My} \quad (2.199)$$

The linear direct stiffness $K_{3,Fz\text{-}uz}$ is eventually found to be of the form:

$$K_{3,Fz-uz} = 1/\{(c_1^2 + c_3^2)C^{(1)}_{1,uz-Fz} + [-2c_1c_2 + 2(l_1 + l_2)c_3^2 + 2c_3c_4]C^{(1)}_{1,uz-My} + [c_2^2 + (l_1 + l_2)^2 c_3^2 + 2c_3c_4(l_1 + l_2) + c_4^2] C_{1,\theta y-My} + (c_1^2 + c_3^2)C^{(2)}_{2,uz-Fz}/8 + [l_1c_1^2 - c_1c_2 + (l_1 + l_2/2)c_3^2 + c_3c_4]C^{(2)}_{2,uz-My}/2 + [l_1^2c_1^2 + c_2^2 - 2l_1c_1c_2 + (l_1 + l_2/2)^2 c_3^2 + 2(l_1 + l_2/2)c_3c_4 + c_4^2]C^{(2)}_{2,\theta y-My}/2 \quad (2.200)$$

where:

$$\begin{cases} c_3 = c_1 - 1 \\ c_4 = l_1 + l_2/2 - c_2 \end{cases} \quad (2.201)$$

The formulation given here allows for two end segments of various shapes, provided they are identical and of double symmetry (as the microhinges treated in this chapter). The same requirement of double symmetry applies also to the middle segment, but usually this can be selected as having constant cross-section. A check has been performed for this model by assuming that all segments have identical constant rectangular cross-section

and, in addition: $l_1 = l_2 = l/3$. By using these particular values the stiffness given in Eq. (2.184) has been obtained, and this validates the more generic model developed here.

Example 2.19

Determine the bending stiffness connected to the midpoint of a microbridge which is formed of two identical segments of length l and constant cross-section of moment of inertia I_{y1} that are placed at the ends and are adjacent to a middle segment of length l and constant cross-section with $I_{y2} = 2\ I_{y1}$.

Solution:

The compliances of the two different compliant segments are:

$$\begin{cases} C^{(i)}_{i,uz-Fz} = l^3/(3EI_{yi}) \\ C^{(i)}_{i,uz-My} = l^2/(2EI_{yi}) \\ C^{(i)}_{i,\theta y-My} = l/(EI_{yi}) \end{cases} \tag{2.202}$$

where i = 1, 2. By using the particular parameters of this problem, it is found that the linear stiffness is:

$$K_{3,Fz-uz} = 1920EI_{y1}/(193l^3) \tag{2.203}$$

Example 2.20

A microbridge is formed of three segments of constant rectangular cross-section, the end portions being identical, as in Fig.2.41. Find the maximum deflection when the central segment is acted upon by a distributed load q.

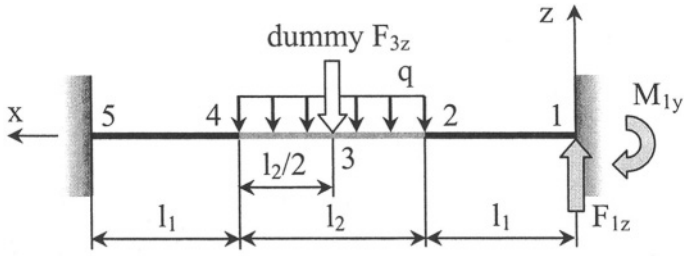

Figure 2.41 Microbridge with distributed load on the middle segment

Solution;

A dummy load ($F_{3z} = 0$ in the end) needs to be applied at point 3 in order to enable calculation of the deflection u_{3z}. The procedure is similar to the

previous ones that have already been presented. The unknown reactions have to be first determined as functions of the distributed load q and the dummy force F_{3z}, followed by calculation of u_{3z}. The calculus tool is again Castigliano's displacement theorem. The bending moments are next given, which provides the means of solving the two above-mentioned tasks:

$$M_b^{(1-2)} = F_{1z}x - M_{1y} \tag{2.204}$$

$$M_b^{(2-3)} = F_{1z}x - M_{1y} - q(x-l_1)^2/2 \tag{2.205}$$

$$M_b^{(3-4)} = F_{1z}x - M_{1y} - q(x-l_1)^2/2 - F_{3z}(x-l_1-l_2/2) \tag{2.206}$$

$$M_b^{(4-5)} = F_{1z}x - M_{1y} - ql_2(x-l_1-l_2/2) - F_{3z}(x-l_1-l_2/2) \tag{2.207}$$

In the end, the deflection at the mid-point 3 is:

$$u_{3z} = ql_2[l_2^4 I_{y1}^2 + 32l_1^4 I_{y2}^2 + 2l_1 l_2 I_{y1} I_{y2}(32l_1^2 + 20l_1 l_2 + 5l_2^2)] / [384E(l_2 I_{y1} + 2l_1 I_{y2}) I_{y1} I_{y2}] \tag{2.208}$$

5.3.2 Torsion

A similar approach can be applied when a torque M_{3x} is applied to the compound microcantilever of Fig. 2.39. The reaction moment at the end 1 is determined to be (by applying the zero rotation angle at that point and through Castigliano's displacement theorem):

$$M_{1x} = M_{3x}/2 \tag{2.209}$$

The torsional stiffness at the midpoint 3 is then calculated as:

$$K_{3,Mx-\theta x} = M_{3x}/\theta_{3x} = 4/(2C_{1,\theta x-Mx}^{(1)} + C_{2,\theta x-Mx}^{(2)}) \tag{2.210}$$

For a microbridge formed of three identical segments of identical rectangular cross-section with $l_1 = l_2 = l/3$, Eq. (2.210) simplifies to:

$$K_{3,Mx-\theta x} = 4/(3C_{1,\theta x-Mx}^{(1)}) = 4GI_t/l \tag{2.211}$$

which is the known equation, also given in Eq. (2.189).

Problems

Problem 2.1

For a constant rectangular cross-section microcantilever, the tip force that corresponds to the tip deflection and slope can be expressed as shown in Eq. (2.21) with the stiffnesses being: $K_{l,Fz\text{-}uz} = 12EI_y/l^3$, $K_{l,Fz\text{-}\theta y} = -6EI_y/l^2$, $K_{l,My\text{-}\theta y} = 4EI_y/l$. However, one can approximate the individual compliances as being the algebraic inverses of the corresponding stiffnesses as: $K_{l,Fz\text{-}uz} = 3EI_y/l^3$, $K_{l,Fz\text{-}\theta y} = 2EI_y/l^2$, $K_{l,My\text{-}\theta y} = EI_y/l$. Determine the maximum relative errors between the force F_{lz} calculated according to the first set of stiffnesses and the same force calculated by the second set of stiffnesses, when $l = 200$ μm, $w = 10$ μm, $t = 2$ μm, $E = 150$ GPa, and $u_{lz} \rightarrow [0.5\ \mu m, 1\ \mu m]$ and $\theta_{ly} \rightarrow [0.01^\circ, 0.1^\circ]$.

Answer:

Maximum relative error = 50%

Problem 2.2

Design a solid rectangular microcantilever such that its linear bending stiffness about the bending-sensitive axis, $K_{l,Fz\text{-}uz}$, is 16 times smaller than the other linear bending stiffness $K_{l,Fy\text{-}uy}$ and 100 times smaller than the axial stiffness $K_{l,Fx\text{-}ux}$.

Answer:

$$\begin{cases} l = c_1 t = 10t \\ w = c_2 t = 4t \end{cases}$$

The thickness can be chosen arbitrarily.

Problem 2.3

Determine the mass that adheres to a constant rectangular microcantilever with $w = 10$ μm, $t = 1$ μm, $l = 150$ μm and $E = 150$ GPa assuming the deposition produces no torsion of the microcantilever. Known are also the tip displacements $\theta_{ly} = 1^\circ$ and $u_{lz} = 1$ μm.

Answer:

$\Delta m = 1.88 \times 10^{-8}$ kg

Problem 2.4

A circularly-filleted microcantilever is used in a magnetic writing application. Find the maximum values of the tip force components F_{ly} and F_{lz} considering that F_{lx} is negligible. The parameters defining the microcantilever are: $E = 200$ GPa, $w = 10$ μm, $l = 100$ μm, $t = 1.5$ μm and $h =$

10 μm. The maximum tip slopes are determined experimentally as: θ_{1x} = 0.01° and θ_{1y} = 0.1°.

Answer:

$$\begin{cases} F_{1y} = \theta_{1x} / (C_{1,\theta x-Mx} h) \\ F_{1z} = \theta_{1y} / C_{1,uz-My} \end{cases}$$

The corresponding numerical values are: F_{1y} = 0.68 μN and F_{1z} = 0.98 μN.

Problem 2.5

In a microcantilever-based force detection application the experimental equipment can sense maximum tip displacements of u_{1z} = 3 μm and θ_{1y} = 0.5°. A rectangular design can be used in a rectangular envelope of l_1 = 200 μm and l_2 = 20 μm. The microfabrication technology produces a thickness of t = 1 μm and the tip has a height of 15 μm. The material is polysilicon with E = 130 GPa. What are the forces F_{1x} and F_{1z} that can be detected by a solid configuration and by a hollow one (both designs have the same square cross-section) ?

Answer:

$$\begin{cases} F_{1z} = K_{1,Fz-uz} u_{1z} + K_{1,Fz-\theta y} \theta_{1y} \\ F_{1x} h = K_{1,Fz-\theta y} u_{1z} + K_{1,My-\theta y} \theta_{1y} \end{cases}$$

For the solid design the forces are: F_{1z} = 0.332 μN and F_{1x} = 2.825 μN.
For the hollow configuration they are: F_{1z} = 0.066 μN and F_{1x} = 0.565 μN.

Problem 2.6

A hollow microcantilever needs to be designed in either a triangular or a rectangular configuration in an application where the direct linear compliance about the sensitive bending axis has to be maximum. If the cross-section is a square with the side t = 1.5 μm and the geometrical envelope for both design variants is a rectangle of length l = 100 μm and width w = 30 μm, decide the design that has to be selected.

Answer:

For the triangular design the main geometric parameters are:

$$\begin{cases} l_1 = l / \cos\alpha \\ \tan\alpha = w/(2l) \end{cases}$$

The triangular-to-rectangular compliance ratio is 1.034, and therefore the triangular design should be utilized in this application.

Problem 2.7

A hollow trapezoid microcantilever is designed to operate in an application where the torsion-produced tip slope θ_{1x} is not available, and therefore the effects of torsion have to be minimum. If the cross-section is square (t = 0.5 μm) and the maximum area where the trapeze can be inscribed is a rectangle defined by l = 200 μm and w = 20 μ, what is the best design for this application ? Known are E = 130 GPa and μ = 0.25.

Answer:

The lengths defining the trapeze are:

$$\begin{cases} l_1 = l / \cos\alpha \\ l_2 = w - 2l\tan\alpha \end{cases}$$

and the trapeze semi-angle α can range between the values of 0 to arctan [w/(21)]. The torsional compliance is minimum for a semi-angle α = 0°, and therefore for a rectangular configuration.

Problem 2.8

Determine the direct linear stiffness about the z-direction at point 3 for the hollow microcantilever sketched in Fig. 2.42. Consider that only the two thin circular portions are compliant and have a square cross-section of side t = 2 μm. The angle α is 90° and the radius r is 100 μm. Young's modulus is E = 130 GPa and Poisson's ratio is μ = 0.25. (Hint: Formulate the compliance matrix for half of the symmetric microcantilever.)

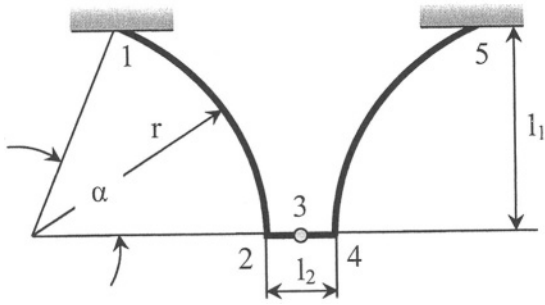

Figure 2.42 Geometry of a hollow circular microcantilever

Answer:

$K_{2,Fz\text{-}uz}$ = 1.124 N/m

Problem 2.9

A constant rectangular cross-section microhinge with l = 50 μm, w = 5 μm has to be replaced by a circularly-filleted one having the same length and

minimum width as the original design in order to increase the axial stiffness by 50%. Determine the fillet radius which will produce this stiffness.

Answer:

The axial stiffness of the circularly-filleted microhinge is 1.5 times the axial stiffness of the rectangular configuration. The fillet radius is $r = 18.3$ μm.

Problem 2.10

A circularly-notched microcantilever is used as a torsional balance in a mass deposition detection application. The constant rectangular segment is defined by $l_1 = 200$ μm and $w_{max} = 50$ μm. The notch width is $w = 2$ μm and the shear modulus is G = 80 GPa. If the notch radius is $r = l_1/2$, what is the thickness t which will produce an overall torsional stiffness of 1.35×10^{-8} Nm?

Answer:

$t = 0.69$ μm.

Problem 2.11

A folded microcantilever has a fixed length l_1 of the longer, identical legs and the same cross-section for all three legs. Determine the length of the middle leg l_2 that would minimize the out-of-the-plane bending stiffness of this design.

Answer:

If the relationship exists between the two lengths: $l_1 = cl_2$, then the linear bending stiffness is minimum when c = 1 (the legs have identical lengths).

Problem 2.12

Design a constant rectangular cross-section microbridge whose torsional-to-bending stiffness ratio is maximum.

Answer:

The stiffness ratio is:

$$K_t / K_b = l^2 / [24(1+\mu)]$$

and therefore the length of the microbridge has to be maximum whereas the material has to have a minimum Poisson's ratio.

Problem 2.13

A microbridge consists of two end corner-filleted microhinges defined by $l_1 = 100$ μm, $r_1 = 20$ μm, $w_1 = 5$ μm, and a middle plate of constant rectangular cross-section defined by $l_2 = 200$ μm, $w_2 = 50$ μm and $t = 2$ μm

(all segments have the same thickness). By also knowing E = 150 GPa, calculate the central transverse force, F_{3z}, which will produce a maximum deflection of $u_{3z} = 3\ \mu m$.

Answer:

$F_{3z} = 122\ \mu N$

Problem 2.14

A microbridge is formed of three constant rectangular cross-section members, of which the end ones are identical, The microbridge is acted upon by a central torque $M_{3x} = 1000 \times 10^{-12}$ Nm. Knowing $l_1 = l_2 = 200\ \mu m$, $t = 2\ \mu m$, $w_1 = 20\ \mu m$, $w_2 = 40\ \mu m$ and G = 60 GPa, determine the maximum angular deformation of the microbridge.

Answer:

$\theta_{3x} = 2.24^{\circ}$

Problem 2.15

A microbridge is formed of three constant rectangular cross-section segments (the end ones being identical) with $I_{y2} = 2I_{y1}$. Find the proper ratio l_2/l_1 which will maximize the mid-point deflection under the action of a distributed load acting on the middle segment. (Hint: Plot $u_{3z}(c)$; $c = l_2/l_1$).

Answer:

The ratio c needs to be maximum.

References

1. S. Morita, R. Wiesendanger, E. Meyer, *Noncontact Atomic Force Microscopy,* London, Imperial College Press, 1999.
2. B.W. Chui, *Microcantilevers for Atomic Force Microscopy,* Kluwer Academic, Boston, 2001.
3. D. Lange, H. Baltes, O. Brand, *Cantilever-based CMOS Nano-Electro-Mechanical Systems,* Berlin, Springer-Verlag, 2002.
4. M. Gad-El-Hak, *The MEMS Handbook,* CRC Press, Boca Raton, 2001.
5. J.A. Pelesko, D.H. Bernstein, *Modeling MEMS and NEMS,* CRC Press, Boca Raton, 2002.
6. M.J. Madou, *Fundamentals of Microfabrication: the Science of Miniaturization,* Second Edition, CRC Press, Boca Raton, 2002.
7. N. Lobontiu, *Compliant Mechanisms: Design of Flexure Hinges,* CRC Press, Boca Raton, 2002.
8. N. Lobontiu, E. Garcia, Two microcantilever designs: lumped-parameter model for static and modal analysis, *Journal of Microelectromechanical Systems,* 13(1), 2004, pp. 41-50.
9. M. Spacek, K.B. Brown, Y. Ma, A.M. Robinson, R.P.W. Lawson, W. Allegretto, CMOS cantilever microstructures as thin film deposition monitors, *Proceedings of the 1999 IEEE Canadian Conference on Electrical and Computer Engineering,* Edmonton, 1999, pp. 1648-1651.

Chapter 3

MICROSUSPENSIONS

1. INTRODUCTION

This chapter introduces the microsuspensions, which are MEMS components that accomplish the double role of supporting other components, which are regularly rigid, and of providing the necessary flexibility in a microdevice that has moving parts. Essentially springs, the microsuspensions are characterized here by means of their stiffnesses, which are derived both about the main direction of motion and about other directions (degrees of freedom) where other motions – usually undesired – may occur. The lumped-parameter stiffness equations of these microcomponents will further be utilized in Chapter 5 in order to study the static response of microdevices that incorporate microsuspensions.

Several microsuspension designs are comprehensively presented, for linear (translatory) motion such as beams, bent beams, U-springs, serpentine springs, bent beam serpentine springs, sagittal springs or folded beams. Other designs, such as the curved-beam springs and the spiral springs, which are intended for rotary motion applications, are also treated in detail. Solved examples are again included in order to better characterize the various designs and to compare their performances. The chapter concludes with a set of proposed problems.

2. MICROSUSPENSIONS FOR LINEAR MOTION

Although the microsuspension designs of this section can be sensitive to rotary motion, they are mainly intended to operate as linear springs in devices that undergo translatory motion.

2.1 Beam Suspensions

The simplest microsuspension is a beam which enables a rigid body to translate, to rotate or to displace in a combined translatory-rotary motion. In

doing so, the beam elastically deforms mainly under bending or/and torsion. Figures 3.1 and 3.2 illustrate two microaccelerometer configurations that are supported by two identical beams (Fig. 3.1) and by four identical beams (Fig. 3.2), respectively. Each beam is fixed at one end by means of an anchor.

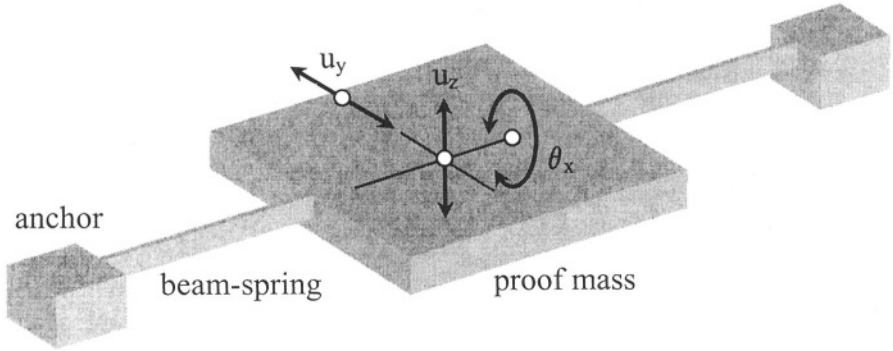

Figure 3.1 Two-beam microaccelerometer

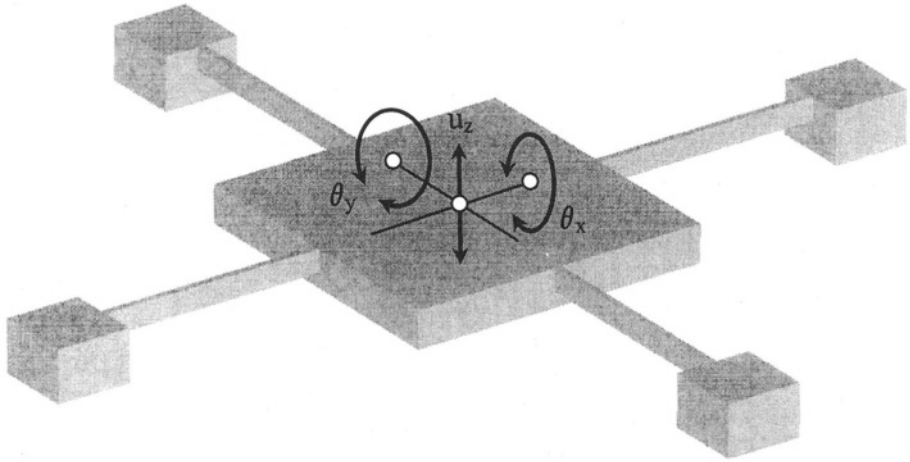

Figure 3.2 Four-beam microaccelerometer

The center proof mass of Fig. 3.1 can perform three different types of motions, namely: translation about the y-axis, out-of-the-plane translation about the z-axis and rotation about the x-axis. Any combination of these basic motions is also enabled. The beams will deflect in bending for each of the translatory motions of the proof mass and will rotate as a result of torsion during the rotary motion of the proof mass. The microaccelerometer of Fig. 3.2 is designed to be sensitive to translation about the z-axis, as well as to

rotations about the x-axis and the y-axis, respectively. Translation about either the x- or y-axis is possible, but at least one of the four members is subject to compression in that case, which might lead to elastic instability (or buckling), as will be discussed in Chapter 5.

Each beam-spring will be defined by means of stiffnesses that related to either bending or torsion. Figure 3.3 is the model of a beam suspension, and indicates the corresponding boundary conditions and the load generated by the central mass inertia when the motion about the z-axis is of interest.

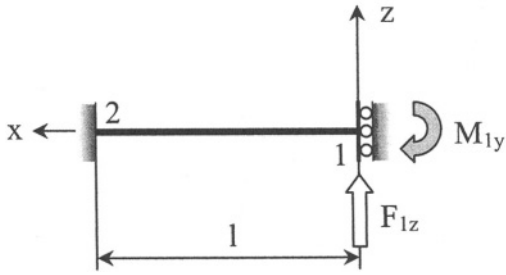

Figure 3.3 Beam-spring model for bending-related stiffness

In order to find the linear direct-bending stiffness $K_{1,Fz\text{-}uz}$ (or simply K_z), the procedure that has been applied within the previous chapters is again utilized. A force F_{1z} is applied and the unknown bending moment reaction M_{1y} is determined followed by calculation of the deflection u_{1z}, which enables specification of the sought stiffness. Both steps are solved by means of Castigliano's displacement theorem. It can be shown that in the case where the beam has a variable cross-section, the stiffness is:

$$K_z = F_{1z} / u_{1z} = 1/(C_{1,uz-Fz} - 2c_z C_{1,uz-My} + c_z^2 C_{1,\theta y-My}) \tag{3.1}$$

where:

$$c_z = C_{1,uz-My} / C_{1,\theta y-My} \tag{3.2}$$

The compliances of Eqs. (3.1) and (3.2) have been given in Chapter 1 for a constant rectangular cross-section beam. By substituting them in Eqs. (3.1) and (3.2), one obtains:

$$K_z = 12EI_y / l^3 \tag{3.3}$$

The bending compliances of Eqs. (3.1) and (3.2) can be expressed in terms of their corresponding stiffnesses, as shown in Chapter 1, in the matrix form:

$$\begin{bmatrix} C_{1,uz-Fz} & C_{1,uz-My} \\ C_{1,uz-My} & C_{1,\theta y-My} \end{bmatrix} = \begin{bmatrix} K_{1,Fz-uz} & K_{1,Fz-\theta y} \\ K_{1,Fz-\theta y} & K_{1,My-\theta y} \end{bmatrix}^{-1} \tag{3.4}$$

By substituting the compliances of Eq. (3.4) in Eqs. (3.1) and (3.2) results in:

$$K_z = K_{1,Fz-uz} \tag{3.5}$$

which shows that the linear direct-bending stiffness of a fixed-guided beam (K_z here) is identical to the one of a fixed-free beam ($K_{1,Fz\text{-}uz}$) – see Example 1.1, for instance. For a fixed-guided beam of constant cross-section, the bending stiffness (see Young and Budynas [1] for instance) is given by Eq. (3.3), which confirms the more generic Eq. (3.5)

The stiffness that is related to bending about the y-axis can be determined similarly, and its equation is:

$$K_y = F_{1y} / u_{1y} = 1/(C_{1,uy-Fy} - 2c_y C_{1,uy-Mz} + c_y^2 C_{1,\theta z-Mz}) \tag{3.6}$$

with:

$$c_y = C_{1,uy-Mz} / C_{1,\theta z-Mz} \tag{3.7}$$

It can be shown that this stiffness of the fixed-guided beam is equal to the stiffness of its corresponding fixed-free beam, namely:

$$K_y = K_{1,Fy-uy} \tag{3.8}$$

Similarly, the torsion stiffness of this configuration is:

$$K_t = K_{1,Mx-\theta x} \tag{3.9}$$

where $K_{1,Mx\text{-}\theta x}$ is the torsional stiffness of the same-geometry, fixed-free beam. When subject to axial extension, the resulting stiffness at the guided end 1 is:

$$K_x = K_{1,Fx-ux} \tag{3.10}$$

where $K_{1,Fx\text{-}ux}$ is the axial stiffness of the fixed-free beam. Defining the axial stiffness of a beam spring makes physical sense as point 1 of Fig. 3.3 can be attached to a rigid mass (such as the proof mass of Fig. 3.1) that might translate about the x-direction and cause the beam to deform axially.

Example 3.1

A constant square cross-section beam is connected to a shuttle mass in a bending-sensitive accelerometer. Design the beam-spring such that it can sense a minimum tip force of $F_{1z} = 100\ \mu N$ when a displacement sensor, as the one sketched in Fig. 3.4, can detect linear displacements with an accuracy of $u_{1z} = 0.1\ \mu m$. Consider that $t/l = \beta\ (\beta = 0.05)$ and that $E = 130 \times 10^9\ N/m^2$. Design also a circular corner-filleted microhinge, having the fillet radius $r/l = \alpha\ (\alpha = 0.1)$ and w = t, in addition to the other properties of the constant cross-section beam (w and t are the cross-sectional dimensions).

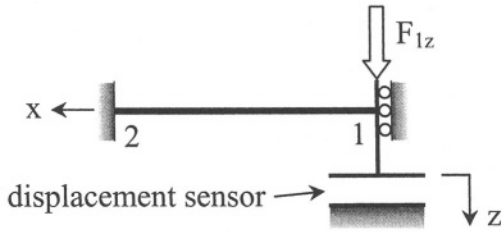

Figure 3.4 Model of a beam spring with displacement sensing

Solution:

The stiffness of the constant cross-section beam is given in Eq. (3.3), which, after substitution of the cross-sectional moment of inertia:

$$I_y = t^4 / 12 \tag{3.11}$$

and of the relationship between t and l, produces the following length of the constant cross-section beam:

$$l = F_{1z} / (\beta^4 E u_{1z}) \tag{3.12}$$

or, numerically, $l = 123\ \mu m$. Accordingly, the thickness of the square cross-section is: $t = l/20 = 6.15\ \mu m$.

For the circular corner-filleted microhinge, the bending-related stiffness has explicitly been given in Eqs. (2.114), (2.117), (2.118) and (2.119) – Chapter 2. If all the necessary substitutions are made, the length of the microflexure is $l = 46.4\ \mu m$, $t = 2.3\ \mu m$ and $r = 4.6\ \mu m$. It can be seen that the length of the constant cross-section beam is almost three times larger than the length of the circular corner-filleted microhinge.

Example 3.2

An angular accelerometer is suspended by mean of two torsion beams at its ends, as shown in Fig. 3.2. A torque M_{1x} is expected to act on a beam-

spring at its connection point to the mass. Compare the maximum rotation angle of a constant rectangular cross-section beam when w = 5 t with the maximum rotation angle of a right elliptic microhinge having the same length and minimum width with the constant cross-section design, and a root parameter b = 1/5.

Solution:

The maximum rotation angle generated by a torsion hinge is:

$$\theta_{1x} = M_{1x} / K_t \tag{3.13}$$

The ratio of the maximum rotation angle for a constant rectangular cross-section spring to the similar rotation angle corresponding to a right elliptic microhinge is:

$$r_{\theta x} = \theta^*_{1x} / \theta^e_{1x} = K^e_t / K^*_t \tag{3.14}$$

where the superscript e denotes elliptic. Figure 3.5 is a three-dimensional plot of this ratio as a function of the minimum width w and length 1. It can be seen the elliptical hinge is up to 6 times stiffer than the corresponding constant rectangular cross-section beam-spring.

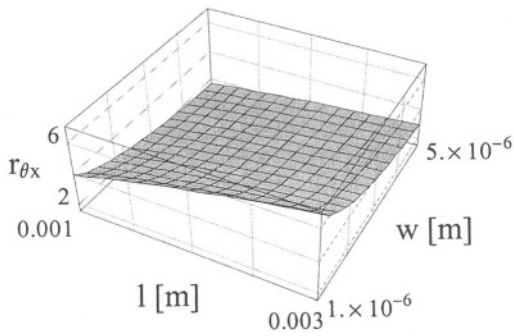

Figure 3.5 Constant cross-section versus right elliptic torsion microhinges by means of the rotation angle

Example 3.3

Determine the linear direct-bending stiffness K_y of one of the four inclined beams which connect to the central mass of Fig. 3.6 (a) and compare this stiffness to the stiffness of a beam with no inclination ($\alpha = 0$ in Fig. 3.6 (b)).

Solution:

The procedure followed previously for the non-inclined beam-spring also applies here, but in addition to calculating the unknown bending moment M_{1z}, the reaction force F_{1x}, as sketched in Fig. 3.6 (b), needs to be calculated in the beginning.

Because both the rotation θ_{1z} and the displacement u_{1x} are zero, these two conditions will provide the equations to solve for M_{1z} and F_{1x}. They can be expressed in terms of F_{1y} and therefore the displacement u_{1y} can now be determined such that the sought stiffness is expressed as:

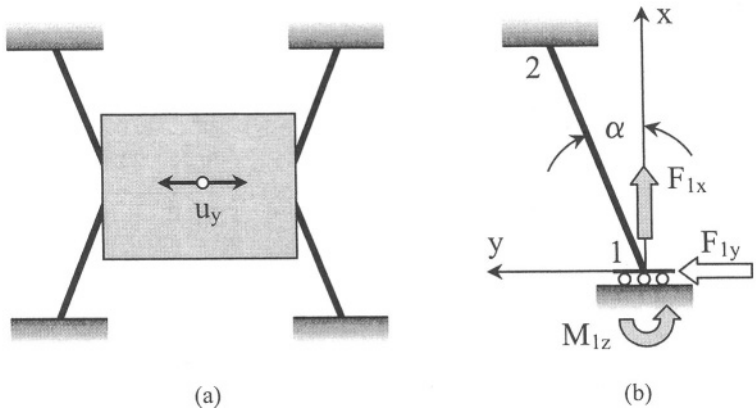

Figure 3.6 Inclined beam spring: (a) accelerometer configuration; (b) Geometry, loads and reactions

$$K_y = F_{1y}/u_{1y} = 1/[(\sin\alpha + a_2\cos\alpha)^2 C_{1,ux-Fx} + (\cos\alpha - a_2\sin\alpha)^2 C_{1,uy-Fy} - 2a_1(\cos\alpha - a_2\sin\alpha)C_{1,uy-Mz} + a_1^2 C_{1,\theta z-Mz}] \quad (3.15)$$

where:

$$a_1 = 2C_{1,ux-Fx}C_{1,uy-Mz}\cos\alpha/\{C_{1,\theta z-Mz}(C_{1,ux-Fx} + C_{1,uy-Fy}) - C_{1,uy-Mz}^2 + [C_{1,\theta z-Mz}(C_{1,ux-Fx} - C_{1,uy-Fy}) + C_{1,uy-Mz}^2]\cos(2\alpha)\} \quad (3.16)$$

and:

$$a_2 = -[C_{1,\theta z-Mz}(C_{1,ux-Fx} - C_{1,uy-Fy}) + C_{1,uy-Mz}^2]\sin\alpha\cos\alpha / [C_{1,\theta z-Mz}C_{1,ux-Fx}\cos^2\alpha + (C_{1,\theta z-Mz}C_{1,uy-Fy} - C_{1,uy-Mz}^2)\sin^2\alpha] \quad (3.17)$$

By taking $\alpha = 0$ in Eq. (3.15), (3.16) and (3.17), Eqs. (3.6) and (3.7) are retrieved, as expected. Equation (3.15) can also be expressed in terms of

stiffnesses by utilizing the matrix transformation of Eq. (3.4), and the stiffness K_y becomes:

$$K_y = 1/\{[a_1^2 K_{1,Fy-uy} + (\cos\alpha - a_2 \sin\alpha)^2 K_{1,Mz-\theta z} + 2a_1(\cos\alpha - a_2 \sin\alpha)K_{1,Fy-\theta z}]/(K_{1,Fy-uy}K_{1,Mz-\theta z} - K_{1,Fy-\theta z}^2) + (a_2 \cos\alpha + \sin\alpha)^2 / K_{1,Fx-ux}\} \quad (3.18)$$

Equation (3.18) simplifies to Eq. (3.8) when $\alpha = 0$, which checks the validity of the generic model. Figure 3.7 plots the ratio of the stiffnesses that are given in Eqs. (3.8) and (3.18) in terms of the parameter α and a parameter c (it has been assumed that the length and width are related as l = cw). It can be seen that the stiffness of the straight beam increases noticeably, compared to the stiffness of the inclined beam. When the inclination angle α and the parameter c increase towards their upper limits in the selected ranges, the stiffness ratio reaches a local maximum.

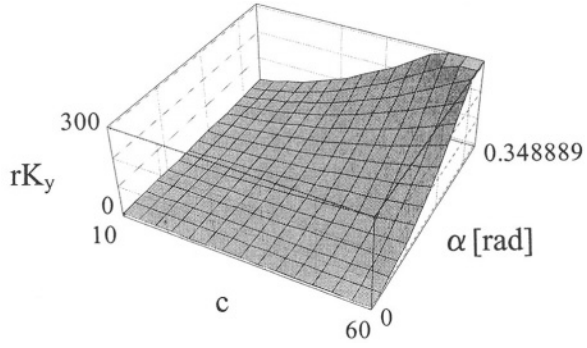

Figure 3.7 Inclined-to-straight beam-spring stiffness ratio

2.2 Bent Beam Suspensions

A spring design which is formed of two compliant straight segments that are perpendicular can be utilized to enable the two-axis motion of a rigid, such as the one shown in Fig. 3.8, where four springs support the central mass symmetrically. While the body translates about one of the directions indicated in the figure, the spring leg that is directed perpendicularly to the motion direction will bend, whereas the other leg will be subject to axial extension/compression in addition to bending. Figure 3.9 indicates the geometry of a *bent beam suspension* (also called *corner spring*), where the two legs have different lengths. The boundary conditions are assumed to be fixed-free, as also indicated in the same figure. The main deformations of a bent beam spring are planar and they result from the two-dimensional motion

of the central mass. However, the bent beam is also sensitive to z-axis parasitic loading, generated by the weight of the central mass. As a consequence, in-plane stiffnesses about the x- and y-directions, as well as the out-of-the-plane stiffness about the z-direction will be derived for this microsuspension.

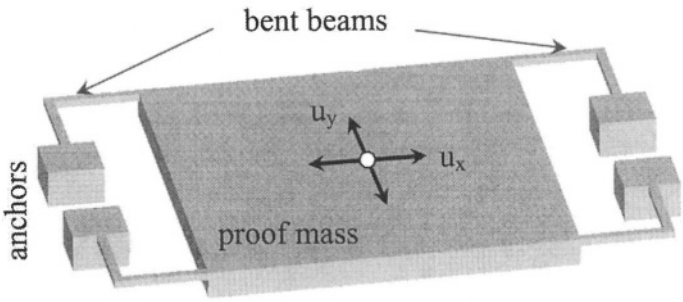

Figure 3.8 Rigid body and four bent beam springs for planar motion

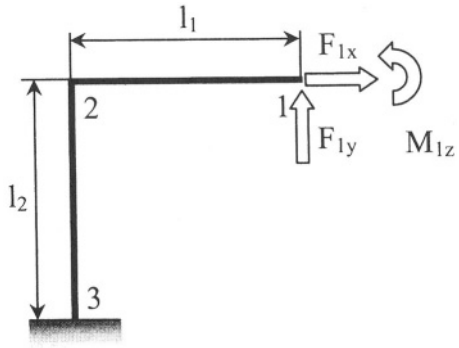

Figure 3.9 Geometry of a bent beam microsuspension

The in-plane deformations of the bent beam can be studied by applying the loads F_{1x}, F_{1y} and M_{1z} and by calculating the corresponding tip displacements u_{1x}, u_{1y} and θ_{1z} through Castigliano's displacement theorem. The strain energy collects contributions from bending and axial loading on the two segments, 1-2 and 2-3. The tip deformations can be related to the tip loads by means of a compliance matrix in the form:

$$\begin{Bmatrix} u_{1x} \\ u_{1y} \\ \theta_{1z} \end{Bmatrix} = \begin{bmatrix} C_{1,ux-Fx} & C_{1,ux-Fy} & C_{1,ux-Mz} \\ C_{1,ux-Fy} & C_{1,uy-Fy} & C_{1,uy-Mz} \\ C_{1,ux-Mz} & C_{1,uy-Mz} & C_{1,\theta z-Mz} \end{bmatrix} \begin{Bmatrix} F_{1x} \\ F_{1y} \\ M_{1z} \end{Bmatrix} \tag{3.19}$$

The terms of the compliance matrix are:

$$C_{1,ux-Fx} = C^{(1)}_{1,ux-Fx} + C^{(2)}_{2,uy-Fy} \tag{3.20}$$

$$C_{1,ux-Fy} = -l_1 C^{(2)}_{2,uy-Mz} \tag{3.21}$$

$$C_{1,ux-Mz} = -C^{(2)}_{2,uy-Mz} \tag{3.22}$$

$$C_{1,uy-Fy} = C^{(1)}_{1,uy-Fy} + C^{(2)}_{2,ux-Fx} + l_1^2 C^{(2)}_{2,\theta z-Mz} \tag{3.23}$$

$$C_{1,uy-Mz} = C^{(1)}_{1,uy-Mz} + l_1 C^{(2)}_{2,\theta z-Mz} \tag{3.24}$$

$$C_{1,\theta z-Mz} = C^{(1)}_{1,\theta z-Mz} + C^{(2)}_{2,\theta z-Mz} \tag{3.25}$$

The superscripts (1) and (2) refer to the first segment 1-2 and to the second one 2-3, respectively. The compliances of the right-hand side of Eqs. (3.20) through (3.25) are calculated for each of the two members with respect to their local frames. In doing so, members of different geometries (defined as free-fixed microhinges) can be utilized in a bent beam design. A stiffness matrix can be defined by inverting the compliance matrix of Eq. (3.19):

$$\begin{bmatrix} K_{1,Fx-ux} & K_{1,Fx-uy} & K_{1,Fx-\theta z} \\ K_{1,Fx-uy} & K_{1,Fy-uy} & K_{1,Fy-\theta z} \\ K_{1,Fx-\theta z} & K_{1,Fy-\theta z} & K_{1,Mz-\theta z} \end{bmatrix} = \begin{bmatrix} C_{1,ux-Fx} & C_{1,ux-Fy} & C_{1,ux-Mz} \\ C_{1,ux-Fy} & C_{1,uy-Fy} & C_{1,uy-Mz} \\ C_{1,ux-Mz} & C_{1,uy-Mz} & C_{1,\theta z-Mz} \end{bmatrix}^{-1} \tag{3.26}$$

In the case the two compliant segments of the bent beam are identical, the particularly-important in-plane stiffnesses are:

$$\begin{aligned} K_x = K_{1,Fx-ux} = [\, & l_1^2 (C^{(1)}_{1,\theta z-Mz})^2 - (C^{(1)}_{1,uy-Mz})^2 + 2(C^{(1)}_{1,ux-Fx} \\ & + C^{(1)}_{1,uy-Fy} - l_1 C^{(1)}_{1,uy-Mz})] \,/\{[\, C^{(1)}_{1,\theta z-Mz}(C^{(1)}_{1,ux-Fx} + C^{(1)}_{1,uy-Fy}) \\ & - (C^{(1)}_{1,uy-Mz})^2\,][\, 2(C^{(1)}_{1,ux-Fx} + C^{(1)}_{1,uy-Fy}) + l_1(l_1 C^{(1)}_{1,\theta z-Mz} - 2C^{(1)}_{1,uy-Mz}\,]\} \end{aligned} \tag{3.27}$$

$$\begin{aligned} K_y = K_{1,Fy-uy} = & [\, 2C^{(1)}_{1,\theta z-Mz}(C^{(1)}_{1,ux-Fx} + C^{(1)}_{1,uy-Fy}) - (C^{(1)}_{1,uy-Mz})^2\,] \,/ \\ & \{[\, C^{(1)}_{1,\theta z-Mz}(C^{(1)}_{1,ux-Fx} + C^{(1)}_{1,uy-Fy}) - (C^{(1)}_{1,uy-Mz})^2\,][\, 2(C^{(1)}_{1,ux-Fx} \\ & + C^{(1)}_{1,uy-Fy}) + l_1(l_1 C^{(1)}_{1,\theta z-Mz} - 2C^{(1)}_{1,uy-Mz}\,]\} \end{aligned} \tag{3.28}$$

When the axial deformations are negligible compared to the bending deformations, Eqs. (3.27) and (3.28) can still be used by considering that the axial compliances of the two segments are zero (axially rigid members).

The mention was made in Chapter 2 that the stiffnesses defined by inverting the compliance matrix are different from the stiffnesses that are calculated as:

$$\begin{cases} \overline{K}_x = F_{1x} / u_{1x} = 1 / C_{1,ux-Fx} \\ \overline{K}_y = F_{1y} / u_{1y} = 1 / C_{1,uy-Fy} \end{cases} \tag{3.29}$$

and that the stiffnesses of Eqs. (3.27) and (3.28) should be used when forces need to be calculated based on known displacements. However, Eqs. (3.29) are used as definition relationships and their values can be obtained by using the transformation Eqs. (2.25) of Chapter 2 from the stiffnesses of Eqs. (3.26).

The out-of-the-plane definition stiffness can be determined by applying a force F_{1z} at point 1 of Fig. 3.9 about a direction perpendicular to the bent beam's plane and by calculating the corresponding displacement. By taking bending and torsion into account, the z-direction stiffness is:

$$\overline{K}_z = F_{1z} / u_{1z} = 1 / (C^{(1)}_{1,uz-Fz} + C^{(2)}_{2,uz-Fz} + l_1^2 C^{(1)}_{1,\theta y-My}) \tag{3.30}$$

Example 3.4

Calculate the mam stiffnesses of a bent beam microsuspension with identical legs and of constant rectangular cross-section. Evaluate the errors in calculating K_x by its definition – Eqs. (3.29) – as opposed to the compliance derived stiffness K_x of Eq. (3.27).

Solution:

For this particular case, the linear in-plane stiffnesses are equal, namely:

$$K_x = K_y = Ew^3 t(5l_1^2 + 2w^2 / [2l_1(4l_1^4 + 5l_1^2 w^2 + w^4)] \tag{3.31}$$

and the z-axis stiffness is:

$$\overline{K}_z = EGw^3 t^3 / [(3Et^2 + 8Gw^2) l_1^3] \tag{3.32}$$

It has been considered that w << t (very thin cross-section) and therefore:

$$I_t = w^3 t / 3 \tag{3.33}$$

The ratio of the x-axis stiffnesses becomes:

$$K_x / \overline{K}_x = 1 + 3l_1^2 / [2(l_1^2 + w^2)] \tag{3.34}$$

and for $l_1 \rightarrow [100\ \mu m, 200\ \mu m]$ and $w \rightarrow [1\ \mu m, 2\ \mu m]$, this ratio is almost constant with a 2.5 approximate value.

2.3 U-Springs

Microsprings that have the approximate shape of the letter U (called here *U-springs*) are mainly used in applications involving translatory motion of rigid bodies. Due to symmetry about the axial (motion) direction, the proof mass can translate about that axis, as suggested in Fig. 3.10.

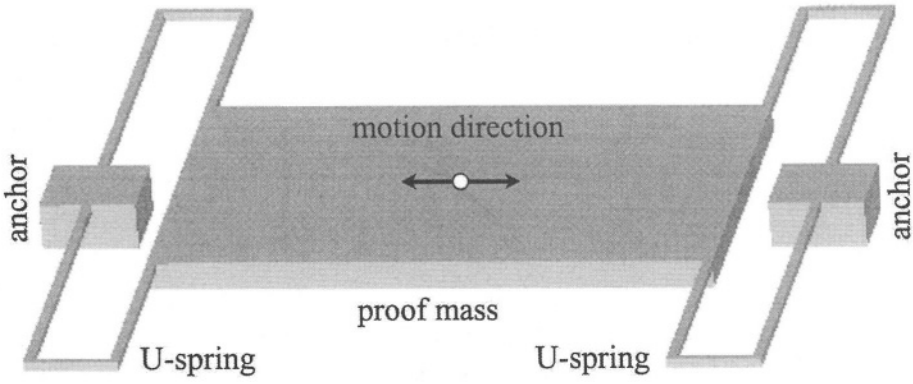

Figure 3.10 Proof mass in translatory motion with four U-springs attached frontally

Other (parasitic) motions, either planar or out-of-the-plane (especially due to the self-weight of the proof mass) are also possible, hence quantifying the stiffnesses about the direction perpendicular to the motion direction and the direction perpendicular to the plane of the microdevice of Fig. 3.10 will also be done, in addition to formulating the main stiffness about the motion direction.

Figure 3.11 pictures a U-spring with the reference frame that is used to define the linear stiffnesses of interest, and which are K_x (the stiffness related to the main translatory motion of the proof mass shown in Fig. 3.10), K_y (the stiffness defining the elastic properties of the U-spring when the body translates about a direction perpendicular to the main one and is contained in the plane of the microdevice) and K_z (the stiffness which describes the spring behavior for the case of an out-of-the-plane motion about the z-direction, as indicated in Fig 3.11).

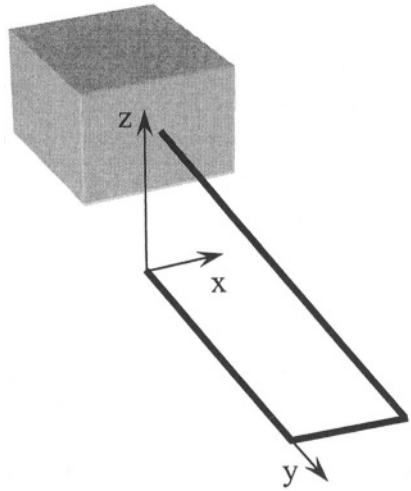

Figure 3.11 U-spring model with boundary conditions, main degrees of freedom, and corresponding forces

As a result of these three translatory motions of the shuttle, the true boundary condition at point 1 in Fig. 3.11 is a forced translation about the x-axis. However, as a simplification to the real situation, it may be considered that point 1 is free to move, as also assumed previously with the bent beam microsuspension. Because the force acting at that point is basically directed about the same direction, the errors of considering point 1 as free are expected to be small. Three different configurations will be analyzed in the following: one with sharp corners, a second one where the short straight link of the model is substituted by half a circle, and a third variant with filleted corners.

2.3.1 U-spring with Sharp Corners (Configuration # 1)

Configuration # 1 is formed of three elastic segments, as shown in Fig. 3.12. In order to keep the formulation valid for a generic case, they can have different but constant cross-sections. It will also be considered that only bending of each of the three segments contribute to the total strain energy of the spring. The in-plane compliances are calculated by applying the loads $\mathbf{F}_{1x}$, $\mathbf{F}_{1y}$ and $\mathbf{M}_{1z}$, as shown in Fig. 3.12, and by calculating the corresponding displacements $\mathbf{u}_{1x}$, $\mathbf{u}_{1y}$ and $\boldsymbol{\theta}_{1z}$. Castigliano's displacement theorem is applied again in order to calculate these displacements. A compliance matrix of the type shown in Eq. (3.19) can be formulated, whose terms are:

$$C_{1,ux-Fx} = [l_1^3 / I_{z1} + 3l_1^2 l_2 / I_{z2} + l_3(3l_1^2 - 3l_1 l_3 + l_3^2) / I_{z3}] / (3E) \quad (3.35)$$

$$C_{1,ux-Fy} = -l_2[l_1 l_2 / I_{z2} + l_3(2l_1 - l_3)/I_{z3}]/(2E) \tag{3.36}$$

$$C_{1,ux-Mz} = [l_1^2 / I_{z1} + 2l_1 l_2 / I_{z2} + l_3(2l_1 - l_3)/I_{z3}]/(2E) \tag{3.37}$$

$$C_{1,uy-Fy} = l_2^2(l_2 / I_{z2} + 3l_3 / I_{z3})/(3E) \tag{3.38}$$

$$C_{1,uy-Mz} = -l_2(l_2 / I_{z2} + 2l_3 / I_{z3})/(2E) \tag{3.39}$$

$$C_{1,\theta z-Mz} = (l_1 / I_{z1} + l_2 / I_{z2} + l_3 / I_{z3})/E \tag{3.40}$$

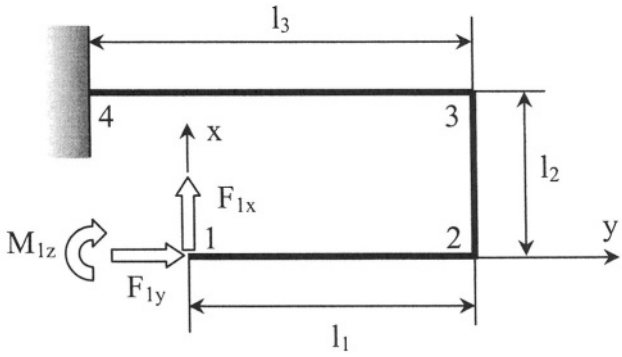

Figure 3.12 U-spring design with sharp corners

The stiffness K_x is the element of the stiffness matrix (which is the inverse of the compliance matrix consisting of the elements defined in Eqs. (3.35) through (3.40)) located on the first row and first column. Similarly, the stiffness K_y is the element placed on the second row – second column position of the same stiffness matrix. The definition stiffnesses are simply the inverses of the corresponding compliances, $C_{1,ux\text{-}Fx}$ and $C_{1,uy\text{-}Fy}$.

The stiffness about the z-direction is calculated in the definition sense that has been introduced in the previous chapters and was also mentioned previously in Eq. (3.30) for instance. Its expression is found by taking the ratio of a force F_{1z} which is applied at point 1 in Fig. 3.12 about a direction perpendicular to the plane of the microdevice to the corresponding displacement u_{1z}, namely:

$$\overline{K}_z = F_{1z} / u_{1z} = \{l_2(l_1^2 / I_{t2} + l_2 l_3 / I_{t3})/G + [l_1^3 / I_{z1} + l_2^3 / I_{z2} + l_3(3l_1^2 - 3l_1 l_3 + l_3^2)/I_{z3}]/(3E)\}^{-1} \tag{3.41}$$

Example 3.5

Analyze the change in the main compliance of a U-spring when the axial deformations are also taken into account. Consider that the three legs have identical constant rectangular cross-sections.

Solution:

In the case where the axial deformations are considered, the strain energy will include terms induced by the axial effects, in addition to bending-produced ones, but the procedure of calculating the main compliance, $C_{1,ux\text{-}Fx}$ remains the same. For a constant rectangular cross-section, the ratio of the bending-related compliance to the compliance that considers both bending and axial effects becomes:

$$r_{Cx} = 1 + l_2 w^2 / \{4[l_1^3 - 3l_1 l_3^2 + l_3^3 + 3l_1^2(l_2 + l_3)]\} \tag{3.42}$$

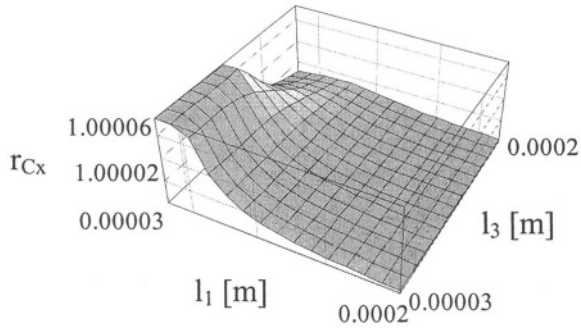

Figure 3.13 Compliance ratio in terms of l_1 and l_3

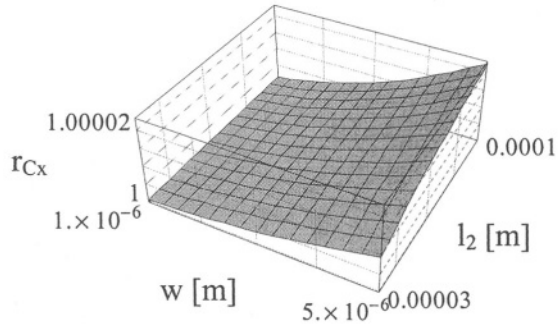

Figure 3.14 Compliance ratio in terms of w and l_2

Equation (3.42) indicates that the model including bending effects generates a compliance about the main direction of action which is very slightly larger than the compliance yielded by the model that adds axial effects to bending. Figure 3.13 is the plot of the compliance ratio of Eq. (3.42) as a function of l_1 and l_3 when $w = 2\ \mu m$ and $l_2 = 50\ \mu m$. Similarly, Fig. 3.14 is the plot of the same compliance ratio in terms of w and l_2 when $l_1 = l_3 = 200\ \mu m$. As both figures indicate, the compliance ratio is in the very close vicinity of 1 when the design variables of Eq. (3.42) span relatively wide ranges, which indicates that neglecting the axial effects has little influence on the main compliance.

Example 3.6

Find the definition stiffness of a U-spring about the y-direction in the case where the middle leg has a small length l_2, which implies considering the additional shearing effects and associated deformations. Compare the resulting stiffness with the regular one determined by means of the compliance $C_{1,uy\text{-}Fy}$ of Eq. (3.38) in the case where $l_2 = 5\ \mu m$ and $w = 1\ \mu m$.

Solution:

When the length l_2 is only about 3-5 times greater than the largest cross-sectional dimension, the deformation produced by the shearing force $S_2 = F_{1y}$ has to be accounted for in addition to bending. The displacement at point 1 about the y-direction in Fig. 3.12 is calculated by means of Castigliano's displacement theorem as:

$$u_{1y} = \frac{\partial U}{\partial F_{1y}} = 1/(EI_z)\left(\int_0^{l_2} M_2 \frac{\partial M_2}{\partial F_{1y}} dx + \int_0^{l_3} M_3 \frac{\partial M_3}{\partial F_{1y}} dx\right) + \frac{\kappa}{GA}\int_0^{l_2} S_2 \frac{\partial S_2}{\partial F_{1y}} dx \tag{3.43}$$

where the subscripts in bending moments M and shearing force S indicate the specific segment out of the three ones making up together the U-spring. The linear stiffness about the y-direction can be expressed according to its definition as:

$$\overline{K}_y = F_{1y}/u_{1y} = 3EGAI_z/\{l_2[3\kappa EI_z + GAl_2(l_2 + 3l_3)]\} \tag{3.44}$$

whereas the same stiffness which only considers bending is:

$$\overline{K}_y = 3EI_z/[l_2^2(l_2 + 3l_3)] \tag{3.45}$$

By constructing the ratio of the y-axis stiffness in Eq. (3.44) to the stiffness of Eq. (3.45), the plot of Fig. 3.15 can be drawn in terms of the lengths l_2 and l_3

for $\kappa = 6/5$. It can be seen that the stiffness ratio is almost constant and equal to 1, which indicates that the shearing effects are not particularly large.

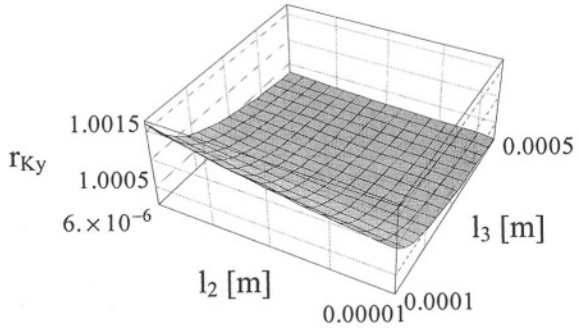

Figure 3.15 Stiffness ratio K_y in terms of l_1 and l_3

2.3.2 U-spring with Circular Short Link (Configuration # 2)

As Fig. 3.16 shows it, configuration # 2 incorporates a semi-circular portion instead of the straight segment 2-3 of the previous design.

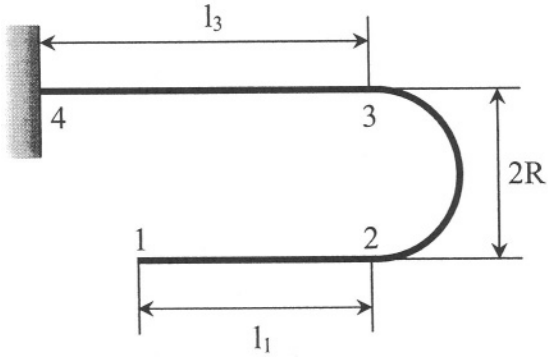

Figure 3.16 U-spring design with circular short link

There are two possibilities, connected to the form factor of the semi-circular section. It is known (see Young and Budynas [1], for instance) that for thin curved beams, when the ratio of the radius R to the cross-sectional width w is greater than 10, the deformations of the curved beam can safely be treated by using the tools applicable to straight beams. By applying the same procedure that has been used for the U-spring configuration # 1, and by only taking bending of the three segments into account, the in-plane compliances of the constant cross-section design are:

$$C_{1,ux-Fx} = \{2(l_1^3 + l_3^3) + 6l_1[l_1(l_3 + 3\pi) - l_3^2 + 4R^2] + 3\pi R^3\}/(6EI_z) \quad (3.46)$$

$$C_{1,uy-Fy} = -R[l_1(2l_3 + \pi R) + 2R^2 - l_3^2]/(EI_z) \quad (3.47)$$

$$C_{1,ux-Mz} = [l_1^2 - l_3^2 + 4R^2 + 2l_1(l_3 + \pi R)]/(2EI_z) \quad (3.48)$$

$$C_{1,uy-Fy} = R^2(8l_3 + 3\pi R)/(2EI_z) \quad (3.49)$$

$$C_{1,uy-Mz} = -R(2l_3 + \pi R)/(EI_z) \quad (3.50)$$

$$C_{1,\theta z-Mz} = (l_1 + l_3 + \pi R)/(EI_z) \quad (3.51)$$

By arranging these compliances into a 3 by 3 symmetric compliance matrix, the corresponding stiffness matrix can be obtained through inversion of this compliance matrix. When the definition stiffnesses are needed, then simple inversion of the individual compliances of Eqs. (3.46) through (3.51) will produce these stiffnesses.

For designs where the circular segment is relatively short (R < 10 w), Young and Budynas [1] recommend using the following bending energy:

$$U = \int_l M_b^2/(2eEA)ds \quad (3.52)$$

where e is the eccentricity, which, for a rectangular cross-section, can be calculated by means of Eq. (1.122). By applying again Castigliano's displacement theorem for the configuration of Fig. 3.16 in the presence of the tip loads $\mathbf{F}_{1x}$, $\mathbf{F}_{1y}$ and $\mathbf{M}_{1z}$ (not shown in Fig. 3.16), the resulting displacements $\mathbf{u}_{1x}$, $\mathbf{u}_{1y}$ and θ_{1z} can be found by means of the following compliances:

$$C_{1,ux-Fx} = \{2eA(l_1^3 + 3l_1^2 l_3 - 3l_1 l_3^2 + l_3^3) + 3I_z(2\pi l_1^2 + 8l_1 R + \pi R^2)\}/(6eEAI_z) \quad (3.53)$$

$$C_{1,ux-Fy} = -R[eAl_3(2l_1 - l_3) + I_z(\pi l_1 + 2R)]/(eEAI_z) \quad (3.54)$$

$$C_{1,ux-Mz} = [eA(l_1^2 + 2l_1 l_3 - l_3^2) + 2I_z(\pi l_1 + 2R)]/2eEAI_z) \quad (3.55)$$

$$C_{1,uy-Fy} = R^2(8eAl_3 + 3\pi I_z)/(2eEAI_z) \quad (3.56)$$

$$C_{1,uy-Mz} = -R(2eAl_3 + \pi I_z)/(eEAI_z) \tag{3.57}$$

$$C_{1,\theta z-Mz} = [eA(l_1 + l_3) + \pi I_z]/(eEAI_z) \tag{3.58}$$

The out-of-the-plane definition stiffness is found by applying a force F_{1z} at the free point of the spring in Fig. 3.16, perpendicularly to the plane of the figure. This stiffness is the ratio of the applied force and the resulting deflection to its equation is:

$$\begin{aligned}\overline{K}_z &= 6EGI_yI_t/\{3EI_yR[8l_3R + \pi(l_1^2 - 2l_1R + 3R^2)] \\ &+ GI_t[2(l_1^3 + 3l_1^2l_3 - 3l_1l_3^2 + l_3^3) + 3\pi l_1^2R + 6\pi l_1R^2 + 3\pi R^3]\}\end{aligned} \tag{3.59}$$

2.3.3 U-spring with Filleted Corners (Configuration # 3)

Configuration # 3 is sketched in Fig. 3.17 where the middle segment is composed of two quarter-circles encompassing a straight line such that overall, this spring configuration is made up of five segments.

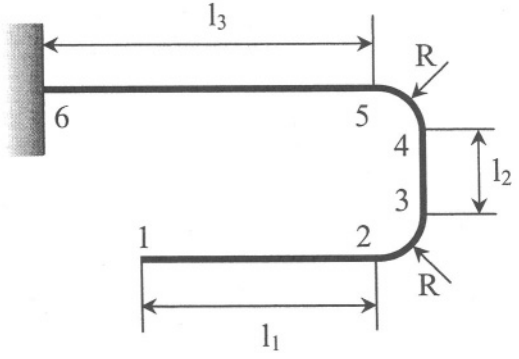

Figure 3.17 U-spring design with circularly-filleted corners

For a thin configuration where the radius-to-width ratio R/w is larger than 10, and in the case where all segments have the same constant cross-section, the in-plane compliances can be determined by following the procedure that has been used for the other U-spring configurations. Their expressions are:

$$\begin{aligned}C_{1,ux-Fx} &= \{2(l_1^3 + l_3^3) + 3R^2(2l_2 + \pi R) + 6l_1[l_1(l_2 + l_3 + \pi R) \\ &- l_3^2 + 2R(l_2 + 2R)]\}/(6EI_z)\end{aligned} \tag{3.60}$$

$$C_{1,ux-Fy} = -(l_2 + 2R)[l_1(l_2 + 2l_3 + \pi R) + R(l_2 + 2R) - l_3^2]/(2EI_z) \quad (3.61)$$

$$C_{1,ux-Mz} = [l_1^2 - l_3^2 + 2l_1(l_2 + l_3 + \pi R) + 2R(l_2 + 2R)]/(2EI_z) \quad (3.62)$$

$$C_{1,uy-Fy} = \{2l_2^2(l_2 + 3l_3) + 3l_2R[8l_3 + (\pi + 2)l_2] + 6R^2[4l_3 + (\pi + 3)l_2] + 9\pi R^3\}/(6EI_z) \quad (3.63)$$

$$C_{1,uy-Mz} = -(l_2 + 2R)(l_2 + 2l_3 + \pi R)/(2EI_z) \quad (3.64)$$

$$C_{1,\theta z-Mz} = (l_1 + l_2 + l_3 + \pi R)/(EI_z) \quad (3.65)$$

For a relatively-thick design (R / w < 10), the in-plane compliances are:

$$C_{1,ux-Fx} = \{3I_z(2\pi l_1^2 + 8l_1R + \pi R^2) + 2eA[l_1^3 + l_3^3 + 3l_1^2(l_2 + l_3) + 3l_2R^2 - 3l_1(l_3^2 - 2l_2R)]\}/(6eEAI_z) \quad (3.66)$$

$$C_{1,ux-Fy} = -(l_2 + 2R)[I_z(\pi l_1 + 2R) + eA[l_1(l_2 + 2l_3) - l_3^2 + l_2R]/(2eEAI_z) \quad (3.67)$$

$$C_{1,ux-Mz} = \{2I_z(\pi l_1 + 2R) + eA[l_1^2 + 2l_1(l_2 + l_3) - l_3^2 + 2l_2R]\}/(2eEAI_z) \quad (3.68)$$

$$C_{1,uy-Fy} = \{3I_z[\pi l_2^2 + 2(\pi + 2)l_2R + 3\pi R^2] + 2eA[l_2^3 + 3l_2^2(l_3 + R) + 3l_2R(4l_3 + R) + 12l_3R^2]\}/(6eEAI_z) \quad (3.69)$$

$$C_{1,uy-Mz} = -(l_2 + 2R)[eA(l_2 + 2l_3) + \pi I_z]/(2eEAI_z) \quad (3.70)$$

$$C_{1,\theta z-Mz} = [eA(l_1 + l_2 + l_3) + \pi I_z]/(eEAI_z) \quad (3.71)$$

As Fig. 3.17 indicates, when the radius of the two circular portions is zero, the current design transforms into the design configuration # 1, whereas when $l_2 = 0$, configuration # 3 changes into configuration # 2. Checks have been performed in order to verify whether the corresponding stiffnesses of either configurations #1 or # 2 are retrieved by using the particular geometric parameters limits mentioned above. When R → 0, Eqs. (3.60) through (3.65) transform indeed into Eqs. (3.35) through (3.40), respectively, which define

configuration # 1. Similarly, when $l_2 \to 0$, the same Eqs. (3.60) through (3.65) change into Eqs. (3.46) through (3.51), respectively, which define configuration # 2. All these calculations confirm the correctness of the equations derived here.

The out-of-the-plane stiffness for this configuration # 3 is:

$$\begin{aligned}\bar{K}_z = {} & 12EGI_y I_t / \{3EI_y \{4l_2(l_1^2 + l_2 l_3) + R[12l_1 l_2 + 2\pi l_1^2 + l_2(16l_3 \\ & + \pi l_2)] + 2R^2[8l_1 + 8l_3 + (\pi + 6)l_2] + 6\pi R^3\} + GI_t[4l_1^3 + 4(l_2^3 + l_3^3) \\ & + 3(\pi + 4)l_2^2 R + 6(\pi + 2)l_2 R^2 + 6\pi R^3 - 12l_1(l_3^2 + l_2 R) + \\ & 6l_1^2(2l_3 + \pi R)]\}\end{aligned} \tag{3.72}$$

Example 3.7

Decide which of the three U-spring configurations is the most compliant about the main direction of motion when compliant members of all design variants have the same rectangular cross-section and can be inscribed each in the same rectangle of sides equal to 100 μm and 200 μm. Also known are l_2 = 100 μm, w = 5 μm and t = 1 μm.

Solution:

The $C_{1,ux\text{-}Fx}$ compliances of the three U-spring configurations will be compared by analyzing compliance ratios. It can be seen that while the first two configurations have their compliances determined by the parameters given in this example, the third configuration can have various compliances because the radius R can take any value from 0 to $l_2/2$.

The following compliance ratios are discussed:

$$\begin{cases} rC^{(1-3)} = C^{(1)}_{1,ux-Fx} / C^{(3)}_{1,ux-Fx} \\ rC^{(2-3)} = C^{(2)}_{1,ux-Fx} / C^{(3)}_{1,ux-Fx} \end{cases} \tag{3.73}$$

where the superscripts 1, 2 and 3 denote the first, second and third configuration, respectively.

Figure 3.18 is the plot of the first ratio defined in Eqs. (3.73) as a function of the radius R, in the case R / w > 10 for configuration # 3. Similarly, Fig. 3.19 pictures the second ratio of Eq. (3.73). As Fig. 3.18 indicates it, the design configuration # 1 is more compliant than the design configuration # 3, but they tend to be equal for small radii. Configuration # 2 is less compliant than configuration # 3, but for large radii, the two designs have almost identical compliances. Similar plots are drawn in Figs. 3. 20 and 3.21 when R / w < 10 for configurations # 2 and # 3.

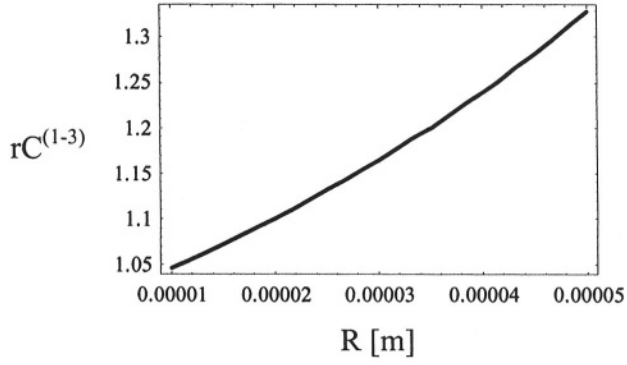

Figure 3.18 Compliance comparison: configuration # 1 versus configuration # 3 (R / w > 10 for configuration # 3)

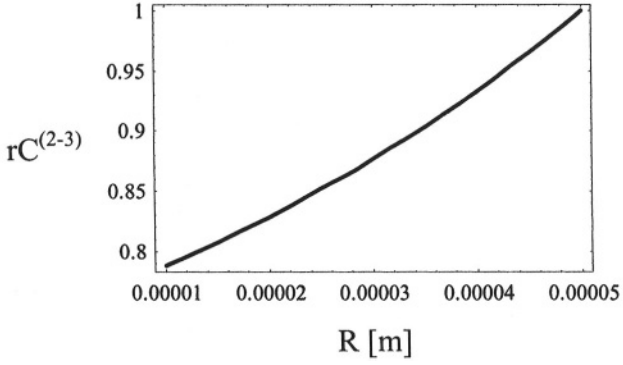

Figure 3.19 Compliance comparison: configuration # 2 versus configuration # 3 (R / w > 10 for both designs)

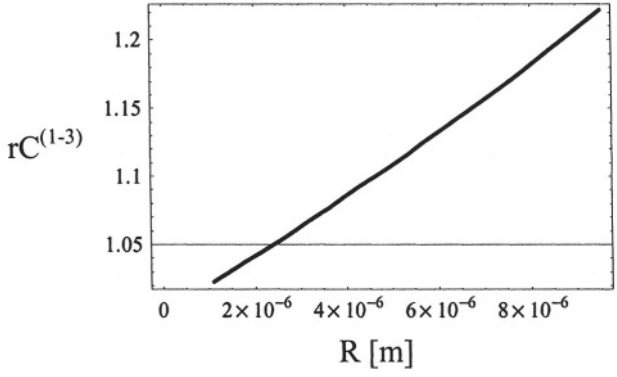

Figure 3.20 Compliance comparison: configuration # 1 versus configuration # 3 (R / w < 10 for configuration # 3)

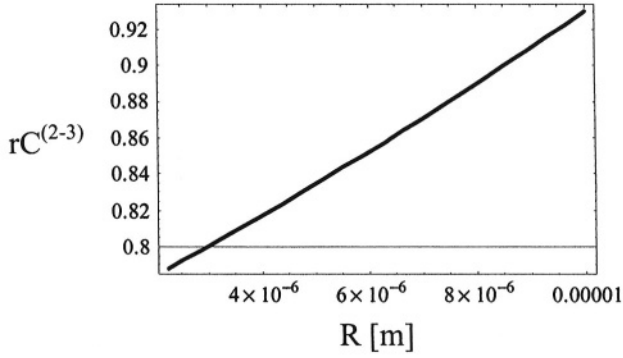

Figure 3.21 Compliance comparison: configuration # 2 versus configuration # 3 (R / w < 10 for both designs)

The trends that have been mentioned for the case where R / w > 10 are also seen when R / w < 10. As a conclusion, configuration # 1 is the most compliant about the x-direction, followed by configuration # 3 and configuration # 2, which is the stiffest.

Example 3.8

Compare the performance of the U-spring configurations # 1 and # 3 in terms of the out-of-the-plane stiffness about the z-direction in the case where $l_1 = l_2 = l_3$, w = 10 t and $R = l_2/c$, where c is a parameter. Consider the stiffness equations according to the definition.

Solution:

Again, the following stiffness ratio can be analyzed:

$$r\bar{K}^{(3-1)} = \bar{K}_z^{(3)} / \bar{K}_z^{(1)} \tag{3.74}$$

Figure 3.22 is a two-dimensional plot showing the variation of the stiffness ratio defined in Eq. (3.74) as a function of the parameter c, when c ranges from 2 to 20. It can be seen that configuration # 3 is stiffer than configuration # 1 (the stiffness ratio is larger than 1) in the particular case of this example, and that for relatively small values of c the stiffnesses of the two designs are quite different.

On the other end of the spectrum, the difference in stiffness between the two design configurations diminishes as the parameter c increases, and this situation should be expected because when the parameter c increases the corner radius decreases, and therefore configuration # 3 approaches the limit case of configuration # 1 which is defined by R = 0.

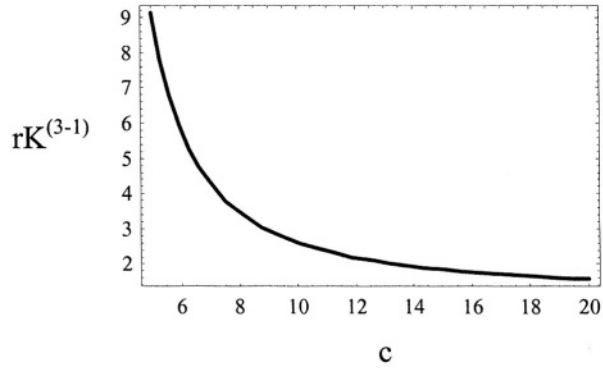

Figure 3.22 K_z stiffness comparison: configuration # 3 versus configuration # 1

2.4 Serpentine Springs

Another solution for springs that support a proof mass frontally is the serpentine spring. Figure 3.23 is a three-dimensional drawing of a pair of serpentine springs connected to a proof mass that can move and alternatively extend and compress each spring. The in-plane motion about a direction perpendicular to the one indicated in Fig. 3.23 is also possible for the same arrangement of the springs. A serpentine spring is formed of one or several series-connected units, as the one shown in Fig. 3.24, where also indicated are the defining geometric parameters of the unit. When the units are identical, a final configuration of the type sketched in Fig. 3.25 is obtained; when the units scale down in their l_1 dimension, linearly for instance, a design such as the one sketched in Fig. 3.26 can be conceived, but the scaling law can be, in general, different than the linear one exemplified here.

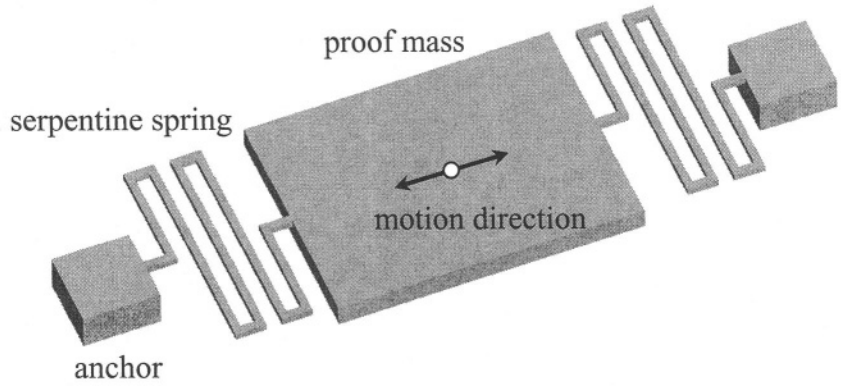

Figure 3.23 Pair of serpentine springs attached frontally to a moving mass

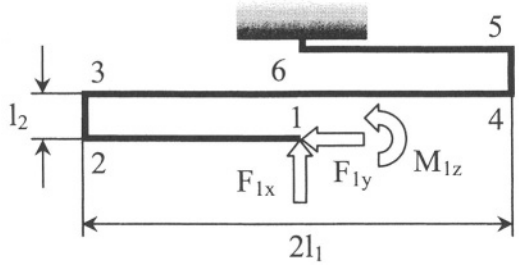

Figure 3.24 Serpentine base unit with defining geometry

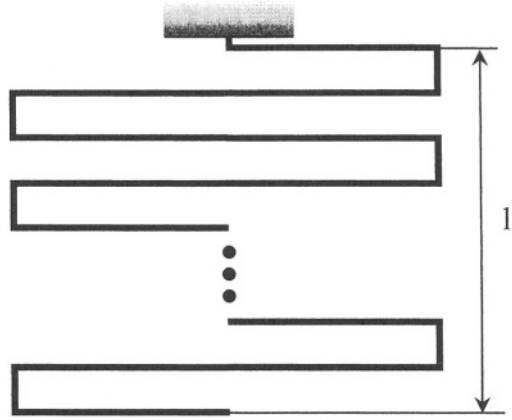

Figure 3.25 Serpentine spring configuration with identical units

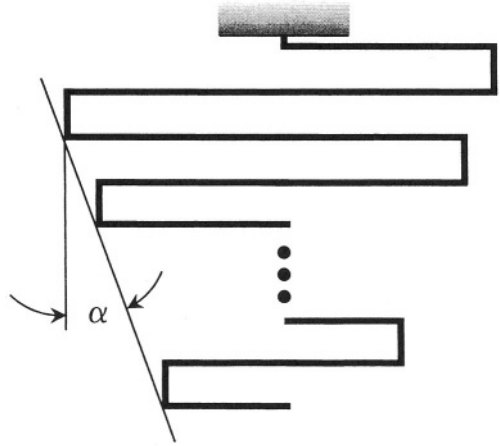

Figure 3.26 Serpentine spring configurations with linearly scaled units

It is therefore sufficient to define the compliances or stiffnesses of a unit, because the compound serpentine springs are formed by series connection of several base units. Figure 3.27 is a three-dimensional model of a serpentine unit with the local reference frame. The in-plane compliances can be found based on Fig. 3.24, which shows the applied loads F_{1x}, F_{1y} and M_{1z}. By using Castigliano's displacement theorem (in the case where only bending is accounted for and the 5 segments composing the base unit are assumed to have identical constant cross-sections), the corresponding displacements u_{1x}, u_{1y} and θ_{1z} are determined. The compliances that form the 3 by 3 symmetric compliance matrix of Eq. (3.19) are given below.

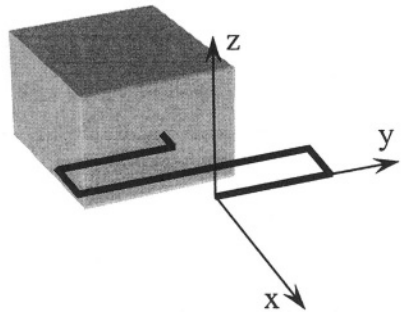

Figure 3.27 Three-dimensional view of a serpentine base unit with boundary conditions and loads for stiffness calculations

$$C_{1,ux-Fx} = 2l_1^2(2l_1 + 3l_2)/(3EI_z) \tag{3.75}$$

$$C_{1,ux-Fy} = -l_1 l_2(l_1 + 2l_2)/(EI_z) \tag{3.76}$$

$$C_{1,ux-Mz} = l_1(l_1 + 2l_2)/(EI_z) \tag{3.77}$$

$$C_{1,uy-Fy} = 2l_2^2(9l_1 + 4l_2)/(3EI_z) \tag{3.78}$$

$$C_{1,uy-Mz} = -2l_2(2l_1 + l_2)/(EI_z) \tag{3.79}$$

$$C_{1,\theta z-Mz} = 2(2l_1 + l_2)/(EI_z) \tag{3.80}$$

As mentioned previously, the definition stiffnesses can be found by simply taking the algebraic inverses of the compliances formulated in Eqs. (3.75) through (3.80). If the loads F_{1x}, F_{1y}, M_{1z} need to be calculated when the corresponding displacements at point 1 – Fig. 3.24 – are known, then a stiffness matrix has to be determined by inverting the compliance matrix of Eq. (3.19) and which contains the terms of Eqs. (3.75) through (3.80).

The definition stiffness about the z-direction is determined by applying a force F_{1z} (not shown in Fig. 3.24) and by calculating the corresponding displacement u_{1z} (when bending and torsion are taken into consideration), as done with previous spring designs. The equation of this stiffness is:

$$\overline{K}_z = M_{1z} / u_{1z} = 3EGI_y I_t / [6EI_y l_1 l_2 (l_1 + 3l_2) + 4GI_t (l_1^3 + 2l_2^2)] \quad (3.81)$$

There are situations where the rigid body which attaches frontally to two spiral springs undergoes a rotation about its longitudinal (x) axis. In this case, each spiral spring will be subject to torsion, and therefore the torsional stiffness is of interest. By applying a moment M_{1x} at the free end 1 – this moment is not drawn in Fig. 3.24 – the torsional stiffness of a serpentine spring unit is:

$$\overline{K}_t = M_{1x} / \theta_{1x} = EGI_y I_t / [2(EI_y l_2 + 2GI_t l_1)] \quad (3.82)$$

Equation (3.82) took into consideration that the long legs are subject to bending about the in-plane direction y, whereas the short legs are loaded in torsion about their longitudinal axes.

Example 3.9

Design a basic serpentine spring in such a manner that the following stiffness relationship apply: $K_z / K_x = 0.0024$ (both stiffnesses are calculated in the definition sense). The rectangular cross-section is constant is defined by $w = 10\ \mu m$ and $t = 1\ \mu m$. Poisson's ratio is $\mu = 0.25$.

Solution:

By using the following equations for the cross-sectional properties:

$$\begin{cases} I_z = w^3 t / 12 \\ I_y = w t^3 / 12 \\ I_t = w t^3 / 3 \end{cases} \quad (3.83)$$

the stiffness condition, which is:

$$\overline{K}_z = 0.0024 \overline{K}_x \quad (3.84)$$

results in an equation that can be solved for the length of the short leg l_2 in terms of the length of the other leg l_1, as plotted in Fig. 3.28. It can be seen that in order to satisfy the requirements of the example, the length l_2 varies almost linearly with l_1.

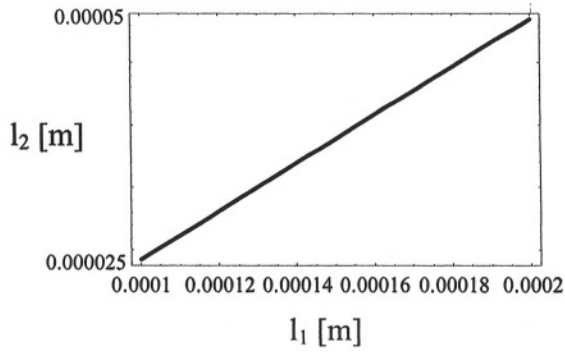

Figure 3.28 Short leg's length as a function of the long leg's length

Example 3.10

Compare the total axial stiffness of a serpentine spring which has 5 linearly-scaled units to the axial stiffness of another serpentine spring which contains 5 identical units. The width of the third (middle) unit in the scaled version is equal to the width of the units in the other design, which is $2l_1$. Assume the two configurations are built of the same material and have identical constant rectangular cross-sections. The legs are defined by $l_1 = 100$ μm and $l_2 = 40$ μm.

Solution:

The total stiffness of each configuration is given by the rule of series connection (which is also treated in Chapter 5) and therefore its expression is determined as:

$$1/K_x = \sum_{i=1}^{5} 1/K_{xi} \tag{3.85}$$

For the configuration with identical units the, K_{xi} factors of Eq. (3.85) are identical, and can be calculated by inverting the compliance $C_{1,ux\text{-}Fx}$ of Eq. (3.75) with the appropriate length l_1. For the scaled version, one needs to calculate the length $l_{1,i}$ for each of the units. It is known that the length of the unit in the middle of the second design is equal to the length of the identical units in the first design, namely.

$$l_{1,3} = l_1 \tag{3.86}$$

The lengths of the other four units can be calculated with the aid of Fig. 3.26 as:

$$\begin{cases} l_{1,1} = l_1 - 4l_2 \tan\alpha \\ l_{1,2} = l_1 - 2l_2 \tan\alpha \\ l_{1,4} = l_1 + 2l_2 \tan\alpha \\ l_{1,5} = l_1 + 4l_2 \tan\alpha \end{cases} \tag{3.87}$$

The ratio of the non-scaled to the scaled stiffness becomes a function of only the angle α and is plotted in Fig. 3.29.

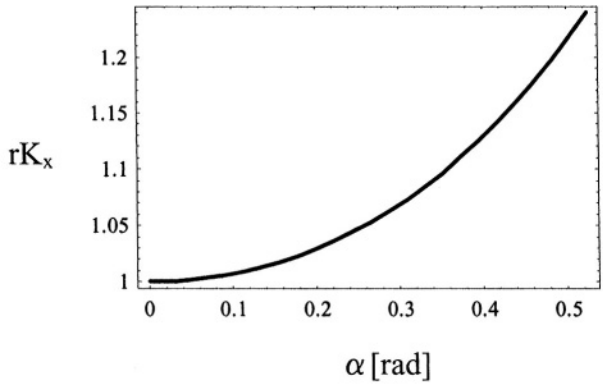

Figure 3.29 K_x stiffness ratio comparing a non-scaled to a scaled serpentine designs

2.5 Bent Beam Serpentine Springs

One disadvantage of the bent beam spring suspension is that for any of the two in-plane translations of the central body, one spring's leg will be in compression, and the load produced by the moving mass might reach the critical limit that will generate buckling of that leg. A modality to circumvent this drawback is two utilize the bent beam in a serpentine configuration, as shown in Fig. 3.30, where each of the four identical springs is formed by adding another scaled-down bent beam.

The result will be that the net cross-section which opposes the compressive load is almost doubled, and there is additional rigidizing by the short segment (of length l_2 in Fig. 3.31) so that the value of the buckling load is substantially raised. In addition, the segments that have been mostly acted upon by axial loads in a bent beam microspring, are loaded in bending for a bent beam serpentine microsuspension, and this is the natural manner of deformation for these compliant members.

The in-plane compliances are determined again by calculating the displacements at point 1 in Fig. 3.31 as produced by the loads F_{1x}, F_{1y} and M_{1z} under the assumptions that the cross-section is constant and identical for

all segments, and that only bending contributes to the elastic deformation of the member.

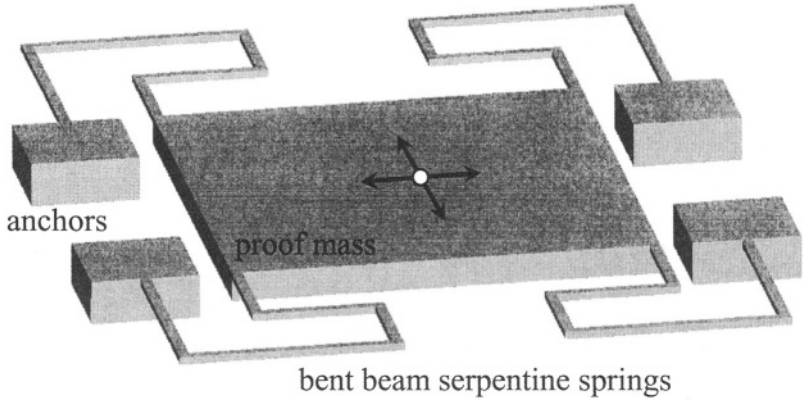

Figure 3.30 Microaccelerometer with four identical bent beam serpentine springs

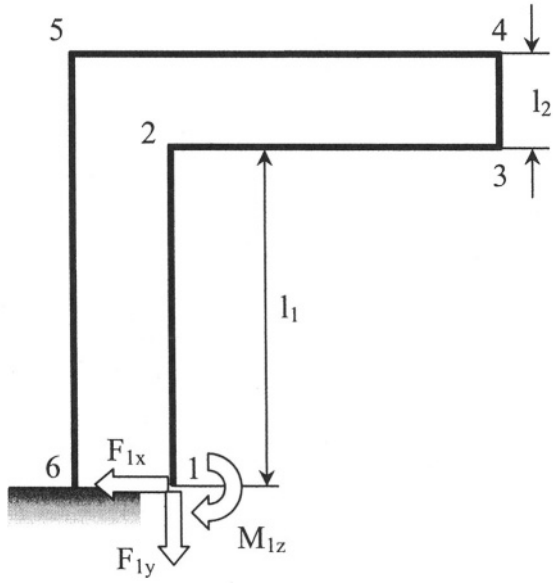

Figure 3.31 Geometry of a bent beam serpentine spring

The six in-plane compliances are:

$$C_{1,ux-Fx} = [8l_1^3 + 15l_1l_2(l_1 + l_2) + 5l_2^3] / (3EI_z) \tag{3.88}$$

$$C_{1,ux-Fy} = -l_1(l_1 + l_2)^2 / (EI_z) \tag{3.89}$$

$$C_{1,ux-Mz} = (3l_1^2 + 4l_1l_2 + 2l_2^2)/(EI_z) \tag{3.90}$$

$$C_{1,uy-Fy} = [2l_1^3 + 3l_1l_2(l_1 + l_2) + 4l_2^2](3EI_z) \tag{3.91}$$

$$C_{1,uy-Mz} = -(2l_1^2 + 4l_1l_2 + l_2^2)/(2EI_z) \tag{3.92}$$

$$C_{1,\theta z-Mz} = (4l_1 + 3l_2)/(EI_z) \tag{3.93}$$

The out-of-the-plane definition stiffness will again consider bending and torsion, and is calculated by applying a force F_{1z} at point 1 in Fig. 3.31. Its equation is:

$$\begin{aligned}\overline{K}_z = {} & 3EGI_yI_t/\{6EI_y(l_1 + l_2)(l_1^2 + l_1l_2 + l_2^2) + GI_t \\ & + [4l_1^3 + 6l_1l_2(l_1 + l_2) + 3l_2^3)]\}\end{aligned} \tag{3.94}$$

Example 3.11

A bent beam serpentine spring and a bent beam spring occupy the same square area. Which of the two microsuspensions is the stiffest in terms of the main stiffness assuming they are built of the same material and they have identical cross-sections ?

Solution:

Both springs are inscribed in a square area of side l_1. The definition stiffnesses for the two springs are expressed by inversion of the corresponding compliances of Eqs. (3.88) and (3.20), respectively.

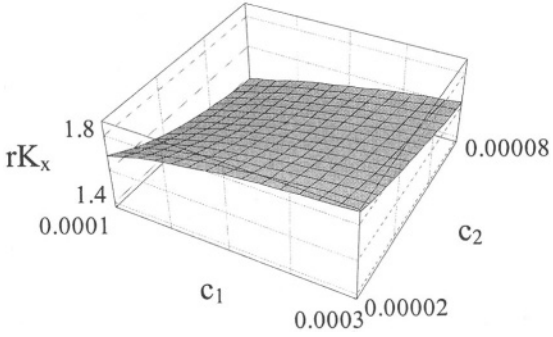

Figure 3.32 K_x stiffness ratio comparing a bent beam spring to a serpentine bent beam spring

By considering that:

$$\begin{cases} l_1 = c_1 l_2 \\ l_2 = c_2 w \end{cases} \tag{3.95}$$

the bent beam to bent beam serpentine stiffness ratio can be evaluated in terms of only the parameters c_1 and c_2 introduced in Eq. (3.95). Figure 3.32 is the three-dimensional plot of this ratio, and it can be seen that the bent beam design is stiffer than the corresponding bent beam serpentine variant.

2.6 Sagittal Springs

Figure 3.33 illustrates another design that utilizes a pair of sagittal springs. This spring configuration can also be employed as a displacement amplification microdevice (this will be shown later in Chapter 5), because an input motion about the long axis can be amplified (sometimes by factors larger than 10) about the direction perpendicular to it, very much similar to the action of a bow-arrow system. The three definition stiffnesses, K_x, K_y (both are in-plane stiffnesses) and K_z (the out-of-the-plane stiffness), will be expressed for a sagittal spring configuration. In order to do determine the K_x stiffness, which defines the spring action about the direction of motion of the shuttle mass, as shown in Fig. 3.33, half of the entire microsuspension will be analyzed, as sketched in Fig. 3.34. The identical links 2-3 and 4-5 of Fig. 3.34 are the only ones being compliant.

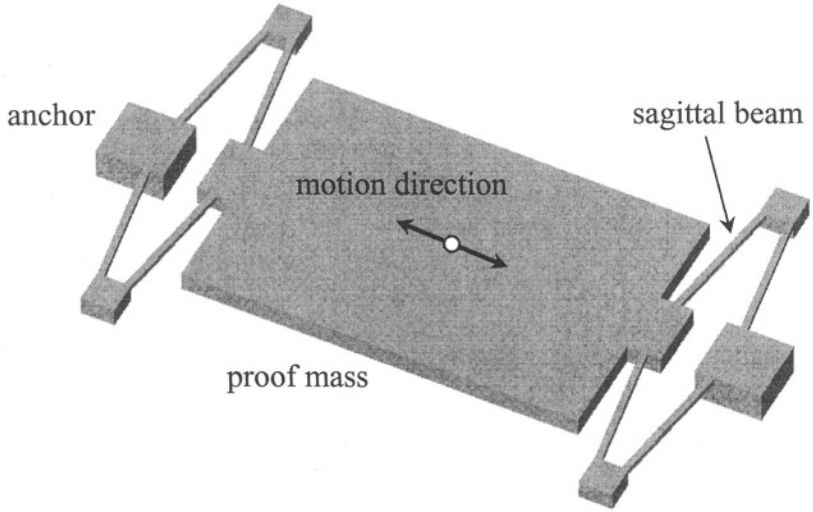

Figure 3.33 Microaccelerometer with two frontal sagittal springs

A first-level design and modeling approach would be the one considering constant cross-section compliant microhinges, but they could also be of a different shape, such as corner-filleted or be a series combination of different compliant segments in order to achieve specific design requirements. It is considered here that both compliant links have the same constant cross-section, and that only bending is taken into account.

By applying a force F_{1x} at point 1 in Fig. 3.34, the corresponding displacement u_{1x} can be found which will enable determining the required stiffness K_x. As previously mentioned, the reactions M_{1z} and F_{1y} need to be calculated by solving the equations: $\theta_{1z} = 0$ and $u_{1y} = 0$, which are set up by applying Castigliano's displacement theorem.

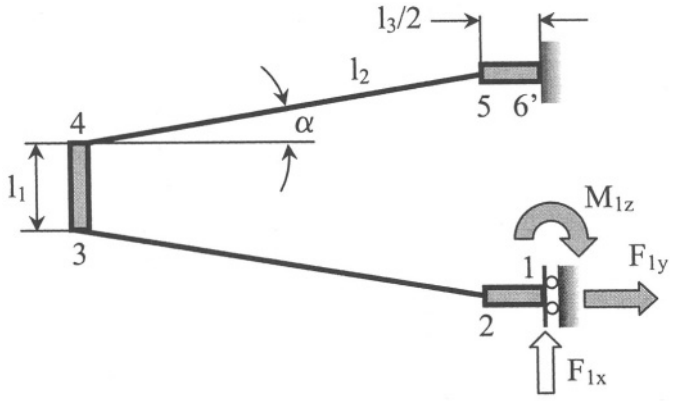

Figure 3.34 Half-model of a sagittal spring for x-stiffness calculation

It can be shown that the stiffness about the motion direction of the half model is:

$$K_x' = 6EI_z / (l_2^3 \cos^2 \alpha) \tag{3.96}$$

By taking $\alpha = 0$ in Eq. (3.96) results in:

$$K_x' = 6EI_z / l_2^3 \tag{3.97}$$

which is the stiffness for a U-spring formed of two parallel fixed-free beams of length l_2. When the cross-section of the two identical compliant members of Fig. 3.34 is variable, Equation (3.96) can be generalized to the form:

$$K_x' = K_{2,Fy-uy} / (2\cos^2 \alpha) \tag{3.98}$$

where $K_{2,Fy\text{-}uy}$ is the direct linear bending stiffness of the compliant member 2-3, calculated at point 2 with respect to point 3 and in a local reference frame placed at 2. Obviously, any of the hinge designs that have been presented in Chapter 2 can be implemented in the sagittal microspring. However, one complete sagittal microspring is composed of two identical parts (as the one drawn in Fig. 3.34) that are connected in parallel, and thus the total stiffness about the x-direction is:

$$K_x = 2K_x' \tag{3.99}$$

The other in-the-plane stiffness, K_y, can similarly be determined by using the sketch of Fig. 3.35. A force F_{1y} is applied at that point and by calculating the corresponding displacement u_{1y}, the sought stiffness is found to be:

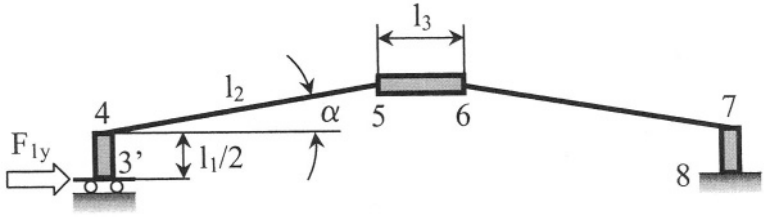

Figure 3.35 Half-model of a sagittal spring for y-stiffness calculation

$$K_y' = F_{1y} / u_{1y} = 6EI_z /(l_2^3 \sin^2 \alpha) \tag{3.100}$$

where, again, just the bending has been taken into account. Equation (3.100) can be generalized to the form:

$$K_y' = K_{4,Fy-uy} /(2\sin^2 \alpha) \tag{3.101}$$

where $K_{4,Fy\text{-}uy}$ is the direct linear bending stiffness of the microhinge 4-5 of variable cross-section, and which can be of variable cross-section. The stiffness is calculated at point 4 in Fig. 3.35 with respect to a local frame. The total stiffness of a sagittal microspring is twice the stiffness of one half because the two half components are connected in parallel, and therefore:

$$K_y = 2K_y' \tag{3.102}$$

The out-of-the-plane stiffness about the z-direction can be found by applying a force F_{1z} and by determining the corresponding displacement u_{1z} at point 1 in Fig. 3.34. It is however necessary to first determine the reaction moment M_{1y} (M_{1y} and F_{1z} are not shown in Fig. 3.34) by means of the related

condition $\theta_{1y} = 0$. Eventually, the z-axis stiffness is calculated by considering bending and torsion of the two compliant members (the cross-section is considered constant) and its (quite complex) expression is:

$$\begin{aligned}\overline{K}_z' = 12\{&6[(l_3-2c)^2\sin^2\alpha + 2(l_1+2l_2\sin\alpha)[l_1\cos\alpha \\ &+ (2l_2\cos\alpha + l_3 - 2c)\sin\alpha]\cos\alpha]/(GI_t) + [6l_1^2 + 14l_2^2 \\ &+ 3(l_3-2c)^2 + 3[(l_3-2c)^2 - 2(l_1^2+2l_2^2)]\cos(2\alpha) - 6(2c \\ &- l_3)(l_2 - 2l_1\sin\alpha)\cos\alpha + 6l_2[(l_3-2c)\cos(3\alpha) \\ &+ l_2\cos(4\alpha) + 4l_1\sin\alpha - 2l_1\sin(3\alpha)]]/(EI_y)\}^{-1}/l_2\end{aligned} \tag{3.103}$$

with:

$$\begin{aligned}c = \{&GI_t[l_3\cos\alpha + l_2\cos(2\alpha)]\cos\alpha + (EI_y - GI_t)l_1\sin\alpha\cos\alpha \\ &+ EI_y(l_3 + 2l_2\cos\alpha)\sin^2\alpha\}/[2(GI_t\cos^2\alpha + EI_y\sin^2\alpha]\end{aligned} \tag{3.104}$$

Example 3.12

A sagittal spring needs to be as insensitive as possible to the action of external forces that act about the y-direction while maintaining a good compliance about the motion direction. What is the inclination angle α that would accomplish these objectives for a given constant rectangular cross-section ?

Solution:

The conditions of the problem require maximizing the following stiffness ratio:

$$rK = K_y / K_x \tag{3.105}$$

By using the definition Eqs. (3.98) and (3.101), the ratio of Eq. (3.105) becomes:

$$rK = 1/\tan^2\alpha \tag{3.106}$$

and therefore the stiffness ratio is maximum when the inclination angle is minimum, i.e. $\alpha = 0$. A practical solution will take a very small value of α.

2.7 Folded Beams

Another microspring configuration that is being utilized to spring-couple to the translatory motion of a proof mass is shown in Fig. 3.36 where two

pairs of so-called folded beams are placed on the sides of the moving mass. Unlike the other configurations where the springs have been coupled in a serial fashion at both ends of the mass and aligned with the motion direction, each of the folded-beam springs are placed in parallel to the mass by supporting it from the two sides.

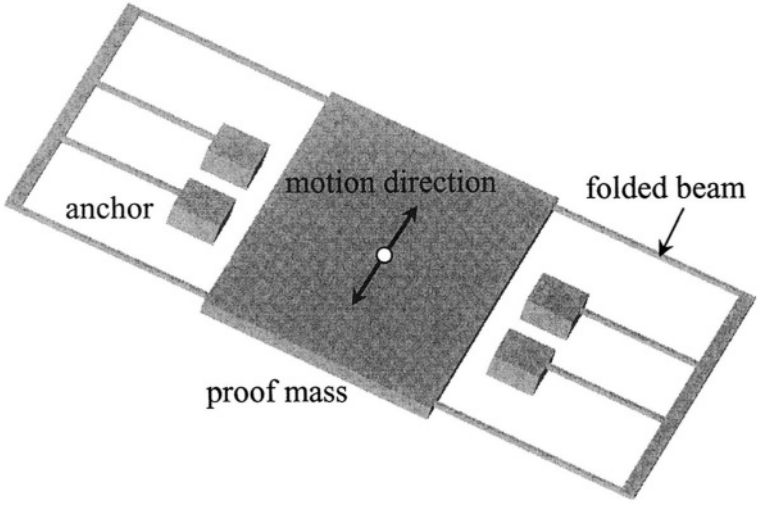

Figure 3.36 Two folded-beam springs attached to the sides of a moving proof mass

The aim is again to determine the spring stiffnesses about the three possible translatory motions of the center mass, namely the x-direction (the motion direction indicated in Fig. 3.36), the y-direction (the other in-plane direction, which is perpendicular on the x-direction) and the out-of-the-plane z-direction. In order to find these stiffnesses, it is sufficient to analyze just half of one folded-beam spring, as pictured in Fig. 3.37.

When only the links denoted by 2-3 and 4-5 in Fig. 3.37 are compliant, and each of the segments has a constant cross-section, the simplest expression of the x-axis stiffness is:

$$K_x' = 12E(I_{z1}/l_1^3 + I_{z2}/l_2^3) \tag{3.107}$$

which simply considers that the two compliant segments behave as two beams in parallel with respect to the x-motion. As a consequence, the resulting stiffness is the sum of the two component stiffnesses. When the two compliant segments have variable cross-sections, Eq. (3.107) can be written as:

$$K_x' = K_{Fy-uy}^{(1)} + K_{Fy-uy}^{(2)} \tag{3.108}$$

where the superscripts 1 and 2 denote the 2-3 and 4-5 members, and the subscript *Fy-uy* indicates the direct linear bending stiffness of the compliant members with respect to their local frames.

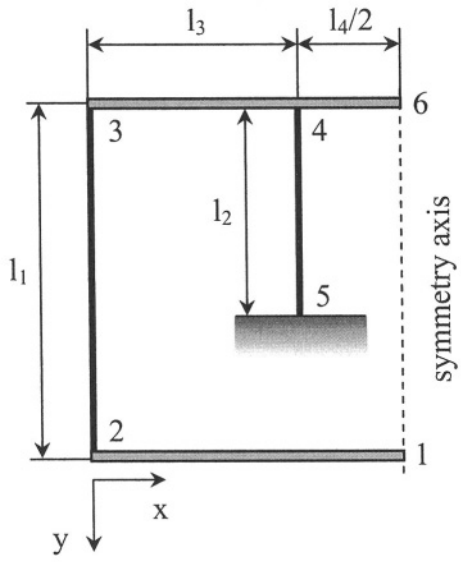

Figure 3.37 Half-model of a folded-beam spring

Because one entire folded-beam spring is composed of two identical halves (as the one sketched in Fig. 3.37) connected in parallel, the total stiffness is:

$$K_x = 2K_x' \tag{3.109}$$

The stiffness about the y-axis, the other in-plane motion direction, which is perpendicular to the main (motion) direction, can be found by considering that a force F_y is applied axially to all four compliant bars. In this situation the bars will only deform axially, and because they are placed in parallel, the total stiffness about the y-direction is:

$$K_y = 2E/(A_1/l_1 + A_2/l_2) \tag{3.110}$$

where it has been considered that the two compliant links have constant cross-sections. When the cross-sections are variable, Eq. (3.110) changes to:

$$K_y = 2(K_{Fx-ux}^{(1)} + K_{Fx-ux}^{(2)}) \tag{3.111}$$

The terms in the right-hand side of Eq. (3.111) are the axial stiffnesses of the two compliant members, taken with respect to their local frames (their x-axes are parallel to their length dimensions).

The spring stiffness about the out-of-the-plane motion (the z-direction) of the mass can be found by also using Fig. 3.37. A force F_{1z} is applied at point 1 about the z-direction and the corresponding u_{1z} (out-of-the-plane) displacement can be determined by considering bending and torsion of the two compliant members. The z-direction stiffness of the half-model is:

$$\overline{K}_z' = 3E/[l_1^3/I_{y1} + l_2(3l_1^2 - 3l_1l_2 + l_2^2)/I_{y2}] \tag{3.112}$$

which is valid when the two compliant segments are of constant cross-sections. The whole folded-beam microspring is formed of two parallel-connection identical parts (as the one sketched in Fig. 3.37), and therefore the stiffness of the full microspring is:

$$\overline{K}_z = 2\overline{K}_z' \tag{3.113}$$

Example 3.13

In a folded-beam microsuspension, the long legs cannot exceed a maximum length of $l_{1,max} = 200\ \mu m$. What is the length of the short legs which would produce a specified stiffness $K_x = 60$ N/m of the microsuspension about the motion direction for a given rectangular cross-section and material properties ($w = t = 5\ \mu m$, E = 130 GPa) ?

Solution:

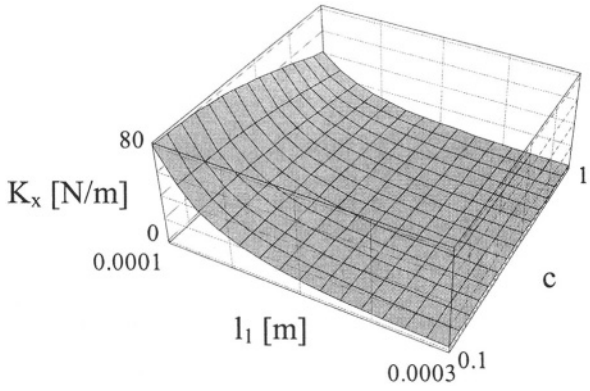

Figure 3.38 Stiffness K_x for a folded-beam suspension

If the short leg length is connected to the length of the long leg as:

$$l_2 = cl_1 \tag{3.114}$$

and for the given moment of inertia and Young's modulus, the stiffness K_x depends on l_1 and c, as shown in Fig. 3.38. The stiffness K_x decreases with l_1 and c increasing. For the values of l_{1max} and K_x the solution is c = 0.94, and therefore the length of the short leg is $l_2 = 188\ \mu m$.

Example 3.14

A sagittal suspension and a folded-beam spring can be inscribed within the same a x b rectangular area ($a = 300\ \mu m$, $b = 200\ \mu m$). What are their stiffnesses about the motion direction, in the case both designs have the same cross-section of their compliant members ? Consider that $\alpha = 15°$ and $l_1 = 2l_3$ for the sagittal spring, and that $l'_3 = l'_4$ for the folded-beam suspension.

Solution:

When both designs are inscribed in the given rectangular area, the main dimensions of the sagittal suspension are related by the following relationships:

$$\begin{cases} a = l_3 + 2l_2 \cos\alpha \\ b = l_1 + 2l_2 \sin\alpha \end{cases} \tag{3.115}$$

which yield $l_2 = 149.429\ \mu m$. The conditions for the folded-beam design are:

$$\begin{cases} a = 2l'_3 + l'_4 \\ b = l'_1 \end{cases} \tag{3.116}$$

and they result in: $l_1' = 200\ \mu m$.

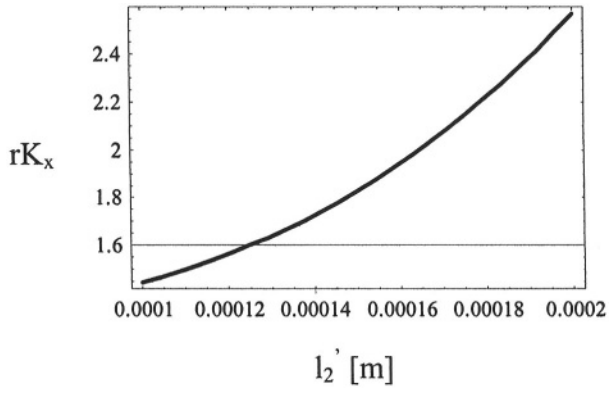

Figure 3.39 K_x stiffness ratio of sagittal spring versus folded-beam spring

By also using the other numerical values, one can study the sagittal-to-folded-beam stiffness ratio rK_x, which is plotted in Fig. 3.39 as a function of the length l_2' of the folded beam. It can be seen that the sagittal design is approximately 2.5 times stiffer than a corresponding folded-beam configuration for small lengths of the middle compliant leg.

3. MICROSUSPENSIONS FOR ROTARY MOTION

Several microsuspensions are studied in this section, which are designed for implementation in rotary-motion micromechanisms. Similar to the microsuspension configurations that are used in linear-motion applications and which were shown to be able to accommodate rotary motion as well, the rotary microsprings can also be sensitive to linear motion.

3.1 Curved-Beam Springs

rigid bodies undergoing translatory motion. A microspring design is analyzed here that can function as a torsional suspension for rotary motion. Figure 3.40 is a two-dimensional sketch showing several identical curved springs that are attached to a central hub at one end and to a tubular shaft (which is concentric with the inner hub) at the other end. The set of curved beams (they can also be straight beams) act as both suspensions and springs, as they connect the hub and the central shaft and elastically oppose the relative rotary motion between the two rigid components.

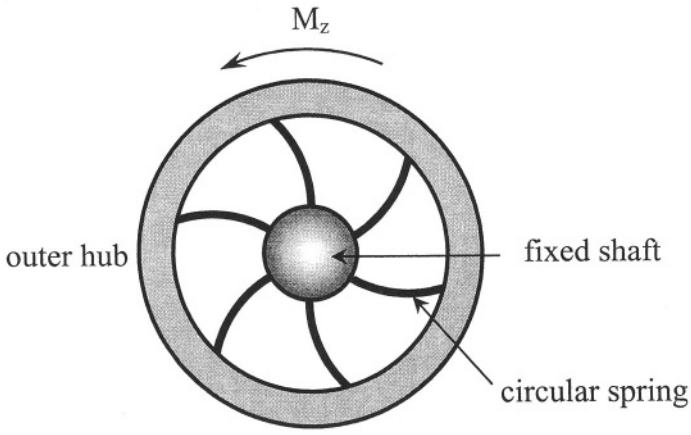

Figure 3.40 Set of curved beams acting as springs for the concentric hub-hollow shaft system

It is of main interest to find the total stiffness of the curved spring set in terms of the relative rotation between hub and the outer hollow shaft. Under

the action of an external torque M_z that is applied to the outer shaft, for instance (case where the inner hub is supposed to be fixed), the relative rotation angle is expressed by the equation:

$$M_z = K_t \theta_z \tag{3.117}$$

The torsion stiffness is:

$$K_t = nK_{1,Mz-\theta z} \tag{3.118}$$

where n is the number of beams and $K_{1,Mz-\theta z}$ is the rotation stiffness of the curved beam shown in Fig. 3.41 and which is defined by a radius R, a center angle α and a constant rectangular cross-section.

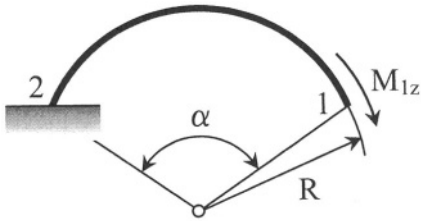

Figure 3.41 Curved spring with defining planar geometry

This stiffness can be determined by utilizing the compliance formulation that has been introduced in Chapter 1 for a relatively-thin curved beam. It has been shown there that the in-plane deformation of a curved beam is defined by a set of six compliances, which have explicitly been derived, and arranged into a compliance matrix – Eq. (1.127). It is known that the inverse of the compliance matrix is the related stiffness matrix, and therefore Eq. (3.26) also applies to this case. Through inversion of the compliance matrix of the right-hand side in Eq. (3.26) and by using the corresponding individual compliance Eqs. (1.156) to (1.161), it is found that:

$$\begin{aligned} K_{1,Mz-\theta z} = EI_z[&-9+6\alpha^2+16\cos\alpha-7\cos(2\alpha)-4\alpha(2 \\ &+\cos\alpha)\sin\alpha]/\{R[-9\alpha+2\alpha^3+8\alpha\cos\alpha+\alpha\cos(2\alpha) \\ &+8\sin\alpha+4\sin(2\alpha)]\} \end{aligned} \tag{3.119}$$

Of interest is also the suspension capacity of the curved spring set as the self-weight of the supported member (the outer hollow shaft in this case) can displace it downward about the z-axis. The corresponding linear stiffness about the z-axis can be calculated as:

$$K_z = nK_{1,Fz-uz} \tag{3.120}$$

where $K_{1,Fz-uz}$ is the out-of-the-plane stiffness of one curved spring. The six out-of-the-plane compliances of a thin curved member have explicitly been formulated in Eqs. (1.139) to (1.143) and Eq. (1.163), respectively. The linear stiffness can be found by inverting the compliance matrix of Eq. (1.137), which results in:

$$\begin{bmatrix} K_{1,Fz-uz} & K_{1,Fz-\theta x} & K_{1,Fz-\theta y} \\ K_{1,Fz-\theta x} & K_{1,Mx-\theta x} & K_{1,Mx-\theta y} \\ K_{1,Fz-\theta y} & K_{1,Mx-\theta y} & K_{1,My-\theta y} \end{bmatrix} = \begin{bmatrix} C_{1,uz-Fz} & C_{1,uz-Mx} & C_{1,uz-My} \\ C_{1,uz-Mx} & C_{1,\theta x-Mx} & C_{1,\theta x-My} \\ C_{1,uz-My} & C_{1,\theta x-My} & C_{1,\theta y-My} \end{bmatrix}^{-1} \tag{3.121}$$

As a consequence, the individual stiffness $K_{1,Fz-uz}$ is:

$$\begin{aligned} K_{1,Fz-uz} = {} & 4EGI_t I_y [(2-\pi)EI_y - (\pi+2)GI_t] / \{ R^3 [(\pi-2)(\pi \\ & -2\alpha)E^2 I_y^2 + 2[8-4(\pi-1)\alpha+\pi(\pi-4)]EGI_t I_y + [16+\pi(\pi-6) \\ & -6(\pi+2)\alpha]G^2 I_t^2 - 2[(\pi-2)EI_y + (\pi+2)GI_t][(GI_t - EI_y) \\ & \sin\alpha\cos\alpha - 4GI_t]] \} \end{aligned} \tag{3.122}$$

Example 3.15

Find the tip angle of a curved microbeam which is part of a rotary (torsional) spring suspension which connects an inner shaft of diameter d to an outer hub of interior diameter D (D = 2d), in a way that would maximize the spring's compliance with respect to an external torque for a given rectangular cross-section and material properties. Consider that w = t = 2 μm, d = 20 μm and E =125 GPa.

Solution:

The tip angle of the curved spring can be expressed as:

$$\sin\alpha = (D-d)/(4R) \tag{3.123}$$

and therefore this condition has to be used in Eq. (3.119), which gives the torsional stiffness of such a spring. The stiffness of interest is plotted in Fig. 3.42 in terms of the shaft diameter d and the radius of the curved spring R by utilizing the given numerical values. As the figure shows, the stiffness is larger for larger values of d and smaller values of R. As a consequence, one has to select these parameters accordingly, namely small values for d and large values for R.

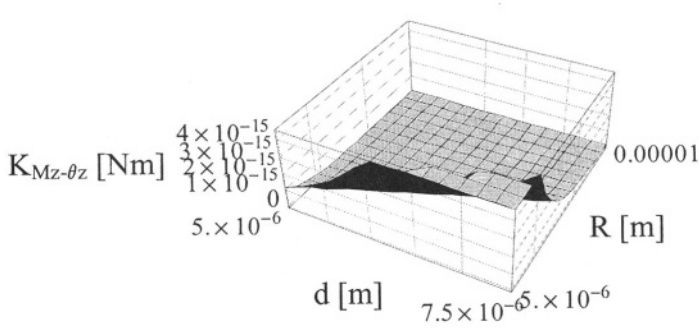

Figure 3.42 Torsion stiffness plot

3.2 Spiral Springs

Another microsuspension variant for rotary motion is the spiral spring. Two designs will be presented next, the spiral spring with small number of turns and the spiral spring with large number of turns. Both designs will consider thick and thin configurations.

3.2.1 Spiral Spring with Small Number of Turns

3.2.1.1 Thick Spiral Spring

A spiral spring that has a small number of turns is sketched in Fig. 3.43. The inner end is fixed whereas the outer one is free. The outer (maximum) radius is r_2 and the inner (minimum) one is r_1.

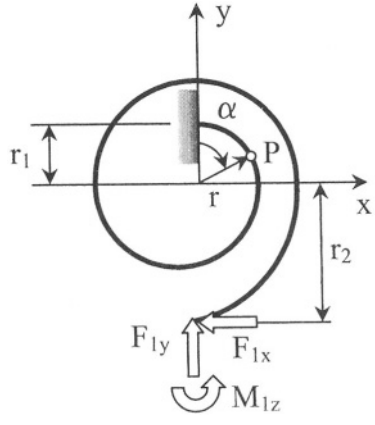

Figure 3.43 Spiral spring with small number of turns

An arbitrary point is situated an angle α measured from the vertical line passing through the fixed end.

The radius r corresponding to the generic point P of Fig. 3.43 can be calculated in the case it varies linearly as:

$$r = r_1 + \alpha(r_2 - r_1)/\alpha_{max} \tag{3.124}$$

where α_{max} is the maximum angle subtended by the spiral. The aim here is to determine the in-plane compliances that relate the loads F_{1x}, F_{1y}, M_{1z}, which are shown in Fig. 3. 43, to the corresponding displacements u_{1x}, u_{1y} and θ_{1z}. The Castigliano's displacement theorem is applied in order to find the six compliances of the 3 x 3 symmetric compliance matrix. In the case of a relatively thick spiral spring (where the maximum radius r_2 is less than 10 times the cross-sectional width w), the bending energy is expressed in Eq. (3.52) and the bending moment is:

$$M_b = M_1 + F_{1x}(r_2 + r\sin\alpha) - F_{1y} r\cos\alpha \tag{3.125}$$

The resulting in-plane compliances are:

$$\begin{aligned} C_{1,ux-Fx} = \{ & 2\alpha_{max}[(2\alpha_{max}^2 - 3)r_1^2 + [3 + 2\alpha_{max}(\alpha_{max} - 12)] \\ & r_1 r_2 + 14\alpha_{max}^2 r_2^2] + 6r_2\alpha_{max}[8r_2\alpha_{max}\cos\alpha_{max} + (r_1 - r_2) \\ & (\cos(2\alpha_{max}) + 8\sin\alpha_{max})] + 3[r_1^2 - 2r_1 r_2 + (1 - 2\alpha_{max}^2)r_2^2] \\ & \sin(2\alpha_{max}\}/(24eAE\alpha_{max}^2) \end{aligned} \tag{3.126}$$

$$\begin{aligned} C_{1,ux-Fy} = & \{(2\alpha_{max}^2 - 1)r_1^2 + (2 - 8\alpha_{max})r_1 r_2 - (1 - 8\alpha_{max})r_2^2 \\ & + [r_1^2 - 2r_1 r_2 + (1 - 2\alpha_{max}^2)r_2^2](\cos(2\alpha_{max}) - 4r_2(r_1 - r_2) \\ & \alpha_{max}\cos\alpha_{max}(\sin\alpha_{max} - 2) - 8r_2^2\alpha_{max}^2\sin\alpha_{max}\}/(8eAE\alpha_{max}^2) \end{aligned} \tag{3.127}$$

$$\begin{aligned} C_{1,ux-Mz} = & [r_1(\sin\alpha_{max} - \alpha_{max}) + r_2(\alpha_{max}^2 + \alpha_{max}\cos\alpha_{max} \\ & - \sin\alpha_{max})]/(eAE\alpha_{max}) \end{aligned} \tag{3.128}$$

$$\begin{aligned} C_{1,uy-Fy} = & \{6r_1(r_1 - r_2)\alpha_{max} + 4(r_1^2 + r_1 r_2 + r_2^2)\alpha_{max}^3 + 6r_2(r_2 - r_1) \\ & \alpha_{max}\cos(2\alpha_{max}) - 3[r_1^2 - 2r_1 r_2 + (1 - 2\alpha_{max}^2)r_2^2]\sin(2\alpha_{max})\} \\ & /24eAE\alpha_{max}^2 \end{aligned} \tag{3.129}$$

$$C_{1,uy-Mz} = [r_1(\cos\alpha_{max} - 1) + r_2(1 - \cos\alpha_{max} - \alpha_{max}\sin\alpha_{max})] / (eAE\alpha_{max}) \quad (3.130)$$

$$C_{1,\theta z-Mz} = \alpha_{max} / (eAE) \quad (3.131)$$

Example 3.16

What is the torsional stiffness of a thick spiral spring with square cross-section ($t = 2\ \mu m$) microfabricated of a material with E = 135 GPa when the maximum angle α_{max} is 270° ? Also consider that $r_1 = 20\ \mu m$ and $r_2 = 30\ \mu m$.

Solution:

The definition torsional stiffness is the inverse of the torsional compliance. As Eq. (3.131) shows, the eccentricity e needs to be calculated. An average radius of $25\ \mu m$ is taken which gives an eccentricity of 1.334×10^{-8} m by way of Eq. (1.122), Chapter 1. By substituting the other numerical values into Eq. (3.131), the torsional stiffness is $K_{Mz\text{-}\theta z} = 1.529 \times 10^{-9}$ Nm.

3.2.1.2 Thin Spiral Spring

For a thin spiral, according to the theory presented in Chapter 1, only the bending moment is taken into consideration, and the elastic deformations are calculated by means of the equations pertaining to straight beams. By applying again Castigliano's displacement theorem, and by considering the bending moment of Eq. (3.125), the six in-plane compliances which are of interest can be expressed as:

$$\begin{aligned} C_{1,ux-Fx} = \{&(3 - 6\alpha_{max}^2 + 2\alpha_{max}^4)r_1^3 + \{2\alpha_{max}[32 + \alpha_{max}[3 \\ &+ \alpha_{max}(\alpha_{max} - 16)]] - 9\}r_1^2 r_2 + (9 - 128\alpha_{max} + 10\alpha_{max}^4)r_1 r_2^2 \\ &+ (-3 + 64\alpha_{max} + 10\alpha_{max}^4)r_2^3 + 32\alpha_{max}r_2[-2r_1^2 + 4r_1 r_2 + (\alpha_{max}^2 \\ &- 2)r_2^2]\cos\alpha_{max} - 3(r_1 - r_2)[r_1^2 - 2r_1 r_2 + (1 - 2\alpha_{max}^2)] \\ &\cos(2\alpha_{max}) + 2\alpha_{max}r_2[32\alpha_{max}(r_1 - r_2)r_2\sin\alpha_{max} + [3r_1^2 \\ &- 6r_1 r_2 + (3 - 2\alpha_{max}^2)r_2^2]\sin(2\alpha_{max})]\} / (16EI_z\alpha_{max}^3) \end{aligned} \quad (3.132)$$

$$\begin{aligned} C_{1,ux-Fy} = \{&2\alpha_{max}r_1[(2\alpha_{max}^2 - 3)r_1^2 + 2(3 - 8\alpha_{max})r_1 r_2 \\ &+ (16\alpha_{max} - 3)r_2^2] + 32\alpha_{max}^2(r_1 - r_2)r_2^2\cos\alpha_{max} + 2\alpha_{max}r_2[3r_1^2 \\ &- 6r_1 r_2 + (3 - 2\alpha_{max}^2)r_2^2]\cos(2\alpha_{max}) - 16\alpha_{max}r_2[-2r_1^2 + 4r_1 r_2 \\ &+ (\alpha_{max}^2 - 2)r_2^2]\sin\alpha_{max} + 3(r_1 - r_2)[r_1^2 - 2r_1 r_2 + (1 - 2\alpha_{max}^2)r_2^2] \\ &\sin(2\alpha_{max})\} / (16EI_z\alpha_{max}^3) \end{aligned} \quad (3.133)$$

$$C_{1,ux-Mz} = \{-2(\alpha_{max}^2 - 2)r_1^2 + (\alpha_{max}^3 - 8)r_1 r_2 + (4 + \alpha_{max}^3)r_2^2 + [-4r_1^2 + 8r_1 r_2 + 2(\alpha_{max}^2 - 2)r_2^2]\cos\alpha_{max} + 4(r_1 - r_2)r_2 \alpha_{max}\sin\alpha_{max}\}/(2EI_z\alpha_{max}^2) \quad (3.134)$$

$$C_{1,uy-Fy} = \{(-3 + 6\alpha_{max}^2 + 2\alpha_{max}^4)r_1^3 + (9 - 6\alpha_{max}^2 + 2\alpha_{max}^4) r_1^2 r_2 + (2\alpha_{max}^4 - 9)r_1 r_2^2 + (3 + 2\alpha_{max}^4)r_2^3 + 3(r_1 - r_2)[r_1^2 - 2r_1 r_2 + (1 - 2\alpha_{max}^2)r_2^2]\cos(2\alpha_{max}) + 2\alpha_{max} r_2[-3r_1^2 + 6r_1 r_2 + (2\alpha_{max}^2 - 3)r_2^2]\sin(2\alpha_{max})\}/(16EI_z\alpha_{max}^3) \quad (3.135)$$

$$C_{1,uy-Mz} = \{[2r_1^2 - 4r_1 r_2 + (2 - \alpha_{max}^2)r_2^2]\sin\alpha_{max} - 2\alpha_{max}(r_1 - r_2)(r_1 - r_2\cos\alpha_{max})\}/(EI_z\alpha_{max}^2) \quad (3.136)$$

$$C_{1,\theta z-Mz} = \alpha_{max}(r_1 + r_2)/(2EI_z) \quad (3.137)$$

Example 3.17

Consider that point 1 in Fig. 3.43 is confined to move about the x-direction. Find the stiffness of a thin spiral spring with small number of turns knowing $\alpha_{max} = 360^o$, $I_z = 2 \times 10^{-24}$ m^4 and $E = 135 \times 10^9$ N/m^2.

Solution:

The stiffness about the x-direction in this case can be found after determining the reactions F_{1y} and M_{1z}. When taking into account that the y-displacement and z-rotation at point 1 are zero, the unknown reactions can be written in terms of F_{1x} in the form:

$$\begin{cases} F_{1y} = c_y F_{1x} \\ M_{1z} = c_z F_{1x} \end{cases} \quad (3.138)$$

where c_y and c_z are functions of r_1, r_2 and α_{max}. After finding the x-displacement at point 1 as a function of F_{1x} and the geometry/material properties defining the spiral, the corresponding stiffness about the x-direction (according to the definition) can be expressed as:

$$K_x = EI_z f(r_1, r_2, \alpha_{max}) \quad (3.139)$$

The function $f(r_1, r_2, \alpha_{max})$ is too complex to be presented here, but Fig. 3.44 shows the variation of the stiffness about the x-direction as a function of the

radii r_1 and r_2 for the particular parameters given here. It can be noticed that that K_x decreases quasi-linearly with r_1 and r_2 increasing.

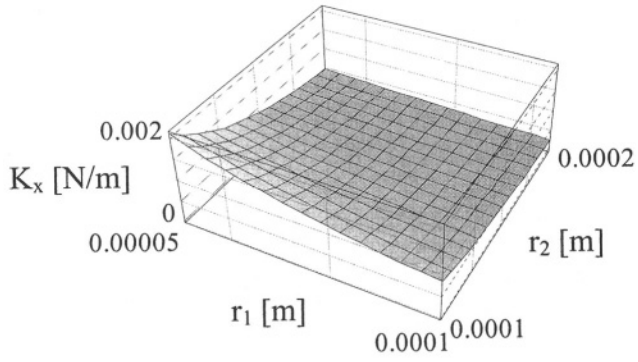

Figure 3.44 Stiffness K_x as a function of r_1 and r_2

Example 3.18

A thin spiral spring has to be designed within a circular area of radius R. Find the rectangular cross-section of the spring with a given thickness-to-width ratio and a given ratio of the maximum-to-minimum radii that would produce the best compliance in torsion for a given material. Consider that $t = 2\ \mu m$, $R = 200\ \mu m$, $\alpha_{max} = 300^o$ and E = 150 GPa.

Solution:

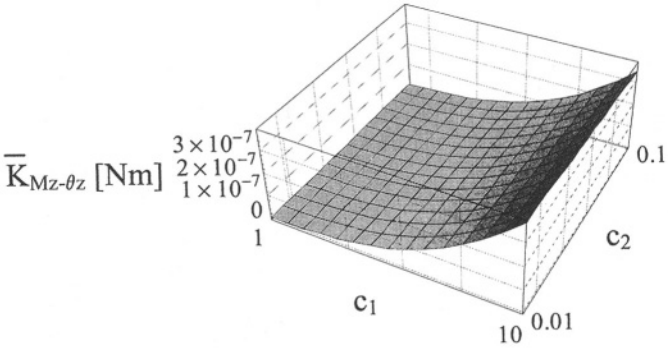

Figure 3.45 Stiffness ratio

The following relationships:

$$\begin{cases} w = c_1 t \\ r_1 = c_2 r_2 \end{cases} \tag{3.140}$$

are substituted into Eq. (3.137), which defines the torsion compliance. The corresponding definition stiffness is the inverse of the compliance. The plot of Fig. 3.45 is drawn in terms of c_1 and c_2. It can be seen that the influence of c_2 is not marked in comparison to c_1. The latter parameter should be small in order to reduce to stiffness (and implicitly to increase the compliance).

3.2.2 Spiral Spring with Large Number of Turns

The case of a spiral with a large number of thin turns, as the one pictured in Fig. 3.46, is studied now.

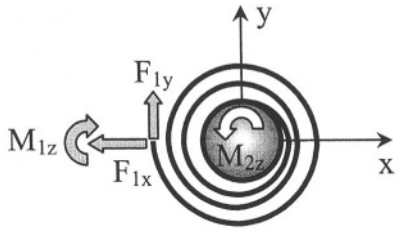

Figure 3.46 Spiral with a relatively large number of turns

The outer end is clamped whereas the inner end is fixed to a shaft that can rotate under the action of a torque M_{2z}. The torsion stiffness (relating M_{2z} to the rotation angle θ_{2z}) is of interest here. The bending moment at a generic point of coordinates x and y is:

$$M_b = M_{1z} + F_{1x} y + F_{1y}(r_2 + x) \tag{3.141}$$

The following approximate equilibrium equation applies:

$$M_{2z} = M_{1z} + F_{1y} r_2 \tag{3.142}$$

By combining Eqs. (3.141) and (3.142), the bending moment becomes:

$$M_b = M_{2z} + F_{1x} y + F_{1y} x \tag{3.143}$$

By applying Castigliano's displacement theorem, the forces F_{1x} and F_{1y} can be expressed in terms of M_{2z}, and, in the end, the rotational stiffness of the spiral spring is found to be (as also shown in Chironis [2] and Wahl [3]):

$$K_{rz} = EI_z / l \tag{3.144}$$

where l is the total length of the spiral.

Problems

Problem 3.1

The polysilicon fixed-guided beam of Fig. 3.4 has a length of $l = 200\ \mu m$ and a constant rectangular cross-section with $w = 6\ \mu m$ and $t = 1\ \mu m$. Young's modulus is E = 150 GPa. The beam is used in an accelerometer whose measuring unit can read displacements with a precision of $u_{1z} = 0.2\ \mu m$. What is the minimum force that can be detected by this microsystem ?

Answer:

$F_{1z} = 2.25 \times 10^{-8}$ N

Problem 3.2

An inclined beam is used in a static application where the stiffness about the active direction of motion, K_y, is two times smaller than it should be. Determine the inclination angle of the beam that would achieve the stiffness objective (see Fig. 3.6 (b)). Known are $l = 100\ \mu m$, $w = t = 2\ \mu m$, $\alpha_0 = 10^o$, $E = 130 \times 10^9\ N/m^2$.

Answer:

$\alpha = 14.27^o$

Problem 3.3

The ratio of the K_x stiffness to the K_y stiffness of a bent beam spring, as the one sketched in Fig. 3.9, has to be of a fixed value r. What is the length of the beam's square cross-section side that would produce this result and what is the permissible range of r ? Consider that $l_2 = cl_1$.

Answer:

$$t = \sqrt{[(4+c)c^3 - 4c - 1] / [(c-r)(c+1)l_1}$$

and therefore:

$$(1+4c)/[c^3(4+c)] < r < c$$

Problem 3.4

A U-spring is designed according to the prescriptions of configuration # 1, Fig. 3.12. It has a constant rectangular cross-section with $w = 5\ \mu m$ and t =

2 μm and Young's modulus is E = 130 GPa. The application where the U-spring is incorporated into requires that $l_3 = 2\,l_1$ and $l_2 = l_1/2$. Determine the length l_1 that produces a maximum stiffness of = 0.3 N/m about the direction of motion (calculated according to the definition).

Answer:

$l_1 = 98.75\ \mu$m

Problem 3.5

A configuration # 2 U-spring (see Fig. 3.16) has to replace a configuration # 1 U-spring (see Fig. 3.12) in order to increase the stiffness about the active direction of motion, K_x. If the geometrical envelope, the cross-section and the material properties are identical for the two designs, what is the factor of improvement in K_x that is achieved by this design change ? Consider that $l_3 = 2l_1$ and $l_2 = l_1$ for configuration # 1 and use the stiffness expressions according to the definition.

Answer:

The stiffness of configuration # 2 is 1.226 times larger than the stiffness of configuration # 1.

Problem 3.6

A configuration # 3 U-spring, as the one shown in Fig. 3.17, is used in a microaccelerometer dynamic application instead of a configuration # 1 U-spring in order to reduce stress concentration at the sharp corners. Known are w = 15 μm, t = 2 μm, l_1 = 300 μm, l_2 = 200 μm, l_3 = 400 μm, R = 100 μm, E = 150 GPa and G = 60 GPa. Find the change in the out-of-the-plane stiffness.

Answer:

Stiffness for configuration # 1 is 19.97 N/m.

Stiffness for configuration # 3 is 6.37 N/m.

Problem 3.7

A bent beam spring (shown in Fig. 3.9) and a configuration # 1 U-spring (as sketched in Fig. 3.12) are microsuspension candidates in an application where the compliance about the in-plane y-direction has to be minimum. When both springs have the same square cross-section (t = 3 μm), are built of the same material and, additionally, the following geometry constraints have to be complied with: $l_3 = 2l_2 = 2l_1 = l = 100\ \mu$m (l is the leg length of the bent beam spring), which design is best suited for the task ?

Answer:

The compliance of the bent beam spring is 4.57 times larger than the compliance of the U-spring, so the U-spring is the option.

Problem 3.8

A basic serpentine spring of very thin cross-section ($t << w$) with a given value of its long leg, l_1, has to be stiff about the out-of-the-plane (z) direction and compliant in torsion. Select a length l_2 which will satisfy these requirements. (Hint: Analyze the $K_z / (l_1^2 K_t)$ ratio).

Answer:

The ratio is maximum (which means the numerator is maximum and the denominator is minimum) for a given l_1 when l_2 is minimum.

Problem 3.9

What is the main compliance of a linearly-scaled serpentine spring that contains two units ? The length of the smaller unit's long leg is $l_1 = 100\ \mu m$, the shorter leg's length is $l_2 = 20\ \mu m$, $\alpha = 30^o$, $w = t = 5\ \mu m$ and E = 140 GPa.

Answer:

The compliance is the sum of the two units compliances; $C_{1,ux\text{-}Fx} = 0.662$ m/N.

Problem 3.10

Compare the two linear in-plane compliances of a bent beam serpentine spring that is microfabricated of polysilicon with E = 130 GPa, G = 40 GPa, $w = 10\ \mu m$, $t = 1\ \mu m$, $l_1 = 10\ l_2 = 200\ \mu m$.

Answer:

$C_{1,uy\text{-}Fy} / C_{1,ux\text{-}Fx} = 0.242$

Problem 3.11

Find the out-of-the-plane deflection of a bent beam serpentine spring with $l_1 = 150\ \mu m$, $l_2 = 30\ \mu m$, $w = 20\ \mu m$, $t = 2\ \mu m$, E = 135 GPa, G = 42 GPa under the action of a force of $F_{1z} = 5\ \mu N$. Also calculate the deflection of a similar bent beam spring with $l = l_1$ under the same loading and having all other geometrical and material properties identical to the ones of the bent beam serpentine spring.

Answer:

Stiffness of bent beam serpentine spring is 36.219 N/m.

Stiffness of bent beam spring is 11.808 N/m.

Problem 3.12

A configuration # 1 U-spring (with the boundary conditions of Fig. 3.12) with $l_1 = l_3$ and a sagittal spring (Figure 3.35), both inscribed in the same rectangular area $l_1 \times l_2$, are possible solutions for an application where relatively high K_y (definition) stiffness is required. Determine the best design solution, when $l_1 = 100\ \mu m$, $l_2 = 50\ \mu m$, $\alpha = 15^o$, $w = t = 4\ \mu m$, E = 140 GPa.

Answer:

Stiffness of U-spring is 10.24 N/m.

Stiffness of sagittal spring is 372.46 N/m (for $l_3 = 0$)

Problem 3.13

A folded-beam spring as the one sketched in Fig. 3.37 is microfabricated by a technology which imposes a thickness of $t = 2\ \mu m$. Find the cross-sectional width w of its two compliant legs assuming that $l_1 = 2\ l_2 = 200\ \mu m$, E = 150 GPa and when a stiffness $K_x = 50$ N/m needs to be produced.

Answer:

$w = 18.52\ \mu m$

Problem 3.14

Find the number of curved springs with $w = t = 3\ \mu m$, $R = 100\ \mu m$, $\alpha = 15^o$ and E = 130 GPa, which combined as shown in Fig. 3.40 will be able to produce a rotation angle of 2° under an external torque of $5000\ \mu N\mu m$.

Answer:

n = 4

Problem 3.15

A thin spiral spring with a small number of turns and with its external end free, needs to have its $C_{1,ux\text{-}Fx}$ compliance 5 times larger than $C_{1,uy\text{-}Fy}$ in an application where $r_1 = 100\ \mu m$ and $\alpha_{max} = 270^o$. Determine the external radius r_2.

Answer:

$r_2 = 154.46\ \mu m$

References

1. W.C. Young, R.G. Budynas, *Roark's Formulas for Stress and Strain,* Seventh Edition, McGraw Hill, New York, 2002.

2. N.P. Chironis – Editor, *Spring Design and Application,* McGraw-Hill Book Company, New York, 1961.

3. A.M. Wahl, *Mechanical Springs,* McGraw-Hill Book Company, Second Edition, New York, 1963.

Chapter 4

MICROTRANSDUCTION: ACTUATION AND SENSING

1. INTRODUCTION

This chapter analyzes the main forms of MEMS *actuation* and *sensing,* also known together as *transduction* methods. The actuation basically converts a form of energy, such as electric or thermal, into mechanical motion by various means. The performance of a specific actuation method is usually qualified through mechanical amounts, such as force/moment or linear/rotary displacement. Conversely, in sensing, an already-existing mechanical motion or the effects of the microdevice interaction with its environment need to be evaluated by transforming the mechanical energy corresponding to motion into another type of energy, which can directly be measured.

On the other hand, one microdevice can be used as either actuator or sensor. An electrostatic comb drive, for instance, can function as an actuator when is supplied with electric energy and sets into motion a microdevice, but, equally, it can be used as a sensor in a microdevice that is actuated by a different source in order to measure displacements by quantifying electric capacitance changes. However, the relationship between mechanical displacement and capacitance variation is unique. In other words, a unique equation governs a specific transduction form, which can be used conveniently to describe either actuation or sensing, through calculation of the corresponding output amount in terms of the input quantities.

Studied in this chapter are transduction methods such as thermal, electrostatic, electromagnetic and magnetic, piezoelectric, piezomagnetic, by means of shape memory alloys, and through bimorphs and multimorphs. Transduction is energetically imperfect, as one form of energy cannot convert into another form of energy without losses (which can be substantial at times), but this subject, which needs further research, especially regarding the mechanisms that are involved in energy conversion, is not approached here.

2. THERMAL TRANSDUCTION

2.1 Introduction

The thermal actuation has the benefit of producing relatively large forces and/or displacements but these performances come at the expense of large input energy and at relatively low frequencies because of the time necessary to reach thermal equilibrium (which is necessary for reproducible operation).

The principle of linear thermal expansion is sketched in Fig. 4.1 where a fixed-free bar of length 1 is shown that expands through heating by a quantity Δl, which can be determined as:

$$\Delta l = u_{1x} = \alpha l \Delta T \tag{4.1}$$

where α is the material coefficient of linear thermal expansion (measured in 1/°C) and ΔT is the temperature variation. Notice that when $\Delta T < 0$ the bar compresses ($\Delta l < 0$), and vice versa, the bar expands ($\Delta l > 0$) when the temperature increases ($\Delta T > 0$), as the case is with the example shown in Fig. 4.1.

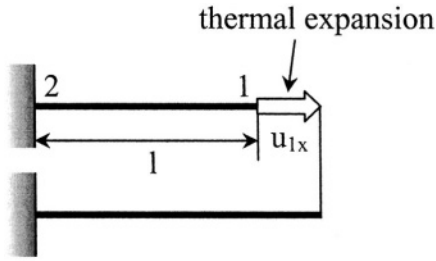

Figure 4.1 Fixed-free bar expanding axially under a temperature increase

This device is probably the simplest thermal actuator as the free end 1 can be coupled to a microdevice at a port where actuation is needed. The thermal displacement of Eq. (4.1) can also be produced by an equivalent force that acts at the free end 1, and which is:

$$F_{1x} = EA\Delta l / l = EA\alpha\Delta T \tag{4.2}$$

where E is the material Young's modulus and A is the cross-sectional area. Equation (4.1) has been used to determine the final form of Eq. (4.2).

The output capacity of an actuator, such as the simple thermal bar, depends on the load is has to overcome. Let us assume that an axial load is applied opposing the free expansion of a fixed-free bar, and let us consider that this force can increase up to a certain level that will completely

annihilate the thermal expansion of the heated bar. As long as the external force is less than this threshold value, usually called *bloc force,* the total displacement of the tip of the bar is the difference of two opposing deformations, namely:

$$u_{1x} = \alpha l \Delta T - Fl/(EA) \tag{4.3}$$

where F is the external force. Equation (4.3) can be rewritten in the form:

$$F = EA\alpha\Delta T - EAu_{1x}/l \tag{4.4}$$

There is a linear relationship between the external force and the total linear expansion, as Eq. (4.4) indicates. For zero axial displacement ($u_{1x} = 0$), the force is maximum and equal to the bloc force:

$$F_b = EA\alpha\Delta T \tag{4.5}$$

whereas its minimum value of zero occurs for the *free displacement* u_0, which is:

$$u_0 = \alpha l \Delta T \tag{4.6}$$

Several of the actuators that are going to be presented in this chapter behave similarly to the thermal actuator, and their force-displacement characteristic can be written in the form:

$$F = F_b - (F_b/u_0)u \tag{4.7}$$

The linear relationship of Eq. (4.7) is plotted in Fig. 4.2.

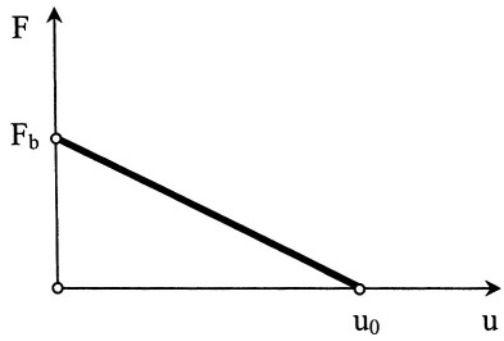

Figure 4.2 External force working against constant actuation force in terms of the output displacement

As Eq. (4.7) suggests, this relationship is fully determined by means of the two parameters, the bloc force F_b and the free displacement u_0, and therefore these two amounts will be formulated for the types of actuators that behave similarly.

2.2 Bent Beam

By changing the boundary conditions of the fixed-free bar analyzed previously, bending and different levels of actuation can be achieved through thermal heating, such as in the example of the bent beam (discussed also by Que et al. [1] and Gianchandani and Najafi [2] for instance) that is sketched in Fig. 4.3.

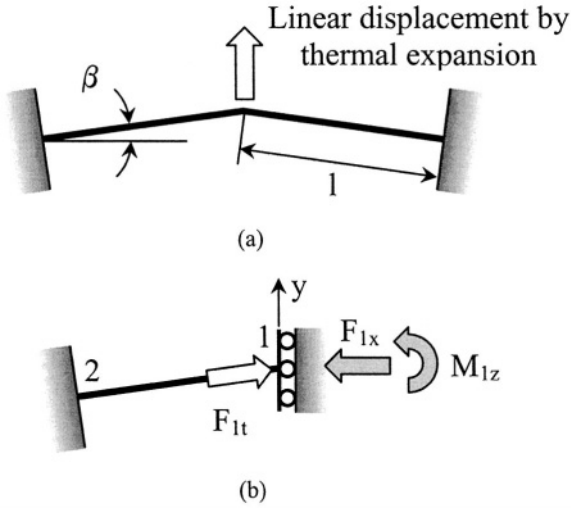

Figure 4.3 Bent beam: (a) Geometry and boundary conditions; (b) Half model with actuation force and support reactions

When the temperature increase does not reach levels that would produce buckling of the bent beam (and which will be analyzed later in this book), the mutually constrained thermal expansion of the two beams making up the device will result in a linear motion by the combined bending of the beams, as suggested in Fig. 4.3 (a). Because of the system's symmetry, it is sufficient to analyze only half of the model, as indicated in Fig. 4.3 (b). Point 1 will be forced to move about the y-axis. By applying a temperature increase to the component of Fig. 4.3 (b), the free expansion is impeded by the two supports, and the only way the member can deform is through bending, which will move the end 1 vertically upwards in the figure. Figure

4.4 is the picture of a real thermal actuator which consists of five bent beams that are placed in parallel, in order to enhance the output force capabilities.

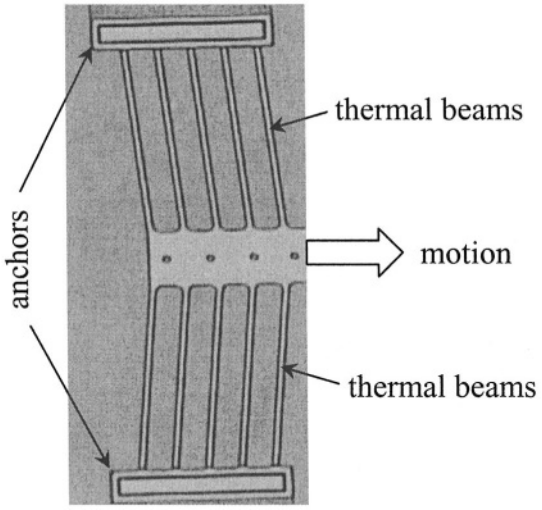

Figure 4.4 Bent beam actuator realized by the MUMPs technology

In order to determine the two performance parameters that have been defined for a straight free-fixed bar under thermal heating, and which are the free displacement and the bloc force, it can be considered that the beam is subject to a force which is the equivalent of the free expansion at end point 1, as given in Eq. (4.2), and which has been denoted as F_{1t} (to highlight its thermal nature) in Fig. 4.3 (b). As a result of boundary constraints, the support reacts with the force F_{1x} and the moment M_{1z}, which have to be determined first. This can be done by using the conditions of zero displacement about the x-axis and zero rotation about the z-axis at point 1, together with Castigliano's displacement theorem. The deflection at point 1 about the y-direction can be found similarly after calculating F_{1x} and M_{1z}, by applying the same theorem and by considering that bending and axial deformations produce the total strain energy. The equation for u_{1y} is:

$$u_{1y} = u_0 = A\alpha\Delta Tl^3 \sin\beta / (12 I_z \cos^2\beta + Al^2 \sin^2\beta) \qquad (4.8)$$

where A and I_z are the cross-sectional area and moment of inertia about the z-axis, respectively. Equation (4.8) indicates that the deflection at point 1 depends linearly on the temperature increase and non-linearly on the geometric parameters defining the half bent beam. An example will be analyzed next that studies the free displacement in terms of the defining geometry.

Example 4.1

A bent beam thermal actuator has a rectangular cross-section defined by the width w and the thickness t. Known are the following material properties which correspond to polysilicon: E = 130 GPa and $\alpha = 2.33 \times 10^{-6}$ 1/°C. For a temperature increase of $\Delta T = 50^{o}$, analyze the influence of the geometry defining the bent beam on the free displacement.

Solution:

Figures 4.5 and 4.6 are two plots showing the variation of the output displacement in terms of the defining geometry. For the simulation of Fig. 4.5 it has been considered that w = 5 μm and t = 1 μm.

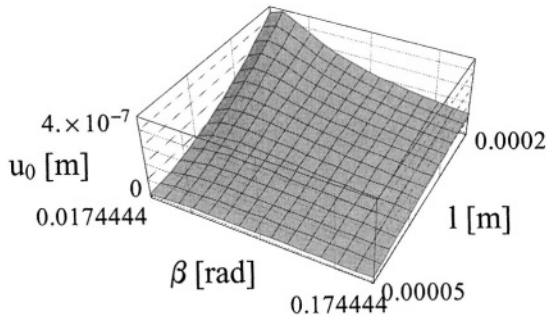

Figure 4.5 Free displacement in a bent beam as a function of beam length and inclination angle

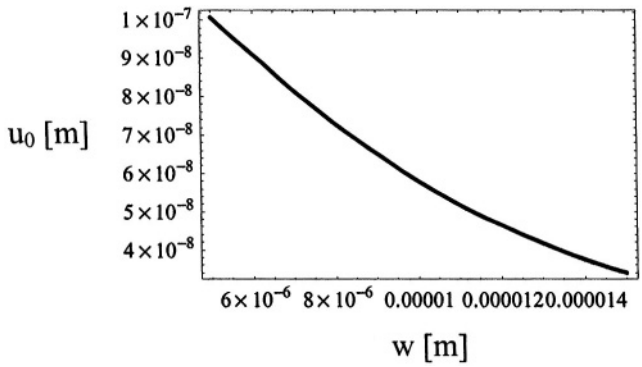

Figure 4.6 Free displacement in a bent beam as a function of cross-section width

The simulation of Fig. 4.6 took the same numerical values, except for w, which is the variable here, and for l = 100 μm and $\beta = 5^{o}$. It can be seen that the free displacement decreases in a non-linear fashion when the inclination

angle increases, and is larger for larger lengths – Fig. 4.5, as expected. Increasing the cross-sectional width reduces the free displacement, as shown in Fig. 4.6. The thickness t of the beam cancels out in Eq. (4.8).

The bloc force, as previously introduced, is the force that has to be applied at point 1 about the y-direction in order to annihilate the output y-displacement at the same point produced by application of a temperature increase – Fig. 4.3 (b). The force is determined by following a procedure similar to the ones already presented and its equation is:

$$F_{1y} = F_b = 3\alpha\Delta TEA^2 I_z l^2 \sin\beta / [(12 I_z \cos^2\beta + Al^2 \sin^2\beta)(Al^2 \cos^2\beta + 3 I_z \sin^2\beta)] \tag{4.9}$$

Example 4.2

Analyze the relationship between the bloc force and the geometric parameters that define the bent beam actuator of Example 4.1.

Solution:

The same numerical values have been used here as in the case of the output displacement studied in Example 4.1. Figures 4.7 and 4.8 are two plots that show the variation of F_b as a function of the defining geometric parameters, namely inclination angle, length and cross-sectional dimensions.

The plot of Fig. 4.7 indicates that the bloc force is larger at smaller lengths where it also reaches a local maximum. For longer elements, the bloc force is almost constant when the inclination angle varies. However, the bloc force is larger for small inclination angles, as seen in Fig. 4.7. As expected, the bloc force increases quasi-linearly with increasing the cross-sectional dimensions w and t, as shown in Fig. 4.8.

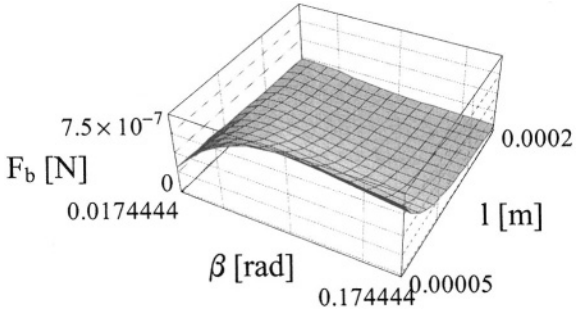

Figure 4.7 Bloc force in a bent beam as a function of beam length and inclination angle

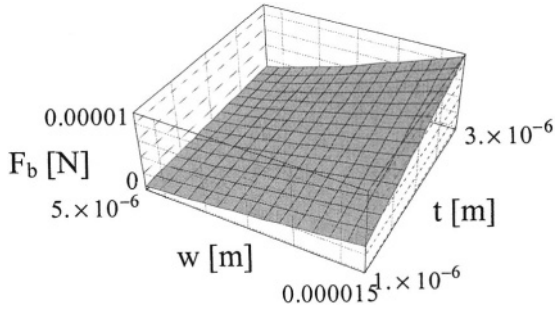

Figure 4.8 Bloc force in a bent beam as a function of cross-sectional width and thickness

Example 4.3

Compare a fixed-free bar and a bent beam half model in terms of their free displacement and bloc force assuming they have identical lengths, cross-sections, material properties and are subjected to the same temperature increase.

Solution:

It is useful to analyze the following two ratios that relate the output displacement and bloc force of the two thermal actuators, namely:

$$\begin{cases} ru_0 = u_0^{bb} / u_0^s \\ rF_b = F_b^{bb} / F_b^s \end{cases} \tag{4.10}$$

where the subscripts *bb* and *s* denote bent beam and straight, respectively.

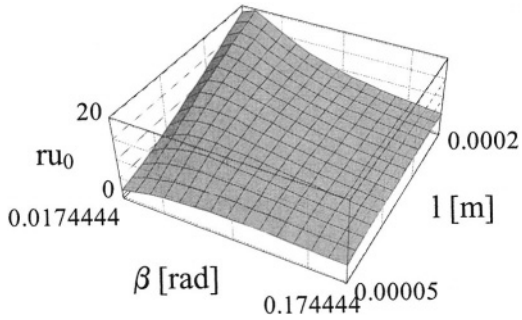

Figure 4.9 Bent beam versus straight bar in terms of free displacement as a function of inclination angle and length

By using Eqs. (4.8) and (4.6), the first ratio of Eq. (4.10) becomes:

$$ru_0 = Al^2 \sin\beta / (6I_z \cos^2\beta + Al^2 \sin^2\beta) \tag{4.11}$$

and is larger than one, which indicates that the displacement produced by a bent beam is always larger than the axial deformation of a fixed-free beam. Figures 4.9 and 4.10 are the plots of the ratio defined in Eq. (4.11) in terms of the geometric parameters. The free displacement of the bent beam can be 20 times larger than the one of a straight bar, for smaller inclination angles and larger lengths, as shown in Fig. 4.9. For larger cross-sectional widths, the free displacement ratio of Eq. (4.11) decreases almost to unity, as illustrated in Fig. 4.10.

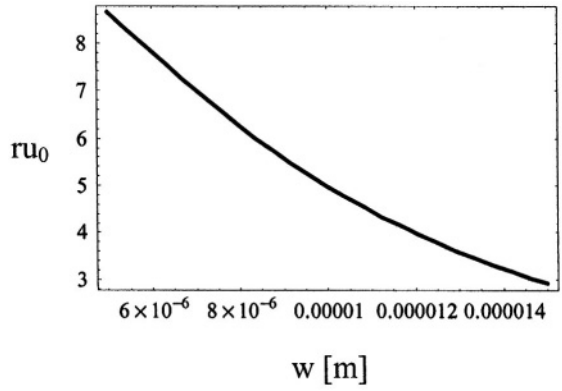

Figure 4.10 Bent beam versus straight bar in terms of displacement output as a function of leg width

The bloc force ratio of Eq. (4.10) becomes, by way of Eqs. (4.9) and (4.5):

$$rF_b = 3AI_z l^2 \sin\beta / [(6I_z \cos^2\beta + Al^2 \sin^2\beta)(3I_z \sin^2\beta + Al^2 \cos^2\beta)] \tag{4.12}$$

This time, as Eq. (4.12) suggests, the ratio is less than 1, and therefore the bloc force of the fixed-free bar is always larger than that of the corresponding bent beam. Figures 4.11 and 4.12 contain two similar plots showing that the bloc force of the bent beam increases relative to the one of the fixed-free bar for larger cross-section dimensions (the dimension w, specifically), smaller inclination angles and smaller lengths. Figures 4.12 and Fig. 4.10 are drawn in terms of the parameter w, as t cancelled out in Eqs. (4.12) and (4.11), respectively.

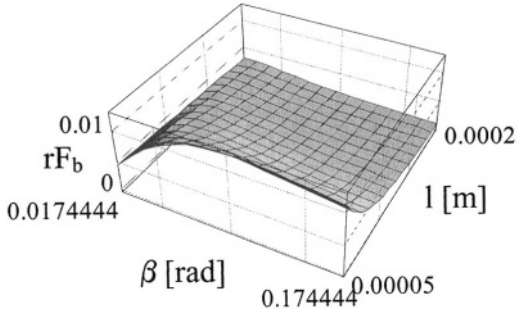

Figure 4.11 Bent beam versus straight bar in terms of bloc force as a function of inclination angle and length

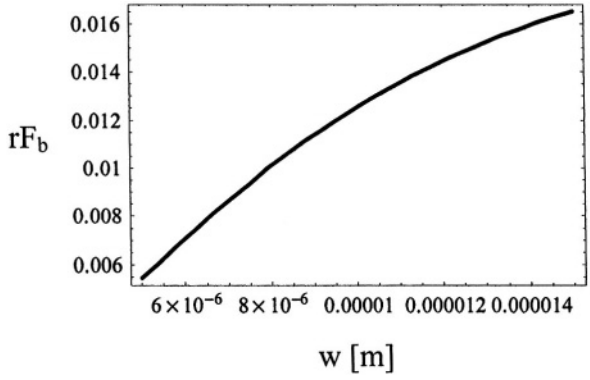

Figure 4.12 Bent beam versus straight bar in terms of bloc force as a function of leg's width

2.3 Two-Beam Thermal Actuator

A two-beam thermal actuator is sketched in Fig. 4.13 (a) consisting of two parallel beams of dissimilar lengths and a connecting rigid link. When the longer beam is heated, its free thermal expansion is prevented by the rigid connecting link as well as by its own fixed end.

The resulting deformed shape, which is sketched in Fig. 4.13 (b), is produced by bending of both the thermally-active (long) beam and the passive (short) one. The geometric parameters defining this actuator system are given in Fig. 4.14. The result of prevented thermal expansion can be modeled by a force F_{2t}, which is applied parallel to the heated beam at its end, and which is given in Eq. (4.2). As mentioned previously, the free displacement and the bloc force fully defined the performance of a thermally-driven fixed-free bar.

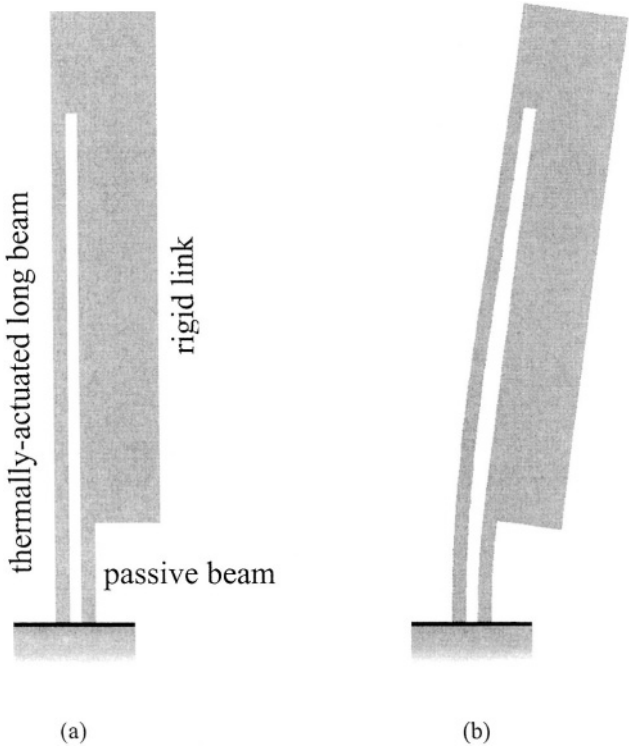

Figure 4.13 Two-beam thermal actuator: (a) original shape; (b) deformed shape

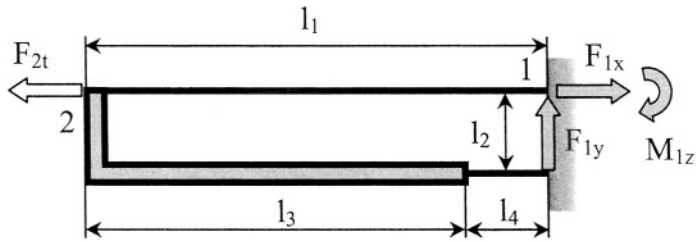

Figure 4.14 Geometry and loads resulting from thermal actuation and boundary supports

As a consequence, the two-beam thermal actuator can be qualified by the free displacement at point 2 about the y-direction, $u_0 = u_{2y}$, and the bloc force, $F_b = F_{2y}$, that needs to be applied at the same point in order to completely bloc the actuator. Another qualifier that can be used to supplement characterizing this actuator is the free rotation being produced through heating at the same point 2. In order to achieve either of these tasks, it is necessary to find the unknown reactions at the fixed end, F_{1x}, F_{1y} and M_{1z}. As previously done, they are found by solving the corresponding equations showing that the two translations and the rotation are zero at that point. The respective

displacements can be formulated by considering the strain energy stored in the two beams through bending and axial effects, and by applying Castigliano's displacement theorem. After determining the three reactions as functions of F_{2t} and the system's geometry, the rotation at point 2 can be found similarly, and its equation is:

$$\theta_{2z} = Al_1^2 l_2 l_4 (l_1^2 - l_1 l_4 + l_4^2)\alpha\Delta T / [Al_1 l_2^2 l_4 (l_1^2 - l_1 l_4 + l_4^2) + I_z (l_1^4 + 4l_1^3 l_4 - 6l_1^2 l_4^2 + 4l_1 l_4^3 + l_4^4)] \quad (4.13)$$

It has been assumed in Eq. (4.13), as well as in all following equations of this sub-section, that the two beams have identical cross-sections and are built of the same material. The free displacement at point 2 is found to be:

$$u_0 = u_{2y} = Al_1^2 l_2 l_4 [-l_1 l_4^3 + 2(l_3 + l_4) l_4^3 + l_1^3 (2l_3 + l_4)]\alpha\Delta T / \{2[Al_1 l_2^2 l_4 (l_1^3 + l_4^3) + I_z (l_1 + l_4)(l_1^4 + 4l_1^3 l_4 - 6l_1^2 l_4^2 + 4l_1 l_4^3 + l_4^4)]\} \quad (4.14)$$

The bloc force can be found by expressing first u_{2y} as a function of F_{2y} and then taking $u_{2y} = 0$. This gives the bloc force as:

$$F_b = F_{2y} = \{6EAI_z l_1 l_2 [-l_1 l_4^3 + 2l_4^3 (l_3 + l_4) + l_1^3 (2l_3 + l_4)]\alpha\Delta T / \{Al_1^3 l_2^2 l_4^3 + 4I_z (l_1 + l_4)[l_1^2 l_4^3 - 3l_1 l_4^3 (l_3 + l_4) + 3l_4^3 (l_3 + l_4)^2 + l_1^3 (3l_3^2 + 3l_3 l_4 + l_4^2)]\} \quad (4.15)$$

It is interesting to study how the length parameters l_1, l_2 and l_4 influence the performance of the two-beam thermal actuator, for instance the free displacement of Eq. (4.14), as discussed in the following example.

Example 4.4

Analyze the free displacement of a two-beam actuator by expressing l_2 and l_4 as fractions of the length l_1. The following geometric and material values are known: l_1 = 200 μm, w = t = 1 μm, $\Delta T = 40°$, $\alpha = 1.1 \times 10^{-6}$ 1/°, E = 130 GPa.

Solution:

Considering that $l_3 = l_1 - l_4$ (see Fig. 4.14) and that the short lengths l_2 and l_4 are fractions of the long beam's length l_1, namely:

$$\begin{cases} l_2 = c_2 l_1 \\ l_4 = c_4 l_1 \end{cases} \quad (4.16)$$

the free displacement is plotted in terms of c_2 and c_4, as shown in Fig. 4.15.

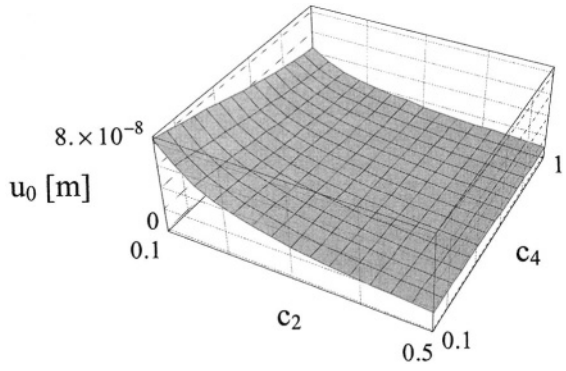

Figure 4.15 Free displacement of a two-beam thermal actuator in terms of the length fractions

It can be seen that the free displacement is larger when both the short beam and the short connecting link are small relative to the active beam length l_1 and that u_0 depends non-linearly on the coefficient c_2 and quasi-linearly on the coefficient c_4 of Eq. (4.16).

The thermal microactuators that have been studied here can also function as sensors in the sense that they can be placed in an environment where thermal changes are expected. The amount of mechanical deformation being produced through thermal variation, which can be evaluated experimentally, will furnish the corresponding amount of temperature change by reversal of the cause-effect relationship utilized in the actuation-type equations presented thus far. Two other transducers, the bimorph and the multimorph, which can also operate thermally, will be presented later in this chapter.

3 ELECTROSTATIC TRANSDUCTION

3.1 Introduction

Electrostatic actuation and sensing are largely utilized in MEMS transducers due to advantages such as sensitivity, fast response, precision, relatively easy fabrication, or integration with CMOS technology. Drawbacks of the electrostatic transduction, which can be linear or rotary, include the relatively small amounts of actuation force and capacitance variation. Figure 4.16 gives a graphic representation of the underlying principle of electrostatic transduction. By charging two bodies with equal and opposite charges (+q and –q), capacitive-type attraction forces between the two bodies can be generated potentially about the three Cartesian directions. Charging can be done by means of an external voltage, either direct-current

(DC) or alternating-current (AC), and thus actuation is achieved. Conversely, when relative motion about one of the three Cartesian directions indicated in the figure takes place, the change in the gap between two adjacent bodies will translate in a capacitive change that can further be used as a sensing metric of the mechanical motion in an external circuit. The attraction force between two oppositely-charged plates is generated by the electric field E, as shown in Fig. 4.17.

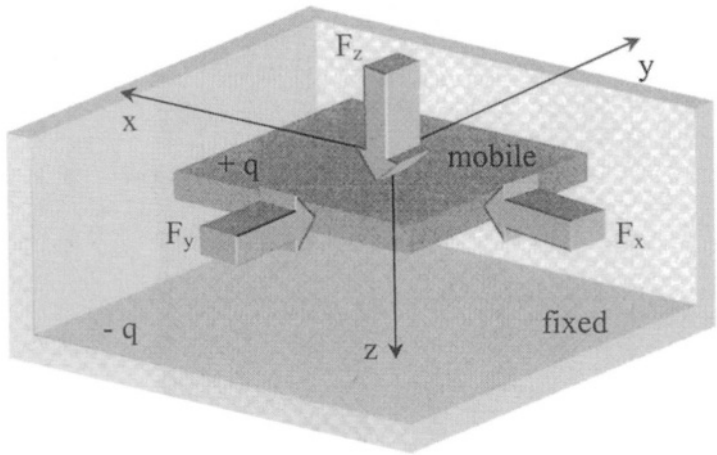

Figure 4.16 Potential motion directions of a charged mobile plate when attracted by three fixed Cartesian wall-plates

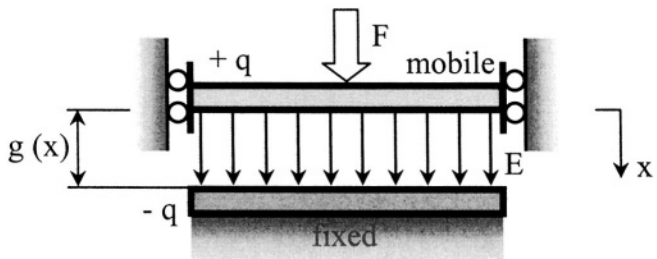

Figure 4.17 Attractive nature of the electrostatic force between two charged plates

MEMS devices that use the electrostatic-force principles for transduction are most of the time designed to be sensitive about one direction of motion. A simple solution that prevents motion about one direction, while enabling mobility about a different axis, is shown in Fig. 4.18. By placing the mobile central member symmetrically in terms of the y-axis with respect to the fixed

mating counterpart, the attraction forces about the y-direction cancel out, and therefore the only motion will be along the x-axis, where the attraction force F_x is unbalanced. This principle can be extended to the three-dimensional space, as another direction can be denied mobility, by using symmetry about the corresponding out-of-the-plane z-axis.

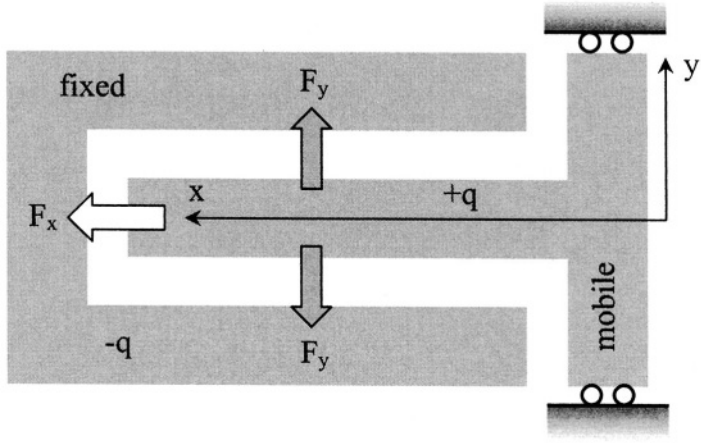

Figure 4.18 Using symmetry to enable motion about a given direction while blocking motion about a different direction

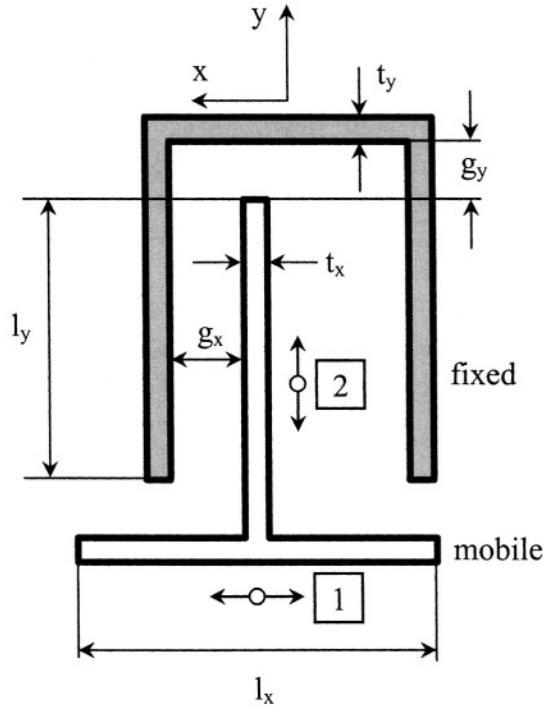

Figure 4.19 Transverse (or parallel-plate, 1) versus longitudinal (or comb-finger, 2) motions in an interdigitated microdevice

In the majority of MEMS applications, the actuation force or the sensing signal are insufficient when only one pair of moving-fixed parts are being utilized. The practical solution to this problem is to couple several pairs of such mating members in a comb-type configuration. Figure 4.19 sketches an interdigitated pair with the main geometric parameters. The motion about direction 1 in this figure is usually referred to as *parallel-plate* whereas the other possible motion, about direction 2, is generally named *comb-finger* motion. However, the interdigitated designs are used for both motions, and therefore, in order to avoid confusion, the alternative denominations of *transverse* and *longitudinal* will be used to indicate motions about the 1 and 2 directions, respectively.

These two types of motions are the main technological applications in planar MEMS, and they will be presented in the following sub-sections. The potentially-variable distances between the moving and fixed parts are the gaps, denoted by g_x and g_y in Fig. 4.19 in order to indicate the axis they refer to. Similarly, the thickness of a fixed/free member is indicated by either t_x or t_y, depending on the axis. These two main directions of transductions are better indicated in Fig. 4.20. The guided supports are just a notional representation because pure roller bearings are rare in MEMS design. The motion directionality is rather achieved by using a proper spring suspension, as the ones studied in the previous chapter.

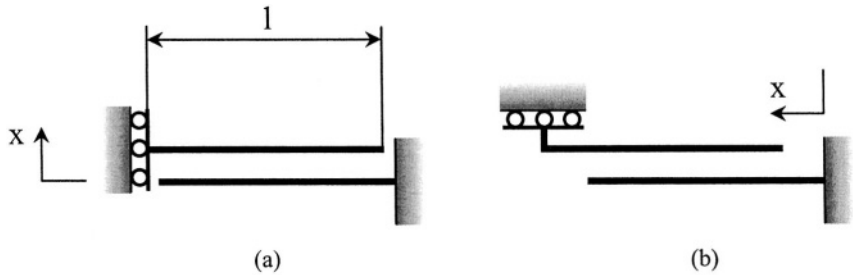

Figure 4.20 Main electrostatic linear transduction motions: (a) Transverse; (b) Longitudinal

The transverse and longitudinal transduction principles will be presented next, as well as another electrostatic method which uses microcantilevers for out-of-the-plane actuation/sensing. It should be mentioned that the purpose of studying the actuation is to define the actuation force that is produced electrostatically, whereas the objective of characterizing the sensing is to determine the capacitance variation as a function of the changing in gap. Figure 4.21 is the picture of a transverse electrostatic sensing device that was fabricated by the MUMPs technology. The upper row of plates is mobile whereas the two rows at the bottom of the figure support the fixed plates. It can be seen that a pair of fixed plates is placed between two mobile plates in

this design, which creates a differential sensing capacity that increases the overall reading performance.

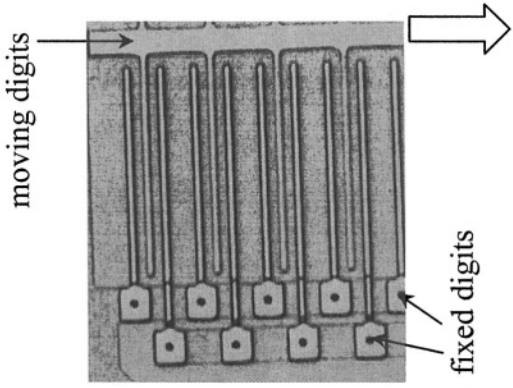

Figure 4.21 Electrostatic transverse transduction microdevice (MUMPS technology)

Similarly, Fig. 4.22 shows another MUMPs device that realizes transduction by using the longitudinal principle.

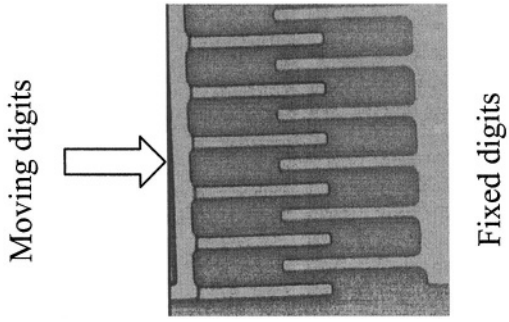

Figure 4.22 Electrostatic longitudinal transduction microdevice (MUMPS technology)

3.2 In-Plane Transverse (Parallel-Plate) Transduction

3.2.1 Actuation

According to the motion direction 1 of Fig. 4.19, and when the mobile plate moves a distance x from its initial position, the capacitance of a transverse-type transducer is:

$$C(x) = \varepsilon A / g_x = \varepsilon l_y l_z / (g_{0,x} - x) \qquad (4.17)$$

where ϵ is the electric permittivity, l_z is the overlap out-of-the-plane dimension, $g_{0,x}$ is the initial gap in the x-direction, and x is the displacement produced through attraction electrostatic forces. The initial-condition (no actuation) capacitance can be found by taking x = 0 in Eq. (4.17), namely:

$$C_0 = \varepsilon l_y l_z / g_{0,x} \tag{4.18}$$

As Eqs. (4.17) and (4.18) suggest, the variability in capacitance is only produced through changing of the gap between the two plates because the overlapped area $A = l_y l_z$ is constant for a transverse electrostatic actuator.

When a voltage V is supplied externally, the electrostatic energy is:

$$U_e = C(x)V^2 / 2 \tag{4.19}$$

The corresponding attraction force between the fixed and the mobile plates is defined as the partial derivative of the electrostatic energy in terms of displacement (which is similar to Castigliano's displacement theorem), and is calculated by using Eqs. (4.18) and (4.19) as:

$$F = \partial U_e / \partial x = \varepsilon l_y l_z V^2 / [2(g_{0,x} - x)^2] \tag{4.20}$$

The initial force (when the two plates are $g_{0,x}$ apart) is:

$$F_0 = \varepsilon l_y l_z V^2 / (2g_{0,x}^2) \tag{4.21}$$

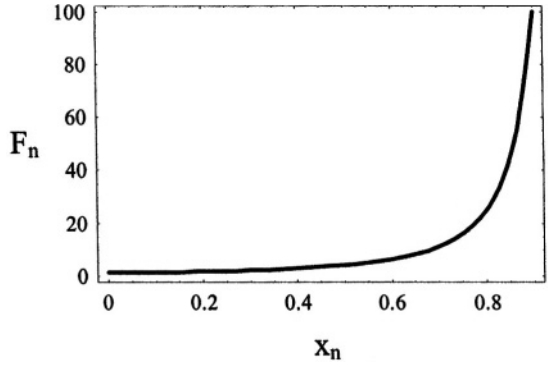

Figure 4.23 Normalized force in terms of normalized displacement for a transverse electrostatic actuator

By using the non-dimensional amounts:

$$\begin{cases} x_n = x / g_0 \\ F_n = F / F_0 \end{cases} \tag{4.22}$$

Eqs. (4.20) and (4.21) can be combined into:

$$F_n = 1/(1 - x_n)^2 \tag{4.23}$$

Equation (4.23) is plotted in Fig. 4.23, which shows the non-linear relationship between the normalized force and the normalized displacement. It can be seen that the attraction force is 100 times larger than the initial-gap force when the gap is 10% of the initial value.

In many practical applications, several identical pairs of transverse actuators are used in order to increase the total force, and this principle is exemplified in the picture of the MUMPs microdevice shown in Fig. 4.21 where two fixed digits were placed in the space created by two mobile ones. Another solution is sketched in Fig. 4.24 where one digit of the movable part is placed closer to one digit of the fixed counterpart, in such a way that the attraction force generated by the resulting gap is larger than the opposite force that is produced through the larger gap between the mobile digit and the other neighboring fixed digit.

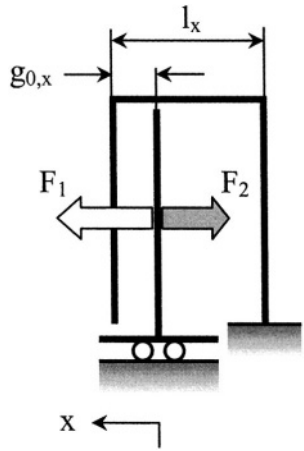

Figure 4.24 Digitated arrangement in a transverse electrostatic actuator

The resulting force in this case is simply the difference between the two force components, namely:

$$F' = F_1 - F_2 = \varepsilon A V^2 [1/(g_{0,x} - x)^2 - 1/(l_x - g_{0,x} + x)^2] / 2 \tag{4.24}$$

If *n* such pairs are used, the total force will be *n* times larger than the force given in Eq. (4.24). It is interesting to assess the relative force loss that occurs when using the arrangement of Fig. 4.24 in comparison to the pure one-pair transverse actuation, as shown in the following example.

Example 4.5

Compare the two-pair transverse actuator of Fig. 4.24 with the single-pair design of Fig. 4.20 (a) in terms of the output force.

Solution:

By considering that the initial gap can be written as a fraction of the actuator spacing l_x as:

$$g_{0,x} = cl_x \tag{4.25}$$

the following force ratio can be formed:

$$(F - F')/F = (cl_x - x)^2 / [(1-c)l_x + x]^2 \tag{4.26}$$

where F is given in Eq. (4.20) and F' in Eq. (4.24). The force ratio of this equation is plotted in Fig. 4.25 as a function of the fraction c and the distance x, in the case where l_x = 50 μm. The relative force difference of Eq. (4.26) increases non-linearly with c increasing and decreases quasi-linearly when x increases. When c = 0.5, which means that the mobile plate is symmetrically placed with respect to the two fixed plates, the relative difference is 1 (or 100%), as it should be, due to the fact that there is no resulting force (F' = 0) to act on the mobile plate.

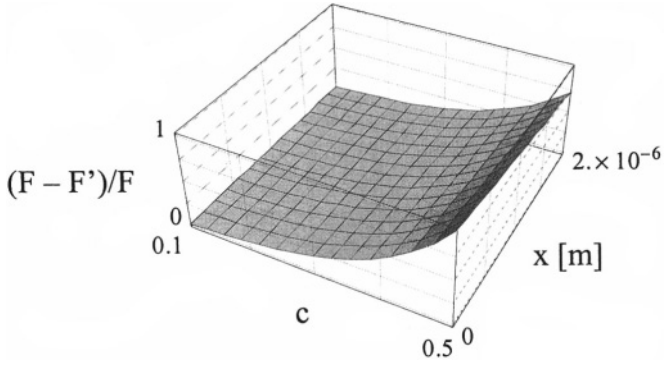

Figure 4.25 Relative difference between force produced by simple transverse actuator pair and interdigitated configuration

3.2.2 Sensing

The same device, as has been mentioned previously, can be utilized to perform motion sensing when the mobile plate is actuated externally. The gap change between two plates will result in a capacitance change that relates to a voltage variation of an external circuit comprising the capacitor. As Eq. (4.17) suggests, the capacitance depends on the distance x, and therefore the following equation can be written for the capacitance variation:

$$\Delta C = \partial C / \partial x \Delta x \tag{4.27}$$

where the partial derivative of Eq. (4.27) is called *sensitivity* and is calculated as:

$$\partial C / \partial x = \varepsilon A / (g_{0,x} - x)^2 \tag{4.28}$$

By analyzing Eqs. (4.27) and (4.28), it is evident that a change in distance translates in a change in capacitance, on one hand, and, on the other hand, this relationship is not linear because the sensitivity of Eq. (4.28) is not constant. The capacitance variation can be related to a voltage variation because voltage is defined as charge over capacitance:

$$U = Q / C \tag{4.29}$$

By assuming that the charge remains constant, one can find the voltage variation by differentiating Eq. (4.29), namely:

$$\Delta U = -Q \Delta C / C^2 \tag{4.30}$$

and therefore the voltage change can be related to a capacitance change, which corresponds to a gap variation, in the form:

$$\Delta U = -Q(\varepsilon A) / \Delta x \tag{4.31}$$

Equation (4.31) indicates that the voltage variation, which can be monitored in an external electric circuit, is inversely proportional to the distance change. Another form of Eq. (4.31) can be obtained by using Eqs. (4.28) through (4.30) as:

$$\Delta U = -U \Delta x / (g_{0,x} - x) \tag{4.32}$$

3.3 In-Plane Longitudinal (Comb-Finger) Transduction

3.3.1 Linear Transduction

3.3.1.1 Actuation

The other possibility of in-plane actuation is illustrated in Fig. 4.26, which shows two adjacent plate digits, one fixed and the other one mobile, the latter one moving parallel to the former one. By charging the two plates with equal and opposite charges, +q and –q, the electric field will generate attractive forces between the two plates, with the net result that the mobile plate will move to the right in the figure.

In order to simplify notation, no subscript is used to refer the gap because the gap is constant, as shown in Fig. 4.26. The overlap area will vary this time, since the engaging distance over the direction of motion changes. The capacitance is:

$$C = \varepsilon(l_o + y)l_z / g \tag{4.33}$$

where l_z is the plate's dimension perpendicular to the plane of the drawing.

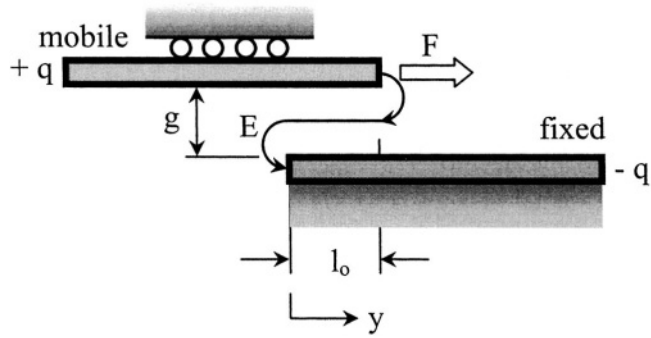

Figure 4.26 Principle of longitudinal electrostatic actuation

The force that generates the motion to the right can be calculated by means of the definition given in Eq. (4.20) and its expression is:

$$F = \varepsilon l_z V^2 /(2g) \tag{4.34}$$

It can be seen that the actuation force is constant, as contrasted to the case of a transverse actuator where the force varied with the distance in a non-linear manner. The plus sign indicates that the electrostatic force favors the increase

of distance y (or the increase of the overlap region between two adjacent plates).

When several pairs of mobile-fixed digits are utilized, the total force increases to a value which is *n* times larger than the force of Eq. (4.34), where *n* is the number of gaps.

3.3.1.2 Sensing

Conversely, the device sketched in Fig. 4.26 can be utilized as a sensing tool when the motion of the mobile plate is generated externally through connection of the mobile digits to a source of motion that is of interest. The capacitance variation can be calculated similarly to the case of a transverse sensing device, and its equation is:

$$\Delta C = \varepsilon l_z \Delta y / g \tag{4.35}$$

where:

$$\varepsilon l_z / g = \partial C / \partial y \tag{4.36}$$

is the sensitivity of the linear longitudinal transducer, and is constant, which is a major advantage of the longitudinal configuration over the transverse design. Similarly to the transverse sensing case, the change in voltage – Eq. (4.30) – can be expressed here as:

$$\Delta U = -U\Delta y /(l_0 + y) \tag{4.37}$$

In the case where *n* fixed-free digit pairs are used, the total change in capacitance will be *n* times the value of Eq. (4.35) because the capacitors are connected in parallel.

Example 4.6

Compare the voltage gain ΔU of an electrostatic transverse sensor with the one of a longitudinal sensor assuming that the initial overlap length l_o of the longitudinal sensor is five times larger than the initial gap $g_{0,x}$ of the transverse sensor.

Solution:

By using the subscripts *t* for transverse and *l* for longitudinal, the following voltage gain ratio can be formed by using Eqs. (4.32) and (4.37):

$$\Delta U_t / \Delta U_l = \Delta x(l_o + y)/[(g_{0,x} - x)\Delta y] \tag{4.38}$$

One can take:

$$\begin{cases} x = c_x g_{0,x} \\ y = c_y l_o \end{cases} \tag{4.39}$$

and consider that the displacement input is the same for both sensors, namely: $\Delta x = \Delta y$. Equation (4.38) can be written in this case as:

$$r_{\Delta u} = \Delta U_t / \Delta U_l = 5(1 + c_y)/(1 - c_x) \tag{4.40}$$

The voltage gain ratio of Eq. (4.40) has been plotted in Fig. 4.27 for the case where the parameter c_x ranges between 0 and 0.8 and c_y takes values between 0 and 1.

As shown in Fig. 4.27, the voltage gain by the transverse principle can be 5 to 60 times higher than the one of the longitudinal method for the particular condition of this problem, but this is dictated by the particular assumption connecting the initial gap and the overlap length.

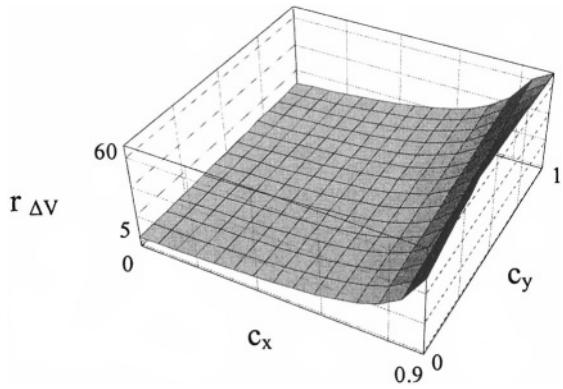

Figure 4.27 Voltage gain: transverse versus longitudinal electrostatic sensors

3.3.2 Rotary Transduction

The longitudinal principle of transduction can also be applied to generate/sense rotary motion. When fixed-free digit pairs are placed concentrically, as sketched in Fig. 4.28, the relative rotary motion can be generated or monitored in a manner similar to the one describing the linear longitudinal transduction.

3.3.2.1 Actuation

Application of an external electric field in a pair of fixed-mobile plates that can sustain relative rotary motion through adequate boundary conditions will generate tangential forces which will rotate the mobile part. Figure 4.29 shows a pair of conjugate digits that are disposed at a radius R_i with respect to a rotation center.

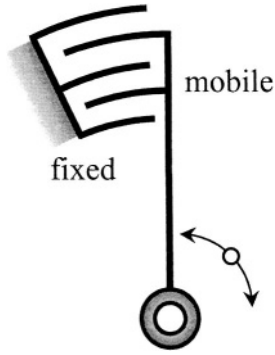

Figure 4.28 In-plane rotary transduction

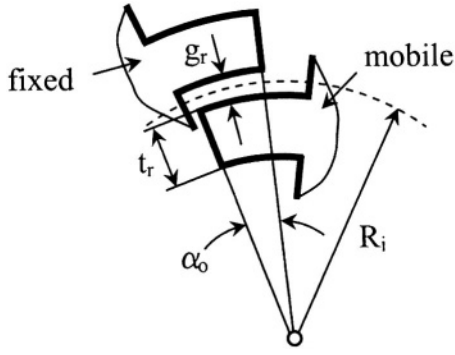

Figure 4.29 Geometry of a fixed-mobile digit pair for in-plane rotary transduction

The initial overlapping area between the fixed and the mobile digits is defined by an angle α_o, as sketched in the Fig. 4.29. The radius R_i defining the corresponding gap suggests that several pairs can be placed concentrically at different radii. The two curvilinear digits will have a relative rotary motion defined by a variable angle α and the capacitance pertaining to this angular motion is:

$$C_i = \varepsilon l_z R_i(\alpha_o + \alpha)/g_r \tag{4.41}$$

where g_r is the radial gap. The force that is generated through application of the voltage U is found as:

$$F_i = \partial U_e / \partial s_i = (\partial U / \partial \alpha)(\partial \alpha / \partial s_i) \tag{4.42}$$

By using the definition equation of the electrostatic energy, Eq. (4.19), and by considering that:

$$ds_i = R_i d\alpha \tag{4.43}$$

the tangential force becomes:

$$F_i = \varepsilon l_z U^2 /(2g_r) \tag{4.44}$$

Equation (4.44) shows that the generated force is constant for a given voltage U and defining geometry, and is independent on the radial position of the capacitor. However, because the relative motion is rotary, it is useful to determine the torque that results from the combined action of all the tangential forces that act at potentially *n* radial gaps. The moment produced by the force F_i at a radius R_i is:

$$M_i = F_i R_i \tag{4.45}$$

The generic radius R_i can be expressed in terms of a minimum radius R_{min} as:

$$R_i = R_{min} + (i-1)(g_r + t_r) \tag{4.46}$$

where t_r is indicated in Fig. 4.29 as the digit radial thickness. The total torque results by adding up all individual torques, each corresponding to one of the *n* gaps. Its equation is:

$$M = \sum_{i=1}^{n}(F_i R_i) = n\{R_{min} + [n(n+1)/2 - 1](g_r + t_r)\}\varepsilon l_z U^2 /(2g_r) \tag{4.47}$$

3.3.2.2 Sensing

When the relative rotary motion is produced externally, the transducer shown schematically in Fig. 4.29 will function as a sensor that can monitor the rotation angle. Similar to the linear design, the rotary device will detect a

capacitance change when the relative angle between the fixed and the free digits varies, according to the equation:

$$\Delta C_i = \varepsilon l_z R_i \Delta\alpha / g_r \tag{4.48}$$

The gaps form an equivalent capacitor whose change in capacitance is the sum of the individual capacitance changes, so that the total capacitance variation is:

$$\Delta C = \sum_{i=1}^{n} (\Delta C_i) = n\{ R_{min} + [n(n+1)/2 - 1](g_r + t_r)\}\varepsilon l_z / g_r \Delta\alpha \tag{4.49}$$

The total capacitance change can be transformed in voltage by proper inclusion of the capacitors in an external electric circuit. The voltage variation is expressed as:

$$\Delta U = U\Delta\alpha / (\alpha_o + \alpha) \tag{4.50}$$

3.4 Out-of-the-Plane Microcantilever-based Transduction

The electrostatic attraction can also be utilized in transduction applications that are based on out-of-plane relative motion, such as the case is with microcantilevers. Figure 4.30 illustrates this principle whereby a microcantilever will bend towards an underlying pad of length l_o, either when the two parts are charged externally with equal and opposite charges, or when bending of the microcantilever is achieved externally, and the change in gap between the two conjugate parts is monitored by a variation in capacitance. In essence, the problem here is one resembling the transverse principle of transduction, but the major difference, which is also computationally paramount, consists in the gap not being constant along the overlapping region. Moreover, determining the basic relationship between the capacitance change and the gap change, which is fundamental to both actuation and sensing, means solving an integral-differential equation and this can only be done by means of numerical methods. This electrostatic transduction principle will briefly be discussed in the following, together with a numerical example illustrating the calculation procedure.

When applying external charges on the microcantilever and the pad that are equal and opposite in sign, the compliant microcantilever will be attracted by the fixed pad and will bend towards it. In doing so, the gap between the two parts will vary along the overlapping length l_o according to the quasistatic equilibrium between actuation forces and elastic properties of the microcantilever. Thus, the posed problem is not purely an actuation one, as the elastic features of the microcantilever condition the entire situation,

but it will be seen a bit later in this chapter that similar cases do exist where other forms of actuation cannot be separated from the underlying elasticity properties of structures.

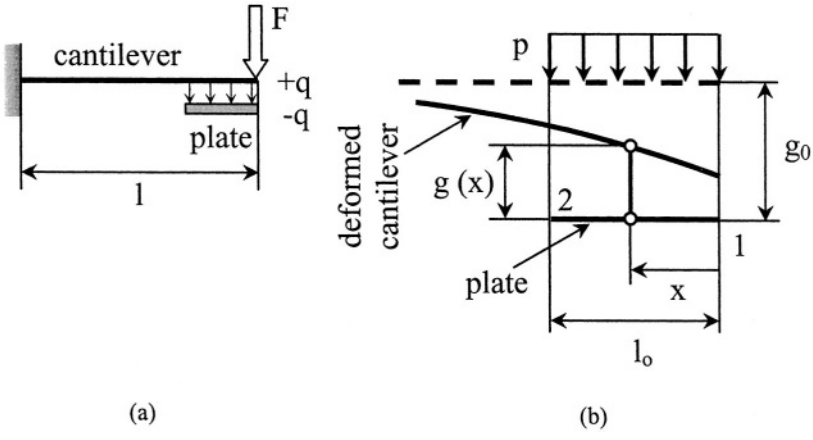

Figure 4.30 Out-of-plane electrostatic transduction by microcantilevers: (a) Boundary conditions and geometry; (b) Detail with distributed electrostatic loading

A procedure will be detailed next giving the maximum tip deflection (at point 1 in Fig. 4.30 (b)) under the action of the electrostatic forces, and this will qualify the actuation side of this microdevice. The variable gap over the actuation length l_o is:

$$g(x) = g_0 - u_z(x) \tag{4.51}$$

where g_0 is the gap between the undeformed microcantilever and the plate, and $u_z(x)$ is the deflection at abscissa x. The force acting on an elementary length dx can be considered constant and equal to:

$$dF = \varepsilon U^2 w dx / [2(g_0 - u_z(x))^2] \tag{4.52}$$

and therefore the distributed force that acts on the overlapping zone (force per unit length) can be expressed as:

$$p(x) = dF / dx = \varepsilon V^2 w / [2(g - u_z(x))^2] \tag{4.53}$$

The tip deflection u_{lz} can be expressed by applying Castigliano's displacement theorem which takes into account the strain energy produced through bending of the entire microcantilever, namely:

$$u_{1z} = \partial U_b / \partial F = 1/(EI_z)[\int_0^{l_0} M_{b1}(\partial M_{b1}/\partial F)dx + \int_{l_0}^{l} M_{b2}(\partial M_{b2}/\partial F)dx] \quad (4.54)$$

with:

$$\begin{cases} M_{b1} = -Fx - x\int p(x)dx + \int xp(x)dx, \ 0 \le x \le l_o \\ M_{b2} = -Fx - x\int_0^{l_0} p(x)dx + \int_0^{l_0} xp(x)dx, \ l_o \le x \le l \end{cases} \quad (4.55)$$

where F is a dummy force applied to the microcantilever at the free end 1. By applying the assumptions that the deflection varies according to a quadratic distribution over the overlapping length (see Kovacs [3] for instance), namely:

$$u_z(x) = (1 - x/l)^2 u_{1z} \quad (4.56)$$

it is possible to simplify Eq. (4.54) – which contains u_{1z} and u_z (x) as unknowns – to an equation which only contains u_{1z} as unknown. Although simpler, this equation is still an integral-differential one, which can be solved only numerically. The final solution is complex and is not given here, but an example will be studied next to better illustrate this problem.

Example 4.7

Determine the free tip deflection of a microcantilever defined by l = 200 μm, w = 10 μm and t = 2 μm when a voltage U = 50 V acts electrostatically on the overlap length l_o. The initial gap between the microcantilever and its corresponding fixed actuation plate is g_0 = 2 μm. The microcantilever's material has a Young's modulus of E = 130 GPa, and the permittivity of the free space is $\epsilon_0 = 8.8 \times 10^{-12}$ F/m. Assume that the overlap length l_o can range in the [20 μm; 75 μm] interval.

Solution:

The solution to Eq. (4.54) was obtained by using the calculation procedure that has previously been outlined, based on the numerical values of this problem. When the overlap length was given values in the specified range, the tip deflection values that are plotted in Fig. 4.31 have been obtained. As Fig. 4.31 indicates, the tip deflection of the microcantilever increases quasi-linearly with the overlap length increasing.

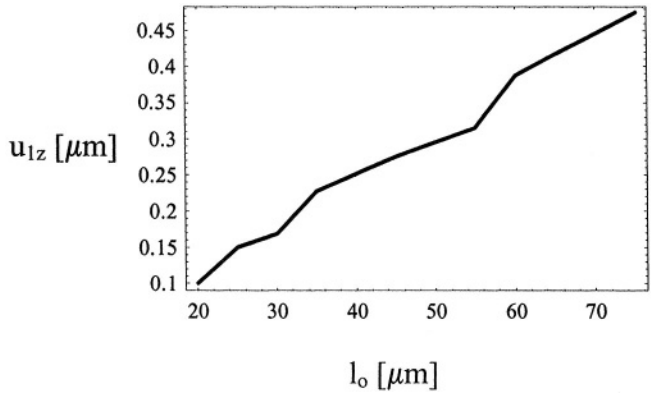

Figure 4.31 Tip displacement as a function of overlap length for an electrostatically-actuated microcantilever

4 ELECTROMAGNETIC/MAGNETIC TRANSDUCTION

The electromagnetic and magnetic effects are generally recognized to produce larger forces at larger air gaps, compared to the electrostatic actuation/sensing methods. In many MEMS designs, electromagnetic and magnetic transduction methods are utilized concurrently in order to enhance the performance of the microdevice.

4.1 Electromagnetic Transduction

The electromagnetic actuation and sensing are based on the interaction between the electric current and an external magnetic field. Figure 4.32 shows a linear conductor carrying a current I, and placed in an external magnetic field B. The Lorentz force that corresponds to this interaction is defined by the vector product:

$$\overline{F} = I\overline{l} \times \overline{B} \tag{4.57}$$

and its magnitude is:

$$F = IlB\sin\alpha \tag{4.58}$$

where l is the length of the conducting wire and α is the angle between the directions of I and B. As Eq. (4.58) indicates, the vectors B and Il need to make a non-zero angle α, in order that a Lorentz force be produced.

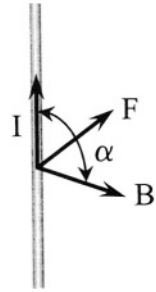

Figure 4.32 Lorentz force acting on a linear wire carrying a current I in an external magnetic field B

This general principle is implemented in MEMS devices by means of loops that can be either circular or rectangular. Figure 4.33 sketches a rectangular loop which can be placed on a mobile structure for instance. The loop carries the current I and is placed in an external magnetic field B, which is parallel to the plane of the loop, as indicated in the same figure.

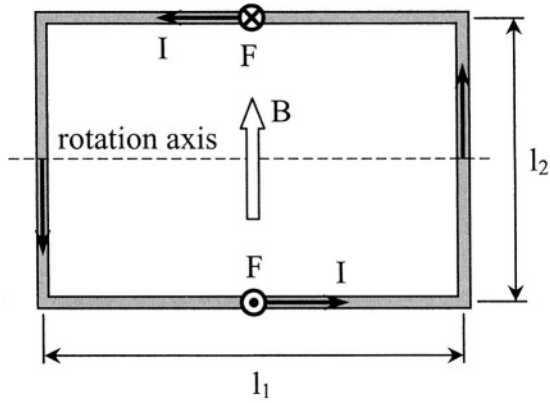

Figure 4.33 Rectangular loop carrying a current in an external magnetic field

Because the field B is parallel to the current in the shorter arms of the loop (of length l_2), there is no force acting on those sides. However, there will be two forces acting on each of the longer arms, one entering the loop's plane (it is indicated by an x in a circle) and the other one exiting the same plane (it is shown by a point in a circle). According to the Lorentz force definition of Eq. 4.57, these two forces are equal and opposite, and their value is:

$$F = Il_1B \tag{4.59}$$

As a consequence, there is no force resultant acting on the loop, but there is a couple produced by the two parallel and opposite forces of Fig. 4.33. The moment of this couple is:

$$M = Il_1l_2B \tag{4.60}$$

and its effect is to rotate the loop about the axis indicated in the same figure.

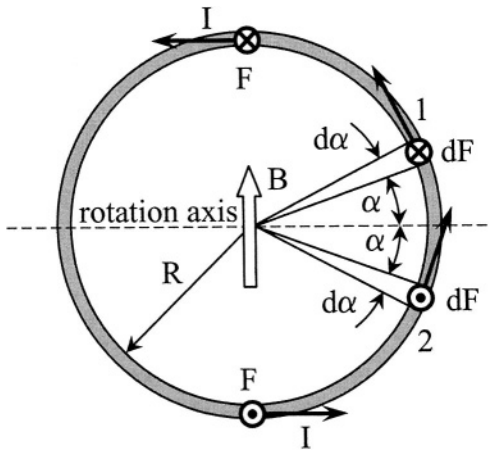

Figure 4.34 Circular loop carrying a current in an external magnetic field

A similar result can be obtained by using a circular loop of radius R, as the one pictured in Fig. 4.34. The Lorentz force acting on a circular segment of length dl, which is defined by an angle $d\alpha$, is:

$$d\vec{F} = Id\vec{l} \times \vec{B} \tag{4.61}$$

and its magnitude is:

$$dF = IRB\sin\alpha d\alpha \tag{4.62}$$

The total force acting on the circular loop can be found by summing up all these elementary forces, which means calculating the following integral:

$$F = \oint dF = \int_0^{2\pi} IRB\sin\alpha d\alpha = 0 \tag{4.63}$$

so, again, there is no resultant force acting on the loop. If one now considers two elementary lengths that are situated at an angle α, disposed

symmetrically with respect to the horizontal diameter of the circular loop, two forces dF, which are equal and opposite according to Eq. (4.62), will produce an elementary couple about the horizontal diameter, and the corresponding moment is:

$$dM = 2R\sin\alpha dF \tag{4.64}$$

The total moment that will tend to rotate the loop about the horizontal diameter, as indicated in Fig. 4.34, can be calculated as:

$$M = \int_0^{\pi} dM = \pi R^2 IB \tag{4.65}$$

By comparing Eqs. (4.60) and (4.65) it can be seen that the moments for both the rectangular and the circular loops can be written as:

$$M = IAB \tag{4.66}$$

where A is the area of the loop. This remark enables to generalize the formulation of the mechanical moment produced in a loop carrying a current when subject to an external magnetic field in the vector form:

$$\overline{M} = \overline{m} \times \overline{B} \tag{4.67}$$

where m is called the *magnetic dipole moment* – see Sadiku [4], for instance, and is calculated as:

$$\overline{m} = IA\overline{n}_A \tag{4.68}$$

where $\mathbf{n_A}$ is the direction perpendicular to the loop's plane. In the case *n* loops are used to increase the actuation/sensing capacity, the corresponding bending moment of Eq. (4.67) will be *n* times larger.

One of the simplest implementations of using a loop carrying current for actuation/sensing purposes in MEMS is to place the respective loop at the free end of a cantilever beam, as discussed in the next example.

Example 4.8

A microcantilever is used to sense an external magnetic field whose direction is known, as sketched in Fig. 4.35. Determine the value of the magnetic field B, assuming that the geometry and the material properties of the microcantilever are known, as well as the tip slope, which is measured experimentally.

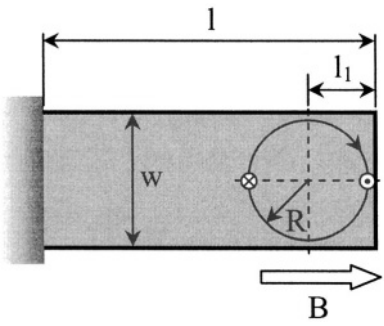

Figure 4.35 Microcantilever for Lorentz-based magnetic field detection

Solution:

The interaction between the external field B and the current in the circular loop will tend to rotate the loop about an axis that is perpendicular to the length direction and passes through the loop's center. The value of this moment is given in Eq. (4.65). It can be shown that application of this moment will produce a slope at the microcantilever's tip according to:

$$\theta_{1y} = M(l - l_1)/(EI_y) \tag{4.69}$$

By combining Eqs. (4.65) and (4.69), the external field becomes:

$$B = EI_y\theta_{1y}/[\pi R^2 I(l - l_1)] \tag{4.70}$$

where the inertia moment of the microcantilever's cross-section is:

$$I_y = wt^3/12 \tag{4.71}$$

4.2 Magnetic Transduction

The principle of magnetic actuation/sensing is similar to the one defining the electromagnetic-based operation. A magnet that is placed in an external magnetic field will be acted upon or will sense forces/moments that result from the interaction between the own magnetic field of the magnet and the external magnetic field. Figure 4.36 (a) illustrates a short magnet of length l (which is pictured as a vector departing from the south pole S and arriving at the north pole N of the magnet), together with the field lines that go externally from the N pole and close in the S pole. Similar to a loop carrying a current I, a *magnetic dipole moment* m can be defined in the form:

$$\overline{m} = q_m \overline{l} \tag{4.72}$$

where q_m is the *isolated magnetic charge* or the *pole strength* – Sadiku [4]. As shown in Eq. (4.72), the vectors m and l are parallel.

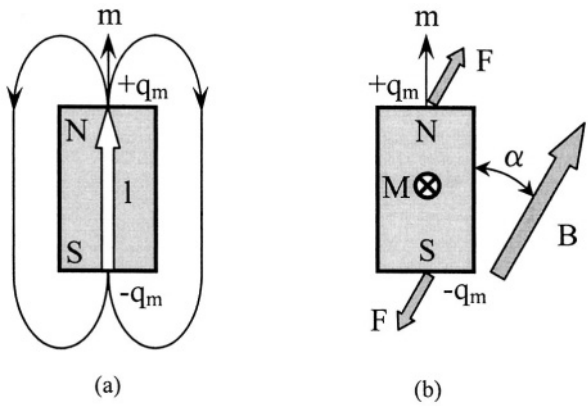

Figure 4.36 Short magnet: (a) Magnetic field; (b) Interaction with an external magnetic field

When this magnet is placed in an external magnetic field, as shown in Fig. 4.36 (b), a couple will act on the magnet about a direction perpendicular to its plane, and will attempt to align the magnet with the external field. The moment of this couple can be calculated by the generic Eq. (4.67), which becomes:

$$M = q_m l B \sin\alpha \tag{4.73}$$

The same moment of Eq. (4.73) can be conceived as being the effect of two equal and opposite forces that act at the magnet's poles and are defined as – Sadiku [4]:

$$\overline{F} = q_m \overline{B} \tag{4.74}$$

The two forces are opposite because the magnetic charge is positive at one pole and negative at the other, as shown in Fig. 4.36, and, as a consequence, no resultant force will act on the magnet, just the couple produced by the two forces, which is equal to:

$$M = Fl \sin\alpha \tag{4.75}$$

By combining Eqs. (4.74) and (4.75), the moment of Eq. (4.73) is retrieved.

The value of q_m is not readily available in the literature because this amount is rather a conceptual descriptor. A way of finding its value in terms of other known amounts is briefly mentioned next. The magnetic dipole moment m can be expressed as:

$$m = M_m A l \tag{4.76}$$

where M_m is called *magnetization,* and for a linear and isotropic magnetic material can be related to the magnetization field of the magnet as:

$$M_m = B_m(\mu_r - 1)/(\mu_0 \mu_r) \tag{4.77}$$

where μ_0 is the *magnetic permeability of the free space,* and μ_r is the *relative permeability of the magnet,* defined as the ratio of its permeability to the permeability of the free space. The relative permeability of a given material, other than air, is always larger than 1 and values are given for different magnetic materials in the literature. By combining Eqs. (4.72), (4.76) and (4.77) results in:

$$q_m = B_m A(\mu_r - 1)/(\mu_0 \mu_r) \tag{4.78}$$

For anisotropic materials, the situation is a bit more complex because the relative permeability cannot be represented by a single value. More details on anisotropic magnetic material behavior can be found in Jakubovics [5] for instance, and application of the anisotropic magnetic properties is explained in more detail in Judy and Muller [6].

An attraction force ca be generated between a permanent magnet and a ferroelectric layer (which can be magnetized), as a means of magnetic transduction. Figure 4.37 is a sketch showing this principle.

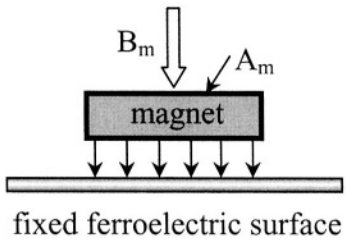

Figure 4.37 Magnetic force between a permanent magnet and a ferroelectric substrate

The magnetic force can be calculated – see McCraig and Clegg [7] – as:

$$F = B_m^2 A_m /(2\mu_0) \tag{4.79}$$

where B_m is the magnetic field created by the magnet, A_m is the magnet area normal to the field and μ_0 is the permeability of the free space.

4.3 Magnetic-Electromagnetic Transduction

Several MEMS applications use the interaction between the electromagnetic and magnetic fields in order to enhance the transduction capabilities. Combining a coil carrying a current with a permanent magnet, such that their fields are parallel, is an example where a force is generated along the two fields' directions. This force and the microsystem's geometry are illustrated in Fig. 4.38 (a).

There are two different ways to calculate the force between the two components. One method is to transform the real magnet into an equivalent coil, as sketched in Fig. 4.38 (b), based on the fact that the magnet and the equivalent coil have the same magnetic moment m, which leads to the equation:

$$q_m t_m = I_2 A_2 \tag{4.80}$$

The interaction force can be calculated as the partial derivative of the total magnetic-electromagnetic energy U_m in terms of direction as:

$$F = \partial U_m / \partial t_g = m \partial B_1 / \partial t_g \tag{4.81}$$

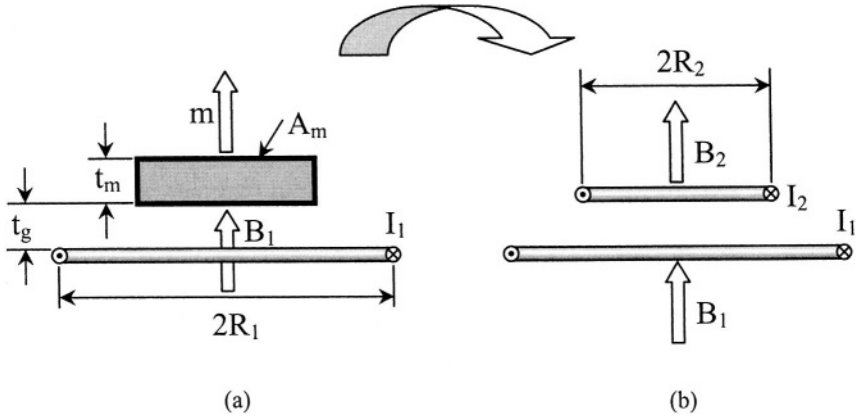

Figure 4.38 Magnetic-electromagnetic interaction: (a) Coil and permanent magnet; (b) Equivalent coil-coil

The magnetic energy can be calculated as the sum:

$$U_m = 1/2 L_{11} I_1^2 + L_{21} I_1 I_2 + 1/2 L_{22} I_2^2 \tag{4.82}$$

where L_{11} and L_{22} are the *direct inductances* of the two coils and L_{12} is the *mutual inductance* connecting the two coils. These inductances are:

$$\begin{cases} L_{11} = \int_{A_1} B_1 dA / I_1 \\ L_{12} = \int_{A_1} B_2 dA / I_2 \\ L_{22} = \int_{A_2} B_2 dA / I_2 \end{cases} \tag{4.83}$$

It can be shown that in the case where B_1 is constant over the equivalent coil, the force of Eq. (4.81) reduces – as shown in Seely and Poularikos [8] – to:

$$F = 3\mu_0 A_1 n_1 I_1 A_2 I_2 t_g / [2\pi (R_1^2 + t_g^2)^{5/2}] \tag{4.84}$$

Another way of calculating the interaction force between the coil and the magnet of Fig. 4.38 (a) is by expressing the magnetic-electromagnetic energy in a different fashion, namely:

$$U_m = (n_1 I_1 + \mu_m B_m t_m)^2 / (2\Re) \tag{4.85}$$

where R is the *magnetic reluctance* of the portion of magnetic line comprising the coil, air gap and magnet, and which is calculated as:

$$\Re = \Re_{coil} + t_g / (\mu_0 A_m) + t_m / (\mu_m A_m) \tag{4.86}$$

If there was no magnetic core inside the coil, then R_{coil} is zero in the equation above. By applying the definition of Eq. (4.81), the interaction force becomes:

$$F = (n_1 I_1 + \mu_m B_m t_m)^2 / [(2\mu_0 A_m)\Re^2] \tag{4.87}$$

Example 4.9

A circular coil of radius R_1 is placed at the end of a microcantilever, as shown in Fig. 4.35. A magnet defined by its area A_m, thickness t_m and inductance B_m is fixed under the coil, such that an air gap t_g is formed between the magnet and the coil. Determine the current I_1 of the coil that will

reduce the initial gap by half. It is assumed the microsystem is operating in air and that the circular loop has one coil only.

Solution:

It can be shown that the force which needs to be applied at a distance l_1 measured from the free end in order to produce a deflection of $t_g/2$ at the free end of the microcantilever of length l is:

$$F = 3EI_y t_g /[(l-l_1)^2(2l+l_1)] \tag{4.88}$$

This force is produced by the magnet-coil interaction, and, as a consequence is also given in Eq. (4.87). By equating Eqs. (4.87) and (4.88), the following equation is obtained for the current I_1:

$$I_1 = [\Re\sqrt{6\mu_0 A_m EI_y t_g /(2l+l_1)}\,/(l-l_1) - \mu_m B_m t_m] / n_1 \tag{4.89}$$

The reluctance of the system is in this case:

$$\Re = t_g /(\mu_0 A_m) + t_m /(\mu_m A_m) \tag{4.90}$$

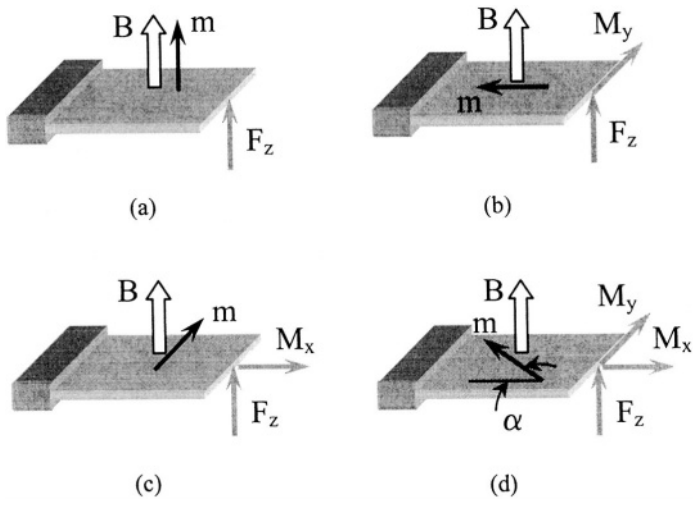

Figure 4.39 Magnetized microcantilever in electromagnetic field: (a) m is parallel to B; (b) m directed parallel to the microcantilever length; (c) m is perpendicular to the microcantilever length; (d) m has an arbitrary direction in the microcantilever plane

Another possibility of combining magnetic and electromagnetic fields is to utilize thin microcantilevers of different magnetizations in order to realize

the interaction with an external electromagnetic field, as suggested by Kruusing and Mikli [9] for instance. Figure 4.39 shows four different cases of magnetization m of a microcantilever that is placed in an external electromagnetic field B, whose direction is assumed to be constant. The interaction between the magnetization vector and the external electromagnetic field vector B results in a force and a moment that act on the cantilever and which are figuratively shown in Figs. 4.39 (a) through (d). The force and the moment are calculated as:

$$\begin{cases} \overline{M} = \overline{m} \times \overline{B} \\ \overline{F}_z = m\partial\overline{B} / \partial z \end{cases} \tag{4.91}$$

It can be seen that in the case where the electromagnetic field B varies about the z-direction, a force F_z will be produced about the same direction, and will bend the microcantilever, irrespective of the direction of magnetization. The moment, however, according to the definition of Eq. (4.91) will have different directions, as a function of the magnetization direction. In the case of Fig. 4.39 (b), the total moment will be a pure bending moment combining to the bending effect produced by the force F_z, whereas Fig. 4.39 (c) depicts the situation where the moment is a torsional one. When m has an arbitrary direction, as shown in Fig. 4.39 (d), the resulting moment can be resolved into a bending component and a torsion component.

Example 4.10

A microcantilever of length l and cross-sectional dimensions w and t is magnetized about a direction α, as shown in Fig. 4.39 (d). The microdevice is used to monitor a constant external field B, as sketched in the same figure. An optical system can measure a maximum slope $\theta_{1\max}$ at the microcantilever tip. What is the maximum value of the magnetic field that can be detected by this sensing microsystem ?

Solution

There will be no force acting at the free end, because the external field is assumed constant. The moment produced at that end can be resolved into a torsional component and a bending one. The later one has the expression:

$$M_{1y} = mB\sin\alpha \tag{4.92}$$

The tip slope can be found as:

$$\theta_{1y} = M_{1y}l /(EI_y) \tag{4.93}$$

By combining Eqs. (4.92) and (4.93) results in:

$$\theta_{1y} = mBl \sin\alpha /(EI_y) \tag{4.94}$$

The tip angle produced through torsion about the longitudinal x-axis is:

$$\theta_{1x} = mBl \cos\alpha /(4EI_y) \tag{4.95}$$

Equation (4.95) has taken into account that for a thin cantilever, the torsional rigidity is 4 times higher than the bending one – see Chapter 2. By taking the ratio of the two tip angles results in:

$$\theta_{1y} / \theta_{1x} = 4 \tan\alpha \tag{4.96}$$

As a consequence, $\theta_{1y} > \theta_{1x}$ for $\alpha > 14^o$ ($\alpha = 14^o$ is solution to Eq. (4.96)) and:

$$B_{max} = EI_y \theta_{1max} /(m \sin\alpha) \tag{4.97}$$

When $\alpha < 14^o$, $\theta_{1y} < \theta_{1x}$, which gives:

$$B_{max} = 4EI_y \theta_{1max} /(m \cos\alpha) \tag{4.98}$$

5 PIEZOELECTRIC (PZT) TRANSDUCTION

The piezoelectric materials have the property of becoming electrically polarized in the presence of an externally applied load/deformation. The degree of polarization is proportional to the level of mechanical deformation, as well as is dependent on the direction of the applied strain. This mechanical-to-electrical energy conversion is known as *direct piezoelectric effect,* and crystals such as the quartz naturally exhibit this property. Piezoelectric materials are also capable to responding in a linear manner to the reverse excitation, in the sense that external application of a field will generate mechanical deformation through the *reverse piezoelectric effect* (also called *electrostriction*). Examples of piezoelectric materials largely utilized in industrial/research applications are polycrystalline ceramic materials such as the PZT (lead zirconate titanate) or semi-crystalline polymers such as the PVDF (polyvinylidene fluoride). For such materials, the component dipoles (molecules that are partly charged positively and partly charged negatively) are randomly arranged in a lattice, but application of an external electric field to such an *unpoled* structure will *pole* it, namely arrange and direct the dipoles about a direction parallel to that of the external field, as sketched in Fig. 4.40.

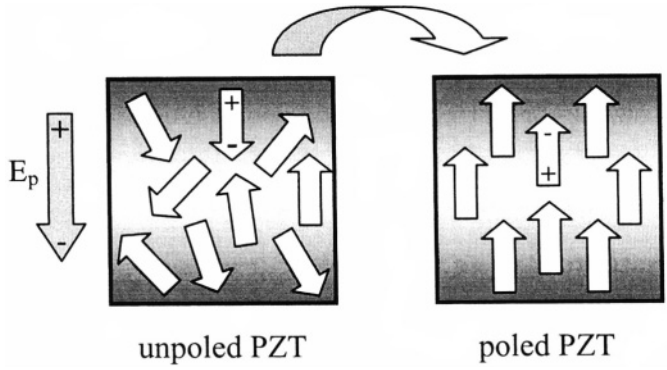

Figure 4.40 Poling of a piezoelectric material by means of an external electric field E_p

It should be mentioned that below a critical temperature, called the *Curie point* (in honor of Jacques and Pierre Curie who discovered the piezoelectric phenomenon in 1880), a piezoelectric material has a tetragonal symmetry with the dipoles arranged such that the positive and negative poles are not coincident.

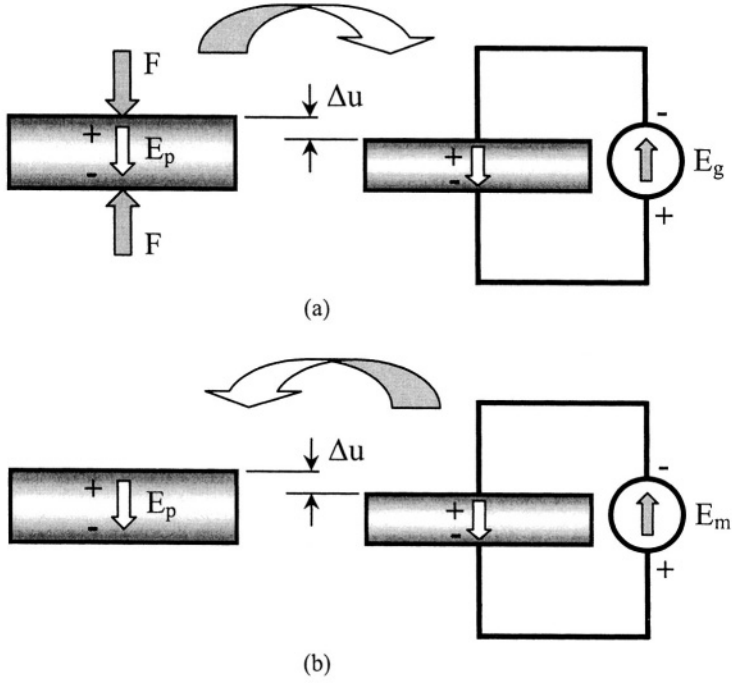

Figure 4.41 Piezoelectric transaction: (a) sensing through the direct piezoelectric effect; (b) actuation through the reversed piezoelectric effect

Application of an electric field can modify the distances between dipoles and arrange them adequately in a poled configuration. However, over the Curie point, the crystalline structure is cubic and symmetric with no dipoles as the negative and positive poles do coincide. As a consequence, poling cannot be applied and therefore the piezoelectric effect cannot be produced over this critical point.

The two principles, the direct and the reversed piezoelectric effects, can be utilized for transduction purposes in both macro-scale and micro-scale applications, and Fig. 4.41 gives a sketch of both phenomena. Application of the external compressive forces F in Fig 4.41 (a) will compress the poled piezoelectric material by a quantity Δu, which, in turn, will generate a field E_g (*g* stands for generated) and the corresponding current in an external electric circuit. The direction of the generated field in this case opposes the mechanical action, as it tries to restore the piezoelectric material to its initial dimensions. The reverse piezoelectric effect is shown in Fig. 4.41 (b). Application of an external field E_m (*m* stands for motor) in opposition to the poling field E_p will generate an expansion of the piezoelectric sample by a quantity Δu. Both examples also show that the direct and reversed piezoelectric effects are directional, in terms of both electrical field and mechanical deformation.

Figure 4.42 shows a piezoelectric plate with its geometric axes x, y and z (which usually is parallel to the plate's thickness, which is also the poling direction). The numbers 1, 2 and 3 indicate directions along which electrical/mechanical physical amounts can be aligned to, as briefly explained next.

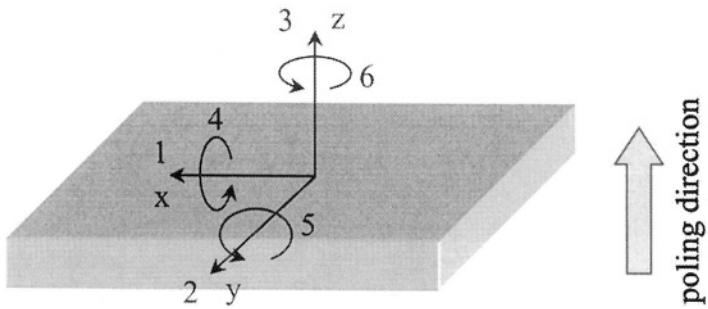

Figure 4.42 Directions for electrical/mechanical vectors defining the piezoelectric behavior

The numbers 1 to 6 are used in the literature to indicate the six different stresses/strains that are set at a point in the three-dimensional space. While electrical fields are vectors that can be applied about the directions 1, 2 or 3, and so are also the normal mechanical stresses (denoted by the symbol σ in Chapter 1), the numbers 4, 5 and 6 are used to denote the three shear stresses

that have been introduced in the same Chapter 1 as τ_{xy}, τ_{yz} and τ_{zx}. The shear stress τ_{xy}, for instance, produces rotation about the direction 6 of Fig. 4.42, and similarly, τ_{yz} generates the rotation 4 whereas τ_{zx} gives rotation about direction 5. The subscripts 4, 5 and 6 are used to denote these directions.

The deformation of a piezoelectric body in the presence of both external mechanical loading and electric field is calculated in the linear domain as the sum of a mechanically-produced deformation and an electrically-generated displacement, according to the matrix equation:

$$\{\varepsilon\}_m = [c^E]\{\sigma\} + [d]\{E\} \tag{4.99}$$

where $\{\epsilon\}_m$ is the total *strain vector* (the subscript *m* means mechanical and is used to distinguish this vector from the permittivity vector, which has the same notation) defined as:

$$\{\varepsilon\}_m = \{\varepsilon_1\ \varepsilon_2\ \varepsilon_3\ \gamma_4\ \gamma_5\ \gamma_6\}^T \tag{4.100}$$

$\{\sigma\}$ is the *stress vector,* similarly defined as:

$$\{\sigma\} = \{\sigma_1\ \sigma_2\ \sigma_3\ \tau_4\ \tau_5\ \tau_6\}^T \tag{4.101}$$

and {E} is the *electric field vector,* having three components:

$$\{E\} = \{E_1\ E_2\ E_3\}^T \tag{4.102}$$

The two matrices that enter Eq. (4.99) are the *compliance matrix* $[c^E]$, which is calculated for constant field (the electrodes of the piezoelectric component are shortcut) and is a 6 x 6 symmetric matrix defined as:

$$[c^E] = \begin{bmatrix} c_{11} & c_{12} & c_{13} & c_{14} & c_{15} & c_{16} \\ c_{12} & c_{22} & c_{23} & c_{24} & c_{25} & c_{26} \\ c_{13} & c_{23} & c_{33} & c_{34} & c_{35} & c_{36} \\ c_{14} & c_{24} & c_{34} & c_{44} & c_{45} & c_{46} \\ c_{15} & c_{25} & c_{35} & c_{45} & c_{55} & c_{56} \\ c_{16} & c_{26} & c_{36} & c_{46} & c_{56} & c_{66} \end{bmatrix} \tag{4.103}$$

and the *charge constant matrix,* defined as:

$$[d] = \begin{bmatrix} d_{11} & d_{12} & d_{13} \\ d_{21} & d_{22} & d_{23} \\ d_{31} & d_{32} & d_{33} \\ d_{41} & d_{42} & d_{43} \\ d_{51} & d_{52} & d_{53} \\ d_{61} & d_{62} & d_{63} \end{bmatrix} \tag{4.104}$$

The first subscript of a d_{ij} term of Eq. (4.104) represents the direction of application of the electric field, whereas the second subscript indicates the direction of measuring the strain. An example will be studied next in order to better understand the physical meaning of the amounts introduced in Eqs. (4.99) through (4.104).

Example 4.11

Determine the total strain about the thickness direction for the fixed-free piezoelectric plate of Fig. 4.42, which is subject to a force $F = 500\ \mu N$ in the presence of an electric field $E_3 = 100$ V/m (the two vectors are parallel). The material has a Young's modulus of E = 48 GPa, and a charge constant $d_{33} = 360 \times 10^{-12}$ m/V. The area of the cross-section normal to the external force is $A = 10^{-8}\ m^2$.

Solution:

The only mechanical stress is the one generated by the force F, about the direction z (or 3). As a consequence, the matrix Eq. (4.99) reduces to a single algebraic equation, namely:

$$\varepsilon_3 = c_{33}\sigma_3 + d_{33}E_3 \tag{4.105}$$

Both terms are compressive as the mechanical load and the electrical field (in conjunction with the piezoelectric poling field) generate deformations (strains) about the negative direction of axis 3. The first term in the right-hand side of Eq. (4.105) is the mechanical strain, which in this case can be calculated as:

$$\varepsilon_m = F / EA \tag{4.106}$$

By combining Eqs. (4.105) and (4.106) and by using the given numerical values, the total strain about the direction 3 becomes: $\epsilon_3 = 140.166 \times 10^{-9}$.

An equation similar to Eq. (4.99) can be written to express the piezoelectric effects as:

$$\{D\} = [d]^T\{\sigma\} + [\varepsilon_e^{\sigma}]\{E\} \tag{4.107}$$

where {D} is the *dielectric displacement vector* and $[\epsilon_e^{\sigma}]$ is the *electrical permittivity matrix* (the subscript σ indicates that the matrix is determined under constant-stress conditions). The vector {D} is defined as:

$$\{D\} = \{D_1 \; D_2 \; D_3\}^T \tag{4.108}$$

and the symmetric permittivity matrix is:

$$[\varepsilon_e^{\sigma}] = \begin{bmatrix} \varepsilon_{11} & \varepsilon_{12} & \varepsilon_{13} \\ \varepsilon_{21} & \varepsilon_{22} & \varepsilon_{23} \\ \varepsilon_{31} & \varepsilon_{32} & \varepsilon_{33} \end{bmatrix} \tag{4.109}$$

When premultiplying Eq. (4.99) by the vector 1/2 $\{\sigma\}^T$, the following equation is obtained, which contains only specific energy (energy per unit volume) terms:

$$\frac{1}{2}\{\sigma\}^T\{\varepsilon_m\} = U_m + U_{PZT} \tag{4.110}$$

where U_m is the *mechanical energy* and is formulated as:

$$U_m = \frac{1}{2}\{\sigma\}^T[c^E]\{\sigma\} \tag{4.111}$$

and U_{PZT} is the *piezoelectric energy* defined as:

$$U_{PZT} = \frac{1}{2}\{\sigma\}^T[d]\{E\} \tag{4.112}$$

The following equation can be obtained from Eq. (4.107) through left-multiplication by 1/2 $\{E\}^T$:

$$\frac{1}{2}\{E\}^T\{D\} = U_{PZT} + U_e \tag{4.113}$$

where the *electric energy* U_e is:

$$U_e = \frac{1}{2}\{E\}^T[\varepsilon_e^{\sigma}]\{E\} \tag{4.114}$$

The energy formulation is useful as it allows introducing an amount, the piezoelectric *coupling factor,* which is defined as:

$$k_{pe} = \sqrt{U_{PZT}^2 / (U_m U_e)} \tag{4.115}$$

and which gives the measure of the degree of energy conversion efficiency.

Example 4.12

Determine the coupling factor k_{pe} for the case defined in Example 4.11 knowing that the electrical permittivity ϵ_{33} is 15×10^{-9} F/m.

Solution:

For the particular problem of the previous example, the stress vector reduces to the σ_3 component. Similarly, the compliance matrix is single-termed as it only contains c_{33}, the permittivity matrix reduces to its ϵ_{33} component, and the electric field vector reduces to E_3. The piezoelectric energy will be in this case:

$$U_{PZT} = \frac{1}{2} d_{33} E_3 \sigma_3 \tag{4.116}$$

The mechanical energy is:

$$U_m = \frac{1}{2} c_{33} \sigma_3^2 \tag{4.117}$$

and the electrical energy simplifies to:

$$U_e = \frac{1}{2} \varepsilon_{33} E_3^2 \tag{4.118}$$

By substituting Eqs. (4.116), (4,117) and (4.118) into the definition equation – Eq. (4.115), the following equation is obtained for the coupling factor:

$$k_{pe} = d_{33} / \sqrt{c_{33} \varepsilon_{33}} \tag{4.119}$$

and it can be shown by analyzing the strain-stress relationship of Eq. (4.105) – Example 4.11 – that $c_{33} = 1/E$ (where E is the Young's modulus about direction 3 or z). As a consequence, Eq. (4.119) yields a coupling factor of approximately 0.2.

The case of utilizing piezoelectric layers sandwiched with other structural or active layers in bimorph/multimorph microcantilevers for

transduction purposes will be studied later in this chapter. The piezoelectric layers (ZnO is a material frequently used in MEMS) can be deposited to the substrate through sol-gel spin coating, which enables deposition of thicknesses of up to 50 μm.

6 PIEZOMAGNETIC TRANSDUCTION

Ferromagnetic materials such as alloys containing iron, cobalt or nickel are *piezomagnetic,* a property which is the magnetic counterpart of piezoelectricity. Piezomagnetic materials produce therefore both the *direct effect,* which consists of generation of a magnetic field under adequate mechanical load and the reversed effect (generally known as *magnetostriction),* which implies mechanical deformation as a result of magnetization. The dimensional change under the action of an external magnetic field in piezomagnetic materials is produced through alignment of the material magnetic domains in accordance to the external field, which creates internal motion and rearrangement with the macroscopic result of dimensional alteration. Figure 4.43 depicts such a situation, whereby an iron-based piezomagnetic alloy, such as Permalloy, elongates through application of a magnetic field.

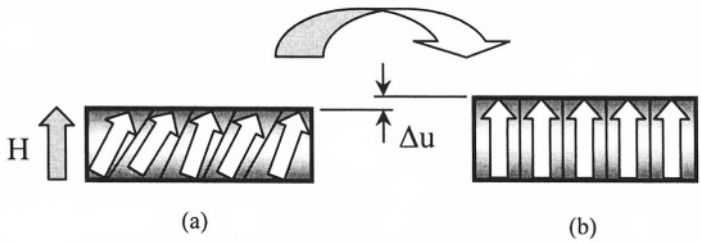

Figure 4.43 Elongation of an iron-based alloy under the action of the magnetic field

Other ferromagnetic compounds, such as those containing nickel, display the reversed response and contract under the action of an external magnetic field. Materials that expand are also called *positive magnetostrictive,* whereas the ones that do contract are alternatively named *negative magnetostrictive,* as shown by Jakubovics [5] for instance. The anisotropy in magnetized piezo-materials is reflected in the sensitivity to the direction of an external magnetic field. In a positive magnetostrictive material, application of an external magnetic field about a direction parallel to the polarization direction will lengthen the dimension parallel to that direction and will shorten the other two dimensions, as sketched in Fig. 4.44 (a), which is the top-view of a piezomagnetic plate. On the contrary, when the magnetic field is applied perpendicularly to the polarization direction, the material will contract about the polarization direction and will extend about the external field's direction,

as suggested in Fig. 4.44 (b). For a negative magnetostrictive material the deformation instances presented above reverse.

The similarity with the piezoelectric materials also extends in the modeling domain where the magneto-elastic equations replicate the electro-elastic ones describing the piezoelectric effect. In essence, the equations that describe the magnetostrictive effect can be written as:

$$\{\varepsilon\}_m = [c^H]\{\sigma\} + [d_{ma}]\{H\} \tag{4.120}$$

It can be seen by comparing Eq. (4.120) to Eq. (4.99) that, formally, the only difference consists in using the *magnetic field* H for magnetostrictive effects instead of the electric field describing the piezoelectric effects. The subscript *ma* was used to designate the *magnetic charge constant matrix,* whereas the superscript *H* indicates that the compliance matrix is calculated under constant-field conditions.

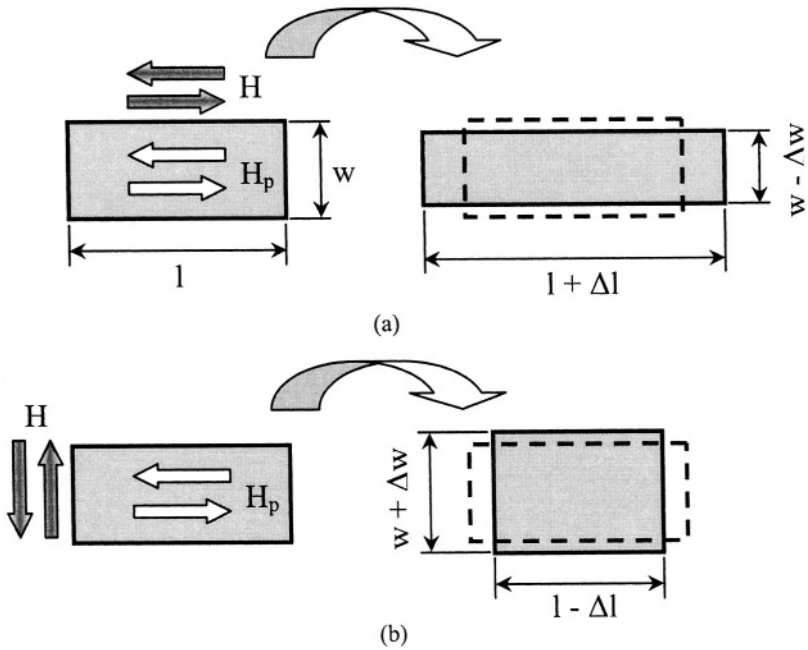

Figure 4.44 Deformation of a positive magnetostrictive material when: (a) the external magnetic field is parallel to the polarization direction; (b) the external magnetic field is perpendicular to the polarization direction

An equation similar to Eq. (4.107) also applies for piezomagnetic materials in the form:

$$\{B\} = [d]^T\{\sigma\} + [\mu^\sigma]\{H\} \tag{4.121}$$

where the induction vector {B} replaces the dielectric displacement vector {D}, the *magnetic permeability matrix* $[\mu]$ substitutes the electrical permittivity matrix $[\epsilon]$ (both calculated for constant stress), and the magnetic field H is used instead of the electric field E. The changes mentioned here in Eqs. (4.120) and (4.121) are also valid for the two problems solved that studied the piezoelectric effect. The remark has to be made that the coupling factor is defined here as:

$$k_{pm} = \sqrt{U_{pm}^2 / (U_{mech} U_{ma})} \tag{4.122}$$

where the *piezomagnetic energy* is:

$$U_{pm} = \frac{1}{2} \{\sigma\}^T [d_{ma}] \{H\} \tag{4.123}$$

and the *magnetic energy* is:

$$U_{ma} = \frac{1}{2} \{H\}^T [\mu^\sigma] \{H\} \tag{4.124}$$

Piezomagnetic materials, such as Terfenol-D, can be deposited in thin or thick layers on various substrates in order to create composite microcantilevers that can be used for MEMS actuation purposes especially, as will be shown in the sections presenting the bimorphs and the multimorphs, later in this chapter.

7 SHAPE MEMORY ALLOY (SMA) TRANSDUCTION

The *shape memory alloys,* in their bulk (macroscopic) form, are utilized in many applications, particularly in the medical industry and are mainly noted for two properties: the *shape memory effect* (SME) and the *superelasticity* (SE). Shape memory alloy thin films are shown to preserve the important advantages of SMAs in macro-scale designs, namely the large levels of actuation force and deformation, while substantially improving (reducing) the response time (which is a deficiency of macro-scale SMA designs) due to higher surface-to-volume ratios. Medical applications include arch wires for orthodontic correction, dental implants (teeth-root prostheses) and the attachments for partial dentures, orthopedics where SMA plates are used as prosthetic joints to attach broken bones, the spinal bent calibration bar (the Harrington bar), actuators in artificial organs such as heart or kidney, active endoscopes and guidewires. Other SMA applications are free and

constrained recovery, force actuation, flow control and actuation at microscale. Micrometer-order thick titanium-nickel (Ti-Ni) films that were sputter-deposited have demonstrated excellent actuation and reaction-time properties.

The shape memory effect (SME) was discovered in a gold-cadmium (Au-Cd) alloy as early as 1951, whereas the same effect in Ti-Ni alloys was reported in 1963. More details regarding the structure, properties and applications of shape memory alloys can be found in Otsuka and Wayman [10] who gave a synthetic view on the evolution lines in the shape memory alloy research. The shape memory effect consists in a phase transformation of an alloy under thermal variation. At lower temperatures, the *martensite* phase of an SMA – with lower symmetry and therefore more easily deformable – is stable, whereas at higher temperatures, the *austenite* phase (also called the parent phase) – of cubic, higher symmetry, which renders the SMA less compliant/deformable under mechanical action – is stable.

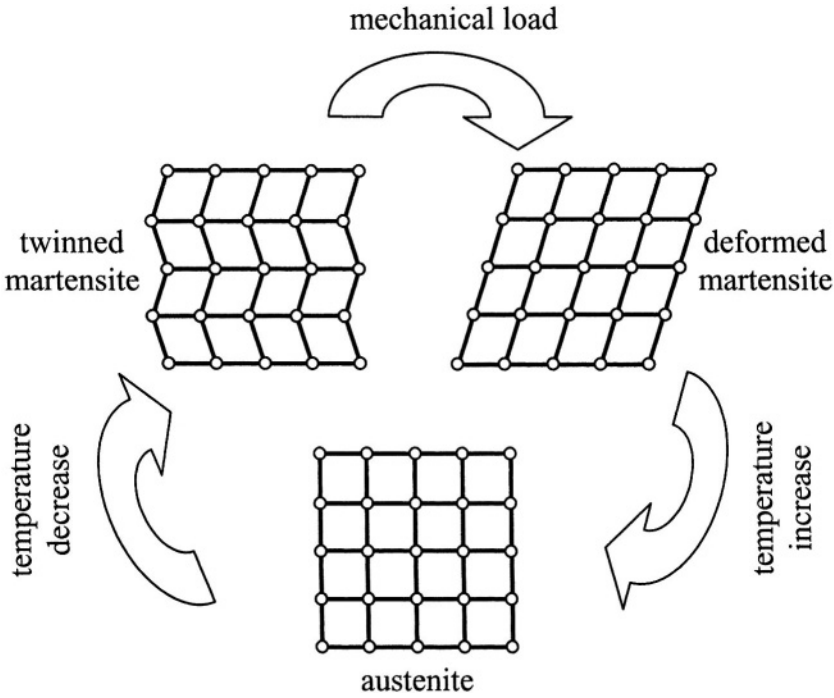

Figure 4.45 Thermo-mechanical cycle in a SMA with shape memory effect

It is thus possible to utilize the sequence of Fig. 4.45 in order to realize the SME. A temperature decrease is first applied which initiates the *martensitic transformation* from austenite to martensite. By subsequently applying the mechanical load, the SMA component in its martensitic phase (which is called *twinned martensite,* with at least two orientations of its potential deformation) at low temperature can be altered into deformed

martensite (since this phase is more compliant), with relatively low levels of external intervention. By further increasing the temperature over a critical value, which triggers the *reversed martensite-austenite transformation,* whereby the higher-symmetry crystallographic orientation of the parent (austenite) phase becomes stable, the component changes its shape to its original condition, and thus it *remembers* it. The reversed transformation will take place upon heating when the martensite becomes unstable.

Usually, the shape memory alloys produce the *one-way* SME, as depicted in Fig. 4.46 (a), and therefore the cyclic martensite-austenite transformation is not possible, as the deformed martensite state cannot be reached through cooling of the austenite phase. However, there are SMAs which remember both states, as sketched in Fig 4.46 (b), and such compositions are called *two-way* shape memory alloys. In MEMS applications, the SMA layers that are currently being used as actuators/sensors are mainly capable of reacting through the one-way SME.

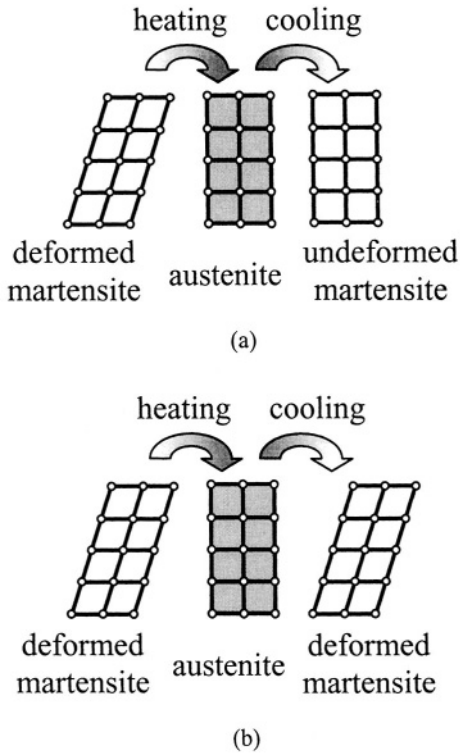

Figure 4.46 SMA effects: (a) one-way SME; (b) two-way SME

The load-deformation (or equivalently, stress-strain) characteristics of the martensite and austenite are schematically shown in Fig. 4.47 when the loading increases gradually about the directions indicated by the arrows. The

difference in slope between the two phases over the first deformation stage is the result of the fact that the austenite is stiffer than the martensite, due to its higher cubic symmetry, and this is the core feature enabling the utilization of SMAs as actuators/sensors in macro/micro applications. The martensite characteristic displays a quasi-horizontal portion (called the *plateau region*) where a component in this state can be deformed with virtually no increase in the external load.

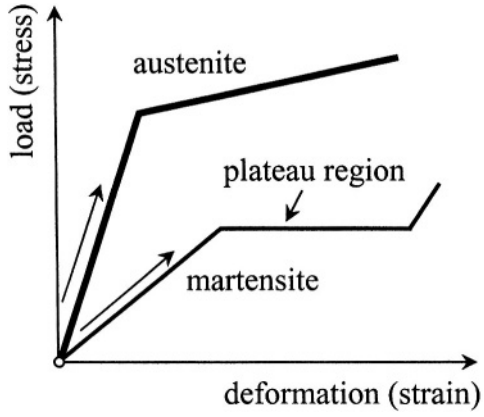

Figure 4.47 Load-deformation characteristics of the martensite and austenite phases of a typical SMA

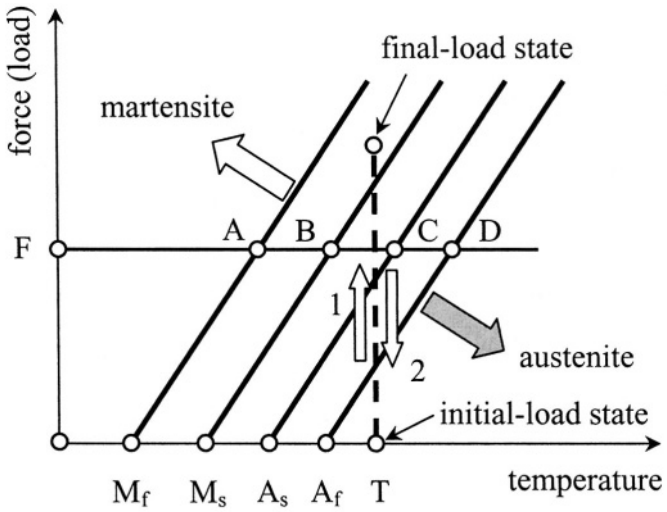

Figure 4.48 Superelastic (SE) effect in a shape memory alloy

The other important feature of certain SMAs, the *superelasticity* (sometimes called *pseudoelasticity*), is depicted in Fig. 4.48. Figure 4.48 shows the force-temperature characteristics of four different SMA compositions, each of them corresponding to a temperature which is relevant to either the martensitic transformation or the reversed one. The temperatures denoted by M_s and M_f symbolize the *start* of the martensitic transformation and the end *(finish)* of it, respectively. Similarly, A_s and A_f represent the same points for the austenite phase. For temperatures smaller than M_f the entire composition is martensite, whereas for temperatures higher than A_f the SMA is completely in its austenitic phase, in the absence of loading. Obviously, for temperatures within the $M_f - A_f$ range, the SMA contains both phases. The SE effect, as suggested in this figure, consists in heating the SMA over the point A_f (where only the austenite exists in stable condition), and loading the mechanical component at constant temperature (isothermally) – direction 1 in Fig. 4.48. In doing so, a final state can be reached where the martensite fraction predominates and where large *superelastic* deformations of 15-18% can be achieved easily, since the plateau region permits it. By downloading the mechanical component, along direction 2 in the same figure, it is possible to reach the initial state. However, the generation of the SE effect is more complex and manifests itself as a spontaneous, stress-free phenomenon, which takes place in certain shape memory alloys after many cycles of so-called *training.* Training consists of combined thermal and mechanical loading which alters the crystallographic structure of an SMA in order to favor SE behavior – Otsuka and Wayman [10].

The mechanics of shape memory alloy actuation/sensing are exemplified by the simple experiment illustrated in Fig. 4.49 where a weight is attached to a SMA wire.

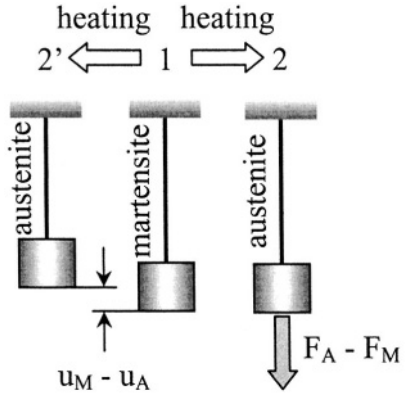

Figure 4.49 SMA transformation as a source for actuation/sensing

It is assumed that in state 1, the SMA wire is in martensitic phase and is deformed by the gravity force exerted on it through the attached weight. In case the temperature increases over the critical reversed transformation value, the austenitic transformation takes place and the natural tendency of the wire is to shrink and remember its original austenitic phase. In order to keep the wire's length unchanged, an external force directed downward has to be applied. This scenario is indicated by the sequence 1-2 in Figs. 4.49 and 4.50, which attempt to explain the change in force by the jump from the martensite characteristic (point 1) to the austenite characteristic (point 2).

As a consequence, the force gain during the 1-2 phase is equal to:

$$\Delta F = F_A - F_M = (K_A - K_M)u_M \tag{4.125}$$

where *A* and *M* stand for austenite and martensite, respectively. For a wire, the stiffness can be expressed as:

$$K = EA/l \tag{4.126}$$

where A is the cross-sectional area, l is the length and E is Young's modulus. It is therefore clear that the force of Eq. (4.125) is due to the difference in Young's moduli between austenite and martensite. Obviously, this simple force generation mechanism can be used in actuation.

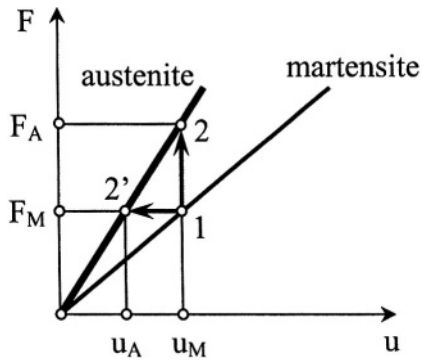

Figure 4.50 Force and stroke potentially gained through SMA transformation in the wire-weight device

Conversely, when no external force is applied during the heating and the corresponding martensite-austenite transformation, the SMA wire will shrink, as sketched in the 1-2' sequence of both Figs. 4.49 and 4.50. The displacement gained in this case is:

$$\Delta u = u_M - u_A = F_M(1/K_M - K_A) \tag{4.127}$$

and the underlying mechanism can be utilized in micro-scale sensing for instance.

Example 4.13

A circular, circumferentially-clamped SMA membrane in martensitic state is deformed through an external pressure such that a maximum central deflection u_0 is reached. A temperature increase of ΔT is applied to the membrane and the martensite transforms completely in austenite. Find the maximum force that can be generated through this reversed transformation. Consider that the membrane is defined by a radius $R = 50\ \mu m$ and thickness $t = 1\ \mu m$. The elastic properties of the austenite and martensite are: $E_A = 80 \times 10^9\ N/m^2$, $\mu_A = 0.35$, $E_M = 27 \times 10^9\ N/m^2$, $\mu_M = 0.3$ (after Otsuka and Wayman [10]). Also consider that $u_0 = 2\ \mu m$.

Solution:

The maximum force that can be generated during the membrane's martensitic-austenitic transformation equals the force that is needed to prevent any resulting deformation, and the stiffness of a clamped circular plate that is acted upon by a force placed at the symmetry center perpendicularly to the membrane plane is given in Eq. (1.231), Chapter 1. As a consequence, the maximum (bloc) force becomes:

$$\Delta F = F_A - F_M = (K_A - K_M)u_0 = 16\pi(D_A - D_M)u_0 / R^2 \qquad (4.128)$$

The flexural rigidities in austenitic and martensitic phase are:

$$\begin{cases} D_A = E_A t^3 / [12(1-\mu_A^2)] \\ D_M = E_M t^3 / [12(1-\mu_M^2)] \end{cases} \qquad (4.129)$$

By using the numerical values of this problem, the maximum force is found to be of 0.206 mN.

8 BIMORPH TRANSDUCTION

8.1 Generic Formulation

Bimorphs are composed of two layers of different materials laid upon each other as sketched in Fig. 4.51 (a). In general, one layer is active, in the sense that it can deform axially upon application of a specific type of energy. Because the two layers are sandwiched together, the free axial deformation of the top layer is constrained by the bottom layer and, as a result, the composite beam will bend. When the top layer shrinks, the resulting deformed shape of the beam is the one shown in Fig. 4.51 (b). When the free

shrinking of the top layer generates a strain ϵ_0, the bottom fibers of the top layer are prevented from fully shrinking by the adjacent bottom passive layer. As a consequence, there is a distribution in the axial deformation, from a maximum shrinking in the free top fiber to a minimum shrinking registered in the bottom (interface) fiber of the active layer. The same deformation trend is followed by the bottom (passive) layer due to its attachment to the top layer.

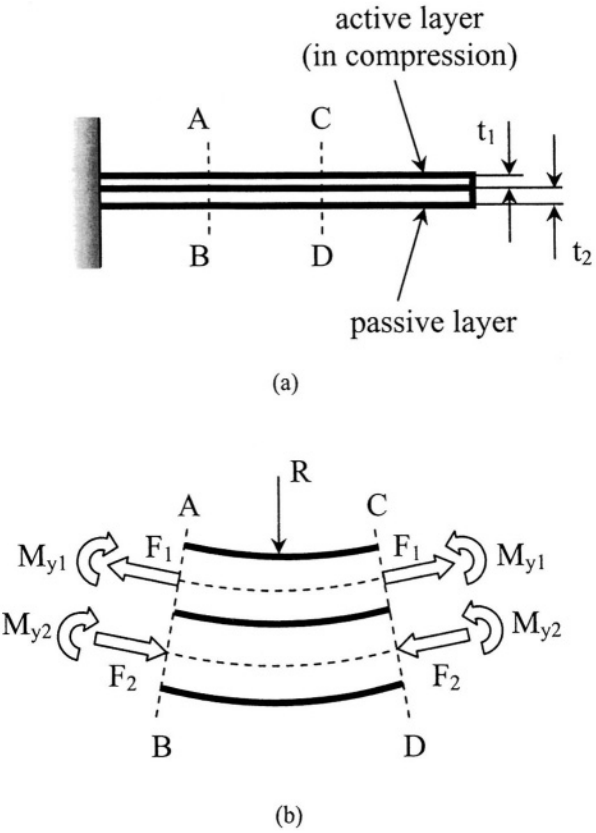

Figure 4.51 Bending deformation of a bimorph with shrinking top active layer: (a) general configuration; (b) Detail of deformed sandwich

Figure 4.51 (b) also indicates the forces and moments that are acting on each of the two layers, as produced by the induced free strain ϵ_0. If one analyzes the interface fiber belonging to the active layer, there are three types of strains that linearly superimpose under the assumption of small deformations, namely: the free strain ϵ_0, an axial strain generated by the action of the force F_1 and another strain component resulting from the bending of this layer. The same interface fiber also belongs to the bottom

layer, and the strains on it are an axial compressive strain due to the force F_2 and a bending strain. Because the strains on this interface should be identical, it follows that:

$$-\varepsilon_0 + F_1/(E_1/A_1) + t_1/(2R) = -F_2/(E_2/A_2) - t_2/(2R) \quad (4.130)$$

It should be noticed that the free strain is compressive (according to the initial assumption), whereas the axial strain is extensional (the force F_1 has the tendency of extending the top layer) as well as the bending strain (since the interface fiber is under the neutral axis of the bent beam which has its center of curvature upwards, as shown in Fig. 4.51 (b)). Similar reasoning explains the signs of the strain components pertaining to the interface fiber of the bottom layer – the right-hand side of Eq. (4.130).

Because there is no net axial force acting on the composite beam, it follows that the two forces should be equal, namely:

$$F_1 = F_2 = F \quad (4.131)$$

As also indicated in Fig. 4.51 (b), there should be a relationship between the bending effects produced on the right side section C-D of the form:

$$F(t_1 + t_2)/2 = M_{y1} + M_{y2} \quad (4.132)$$

The bending moments M_{y1} and M_{y2} can be expressed according to the engineering beam theory, as:

$$\begin{cases} M_{y1} = E_1 I_{y1}/R \\ M_{y1} = E_2 I_{y2}/R \end{cases} \quad (4.133)$$

Equation (4.133) took into consideration that bending of the two layers takes place independently, about the neutral (symmetry) axis of each component, such that both deform as circles with the same curvature radius R. By combining Eqs. (4.130) through (4.133), the unknown radius of curvature is found to be:

$$R = \{4E_2A_2(E_1I_{y1} + E_2I_{y2}) + E_1A_1[4E_1I_{y1} + E_2(4I_{y2} + A_2(t_1 + t_2)^2)]\}/[2E_1E_2A_1A_2\varepsilon_0(t_1 + t_2)] \quad (4.134)$$

Equation (4.134) is quite generic as the free strain ϵ_0 can be generated by a variety of means, for instance thermally, piezoelectrically or through shape-memory effects. Each of these transduction solutions will be discussed individually in the following.

It has also been shown in Chapter 1 that the bending of a sandwich beam can be described by an equivalent bending rigidity $(EI_y)_e$, which was defined in Eq. (1.180) in terms of individual material and geometry properties of the component layers. The bending moment that needs to be applied at the cantilever's tip in order to produce the curvature radius of Eq. (4.134) is determined as:

$$M_y = (EI_y)_e / R \tag{4.135}$$

Equation (4.134) or Eq. (4.135) can serve as a metric in comparing the different possibilities of actuating a bimorph with a given geometry, but in actuality only the peculiarities of the free strain ϵ_0 will dictate the differences in bending between two physically-identical bimorphs that are actuated by means of different sources.

When used as an actuator, the bimorph needs to be characterized in terms of its free displacement and bloc force capabilities, as mentioned in the beginning of this section. For a fixed-free (cantilever) configuration, the free displacement can be calculated as:

$$u_0 = u_{1z} = M_y l^2 / [2(EI_y)_e] \tag{4.136}$$

where the equivalent rigidity $(EI_y)_e$ is given in Eq. (1.180) of Chapter 1. Similarly, the force that will bloc the tip motion of a bimorph can be calculated as:

$$F_b = F_{1z} = 3M_y / (2l) \tag{4.137}$$

For a bimorph with given cross-section, material and induced-strain properties, the free displacement is proportional to the square of the length, as indicated by Eq. (4.136), whereas the bloc force of Eq. (4.137) is inversely proportional to the bimorph length.

The generic equations presented thus far can also be utilized as metric tools in quantifying the mechanical motion or the environmental changes by means of bimorph-based sensors. A variation of the tip bending moment or deflection translates in an induced strain, and this latter amount can easily be converted into an electrical signal for instance.

8.2 Thermal Bimorph

In a thermal bimorph, as the name indicates, the source strain ϵ_0 is induced thermally. In the hypothesis that the temperature of the upper layer of Fig. 4.51's bimorph decreases by ΔT (such that shrinking of this layer is possible, according to the assumptions here), the induced strain is:

$$\varepsilon_0 = \Delta l / l = \alpha \Delta T \tag{4.138}$$

Equation (4.138) has to be substituted into Eq. (4.134) in order to determine the curvature radius of a thermal bimorph.

A more realistic case is when both layers of a bimorph are exposed to the same temperature variation. For instance, when $\alpha_2 > \alpha_1$, the lower layer has a tendency to expand more than the upper layer and this situation is equivalent to only decreasing the temperature of the upper layer. This design was analyzed as early as 1925 by S. Timoshenko [11], who called the thermal bimorph a *bi-metal thermostat* since the materials of the two layers were metals. By following a procedure similar to the one already presented in the introduction to this sub-section, it can be shown that Eq. (4.134) remains valid by taking:

$$\varepsilon_0 = (\alpha_2 - \alpha_1)\Delta T \tag{4.139}$$

Example 4.14

Compare the bending performance of two physically-identical thermal bimorphs, when for one of them the lower layer is heated by a temperature ΔT, whereas for the other bimorph both layers are heated by the same temperature. Assume that $\alpha_2 > \alpha_1$.

Solution:

Equation (4.134) gives the curvature radius for both bimorph designs by means of the induced strain of either Eq. (4.138) – for the design with one heated layer, or Eq. (4.139) – for the configuration with both layers heated. The ratio of the two radii is simply:

$$R_1 / R_2 = (\alpha_2 - \alpha_1) / \alpha_1 = \alpha_2 / \alpha_1 - 1 \tag{4.140}$$

Although $\alpha_2 > \alpha_1$, the ratio of Eq. (4.140) is larger than 1 only when $\alpha_2 > 2\alpha_1$, and therefore the radius of curvature of the bimorph with one heated layer is greater than the radius of the similar bimorph with both layers heated. When $\alpha_2 < 2\alpha_1$, the ratio of Eq. (4.140) is less than 1, which indicates that $R_1 < R_2$.

8.3 Piezoelectric (PZT) Bimorph

When one of the layers forming the bimorph (for instance the upper one) is made up of a piezoelectric material, the free strain of this layer can be expressed, according to Eq. (4.99), as:

$$\varepsilon_0 = d_{31} E = d_{31} \Delta U / t_1 \tag{4.141}$$

where it has to be assumed that the voltage variation ΔU is negative, in order to comply with the assumption of the generic case that the upper layer is under free compression.

Example 4.15

Calculate the voltage that needs to be applied to a piezoelectric bimorph in order to achieve the bending capability of a thermal bimorph which has the same physical configuration. Assume that $d_{31} = 9 \times 10^{-11}$ m/V, $\alpha = 2.3 \times 10^{-6}$ 1/°C, $t_1 = 2$ μm.

Solution:

A piezoelectric bimorph can be compared to a physically-identical thermal bimorph by means of the free strain, and it can be seen from Eqs. (4.141) and (4.138) that the ratio of the free strain is:

$$\varepsilon_0^{PZT} / \varepsilon_0^{th} = d_{31} \Delta U / (t_1 \alpha \Delta T) \tag{4.142}$$

Equal bending capability of the two bimorphs means equal free strains and therefore:

$$\Delta U = (t_1 \alpha / d_{31}) \Delta T \tag{4.143}$$

Equation (4.143) indicates that for given material and geometric properties of the two bimorphs, the voltage is proportional to the temperature variation and the proportionality constant in the parenthesis of Eq. (4.143) is 0.025 V/°C. Figure 4.52 shows the plot of voltage variation as a function of the temperature variation in this problem.

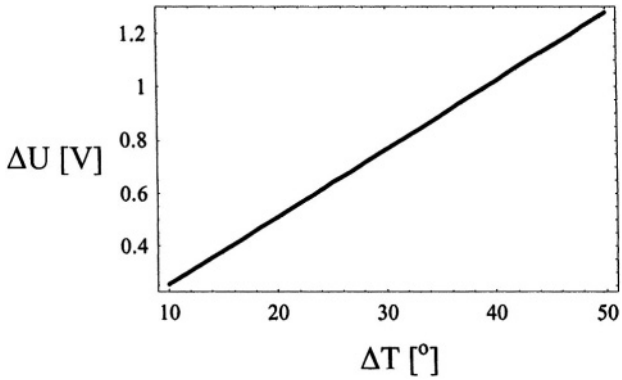

Figure 4.52 Voltage variation in terms of temperature variation in a piezoelectric-versus-thermal bimorph comparison

As the figure indicates, a voltage variation of about 1.2 V is necessary to apply to a piezoelectric bimorph in order to achieve the same bending radius as in a thermal bimorph which is subject to a temperature variation of 50°.

8.4 Piezomagnetic Bimorph

As discussed in the section introducing the piezomagnetic materials, a component made out of such a material can either expand or contract about a given direction as a function of the type of piezomagnetism (positive or negative) and of the directional relationship between the polarization field and the external magnetic field. In any situation, however, the amount of strain is usually denoted by λ and is equal to:

$$\lambda = \Delta l / l \tag{4.144}$$

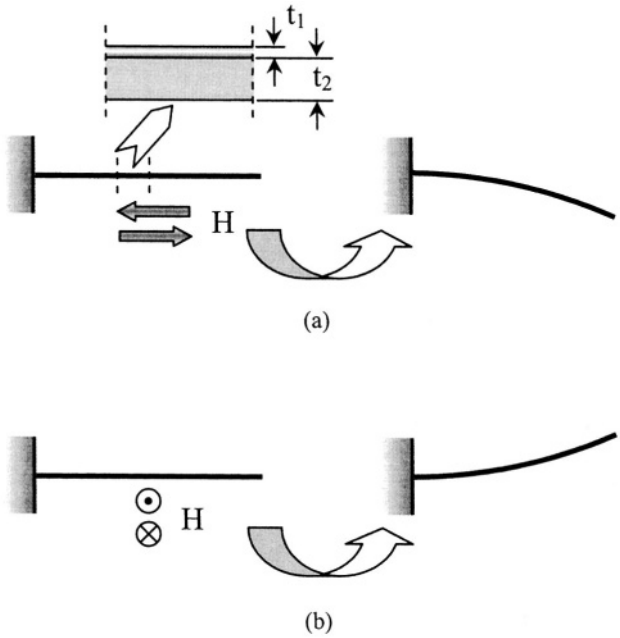

Figure 4.53 Bimorph with positive piezomagnetic active layer: (a) external magnetic field is parallel to polarization field; (b) external magnetic field is perpendicular to polarization field

When a piezomagnetic material is attached to a structural layer (in MEMS this is generally done by magnetron sputtering) in a cantilever-type configuration, the resulting bimorph can bend in the presence of an external magnetic field. Figure 4.53 for instance shows a bimorph that contains a positive piezomagnetic layer attached to a thicker structural layer. Assuming that the piezomagnetic direction of polarization is parallel to the length of the

microcantilever, two situations are possible, in terms of the direction of the external magnetic field. When the field is parallel to the polarization direction, as indicated in Fig. 4.53 (a), the piezomagnetic layer will stretch and the bimorph will bow downward. When the external magnetic field is perpendicular to the polarization direction, as shown in Fig. 4.53 (b), the piezomagnetic material will contract and will bow the bimorph upward. The material properties that define the coupled magnetic-mechanical behavior of a piezomagnetic material are generally determined experimentally, and the strain of Eq. (4.144) can be found as a function of the applied magnetic field. An example of piezomagnetic bimorph will be solved next.

Example 4.16

Find the tip bending moment produced by an amorphous negative piezomagnetic bimorph when the external magnetic field acts as shown in Fig. 4.53 (b). Assume that the polysilicon substrate is individually heated by $\Delta T = 50^{o}$. The induced strain has a value of $\lambda = 250 \times 10^{-6}$ for a field of H = 1000 Oe. The thicknesses of the two layers are $t_1 = 1\ \mu m$ and $t_2 = 5\ \mu m$ and the common width is $w = 30\ \mu m$. The elastic properties are: $E_1 = 10$ GPa and $E_2 = 165$ GPa, and the coefficient of linear thermal expansion is $\alpha_2 = 2.3 \times 10^{-6}$ 1/°C for the polysilicon.

Solution:

The deformation of this bimorph is the one sketched in Fig. 4.53 (a) because the piezomagnetic material is negative and has the opposite reaction compared to a positive material under identical external magnetic influence. The interface strain equation is in this case:

$$F/(E_1A_1)+t_1/(2R)-\lambda_1=-F/(E_2A_2)-t_2(2R)+\alpha_2\Delta T \qquad (4.145)$$

By coupling this equation with the curvature radius Eq. (4.134) – where $\epsilon_0 = \lambda_1 + \alpha_2 \Delta T$ – and the moment equilibrium Eq. (4.132), the equation of the tip bending moment becomes:

$$M = E_1E_2(E_1t_1^3+E_2t_2^3)(\lambda_1+\alpha_2\Delta T)t_1t_2(t_1+t_2)w/\{2[E_1t_1^4 + E_2t_2^4+2E_1E_2t_1t_2(2t_1^2+3t_1t_2+2t_2^2)]\} \qquad (4.146)$$

and its numerical value is $M = 2.635 \times 10^{-9}$ Nm.

8.5 Shape Memory Alloy (SMA) Bimorph

An SMA bimorph is formed of a layer of shape memory alloy (sputter-) deposited over a substrate layer. The following scenario can be envisioned for actuation: the bimorph is heated from a temperature T_0 to a temperature

T_1 which might be selected to coincide with A_s, which marks the start of the austenitic transformation. Assuming that the substrate has a higher coefficient of linear expansion, the bimorph will bend, due to the dissimilarity in the linear expansion coefficients of the two materials, in the way shown in the generic Fig. 4.51 (b). Being in martensite phase, the SMA is easily deformable. Further increasing the temperature from $T_1 = A_s$ to a temperature T_2 above the point A_f (where all the SMA is in austenitic form) will cause the SMA to shrink, which will produce more bending in the bimorph. The equations which define the deformation over the first temperature variation can be written as:

$$F/(E_M A_1) + t_1/(2R) + \alpha_M (T_1 - T_0) = -F/(E_2 A_2) - t_2/(2R) + \alpha_2 (T_1 - T_0) \tag{4.147}$$

and:

$$F(t_1 + t_2)/2 = E_M I_1 / R + E_2 I_2 / R = M \tag{4.148}$$

Equations (4.147) and (4.148) can be solved for the curvature radius, which is:

$$R = \{4E_M A_1 (E_M I_1 + E_2 I_2) + E_2 A_2 [4E_2 I_2 + [4I_1 + (t_1 + t_2)^2 A_1] E_m\} / [2A_1 A_2 (\alpha_2 - \alpha_M) E_M E_2 (t_1 + t_2)(T_1 - T_0)] \tag{4.149}$$

The bending moment M is given by Eq.(4.148). During the second phase, new forces and a new bending moment are set by the relative shrinking of the SMA layer, and the corresponding equations are:

$$F'/(E_A A_1) + t_1/(2R') + \alpha_A (T_2 - T_1) = -F'/(E_2 A_2) - t_2/(2R') + \alpha_2 (T_2 - T_1) \tag{4.150}$$

and:

$$F'(t_1 + t_2)/2 = E_A I_1 / R' + E_2 I_2 / R' = M' \tag{4.151}$$

Similarly, Eqs. (4.150) and (4.151) are solved for the new radius, which is:

$$R' = \{4E_A A_1 (E_A I_1 + E_2 I_2) + E_2 A_2 [4E_2 I_2 + [4I_1 + (t_1 + t_2)^2 A_1] E_A\} / [2A_1 A_2 (\alpha_2 - \alpha_A) E_A E_2 (t_1 + t_2)(T_2 - T_1)] \tag{4.152}$$

whereas M' is given by Eq. (4.151). As previously, the subscript *M* denotes martensite and the subscript *A* symbolizes austenite.

Example 4.17

A bimorph cantilever is formed of an SMA layer with thickness t_1 and is deposited on a polysilicon substrate with thickness t_2. An external bending moment M is applied at the free end in the positive manner (the SMA layer is stretched), followed by a temperature increase that takes the bimorph from an initial value $T_1 < A_s$ to a final one, $T_2 > A_f$. Determine the final configuration of the SMA-based bimorph.

Solution:

The external moment M which is applied to the SMA bimorph acts as a constant bias moment, and is plotted in Fig. 4.54 against the curvature of the bimorph. At T_1 the SMA is in martensitic state and the moment-curvature relationship is of the form:

$$M_M = (EI_y)_e \rho \tag{4.153}$$

where the equivalent moment of inertia has been calculated in Chapter 1 by means of Eq. (1.180) where one has to take E_M instead of E_1. The amounts z_1, z_2 and z_N are the positions of the symmetry axes of the two layer and the position of the neutral axis, respectively (they are needed in Eq. (1.180)). The latter amount, z_N, is given in Eq. (1.178).

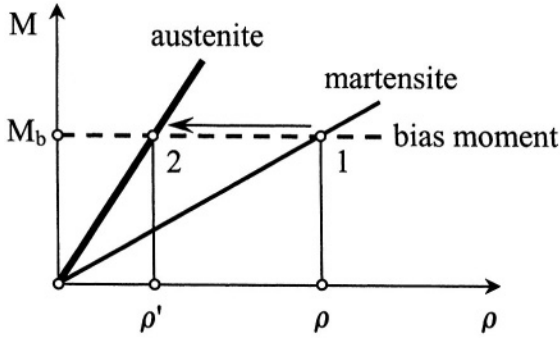

Figure 4.54 SMA bimorph with bias spring

At the operation point, the bending moment of the martensitic SMA is equal to the bias moment M_b and therefore the curvature is:

$$\rho = M_b / (EI_y)_e \tag{4.154}$$

The change in temperature and the subsequent phase transformation from martensite to austenite sends the operation point from the curve corresponding to the martensitic SMA, with lower Young's modulus, to the curve representing the bending moment-curvature characteristic for the SMA in the austenitic state, where Young's modulus is larger. For the latter state, the curvature is:

$$\rho' = M_b / (EI_y)_e' \tag{4.155}$$

where, again, the bending rigidity is calculated by Eq. (1.180), Chapter 1, by taking E_A instead of E_1.

8.6 Bimorph with Dissimilar-Length Components

The bimorph configurations discussed thus far had identical lengths of their components. There are also situations where one of the two layers is shorter than the other. Figure 4.55 sketches such a design where the two layers do not overlap completely. As shown previously, it is possible to determine the bending moments M that are generated through induced strains and act at the ends of the shorter layer, which mark the boundaries of the overlapping region. It has also been shown in Chapter 1 that an equivalent bending rigidity $(EI_y)_e$ can be calculated for the length l_1. As a consequence, it is possible to quantify the free displacement and the bloc force of this type of actuator at its free end.

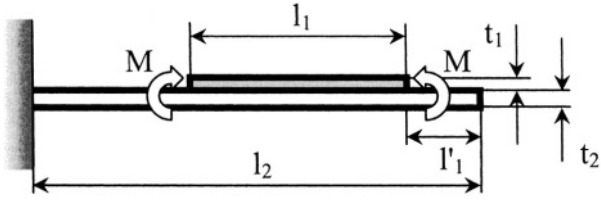

Figure 4.55 Bimorph with dissimilar-length layers

The free displacement, for instance, is given by the equation:

$$u_0 = u_{1x} = l_1(l_1 + 2l_1')M / [2(EI_y)_e] \tag{4.156}$$

where the bending moment M is given in Eq. (4.135) and the equivalent rigidity can be calculated as shown in Eq. (1.180) of Chapter 1. The force

that needs to be applied at the bimorph's free end in order to bloc the actuator is calculated as previously detailed and is:

$$F_b = F_{1z} = 3E_1 I_{y1} l_1 (l_1 + 2l_1')M / \{2[l_1 E_1 I_{y1}(l_1^2 + 3l_1 l_1' + 3l_1'^2) + (EI_y)_e(l_2^3 - l_1^3 - 3l_1 l_1'(l_1 + l_1'))]\} \quad (4.157)$$

Example 4.18

Study the relationship between the short patch length l_1 and its position l_1' on the microcantilever to the free displacement produced by a bimorph with dissimilar lengths.

Solution:

For given thicknesses and material properties of the bimorph, the free displacement expressed in Eq. (4.156) depends on two parameters: the position of the shorter patch, l'_1 and its length, l_1. It can be shown that the free displacement is proportional to the function:

$$fu_0 = l_1(l_1 + 2l_1') \quad (4.158)$$

Figure 4.56 is a three-dimensional plot of the function defined in Eq. (4.158). It can be seen that in order to maximize this function, and consequently the free displacement, the upper layer should be placed towards the root of the actuator and its length should be as large as possible.

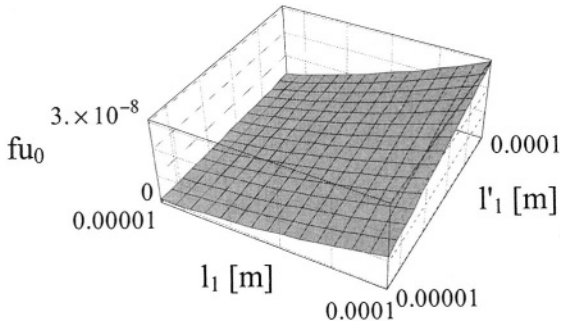

Figure 4.56 Free displacement function plot in terms of length and position of active layer

9 MULTIMORPH TRANSDUCTION

A multimorph is composed of more than two structural layers that are sandwiched together. Strain can be induced externally in each or just some of the layers, and the differential axial deformation, which is the result of

different layer material properties, results in bending of the multimorph that can be used for either actuation or sensing purposes. Using three or more active layers in a compound microcantilever allows for more power to be produced by the actuator (the stiffness of the resulting structure is larger because of more beams in parallel) or for combining actuation and sensing together in the same device. Figure 4.57 shows a three-layer multimorph with its reference frame.

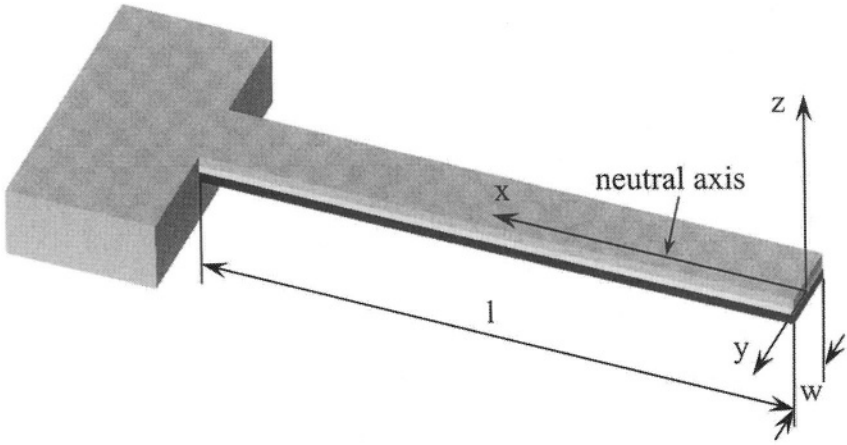

Figure 4.57 Three-layer multimorph with geometry and reference frame

The model developed next, together with the related solved examples and more detailed derivation can be found in Garcia and Lobontiu [12]. Figures 4.58 (a) and (b) illustrate the multimorph composition and its deformed shape.

The interface fiber between layers *i* and *i+1* has a unique deformation and therefore the strains of the two neighboring layers at this interface should be identical. By applying the principle of linear superposition, the resulting strain comprises three terms: one is produced by axial deformation of a layer, the second is produced by bending and the third term considers the strain which can be induced externally. As a consequence, the strain continuity equation at the interface between layers *i* and *i+1* is:

$$\frac{F_i}{E_i A_i}+\frac{t_i}{2R}+\varepsilon_i=\frac{F_{i+1}}{E_{i+1}A_{i+1}}-\frac{t_{i+1}}{2R}+\varepsilon_{i+1},\ i=1\rightarrow n-1 \qquad (4.159)$$

Since there is no external load acting axially, the sum of all the forces F_i needs to be zero:

$$\sum_{i=1}^{n} F_i = 0 \tag{4.160}$$

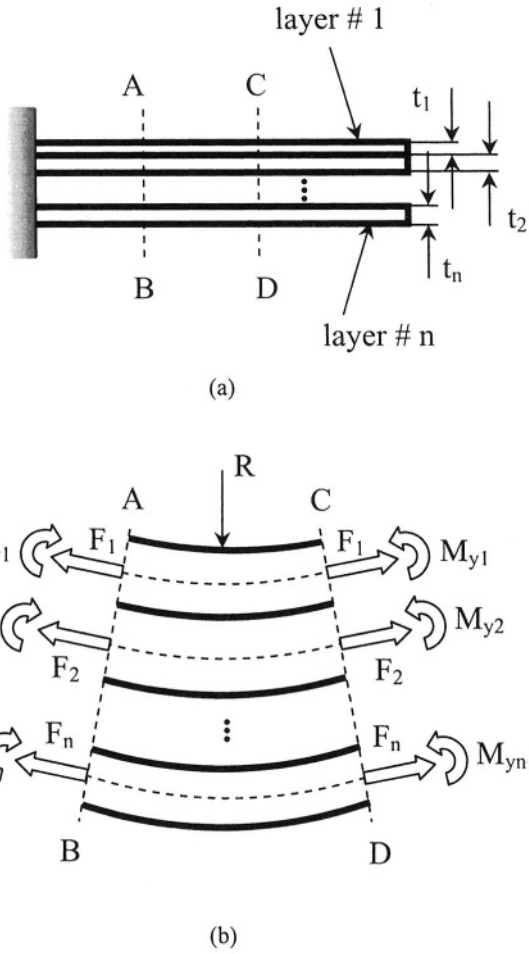

Figure 4.58 Generic multimorph beam: (a) side view with undeformed geometry; (b) close-up of bent segment

Equation (4.159) can be rewritten as:

$$F_{i+1} = E_{i+1}A_{i+1}\left(\frac{F_i}{E_i A_i} + \frac{t_i + t_{i+1}}{2R} + \varepsilon_i - \varepsilon_{i+1}\right), i = 1 \rightarrow n-1 \tag{4.161}$$

By successively applying Eq. (4.161), the force on a particular layer can be expressed in terms of the force on the previous layer, which, in turn, depends

on the force of the previous layer, and so on, such that, in the end, the particular force is expressed in terms of F_1. Also demonstrated in [12] is that the generic force F_i is expressed as:

$$F_i = C_i / R + D_i \tag{4.162}$$

with:

$$C_i = \frac{E_i A_i}{2}\{t_1 + 2\sum_{k=2}^{i-1} t_k + t_i - \frac{\sum_{i=2}^{n}[E_i A_i(t_1 + 2\sum_{k=2}^{i-1} t_k + t_i)]}{E_1 A_1 + \sum_{i=2}^{n} E_i A_i}\} \tag{4.163}$$

and:

$$D_i = E_i A_i\{\varepsilon_1 - \varepsilon_i - \frac{\sum_{i=2}^{n}[(\varepsilon_1 - \varepsilon_i)E_i A_i]}{E_1 A_1 + \sum_{i=2}^{n}(E_i A_i)}\} \tag{4.164}$$

The curvature radius can be expressed as:

$$R = \sum_{i=1}^{n}[E_i I_{yi} - C_i(z_N - z_i)] / \sum_{i=1}^{n}[D_i(z_N - z_i)] \tag{4.165}$$

The individual moments which are produced by pure bending about each individual neutral (symmetry) axis are defined as:

$$M_{yi} = E_i I_{yi} / R \tag{4.166}$$

The total bending moment can therefore be calculated as:

$$M_y = \sum_{i=1}^{n} M_{yi} = \sum_{i=1}^{n}(E_i I_{yi}) / R \tag{4.167}$$

Example 4.19

Determine the curvature radius in a three-layer multimorph cantilever having the characteristics given in Table 1 in the case of applying a temperature increase of $\Delta T = 60^{\circ}$. The length of the composite cantilever is 50

μm and the common width of the layers is w = 10 μm. Use the analytic model developed herein, as well as an independent finite element simulation.

Table 1. Material and geometric parameters of a three-layer cantilever

	t [μm]	E [GPa]	α [1/°]
Layer # 1	1	200	1.1×10^{-6}
Layer # 2	2	150	1.3×10^{-6}
Layer # 3	2	130	1.6×10^{-6}

Solution:

The Ansys software has been used to run the finite element analysis, with two-dimensional elements having the material properties of Table 1. The tip slope was 0.02° which translated into a curvature radius of approximately R = 0.11 m. The analytic model proposed here resulted in a curvature radius of R = 0.1 m, and therefore there is agreement between the two methods, and this particular example constitutes another check of the accuracy of the proposed model.

Example 4.20

An anti-parallel trimorph is formed of two identical active layers that are laminated on a middle structural layer. When the two external layers are actuated such that one compresses and the other one stretches, desirably by the same amount of strain, an *anti-parallel* configuration is achieved with enhanced actuation/sensing capabilities. Assuming the two active layers are made of PZT material and that the middle layer is a polysilicon substrate, determine the bending moment that can be achieved by this structure when applying a +120/ -120 V variation on the two PZT layers.

Solution:

Assuming the top PZT layer shrinks under the negative voltage variation, and the other PZT layer stretches when subject to the positive voltage variation, the strains induced in the two layers are:

$$\begin{cases} \varepsilon_1 = d_{31}\Delta U / t_1 \\ \varepsilon_3 = d_{31}\Delta U / t_3 \end{cases} \tag{4.168}$$

By utilizing the conditions of Eq. (4.168) into the generic multimorph model, one obtains the following particular equation for the curvature radius R:

$$R = \{ E_1 [A_1 (t_1 + t_2)^2 - 4 I_{y1}] - 2 E_2 I_{y2} \} / [2 E_1 A_1 (t_1 + t_2) \varepsilon_1] \tag{4.169}$$

The tip bending moment is:

$$M = \{2E_1A_1(2E_1I_{y1} + E_2I_{y2})(t_1 + t_2)d_{31}\Delta V / \{t_1\{E_1[A_1(t_1 + t_2)^2 - 4I_{y1}] - 2E_2I_{y2}\}\} \quad (4.170)$$

The PZT-generated strain, as defined in Eq. (4.141), has been used in Eq. (4.170). It should be mentioned here that the neutral axis coincides with the longitudinal symmetry axis of the middle layer, namely:

$$z_N = t_1 + t_2 / 2 \quad (4.171)$$

and that the axial force on the middle layer is zero, whereas the forces on the two external layers are equal and opposite: $F_1 = - F_3$.

Example 4.21

A multimorph can combine three of the active effects analyzed so far, namely the thermal, piezoelectric and shape memory effects in order to produce actuation, sensing or both. Figure 4.59 shows the longitudinal disposition, from top to bottom, of a piezoelectric (PZT) layer, an electric insulator layer (such as silicon nitride and whose thickness is negligible compared to the other layers' thicknesses), a shape memory alloy (SMA) layer and a structural layer (made up of polysilicon). Analyze the behavior of this multimorph transducer.

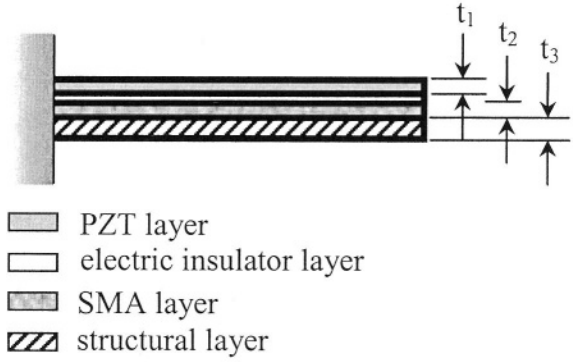

Figure 4.59 Side view of a PZT-SMA-based multimorph

Solution:

One can assume that initially the PZT layer can function as the actuator agent, when subject to a voltage variation which will shrink its original length and this will bend the multimorph, as shown in Fig. 4.58 (b) for a generic

multimorph. The SMA layer, being at low/martensitic temperature, can easily be deformed, as driven by the PZT deformation.

If a temperature increase is subsequently applied so that the SMA's martensite phase transforms into austenite, the SMA layer will shrink, becoming the actuator, and the multimorph will further bend. If no voltage is supplied to the PZT during the SMA actuation, the PZT can act as a sensor because the change in strain translates in a proportional voltage change. As a consequence, the sandwich device can function as both actuator and sensor by switching the functions of the PZT layer.

It is of interest to quantify the level of actuation, as well as the relationship defining the voltage detection during the second phase, when SMA is the actuator and the PZT layer is the sensor. By using the generic multimorph model, it is possible to calculate the curvature radius R, as well as the corresponding tip moment acting on the bender. At the same time, the voltage generated through SMA-driven deformation into the PZT layer can be evaluated by considering the strain on its lower fiber as being produced through bending and axial deformation, namely:

$$\Delta U = \frac{t_1}{d_{31}}\left(\frac{F_1}{E_{PZT}A_1} + \frac{t_1}{2R}\right) \tag{4.172}$$

where the axial force F_1 acting on the PZT layer is:

$$F_1 = E_1A_1\{E_2A_2[2(\alpha_1-\alpha_2)\Delta TR + t_1 + t_2] + E_3A_3[2(\alpha_1-\alpha_3)\Delta TR + t_1 + 2t_2 + t_3]\}/[2R(E_1A_1 - E_2A_2 + E_3A_3)] \tag{4.173}$$

and the curvature radius corresponding to SMA-generated bending is expressed as:

$$R = A/B \tag{4.174}$$

where:

$$A = 12(E_2A_2 + E_3A_3)(E_1I_1 + E_2I_2 + E_3I_3) + E_2E_3A_2A_3(3t_2^2 + 7t_2t_3 + 4t_3^2) - E_1A_1\{12E_1I_1 + 12E_3I_3 + 3E_2[4I_2 + A_2(t_1+t_2)^2] + E_3A_3(t_1 + 2t_2 + t_3)(3t_1 + 6t_2 + 4t_3)\} \tag{4.175}$$

and:

$$B = 2\Delta T\{[E_2E_3A_2A_3(\alpha_3-\alpha_2)(3t_2 + 4t_3) + E_1A_1[3E_2A_2(\alpha_2-\alpha_1)(t_1+t_2) + E_3A_3(\alpha_3-\alpha_1)(3t_1 + 6t_2 + 4t_3)]]\} \tag{4.176}$$

10 OTHER FORMS OF TRANSDUCTION

Actuation and sensing can be produced by other means, as well. Figure 4.60 for instance, shows an elastic, membrane-like layer that covers an enclosure. If heating is provided to an element in the enclosure, the gas trapped inside the enclosure will expand and the resulting pressure will deform the membrane outward.

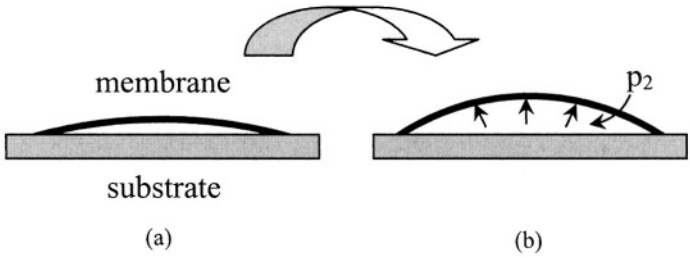

Figure 4.60 Actuation by gas expansion and elastic membrane: (a) Initial undeformed state; (b) High-pressure deformed state

In the case of a general gas transformation, the pressure after the temperature increase ΔT has been applied can be calculated as:

$$p_2 = p_1 V_1 (T_1 + \Delta T)/(T_1 V_2) \tag{4.177}$$

Another equation can be written relating the pressure in the final state p_2 with the deformation, and therefore the new volume V_2, and the solution to these two equations will characterize the transduction problem.

The membrane can also deform by introducing fluids under pressure in the provided enclosure, such that the case is with *hydraulic* or *pneumatic* transduction.

Hydrogels, which can undergo large volume changes (swelling or shrinking) under diverse stimuli such as variations in the water pH, solute concentration, electric field, light or temperature, are also utilized in MEMS transduction, as microcomponents that actuate flow-control components in microfluidics – see, for instance, Liu, Yu and Beebe [13] . Hydrogel-based transduction needs no external power and is capable of producing relatively large amounts of displacement and force in actuation, and to be very sensitive to small environmental changes. Reducing the scale of hydrogel MEMS components improves the time response of swelling-unswelling.

Electroactive polymers (EAP), also called *artificial muscles,* are actually electrostrictive materials which can reversibly change shape through electric field exposure, and are consequently used as transduction materials, especially in multimorph configurations.

Other transduction implementations, especially in microfluidics, utilize various basic principles such as *dielectrophoresis, surface-tension, liquid-vapor phase change* or *microbubbles.*

Problems

Problem 4.1

A bent beam thermal actuator needs to be able to deliver its mechanical output around an operation point that lies within a domain bounded by [u_{min}, u_{max}] and [F_{min}, F_{max}]. Determine the inclination angle satisfying this condition. Known are also the length l, the cross-sectional area A and the moment of inertia I_z.

Answer:

$$cos(2\beta) = [6EAI_z(u_{max} - u_{min}) - l(3I_z + Al^2)(F_{max} - F_{min})] /$$
$$[l(Al^2 - 3I_z)(F_{max} - F_{min})]$$

Problem 4.2

Determine the optimal value of the inclination angle β of a bent beam thermal sensor that will maximize the free displacement for a temperature increase $\Delta T = 40^o$. Known are the coefficient of thermal expansion $\alpha = 2.3 \times 10^{-6}$ 1/°C, the length $l = 100\ \mu m$, and the cross-sectional dimensions $w = t = 10\ \mu m$.

Answer:

$\beta = 5.77^o$, $u_{max} = 4.62 \times 10^{-8}$ m

Problem 4.3

A two-beam polysilicon thermal sensor is defined by the following geometric parameters: $l_1 = 200\ \mu m$, $l_2 = l_4 = 10\ \mu m$. Design the rectangular cross-section of this sensor (w and t) which will produce a tip rotation $\theta_{2z} = 0.1^o$ under a temperature increase of $\Delta T = 80^o$ C. The coefficient of thermal expansion is 1.8×10^{-6} 1/°.

Answer:

$w = 5.6\ \mu m$; t can be chosen arbitrarily

Problem 4.4

A geometric envelope of $200\ \mu m \times 15\ \mu m$ is available for the design of a thermal actuator of maximum bloc force. In case the cross-section of the flexible beams is specified ($w = t = 5\ \mu m$), decide whether a bent beam actuator or a two-beam design constitutes the best solution. (Hint: Study the bloc force ratio).

Answer:

The bloc force of the two-beam thermal actuator is up to 80 times larger than the bloc force of a bent beam actuator, for very small lengths l_4 of the short leg of the two-beam design.

Problem 4.5

A transverse (plate-type) electrostatic device is used as a capacitive sensor. Design the sensor such that when the mobile plate travels between the limit positions $x_{min} = g_{0,x}/5$ and $x_{max} = g_{0,x}/3$, the capacitance variation is no less than a minimum value ΔC_{min}.

Answer:

$g_{0,x} = \varepsilon l_y l_z / (4\Delta C_{min})$; the area $l_y l_z$ Can be chosen arbitrarily;

Problem 4.6

Design a longitudinal (comb-type) electrostatic actuator of given sensitivity ∂C/∂y that is expected to deliver an output force F.

Answer:

$$l_z = g(\partial C / \partial y) / \varepsilon ; \; F = (\partial C / \partial y) U^2 / 2$$

Problem 4.7

A rotary electrostatic actuator with a single gap $g_r = 1$ μm produces a maximum torque M_1, which is 1.5 times less than the desired effective value M_{eff}. By keeping the existing gap, other conjugate pairs are added radially in order to meet the objective. Find the number of total gaps (radial digit pairs) that will enable achieving the level of torque needed when $t_r = 1$ μm and $R_{min} = 100$ μm.

Answer:

n = 2

Problem 4.8

A microcantilever of given dimensions l = 150 μm, w = 15 μm and t = 1 μm is used as an electrostatic actuator. Find the gap between the microcantilever and its mating pad (assuming both have the same length) that will produce a tip deflection of 0.8 μm under application of a 80 V voltage. The material properties are E = 120 GPa and $\epsilon = 8.8 \times 10^{-12}$ F/m.

Answer:

g = 2.4 μm

Problem 4.9

Find the net effect on a loop having the geometry shown in Fig. 4.61 (where R = l/2) and carrying a current I when subject to an external field B.

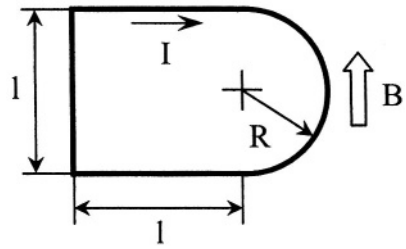

Figure 4.61 Loop carrying a current in a magnetic field

Answer:

Rotation of the loop about an in-plane direction perpendicular on B and passing through the semi-circle center; total moment = $(1 + \pi/8)\, BIl^2$;

Problem 4.10

Find the deflection at the midpoint of the microbridge shown in Fig. 4.62, which is produced by the interaction between the fields of a permanent magnet attached to the microbridge and the fixed coil carrying a current I_1. The microcantilever cross-section is defined by a width w and a thickness t.

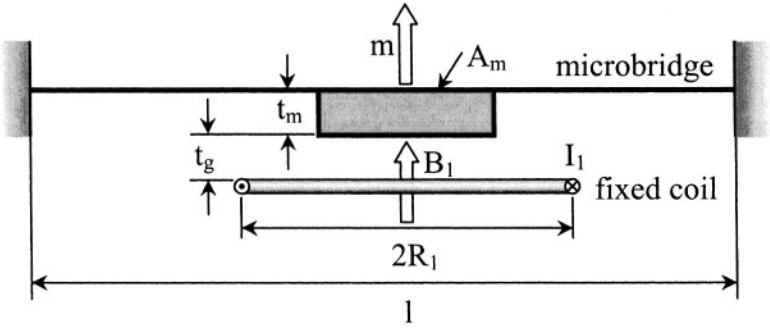

Figure 4.62 Magnetic-electromagnetic interaction via flexible microbridge

Answer:

$$u = l^3 A_1 t_m n_1 I_1 q_m \mu_0 t_g \,/[\pi 128 E I_y (R_1^2 + t_g^2)^{5/2}]$$

Problem 4.11

A microcantilever is magnetized as indicated in Fig. 4.39 (c). Determine the actuation effects at the free end when the external filed is defined by the law: $B = B_0\, e^{-az}$ and the magnetic field source is located underneath the free

end at a distance h. Known are the cross-sectional dimensions w and t, and the magnetization m of the magnet.

Answer:

$$\begin{cases} u_z = -4l^3 maB_0 e^{-ah} /(Ewt^3) \\ \theta_x = 3lmB_0 e^{-ah} /(Gwt^3) \end{cases}$$

Problem 4.12

A thin sheet is constructed of piezoelectric material of cross-sectional dimensions w and t, and dielectric constant d_{31}. The piece is polarized over its thickness direction 3 and is subject to bending moments M that are applied at its ends. A total strain ϵ_t is measured on one of the sides of the piezoelectric sheet. Calculate the corresponding voltage that is generated.

Answer:

$$\Delta U = t[\varepsilon_t - 6M /(Ewt^2)] / d_{31}$$

Problem 4.13

Find the bloc force that has to be applied to a piezomagnetic bloc of cross-sectional area A and Young's modulus E. The piece is magnetized about its height direction by means of a magnetic field H. Also determine the coupling coefficient. Known are the magnetic charge constant d_{33}, the magnetic permeability μ_{33} and the magnetic compliance c_{33}.

Answer:

$$\begin{cases} F = EAd_{33}H \\ k = d_{33} / \sqrt{c_{33}\mu_{33}} \end{cases}$$

Problem 4.14

A clamped square membrane constructed of SMA with side l and thickness t is deformed while in martensitic state by application of a uniform pressure p. A temperature variation, which brings the martensite into austenite phase, is applied subsequent to removing the initial pressure. Determine the variation in the maximum deflection. Known are Young's modulii in martensitic and austenitic states, E_M and E_A, as well as Poisson's ratio μ. (Hint: use Eq. (1.233) with the first two terms of the infinite series expansion.)

Answer:

$$\Delta u = 12(1-\mu^2)(E_A - E_M)l^4 p /(19\pi^6 E_A E_M t^3)$$

Problem 4.15

A bimorph is constructed of two different materials, having $E_1 = 130$ GPa , $\alpha_1 = 2 \times 10^{-6}$ 1/°C , $E_2 = 150$ GPa , $\alpha_2 = 2.4 \times 10^{-6}$ 1/°C. Find the thicknesses t_2 when $t_1 = 1$ μm and $l = 200$ μm. The tip slope $\theta_1 = 0.2^o$ is produced by a temperature increase of $\Delta T = 60^o$ C.

Answer:

$t_2 = 2.05$ μm

Problem 4.16

A bimorph is formed of two layers, the active one being piezomagnetic and the substrate being polysilicon. Find the length of the bimorph when a tip bloc force of 20 μN needs to be produced with an induced strain $\lambda = 0.001$. Known are $E_1 = 10$ GPa, $E_2 = 160$ GPa, $t_1 = 1.5$ μm, $t_2 = 7.5$ μm, $w = 10$ μm.

Answer:

$l = 185.42$ μm

Problem 4.17

A bimorph sensor is formed of a piezoelectric layer attached to a structural polysilicon layer of given thickness t_2. Determine the variation ΔE in the external field when a tip deflection of 0.2 μm is measured optically. The following parameters are known: $d_{31} = 8.5 \times 10^{-11}$ m/V, $E_1 = 5$ GPa, $E_2 = 160$ GPa, $l = 150$ μm, $w = 15$ μm, $t_1 = 1.2$ μm, $t_2 = 5$ μm.

Answer:

$\Delta E = 3.73 \times 10^6$ Vm

Problem 4.18

A bimorph with dissimilar-length components utilizes thermal expansion for temperature change detection. Find the temperature variation ΔT when a tip deflection of 0.1 μm is measured experimentally. Known are the following amounts: $l_2 = 200$ μm, $l_1' = 0$, $l_1 = 3l_2/4$, $w = 10$ μm, $t_1 = t_2 = 5$ μm, $\alpha_1 = 1.8 \times 10^{-6}$ 1/°C, $\alpha_2 = 3 \times 10^{-6}$ 1/°C, $E_1 = 125$ GPa, $E_2 = 140$ GPa.

Answer:

$\Delta T = 49.42^o$

Problem 4.19

A three-layer multimorph is constructed to function as a thermal actuator. Determine the tip deflection that this actuator is capable of producing under a temperature increase of $\Delta T = 80^o$. It is known that $l = 350$ μm, $w = 8$ μm, $t_1 = t_2 = t_3 = 2$ μm, $E_1 = 120$ GPa, $E_2 = 130$ GPa, $E_3 = 150$ GPa, $\alpha_1 = 1.2 \times 10^{-6}$ 1/°C, $\alpha_2 = 1.5 \times 10^{-6}$ 1/°C, $\alpha_3 = 1.8 \times 10^{-6}$ 1/°C.

Answer;

$u_z = 0.84\ \mu m$

Problem 4.20

Positive and negative magnetostrictive layers, of identical thickness, are attached on both sides of a polysilicon layer. Determine the tip slope when an external magnetic field induces opposite strains $\lambda_1 = -\lambda_2 = 0.00012$ in the two piezomagnetic layers. Known are: $l = 200\ \mu m$, $w = 12\ \mu m$, $t_1 = t_3 = 0.5\ \mu m$, $t_2 = 1\ \mu m$, $E_1 = E_3 = 9$ GPa, $E_2 = 150$ GPa.

Answer:

$\theta_z = 1.2^o$

References

1. L. Que, J.-S. Park, Y.B. Gianchandani, Bent beam electrothermal actuators – Part I: single beam and cascaded devices, *Journal of Microelectromechanical Systems,* 10 (2), pp. 247-254, 2001.

2. Y.B. Gianchandani, K. Najafi, Bent beam strain sensors, *Journal of Microelectromechanical Systems,* 5(1), pp. 52-58, 1996.

3. G.T.A. Kovacs, *Micromachined Transducers Sourcebook,* McGraw-Hill, Boston, 1998.

4. M.N.O. Sadiku, *Elements of Electromagnetics,* Third Edition, Oxford University Press, New York, 2001.

5. J.P. Jakubovics, *Magnetism and Magnetic Materials,* The University Press, Cambridge, 1994.

6. J.W. Judy, R.S. Muller, Magnetic microactuation of torsional polysilicon structures, *Sensors and Actuators A,* 53 (1-3), pp. 392-397, 1996.

7. M. McCraig, A.G. Clegg, *Permanent Magnets in Theory and Practice,* Second Edition, John Wiley & Sons, New York, 1989.

8. S. Seely, A.D. Poularikos, *Electromagnetics – Classical and Modern Theory and Applications,* Marcel Dekker, New York, 1979.

9. A. Kruusing, V. Mikli, Flow sensing and pumping using flexible magnet beams, *Sensors and Actuators A,* 52, pp. 59-64, 1996.

10. K. Otsuka and C.M. Wayman – Editors, *Shape Memory Materials,* Cambridge University Press, Cambridge, 1999.

11. S. Timoshenko, Analysis of bi-metal thermostats, *Journal of the Optical Society of America,* 11, pp 233-255,1925.

12. E. Garcia, N. Lobontiu, Induced-strain multimorphs for microscale sensory actuation design, *Smart Structures and Materials,* 13, pp. 725-732, 2004.

13. R.H. Liu, Q. Yu, D.J. Beebe, Fabrication and characterization of hydrogel-based microvalves, *Journal of Microelectromechanical Systems,* 11 (1), pp. 45-53, 2002.

Chapter 5

STATIC RESPONSE OF MEMS

1. INTRODUCTION

This chapter studies the static response of microsystems by modeling the combined effects of actuation, sensing and elastic suspension. The number of microdevices that can be custom-built by integrating spring designs such as those presented in Chapters 2 and 3 with rigid parts and transduction principles, as the ones analyzed in Chapter 4, is vast, and the present chapter contains just a sample of the extended pool of MEMS applications. The static equilibrium equations are used for either translatory or rotary motion in order to qualify the performance of various classes of MEMS, starting from the simplest designs (with one suspension unit and one transduction unit) to more complex ones (comprising several spring microsuspensions together with either actuation or sensing units or with both actuation and sensing capabilities). The large deformations of mechanical microsuspensions are analyzed in MEMS applications that deform either axially or through bending. The buckling phenomenon, as applied to straight and curved microcomponents, is also addressed together with the post-buckling and accompanying large-deformation phenomena. Later, the stresses and yield criteria for combined stresses are presented for several MEMS applications. Fully-solved examples supplement the text in order to better explain the various topics of this chapter, and a set of proposed problems completes the presentation.

2. SINGLE-SPRING MEMS

One of the simplest MEMS configurations comprises one microsuspension (spring) and the actuation/sensing component. The equilibrium in such situations is produced when the actuation force/moment and the opposing elastic force/moment are equal. Several practical applications will be analyzed next, including microdevices that are designed for linear or rotary (mainly electrostatic) transduction and flexure microhinge MEMS.

2.1 Transverse Electrostatic Actuation with Microsuspension

By coupling the transverse (plate-type) electrostatic transduction that has been introduced in Chapter 4 to one of the microsuspensions presented in Chapter 3 leads to the model shown in Fig. 5.1.

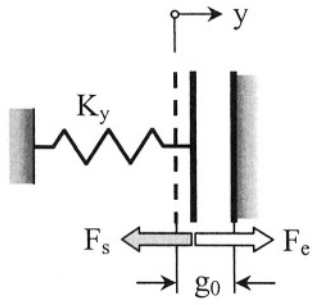

Figure 5.1 Model of transverse electrostatic actuation and microsuspension

The maximum gap between the fixed and the mobile plates, g_0, occurs initially for y = 0. The static equilibrium sets in when the two opposing forces, the electrostatic and the spring force, are equal:

$$F_e = F_s \tag{5.1}$$

The force produced through transverse electrostatic actuation was given in Chapter 4 and is rewritten here as:

$$F_e = \varepsilon A U^2 / [2(g_0 - y)^2] \tag{5.2}$$

whereas the elastic force is:

$$F_s = K_y y \tag{5.3}$$

Figure 5.2 shows the force-displacement plots of these two forces. As Fig. 5.2 indicates, there are two points of equilibrium, E_1 and E_2, where the two forces are equal for specified spring and electrostatic actuation properties. However, only the first equilibrium point, E_1, is stable because of the fact that the slope of the electrostatic force is smaller than the (constant) slope of the elastic force, whereas at point E_2 the slope of the electrostatic force is larger than the one of the elastic force.

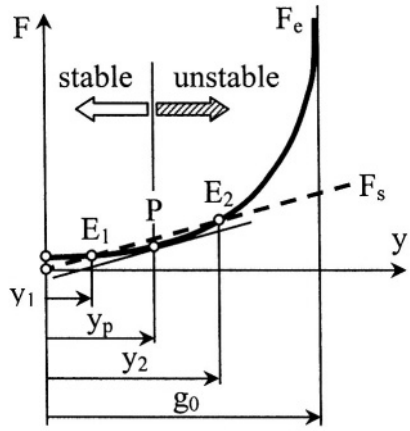

Figure 5.2 Electrostatic and spring forces versus displacement

It is known that an equilibrium point, one for which the total force, defined as:

$$F = F_e - F_s \tag{5.4}$$

is zero, has stable properties when the force derivative is negative, namely:

$$\partial F / \partial x < 0 \tag{5.5}$$

The limit point separating the stable region from the unstable one can be found by solving the equation system:

$$\begin{cases} F = 0 \\ \partial F / \partial x = 0 \end{cases} \tag{5.6}$$

where the total force F is determined by means of Eqs. (5.2), (5.3) and (5.4). By solving the equation system (5.6) in terms of position and corresponding voltage, the following solution is obtained:

$$\begin{cases} y_p = g_0 / 3 \\ U_p = 2\sqrt{6} / 9 \sqrt{K_y g_0^3 / (\varepsilon A)} \end{cases} \tag{5.7}$$

The force corresponding to this point can be found by substituting y_p of Eq. (5.7) into either Eq. (5.2) or Eq. (5.3), and its expression is:

$$F_p = 9\varepsilon A U^2 / (8 g_0^2) = K_y g_0 / 3 \qquad (5.8)$$

The values of y_p and F_p define the point P of Fig. 5.2, which characterizes the phenomenon known as *pull-in.* For forces less than F_p of Eq. (5.8), the slope of the electrostatic force is smaller than the one of the spring force (which is equivalent to saying that the slope of the total force F is less than zero) and the system is stable. When the forces are larger than F_p, the situation reverses and the slope of F is greater than zero, which means that the system becomes unstable. As a consequence, for displacements that are larger than one-third of the initial gap g_0, the mobile plate collapses (it is *pulled-in*) against the fixed one, irrespective of the microspring design. This also explains the reason why the equilibrium point E_1 is stable (it is positioned to the left of y_p), and the other equilibrium point E_2 is unstable.

The particular situation where Eqs. (5.7) and (5.8) are valid is pictured in Fig. 5.3. Compared to the generic case of Fig. 5.2, the actuation voltage U needs to be increased or the spring has to adequately be redesigned, in order for the spring force characteristic to be tangent to the electrostatic force characteristic, as shown in Fig. 5.3. By increasing the voltage for instance, the force-displacement curve representing the electrostatic actuation will translate upward until it becomes tangent to the spring characteristic.

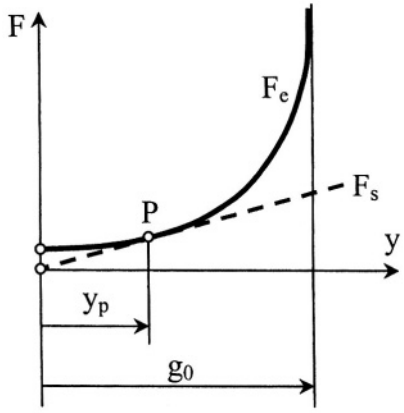

Figure 5.3 Single-point equilibrium in transverse electrostatic actuation and microspring

Example 5.1

A transverse electrostatic actuator is serially coupled to a spring of stiffness $K_y = 0.3$ N/m. Find the actuation voltage that will result in the stable equilibrium position being related to the pull-in position as: $y_1 = y_p/3$. Known are the following amounts: $g_0 = 5\ \mu$m, $A = 100\ \mu m^2$, $\epsilon = 8.8 \times 10^{-12}$ F/m.

Solution:

As previously shown, the conditions for stable static equilibrium are:

$$\begin{cases} F_e = F_s \\ \partial F_e / \partial x - \partial F_s / \partial x < 0 \end{cases} \tag{5.9}$$

The electrostatic force F_e and the spring force F_s are given in Eqs. (5.2) and (5.3), respectively. The value of the pull-in displacement y_p is also given in the second Eq. (5.7). By combining these equations with the relationship between y_1 and y_p, it is found that the voltage is U = 86.6 V.

2.2 Flexure-Spring Microdevices

Flexure-spring microdevices are used as acceleration sensors in automotive control systems of airbags, chassis or navigation monitoring. The simplest microaccelerometer consists of a flexure hinge and a tip mass, as pictured in Fig. 5.4 (a).

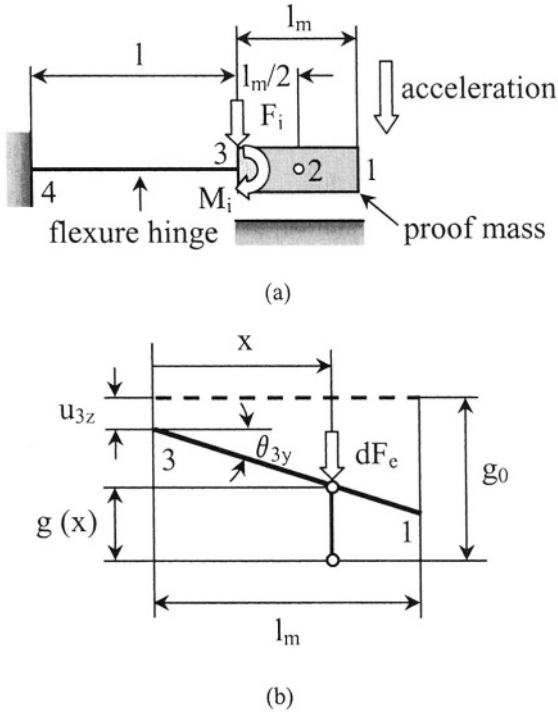

Figure 5.4 Flexure-hinge microaccelerometer: (a) side view with schematic configuration; (b) detail with displaced proof-mass

By assuming that the acceleration of the monitored system acts perpendicularly to the flexure-hinge microaccelerometer, it is possible to evaluate this acceleration by means of a measured amount, such as the deflection or the slope of the deformed flexure as shown next. It can be considered that the inertia force acts at point 2, the center of the proof mass – Fig. 5.4 (a), which means the flexure hinge is loaded at its tip 3 by the inertia force F_i and the moment M_i. The slope and deflection at point 3 can be found by using the compliance formulation of Chapter 2 as:

$$\begin{cases} \theta_{3y} = C_{uz-My} F_i + C_{\theta y-My} M_i \\ u_{3y} = C_{uz-Fz} F_i + C_{uz-My} M_i \end{cases} \tag{5.10}$$

where the compliances above define any of the flexure microhinges that have been analyzed in Chapter 2. The inertia force and moment are:

$$\begin{cases} F_i = ma \\ M_i = mal_m / 2 \end{cases} \tag{5.11}$$

The unknown acceleration a can be determined when either the slope or the deflection of Eqs. (5.10) can be measured directly (experimentally), namely:

$$a = u_{3z} / [\, m(C_{uz-Fz} + C_{uz-My} l_m / 2)] \tag{5.12}$$

or:

$$a = \theta_{3y} / [\, m(C_{uz-My} + C_{\theta y-My} l_m / 2)] \tag{5.13}$$

Example 5.2

Determine the external acceleration by means of a flexure-hinge microaccelerometer (as the one sketched in Fig. 5.4 (a)) whose gap is measured electrostatically.

Solution:

An elementary electrostatic force dF_e can be formulated that corresponds to a length dx (not shown in Fig. 5.4 (b)) and to the gap g(x). This force is:

$$dF_e = \varepsilon U^2 l_1 dx / [\, 2g(x)^2 \,] \tag{5.14}$$

The variable gap g(x), as shown in Fig. 5.4 (b), is:

$$g(x) = g_0 - u_{3z} - (l_m - x)\theta_{3y} \tag{5.15}$$

The total electrostatic force can be calculated by integrating Eq. (5.14) over the length l_m and by using Eqs. (5.10) and (5.11), namely:

$$F_e = 2\varepsilon U^2 l_1 l_m /\{[a(2C_{uz-Fz} + l_m C_{uz-My})m - 2g_0][a[2C_{uz-Fz} + l_m(3C_{uz-My} + l_m C_{\theta y-My})]m - 2g_0]\} \quad (5.16)$$

This electrostatic force is equal to the inertia force that is generated by the external acceleration and the mass of the proof mass, as given in the first Eq. (5.11). The acceleration a can be determined by solving the third-degree algebraic equation that results by equating Eq. (5.16) and the first Eq. (5.11).

2.3 Rotary Microdevices

Rotary actuation and sensing, together with appropriate suspensions, are used in microgyroscopes for instance that are utilized to detecting changes in the direction of rotation of navigational systems such as those implemented in cars. The rotary portion of a microgyroscope consists at its minimum of actuation, sensing and suspension. An example, similar to the one analyzed by Geiger et al. [1], is sketched in Fig. 5.5, where two pairs of rotary electrostatic actuators (connected in parallel) are disposed symmetrically to ensure balancing of the microdevice. Two similar sensing pairs (also in parallel connection) are disposed 90° with respect to the actuator units. The outer mobile hub and the inner fixed post are connected by means of a spiral spring.

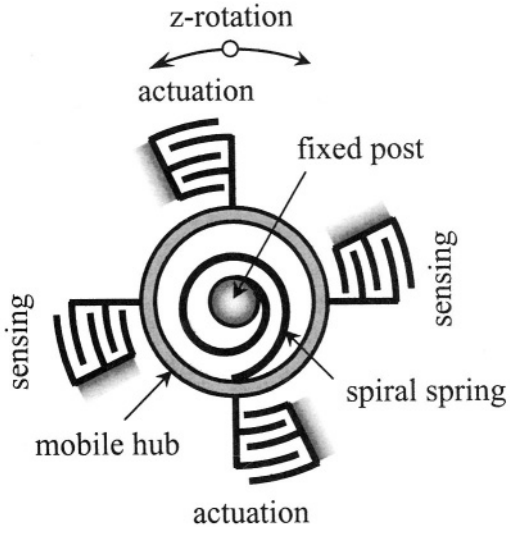

Figure 5.5 Rotary electrostatic transduction with spiral-spring microsuspension

Other suspension solutions, with several microsprings, such as those of Figs. 5.6 (a) and (b), are also possible.

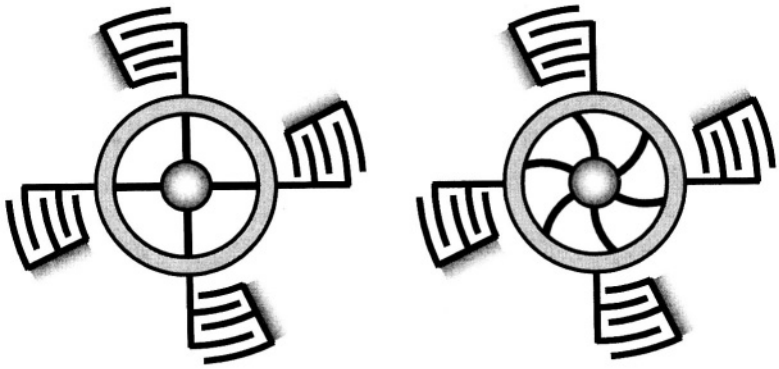

Figure 5.6 Rotary electrostatic transduction with: (a) straight-beam microsuspensions; (b) curved-beam microsuspensions

Application of a voltage differential between the fixed and mobile electrodes of the two actuation units generates a couple that will rotate the mobile hub. The maximum rotation angle under static actuation is given by the equilibrium between the actuation torque and the elastic restoring couple produced by the spiral spring. The two sensing units will detect the rotation angle as a change in capacitance, as shown in Chapter 4. Comparing the angle predicted by capacitance reading to the angle that results from the torque balance equation can give an insight on the actuation losses, as detailed in the following example.

Example 5.3

The microdevice pictured in Fig. 5.5 operates in an environment with $\epsilon = 8.8 \times 10^{-12}$ F/m and is actuated electrostatically by a voltage U = 80 V. The readout units indicate a capacitance variation of $\Delta C = 1.46 \times 10^{-14}$ F. Consider that each transduction unit is formed of n = 10 gaps and that $g_r = 3$ μm, $t_r = 5$ μm, $l_z = 5$ μm and $R_{min} = 300$ μm – see Fig. 4.29. The spiral microsuspension is defined by $r_1 = 100$ μm, $r_2 = 180$ μm, $\alpha_{max} = 420^o$ – see Fig. 3.43, $w = t = 5$ μm (the cross-sectional dimensions) and Young's modulus is 160 GPa. Find the relative error in the rotation angle between the model-predicted value and the actual value read by the sensing units.

Solution:

The torque equilibrium in the position of static balance requires that the electrostatic actuation torque be equal to the restoring torque produced by the spiral spring, namely:

$$M_e = M_s \tag{5.17}$$

where the actuation torque M_e is twice the value determined in Eq. (4.47) of Chapter 4 (there are two parallel actuators in Fig. 5.5). The elastic torque can be expressed as:

$$M_s = \Delta\alpha / C_{\theta z - Mz} \tag{5.18}$$

where $\Delta\alpha$ is the rotation angle of the mobile hub and $C_{\theta z\text{-}Mz}$ is the rotation compliance of the spiral spring, which has been defined in Eq. (3.137) of Chapter 3 for thin spiral springs. Equation (5.18) uses the simplifying assumption that the rotation compliance is simply the inverse of the corresponding stiffness.

By combining Eqs. (5.17), (5.18), (4.47) and (3.137) together with the numerical data of this example, the predicted value of the rotation angle is found to be $\Delta\alpha = 4.84^o$. The capacitance change, as provided by the two sensing units, relates to the actual rotation angle according to Eq. (4.49) of Chapter 4 (the total capacitance variation is twice the value given by Eq. (4.49) because there are two sensing units in parallel) and a value of $\Delta\alpha' = 3.9^o$ results from the measurement. The relative (percentage) error between the model and actual rotation angles is therefore equal to $100\ (\Delta\alpha - \Delta\alpha') / \Delta\alpha = 19.4\ \%$.

3. TWO-SPRING MEMS

Two springs can be coupled either in series or in parallel and the resulting stiffness is found as a combination of the individual springs' stiffnesses. Figure 5.7 illustrates the models that give the equivalent stiffness for spring parallel/serial connection.

The equivalent parallel and series stiffnesses, as well-known from elementary mechanics, are calculated as:

$$\begin{cases} K_p = K_1 + K_2 \\ 1/K_s = 1/K_1 + 1/K_2 \end{cases} \tag{5.19}$$

Equations (5.19) are specified for linear springs, but they are also valid for rotary springs, which can similarly be coupled either in series or parallel. The same equations can be extrapolated in design cases where more than two microsprings are connected in parallel/series.

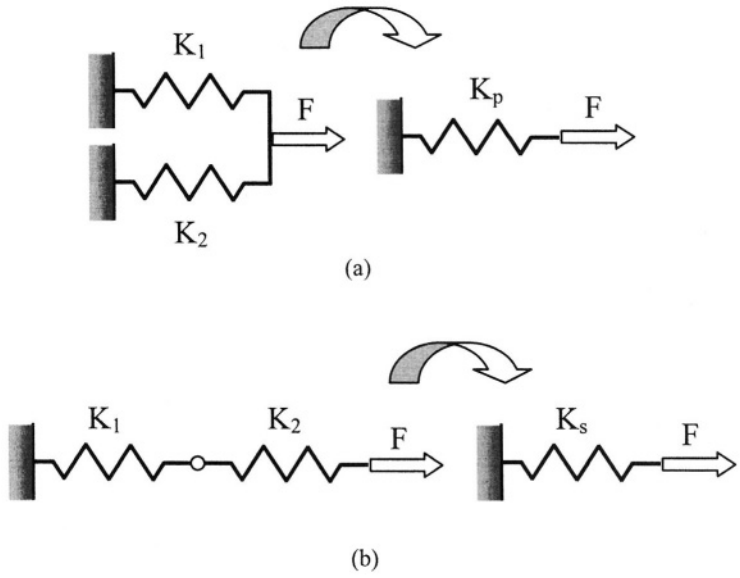

Figure 5.7 Two-spring connection: (a) Parallel; (b) Serial

3.1 Flexure-Spring Microdevices

The model of a MEMS comprising a mass physically supported by two suspensions that enable linear motion about an out-of-the-plane axis z, is sketched in Fig. 5.8 (a).

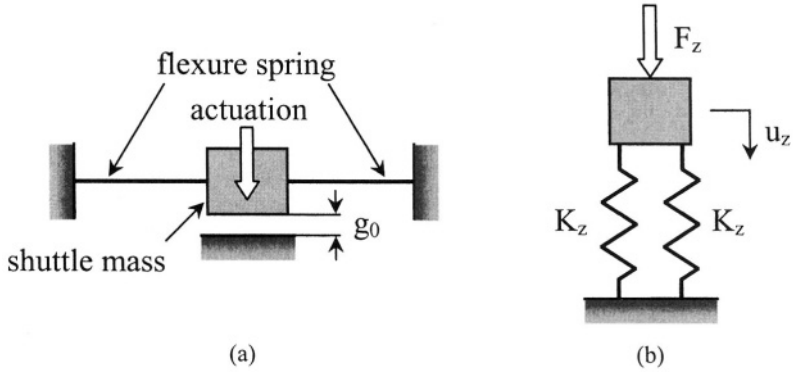

Figure 5.8 MEMS with two flexure springs in parallel: (a) Configuration; (b) Equivalent spring model

The device of Fig. 5.8 (a) can be used as an electrical switch or a microaccelerometer for instance. The middle link (shuttle mass for microaccelerometers) will displace about the z-direction through either

actuation when it will touch another fixed component and close an electrical circuit (in a microswitch application) or through inertial acceleration (in a microaccelerometer). Figure 5.8 (b) shows the equivalent spring model of the MEMS design of Fig. 5.8 (a). The static response of this system is characterized by the equation:

$$u_z = F_z /(2K_z) \tag{5.20}$$

Example 5.4

Find the minimum actuation voltage that will move the central link a distance $y = g_0/4$ (where $g_0 = 2$ μm) in an electrical microswitch with two identical flexure hinges, as the one sketched in Fig. 5.8 (a). Young's modulus is E = 160 GPa, the electrical permittivity is $\varepsilon = 8.5 \times 10^{-12}$ F/m and the actuation area is $A = 100 \times 10^{-12}$ m^2.

(a) The flexure hinges are 100 μm long and have constant rectangular cross-section with w = t = 1 μm.

(b) The flexure hinges are right circularly-filleted with r = 1 and w = t = 1 μm

Solution:

In both cases, the actuation voltage can be found by solving Eq. (5.20) after substituting the electrostatic actuation force of Eq. (5.2).

(a) For the constant cross-section flexure hinge, the stiffness is $12EI_y/l^3$ and therefore a voltage of U = 29.1 V is obtained by solving Eq. (5.20).

(b) For the right circularly-filleted flexure hinge, as the one shown in Fig. 2.14, Chapter 2, the K_z stiffness is found by inverting the symmetric compliance matrix which is formed of $C_{l,uz\text{-}Fz}$, $C_{l,uz\text{-}Fy}$ and $C_{l,\theta y\text{-}My}$ of Eqs. (2.72), (2.73) and (2.74), respectively. By using again Eq. (5.20), the voltage corresponding to this design is U = 98.16 V.

3.2 Other Linear-Motion Microdevices

Several examples of two-spring linear-motion microdevices are presented next. One class of linear-motion MEMS comprises microdevices whose linear motion takes place in an x-y plane, as shown in Fig. 5.9 (a). Adding to the active planar motion, the effects of gravity about the z-direction (which is perpendicular to the x-y plane) might play an important, although undesired, role.

In addition to the spring-type stiffness of the two suspensions about the x-axis, the self weight of the central mass solicits the flexibility of the same suspensions about the out-of-the-plane z-axis, as indicated in Fig 5.9 (b). Various suspensions have been studied in Chapter 3 and their stiffnesses about both the x- and z-axes have explicitly been given.

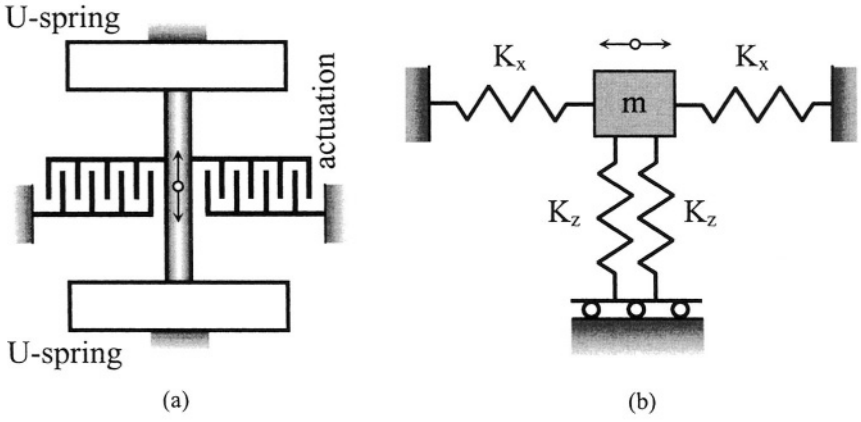

Figure 5.9 (a) Top view of a two-spring linear-motion microdevice; (b) Rotated side view of model with mass and two suspensions

Through actuation about the x-direction, the central rigid link will move to the right for instance, as shown in Fig. 5.10, and will generate reaction forces by the stiffnesses opposing the motion. The midpoint P will move to a position P' in the x-z plane under the combined action of the actuation force F_a, elastic forces F_{e1}, F_{e2} and F_{e3} and gravity G. While the actuation force can be generated by a variety of means, as described in the previous chapter, the elastic forces are calculated as:

$$\begin{cases} F_{e1} = K_x \Delta x_1 \\ F_{e2} = K_x \Delta x_2 \\ F_{e3} = 2K_z \Delta z \end{cases} \tag{5.21}$$

where Δx_1, Δx_2 and Δz represent the deformations of the left, right and vertical spring, respectively. The elastic force about the z-direction took into account that two springs are connected in parallel.

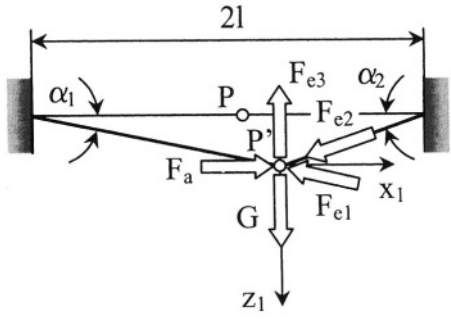

Figure 5.10 Model for mass and two suspensions with stiffness about the x and z directions

Equilibrium about the local x_1 and z_1 axes results in the equations:

$$\begin{cases} F_a = F_{e1}\cos\alpha_1 + F_{e2}\cos\alpha_2 \\ G + F_{e2}\sin\alpha_2 = F_{e1}\sin\alpha_1 + F_{e3} \end{cases} \tag{5.22}$$

and the motion of the midpoint P to the final position P' is expressed by means of the equation:

$$\begin{cases} (l + \Delta x_1)\cos\alpha_1 + (l - \Delta x_2)\cos\alpha_2 = 2l \\ (l + \Delta x_1)\sin\alpha_1 = (l - \Delta x_2)\sin\alpha_2 \approx \Delta z \end{cases} \tag{5.23}$$

By using the following small-displacement assumptions:

$$\begin{cases} \sin\alpha_1 \approx \alpha_1 \\ \sin\alpha \approx \alpha_2 \\ \cos\alpha_1 \approx \cos\alpha_2 \approx 1 \end{cases} \tag{5.24}$$

the solution to Eqs. (5.22) and (5.23) gives:

$$\alpha_1 = mgK_x(F_a - 2K_x l)/[F_a^2(K_x + K_z) - 4K_x^2 K_z l^2] \tag{5.25}$$

$$\Delta x_1 \approx \Delta x_2 = F_a/(2K_x) \tag{5.26}$$

These amounts enable calculation of the final position (point P') as:

$$\begin{cases} \Delta x = (l + \Delta x_1)\cos\alpha_1 - l \approx \Delta x_1 \\ \Delta z = (l + \Delta x_1)\sin\alpha_1 \approx (l + \Delta x_1)\alpha_1 \end{cases} \tag{5.27}$$

where Δx and Δz are the displacements of the midpoint P after application of the actuation force F_a.

Example 5.5

Evaluate the errors that correspond to ignoring the suspensions' stiffness about the z-direction in a two-suspension MEM. Determine the actuation force which is necessary to make this error zero.

Solution:

In the case where $K_z = 0$, Eq. (5.25) becomes:

$$\alpha_1' = mg(F_a - 2K_x l)/F_a^2 \tag{5.28}$$

whereas Eq. (5.26) remains unchanged. It can be seen that there is a non-zero out-of-the-plane motion about the z-direction because the second Eq. (5.27) in combination with Eq. (5.28) give a non-zero value of Δz. The following relative error is introduced:

$$e_z = (\Delta z - \Delta z')/\Delta z \tag{5.29}$$

when $\Delta z'$ is calculated by means of the second Eqs. (5.27) and (5.28). This error reduces to:

$$e_z = (\alpha_1 - \alpha_1')/\alpha_1 = K_z(4k_x l^2/F_a^2 - 1/K_x) \tag{5.30}$$

As Eq. (5.30) shows, the error is dependent on both the device characteristics, such as stiffnesses and geometry, and the actuation force. The errors are zero when:

$$F_a = 2l\sqrt{K_x K_z} \tag{5.31}$$

Example 5.6

Consider the case where, due to imperfections, the actuation force makes a small angle α with the horizontal direction, in the x-z plane of Fig. 5.10. Evaluate the errors introduced by this imperfection.

Solution:

According to Fig. 5.10, the angle formed by the left segment with the horizontal direction is in this case:

$$\alpha_1' = K_x(\alpha F_a + mg)(F_a - 2K_x l)/[F_a^2(K_x + K_z) - 4K_x^2 K_z l^2] \tag{5.32}$$

and the horizontal projections of the two springs' deformations are given by Eq. (5.26) under the assumptions of small-displacements. By combining Eqs. (5.25) and (5.32), results in the following error function, defined in Eq. (5.29):

$$e_z = \alpha F_a/(mg) \tag{5.33}$$

Equation (5.33) indicates that for the linearized, small-displacement case, the error in the z-displacement varies linearly with the inclination angle of the actuation force, and obviously, the error is zero when the angle of the actuation force is zero.

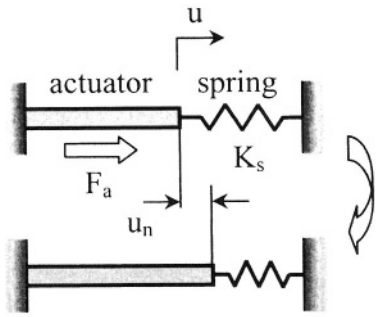

Figure 5.11 Linear actuator working against spring

In many situations, linear actuators, such as thermal, work against one or several springs that are designed to oppose the generated force/motion. An example is sketched in Fig. 5.11, where a bar functions as an actuator as it expands through thermal heating. Coupled to the thermal bar is a spring of stiffness K_s. Application of a certain temperature increase will displace the actuator-spring connection point to the right by a quantity u_n, as sketched in the figure. This position is the result of the force equilibrium between the actuation force (given generically in Chapter 4 in Eq. (4.7)) and the elastic force developed in the spring, namely:

$$F_b - (F_b / u_0) u_n = K_s u_n \tag{5.34}$$

As discussed in Chapter 4, F_b is the bloc force and u_0 the free displacement of the actuator. The solution to Eq. (5.34) is:

$$u_n = 1/(K_s / F_b + 1/u_0) \tag{5.35}$$

The two characteristics, of the actuator and of the spring, are plotted in Fig. 5.12, and their intersection gives the value u_n of Eq. (5.35).

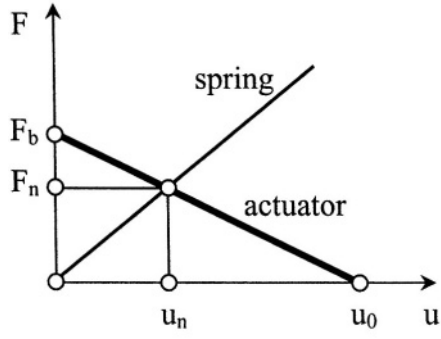

Figure 5.12 Force-displacement characteristics of linear actuator and spring working in series

As the figure indicates, the force F_n corresponding to the *nominal* displacement/deformation u_n can be determined from either the actuator or spring characteristic, as also shown in Eq. (5.34).

Example 5.7

In an optical chopper, as the one sketched in Fig. 5.13, the light coming perpendicularly to a plane can access through slots cut in a mobile plate and trigger a 1-0 type signal. The microdevice is actuated thermally by the two inclined beams at its left. Find the minimum temperature which is necessary to displace the plate by the quantity $p = 0.1\ \mu m$. The inclined beams are defined by: $l = 150\ \mu m$, $w = 3\ \mu m$, $t = 3\ \mu m$, $\alpha = 2^o$ and $E = 150 \times 10^9$ N/m^2.The linear thermal expansion coefficient is $\alpha = 2.6 \times 10^{-6}\ 1/^o$. Ignore the weight of the plate.

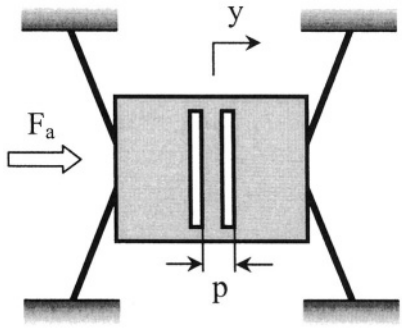

Figure 5.13 Optical chopper design with four bent beams (two can be actuators)

Solution:

The bloc force F_b and free displacement u_0 have been determined in Chapter 4, Eqs. (4.9) and (4.8), for a bent beam thermal actuator, which means that the actuation characteristic of Fig. 5.12 is determined. At the same time, the stiffness of each of the inclined-beam springs are known – given in Eq. (3.18) of Chapter 3. As a consequence, the nominal point of operation is determined, as given by Eqs. (5.34) and (5.35). The equivalent of the four inclined beams is a spring having four times the stiffness of a single beam, and therefore Eq. (5.35) can be written as:

$$p = 1/(4K_y / F_b / + 1/u_0) \tag{5.36}$$

where it has been considered that the displacement corresponding to the nominal operation point u_n should be equal to the required pitch displacement p, and the stiffness K_y is given in Eq. (3.18). It can be seen that the bloc force and free displacement can be put into the following form:

$$\begin{cases} F_b = f_b \Delta T \\ u_0 = f_0 \Delta T \end{cases} \tag{5.37}$$

where:

$$\begin{cases} f_b = 3\alpha E A^2 I_z l^2 \sin\beta / [(12 I_z \cos^2\beta + A l^2 \sin^2\beta)(A l^2 \cos^2\beta \\ + 3 I_z \sin^2\beta)] \\ f_0 = A\alpha l^3 \sin\beta / (12 I_z \cos^2\beta + A l^2 \sin^2\beta) \end{cases} \tag{5.38}$$

Solution of Eq. (5.36), via Eqs. (5.37), gives the following value of the temperature increase ΔT (which is embedded in both F_b and u_0):

$$\Delta T = p(1/f_0 + 4K_y / f_b) \tag{5.39}$$

With the numerical values of this example, the temperature increment has a value of $\Delta T = 779.78\ ^{\circ}C$.

Example 5.8

A two bent beam thermal actuator, as the one sketched in Fig. 5.14 (a), of specified geometry and material properties, has to be evaluated. Its output displacement is determined optically, whereas the output force is measured indirectly by means of the fixed-free constant cross-section beam, which is positioned as shown in the same figure. Determine the Young's modulus of the microdevice, as well as the output force. The geometry of the bent beam is: $l = 100\ \mu m$, $w = t = 3\ \mu m$, $\beta = 2^{\circ}$; the geometry of the test beam is: $l_1 = 55\ \mu m$, $w_1 = t_1 = 0.8\ \mu m$, the coefficient of thermal expansion is $\alpha = 2.59 \times 10^{-6}\ 1/^{\circ}$ and the temperature increase is $\Delta T = 234^{\circ}$.

Solution:

According to the spring model of Fig. 5.14 (b), the force equilibrium equation is:

$$F_a = (2K_{bb} + K_b)u_n \tag{5.40}$$

where the subscript *bb* denotes the bent beam and the subscript *b* stands for the beam dedicated to measuring the actuation force. The thermal actuation force is determined by means of the bloc force and the free displacement, according to Eqs. (4.9) and (4.8) in Chapter 4. Also the stiffness of one bent beam is known – Eq. (3.18) in Chapter 3. The stiffness of the test beam is simply:

$$K_b = 12EI_{1z} / l_1^3 \tag{5.41}$$

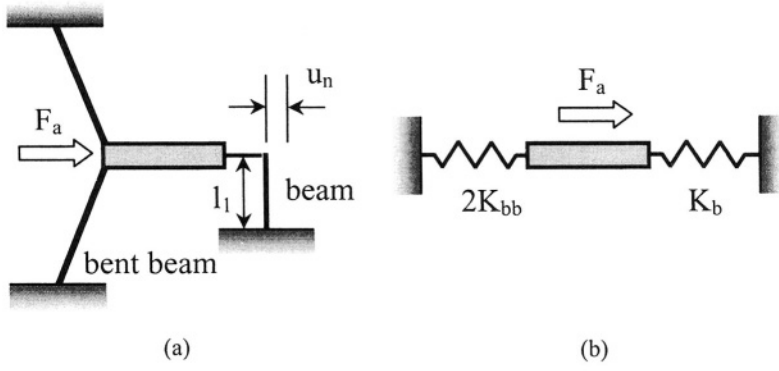

Figure 5.14 Bent beam thermal actuator: (a) microdevice with force beam; (b) equivalent actuation model with springs

As a consequence, the force exerted on the beam by the thermal actuator is:

$$F_b = K_b u_n \tag{5.42}$$

By substituting F_a, K_{bb} (from Chapters 4 and 3, as mentioned) and K_b of Eq. (5.41) into Eq. (5.40), the unknown Young's modulus is E = 347 GPa and the force on the beam is $F_b = 0.8\ \mu N$, according to Eq. (5.42).

Example 5.9

Determine the displacement of the linear micromotor sketched in Fig. 5.15. The actuation is provided by two identical two-beam units (as described in Fig. 4.14, Chapter 4) and additional suspension is added into the system by the two end beams. The beams and the compliant parts of the actuators have identical cross-sections ($w = 2\ \mu m$, $t = 2\ \mu m$). Known is the geometry of the microsystem ($l_1 = 200\ \mu m$, $l_2 = 20\ \mu m$, $l_3 = 140\ \mu m$, $l_5 = 100\ \mu m$), as well as the material properties (E = 150 GPa, $\alpha = 2 \times 10^{-6}\ 1/^{o}$) and the temperature increase ($\Delta T = 200^{o}$).

Solution:

This example is conceptually similar to the previous one, in the sense that two actuators are placed in parallel to increase the amount of horizontal force and to produce a horizontal motion, because of the symmetry. As a result of this similitude, the equation of static equilibrium between the actuation force and the elastic restoring forces of the two beams is:

$$2F_a = 2K_b u_n \tag{5.43}$$

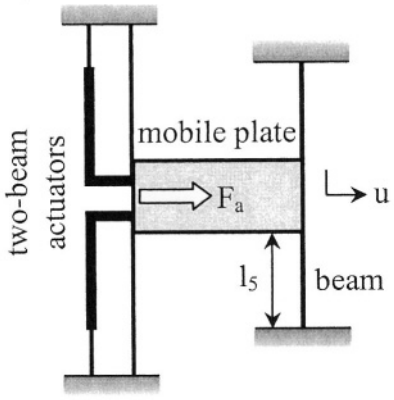

Figure 5.15 Two-beam thermal actuator with beam springs

where the 2 multiplier indicates there are two actuators and two restoring springs. The actuation force for a two-beam thermal device was given in Eqs. (5.34) as a function of the free displacement u_0 and bloc force F_b, which are given in Eqs. (4.14) and (4.15) of Chapter 4 for the two-beam actuator. The stiffness of a fixed-guided beam is:

$$K_b = 12EI_z / l_5^3 \tag{5.44}$$

Therefore, by solving for the output displacement in Eq. (5.43) gives u_n = 0.52 μm.

3.3 Torsion-Spring Microdevices

When a central mass is supported by two springs on the sides and the actuation creates a torque about the hinge longitudinal axis, as shown in Fig. 5.16, the equilibrium equation corresponding to this situation gives the rotation angle resulting from the interplay between actuation and the elastic properties of the two hinges:

$$\theta = M_a /(2K_t) \tag{5.45}$$

One common application of the microdevice of Fig. 5.16 is the so-called *torsion micromirror,* which is sketched in Fig. 5.17 (a). As shown in Figs. 5.17 (a) and (b), a central plate is supported by two torsion hinges. Electrostatic actuation by the plate of dimensions l_1 and l_2 will attract the

central plate and, due to the eccentric nature of these forces, the central plate will rotate with respect to the hinge longitudinal axis.

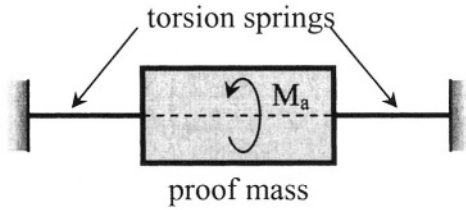

Figure 5.16 Model for mass and two suspensions with torsion loading

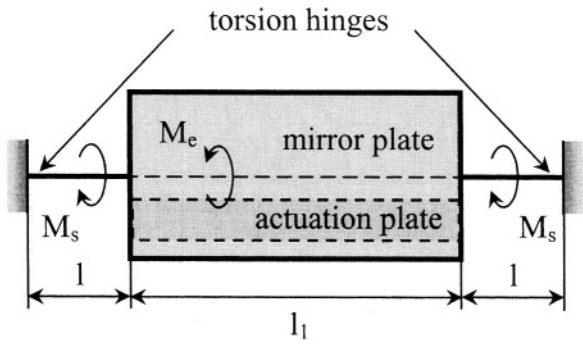

(a)

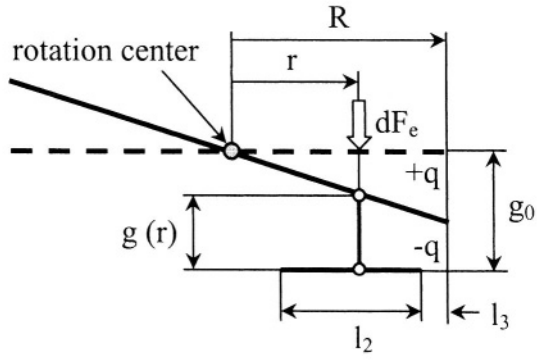

(b)

Figure 5.17 Torsion micromirror. (a) Top view schematic; (b) Detail with rotated plate

When the two torques are in equilibrium, the angle of rotation can be found by means of Eq. (5.45). Another important aspect is the pull-in phenomenon, which has been discussed in this chapter and which defines the

stable operation point. Both aspects will be studied next. A similar analysis is given by Sattler et al. [2] for the particular case where $l_3 = 0$ and $l_2 = R$ (width of the actuation plate is equal to half-width R of the mirror plate).

Figure 5.17 (b) shows the central plate in a rotated position. An elementary electrostatic force dF_e acts on the mobile central (mirror) plate over a length dr (not drawn in Fig. 5.17 (b)), namely:

$$dF_e = \varepsilon U^2 l_1 dr / [2g(r)^2] \tag{5.46}$$

where, under the small-displacement modeling assumption, the variable gap g(r) depends on the initial gap g_0 and the rotation angle θ as:

$$g(r) = g_0 - r\theta \tag{5.47}$$

This force produces an elementary active torque:

$$dM_e = rdF_e \tag{5.48}$$

The total active (electrostatic) torque is the sum of all the elementary torques of Eq. (5.48), and is determined by integration between the limits $R - (l_2 + l_3)$ and $R - l_3$ as:

$$M_e = \varepsilon l_1 U^2 \{ln[(R - l_3)\theta - g_0] / (R - (l_2 + l_3))\theta - g_0] + g_0 l_2 \theta / \{[(R - l_3)\theta - g_0][(R - (l_2 + l_3))\theta - g_0]\}\} / (2\theta^2) \tag{5.49}$$

Equation (5.49) gives the actuation moment that is produced under conditions of *voltage control.* Another possibility is to control the electrostatic model by means of charge, the so-called *charge-control* problem. The elementary charge corresponding to the area determined by l_1 and dr is:

$$dq = \varepsilon E dA = \varepsilon U l_1 dr / g(r) \tag{5.50}$$

The total charge q can be found by integrating Eq. (5.50) between the limits $R - (l_2 + l_3)$ and $R - l_3$. The voltage U can be expressed in terms of capacitance C and charge q as:

$$U = q / C \tag{5.51}$$

and therefore the charge-control actuation equation – the counterpart of the voltage control Eq. (5.49) – is:

$$M_e = q^2\{ln[((R-l_3)\theta - g_0)/(R-(l_2+l_3))\theta - g_0] + g_0 l_2\theta / \{[(R-l_3)\theta - g_0][(R-(l_2+l_3))\theta - g_0]\}\}/\{2\varepsilon l_1 ln^2[(R-l_3)\theta - g_0]/[(R-(l_2+l_3))\theta - g_0]\} \quad (5.52)$$

Equations (5.49) and (5.52) reduce to the equations of Sattler et al. [2], who treated the particular case where $l_3 = 0$ and $l_2 = R$.

As mentioned previously, the active moment of either Eq. (5.49) or Eq. (5.52) is opposed by the elastic spring moment produced through torsion of the two supporting hinges. The spring moment is:

$$M_s = 2K_t\theta \quad (5.53)$$

where K_t is the torsional stiffness of a hinge. At equilibrium, M_e and M_s should balance each other, and the point of stable equilibrium, as discussed for a single-spring microsystem, can be found by solving the equilibrium equations:

$$\begin{cases} M = 0 \\ dM/d\theta = 0 \end{cases} \quad (5.54)$$

where:

$$M = M_e - M_s \quad (5.55)$$

The solution to Eqs. (5.54) is the set (θ_p, U_p), for the voltage-control problem, or the set (θ_p, q_p), for the charge-control problem (the p subscript denotes *pull-in,* as mentioned previously).

Example 5.10

The torsion microdevice of Fig. 5.18 is used to determine the magnitude of an electromagnetic field B which acts in the plane of the middle sensing plate and of the two identical circular corner-filleted microhinges. The rotation angle of the plate is determined experimentally to be 3° when a current I = 20 mA passes through the circular loop of radius R = 80 μm. The shear modulus of the hinges is G = 56.7 GPa and the hinges are defined by l = 100 μm, r = 1/8, t = 0.8 μm and w = 6 μm. Find the external magnetic disturbance B.

Solution:

The torque M that is produced by the interaction between the current I and the external magnetic field B is given in Eq. (4.65) of Chapter 4. This torque rotates the microdevice of Fig. 5.18 by an angle θ according to Eq.

(5.45). The torsional stiffness of a circular corner-filleted microhinge is defined in Eq. (2.121) of Chapter 2. With these particular conditions, the solution becomes B = 0.448 T.

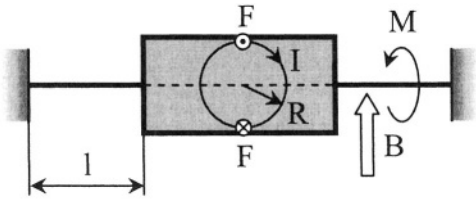

Figure 5.18 Electromagnetic sensor with torsional microhinges

4. MULTI-SPRING MEMS

MEMS such as accelerometers, bridges or filters need be designed with more than two spring microsuspension in order to stabilize/prevent motion about specified directions. Figure 5.19 (a) for instance is the sketch of a microaccelerometer that can sense the motion about the direction perpendicular to the plane of the circular proof mass by means of three flexure hinges. Similarly, Fig, 5.19 (b) shows a proof mass that is supported by four identical springs (microhinges). The out-of-the-plane motion, as well as the planar motion, both indicated in the figure, are possible for this configuration.

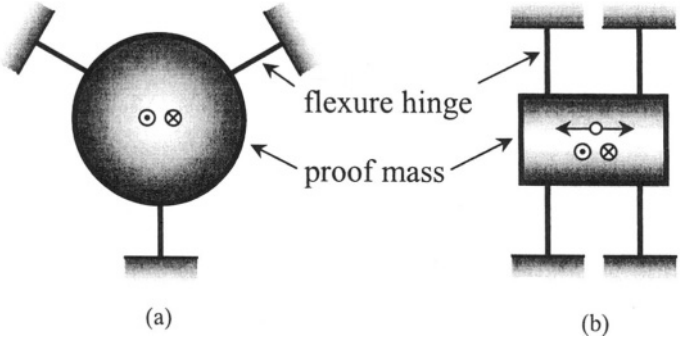

Figure 5.19 Multi-spring MEMS: (a) Three-spring design; (b) Four-spring design

The out-of-the-plane z-displacement at the center of the disc shown in Fig. 5.19 (a) can be calculated as:

$$u_z = F_z /(3K_z) \tag{5.56}$$

whereas the similar motion of the microdevice of Fig. 5.19 (b) is:

$$u_z = F_z /(4K_z) \tag{5.57}$$

Similarly, the linear motion of the proof mass of Fig. 5.19 (b) about an in-plane direction x is:

$$u_x = F_x /(4K_x) \tag{5.58}$$

Example 5.11

Compare the sensitivities of the two microaccelerometers shown in Fig. 5.19 (a) and (b) by considering they have identical proof masses and flexure hinges.

Solution:

The sensitivity of an accelerometer can be defined as the ratio of displacement to the (inertial) force, namely:

$$s = u / F \tag{5.59}$$

By way of Eqs. (5.56) and (5.57) it follows that the sensitivities of the two microaccelerometers relate as:

$$s_a / s_b = 4/3 \cong 1.33 \tag{5.60}$$

which indicates that the three-flexure microaccelerometer is approximately 33% more sensitive than its four-flexure counterpart.

5. DISPLACEMENT-AMPLIFICATION MICRODEVICES

This section discusses lever-based and sagittal displacement-amplification microdevices by analyzing their performance criteria, the most important being the displacement amplification ratio.

5.1 Lever-based Displacement-Amplification Microdevices

Displacement-amplification microdevices are designed based on the principle illustrated in Fig. 5.20. The actuation force F works against the torsional spring of stiffness K_t and produces the rotation angle α which is, according to the moment balance, equal to:

$$\alpha = Fl_1 / K_t \tag{5.61}$$

The horizontal displacement of the tip point 1, which moves to 1' – as shown in Fig. 5.20, is:

$$u_{1y} = l \sin\alpha \tag{5.62}$$

whereas the vertical displacement of the same point is:

$$u_{1x} = (1 - \cos\alpha)l \tag{5.63}$$

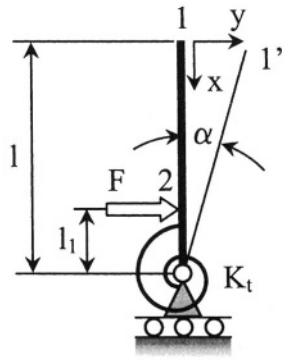

Figure 5.20 Lever-based displacement amplification

At the same time, the displacement of the point 2, where the force F is applied, is:

$$u_{2y} = l_1 \sin\alpha \tag{5.64}$$

and therefore the *displacement amplification,* also called *mechanical advantage,* can be calculated as:

$$a = u_{1y} / u_{2y} = l / l_1 \tag{5.65}$$

Rotation joints, of the type sketched in Fig. 5.20, are rarely produced in MEMS. A more convenient and often-applied solution is to utilize a flexure hinge instead of a classical rotation joint, as discussed in Chapter 2.

Although the motion produced by a flexure hinge is not a pure rotation and is also limited by the bending deformation capability of the flexure, many MEMS designs implement it, especially due to its structural simplicity and ease of microfabrication. Figure 5.21 shows two designs, which are the flexure-based replicas of the lever of Fig. 5.20. The length of the flexure is l_f and its cross-section, generally rectangular, may be constant, or variable.

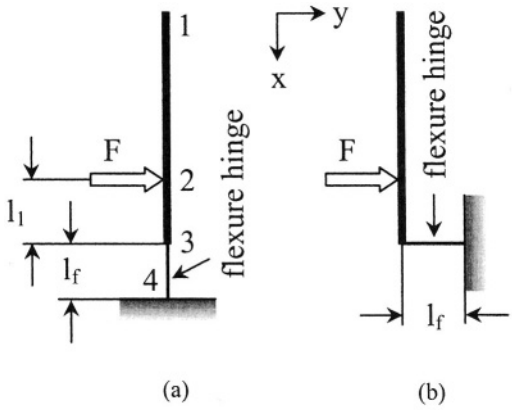

Figure 5.21 Lever-based displacement amplification with flexure hinge: (a) flexure parallel to lever; (b) flexure perpendicular to lever

As detailed in Chapter 1, the rotation angle (slope) and horizontal displacement at point 3 (the tip of the flexure hinge) of the design in Fig. 5.21 (a) can be found when the compliances of the flexure are known in the form:

$$\begin{cases} \theta_{3z} = C_{3,uy-Mz}F + C_{3,\theta z-Mz}Fl_1 \\ u_{3y} = C_{3,uy-Fy}F + C_{3,uy-Mz}Fl_1 \end{cases} \tag{5.66}$$

The rigid lever is tangent to the deformed flexure hinge at the junction point 3, and therefore the position of the lever's free tip can be calculated as:

$$\begin{cases} u_{1y} = u_{3y} + l\sin\theta_{3z} \\ u_{1x} = (1-\cos\theta_{3z})l \end{cases} \tag{5.67}$$

Similarly, the displacement at point 2 about the force direction can be calculated as:

$$u_{2y} = u_{3y} + l_1\sin\theta_{3z} \tag{5.68}$$

such that the displacement amplification becomes:

$$a = u_{1y}/u_{2y} = (u_{3y} + l\sin\theta_{3z})/(u_{3y} + l_1\sin\theta_{3z}) \tag{5.69}$$

For the amplification scheme of Fig. 5.21 (b), point 3 will move due to bending and axial deformations as follows:

$$\begin{cases} u_{3x} = -C_{3,uy-Mz} F l_1 \\ u_{3y} = C_{3,ux-Fx} F \\ \theta_{3z} = C_{3,\theta z-Mz} F l_1 \end{cases} \tag{5.70}$$

The horizontal displacements u_{1y} and u_{2y}, as well as the displacement amplification a are given by Eqs. (5.67), (5.68) and (5.69), respectively. The vertical displacement of point 1 in Fig. 5.21 (b) is:

$$u_{1x} = u_{3x} + (1 - \cos\theta_{3z})l \tag{5.71}$$

Example 5.12

Assess the errors that appear in the amplification produced by the microdevice of Fig. 5.21 (b) when neglecting the axial deformation of the flexure hinge. Consider that the flexure has a constant rectangular cross-section and that $l = 200\ \mu m$ and $l_1 = 15\ \mu m$.

Solution:

When the axial deformation is accounted for, in addition to the bending-produced deformation, the horizontal displacement at point 3 can be calculated by means of Castigliano's displacement theorem as:

$$u_{3y} = F(I_z + Al_1^2)l_f / (EAI_z) \tag{5.72}$$

and the slope at the flexure's tip is:

$$\theta_{3z} = Fl_1 l_f / (EI_z) \tag{5.73}$$

For small displacements, the horizontal motions at points 1 and 2 can be approximated as:

$$\begin{cases} u_{1y} = u_{3y} + l\theta_{3z} \\ u_{2y} = u_{3y} + l_1\theta_{3z} \end{cases} \tag{5.74}$$

and the corresponding displacement amplification becomes:

$$a = u_{1y} / u_{2y} = [I_z + Al_1(l + l_1)] / (I_z + 2Al_1^2) \tag{5.75}$$

By following a similar approach, the amplification for the case where the axial deformations are neglected is:

$$a' = (l + l_1)/(2l_1) \tag{5.76}$$

The relative error between the amplifications given in Eq. (5.76) versus Eq. (5.75) can be expressed as:

$$e = (a' - a)/a = (l - l_1)w^2/\{2l_1[12l_1(l + l_1) + w^2]\} \tag{5.77}$$

and Fig. 5.22 is a plot showing this error as a function of the flexure's cross-sectional width.

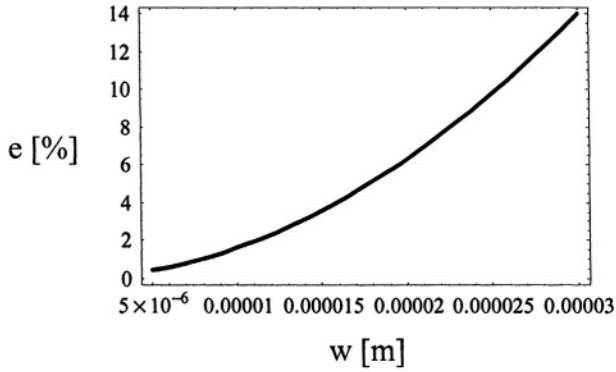

Figure 5.22 Relative errors in the amplification of the microdevice of Fig. 5.21 (b) when axial and bending deformation are considered versus the case when only bending deformation is accounted for

Example 5.13

Compare the final positions of the two amplification devices shown in Figs. 5.21 (a) and (b) when the flexure hinge has constant square cross-section. Consider that F = 10 μN, t = 2 μm, l = 200 μm and E = 160 GPa. Also compare the amplifications produced by the two devices.

Solution:

The needed compliances are:

$$\begin{cases} C_{3,uy-Fy} = 4l_f^3/(Et^4) \\ C_{3,\theta z-Fy} = 6l_f^2/(Et^4) \\ C_{3,\theta z-Mz} = 12l_f/(Et^4) \end{cases} \tag{5.78}$$

The notation of the compliances in Eqs. (5.78) corresponds to the local frame of the flexure, where the y-axis is perpendicular to the flexure's longitudinal axis. By using Eqs. (5.78), in combination to Eqs. (5.66) through (5.71), the displacements of point 1 in the two configurations of Figs. 5.21 (a) and (b) can be determined. If the following substitution is used:

$$\begin{cases} l_1 = c_1 l \\ l_f = c_2 l \end{cases} \tag{5.79}$$

the ratio of the displacements u_{1y} is plotted in Fig. 5.23.

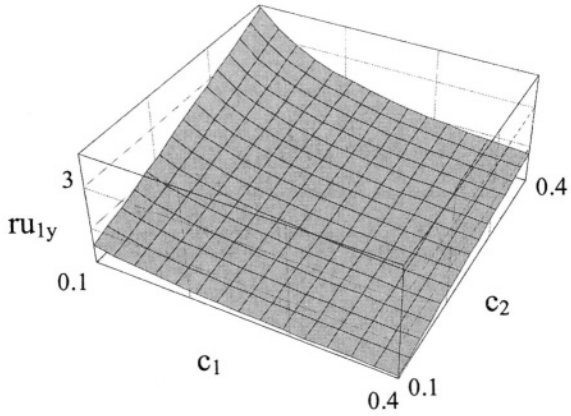

Figure 5.23 Ratio of horizontal displacements for point 1: Fig 5.21 (a) versus Fig. 5.21 (b)

The ratio is larger than 1 for smaller values of c_1 and larger values of c_2, which means when the force F acts closer to the flexure hinge and when the length of the flexure hinge is larger.

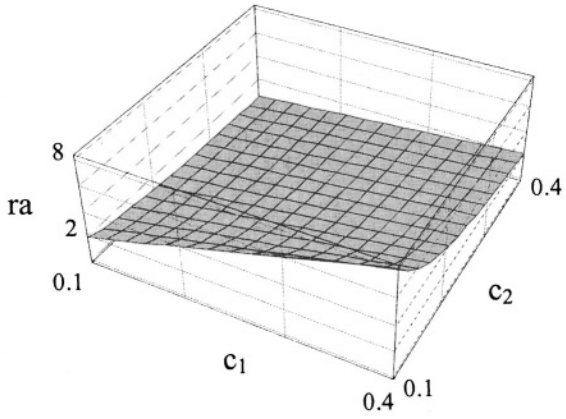

Figure 5.24 Amplification ratio: Fig 5.21 (a) versus in Fig. 5.21 (b)

The amplifications of the two mechanisms are calculated by means of the corresponding equations, and a comparison between the two amplifications is performed through the two device's amplification ratio, as shown in Fig. 5.24. The amplification of the mechanism in Fig. 5.21 (a) is larger than the one produced by the mechanism in Fig. 5.21 (b) for the set of numerical values of this problem, as shown in Fig. 5.24.

Example 5.14

The microdevice of Fig. 5.25 is actuated linearly by a thermal actuator of length l_a. Determine the horizontal displacement at the free tip 1 of the rigid vertical link for a temperature increase ΔT. Known are all geometrical amounts as well the elastic and thermal properties.

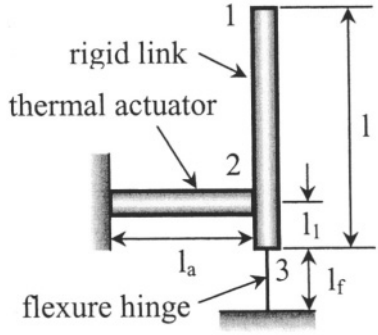

Figure 5.25 Thermally-actuated displacement-amplification microdevice

Solution:

The horizontal displacement at point 2 is given in Eq. (5.68) as a function of the horizontal displacement at point 3 and the slope at the same point. As shown previously for the mechanism of Fig. 5.21 (a), the displacement and rotation can be calculated as:

$$\begin{cases} \theta_{3z} = F_{2y} l_f (2l_1 + l_f)/(2EI_z) \\ u_{3y} = F_{2y} l_f (3l_1^2 + 3l_1 l_f + l_f^2)/(3EI_z) \end{cases} \tag{5.80}$$

where F_{2y} is the force generated by thermal actuation at the interface between the horizontal actuator and the vertical rigid link. The value of F_{2y} is given in Eq. (4.7), Chapter 4 and is rewritten here for convenience:

$$F_{2y} = F_b - F_b u_{2y} / u_0 \tag{5.81}$$

where F_b is the bloc force – Eq. (4.5) and u_0 is the free displacement – Eq. (4.6). By substituting Eqs. (5.81) and (5.80) into Eq. (5.68), an algebraic equation is formed, which can be solved for u_{2y} as:

$$u_{2y} = u_0 / \{1 + 6EI_z u_0 / [F_b l_f (12l_1^2 + 9l_1 l_f + 2l_f^2)]\} \tag{5.82}$$

By combining Eq. (5.82) with the first Eq. (5.67), the horizontal displacement at point 1 becomes:

$$u_{1y} = \{F_b l_f [6l_1(l + l_1) + 3(l + 2l_1) l_f + 2l_f^2] u_0\} / [F_b l_f (12l_1^2 + 9l_1 l_f + 2l_f^2) + 6EI_z u_0] \tag{5.83}$$

5.2 Sagittal Displacement-Amplification Microdevices

Another type of amplification microdevice is the sagittal design, which was presented in Chapter 3 as a suspension component. Figures 5.26, 5.27 and 5.28 are sketches of three sagittal amplifiers.

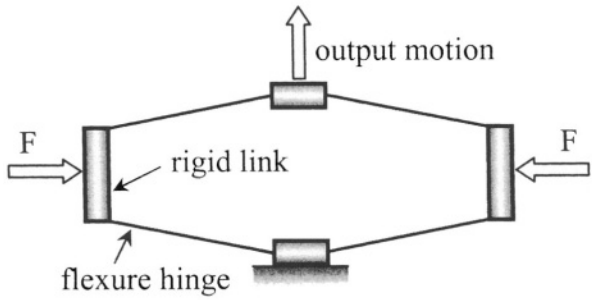

Figure 5.26 Sagittal displacement-amplifying microdevice with four straight flexure hinges

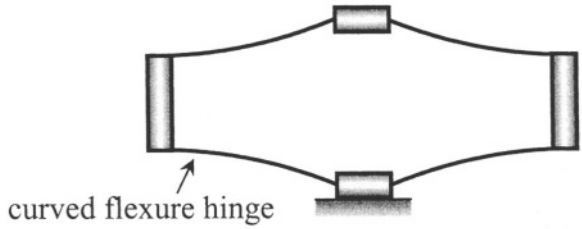

Figure 5.27 Sagittal displacement-amplifying microdevice with four curved flexure hinges

The operation principle of all these devices is rather simple: application of an input force F will generate deformation of the flexure-based mechanisms, and the input displacement corresponding to the force F will be amplified at

the output port, about a direction perpendicular to the input one, due to the inclination in the compliant legs, as shown in Fig. 5.26.

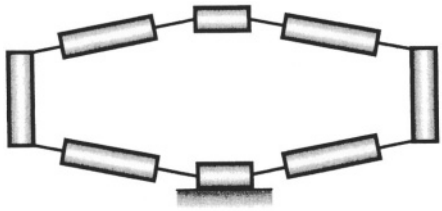

Figure 5.28 Sagittal displacement-amplifying microdevice with eight straight flexure hinges

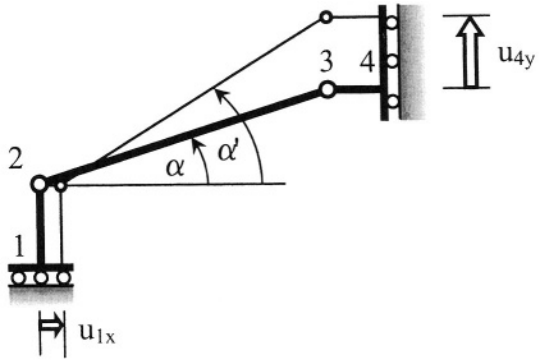

Figure 5.29 Quarter model of sagittal displacement amplifier with rotation joints

Figure 5.29 depicts the quarter model of an amplification mechanism of the type sketched in Fig. 5.26 under the assumption that the flexure hinges are pure rotational joints.

An input displacement u_{1x} translates into the amplified output displacement u_{4y}, as indicated in Fig. 5.29, where the initial position is indicated by thicker lines. For l_1, l_2 and l_3 being the lengths of the three rigid links 1-2, 2-3 and 3-4 respectively, it can be shown that the following geometric relationships do apply:

$$\begin{cases} u_{1x} + l_2 \cos\alpha' = l_2 \cos\alpha \\ l_2 \sin\alpha' = l_2 \sin\alpha + u_{4y} \end{cases} \tag{5.84}$$

By solving Eqs. (5.84) for u_{4y}, it can be shown that the displacement amplification of this device is:

$$a = u_{4y} / u_{1x} = \sqrt{l_2^2 / u_{1x}^2 \sin^2 \alpha + 2 l_2 / u_{1x} \cos \alpha - 1} - l / u_{1x} \sin \alpha \quad (5.85)$$

As Eq. (5.85) indicates, the displacement amplification is not a linear function of the input displacement u_{1x}. Figure 5.30 is a plot of the amplification in terms of the length of the mid link and its original inclination angle (for an input displacement $u_{1x} = 5\ \mu m$), whereas Fig. 5.31 shows the variation of the same amount as a function of the input displacement (when $l_2 = 200\ \mu m$ and $\alpha = 2^o$).

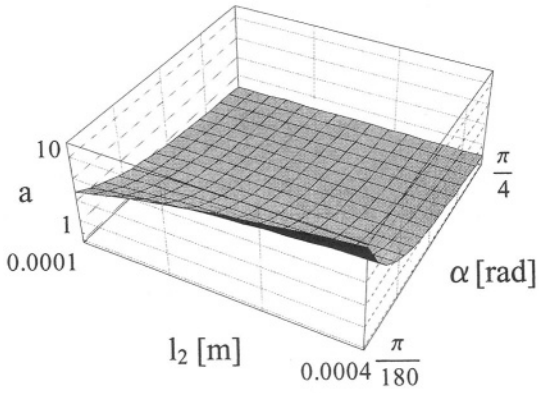

Figure 5.30 Displacement amplification as a function of the main link's length and inclination angle

As expected, the amplification increases with the length l_2 increasing and with the inclination angle α decreasing, as shown in Fig. 5.30. Also, an interesting feature of this device consists in the fact that larger input displacements u_{1x} produce smaller amplifications, as indicated by the plot of Fig. 5.31.

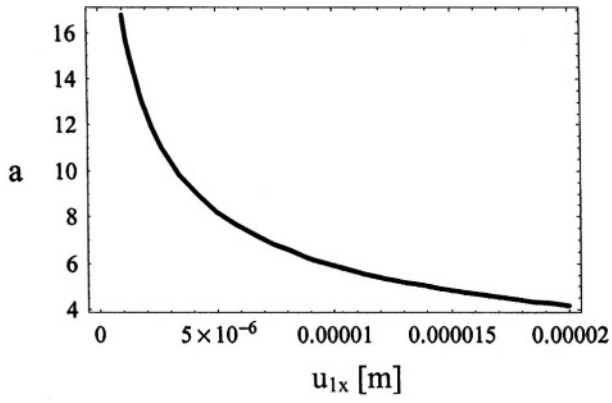

Figure 5.31 Displacement amplification as a function of the input magnitude

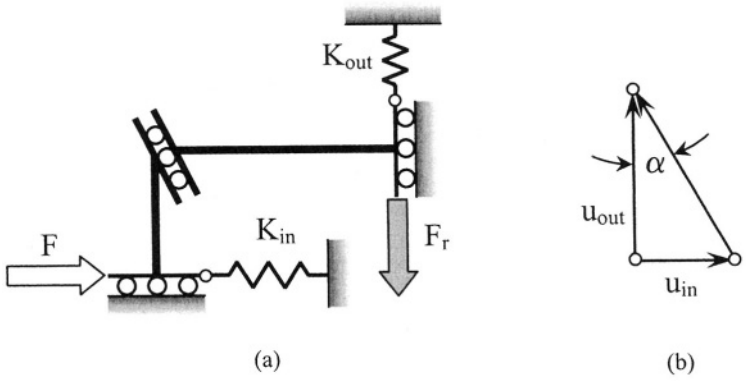

Figure 5.32 Physical quarter-model of sagittal displacement amplifier: (a) spring-based model; (b) displacement diagram

The three mechanisms shown in Figs. 5.26 and 5.27 will be studied next in terms of their displacement amplification capacity, but also they will be characterized in terms of two other important qualifiers: the *input stiffness* and the *output stiffness.* Figure 5.32 (a) is a simplified physical model of the real microdevices of Figs. 5.26, 5.27 and 5.28 describing the spring features by means of two sets of matching wedges that can relatively slip without friction along their mating surfaces. For convenience, the subscript *in* has been used to denote the *input* (horizontal) direction of Fig. 5.32 (a), whereas *out* signifies the *output* (vertical) direction in the same figure.

The actuating (input) force F encounters elastic resistance which can be modeled by the horizontal spring of stiffness K_{in}. At the same time, due to the relative inclination α of the two rigid links, elastic resistance is also set about the perpendicular direction, and this is modeled by the spring of stiffness K_{out}. The same inclination amplifies the input displacement u_{in} to a value u_{out} about the direction perpendicular to the input one, as pictured in Fig. 5.32 (b).

When the work introduced in the system by the action force F entirely balances the work of the resistance force F_r and the potential energy stored in the two elastic springs, the following equation applies:

$$Fu_{in}/2 = F_r u_{out}/2 + K_{in}u_{in}^2/2 + K_{out}u_{out}^2/2 \tag{5.86}$$

where division by the factor of 2 in the work terms has been applied because the respective forces are applied quasi-statically. At the same time, the following relationship holds true:

$$\tan\alpha = u_{in}/u_{out} = 1/a \tag{5.87}$$

from Fig. 5.32 (b). By substituting now Eq. (5.87) into Eq. (5.86), the following equation is obtained:

$$F - aF_r = (k_{in} + a^2 K_{out})u_{in} \tag{5.88}$$

In the particular case where both the active force and the resistance force are zero (the mechanism deforms through application of the input displacement u_{in}), Eq. (5.88) simplifies to:

$$K_{in} = -a^2 K_{out} \tag{5.89}$$

which shows that the displacement amplification a, the input stiffness K_{in} and the output stiffness K_{out} are related. This condition is accurate for a device with pure rotation joints, but is only an approximation for devices utilizing microhinges, as shown in the following.

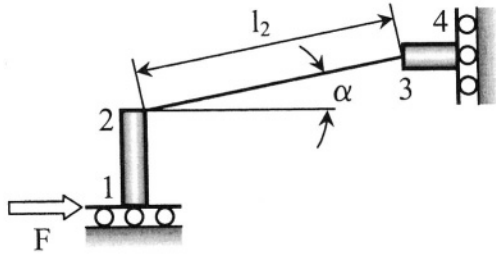

Figure 5.33 Quarter-model of displacement-amplification microdevice with one straight flexure hinge

The micromechanism of Fig. 5.26 will further be studied by formulating the three corresponding qualifiers mentioned above, namely the displacement amplification, input stiffness and output stiffness. A quarter-model will be again employed, as sketched in Fig. 5.33. Essentially, the design of Fig. 5.33 is statically-equivalent to the simplified model of Fig. 5.34, where the two rigid links have been eliminated.

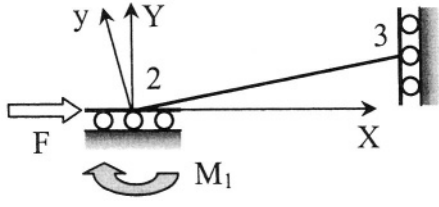

Figure 5.34 Reduced quarter-model of displacement-amplification microdevice with one straight flexure hinge for input stiffness calculation

The approach followed here is the one based on the stiffness approach of Chapter 1 for a straight flexible member. As shown in Fig. 5.34, two sets of reference frames are utilized here: one is the global frame XY, and the other is the local reference frame with its x-axis aligned with the straight flexure hinge. The actuation force F decomposes locally into the F_x and F_y, and therefore, the following matrix equation can be written, according to Castigliano's first theorem:

$$\begin{Bmatrix} F_{1x} \\ F_{1y} \\ M_1 \end{Bmatrix} = \begin{bmatrix} K_{Fx-ux} & 0 & 0 \\ 0 & K_{Fy-uy} & K_{Fy-\theta z} \\ 0 & K_{Fy-\theta z} & K_{Mz-\theta z} \end{bmatrix} \begin{Bmatrix} u_{1x} \\ u_{1y} \\ \theta_{1z} \end{Bmatrix} \tag{5.90}$$

The supplemental part of the subscript which has been used in Chapter 1 to denote the extremity of the flexible member which is assumed free (point 3 here) was eliminated from the notation, because the 2-3 flexure is symmetric. As Eq. (5.90) indicates, axial and bending effects are both taken into account.

In order to determine the input stiffness, a relationship between the force F and the corresponding displacement u_{1X} (taken about the global direction X) is needed. This displacement results from adding up the two local deformations, u_{1x} and u_{1y}, namely:

$$u_{1X} = u_{1x}\cos\alpha - u_{1y}\sin\alpha \tag{5.91}$$

The local deformations u_{1x} and u_{1y} can be expressed from the first two rows of the matrix Eq. (5.90) as:

$$\begin{cases} F\cos\alpha = K_{Fx-ux}u_{1x} \\ -F\sin\alpha = K_{Fy-uy}u_{1y} \end{cases} \tag{5.92}$$

where it has been taken into consideration that F_{1x} and F_{1y} are the projections of F onto the local x-and y-axes. The rotation (slope) at point 2 is zero, because the flexure hinge is rigidly attached to the link 1-2 at that particular point. By combining now Eqs. (5.91) and (5.92), results in the following equation giving the input stiffness:

$$K_{in} = F/u_{1X} = 1/(\cos^2\alpha/K_{Fx-ux} + \sin^2\alpha/K_{Fy-uy}) \tag{5.93}$$

It should be mentioned that Eq. (5.93) is generic in the sense that it can accommodate any shape of a flexure hinge whose required stiffnesses are known.

A similar approach is followed in order to determine the other important stiffness, the output stiffness. Figure 5.35 pictures the reduced quarter-model that corresponds to this case.

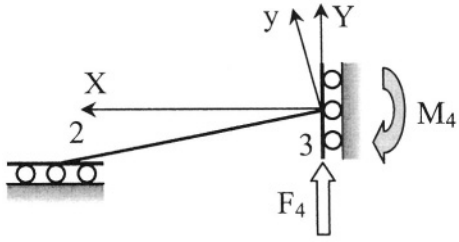

Figure 5.35 Reduced quarter-model of displacement-amplification microdevice with one straight flexure hinge for output stiffness calculation

The force F_4 is originally applied at point 4 of Fig. 5.33, and is transferred at point 3 on the reduced quarter-model of Fig. 5.35. A relationship similar to the matrix Eq. (5.90) can be written, connecting the load components F_{4x}, F_{4y} and M_4 to the deformations, according to the following equations:

$$\begin{cases} F_4 \sin\alpha = K_{Fx-ux} u_{4x} \\ F_4 \cos\alpha = K_{Fy-uy} u_{4y} \end{cases} \tag{5.94}$$

The displacement at 4 about the Y-direction (the direction of the applied force F_4) can be expressed as:

$$u_{4Y} = -u_{4x} \sin\alpha + u_{4y} \cos\alpha \tag{5.95}$$

The output stiffness is found by combining Eqs. (5.94) and (5.95), namely:

$$K_{out} = F_4 / u_{4Y} = 1/(\cos^2\alpha / K_{Fy-uy} - \sin^2\alpha / K_{Fx-ux}) \tag{5.96}$$

The displacement amplification is determined by following a path similar to the one used in finding the output stiffness, the only differences here being that there is no force F_4 and the actuation force F (which is applied at point 1, as shown in Fig. 5.34) will generate a horizontal reaction H_4 at point 4, which can be transferred at point 3, as it was done previously. In this case, the equations connecting local forces to local displacements (deformations) are:

$$\begin{cases} F\cos\alpha = K_{Fx-ux} u_{4x} \\ F\sin\alpha = K_{Fy-uy} u_{4y} \end{cases} \tag{5.97}$$

By combining Eqs. (5.97) and Eq. (5.95) gives the output displacement u_{4Y}, which is produced by application of the force F at the input port 1, namely:

$$u_{4Y} = F/2 \sin 2\alpha (1/K_{Fy-uy} - 1/K_{Fx-ux}) \tag{5.98}$$

The displacement amplification is found by means of Eqs. (5.91), (5.92) and (5.98) as:

$$a = u_{4Y}/u_{1X} = (1/K_{Fy-uy} - 1/K_{Fx-ux}) \sin 2\alpha /[2(\cos^2 \alpha / K_{Fx-ux} + \sin^2 \alpha / K_{Fy-uy})] \tag{5.99}$$

Example 5.15

Check whether the input stiffness K_{in}, output stiffness K_{out} and displacement amplification a of the quarter-model of a microdevice with four straight hinges, as the one pictured in Fig. 5.26, satisfy the condition of Eq. (5.89), which is valid for a similar device with pure rotation joints.

Solution:

If one combines Eqs. (5.93), (5.96) and (5.99), the condition posed in Eq. (5.89) is only possible when:

$$2K_{Fy-uy} \cos(2\alpha) + (K_{Fx-ux} - K_{Fy-uy}) \sin^2(2\alpha) = 0 \tag{5.100}$$

which is equivalent to the particular value of the inclination angle:

$$\alpha = 2 \arccos\{[K_{Fy-uy} + \sqrt{K_{Fy-uy}^2 + (K_{Fx-ux} - K_{Fy-uy})^2}\,] /[(K_{Fx-ux} - K_{Fy-uy})]\} \tag{5.101}$$

Example 5.16

Based on the equations giving the input and output stiffness and the displacement amplification for a quarter-model amplification microdevice, find those amounts that correspond to the full, four-flexure microdevice.

Solution:

The full microdevice comprises four flexures and its spring-based model is shown in Fig. 5.36 (a). There are two branches between the nodal points A and B, the upper one and the lower one, each formed of two identical springs connected in series. The equivalent spring stiffness for each branch is $K_{in}/2$, according to the series connection rule, presented in this chapter. As a consequence, the equivalent spring shown in Fig. 36 (b) results from

combining two springs in parallel, each having the stiffness $K_{in}/2$, and its stiffness is the sum of these two intermediate stiffnesses, namely:

$$K_{in,t} = K_{in}/2 + K_{in}/2 = K_{in} \tag{5.102}$$

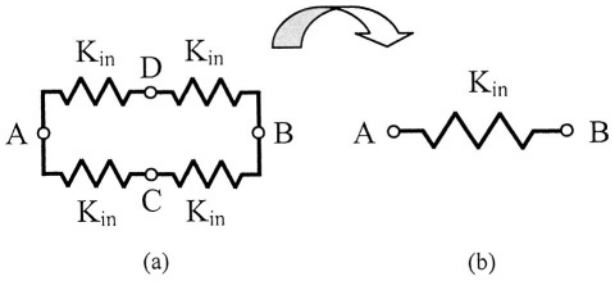

Figure 5.36 Spring-based models: (a) Full four-flexure sagittal amplification microdevice model; (b) Equivalent model

As a consequence, the input stiffness of the whole micromechanism is equal to the stiffness of one quarter of it. Similar reasoning can be applied to demonstrate that the total output stiffness is:

$$K_{out,t} = K_{out}/2 + K_{out}/2 = K_{out} \tag{5.103}$$

by following the left and right branches between points C and D in Fig. 5.36 (a).

The following reasoning can be developed in order to determine the displacement amplification of the full microdevice. A simplified quarter-model amplification device of the type discussed here is sketched in Fig. 5.37 (a), where the input and output displacements are shown (the thicker line indicates the flexure in its final position). The corresponding full microdevice model is shown in Fig. 5.37 (b).

When the full mechanism is analyzed, the input displacement is actually applied from both sides, as indicated schematically in Fig. 5.37 (b) and the output can also be collected at two ports about the direction perpendicular to the input direction. As a consequence, the amplification of the whole microdevice can be calculated as:

$$a_t = 2u_{out}/(2u_{in}) = u_{out}/u_{in} = a \tag{5.104}$$

As the case was with the input and output stiffnesses, Eq. (5.104) indicates that the displacement amplification of the entire sagittal micromechanism is equal to the amplification produced by one quarter model.

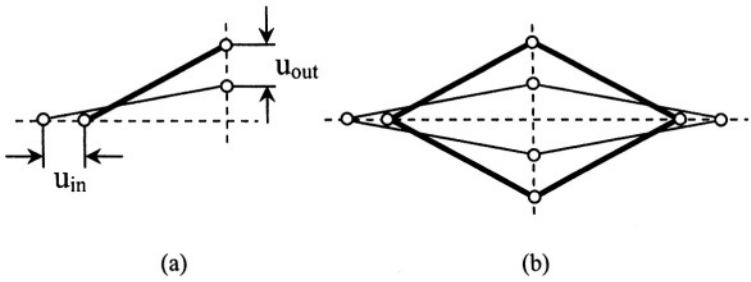

Figure 5.37 Input and output displacements for a sagittal displacement amplification microdevice: (a) quarter model; (b) full model

Example 5.17

Express the input and output stiffnesses, as well as the displacement amplification of the microdevice with four curved flexure hinges sketched in Fig. 5.27. The quarter-model of this sagittal microdevice, together with the defining geometry, are shown in Fig. 5.38.

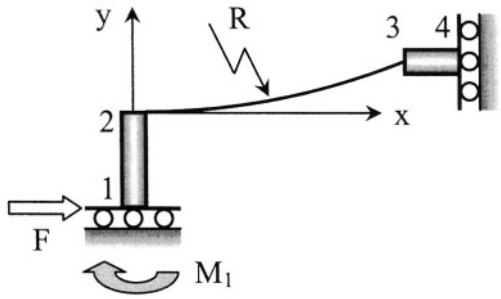

Figure 5.38 Quarter-model of displacement-amplification microdevice with four curved flexure hinges

Solution:

The curvature radius of the flexure is R and the corresponding center angle (not indicated in Fig. 5.38) is α. The lengths of the two adjoining rigid links are l_1 and l_3, respectively. The input stiffness, output stiffness and displacement amplification are calculated in a manner similar to the one used for the straight-flexure quarter-model analyzed previously.

The reaction moment M_1, which is set when the force F acts at point 1, can be found by considering that the rotation at point 2 is zero (the circular flexure remains rigidly connected to the link 1-2 at that point). It is considered that the local frame indicated in Fig. 1.20 of Chapter 1, it is also

used for this example. According to Eq. (1.127) of Chapter 1, the rotation angle at point 2 (which is actually zero) can be written as:

$$\theta_{2z} = C_{ux-Mz} F_{1x} + C_{uy-Mz} F_{1y} + C_{\theta z-Mz} M_{1z} \tag{5.105}$$

where $F_{1x} = F$, $F_{1y} = 0$ (there is no vertical reaction at point 1, and therefore no y-component at point 2) and $M_{1z} = M_1$. By solving Eq. (5.105) for M_1 gives:

$$M_1 = C_{ux-Mz} / C_{\theta z-Mz} F \tag{5.106}$$

The displacement about the x (input) direction at point 1 is given by the same Eq. (1.127) of Chapter 1 as:

$$u_{2x} = u_{1x} = C_{ux-Fx} F + C_{ux-Mz} M_1 \tag{5.107}$$

By substituting M_1 of Eq. (5.106) into Eq. (5.107), produces the following input stiffness equation:

$$K_{in} = F / u_{1x} = C_{\theta z-Mz} / (C_{ux-Fx} C_{\theta z-Mz} + C_{ux-Mz}^2) \tag{5.108}$$

The compliance equations that define the input stiffness are explicitly given in Eqs. (1.133), (1.128) and (1.130) in Chapter 1.

The output stiffness is calculated similarly by assuming that a force F_4 is applied vertically upward at node 4, as shown in Fig. 5.39.

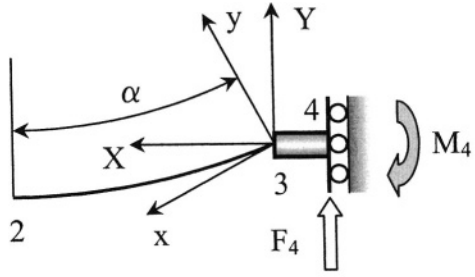

Figure 5.39 Quarter-model with load for output stiffness calculation

An equation can be written in order to express the zero rotation at node 4, and this leads to the unknown moment M_4:

$$M_4 = (C_{ux-Mz} \sin\alpha - C_{uy-Mz} \cos\alpha) / C_{\theta z-Mz} F_4 = c_m F_4 \tag{5.109}$$

The sine and cosine terms appear in Eq. (5.109) because of the inclination of the force F_4 with respect to the local reference frame xy of Fig. 5.39. The displacement about the vertical direction at point 4 results from superimposing the local displacements at that point in the form:

$$u_{4Y} = u_{3Y} = u_{4y}\cos\alpha - u_{4x}\sin\alpha \tag{5.110}$$

where Y and X denote the global reference frame, as shown in Fig. 5.39. By expressing the local displacement components at point 3, according to the generic Eq. (1.127) of Chapter 1, the output stiffness can be formulated as:

$$\begin{aligned} K_{out} = 1/[&(-C_{ux-Fy}\sin\alpha + C_{uy-Fy}\cos\alpha + c_m C_{uy-Mz})\cos\alpha \\ &+ (C_{ux-Fx}\sin\alpha - C_{ux-Fy}\cos\alpha - c_m C_{ux-Mz})\sin\alpha] \end{aligned} \tag{5.111}$$

The amplification factor is found by applying the force F at node 1 (as in the case of finding the input displacement) and by determining the corresponding displacement about the Y-direction at 4. In this case, a horizontal reaction H_4 (not shown in Figs. 5.38 and 5.39) is set at node 4 such that $H_4 = F$. The unknown bending moment at the same node can be found as:

$$M_4 = (C_{ux-Mz}\cos\alpha + C_{uy-Mz}\sin\alpha)/C_{\theta z-Mz}F_4 = c_m' F \tag{5.112}$$

The vertical displacement at node 4 is determined by following the approach previously described and by combining this displacement with u_{1x}, which was determined when formulating the input stiffness. The displacement amplification becomes:

$$\begin{aligned} a = u_{4Y}/u_{1X} = [&(-C_{ux-Fy}\cos\alpha - C_{uy-Fy}\sin\alpha + c_m' C_{uy-Mz})\cos\alpha \\ &+ (C_{ux-Fx}\cos\alpha + C_{ux-Fy}\sin\alpha - c_m' C_{ux-Mz})\sin\alpha]/(C_{ux-Fx} \\ &+ C_{ux-Mz}^2/C_{\theta z-Mz}) \end{aligned} \tag{5.113}$$

Another important aspect is assessing the way these displacement-amplification micromechanisms interact with and can handle external loads that are connected to the output port and are directed about the output direction. A reduced quarter-model of the displacement amplification microdevice is shown in Fig. 5.40, where the actuation force F is opposed by the external (resistive) load F_r.

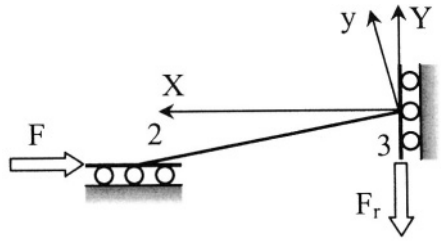

Figure 5.40 Reduced quarter-model of sagittal microdevice with straight flexure hinge under actuation and load

The procedure of finding the output displacement u_{4Y} is similar to the ones applied to find the output stiffness and the displacement amplification for this microdevice. In essence, and without repeating the calculus that has been already detailed previously, the output displacement that is produced under the combined action of the input force F and the resistive force F_r is:

$$u_{4Y} = (F\sin\alpha - F_r\cos\alpha)\cos\alpha / K_{Fy-uy} - (F\cos\alpha + F_r\sin\alpha) \sin\alpha / K_{Fx-ux} \quad (5.114)$$

It is important to determine the maximum value of the resistive force F_r which will bloc the motion at the output port of a sagittal microdevice and which is known as the *bloc force.* By taking $u_{4Y} = 0$ in Eq. (5.114), produces the following equation of the bloc force:

$$F_b = 2(K_{Fx-ux}\cos^2\alpha + K_{Fy-uy}\sin^2\alpha)F/(K_{Fx-ux} - K_{Fy-uy}) \quad (5.115)$$

The displacement amplification microdevices can be combined in various ways in order to tune certain stiffness properties or to augment the absolute output levels that cannot be reached by using a single unit.

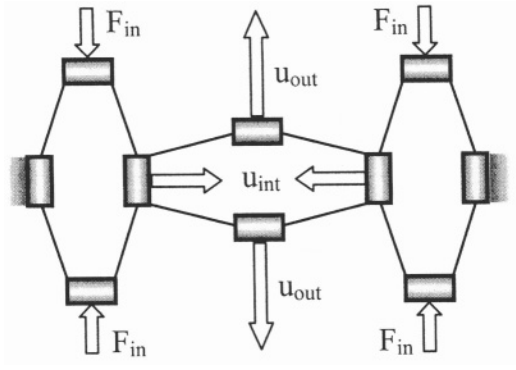

Figure 5.41 Arrangement for displacement amplification enhancement

Figure 5.41 shows an example where two identical units are used to actuate a central unit. The two different units have potentially different stiffness and amplification properties. The input forces F_{in} actuate the two side amplification devices in the way suggested in Fig. 5.41, and their output u_{int} serves as input to the middle amplification microdevice, which produces the bi-directional doubly-amplified output displacements u_{out}. Knowing the amount of actuation force F_{in} it is of interest to determine the output displacement u_{out}. The subscript 1 will be used to denote the side input actuators and the subscript 2 will stand for the middle amplification unit. The displacement amplifications produced by the two units are:

$$\begin{cases} a_1 = u_{out,1} / u_{in} \\ a_2 = u_{out} / u_{in,2} \end{cases} \tag{5.116}$$

However, the input displacement to the middle unit $u_{in,2}$ is the output displacement produced by the first unit $u_{out,1}$, and therefore the two Eqs. (5.116) combine into:

$$u_{out} = a_1 a_2 u_{in} \tag{5.117}$$

The input displacement u_{in} can be expressed as:

$$u_{in} = F_{in} / K_{in,1} \tag{5.118}$$

The input stiffness of the side amplification device is connected to the stiffness at its output port about the output direction, as shown previously. In the present case, the stiffness at the output port of the side device is composed of the output stiffness of this device, coupled in parallel to the input stiffness of the middle microdevice, and therefore, the following equation applies (the minus sign of the original Eq. (5.89) is ignored):

$$K_{in,1} = a_1^2 (K_{out,1} + K_{in,2}) \tag{5.119}$$

By combining Eqs. (5.117), (5.118) and (5.119), yields the absolute output displacement, namely:

$$u_{out} = F_{in} a_2 / [a_1 (K_{out,1} + K_{in,2})] \tag{5.120}$$

In order to increase the output displacement, the amplification of the middle microdevice needs to be high, whereas the amplification of the side microdevices has to be relatively small. Also the output stiffness of the side

units and the input stiffness of the middle unit need to be small in order to produce large output displacements.

6. LARGE DEFORMATIONS

There are MEMS devices which are designed to operate under conditions of large deformations/displacements in order to amplify their output capabilities.

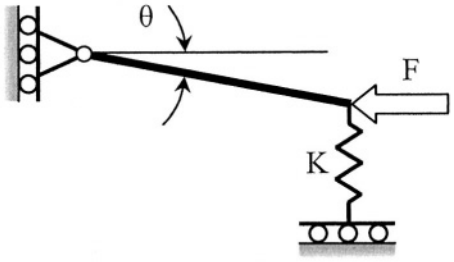

Figure 5.42 Rigid bar with one end pinned and a spring and a load at the other end

While the separation between small and large displacements is rather flexible, the mathematical description and solutions of the two theories are quite different. The small-displacement theory considers that the loading and resulting deformations/displacements of a microcomponent are independent and can be superimposed linearly. The large-displacement theory is non-linear, and effects of different loads do combine and affect each other and, together, they affect the deformed state of a MEMS component. In many instances, an originally non-linear mathematical model can be linearized, especially when the deformations are small, as shown in the example of Fig. 5.42, where the axial force produces an angular rotation θ of the pinned bar of length l, because of an initial misalignment from the horizontal position. The moment equilibrium equation is:

$$Fl\sin\theta = K(l\sin\theta)(l\cos\theta) \tag{5.121}$$

The following small-displacement approximations are used:

$$\begin{cases} \sin\theta \cong \theta \\ \cos\theta \cong 1 \end{cases} \tag{5.122}$$

which transform Eq. (5.121) into:

$$F \cong Kl \tag{5.123}$$

For an elastic body that is acted upon by external loads, the small-displacement theory provides the Cauchy strain-displacement relationships given in Eqs. (1.27) of Chapter 1. However, those equations are just keeping the linear terms of the following more complete equations:

$$\begin{cases} \varepsilon_x = \partial u_x / \partial x + 1/2[(\partial u_x / \partial x)^2 + (\partial u_y / \partial x)^2 + (\partial u_z / \partial x)^2] \\ \varepsilon_y = \partial u_y / \partial y + 1/2[(\partial u_x / \partial y)^2 + (\partial u_y / \partial y)^2 + (\partial u_z / \partial y)^2] \\ \varepsilon_z = \partial u_z / \partial z + 1/2[(\partial u_x / \partial z)^2 + (\partial u_y / \partial z)^2 + (\partial u_z / \partial z)^2] \\ \gamma_{xy} = 1/2(\partial u_x / \partial y + \partial u_y / \partial x + \partial u_x / \partial x \partial u_x / \partial y + \partial u_y / \partial x \partial u_y / \partial y \\ + \partial u_z / \partial x \partial u_z / \partial y) \\ \gamma_{yz} = 1/2(\partial u_y / \partial z + \partial u_z / \partial y + \partial u_x / \partial x \partial u_x / \partial z + \partial u_y / \partial x \partial u_y / \partial z \\ + \partial u_z / \partial x \partial u_z / \partial z) \\ \gamma_{zx} = 1/2(\partial u_z / \partial x + \partial u_x / \partial z + \partial u_x / \partial y \partial u_x / \partial z + \partial u_y / \partial y \partial u_y / \partial z \\ + \partial u_z / \partial y \partial u_z / \partial z) \end{cases} \tag{5.124}$$

which are given, for instance, by Boresi, Schmidt and Sidebottom [3]. An example will be analyzed next in order to better contrast the differences between the small- and large-displacement theories.

Example 5.18

Consider a fixed-free bar of constant cross-section that is acted upon by an axial force at its free end. Compare the maximum displacements corresponding to small- and large-displacement theories. Given are the force F = 200 μN, the cross-sectional area, A = 0.2 μm^2, the length of the bar, l = 200 μm, and Young's modulus, E = 160 GPa.

Solution:

The differential equation given by the small-displacement theory is:

$$\partial u_x / \partial x = F/(EA) \tag{5.125}$$

which is a linear first-order differential equation whose solution gives the well-known maximum displacement at the free end:

$$u_{x,max} = Fl/(EA) \tag{5.126}$$

The first Eq. (5.124) can be expressed for large displacements by means of the non-linear first-order differential equation:

$$1/2(\partial u_x/\partial x)^2 + \partial u_x/\partial x = F/(EA) \qquad (5.127)$$

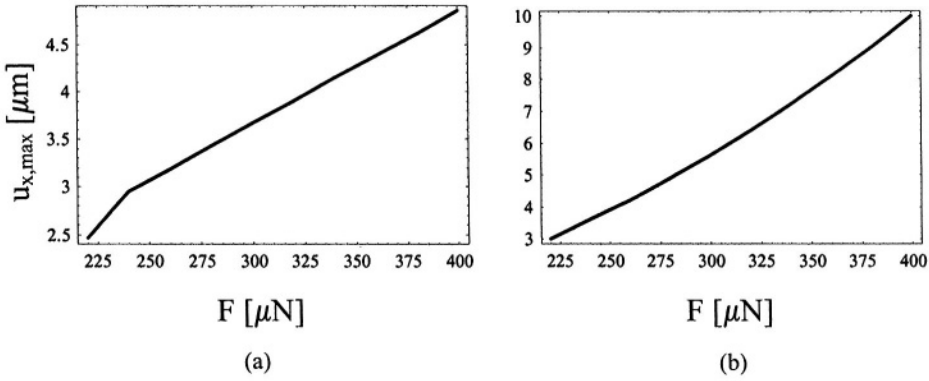

Figure 5.43 Maximum axial displacement of a fixed-free microbar as a function of the extension load according to: (a) large-deformation theory; (b) small-deformation theory

The two plots of Fig. 5.43 show the tip displacements according to the large-deformation theory – Fig. 5.43 (a) – and the small-deformation theory – Fig. 5.43 (b) –, both in terms of the applied force. It can be noticed that the predictions of the small-displacement theory are always higher than the ones of the large-displacement theory –up to more than twice for large axial forces.

Many MEMS do deform by means of beam-like structures, and there are situations where such members are subject to large deformations.

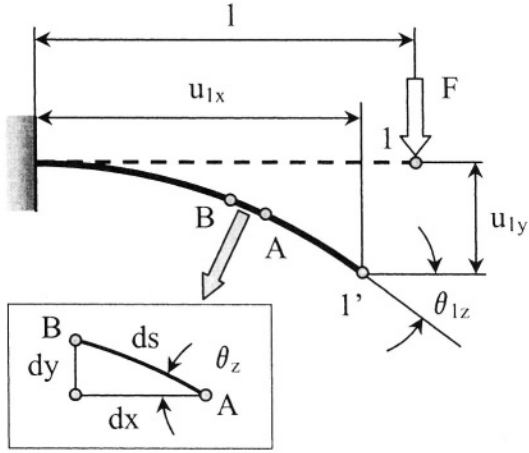

Figure 5.44 Cantilever with tip force producing large deformations

Figure 5.44 shows a microcantilever that is subject to large deformations under the action of a tip force F. It can be seen that, unlike in the small-displacement theory – where it is assumed that the projection of the bent

beam on its original longitudinal direction has the same length with the unbent beam, the horizontal projection of the deformed beam is shorter by the quantity $l - u_{lx}$. Another major difference consists in the fact that the three parameters defining the ultimate position of the microcantilever free tip, namely: u_{lx}, u_{ly} and θ_{lz}, are dependent. In bending, the essential difference between the large- and the small-displacement theories consists in the way the basic differential equation is formulated. While the large-displacement theory takes the exact form:

$$EI_z d^2u_y(x)/dx^2 /\{1+[du_y(x)/dx]^2\}^{3/2} = -M_z \qquad (5.128)$$

the small-deflection theory ignores the slope second power in the denominator of Eq. (5.128), and therefore studies the approximate differential equation:

$$EI_z d^2u_y(x)/dx^2 = -M_z \qquad (5.129)$$

Another form of the exact Eq. (5.128) is:

$$EI_z d\theta_z(x)/ds = -M_z \qquad (5.130)$$

as shown, for instance, by Timoshenko [4] or Gere and Timoshenko [5]. As suggested in Fig. 5.44, the relationships between the curvilinear variable s and its projections on the x and y axes are:

$$\begin{cases} dy = ds \sin\theta_z \\ dx = ds \cos\theta_z \end{cases} \qquad (5.131)$$

By taking into account that the bending moment at a generic position x is simply equal to F times x, Eq. (5.130) can serve to take its derivative in terms of the curvilinear coordinate s by also using Eq. (5.131), which results in:

$$EI_z d^2\theta_z(x)/ds^2 = -F\cos\theta_z \qquad (5.132)$$

The solution to this differential equation, by taking into consideration that the curvature at the free end is zero, becomes:

$$ds = d\theta_z /[k\sqrt{2(\sin\theta_{lz} - \sin\theta_z)}] \qquad (5.133)$$

where:

$$k^2 = F/(EI_z) \qquad (5.134)$$

The length of the beam can be expressed by integrating the differential length ds of Eq. (5.133), namely:

$$l = 1/(\sqrt{2}k) \int_0^{\theta_{1z}} d\theta_z / \sqrt{\sin\theta_{1z} - \sin\theta_z} \tag{5.135}$$

The right-hand side of Equation (5.135) can be expressed in terms of an integral of the form:

$$F(c,\varphi) = \int_0^{\varphi} d\theta_z / \sqrt{1 - c^2 \sin^2\theta_z} \tag{5.136}$$

which is known as an *elliptic integral of the first kind* where c is a constant. Equation (5.135) enables to find the force F that corresponds to a tip slope θ_{1z}.

The maximum tip deflection can be found by solving the first Eq. (5.131), namely:

$$u_{1y} = \int_0^{\theta_{1z}} dy = 1/(\sqrt{2}k) \int_0^{\theta_{1z}} \sin\theta_z d\theta_z / \sqrt{\sin\theta_{1z} - \sin\theta_z} \tag{5.137}$$

Finding u_{1y} implies numerically solving an *elliptic integral of the second kind,* which is defined as:

$$E(c,\varphi) = \int_0^{\varphi} \sqrt{1 - c^2 \sin^2\theta_z}\, d\theta_z \tag{5.138}$$

Similarly, the tip position u_{1x} is determined by integrating the second Eq. (5.131) as:

$$u_{1x} = \int_0^{\theta_{1z}} dx = 1/(\sqrt{2}k) \int_0^{\theta_{1z}} \cos\theta_z d\theta_z / \sqrt{\sin\theta_{1z} - \sin\theta_z} \tag{5.139}$$

An example will be studied now to highlight the differences between the deformations of a beam when calculated by the large-displacement hypotheses versus the small-displacement theory.

Example 5.19

Consider a microcantilever of length l = 300 μm and having a cross-section defined by w = 10 μm and t = 2 μm being acted upon by a force F as

in Fig. 5.44. Find the deformed position at the free end defined by, u_{1x}, u_{1y} and θ_{1z} by using the large-displacement theory and compare it with the results given by the small-displacement theory when the force F increases from 2 μN to 100 μN. Consider that Young's modulus is 130 GPa.

Solution:

The tip angle θ_{1z} is found by solving Eq. (5.135) for the large-displacement theory and Fig. 5.45 (a) is the plot of this angle against the force, whereas Fig. 5.45 (b) shows the angle θ_{1z} when calculated by means of the small-deflection hypotheses, according to which:

$$\theta_{1z} = Fl^2/(2EI_z) \tag{5.140}$$

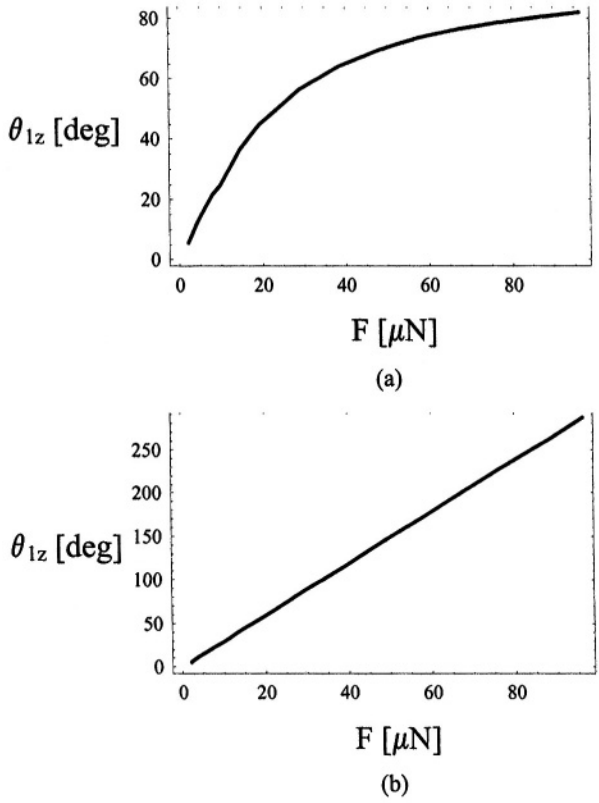

Figure 5.45 Tip rotation angle according to the: (a) large-displacement theory; (b) small-displacement theory

It can be noticed that the predictions of the small-displacement theory are always higher than the ones of the large-displacement model, and for large values of the force F the difference in results is more than 250%.

Equation (5.137) is solved numerically in order to determine the tip deflections of the microcantilever by means of the large-deformation model, and Fig. 5.46 (a) plots the values of u_{1y} versus the force F. The non-linear relationship between load and deformation can be seen again. The tip deflection is calculated by the small-displacement assumptions by means of the known relationship:

$$u_{1y} = Fl^3 /(3EI) \tag{5.141}$$

and Fig. 5.46 (b) shows the linear deflection-force relationship. Again, the predictions by the small-displacement theory are overestimating the tip deflection by significant amounts for large values of the force F.

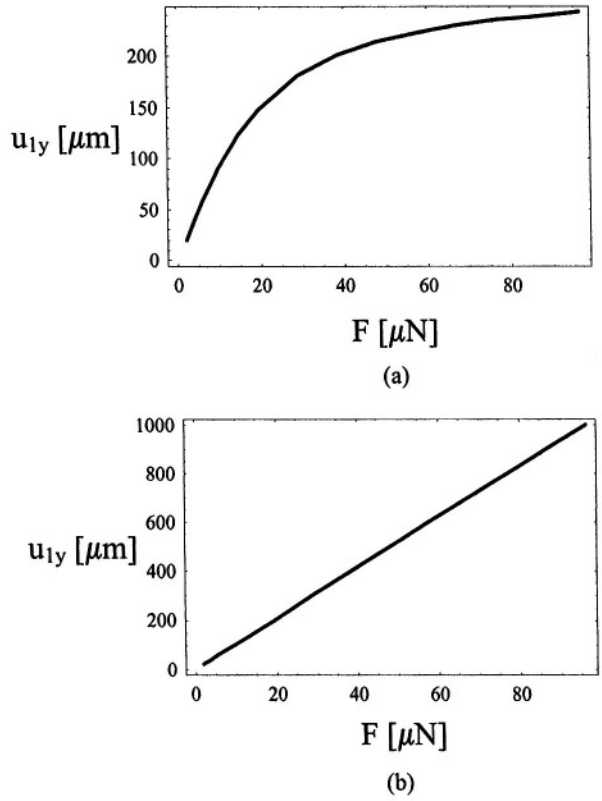

Figure 5.46 Tip deflection according to the: (a) large-displacement theory; (b) small-displacement theory

The tip position u_{1x} is plotted in Fig. 5.47 against the force F, as calculated by means of Eq. (5.139) according to the large-displacement theory. Values as large as $170\ \mu m$ are obtained by the large-displacement model predictions.

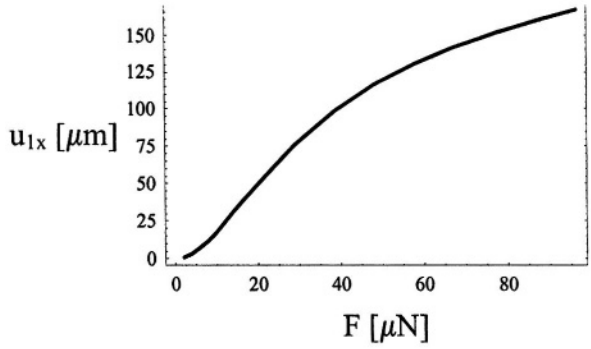

Figure 5.47 Tip deformation about the longitudinal axis according to the large-displacement theory

Example 5.20

Analyze the maximum stresses that are produced through bending of the microcantilever in the preceding example when calculated by both the small- and large-displacement theories.

Solution:

According to the small-displacement theory, the maximum stresses, which are located on the upper fibers of the microcantilever, are calculated as:

$$\sigma_{max}^{s} = M_{max} t/(2I_z) = Flt/(2I_z) \tag{5.142}$$

It has been shown that $d\theta_z/ds$ represents the true curvature, and this fact was used in the large-displacement theory. The radius of curvature is therefore:

$$1/R = d\theta_z/ds \tag{5.143}$$

The maximum strain (on the upper fibers) can be calculated as:

$$\varepsilon_{max} = t/(2R) = t(d\theta_z/ds)_{max}/2 \tag{5.144}$$

By way of Eq. (5.133), which gives the space derivative of the slope according to the large displacement theory, the maximum value invoked in Eq. (5.144) is:

$$(d\theta_z/ds)_{max} = k\sqrt{2\sin\theta_{1z}} \tag{5.145}$$

For materials with linearly-elastic behavior, the stress is the product of the Young's modulus and the corresponding strain, and therefore, by using Eqs.

(5.144) and (5.145), the maximum stress according to the large displacement model is:

$$\sigma^{l}_{max} = Etk\sqrt{sin(\theta_{1z})}/2 \tag{5.146}$$

As a consequence, the following stress ratio can be formulated, based on Eqs. (5.142) and (5.146):

$$r_{\sigma} = \sigma^{s}_{max}/\sigma^{l}_{max} = kl/\sqrt{2sin(\theta_{1z})} \tag{5.147}$$

The stress ratio of Eq. (5.147) is plotted against the force F in Fig. 5.48. It can be seen that by using the small-displacement theory, the stresses are always overevaluated, as compared to the large-displacement theory, up to factors of approximately 2.5 for large values of F. However, at relatively smaller loads, the predictions given by the two methods are almost identical, as also shown in Fig. 5.48, where the stress ratio is very close to 1 for small values of the force F.

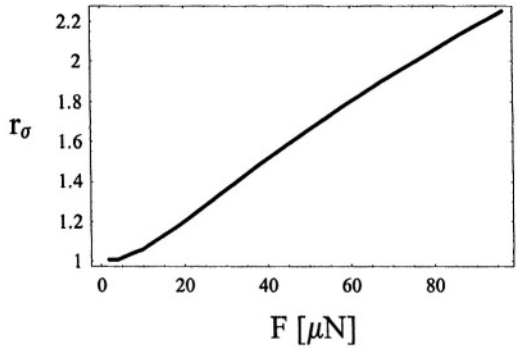

Figure 5.48 Stress ratio as a function of the tip force – Eq. (5.147)

7. BUCKLING

7.1 Introduction

Buckling is associated with structural instability occurring at statical/dynamical loads which are called *critical* and which can produce either failure or large deformations that are unacceptable. The discussion here will be restricted to statically-generated buckling. Figure 5.49 pictures three different situations that are stability-related.

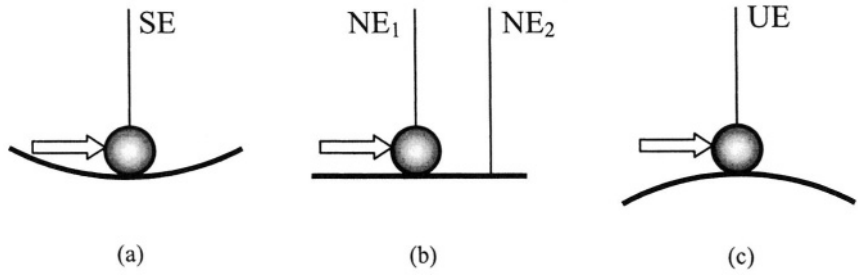

Figure 5.49 Stability-related conditions: (a) Stable; (b) Neutral equilibrium; (c) Unstable

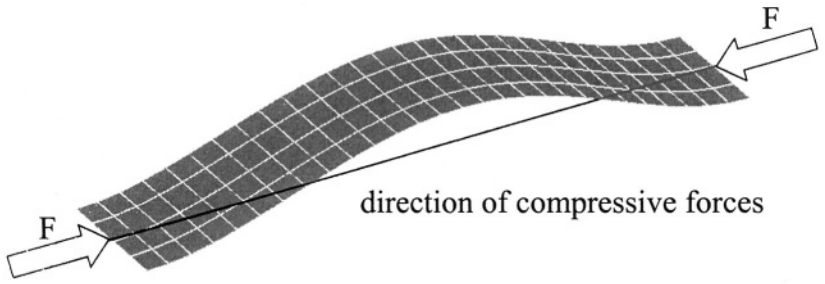

Figure 5.50 Finite element model showing out-of-the-plane buckling of a thin column

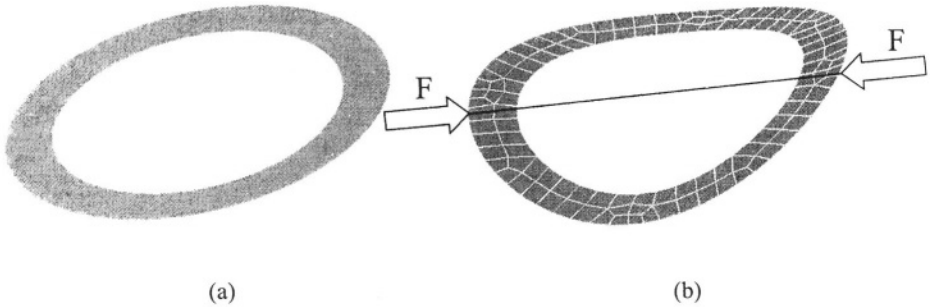

Figure 5.51 Buckling of a thin ring: (a) Undeformed; (b) Finite element model of the out-of-the-plane deformed shape

A perturbation will displace the ball, as shown in Fig. 5.49 (a), but the stable-equilibrium position (denoted by SE) will be regained after the perturbation ceases. In the case of Fig. 5.49 (b), any position is one of equilibrium, for instance the ball will move from one equilibrium position NE_1 to a subsequent one NE_2 after the perturbation ends, and therefore this situation is one of neutral equilibrium (NE). On the contrary, when a perturbation is

applied to the ball sitting at the top of the convex surface of Fig. 5.49 (c), the ball will irreversibly move from its position UE, which is therefore an unstable-equilibrium position. It should be mentioned that the three states of Fig. 5.49 are defined based on small perturbations. When these perturbations are large, there might be changes in the stability condition of a structure leading, for instance, from a stable to an unstable state and vice versa. Figures 5.50 and 5.51 illustrate two examples of structural buckling that might be encountered in MEMS applications.

When the compression forces that are applied about the longitudinal (long) axis of the thin member of Fig. 5.50 reach a certain critical level, the column will lose its equilibrium position and will bend (buckle) outside its plane as shown in the figure. Similarly, when the thin ring of Fig. 5.51 (a) is compressed, it can buckle out of its plane, as illustrated in Fig. 5.51 (b). The cases shown in Figs. 5.50 and 5.51 are representative for the *bifurcation buckling,* where there is a sudden jump from one state/mode of deformation (which is axial) to another mode (which is bending) at a critical level of the compressive load. Another possibility is the *limit-load* or *maximum-load* (also known as *snap-through buckling* – see Chen and Lui [6] for instance) where the jump occurs between two modes that are similar in nature, such as the case is with the arch of Fig. 5.52, which can snap-through (buckle) from one stable bending state (shown with solid line), to a different one (indicated by dotted line) under the action of external pressure.

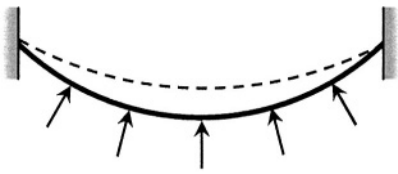

Figure 5.52 *Snap-through* buckling of an arch under external pressure

Figure 5.53 contains the qualitative load-deformation plots of these two buckling variants. Both situations follow the compression-defined path 1-2 up to the point 2 where they separate. In the case of bifurcation buckling, when the critical load is reached at point 2 the deflection increases substantially through bending-produced buckling with the compression force being constant and equal to the critical value. As a consequence, the line 2-3-4 is followed up to the point 4 where either the structure collapses or a limit is reached in deformation. The limit-load or snap-through buckling situation registers a jump in its load-deflection characteristic from point 2 to point 3 (as the 2-3 portion is inadmissible), and snaps to another bending state, shown qualitatively by the segment 3-5, up to the limit point 5. It should be noted that the segment 1-2 doesn't have to be identical for the two buckling cases, but it was drawn so in order to simplify the graphical representation.

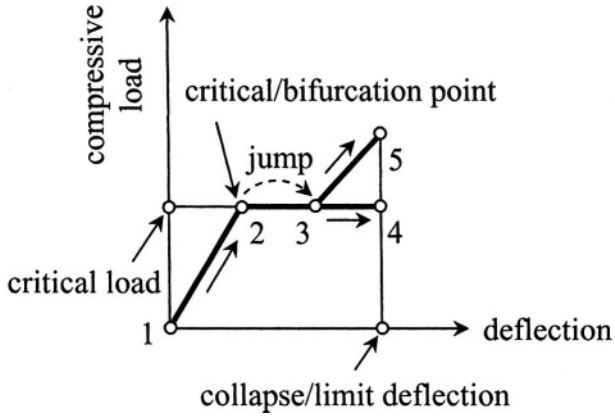

Figure 5.53 Bifurcation versus snap-through buckling

The buckling cases discussed so far (and which are retrieved in significant numbers of MEMS applications) were produced by bending/flexure. There are however cases where buckling is generated through torsion (such as for thin-walled open-section members) or through mixed bending and torsion (for coupled bending-torsional cases), but these situations are beyond the scope of this presentation. Also, from a structural standpoint, members that can buckle include columns (which can sustain only axial loads), beam-columns (which can sustain bending loads, in addition to axial loads), rigid frames (which are formed of two or more rigidly-attached beam-columns), or plates/membranes. The presentation will be limited here to columns and beam-columns (both straight and curved), as the majority of buckling-related MEMS applications are based on these structural members.

Buckling can be either elastic or inelastic, depending on the way the buckling stresses do compare to the *proportionality limit* σ_p, which is shown in the plot of Fig. 5.54 for a ductile material. Long and thin (slender) columns for instance buckle at stress levels that are less the proportionality limit, where the stress-strain characteristic becomes non-linear (the material no longer obeys the Hooke's linear relationship). This type of buckling is therefore elastic and this is the desired form of buckling in MEMS applications, as the microcomponent recovers its original shape after the load has been removed. Relatively short components are generally prone to inelastic buckling, as part of their cross-section is already in the non-linear portion of the stress-strain characteristic of Fig. 5.54 (the 2-3 portion), and therefore this type of buckling is inelastic, so the micromember does not completely regain its original shape. Unless the buckled micromember is going to be discarded, this condition is to be avoided in buckling design.

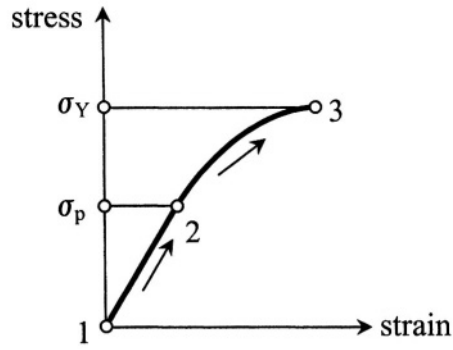

Figure 5.54 Stress-strain curve for a ductile material

7.2 Columns and Beam-Columns

Columns and beam-columns (straight, curved and bent) will be studied next by analyzing their behavior in the elastic domain.

7.2.1 Straight Beam-Columns

The main problem with the elastic buckling is establishing the minimum compressive force (the *critical load*), which is capable of producing buckling. One method of solving this problem is formulating and solving the differential equation of a column subjected to axial compressive load. Most often, the pinned-pinned configuration of Fig. 5.55 is taken as the paradigm example, and will also be utilized here.

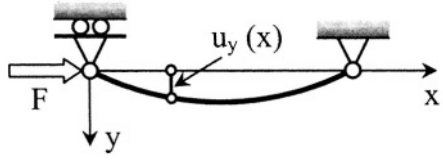

Figure 5.55 Pinned-pinned column in buckling.

The pinned-pinned column is originally straight and its length is 1. Figure 5.55 shows it in buckled condition and indicates the generic deflection $u_y(x)$ which is generated through the action of the compressive axial load F applied at the moving pinned end. The differential equation governing the static bending of this member is:

$$EI_z d^2u_y(x)/dx^2 = -M_z \tag{5.148}$$

As Fig. 5.55 indicates, the bending moment is:

$$M_z = Fu_y(x) \tag{5.149}$$

such that substitution of Eq. (5.149) into Eq. (5.148) results in:

$$d^2u_y(x)/dx^2 + k^2u_y(x) = 0 \tag{5.150}$$

where:

$$k^2 = F/(EI_z) \tag{5.151}$$

From basic differential calculus, it is known that the solution to the homogeneous differential equation (5.150) is of the form:

$$u_y(x) = A\cos(kx) + B\sin(kx) \tag{5.152}$$

where A and B are integration constants that are determined from the boundary conditions. When x = 0, the deflection at that point is $u_y(0) = 0$, and Eq. (5.152) gives A = 0. Similarly, when x = 1, $u_y(l) = 0$, which, after substitution into Eq. (5.152), gives the non-trivial solution:

$$\sin(kl) = 0 \tag{5.153}$$

Equation (5.153) is equivalent to:

$$kl = n\pi, n = 1,2,3,... \tag{5.154}$$

which, combined to Eq. (5.151), gives the equation of the forces that produce buckling as:

$$F = n^2\pi^2 EI_z/l^2 \tag{5.155}$$

Out of the set of forces that are obtained when n = 1, 2, 3,..., the critical buckling load is the smallest one, corresponding to n = 1, and therefore:

$$F_{cr} = \pi^2 EI_z/l^2 \tag{5.156}$$

Boundary conditions that are different from the ones of Fig. 5.55 are also possible in other buckling-related problems, as shown in Fig. 5.56. The

critical buckling load can be calculated for each case following the procedure used in determining the critical load for a pinned-pined column, as detailed in Chen and Lui [6] or Chajes [7]. The critical load can be expressed in the generic manner:

$$F_{cr} = \pi^2 E I_z / l_{eff}^2 \tag{5.157}$$

where l_{eff} is called the *effective length* and is calculated by means of the effective-length factor K as:

$$l_{eff} = Kl \tag{5.158}$$

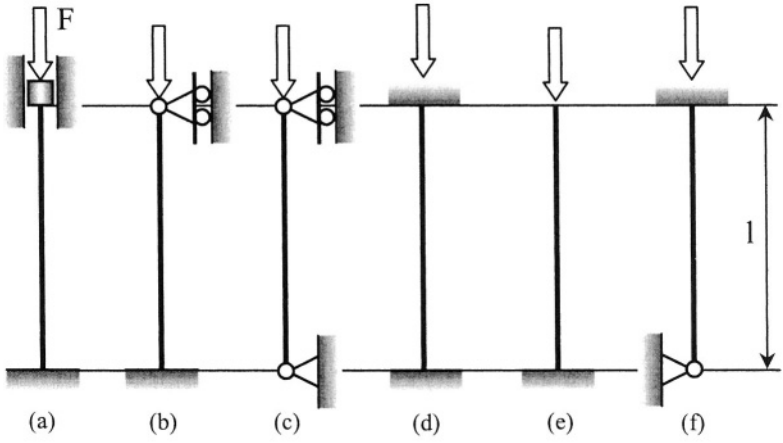

Figure 5.56 Combinations of ideal boundary conditions for beam-columns in buckling: (a) guided-fixed (K = 0.5), (b) pinned-fixed (K = 0.7), (c) pinned-pinned (K = 1), (d) fixed-fixed (K = 1), (e) free-fixed (K = 2), (f) fixed-pinned (K = 2)

Figure 5.56, which shows other combinations of boundary conditions for beam-columns subjected to buckling, also gives the corresponding values of K – after Chen and Lui [6].

Another measure of the elastic buckling is the *critical stress,* which is produced by the compression load, and which can be calculated as:

$$\sigma_{cr} = F / A = \pi^2 E I_z (l_{eff}^2 A) \tag{5.159}$$

By using the *radius of gyration,* which is defined as:

$$r = \sqrt{I_z / A} \tag{5.160}$$

and the *slenderness ratio,* which is:

$$\lambda = l_{eff} / r \tag{5.161}$$

the critical stress of Eq. (5.159) becomes:

$$\sigma_{cr} = \pi^2 E / \lambda^2 \tag{5.162}$$

The critical stress σ_{cr} is plotted against the slenderness ratio λ in Fig. 5.57.

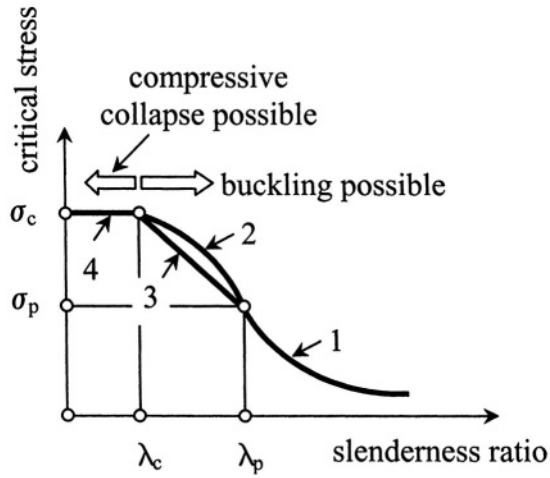

Figure 5.57 Plot of critical stress against the slenderness ratio

The curve denoted by 1 is the graphical representation of the critical stress – slenderness ratio of Eq. (5.162), and therefore the elastic buckling is only possible for values lager than the value λ_p, which corresponds to the material proportionality limit. For values smaller than λ_p, which apply to shorter columns – as the definition Eq. (5.161) shows it, the column might buckle inelastically (the portions 2 or 3) or, for very short columns, buckling is not even possible (the segment denoted by 4). The curve 2 for instance represents the *Engesser model* for inelastic buckling, which uses a formula similar to the one corresponding to the elastic buckling of Eq. (5.162). The only difference with this model is that Young's modulus is no longer constant, and is taken as either the tangent or secant value from the experimental stress-strain curve, or as an average combination of the two values. Another solution is the *Tetmajer-Jasinski model,* which expresses a linear relationship between the critical stress and the slenderness ratio. While the Engesser model works better for metallic components, the Tetmajer-Jasinski model is

more appropriate for aluminum-type materials – Chen and Lui [6]. In MEMS devices, however, the inelastic buckling is not desirable, and redesign has to be performed when a component is plausible to buckle inelastically.

Example 5.21

A guided-fixed beam-column, as the one sketched in Fig. 5.56 (a), which is intended to function as an out-of-the-plane actuator, is designed by mistake such that $\lambda = 0.2\ \lambda_p$. Take the necessary measures in order for the beam column to operate reliably as an actuator. The material of the microcomponent cannot be changed and the length is also specified.

Solution:

Because $\lambda < \lambda_p$, the beam-column will eventually buckle inelastically, as shown in Fig. 5.57, and this is an undesired condition. For elastic buckling it is necessary that the redesigned component have a slenderness ratio larger than the proportionality limit. By considering a rectangular cross-section defined by w and t (w being the in-plane dimension, and w > t), the slenderness ratio in the initial design can be expressed as:

$$\lambda_1 = K_1 l \sqrt{A / I_z} = 2\sqrt{3} K_1 l / t_1 \tag{5.163}$$

when taking into account that:

$$\begin{cases} A = wt \\ I_{min} = I_z = wt^3 / 12 \end{cases} \tag{5.164}$$

Obviously, the new slenderness ratio (of the redesigned microactuator) is expressed similarly as:

$$\lambda_2 = 2\sqrt{3} K_2 l / t_2 \tag{5.165}$$

and the intention is that:

$$\lambda_2 \geq 5\lambda_1 \tag{5.166}$$

in order to insure that the new slenderness ratio is at least equal to the proportionality limit λ_p so that buckling takes place in the elastic domain. Combination of Eqs. (5.163), (5.165) and (5.166) results in the following relationship:

$$K_2 t_1 / (K_1 t_2) \geq 5 \tag{5.167}$$

One way of realizing condition (5.167) is to change the current boundary conditions such that K increases. The highest theoretical value of K is 2, as shown in Fig. 5.56, and this corresponds to either a free-fixed condition – Fig. 5.56 (e) or a fixed-pinned one – Fig. 5.56 (f). This provision would transform Eq. (5.167) into:

$$t_2 \leq 0.8 t_1 \tag{5.168}$$

because $K_1 = 0.5$ and $K_2 = 2$, as indicated in Fig. 5.56. As a consequence, the microactuator will buckle elastically when the boundary is modified according to the previous discussion and when the cross-section thickness is reduced by at least 20%.

7.2.2 Curved Beam-Columns

A pinned-pinned thin curved beam of small curvature is now analyzed, as the one sketched in Fig. 5.58, in order to find its critical load by means of the *energy method.*

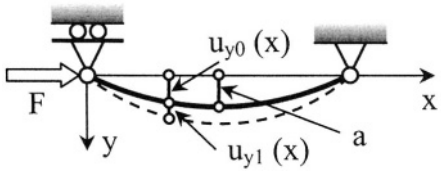

Figure 5.58 Pinned-pinned curved beam of small curvature under axial loading

The original shape of the beam is drawn with thick solid line, whereas the deformed (buckled) shape is shown with a dotted line. The original offset of the curved beam at a position x is denoted by u_{y0} (x) and the maximum offset a is located at the midpoint of the beam whose span is 1. The extra-deformation gained through axially-produced bending is denoted by u_{y1} (x), for the x-position. By following the standard procedure that enables finding the deformed shape of a pinned-pinned beam and under the assumption that the original curved shape of the beam is defined as:

$$u_{y0}(x) = a \sin(\pi x / l) \tag{5.169}$$

Timoshenko [4] derived the following solution for the bent shape of the curved beam:

$$u_y(x) = u_{y0}(x) + u_{y1}(x) = a / (1 - k^2 l^2 / \pi^2) \sin(\pi x / l) \tag{5.170}$$

The energy method which is utilized here as an alternative tool of calculating the critical load states that the strain energy stored in a deformed member is equal to the external work performed by the loads. In the case of the small-curvature beam of Fig. 5.58, only the bending effects have to be accounted for. As a consequence, the strain energy stored in the beam through bending is expressed as:

$$U = \int_0^l M_z^2 /(2EI_z)dx \tag{5.171}$$

The bending moment is produced by the axial force and is equal to:

$$M_z = Fu_y(x) \tag{5.172}$$

By substituting Eqs. (5.170) and (5.172) into Eq. (5.171), the strain energy can be calculated as:

$$U = a^2 lF^2 /[4EI(1-k^2 l^2/\pi^2)^2] \tag{5.173}$$

The work in this case is produced by the force F traveling over a distance u_{1x} about the x-axis, namely:

$$W = Fu_{1x} \tag{5.174}$$

The travel by the force F can be calculated as:

$$u_{1x} = 1/2\int_0^l [du_y(x)/dx]^2 dx \tag{5.175}$$

By taking the x-derivative of $u_y(x)$ of Eq. (5.170) and by substituting it into Eq. (5.175), the work of Eq. (5.174) becomes:

$$W = \pi^2 a^2 F /[4l(1-k^2 l^2/\pi^2)^2] \tag{5.176}$$

By considering the statement of the energy principle, namely:

$$U = W \tag{5.177}$$

it can be found that the critical force is equal to the critical force corresponding to a straight pinned-pinned beam.

The advantage of the curved design, as well as of the next design presented herein (the bent beam column), over the straight configuration is that the curved beam-column produces buckling unidirectionally (outside the curvature center), as it is improbable that buckling will occur the other direction. This feature can be used in applications where buckling is sought not to take place about certain directions, such as towards the substrate. At the same time, the buckling direction of a straight beam-column is completely unpredictable.

7.2.3 Bent Beam Columns

A design which is similar to the small-curvature curved beam of Fig. 5.58 is the one sketched in Fig 5.59. It consists of two symmetric beams which are rigidly attached at the middle of the span 1, and are slightly inclined, making a small angle α with the line joining the two end pins. This design, with different boundary conditions, was studied in the sensing/actuation chapter, when dealing with the bent beam thermal actuator. It is worth emphasizing that when the axial force is less than the critical buckling load, the microstructure still bends, although not through buckling, and this is also valid for the curved beam of the previous sub-section.

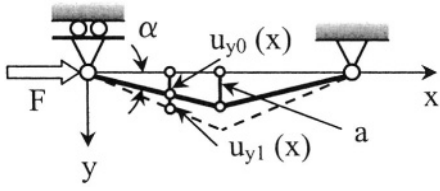

Figure 5.59 Pinned-pinned bent beam under axial loading

Determining the critical load can be done by using the energy method, similarly to the procedure applied to the curved beam. The loading by the force F is statically-equivalent to the loading by a force F_1 applied at the beam's midpoint, as shown in Fig. 5.60. The two loading systems are equivalent when the areas of the two bending moment diagrams are equal, as shown by Timoshenko [4], namely when:

$$Fal/2 = F_1 l^2/8 \tag{5.178}$$

The initial offset of a generic point of the bent beam of Fig. 5.60 is:

$$\begin{cases} u_{y0}(x) = 2ax/l, x < l/2 \\ u_{y0}(x) = 2a(x-l)/l, \text{ for } x > l/2 \end{cases} \tag{5.179}$$

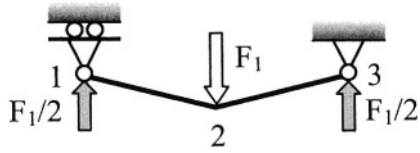

Figure 5.60 Equivalent loading of the pinned-pinned bent beam

The deformation produced through bending by the action of the force F_1 can simply be found by integrating the following differential equations:

$$\begin{cases} EId^2u_{y1}(x)/dx^2 = -F_1x/2, x < l/2 \\ EId^2u_{y1}(x)/dx^2 = -F_1x/2 + F_1(x - l/2), x < l/2 \end{cases} \quad (5.180)$$

and by using the appropriate boundary conditions that are zero deflections at points 1 and 3, as well as equal deflections and equal slopes at point 2. It can be shown that the total offset of the deformed beam is:

$$u_y(x) = \begin{cases} b\sin(kx), x < l/2 \\ b\sin[k(l-x)]), x > l/2 \end{cases} \quad (5.181)$$

where:

$$b = 4a\sin(kl/2)/[lk\sin(kl)] \quad (5.182)$$

By using Eqs. (5.171) and (5.181), it is found that the strain energy is equal to:

$$U = [l - \sin(kl)/k]b^2F^2/(4EI) \quad (5.183)$$

The work done by the axial force is:

$$W = [l + \sin(kl)/k]b^2k^2F/4 \quad (5.184)$$

By equating the strain energy U to the work W, according to the energy principle, gives the expression of the critical force:

$$F_{cr} = \pi^2EI/l^2 \quad (5.185)$$

which is also the solution for a straight beam of length l.

7.3 Post Buckling and Large Deformations

The critical load is found by means of the small-displacement theory, and this cannot predict the displacement/deformations of a beam-column at buckling or for conditions where the axial load exceeds the critical value. However, as mentioned previously, MEMS applications are being specifically designed to produce large output displacement through buckling and therefore knowledge of the true deformation of a buckled member is important. By using the large-deformation theory it is possible to predict the so-called *post-buckling* behavior of a microcomponent, as shown next.

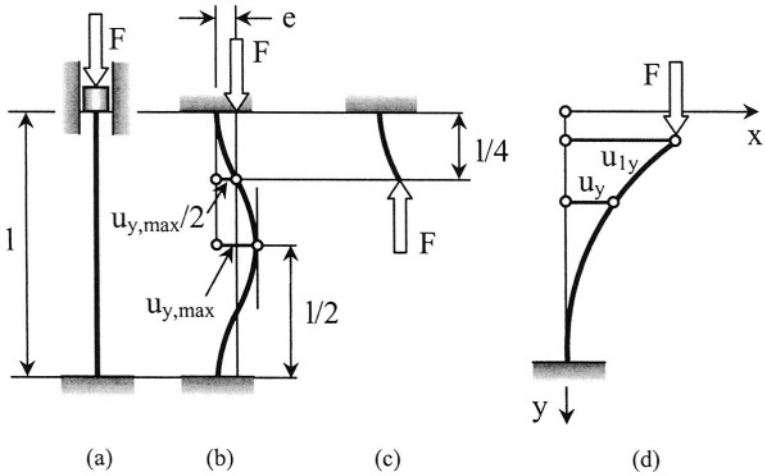

Figure 5.61 Postbuckling and large deformations: (a) straight guided-fixed column; (b) same column in buckled condition; (c) one-quarter length free-fixed column; (d) free-fixed column

The straight guided-fixed column of Fig. 5.61 (a) is the model for many MEMS components that utilize buckling/postbuckling to achieve either large displacements or actuation forces. When the axial force F exceeds the critical buckling value, large deformations are set and the column deflects as shown in Fig. 5.61 (b). The buckled shape of Fig. 5.61 (b) can be divided in four equal segments, one of them (of free-fixed boundary conditions) being shown in Fig. 5.61 (c). As Fig. 5.61 (b) suggests, there is a relationship between a guided-fixed column and a free-fixed one, the latter having the length equal to one quarter the length of the former, as mentioned by Timoshenko [4], for instance.

One consequence of this one-quarter-length relationship is that the buckling load of the guided-fixed column can be calculated from the

buckling load of the free-fixed column by using 1/4 instead of 1. Another important consequence is that the maximum postbuckling deflection of the guided-fixed column is twice the maximum postbuckling deflection of a free-fixed column with one quarter length, as shown in Figs. 5.61 (b) and (c). Calculating the maximum deflection of a free-fixed column is relatively easier and it follows the path described previously when studying the large deflections of a free-fixed beam under the action of a transverse force.

Figure 5.61 (d) is used to briefly formulate the maximum deflection of a postbuckled free-fixed column. By using the same reasoning that has been applied for the beam under the action of a transverse load – Fig. 5.44 – it can be shown that:

$$ds = -d\theta_z / [\sqrt{2}k\sqrt{\cos\theta_z - \cos\theta_{1z}}] \tag{5.186}$$

where ds, θ_z and θ_{1z} are indicated in Fig. 5.44 and k is given in Eq. (5.134). Equation (5.186), coupled to Eq. (5.133), gives the length of beam-column as:

$$l = 1/(\sqrt{2}k) \int_0^{\theta_{1z}} d\theta_z / \sqrt{\cos\theta_z - \cos\theta_{1z}} \tag{5.187}$$

Equation (5.187) is used to determine the force F (which is embedded in k by way of Eq. (5.134)) corresponding to a certain value of the tip slope θ_{1z}. The maximum tip deflection is found by combining Eqs. (5.186) and (5.131), namely:

$$u_{1y} = 1/(\sqrt{2}k) \int_0^{\theta_{1z}} \sin\theta_z d\theta_z / \sqrt{\cos\theta_z - \cos\theta_{1z}} \tag{5.188}$$

Example 5.23

Determine the maximum deflection of a guided-fixed microcolumn as the one sketched in Fig. 5.61 (a) under the compressive action of a force F = 44.4 μN, knowing l = 300 μm, w = 5 μm, t = 1 μm and E = 160 GPa.

Solution:

The critical load of a free-fixed microcolumn having the length equal to 1/4 the length of the analyzed microcolumn is determined by means of Eqs. (5.157) and (5.158) and of Fig. 5.56 (e) – showing that K = 2. The critical load is found to be equal to 1.827 μN. Solving for θ_{1z} in Eq. (5.187) gives a value of 100°, which is further utilized in Eq. (5.188) to find the maximum tip deflection of the free-fixed beam. This value, as mentioned previously, is half the maximum deflection of a guided-fixed microcolumn having four

times the length of the free-fixed microcolumn, which gives a value of $u_{y,max} = 119\ \mu m$ for the sought maximum postbuckling deflection.

8. COMPOUND STRESSES AND YIELDING

8.1 Introduction

Often times, normal and tangential stresses are produced concomitantly in deformable MEMS components. In such cases, the loading produced through actuation needs to ensure that the microcomponents that do deform, do so within the elastic range, so that the part regains its original shape after loading is relieved, and that they do not fail.

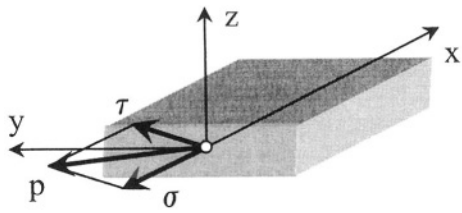

Figure 5.62 Normal (σ), tangential (τ) and resultant (p) stresses on a cross-section

Figure 5.62 shows the cross-section of a MEMS component where normal (perpendicular to the plane) and tangential (within the plane) stresses are produced and combined vectorially to get the resultant stress p. The normal stress σ can be produced by either bending or axial loading whereas the tangential stress τ, which is contained in the yz plane of the cross-section and which has components about the principal axes y and z, can be generated by torsion or shearing, as discussed in Chapter 1. The total stress p can be found as:

$$p = \sqrt{\sigma^2 + \tau^2} \tag{5.189}$$

Failure in MEMS, as the situation where a microcomponent does no longer perform as expected/designed, can occur in the forms of *fracture* (in the case of brittle materials), *yielding* (for ductile materials where the stresses exceed the yield limit), *excessive deformation* (either elastic or plastic), *buckling* or *creep* (deformation under constant load, especially at elevated temperatures) – see for more details Boresi, Schmidt and Sidebottom [3] or Cook and Young [8].

8.2 Yielding Criteria

The MEMS yielding failure will be discussed here under statical loading. In essence, a compound stress resulting from normal and tangential components needs to be less than a limit value in order for the microcomponent to operate reliably. In order to predict the yield response of structural components that are constructed of various materials and under different loading conditions, criteria have been formulated that enable transforming the complex loading into a simpler one, usually the uniaxial tension, for which experimental values of the yield stress are usually experimentally available. A brief presentation of the yield criteria that are most common are presented next, but the interested reader could consult more advanced texts dedicated to this topic, such as Boresi, Schmidt and Sidebottom [3], Ugural and Fenster [9] or Den Hartog [10], to cite just a few sources.

The *von Mises theory* considers that yielding begins when the distortion energy reaches the limiting value and therefore when it is equal to the distortion energy at yielding in a simple tension test. It is known from strength of materials that the actual state of stress and deformation in a component is the superposition (sum) of a *hydrostatic state* (which causes the structure to modify its volume without changing its shape) and a *distorsional state* (which only generates shape modification through pure-shear mechanisms, without altering the structural volume). By equating the distorsion energy corresponding to the real three-dimensional state of stress to the distorsion energy pertaining to a uniaxial tensile stress situation, the von Mises criterion (or theory) gives the following equivalent stress:

$$\sigma_{ech} = \sqrt{[(\sigma_x - \sigma_y)^2 + (\sigma_y - \sigma_z)^2 + (\sigma_z - \sigma_x)^2 + 6(\tau_{xy}^2 + \tau_{yz}^2 + \tau_{zx}^2)]/2} \quad (5.190)$$

It is sometimes considered that the von Mises theory is a particular case of a more generic theory, also known as the *Beltrami-Haigh (total energy) criterion,* which states that yielding initiates when the total strain energy of a structural component under complex loading equals the total strain energy corresponding to yielding in an uniaxial tension/compression. A common particular case of the general three-dimensional state of stress is the *state of plane stresses* where the only non-zero stresses are the normal stress σ_x and the tangential stress τ_{yz}, case where Eq. (5.190) reduces to:

$$\sigma_{ech} = \sqrt{\sigma_x^2 + 3\tau_{yz}^2} \quad (5.191)$$

The *Tresca criterion,* also known as the *maximum shear stress theory,* assumes that yielding most likely occurs when the maximum shear stress in a component under complex load is equal to the maximum (yield) shear stress

in uniaxial tension/compression. As a consequence, the equivalent stress by the Tresca criterion is formulated as:

$$\sigma_{ech} = \sigma_{max} - \sigma_{min} \tag{5.192}$$

where σ_{max} and σ_{min} are the maximum and minimum values of the three principal stresses σ_1, σ_2 and σ_3, which can be calculated as solutions of the third-degree algebraic equation:

$$\sigma^3 - I_1\sigma^2 + I_2\sigma - I_3 = 0 \tag{5.193}$$

with I_1, I_2 and I_3 – the stress invariant – being defined in terms of the three-dimensional state of stress components as:

$$\begin{cases} I_1 = \sigma_x + \sigma_y + \sigma_z \\ I_2 = \sigma_x\sigma_y + \sigma_y\sigma_z + \sigma_z\sigma_x - \tau_{xy}^2 - \tau_{yz}^2 - \tau_{zx}^2 \\ I_3 = \sigma_x\sigma_y\sigma_z + 2\tau_{xy}\tau_{yz}\tau_{zx} - \sigma_x\tau_{yz}^2 - \sigma_y\tau_{zx}^2 - \sigma_z\tau_{xy}^2 \end{cases} \tag{5.194}$$

In a plane stress situation, the Tresca theory predicts that:

$$\sigma_{ech} = \sqrt{\sigma_x^2 + 4\tau_{yz}^2} \tag{5.195}$$

Both von Mises and Tresca yielding criteria are working well for ductile materials.

Example 5.23

A microcantilever of constant rectangular cross-section is utilized in a AFM reading experiment, where, at a given moment in time, the following forces act at its tip, as shown in Fig. 5.63: F_{1x} = 1 μN, F_{1y} = μN and F_{1z} = 5 μN. Determine the maximum stress induced in the microcantilever when its narrow cross-section is defined by w = 20 μm and t = 2 μm. The length of the microcantilever, l = 250 μm, is measured between the vertex of its tip and the anchor root, and the distance h is equal to 5 μm. The microcantilever is metallic with a yield stress of σ_Y = 120 MPa.

Solution:

The most loaded cross-section of the microcantilever is the one located at the anchor root. Bending moments and axial tension combine to produce normal stresses, whereas the tangential stresses are generated by torsion when shearing is ignored. The loading at the microcantilever's fixed root comprises the following components:

$$\begin{cases} N = F_{1x} \\ M_y = F_{1z}l + F_{1x}h \\ M_z = F_{1y}l \\ M_x = F_{1y}h \end{cases} \tag{5.196}$$

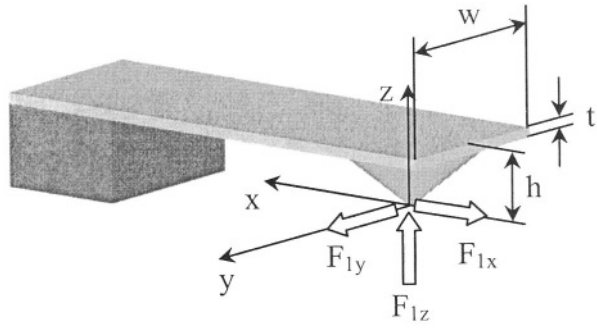

Figure 5.63 Microcantilever for AFM reading acted upon by three tip forces

The von Mises criterion reduces in the case of the constant cross-section to the form given in Eq. (5.191).

Figure 5.64 shows the variation of the normal bending stresses under the action of M_y and M_z, respectively.

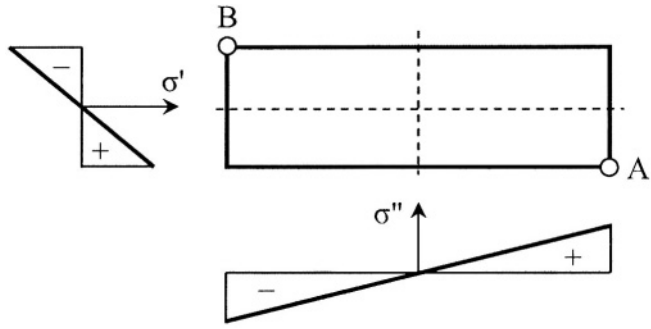

Figure 5.64 Bending-produced stresses over the cross-section

The bending-produced stresses are zero in the symmetry axes, and reach a maximum (either positive – corresponding to tension, or negative – corresponding to compression) on the outer fibers. The bending moment M_y

generates the normal stress σ' and M_z generates σ'', such that the resultant stress is their algebraic sum at any point of the cross-section. As Fig. 5.64 shows, at points A and B the sum is maximum, positive at A and negative at B. In addition to bending, the axial force N also produces tensile stresses σ''', which are constant over the cross-section. It follows that the maximum normal stress is found at A, and is tensile (positive):

$$\sigma_{max} = \sigma_A = \sigma'_A + \sigma''_A + \sigma'''_A = M_y t/(2I_y) + M_z w/(2I_z) + N/A \quad (5.197)$$

It is also known – see Boresi, Schmidt and Sidebottom [3] for instance, that for a narrow cross-section the maximum torsion-produced stress occurs also at one of the edge points – so either A or B – and is equal to:

$$\tau_{max} = 3M_x/(wt^2) \quad (5.198)$$

By recalling that the equivalent stress represents a maximum value, it follows that Eq. (5.195) becomes, by means of Eqs. (5.196) through (5.198):

$$\sigma_{ech} = \sqrt{\{6[(F_{1z}l + F_{1x}h)/t + F_{1y}l/w] + F_{1x}\}^2 + 27F_{1y}^2 h_2/t^2}/(wt) \quad (5.199)$$

The equivalent stress of Eq. (5.199) gives σ_{ech} = 101.6 MPa, which is smaller than the yield stress.

Example 5.24

A U-spring connects to a shuttle mass as in Fig. 5.65 (a). The spring is acted upon by the forces F_{1x} and F_{1z}. The U-spring is constructed of a ductile material with a yield stress of σ_Y = 100 MPa and the spring's cross-section is a narrow rectangle, as shown in Fig. 5.65 (b) with w = 10 μm and t = 1 μm. Known are also l_1 = 100 μm , l_2 = 20 μm, $l_3 = 2l_1$ and F_{1z} =1 μN. Determine the force F_{1x} which will keep the maximum stresses in the microsuspension at the yield threshold.

Solution:

When ignoring the stresses produced by axial and shearing effects, the three segments of the half-model of Fig. 5.65 (a) are subject to the combined action of bending and torsion. The maximum moments occur at the fixed position 4, namely:

$$\begin{cases} M_x = F_{1z}l_1 \\ M_z = F_{1x}l_1 \\ M_y = F_{1z}l_2 \end{cases} \quad (5.200)$$

The normal stresses in this case are produced by the two bending moments, and the maximum value occurs again at one vertex being of the form:

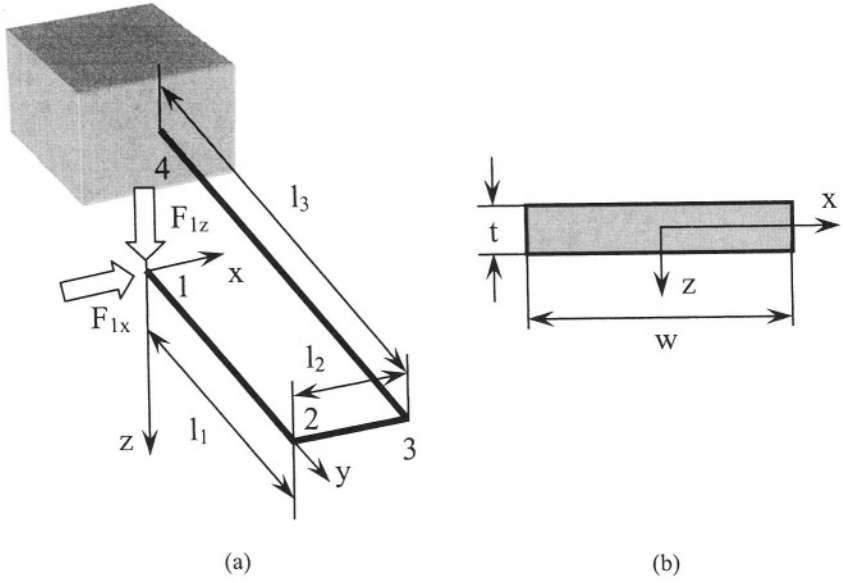

Figure 5.65 Model of a U-spring: (a) geometry and static loading; (b) cross-section

$$\sigma_{max} \approx \sigma = \sigma' + \sigma'' = M_x t/(2I_x) + M_z w/(2I_z) \tag{5.201}$$

Because the cross-section is narrow, the tangential stress which is caused by the torsion moment has its expression given in Eq. (5.198).The von Mises theory results in:

$$\sigma_Y = \sqrt{\sigma_{max}^2 + 3\tau_{max}^2} \tag{5.202}$$

which, by using Eqs. (5.200) and (5.201), gives $F_{1y} = 6.57\ \mu N$.

For this state of stress problem, the Tresca criterion becomes:

$$\sigma_Y = \sqrt{\sigma_{max}^2 + 4\tau_{max}^2} \tag{5.204}$$

The numerical data of this problem results in $F_{1y} = 6.55\ \mu N$.

Problems

Problem 5. 1

The precision-positioning microdevice shown in Fig. 5.66, utilizes transverse electrostatic actuation and a spiral spring. The displacement is

monitored by means of longitudinal electrostatic sensing in a controlled feedback loop. Dimension the electrostatic actuator area A for an initial gap $g_0 = 6\ \mu m$ such that minimum displacement increments $\Delta x = 0.01\ \mu m$ can be produced by minimum voltage increments $\Delta U = 0.5$ V. The spiral spring is defined by $l_1 = 150\ \mu m$, $l_2 = 80\ \mu m$, $I_z = 5 \times 10^{-25}\ m^4$ and E = 160 GPa. The electrical permittivity is $\epsilon = 9 \times 10^{-12}$ F/m. Also determine the pull-in voltage.

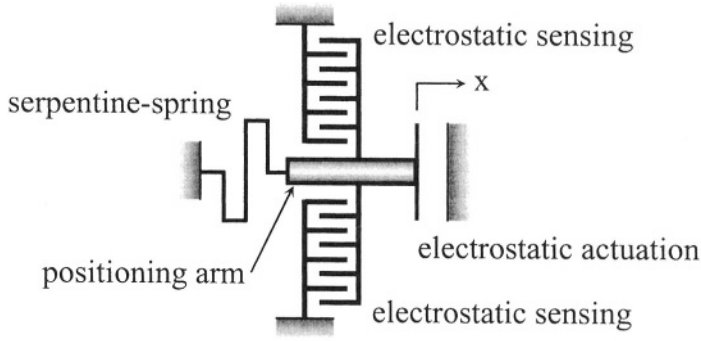

Figure 5.66 One-spring and electrostatic actuation

Answer:

$A = 315\ \mu m^2$; $U_p = 4.72$ V.

Problem 5.2

A microaccelerometer, as the one of Fig. 5.4 (a), uses a constant rectangular cross-section flexure hinge with $l = 150\ \mu m$, cross-section defined by $t = 2\ \mu m$ and $w = 10\ \mu m$, and E = 150 GPa. The tip mass has a length $l_m = 50\ \mu m$ and its mass is $m = 5\ \mu g$. The electrical permittivity is $\epsilon = 8 \times 10^{-12}$ F/m and the initial gap is $g_0 = 8\ \mu m$. The sensor has to be able to detect accelerations as small as $0.0098\ m/s^2$. Determine the voltage that is generated under these circumstances.

Answer:

U=10.11 V

Problem 5.3

The rotary electrostatic transducer of Fig. 5.6 (a) is used instead of the one studied in Example 5.3. Determine the number of beam suspensions having the cross-section defined by $w = t = 2\ \mu m$ that will make this microsystem perform identically to the one of Example 5.3 under identical actuation and geometrical/material conditions.

Answer:

n = 3

Problem 5.4

The microaccelerometer with two flexure microhinges of Fig. 5.67 uses double capacitance readout (parallel capacitance). Find the acceleration knowing that the maximum capacitance variation is $\Delta C = 8 \times 10^{-15}$ C and the voltage generated externally is U = 0.1 V. The microaccelerometer mass is $m = 10 \times 10^{-6}$ kg. Also known are $g_0 = 4$ μm, $\epsilon = 8.8 \times 10^{-12}$ F/m, A = 800 μm^2 (the capacitive area), as well as the parameters of the flexure microhinges: $l = 200$ μm, $w = t = 1$ μm, E = 155 GPa. (Hint: The total capacitance change is the sum of the capacitance variations at the two gaps).

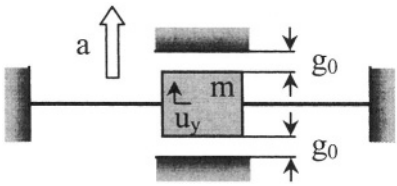

Figure 5.67 Microaccelerometer with double capacitance readout

Answer:

$a = 3.52 \times 10^{-6}$ N/m

Problem 5.5

A microdevice as the one shown in Fig. 5.68 is composed of an electrostatic longitudinal actuator and two beam suspensions, all connected by a central shuttle mass. The microactuator has the following defining parameters: $l_z = 10$ μm, $g = 1.5$ μm, $n = 20$ (the number of gaps), $\epsilon = 1.8 \times 10^{-12}$ F/m and the parameters of one microbeam are: $l = 100$ μm, $w = t = 3$ μm, E = 160 GPa. Find the longitudinal displacement of the shuttle mass when a voltage U = 80 V is applied to the electrostatic actuator unit.

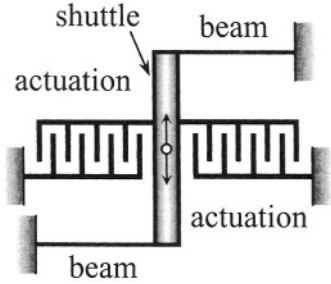

Figure 5.68 Microdevice with electrostatic actuation and beam suspensions

Answer:

Displacement = 2.62 μm

Problem 5.6

The microdevice in Fig. 5.69 combines electrostatic transverse actuation, longitudinal sensing, and two folded-beam microsuspensions. The actuation unit is defined by: $n_a = 20$, $l_y = 20\ \mu m$, $l_z = 10\ \mu m$, $g_{0,x} = 3.5\ \mu m$. The sensing unit has the following parameters: $n_s = 50$, $l_z = 10\ \mu m$, $g = 0.5\ \mu m$. The sensed capacitance change is 1.62×10^{-14} C for a voltage of 100 V actuation-supplied. Determine the model displacement of the central shuttle mass, as well as its real displacement for $\epsilon = 9 \times 10^{-12}$ F/m.

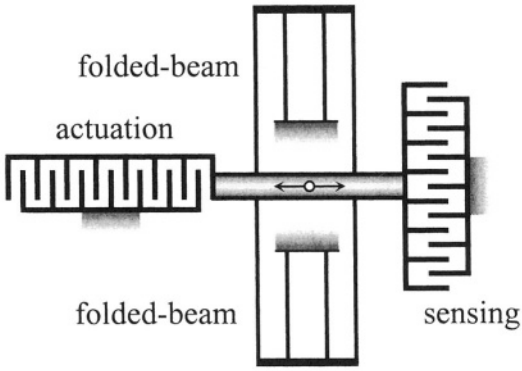

Figure 5.69 Microdevice with electrostatic transverse actuation, longitudinal sensing and folded-beam suspensions

Answer:

Model displacement = 1.92 μm

Experimental displacement = 1.8 μm

Problem 5.7

A torsional microdevice, as the one sketched in Fig. 5.70, is employed to measure the magnitude of an external magnetic field B, which is directed as shown in the same figure. The rotation angle is measured experimentally by optical means and its maximum value is $\theta_x = 1^o$. The radius of the current loop is $R = 100\ \mu m$, the current is $I = 5\ \mu A$ and the parameters defining the two constant cross-section torsion microhinges are $l = 100\ \mu m$, $w = 20\ \mu m$, $t = 1\ \mu m$ and $G = 62$ GPa. Find the external magnetic field B.

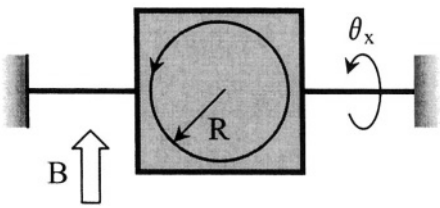

Figure 5.70 Electromagnetic-field sensor with two torsional microhinges

Answer:

B = 918.52 T

Problem 5.8

The microdevice in Fig. 5.71 is used as an angular electrostatic actuator (as in Fig. 5.17) in an application where a rotation angle of $\theta_x = 1.2^o$ needs to be achieved. Find the necessary voltage knowing that: $R = 100\ \mu m$, $l_1 = 300\ \mu m$, $l_2 = R/2$, $l_3 = 0$, $g_0 = 5\ \mu m$, $\epsilon = 9 \times 10^{-12}$ F/m. The torsion microhinges are defined by: $l = 80\ \mu m$, $w = 10\ \mu m$, $t = 1\ \mu m$ and G = 80 GPa.

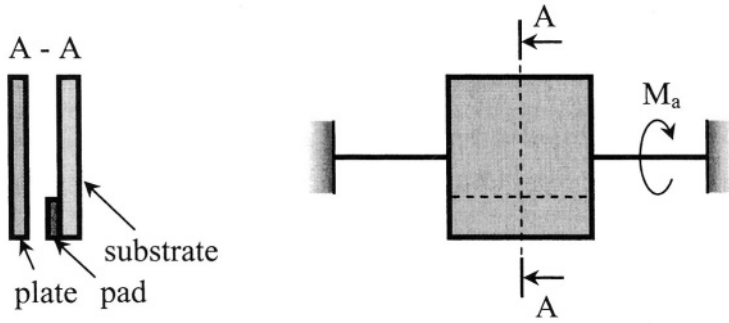

Figure 5.71 Angular electrostatic actuator with torsion microhinges

Answer:

U= 17.34V

Problem 5.9

The four-beam microaccelerometer in Fig. 5.72 is expected to sense an acceleration $a = 0.0001\ m/s^2$. Find the mass that will produce a displacement of the central mass $u_y = 0.01\ \mu m$ when the four identical flexure microhinges are defined by: $l = 260\ \mu m$, $w = t = 1\ \mu m$, E = 165 GPa.

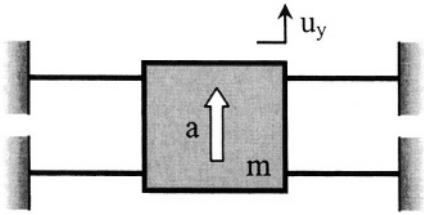

Figure 5.72 Microaccelerometer with four flexure microhinges

Answer:

$m = 93.88 \times 10^{-6}$ kg

Problem 5.10

The plate of the optical chopper in Fig. 5.13 is suspended by means of four inclined beams. Determine the minimum actuation force which is needed to displace the plate by a quantity $p = 0.1\ \mu m$. Ignore the plate's self weight, as well as the suspensions' stiffness about the z-direction.

Answer:

$F_a = 5.82\ \mu N$

Problem 5.11

The bimorph in Fig. 5.73 pushes the hinged mirror microplate with a force F_z such that an amplified out-of-the-plane motion u_z is obtained at the free tip of the microplate. A strain $\epsilon = 0.0002$ is induced in the bimorph. The bimorph is defined by the following geometric and material parameters: $l_a = 280\ \mu m$, $t_1 = t_2 = 5\ \mu m$, $w = 50\ \mu m$, $E_1 = 180$ GPa, $E_2 = 0.8\ E_1$. The two identical torsion microhinges have G = 75 GPa, $w = 4\ \mu m$ and $t = 0.6\ \mu m$. Also known are $l_1 = 10\ \mu m$ and $l_2 = 300\ \mu m$. Find the tip displacement u_z.

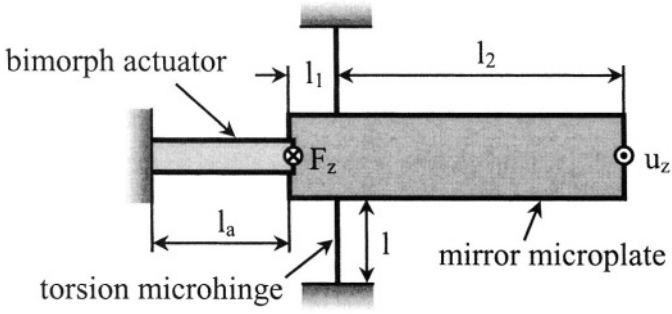

Figure 5.73 Displacement-amplification microdevice with bimorph actuation and torsion microhinges (top view)

Answer:

$u_z = 33\ \mu m$

Problem 5.12

Find the bloc force for a sagittal microdevice with curved flexure hinges, based on the quarter-model of Fig. 5.74.

Answer:

$$F_b = \{[C_{ux-Fx}\cos\alpha + C_{ux-Fy}(\cos\alpha + \sin\alpha) + (C_{ux-Mz} + C_{uy-Mz})c_{m1} + C_{uy-Fy}\sin\alpha]F\}/[C_{ux-Fx}\sin\alpha + C_{ux-Fy}(\sin\alpha - \cos\alpha) + (C_{ux-Mz} + C_{uy-Mz})c_{m2} - C_{uy-Fy}\cos\alpha]$$

$$\begin{cases} c_{m1} = (C_{ux-Mz}\cos\alpha + C_{uy-Mz}\sin\alpha)/C_{\theta z-Mz} \\ c_{m2} = (C_{ux-Mz}\sin\alpha - C_{uy-Mz}\cos\alpha)/C_{\theta z-Mz} \end{cases}$$

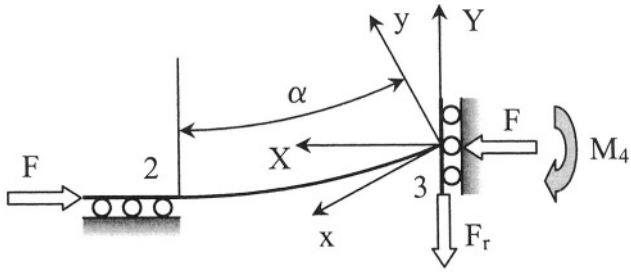

Figure 5.74 Reduced quarter-model of sagittal microdevice with curved flexure hinges

Problem 5.13

A fixed-free microbar having a length $l = 200\ \mu m$ and cross-section area $A = 0.2\ \mu m^2$ is used in a yield tensile test, which indicates that the axial force producing fracture of the microspecimen is $F = 500\ \mu N$ and that the corresponding maximum tip displacement is $3.1\ \mu m$. Find the values of Young's modulus according to the small- and large-deformation models.

Answer:

$E^l = 160$ GPa

$E^s = 129$ GPa

Problem 5.14

The slender microbeam of Fig. 5.75 is utilized to generate large displacements through buckling by means of a thermal actuator. The microbeam is defined by $l = 250\ \mu m$, $w = 5\ \mu m$, $t = 1\ \mu m$ and $E = 165$ GPa, and the actuator by $l_a = 500\ \mu m$, $w_a = t_a = 10\ \mu m$, $E_a = 180$ GPa, $\alpha = 3 \times 10^{-6}\ 1/^o$. The axial displacement at the actuator-microbeam junction is $u = 0.28\ \mu m$ when a temperature increase $\Delta T = 200^o$ is applied to the actuator. Establish if this condition is sufficient to produce buckling of the microbeam.

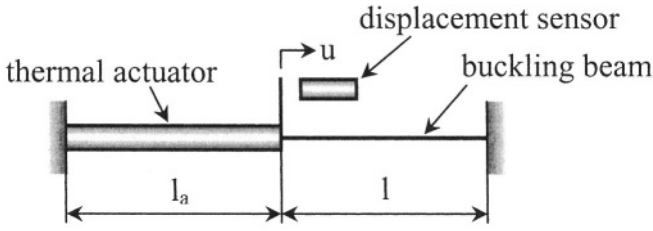

Figure 5.75 Buckling microdevice with thermal actuation and slender beam

Answer:

F = 720 μN (Eq. (4.7)), F_{cr} = 43 μN (for a guided-fixed beam); buckling possible

Problem 5.15

A microplate supported by two carbon nanorods of circular cross-section is used to sense external magnetic fields by means of a current loop, as shown in Fig. 5.76. Find the maximum torsion angle that would keep the stresses in the nanorods under an allowable limit τ_a. Known are the radius of the nanorods circular cross-section, r, their length l and the shear modulus G.

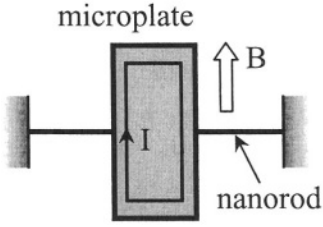

Figure 5.76 Magnetic microsensor with torsion nanorods

Answer:

$$\theta_{x,max} = l\tau_a /(Gr)$$

References

1. W. Geiger et al., Decoupled microgyros and the design principle DAVED, *Sensors and Actuators A,* 95, 2002, pp. 239-249.
2. R. Sattler, F. Plotz, G. Fattinger, G. Wachutka, Modeling of an electrostatic torsional actuator: demonstrated with an RF MEMS switch, *Sensors & Actuators A,* 97-98, 2002, pp. 337-346.
3. A.P. Boresi, R.J. Schmidt, O.M. Sidebottom, *Advanced Mechanics of Materials,* Fifth Edition, John Wiley & Sons, Inc., New York, 1993.
4. S.P. Timoshenko, *Theory of Elastic Stability,* McGraw-Hill Book Company, New York, 1936.
5. J.M. Gere, S.P. Timoshenko, *Mechanics of Materials,* Third Edition, PWS-KENT Publishing Company, Boston, 1990.
6. W.F. Chen, E.M. Lui, *Structural Stability. Theory and Implementation,* Elsevier, New York, 1987.
7. A. Chajes, *Principles of Structural Stability Theory,* Prentice Hall, Englewood Cliffs, 1974.
8. R.D. Cook, W.C. Young, *Advanced Mechanics of Materials,* Macmillan Publishing Company, New York, 1985.
9. A.C. Ugural, S.K. Fenster, *Advanced Strength and Applied Elasticity,* Third Edition, PTR Prentice Hall, Englewood Cliffs, 1995.
10. 1. J.P. den Hartog, *Advanced Strength of Materials,* Dover Publications, New York, 1987.

Chapter 6

MICROFABRICATION, MATERIALS, PRECISION AND SCALING

1. INTRODUCTION

This chapter reviews succinctly some of the microfabrication processes and materials that are currently being used in the MEMS technology. Lithography, surface micromachining, bulk micromachining, micromolding and stereolithography are presented, but existing literature which is specifically dedicated to microtechnology, discusses the aspects mentioned here in far more detail. Another segment of this chapter studies the imperfections that MEMS design still has to overcome, as material property variability, microfabrication limitations and simplifying assumptions in modeling constitute perturbations that alter the would-be ideal MEMS final product. The chapter concludes with a discussion of the scaling laws and of the implications they have when small-scale is involved. Of particular interest is the length and its influence on amounts studied in this book such as stiffnesses and transduction forces. As in the previous chapters, solved examples and proposed problems are included here.

2. MICROFABRICATION

Two basic microfabrication techniques that are used in MEMS production are sketched in Fig. 6.1. *Additive procedures,* as shown in Fig. 6.1 (a), start from a substrate material (such as a commercially-available silicon wafer) and build the microstructure from one free surface of the wafer by adding successively several layers. On the contrary, *subtractive procedures* – Fig. 6.1 (b), start from the same free surface of the substrate material and construct the structural feature by removing (etching away) material until the intended microdevice is obtained. The simple example of Fig. 6.1 is a microcantilever that can ultimately be produced by either of these two basic procedures.

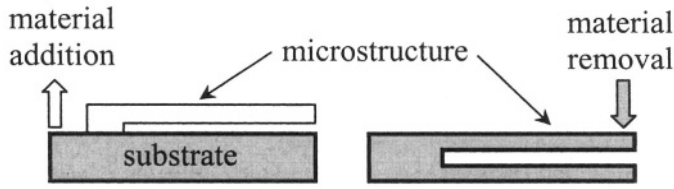

Figure 6.1 Basic MEMS fabrication procedures: (a) additive; (b) subtractive

Additive techniques are very diverse and they include processes such as *growth, physical vapor deposition* (PVD) – which can be performed by evaporation, sputtering, molecular beam epitaxy (MBE), laser ablation or ion plating –, *chemical vapor deposition* (CVD) – which can be done at atmospheric pressure (APCVD) or at low pressure (LPCVD) and can be enhanced by various energy sources such as plasma or laser –, *tape casting, sol-gel deposition, plasma spraying, spin/dip coating, self-assembled monolayers* (SAMs), *micro-spotting* or *microprinting.*

Subtractive microprocessing includes procedures such as *wet* and *dry etching, laser machining, focused ion-beam (FIB) milling, micro electrical discharge machining* (EDM) or *ultrasonic drilling.* An excellent resource material for both additive and subtractive microfabrication procedures is the monograph on microfabrication by Madou [1].

A brief presentation will be given here of the main microfabrication techniques that are currently being employed to produce mechanical microdevices, namely: *lithography, surface micromachining, bulk micromachining, molding,* and *microstereolithography* and *other techniques.* This is an abbreviated presentation, aimed at highlighting the specific fabrication means that are used to produce the micromechanical structures that have been addressed in this book. More details can be found in specialized monographs, such as those of Madou [1] or Gad-el-Hak [2] for instance.

2.1 Lithography

Lithography is a basic microfabrication procedure, which can be implemented in either additive or subtractive procedures. As Fig. 6.2 indicates, there are several lithography categories, such as optical, charged-particle, X-ray and nano-lithography, which will be discussed shortly. Figure 6.3 shows the main steps that are involved in a microlithographic process. In essence, any of the lithography processes mentioned in Fig. 6.2 starts with the deposition of the resist (a polymer that is sensitive to radiation) on top of a substrate material, which can be a commercially-available silicon wafer – Fig. 6.3 (a). This step is followed by selective exposure of the resist to radiation by means of a mask which has transparent areas – the white regions

in Fig 6.3 (b) – and areas that absorb the incident radiation – the black region in the same Fig. 6.3 (b).

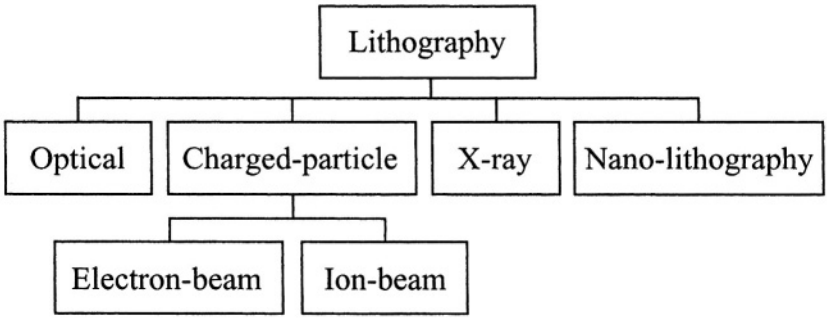

Figure 6.2 Lithography micro fabrication procedures

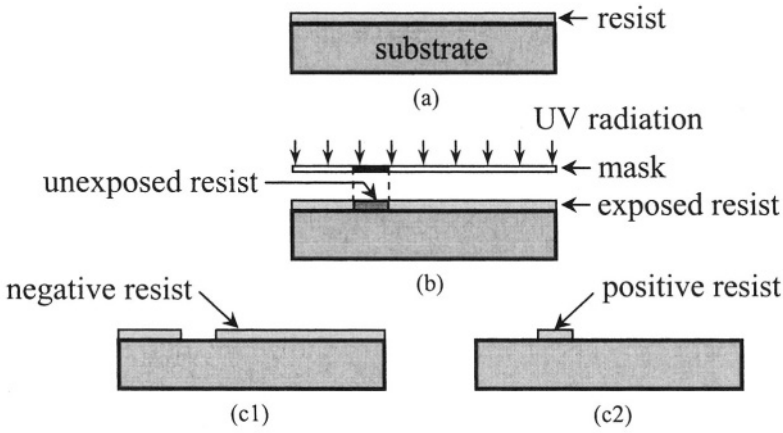

Figure 6.3 Lithography steps: (a) resist deposition; (b) resist exposure; (c1) development of negative resist; (c2) development of positive resist

The mask can either be placed in *contact* with the wafer (which poses problems such as mask alignment and contact deformation/stresses) or in close *proximity* (as in *shadow printing*) of the wafer within a few microns (which eliminates the contact stress problem but introduces limitations to resolution due to diffraction). Both methods produce a one-to-one latent image of the mask onto the resist. The *projection lithography* permits the mask to be spaced away from the wafer such that optic systems can be placed between the mask and the wafer with the effect of reducing the features that are transposed to the resist and of enhancing the resolution. The exposed and unexposed areas of the resist have different solubilities and the exposed

regions are further eliminated through selective dissolving. The radiation-exposed regions of *negative resists* are more soluble than the unexposed ones, whereas for *positive* resists the unexposed areas are more soluble, and therefore the corresponding final results are shown in Figs. 6.3 (c1) where a central cavity is produced in the exposed negative resist, whereas the positive resist of Fig 6.3 (c2) presents two side cavities.

The lithography variants shown in Fig. 6.2 will be described in the following.

2.1.1 Optical Lithography (Photolithography)

In photolithography, resists normally used in the integrated-circuit (IC) industry can be deposited in layers up to 2 μm thick with a film uniformity of 0.1 % through spin-coating techniques, whereby the wafer is rotated at 1000 – 2000 rpm and the viscous resist is layered and attaches to the substrate. Negative resists generally consist of two-components and are based on a rubber-like matrix. The most used positive resist is the polymethylmethacrylate (PMMA) – also utilized in X-ray lithography. The photoresists are usually removed after development but there are also permanent resists such as the polyimide, which can be used to produce flexible microcomponents in MEMS. Thicker photoresist layers can be achieved through casting, polymerization or by using thick sheets of dry resists. PMMA can be deposited in layers 1 cm thick, whereas the epoxy resin known as SU-8 (developed at IBM) can be layered in a single spin coat in films 500 μm thick.

The exposure is realized by using ultra-violet (UV) radiation, which can range from the extreme ultraviolet (EUV) limit defined by wavelengths of 10- 14 nm to the near ultraviolet (NUV) limit, with wavelengths of 350 – 500 nm. The development stage, where selected regions of the resist layer that have been exposed (for positive resists) or unexposed (for negative resists) to UV radiation will be removed, can be wet (through techniques such as immersion or spraying) or dry (by means of oxygen reaction ion etching O_2-RIE, for instance).

The main phases in a classical photolithography process are preceded and followed by various conditioning steps such as cleaning or pre- and post-baking, which are aimed at eliminating the possible contaminants and at assisting in completing the unfinished chemical reactions.

A qualifier that is used as a figure of merit in characterizing the performance of a specific microlithographic technique, but also any other microprocess, is the aspect ratio (AR), which can be defined, based on the prism shown in Fig. 6.4, as:

$$AR = t / min(l_1, l_2) \tag{6.1}$$

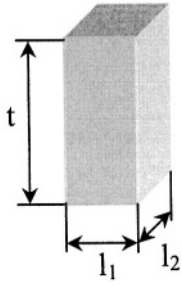

Figure 6.4 Geometrical dimensions of a prismatic feature obtained through lithography

The dimension t defines the thickness of the feature, which depends on the resist thickness, whereas the dimensions l_1 and l_2 describe the cross-section. In the case of photolithography based on the SU-8 material for instance, the aspect ratio can reach a value of 25.

2.1.2 X-Ray Lithography (XRL)

The photolithography techniques are designed to operate in vacuum environment, which challenges the cost-effectiveness of these procedures. Unlike them, the X-ray lithography (XRL) does not need vacuum because there are no particles involved in the process. The XRL uses very short wavelengths, in the range of 10 Angstroms, produced by different sources such as plasma, electron impact tubes and high-energy synchrotrons. The latter source is the most powerful, but also the most expensive. It is however the choice enabling exposure of 500 μm thick layers of PMMA resists (in the so-called deep X-ray lithography, or DXRL) because the specific energy required to produce vertical walls over such large thicknesses is of the order of 3000 J/cm^3, which is difficult to be obtainable by other X-ray sources. The PMMA resist can be deposited on the substrate material by spin-coating of successive thinner layers, by casting or by plasma polymerization.

Both contact and proximity (shadow) printing are feasible variants in XRL, which indicates that only 1:1 reproduction of the mask is possible. Unlike proximity printing in photolithography, which is known to be diffraction-limited, in shadow XRL the very small wavelength eliminates this inconvenience. However, the mask process is quite involved, as the blank regions need to possess good absorbance properties in order to bloc the high-energy X-ray radiation, and metals such as gold or tungsten are used as blanks. The transparent regions of the mask are realized by means of very thin layers of materials such as beryllium, titanium, silicon or silicon nitride.

The results produced through XRL/DXRL techniques include long vertical walls with runouts of less than 0.1 μm for 100 μm length (the *runout* measures the deviation measured perpendicularly to the vertical/thickness

dimension), high reproducibility, very good resolutions (small critical dimensions) and aspect ratios in excess of 100.

2.1.3 Charged-Particle Lithography

Lithography is also performed by using high-current densities in very narrow beams (diameters are in the nanometer range) consisting of either electrons or ions in a sequential (pixel-by-pixel) exposure of the planar domain. The technique is virtually a write-system, which only needs a software mask, stored in the computer's memory, and which is replicated point-by-point on the resist. However, both the *electron-beam lithography (EBL)* and the *ion-beam lithography (IBL)* need a vacuum environment and are serial techniques, which somewhat limit their throughput and cost-effectiveness. Both methods are based on the beam-resist interactions, which result in local solubility changes, which enable further removing of the exposed/unexposed area.

The EBL utilizes high-energy, focused narrow-beam electrons (with energies of the order of 100 keV) that interact and expose resists such as the PMMA. The method is based on short wavelengths (approximately 0.005 nm for 50 keV, as shown by Xia et al. [3]), which produces high resolution levels of 0.25 nm diameter spots. Structures with minimum dimensions in the order of 2 nm can be obtained from thin resist layers (up to 100 nm, which keeps the electron backscattering at low levels), but features of 50 nm can routinely be produced by EBL, as also pointed out by Xia et al. [3].

The IBL also known as *FIBL (focused ion-beam lithography),* as already mentioned, uses ion beams for point-by-point exposure of a resist material. The ion source materials include liquid gallium, indium or gold. The so-called *ion projection lithography* (*IPL*) – Madou [1] – uses thin stencils (membranes with very small circular holes) to direct the incoming flow of hydrogen, helium or argon ions. Compared to the EBL, the IBL has a better resolution and a higher resist exposure sensitivity (almost two orders of magnitude higher, as mentioned by Xia et al. [3]).

2.1.4 Nanolithography

A more comprehensive review of other lithography-based techniques that enable nanofabrication in the combined form of *writing* (creation of a transferable pattern) and *replication* (transfer of a pattern to a material) is given by Xia et al. [3], and Madou [1] for instance, and the main aspects characterizing these methods will be just highlighted here.

Atomic force microscopy (AFM), scanning tunneling microscopy (STM), near-field scanning optical microscopy (NFSOM) or *scanning electrochemical microscopy (SECM),* which are normally used to characterize/define three-dimensional topography at atomic level, can be used to generate patterns in resist materials (through direct contact or through

proximity interaction), patterns which are further exposed and developed in order to produce very fine lithographic architectures.

The *soft lithography* technique employs a patterned elastomer for replication on non-planar surfaces, materials that are not usually being used, or for large areas. Other lithography-based methods that produce features in the nanometer range are the *near-field phase-shifting photolithography* (which uses narrow, very-small-wavelength light sources that can be scanned at 10 nm of the resist surface and thus highly increase the resolution), *topographically-directed photolithography* (where a patterned photoresist layer is utilized instead of a mask to direct the UV radiation through the resist thickness in near-field optical domain), or *lithography with neutral metastable atoms* (where neutral atoms such as argon or cesium are used to directly etch patterns in monolayers through adequate masks).

2.2 Surface Micromachining

Surface micromachining is an integrated-circuit (IC)-related technique, which has a direct relationship with the complementary metal-oxide-semiconductor (CMOS) processes that are used to produce very large scale integration (VLSI) devices, as mentioned by Spearing [4]. Surface micromachining is essentially an additive process which deposits thin layers in a sequential manner on a substrate material.

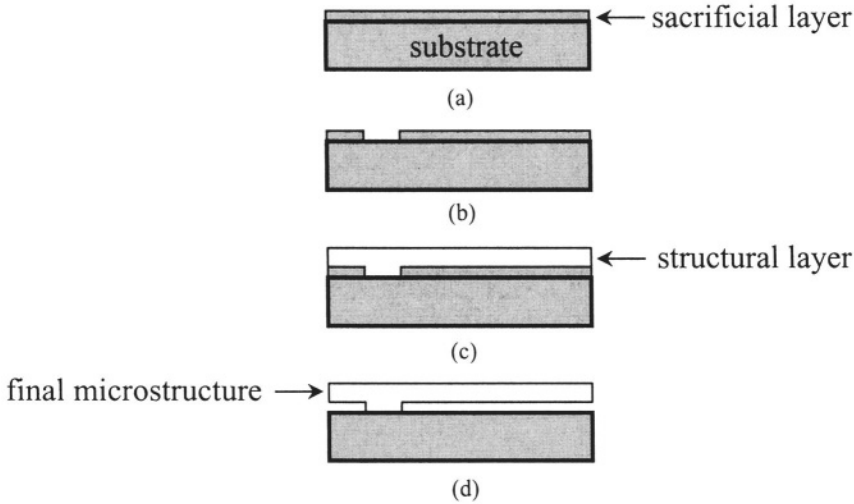

Figure 6.5 Surface micromachining process: (a) deposition of a sacrificial layer; (b) patterning of the sacrificial layer; (c) deposition of the structural layer; (d) etching of the sacrificial layer

Realization of a *structural layer* is produced in combination with another layer, named *sacrificial layer* (also *spacer layer* or *base*) through deposition,

patterning and etching. The very name of surface micromachining is connected to the prevalent planar nature of this process involving microstructures that are formed of thin film layers (thicknesses less than 10 μm). Because surface micromachining and CMOS are related, MEMS that are obtained through surface micromachining can integrate mechanical and electronic microcomponents. Figure 6.5 illustrates the main phases that compose a typical surface micromachining process. The basic process flow of Fig. 6.5 is usually repeated several times in order to obtain rather complex microdevices with thicker structural components. Sandia National Laboratories for instance produces MEMS through the 5-level SUMMiT (Sandia Ultra-Planar Multi-Level MEMS Technology) surface micromachining process, and the former Microelectronics Center of North Carolina offers the 3-level MUMPs (Multi-User Multi-Process) technique.

While the IC-related surface micromachining process emerged in the 1960's and was based on polycrystalline silicon (polysilicon), the first MEMS device was produced by Nathanson and coworkers at Westinghouse Research Laboratory in the mid 1960's, and consisted of a metallic microcantilever implemented in a resonant gate field-effect transistor (FET). The polysilicon has been introduced as the main component in surface-micromachined MEMS by researchers at University of California Berkeley in the mid 1980's, and has remained since then the main structural material utilized in surface micromachining. The preponderance of using polysilicon is due to its very good compatibility with the IC process (which has been pioneered by implementing polysilicon in microelectronics) and to the fact that polysilicon has mechanical properties which are controllable and reproducible (quasi-constant) within narrow error margins. Moreover, compared to single-crystal silicon, which is anisotropic, the polysilicon is isomorphic, and therefore is amenable to simpler mechanical design. Another important feature of polysilicon is the fact that it presents plastic deformation before fracture, whereas the silicon is known to be brittle. The polysilicon is usually deposited by low-pressure chemical vapor deposition (LPCVD) from silane, which can be combined with phosphane or diborane in order to yield doped film layers possessing electric conductivity.

Metals have also been used as structural layers in surface micromachining, and examples include aluminum, tungsten, gold, platinum, iridium, nickel or copper. Other materials that can be incorporated in surface-micromachined MEMS are the polyimide (utilized at creating large-deformation monolithic hinges), silicon nitride (which yields very thin layers with good surface quality), silicon oxide, diamond and silicon carbide (the last two materials being known for high mechanical hardness, chemical inertness and piezoresistive properties).

For polysilicon, the sacrificial layer can be produced out of silicon oxide or phosphosilicate glass (PSG). The accompanying etchant in these cases is hydrofluoric acid (HF), which is used in aqueous solution. For other structural materials, such as metals, the sacrificial layers can be built out of

organic films, as well as of polyimide and parylene, which can be etched away by means of dry plasma procedures.

While surface micromachining is fundamentally bound to produce relatively-thin MEMS, an alternative procedure developed by Keller and coworkers at University of California Berkeley and named HexSil was conceived to generate high aspect ratio microstructures by means of a process that combines surface micromachining and molding, as shown by Bustillo et al. [5], or Madou [1]. The HexSil process, which is pictured in Fig. 6.6, starts with a silicon wafer as the substrate material.

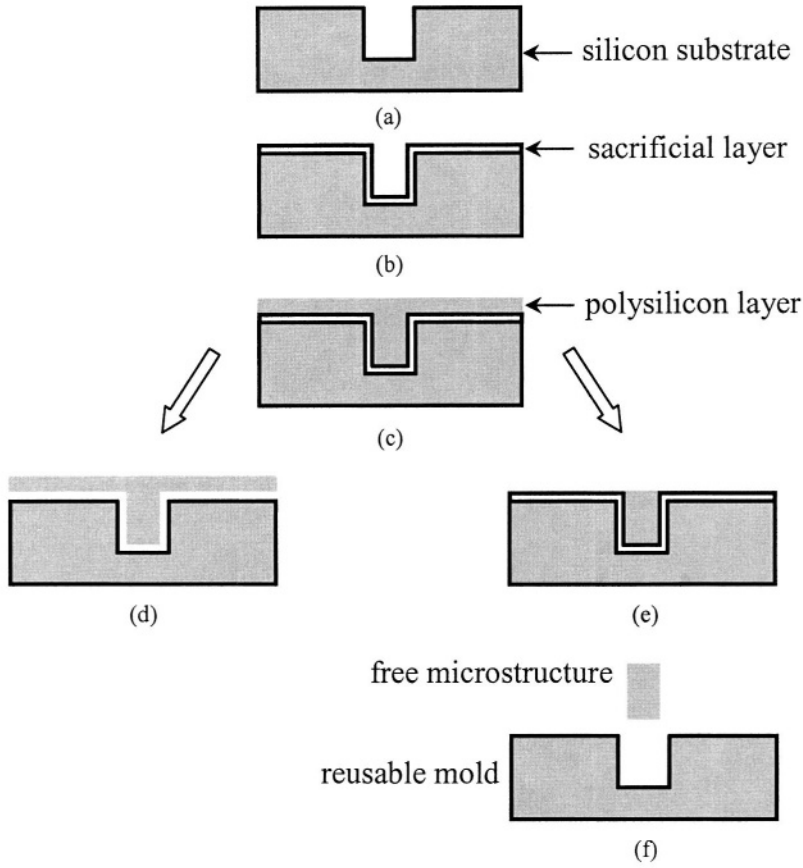

Figure 6.6 HexSil process: (a) DRIE etching of deep vertical trench; (b) deposition of sacrificial layer; (c) deposition of the structural polysilicon layer; (d) etching of the sacrificial layer; (e) chemical-mechanical polishing; (f) etching of the sacrificial layer and full release of microstructure

A deep trench (approximately 100 μm long) is microfabricated in the silicon substrate, as shown in Fig. 6.6 (a), by means of *deep reaction ion-enhanced etching* (DRIE). An oxide sacrificial layer is conformally deposited over the trench and the exposed wafer horizontal surface, as pictured in Fig.

6.6 (b). Over the sacrificial layer and filling the remaining trench gap, polysilicon is deposited, as suggested in Fig. 6.6 (c). The trenched silicon substrate can be used as a mold for another round of HexSil microfabrication. Two different variants are further possible, one being suggested in Fig. 6.6 (d), where the sacrificial layer is directly etched and the resulting polysilicon structure shown in that figure can either be fully released and utilized in further applications or can be still attached to the silicon substrate by hinges not shown in the figure. The second route is shown in the sequence of Figs. 6.6 (e) and 6.6 (f) and consists of chemical-mechanical polishing of the top polysilicon layer – Fig. 6.6 (e), followed by etching of the sacrificial layer – Fig 6.6 (f), which will completely release the structure with the shape shown in this last figure.

2.3 Bulk Micromachining

MEMS bulk micromachining is aimed at removing (etching away) relatively large amounts of material from a substrate in order to produce mechanical devices that can move/deform. Compared to surface micromachining, where the total thickness/depth of a microdevice was technologically limited by the layer thickness and the number of layers, deeper features can be obtained in bulk micromachining, which enables delivering more power/force by the resulting microdevices.

Bulk micromachining procedures can be divided into *wet* and *dry,* the latter category including vapor-phase etching and plasma-phase etching, as shown in Fig. 6.7. These techniques will be discussed shortly. Figure 6.8 gives the process flow for a generic bulk micromachining process yielding a microcantilever for instance. A patterned mask is first layered on top of a substrate such as a silicon wafer – Fig. 6.8 (a). Etching of the two channels shown in Fig. 6.8 (b) follows and eventually, side etching is applied to undercut the microcantilever, as sketched in Figs. 6.8 (c) and 6.8 (d).

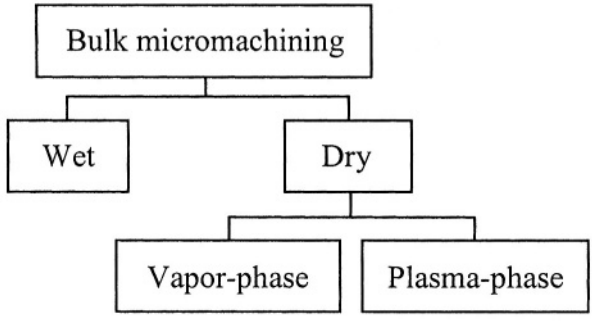

Figure 6.7 Main fabrication techniques in bulk micromachining

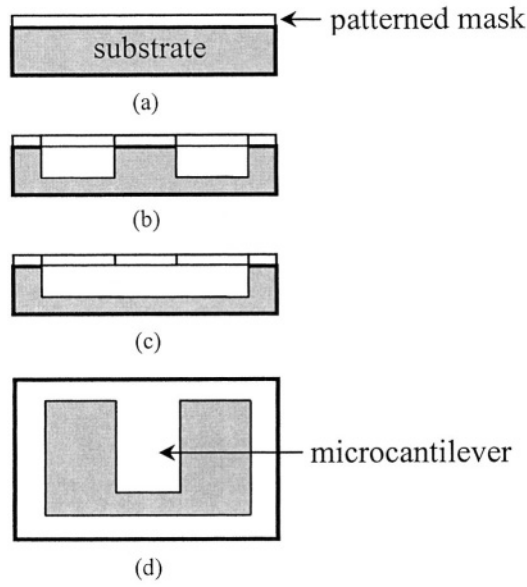

Figure 6.8 Bulk micromachining of a microcantilever: (a) deposition and patterning of a mask; (b) etching of the side channels; (c) undercutting and partial freeing of the microcantilever; d) top view of the microcantilever

Although materials such as quartz, germanium and compounds of gallium and silicon have been reported being used as substrate bases for bulk micromachining – see Madou [1] for more details, the silicon is largely the preferred material utilized for MEMS such as sensors and actuators that are obtained by means of this procedure. Crystalline silicon is commercially available in circular wafers, the most common being the 4 in (100 mm) diameter, 525 μm thick variant and the 6 in (150 mm) diameter, 650 μm thick version. Also available are silicon wafers of 8 and 12 in diameter which are mostly employed in research applications. The silicon is an anisotropic crystalline material with a diamond-like lattice. By using the *Miller-indices* notation, according to which a lattice unit is defined by three Cartesian directions, [100], [010] and [001] – as sketched in Fig. 6.9 (a), it is known that crystalline silicon has three principal planes of anisotropy that are denoted by [100] – Fig. 6.9 (a), [110] – Fig. 6.9 (b) and [111] – Fig. 6.9 (c). Wafers can be cut parallel to one of these three planes and therefore the resulting substrates are named (100) – , (110) – and (111) – oriented silicon wafers. More details on the crystal structure of the silicon and the anisotropy planes can be found in Madou [1] for instance. Experiments with etching of silicon have shown that [111] planes act as etch stoppers as etching rates along directions perpendicular to these planes are substantially lower than

about other directions. This feature is employed in conveniently designing MEMS that can be realized through anisotropic etching.

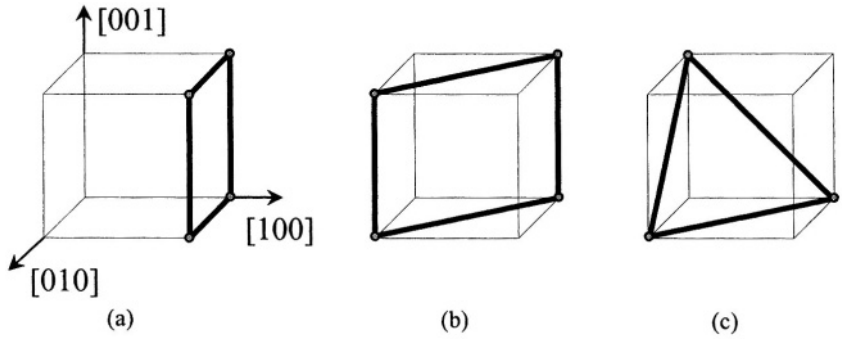

Figure 6.9 Miller indices and planes of interest in a silicon lattice: (a) (100)-oriented silicon; (b) (110)-oriented silicon; (c) (111)-oriented silicon

Figure 6.10 shows one instance of isotropic etching (that can use a metallic substrate) and two examples of anisotropic etching of silicon.

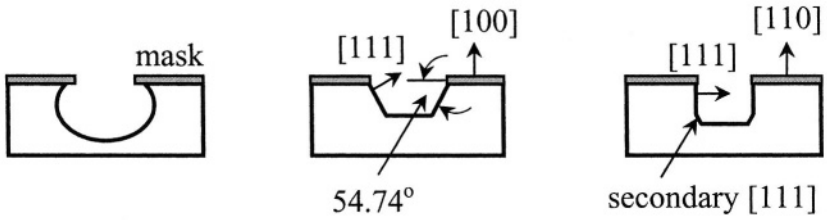

Figure 6.10 Examples of bulk micromachining: (a) isotropic; (b) anisotropic etching of (100) silicon; (c) anisotropic etching of (110) silicon

In isotropic etching the etch rates are equal about any direction and the shape carved in a substrate is like the one illustrated in Fig. 6.10 (a). For a (100) silicon wafer – Fig 6.10 (b), the [111] planes are inclined at 54.74° with respect to the [100] direction (the wafer surface) and because etching rates about directions perpendicular to [111] planes are almost zero, etching stops (or is considerably slowed-down) at those planes. When the process is completed the trapezoid-like cavity of Fig. 6.10 (b) is obtained. For (110) silicon wafers, as the one sketched in Fig. 6.10 (c), the primary [111] planes are perpendicular to the [110] planes. While etching about the direction perpendicular to [110] proceeds with high speed, etching about the [111] direction is inhibited, and the result is the almost-vertical walls shown in Fig. 6.10 (c). Secondary [111] planes also exist at the bottom of the cavity, which locally stop etching and produce the slightly imperfect shape, as indicated in the same figure.

2.3.1 Wet Etching

Wet etching is produced by exposure of the substrate to reactant fluids that can remove material through chemical reactions either isotropically or anisotropically. *Isotropic etching* results in material removal at uniform rates about all directions and produces the rounded shape of Fig. 6.10 (a). The most popular etchant for silicon, as shown by Kovacs et al. [6] for instance, is the *HNA,* which consists of a mixture of hydrofluoric acid (HF), nitric acid (HNO_3) and acetic acid (CH_3COOH). Masking against isotropic wet etching can be ensured by materials such as silicon nitride or silicon dioxide. Light doping (either of the p- or the n-type) of silicon can also be employed for reducing the etching rate to approximately 150 times, as mentioned by Kovacs et al. [6].

Anisotropic etching of silicon is mainly based on the differing reaction speeds about the main anisotropic directions. One of the most popular anisotropic etchant is potassium hydroxide (KOH) and its etch rates about the meaningful directions are: 400 about the [100] direction and 600 about the [110] direction when the etch rate about the etch-stop [111] direction is taken 1 (see Kovacs et al. [6]). The *alkali hydroxide etchants,* such as KOH or NaOH are sometimes incompatible with CMOS technology as they may react with metallic components of the circuitry. The *ammonium hydroxide* (NH_4OH), especially the *quaternary ammonium hydroxide* known as *TMAH,* is CMOS-compatible and is usable in integrated MEMS, although the etching rates are slightly smaller than those produced by alkali hydroxides. *EDP* (ethylenediamine pyrochatechol) is another anisotropic etchant, which produces reductions of 50 times in contact with doped silicon. Like the alkali hydroxides, EDP might react with aluminum components, which is problematic in CMOS devices.

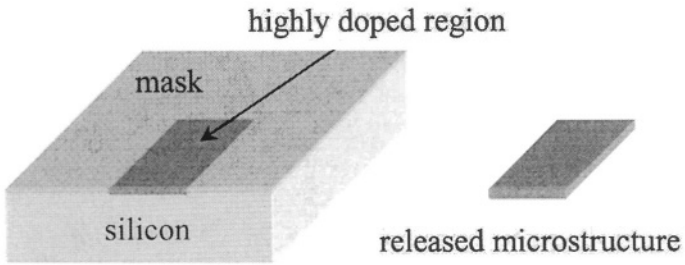

Figure 6.11 Fully-released microstructure by etching a highly doped silicon region

The etch-rate modulation through silicon doping can lead to the extreme design situation pictured in Fig. 6.11, where a highly p-doped (p++) area can

entirely release a structure through etching, and therefore can be a source of building independent micro/nano components that can further be utilized in other applications such as material property testing. This process is also known as the *lost wafer* – Kovacs et al. [6]. Etch rate modulation is also possible by changing the electrical potential between the silicon and the etchant. Wet etching, because of the molecular hydrogen, which is usually a reaction product, might generate local micromasking at the etched surface and further microasperities *(hillocking)* that decrease the surface quality. Among the countermeasures that can be taken to decrease surface roughness, the ultrasonic agitation has been shown to eliminate hillocking altogether.

2.3.2 Dry Etching

As mentioned previously, dry etching can be performed by using either vapor-phase or plasma-phase reactants. Vapor-phase etching is produced by various reactants, one of which is the *xenon difluoride* (XeF_2). This reactant is particularly selective to a large collection of materials, including Au, Al, TiNi, $SiNO_3$, SiO_2, and therefore is CMOS-compatible. It comes however with the down sides of producing relatively rough surfaces and of being able to react to water and further producing HF which might react to SiO_2 microcomponents/masks. A very good surface quality but at a lower etching rate is produced by *interhalogen gases* such as BrF_3 or ClF_3. The laser-driven vapor-phase (also known as LACE) procedure is an alternative which highly accelerates etching rates through very intense local heating and expulsion of free radicals by photolysis, such that very complex shapes can be obtained.

Plasma-phase etching, the other dry-etch category recourses to radio-frequency (RF) power sources through ions that can initiate chemical reactions at room temperature. Fluorine free radicals result from reactant gases in the plasma environment, which attack the silicon and produce SiF_4 that is etched away. Plasma etching is recognized to have high rates and to generate cavities isotropically. Procedures have also been designed to enable anisotropic etching by dry plasma. A solution, for instance, is to use *chlorofluorocarbons* during plasma bombardment with the result that polymer layers are deposited on the walls that are parallel to the ion attack. These layers act as protective coating, and therefore etching advances rapidly only about the ionizing direction. Another technique is the *reaction ion-enhanced etching* (RIE), which can generate structures with aspect ratios as large as 30:1. In RIE, cryogenic cooling of the wafer is utilized with the effect that condensation of reactant gases on the side walls slows down etching about directions perpendicular to these walls. A variant of RIE, the *deep reaction ion-enhanced etching* (DRIE), as mentioned, uses high-density plasma to produce long vertical walls, by applying anisotropic etching through a two-phase sequence composed of etching and protective layer deposition. Light ion exposure during the deposition phase prevents addition of the Teflon-like protective layer on the surface of plasma attack, and

therefore etching about this direction can advance very rapidly. Anisotropies of 30:1 (ratio of etch rates about the unprotected direction versus the protected directions) are reported to have been possible – Kovacs et al. [6]. *Variable anisotropy etching* is another alternative solution to anisotropic plasma-phase etching, which is implemented by switching between isotropic and anisotropic etching during ion exposure. A solution that provides complete etch stop is sketched in Fig. 6.12, where two silicon wafers are attached by bonding, one being bare silicon and the other one having a SiO_2 layer grown on it.

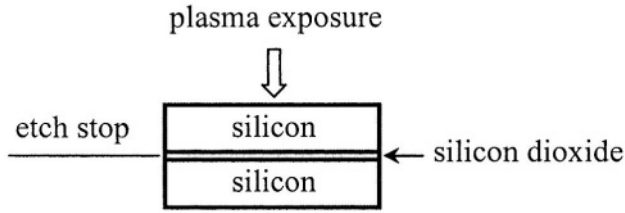

Figure 6.12 Buried etch-stop layer in plasma-phase etching

2.4 Micromolding and the LIGA Process

The MEMS fabrication by means of micromolding creates mechanical microdevices by using a pre-fabricated mold for deposition of the structural material. The surface micromachining HexSil process, which has previously been described, utilizes molding of polysilicon in order to obtain a fully- or partially-released structure. The reusable polysilicon that results after completion of the HexSil variant with fully-released microstructure – Fig. 6.6 (f) – can further be utilized to electroplate a metal on the surface of the polysilicon mold, followed by planarization – Fig 6.13 (a). The metal part is then separated from the master mold, as shown in Fig. 6.13 (b), and can either be used as it is, or can subsequently be used as a mold insert in *precision plastic replication process,* such as *casting, injection molding* or *hot embossing.* Figure 6.13 (c) pictures the schematic of a hot embossing process where the mold insert is pressed against the fluid plastic, which after cooling will retain the shape impressed by the metal mold. The resulting plastic part can either be used per se or can be a lost mold and may generate metal parts in a second electroforming process, as mentioned by Madou [1].

The LIGA acronym comes from the German words Lithographie, Galvanoformung, Abformung meaning lithography, electroplating and molding. Therefore, LIGA is a mixed process consisting of the three microfabrication techniques mentioned above. X-ray lithography and electrodeposition of metals (which is the combination of the first two LIGA phases) were achieved at IBM in the 1975s by Romankiv and coworkers who reported production of high aspect-ratio gold microstructures. The full LIGA

process was first introduced in Germany in the early 1980's by Ehrfeld and coworkers, who added the molding process to the lithography-electroplating sequence, as a way of obtaining very precise micro-scale parts in a very cost-effective way.

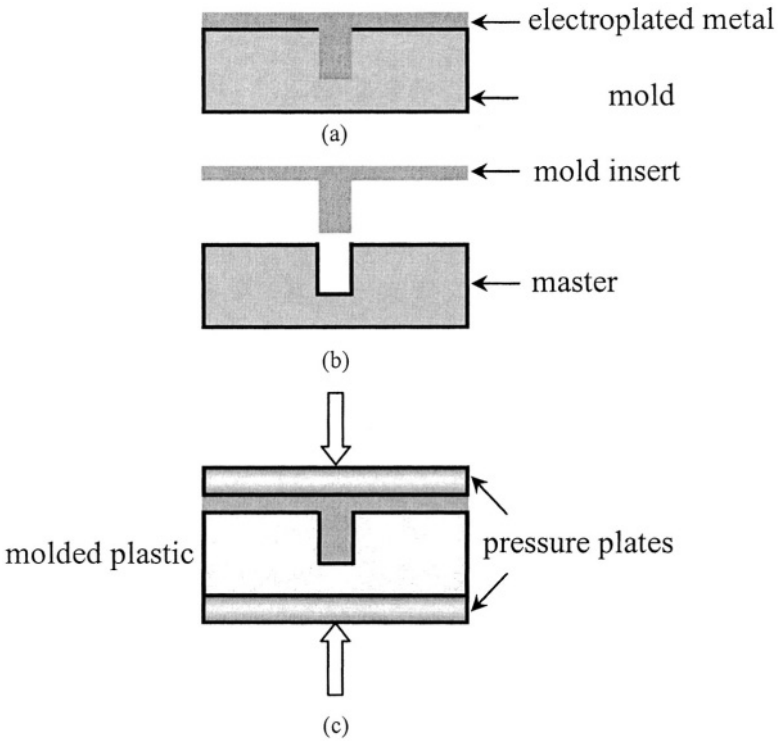

Figure 6.13 Micromolding process: (a) electroplating and planarization of metal; (b) separation of metal mold and master; (c) utilization of the metal mold as an insert in precision plastic hot embossing

Figure 6.14 shows the main steps of a variant of the LIGA process, called SLIGA, which includes the additional step of including and removing a sacrificial layer – see Guckel [7]. It should be mentioned that the typical LIGA process is a single-level microfabrication method which produces fixed prismatic parts. The addition of sacrificial layers such as in the SLIGA technique, results in free, partly-attached members, that can be utilized in MEMS. Utilization of deep X-ray lithography (DXRL) for patterning of thick PMMA resists facilitates microfabrication of metallic parts with large aspect ratios, and application of multiple LIGA steps results in high-aspect ratio systems (HARMS). Transfer of the mask pattern onto the resist layer is performed on a 1:1 scale by means of proximity printing. Advantages of the

LIGA process include the following ones, as mentioned by Malek and Saile [8]: very large structural heights (depths) – up to the order of centimeters – as

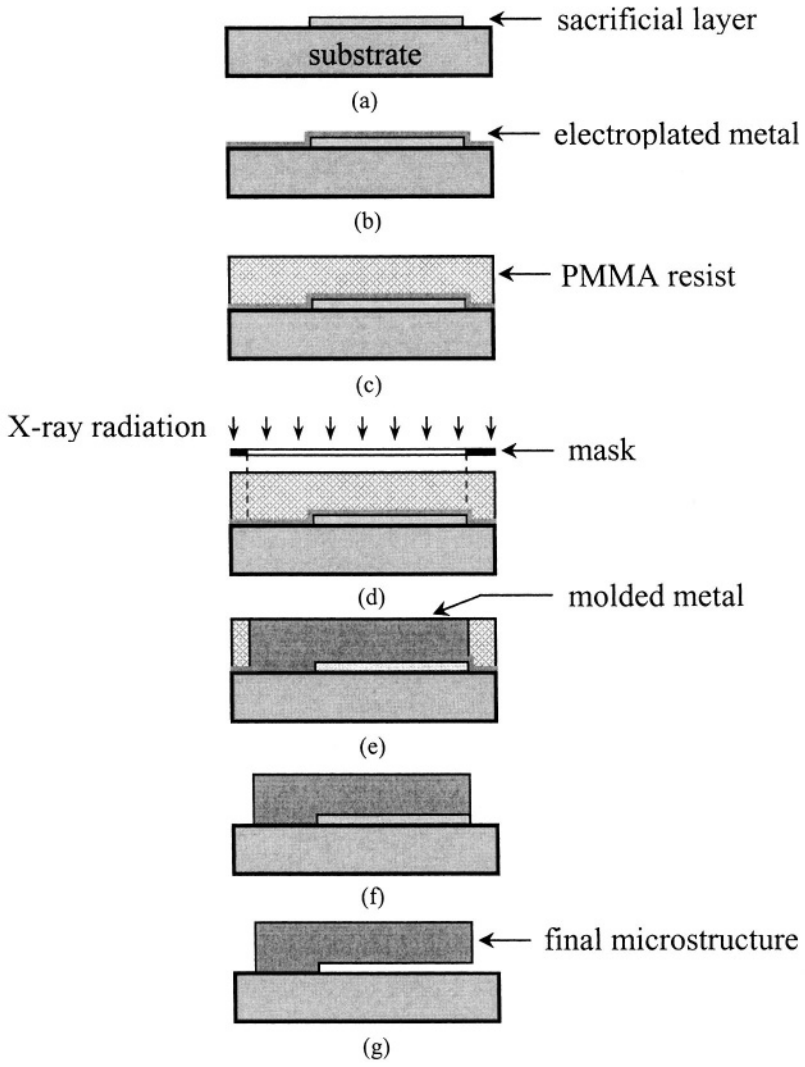

Figure 6.14 The sacrificial LIGA (SLIGA) process: (a) application and patterning of a sacrificial layer; (b) metal electroplating; (c) PMMA resist deposition; (d) X-ray radiation exposure and development; (e) metal molding; (f) removal of PMMA and plating base; (g) etching of sacrificial layer and freeing of microstructure

well as aspect ratios (in excess of 1000) realizable in a single step, large gamut of materials (metals, alloys, polymers, ceramics, composites, multilayer materials), complex shapes (three-dimensional multi-level structures with oblique faces), structural and dimensional accuracy, low

surface roughness (in the order of 20 nm), excellent verticality of surfaces with runouts of the order of 1 mrad, capacity of mixing different-scale features or capacity of combination with other microfabrication process such as surface and bulk micromachining.

The end result of the process shown in Fig. 6.14 is the high aspect ratio microcantilever sketched in Fig. 6.15.

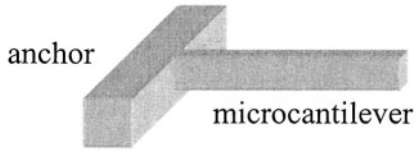

Figure 6.15 High aspect ratio microcantilever (free lateral shape) produced by the SLIGA process

2.5 Microstereolithography and Related Processes

A brief presentation will follow of several other microfabrication processes that are currently being utilized for MEMS production and are collectively known as *microstereolithography.*

Microstereolithography is a technique that evolved from *rapid prototyping* (RP) fabrication and is based on producing three-dimensional microstructures by means of techniques that involve multi-layer stacking through laser-induced polymerization – Bertsch et al. [9]. There are three main categories of microstereolithographic fabrication techniques, namely: vector-by-vector, integral and laser polymerization inside the reactive environment. In *vector-by-vector* processes, the fine focusing of the laser beam is made at the reactive surface, which reduces the attack spot size and improves resolution. Subcategories of this process are the *constrained-surface* method (where the laser beam is sent from a fixed window) and the *free-surface* method (where the reactor is displaced in the three-dimensional space by an x-y-z stage). In *integral microstereolithography,* the image of one layer is projected on the resin surface with high resolution and pre-specified depth. Usual pattern generators are liquid crystal displays (LCDs) and digital micromirror devices (DMDs). Eventually, the *laser polymerization inside the reactive environment* method, as the name suggests, attempts to realize local polymerization underneath the reactant surface in small increments that can be controlled three-dimensionally.

Other processes that are related to microstereolithography are the *polymerization with evanescent waves* (PEW), the *spatial forming* and the *electrochemical fabrication* (EFAB). In a PEW process, multilevel microstructures are directly obtained. This method uses the phenomenon of total reflection and the subsequent generation of evanescent waves (waves

whose intensity decays exponentially over a layer's thickness) to initiate polymerization over maximum thicknesses of the order of 1.5 mm. The *spatial forming* process uses ceramic inks to create a mold in a layer-by-layer fashion. The pre-designed voids are subsequently filled with metal-based inks and after curing and sintering, the final metallic microstructure is freed from the ceramic matrix which crumbles.

Another microstereolithography-related fabrication process is *EFAB (Electrochemical FABrication),* which can produce high aspect ratio microdevices made out of metals, such as nickel, copper or permalloy. EFAB is a batch process that belongs to the family of rapid prototyping (such as stereolithography) and three-dimensional printing. EFAB utilizes the three-dimensional CAD drawing of a microdevice that has to be fabricated and slices the drawing into several cross-sections. For each slice a mask is created by photolithography and all the masks that are needed for the 3D microdevice are created prior to the fabrication process itself. The process flow is sketched in Fig. 6.16.

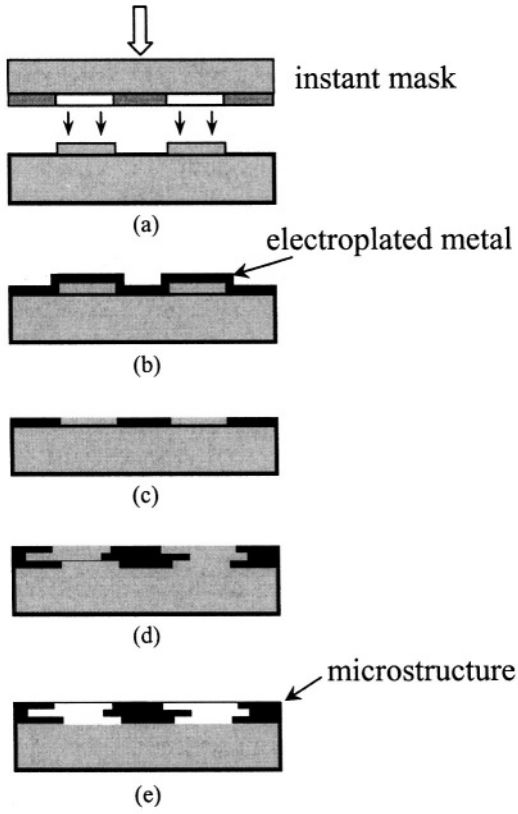

Figure 6.16 EFAB process sequence: (a) Instant masking; (b) metal electroplating; (c) planarization; (d) several (a)-(b)-(c) sequences; (e) removal of sacrificial material

A sacrificial layer (usually copper), which has to be etch-compatible with the metal used for building the microstructure, is pattern-deposited on a substrate material, as shown in Fig. 6.16 (a). An instant mask is pressed against the substrate and injects the support (sacrificial) material through the unobstructed area of the mask. The mask is then removed and electroplating of the structural metallic layer (nickel, for instance) is performed, as sketched in Fig. 6.16 (b). Planarization of the two layers produces the composite structure of Fig. 6.16 (c). These steps are repeated several times with different masks until the multiple-layer structure of Fig. 6.16 (d) is obtained. The final step in the EFAB process is acid etching of the sacrificial layers and release of the structural microdevice – Fig. 6.16 (e). The number of layers is virtually limitless and the fabrication time per layer is of the order of tens of minutes (surface micromachining, for instance, might require a few days for completion of one layer), whereas a layer can be 20 μm thick. Another advantage is that the EFAB process does not require clean room and elevated temperatures.

2.6 Packaging

Mechanical microdevices are integrated with electronic circuitry, which are sensitive to environmental factors such as temperature variations, humidity or electromagnetic interferences, and therefore need protection, which is performed by a process called *packaging* and which follows the microfabrication itself. Figure 6.17 sketches few of the steps that are involved in MEMS packaging

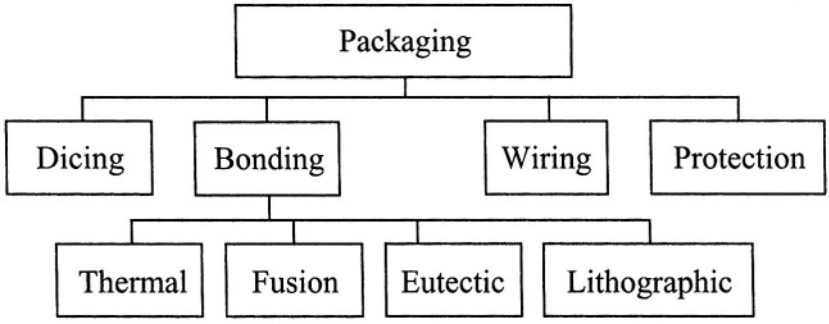

Figure 6.17 Principal phases in MEMS packaging

Through *dicing* or *sawing* the individual microdevices are cut away from the wafer. *Cavity sealing* or *bonding* is utilized to bond the MEMS die to a protective plate or to another die containing the electronic circuitry for instance. Bonding, as indicated in Fig. 6.17, can be realized in several ways, such as: *thermal bonding* (either *anodic* or with *intermediate layers*), *fusion*

bonding (where chemical reactions between the components of the two plates at relatively elevated temperatures create the physical attachment), *eutectic bonding* (a phase mixture such as Au-Si is formed which bonds the two components) or *photolithographic bonding* (which utilizes patterned thick photoresist layers to glue two plates). Other phases in a MEMS packaging process include connection of the die to power/electronic microcomponents and wire bond, die protection (mostly through coating), stress isolation measures and thermal management.

3. MATERIALS

As previously shown, structural members and devices in MEMS are produced from a variety of materials, non-metallic and metallic alike. While some of these materials are strictly used for structural design and others are sacrificial materials being removed in the end of a process, there are a few materials that can be used as either structural or sacrificial components, depending on the application, process technology and the context of combination with other materials. MEMS materials can be *brittle* (they break almost abruptly, without any plastic deformation) or *ductile* (there is a non-linear portion of the stress-strain curve before failure occurs). Silicon and polysilicon, for instance, are brittle materials, whereas MEMS metals are ductile.

All materials, brittle and ductile, need to have their *Young's modulus* determined, as this amount, together with the geometric parameters, defines the stiffness of a microcomponent. *Poisson's ratio* is another important elastic parameter which defines the lateral contraction of a material sample under tension. In addition, brittle materials can fairly be characterized in terms of their mechanical behavior by means of the *fracture strength* (which is the stress at the beginning of fracture). Ductile materials are generally defined by means of the *yield strength* (which is the stress value corresponding to the point on the stress-strain characteristic where the linear behavior ends) and the *ultimate strength* – the stress where failure does occur.

A brief presentation of the main materials that are used in MEMS construction and their main mechanical properties will be given next. It should be emphasized that there are differences – sometimes quite large – in the mechanical properties of the same material between the bulk and thin film forms. At the same time, variability exists for the same mechanical property of a thin film, depending on the method of microfabrication and system of measurement. Possible causes of these large differences are the imperfect models that are used and the fact that the geometry of a real microcomponent cannot be assessed/measured precisely and is often not the ideal one used in the model. An excellent source for up-to-date MEMS material information regarding properties and testing can be found in Sharpe [10], who surveyed the literature dedicated to mechanical properties of MEMS (material property values are mainly cited here from this reference).

The *single-crystal silicon* is a brittle material that can be grown as a single crystal. It can also be processed by bulk micromachining and is the platform for surface micromachining. Because single-crystal silicon is anisotropic, its mechanical properties are direction-dependent, and Sharpe [10] mentions that Young's modulus can vary from 125 GPa to 180 GPa, whereas values of the fracture strength can range from 0.26 GPa to 26.4 GPa (an initial design value larger than 1 GPa is recommended Sharpe [10] and Yi and Kim [11]).

Polysilicon is the most common material in MEMS that is used for structural components. Its mechanical properties are similar to the ones of the single-crystal silicon (Young's modulus of 163 – 166 GPa, Poisson's ratio of 0.22, fracture strength of 1.2 – 3 GPa), but polysilicon is an isotropic material, which can be either deposited or grown. The *silicon dioxide* (SiO_2) – with E = 70 GPa and the fracture strength of 1 GPa – is used as sacrificial material or etch mask – like in the case of dry etching of thick polysilicon, see Zorman and Mehregany [12]. However, SiO_2 can also be incorporated into MEMS as a structural component. Two other members of the same family are the *crystalline quartz* and the *spin-on-glass* (SOG). The *silicon nitride* (Si_3N_4) – 250 GPa Young's modulus, 0.23 Poisson's ratio and 6 GPa fracture strength – is another material that can be utilized for etch masking, but also as a sacrificial material, for electrical insulation, surface passivation or as structural material. Si_3N_4 can be deposited on a substrate by either LPCVD or by plasma. The *diamond-like carbon* and the *silicon carbide* (SiC) are materials that are implemented in MEMS having to operate in harsh environments, where very good mechanical (hardness particularly), thermal and electrical properties are required. Both materials have high mechanical hardness and Young's modulus (1035 GPa for the diamond-like carbon and up to 700 GPa for SiC), high thermal conductivity and electrical stability at temperatures in excess of 300° C. Both materials are also chemically inert. They can be grown, deposited or micromolded by microfabrication processes that have to modify the standard procedures. *Germanium* (Ge) is another inert material, which can be used as either structural component or as sacrificial layer – especially in the polysilicon-germanium compound, which can easily be etched by H_2O_2.

Metals and metal compounds are also well represented in MEMS construction. *Aluminum* (Al) is probably the most utilized as it is also used in and compatible with IC microelectronics. The aluminum is layer-deposited and can function as either structural component or as a sacrificial material in combination, for instance, with the polyimide – which is the structural material. While Young's modulus of bulk aluminum is 70 GPa, for thin-film aluminum it can range from 8 to 40 GPa, and its fracture strength is 0.15 GPa. Other metals, such as *copper* (Cu) (E = 120 GPa, $\sigma_u = 0.35$ GPa) , *nickel* (Ni) (E = 180 GPa, $\mu = 0.3$, $\sigma_u = 0.5$ GPa), *nickel-iron* (Ni-Fe) (E = 120 GPa, $\sigma_u = 1.6$ GPa), *titanium* (Ti) (E = 100 GPa, $\sigma_u = 0.8$ GPa), *tungsten* (W), *zirconium* (Zr), *gold* (Au) (E = 70 GPa, $\sigma_u = 0.3$ GPa), *silver* (Ag) or

platinum (Pt) are incorporated in MEMS as structural components and can be deposited, sputtered or electroplated. Metal compounds that find use in MEMS design are *gallium arsenide* (GaAs) and *indium phosphide* (InP) that are commercially-available as wafers and have piezoelectric and special optical properties. Other metal compounds that exhibit piezoelectric properties are the *zinc oxide* (ZnO) and the *lead zirconate titanate* (PZT).

4. PRECISION ISSUES IN MEMS

4.1 Material Properties Precision

As mentioned previously, material property constants, such as Young's modulus or Poisson's ratio, are often times dependent on the specifics of the microfabrication process and of the experimental setup utilized to measure a MEMS mechanical property. Both factors lead to large variabilities sometimes in the value of a mechanical property for the very same material. A simple example is presented showing the divergence in results when Young's modulus of a material is uncertain.

Example 6.1

A single-crystal silicon microcantilever of constant rectangular cross-section is utilized for atomic force microcopy force reading in a contact application, as sketched in Fig. 6.18. Knowing the length $l = 150\ \mu m$, the cross-sectional dimensions, $w = 10\ \mu m$, $t = 2\ \mu m$, and also the experimental values of the tip displacements $u_{1z} = 4\ \mu m$ and $\theta_{1y} = 3^o$, determine the maximum and minimum values that correspond to these parameters when the Young's modulus is uncertain and can have a minimum value of $E_{min} = 125$ GPa and a maximum value of $E_{max} = 180$ GPa.

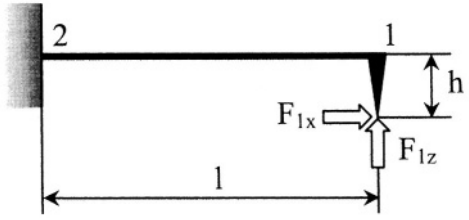

Figure 6.18 Microcantilever in an AFM application

Solution:

As shown in Chapter 2, the tip deflection and slope can be expressed for this case as:

$$\begin{cases} u_{1z} = (F_{1z}l/3 + F_{1x}h/2)l^2/(EI_y) \\ \theta_{1y} = (F_{1z}l/2 + F_{1x}h)l/(EI_y) \end{cases} \tag{6.2}$$

By solving the equation system (6.2) results in:

$$\begin{cases} F_{1z} = 6(2u_{1z} - l\theta_{1y})EI_y/l^3 \\ F_{1x} = 2(2l\theta_{1y} - 3u_{1z})EI_y/(hl^2) \end{cases} \tag{6.3}$$

The moment of inertia is:

$$I_y = wt^3/12 \tag{6.4}$$

By using the numerical values of this example, it is found that the maximum values of the tip forces are $F_{1z,\,max} = 31.15\ \mu N$ and $F_{1x,\,max} = 26.37\ \mu N$ (they correspond to E_{max}), whereas the minimum tip forces are $F_{1z,\,min} = 21.63\ \mu N$ and $F_{1x,\,min} = 18.31\ \mu N$.

To generalize the example discussed above, it should be remembered that Young's modulus influences the stiffness of a microdevice according to:

$$K = E\,f(geometry) \tag{6.5}$$

and therefore chances are that the stiffness will be overestimated by taking the maximum value of Young's modulus, whereas when the minimum value of E is considered, the stiffness will likely be less than the real value. The next example looks at how uncertainty in Poisson's ratio affects the quasi-static behavior of a short microcantilever.

Example 6.2

A short microcantilever constructed from silicon nitride (Si_3N_4) in a solid trapezoid configuration, of the type sketched in Fig. 2.11, Chapter 2, is used to write in a AFM application. Knowing that $l = 75\ \mu m$, $w_{max} = 40\ \mu m$, $w_{min} = 20\ \mu m$, $t = 5\ \mu m$ and $E = 140$ GPa. Consider that the only force acting on the microcantilever tip is F_{1z} and that the tip deflection and slope are measured experimentally as $u_{1z} = 5\ \mu m$, $\theta_{1y} = 1^o$. Determine the force F_{1z} when the Poisson's ratio is known to have values in the [0.21, 0.28] interval.

Solution:

It has been shown in Chapter 1 that for a short beam (where the ratio of the length to the largest cross-sectional dimension is approximately less than 5-7), the direct-bending compliance $C_{uz\text{-}Fz}$ is the one affected by the

consideration of the shearing effects that correspond to relatively-short beams, and is expressed as:

$$C^{s}_{uz-Fz} = C_{uz-Fz} + 2\alpha(1+\mu)C_{ux-Fx} \tag{6.6}$$

where the compliances $C_{uz\text{-}Fz}$ and $C_{ux\text{-}Fx}$ are calculated for long configurations. Chapter 2 gave the bending-related stiffnesses of a solid constant rectangular cross-section microcantilever of trapezoid longitudinal profile, namely $K_{Fz\text{-}uz}$, $K_{Fz\text{-}\theta y}$ and $K_{My\text{-}\theta y}$. It is known that the bending-related compliance matrix is the inverse of the stiffness matrix, and therefore $C_{uz\text{-}Fz}$ can be computed as the element in the first row and first column of the inverse of the stiffness matrix:

$$[K] = \begin{bmatrix} K_{Fz-uz} & K_{Fz-\theta y} \\ K_{Fz-\theta y} & K_{My-\theta y} \end{bmatrix} \tag{6.7}$$

As shown in Chapter 1, the axial compliance is calculated according to Eq. (1.106), and therefore the direct-bending compliance of Eq. (6.6) can be calculated for either μ_{min} or μ_{max}. Now, the following compliance matrix:

$$[C] = \begin{bmatrix} C^{s}_{uz-Fz} & C_{uz-My} \\ C_{uz-My} & C_{\theta y-My} \end{bmatrix} \tag{6.8}$$

will give by matrix inversion the corresponding stiffness matrix which includes shearing effects. As a consequence, the force F_{1z} can be calculated as:

$$F_{1z} = K^{s}_{Fz-uz}u_{1z} + K_{Fz-\theta y}\theta_{1y} \tag{6.9}$$

The maximum value of the tip force is found to be $F_{1z,\,max} = 500.815\ \mu N$ and the minimum force is $F_{1z,\,min} = 500.443\ \mu N$.

This example, too, can be generalized in order to highlight the influence of considering the incertitude in evaluating Poisson's ratio. The equations above, particularly Eq. (6.6), indicate that the direct-bending compliance, which is affected by the shearing effects, can be expressed in the form:

$$C = f_1(geometry) + \mu\, f_2(geometry) \tag{6.10}$$

When the maximum value of Poisson's ratio is taken in Eq. (6.10), the microstructure will be over-evaluated in its compliance, whereas the opposite will happen when taking the minimum value of Poisson's ratio.

4.2 Microfabrication Precision

The microfabrication processes that are utilized for MEMS production can yield sometimes shapes that are not geometrically perfect, either due to limitations of the microfabrication process itself or because of phenomena that take place during or after microfabrication. A few examples will be analyzed pointing out the errors that can result through geometric imprecision.

One such example is provided in wet etching of microstructures that are supposed to have rectangular cross-sections, but instead, the final shape is trapezoid, as shown in Fig. 6.19.

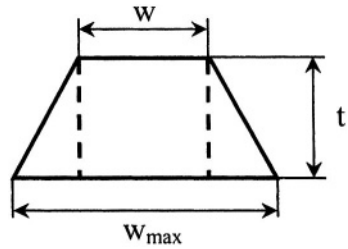

Figure 6.19 Trapezoid cross-section resulted by wet etching of silicon

This geometrical error can increase the net cross-section from the intended rectangular shape (shown with dotted lines in Fig. 6.19) of dimensions w and t to the trapezoid one. As a result, the new cross-sectional properties (area and moments of inertia) will affect both modeling and experimental results. An example will be studied of a fixed-fixed microbeam which is used in a *continuous stiffness measurement (CSM)* technique to determine Young's modulus and the fracture strength, by monitoring the applied force and the resulting deformation at the midspan of the beam – see more details in Li and Bhushan [13], for instance.

Example 6.3

Analyze the errors that are produced in using the continuous stiffness method technique for the experimental evaluation of Young's modulus and the fracture strength of a silicon fixed-fixed microbeam – Fig. 6.20 (a), whose cross-section is trapezoid instead of rectangular. A variable force is applied at the beam's mid-span and its value, together with the resulting deflection, are monitored continuously.

Solution:

It can be shown that the deflection and the corresponding force at the beam's mid-span – Fig. 6.20 (a) – are related as:

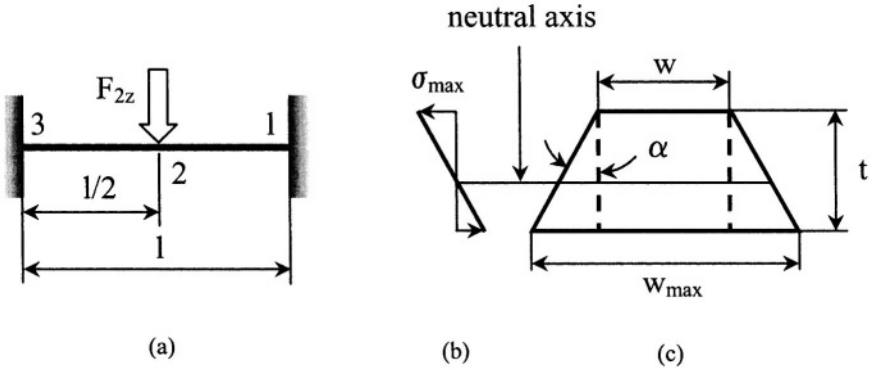

Figure 6.20 Indentation test for material properties evaluation: (a) fixed-fixed microbeam with mid-span loading; (b) bending stresses over cross-section; (c) trapezoid cross-section

$$u_{2z} = F_{2z} l^3 /(48 E I_y) \tag{6.11}$$

which gives Young's modulus equation:

$$E = F_{2z} l^3 /(48 I_y u_{2z}) \tag{6.12}$$

The moment of inertia for the trapezoid cross-section (as shown in Young and Budynas [14] for instance) of Fig. 6.20 (c) is:

$$I_y = (w_{max}^2 + 4 w_{max} w + w^2) t^3 /[36(w_{max} + w)] \tag{6.13}$$

If no geometric imperfection occurred, the moment of inertia of the rectangular cross-section would be:

$$I_y^* = w t^3 /12 \tag{6.14}$$

It is evident that the value of the Young's modulus would be over-evaluated if the rectangular cross-section was used instead of the real trapezoidal one, which has a larger moment of inertia.

The bending moment is maximum at the midspan and its value is:

$$M_{2y} = F_{2z} l /8 \tag{6.15}$$

The maximum stress at that location and on the upper fiber, as shown in Fig. 6.20 (b), can be calculated as:

$$\sigma_{max} = F l z_c /(8 I_y) \tag{6.16}$$

where z_c, the distance from the neutral axis (where the stress is zero, as shown in Fig 6.20 (b)) to the upper fiber, is:

$$z_c = (2w_{max} + w)t / [3(w_{max} + w)] \tag{6.17}$$

In the case of a rectangular cross-section the neutral axis is placed at the cross-section's center, namely:

$$z_c^* = t/2 \tag{6.18}$$

As it can be seen, the position of the neutral axis is another error source in determining the maximum stress (in particular the fracture strength), which ads to the error in the moment of inertia. Two plots are shown in Figs. 6.21 and 6.22, which show errors in Young's modulus and in the maximum stress, when taking a rectangular cross-section of dimensions w and t, instead of a trapezoid one, as shown in Fig. 6.20 (c). Clearly, the error in the Young's modulus is generated by differences in the moments of inertia of the two cross-section, therefore the following relative error function can be evaluated:

$$e_Y = 100(I_y - I_y^*)/I_y \tag{6.19}$$

The long side of the trapezoid can be expressed as:

$$w_{max} = w + 2t\tan\alpha \tag{6.20}$$

where the angle α is the deviation from vertical of the trapezoid's non-parallel sides, as shown in Fig. 6.20 (c).

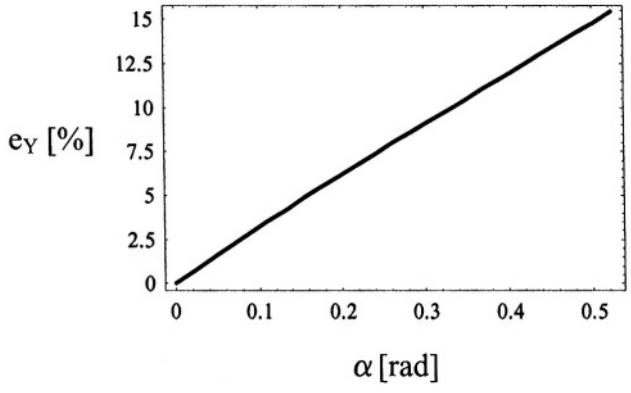

Figure 6.21 Relative errors in the values of Young's modulus

Similarly, a relative error function for stresses can be formulated as:

$$e_\sigma = 100\,(\sigma_{max} - \sigma^*_{max})/\sigma_{max} \tag{6.21}$$

The two error functions are now calculated by using the corresponding equations presented in this example and by taking $w = 6\ \mu m$, $t = 2\ \mu m$ and by considering that the angle α ranges between 0° and 30°. As Figs. 6.21 and 6.22 indicate, the relative errors in considering a rectangular cross-section instead of the real trapezoidal one can be as large as 15% in Young's modulus and 12% in the maximum stress.

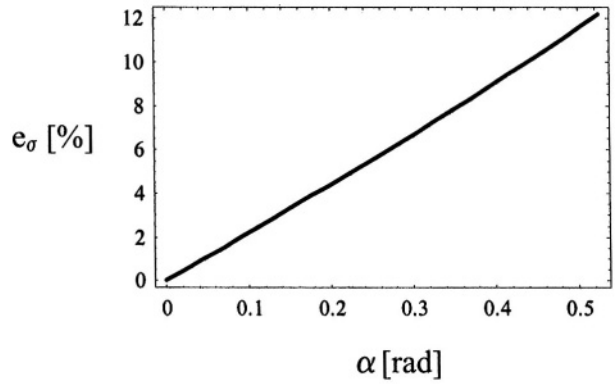

Figure 6.22 Relative errors in the values of the maximum stress

Another source for imprecision in microfabrication is represented by the *residual stresses* that are setup in a microcomponent and which deform it, especially when the microcomponent has a small thickness (it is basically realized as a film). Causes for residual stresses, as mentioned by Madou [1], include gas entrapment or impurity inclusions, microvoids created by gases that are generated during deposition and escape, thermal and lattice mismatches between the film and the substrate, and doping. Often times, the residual (or intrinsic) stresses do combine with thermal stresses that are generated through different thermal expansion coefficients of the substrate and deposited film. Eliminating or reducing the levels of residual stresses (which can reach values in the $10^8 - 5 \times 10^{10}$ dyn/cm^2 – Madou [1]) is generally attempted by post-deposition thermal treatment processes, such as *annealing*. Efforts have been dedicated to evaluating the residual stresses in MEMS, and a few of the specific methods will be presented next. One such method consists of depositing the material of interest as a thin film over a substrate microbeam. The residual stresses, which develop during and after deposition, can be either tensile or compressive, and will bow the sandwiched microbeam in one of the shapes shown in Fig. 6.23. Thin films do not have a stress variation (gradient) over the thickness, as the thickness is

very small. Constant axial stress/strain results in axial forces that can be either compressive or tensile. The situation of Fig. 6.23 (a) corresponds to a film that has inner tensile stresses, and therefore the film has the tendency to expand axially (about a direction parallel to beam's length). Because of the film's attachment to the substrate, the sandwich microbeam will bend downwards, in the way described in Chapter 4 at bimorph transduction. A film with compressive stresses, which tends to shrink axially, will bow the microcantilever in the form pictured in Fig. 6.23 (b).

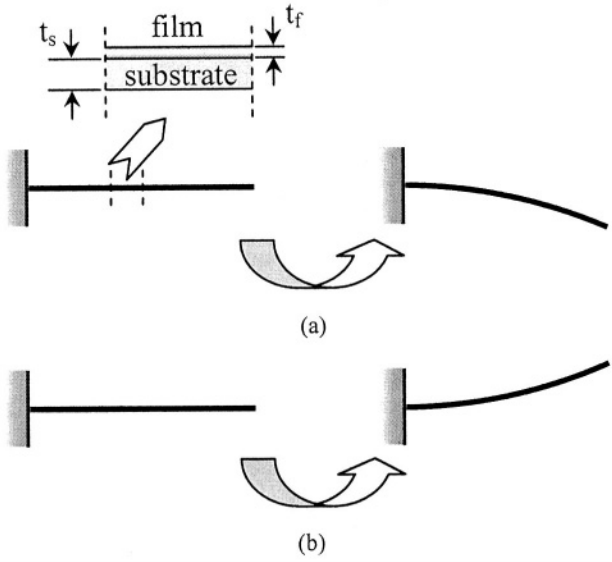

Figure 6.23 Bending effects of residual stresses in thin films deposited on microcantilever substrates: (a) film under tensile stresses; (b) film under compressive stresses

Example 6.4

Determine the residual stress (assumed to be compressive) in a thin film, which is deposited on a microcantilever substrate, Fig. 6.23 (b), by knowing the maximum tip deflection of the microcantilever beam as well as the dimensions and material properties for the film and substrate.

Solution:

It has been shown in Chapter 4 that the bending moment which acts on the upper layer (the film here) is expressed as:

$$M_{fy} = E_f I_{fy} / R \tag{6.22}$$

where the curvature radius – Eq. (4.134) – is calculated as:

$$R = \{4E_s A_s (E_f I_{yf} + E_s I_{ys}) + E_f A_f [4E_f I_{yf} + E_s (4I_{ys} + A_s (t_f + t_s)^2)]\} / [2E_f E_s A_f A_s \varepsilon_r (t_f + t_s)] \tag{6.23}$$

The subscripts *f* and *s* mean film and substrate, respectively, and ϵ_r is the residual strain, which is unknown. By only considering the bending of the film and the tip deflection produced by the moment M_{fy} of Eq. (6.22) results the following equation:

$$u_{1z} = M_{fy} l^2 / (2E_f I_{yf}) \tag{6.24}$$

By combining now Eqs. (6.22), (6.23) and (6.24) gives the residual strain:

$$\varepsilon_r = u_{1z} \{4E_s A_s (E_f I_{yf} + E_s I_{ys}) + E_f A_f [4E_f I_{yf} + E_s (4I_{ys} + A_s (t_f + t_s)^2)]\} / [E_f E_s A_f A_s \varepsilon_r (t_f + t_s) l^2] \tag{6.25}$$

and therefore the corresponding residual stress is simply:

$$\sigma_r = E_f \varepsilon_r \tag{6.26}$$

It should be noticed that measuring the tip deflection, or directly the radius of the deform bimorph, can be done by a variety of procedures, including Raman spectroscopy, infrared spectroscopy, Moiré fringes, laser speckle interferometry or X-rays acoustics. In the case the curvature radius can be measured experimentally, Eq. (6.23) will directly give the residual strain, and then Eq. (6.26) will enable calculation of the corresponding stress.

A similar method for evaluating residual stresses is known as the *disc method,* which utilizes a film that is deposited over a substrate disc. The residual stresses developed in the film will cause the disk to deform (bow), and the deflection at the disk's center is measured and subsequently used to evaluate the residual stress. The Stoney equation is utilized in this case – as given in Madou [1]:

$$\sigma_r = E_f t_s^2 / [6(1 - \mu_f) t_f R] \tag{6.27}$$

Example 6.5

Determine the residual stress in a thin layer which is deposited on a substrate disc of radius r (as shown in Fig. 6.24) when the center deflection u_{1z} is available experimentally. Known are the geometric parameters and material properties of the film and substrate.

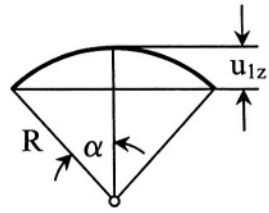

Figure 6.24 Bent circular disc for residual stress evaluation

Solution:

The Stoney formula – Eq. (6.27) gives the residual stress in terms of the curvature radius R, but this parameter might not be available directly. However, the following relationship exists between the center deflection and the curvature radius:

$$u_{1z} = R(1 - \cos\alpha) \tag{6.28}$$

The angle α, as shown in Fig. 6.24, can be approximated to:

$$\alpha = r / R \tag{6.29}$$

where r is the disk radius. Equations (6.28) and (6.29) combine into:

$$u_{1z} = R[1 - \cos(r / R)] \tag{6.30}$$

If one considers the cosine series expansion which retained the first five terms (the second and the fourth terms are zero):

$$\cos(r / R) \cong 1 - r^2 /(2R^2) + r^4 /(24R^4) \tag{6.31}$$

then Eq. (6.30) changes to:

$$24u_{1z}R^3 - 12r^2R^2 + r^4 = 0 \tag{6.32}$$

which is a third-degree equation in R. By solving it, the resulting value of R can be substituted into Eq. (6.27), which gives the residual stress.

Another method dedicated to measuring the residual stresses in thin films, as discussed in Madou [1] for instance, utilizes a series of fixed-fixed microbeams formed of the material whose stresses are of interest. The microbeams have identical cross-sections but different lengths. When the tendency of the microbeam is to expand axially, due to residual stresses, the fixed supports will react with opposing compressive forces, and for a given (critical) length, one particular microbeam (having the critical length) will

buckle and will give the residual stress, as discussed in the following example.

Example 6.6

A series of fixed-fixed microbeams are used in a test to determine the residual stress in a film material. The beams have identical rectangular cross-section defined by w and t, but are of different lengths. An optical system monitors the deflection at mid-span and decides that buckling occurred for the microbeam of length l_c, as shown in Fig. 6.25. Determine the residual stress when the material Young's modulus is known.

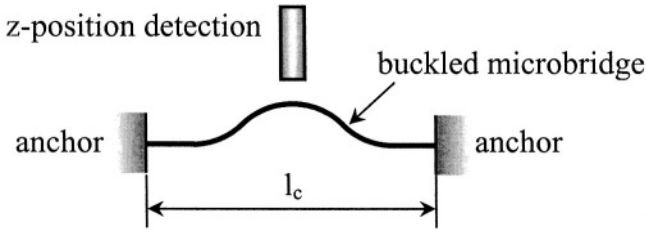

Figure 6.25 Side view of a buckled microbridge for residual stress evaluation

Solution:

In has been shown in the previous chapter that the critical buckling load for a fixed-fixed beam is:

$$F_{cr} = 4\pi^2 E I_{min} / l_c^2 \tag{6.33}$$

This axial force enables calculation of the corresponding axial stress, which is also the residual stress, as:

$$\sigma_{cr} = \sigma_r = F_{cr} / A \tag{6.34}$$

By using:

$$\begin{cases} I_{min} = wt^3 / 12 \\ A = wt \end{cases} \tag{6.35}$$

in combination with Eq. (6.33), the residual stress of Eq. (6.34) can be found as:

$$\sigma_r = \pi^2 E t^2 / (3 l_c^2) \tag{6.36}$$

Another design variant, which utilizes buckling for residual stress evaluation is the *ring crossbar* (also known as *Guckel ring)* of Fig. 6.26, where a beam is fixed at two points on a ring about the ring's diameter. The ring is fixed on a substrate about a direction perpendicular to the beam's direction. Preexisting tensile strain in the ring will compress the crossbar after etch and release, and for a critical length, the crossbar will buckle, and the residual stress can be found as shown in the previous example.

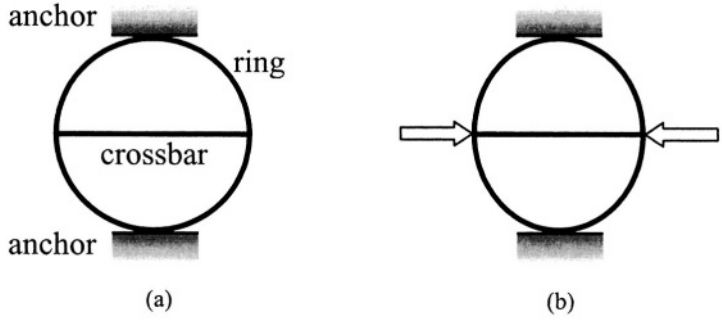

Figure 6.26 Top view of a ring crossbar utilized to measure residual stresses through buckling of the crossbar: (a) undeformed condition; (b) buckled condition

Thick films, too, can present residual stresses because of recrystallization phenomena subsequent to deposition and to insufficient control authority during the deposition process, as highlighted by Madou [1].

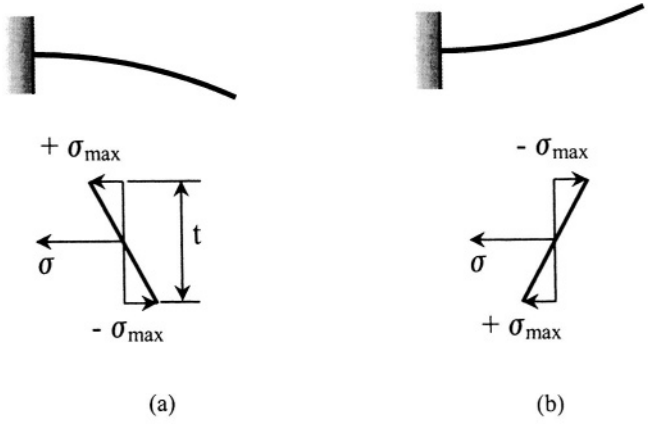

Figure 6.27 Thick-film microcantilevers with residual stresses: (a) tensile stresses on the upper fiber and bent shape; (b) compressive stresses on the upper fiber and bent shape

In such cases, the strain/stress is no longer constant over the film's thickness, and therefore the strain/stress gradient will bend the microcantilever, in one

of the shapes shown in Fig. 6.27. As Fig. 6.27 (a) indicates, the microcantilever will bent downward for a stress gradient with tensile stresses on the upper fiber and compressive stresses on the lower fibers. Upward bending will occur, as shown in Fig. 6.27 (b) when the stress gradient is opposite to the one of Fig, 6.27 (a).

Example 6.7

Find the maximum residual stress in a thick-film microcantilever of the type pictured in Fig. 6.27 (a) when the tip deflection can be measured experimentally and the geometry and material properties of the microbeam are known.

Solution:

For a beam of thickness t and moment of inertia I_y, which is acted upon by a moment M_y, the maximum stress is:

$$\sigma_{max} = M_y t /(2I_y) \tag{6.37}$$

The tip deflection of a microcantilever can be determined as:

$$u_{lz} = M_y l^2 /(2EI_y) \tag{6.38}$$

By combining Eqs. (6.37) and (6.38) results in:

$$\sigma_{max} = Etu_{lz} / l^2 \tag{6.39}$$

As in any classical (large-scale) fabrication technology, the dimensions produced by microfabrication are not the nominal (as-designed) ones because a process leads to inevitable dimensional errors. A linear dimension l for instance can only be guaranteed to statistically range in a $(l - \Delta l \rightarrow l + \Delta l)$ domain. In surface micromachining for example, both gap and solid dimension are subject to such technology limitations, which combined together in a microdevice, can affect the nominal (theoretically-predicted) performance.

Example 6.8

A longitudinal (comb-type) electrostatic microdevice, as the one shown in Fig. 4.26 (Chapter 4), is used in a sensing application. The microfabrication technology produces linear dimensions with tolerances of $-\Delta l$ and $+\Delta l$. Determine the ratio of the maximum to the minimum values of the capacitance sensitivity (Eq. (4.36)) in terms of the tolerance fraction p, where $\Delta l = pl$.

Solution:

The maximum capacitive sensitive can be found from Eq. (4.36) as:

$$\partial C / \partial x\big|_{max} = \varepsilon(l_z + \Delta l_z)/(g - \Delta g) \tag{6.40}$$

Similarly, the minimum capacitive sensing is:

$$\partial C / \partial x\big|_{min} = \varepsilon(l_z - \Delta l_z)/(g + \Delta g) \tag{6.41}$$

The linear dimension variation can be written as:

$$\begin{cases} \Delta l_z = p l_z \\ \Delta g = p g \end{cases} \tag{6.42}$$

By substituting Eqs. (6.42) into Eqs. (6.40) and (6.41), the ratio of the maximum to the minimum sensitivity becomes:

$$\partial C / \partial x\big|_{max} / \partial C / \partial x\big|_{min} = (1+p)^2/(1-p)^2 \tag{6.43}$$

Figure 6. 28 is a plot corresponding to Eq. (6.43).

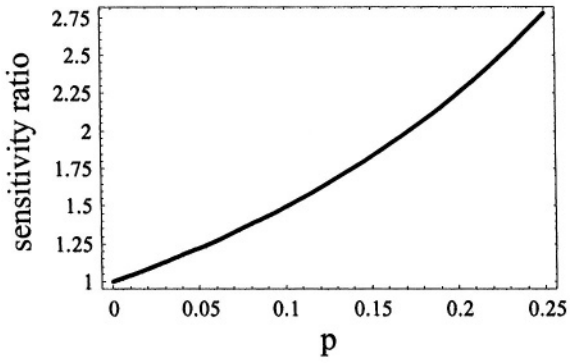

Figure 6.28 Ratio of maximum to minimum capacitive sensitivity ratios as a function of the tolerance fraction

It can be seen that the sensitivity ratio varies non-linearly from a value of 1 for p = 0 (this is the ideal case, when the dimensions are perfect) to a value of approximately 2.75, when p = 0.25.

Although not a microfabrication defect in itself, *stiction* – the phenomenon of adhesion of thin-film structures such as microcantilevers, microbridges or membranes, especially during the wet etching of sacrificial layers – constitutes a source of shape damaging and even mechanical failure

in MEMS. As shown by Mastrangelo and Hsu [15], the magnitude of the forces that are developed through stiction are significant, such that attempts to normally operate microfilm structures that have adhered to the substrate can terminally damage the microdevice. The mechanisms that generate such high levels of forces are the capillary phenomena at the liquid- solid interface in very small interstices, as well as the solid-solid adhesion which is established after contact. However, further discussion and quantitative analysis of this phenomenon is beyond the scope of this book.

4.3 Modeling Precision

Another source of errors in MEMS design is the precision of modeling the mechanical behavior of a microcomponent. Simplifying assumptions are often used to keep the modeling process tractable while preserving the certitude of its prediction accuracy, Examples can be cited where modifications of the basic assumptions used in modeling have to be applied, such as considering the shearing effects for relatively-short beams or using the large deformation theory, when it warranted by reality. It is also very important in MEMS that move through elastic deformation of their components, such as the ones discussed in this book, to separate between the members that can be considered rigid and the ones that cannot. Otherwise, errors – sometimes significant – can be introduced in the stiffness/compliance of the microdevice of interest. An example will be analyzed next, highlighting errors that are produced through modeling assumptions in boundary conditions.

Example 6.9

Evaluate the errors which are generated when considering that the vertical anchor of the microcantilever of in Fig. 6.29 (a) is rigid as opposed to the case when its flexibility is taken into consideration under the loading suggested in Fig. 6.29 (b).

Solution:

It has been shown previously that the displacements at a certain point on a free-fixed chain, as the one considered here, can be calculated by combining the various compliances of the flexible links in terms of the specific configuration of the chain. In this case, the deflection u_{1z} and slope θ_{1y} can be expressed as:

$$u_{1z} = l\{F_{1z}l[l/(3I_{y1}) + h/I_{y2}] + M_{1y}[l/(2I_{y1}) + h/I_{y2}]\}/E \quad (6.44)$$

$$\theta_{1y} = \{F_{1z}l[l/(2I_{y1}) + h/I_{y2}] + M_{1y}(l/I_{y1} + h/I_{y2})\}/E \quad (6.45)$$

Equations (6.44) and (6.45) are solved for F_{1z} and M_{1y}, which can be expressed in the form:

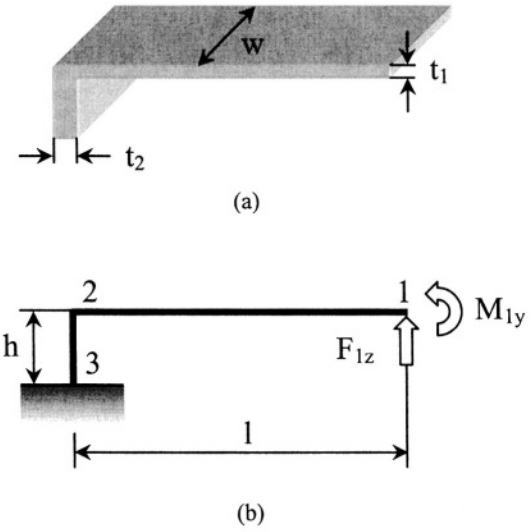

Figure 6.29 Microcantilever with anchor: (a) Three-dimensional sketch; (b) Loading and boundary conditions

$$F_{1z} = K_{Fz-uz}u_{1z} + K_{Fz-\theta y}\theta_{1y} \tag{6.46}$$

$$M_{1y} = K_{Fz-\theta y}u_{1z} + K_{My-\theta y}\theta_{1y} \tag{6.47}$$

where the stiffnesses are:

$$K_{Fz-uz} = 12EI_{y1}(hI_{y1} + lI_{y2})/[(4hI_{y1} + lI_{y2})l^3] \tag{6.48}$$

$$K_{Fz-\theta y} = -6EI_{y1}(2hI_{y1} + lI_{y2})/[(4hI_{y1} + lI_{y2})l^2] \tag{6.49}$$

$$K_{My-\theta y} = 4EI_{y1}(3hI_{y1} + lI_{y2})/[(4hI_{y1} + lI_{y2})l] \tag{6.50}$$

If one takes $h \to 0$ and $I_{y2} \to 0$, then Eqs. (6.48), (6.49) and (6.50) reduce to the known equations for a simple cantilever, namely:

$$K^*_{Fz-uz} = 12EI_1/l^3 \tag{6.51}$$

$$K^{*}_{Fz-\theta y} = -6EI_1 / l^2 \tag{6.52}$$

$$K^{*}_{My-\theta y} = 4EI_1 / l \tag{6.53}$$

The following ratios can be formulated and calculated by means of Eqs. (6.48) through (6.53):

$$rK_{Fz-uz} = (K^{*}_{Fz-uz} - K_{Fz-uz}) / K^{*}_{Fz-uz} = 3hI_{y1}(4hI_{y1} + lI_{y2}) \tag{6.54}$$

$$rK_{Fz-\theta y} = (K^{*}_{Fz-\theta y} - K_{Fz-\theta y}) / K^{*}_{Fz-\theta y} = 2hI_{y1}(4hI_{y1} + lI_{y2}) \tag{6.55}$$

$$rK_{My-\theta y} = (K^{*}_{My-\theta y} - K_{My-\theta y}) / K^{*}_{My-\theta y} = hI_{y1}(4hI_{y1} + lI_{y2}) \tag{6.56}$$

and Fig. 6.30 is the plot of $rK_{My\text{-}\theta y}$ in terms of h and t_2, for the case where l = 200 μm, t_1 = 2 μm and w = 15 μm. Obviously, the relative errors increase when the height h increases and the thickness t_2 decreases.

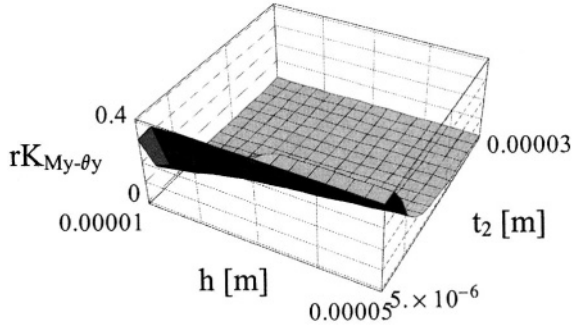

Figure 6.30 Stiffness error when considering the leg compliance in a microcantilever

Other examples of modeling errors have been presented in Chapter 5 when analyzing the out-of-the-plane stiffness of microsuspensions in connection to the regular, in-plane stiffness and motion of microdevices.

5. SCALING

The *theory of similitude* enables comparing the behavior of systems that are similar by extrapolation of the available data (either experimental or numerical) characterizing one system to another system, in order to predict the response of the latter. In many cases data can be acquired by using a laboratory model which suitably produces experimental data. By applying

the theory of similitude, it is possible to scale up or down the model properties and to predict the behavior of a similar system that is built at a different scale. The theory of similitude is implemented by means of the *dimensional analysis,* which is the analytical tool that takes into consideration the dimensions of the pertinent amounts defining a given phenomenon. The dimensional analysis, as shown by Murphy [16] or Taylor [17], produces qualitative relationships, and in combination with experimental/numerical data, yields quantitative results that lead to accurate predictions. The dimensional analysis is based on two axioms, namely:

- Two quantities are numerically equal only when they are qualitatively similar (have the same dimensions). For instance, a quantity that is measured in length units can only be equal to another quantity that is also being measured in length units.
- The magnitude ratio of two similar quantities is independent of the measurement units when the same units are used for both quantities. The width-to-thickness ratio of one microcantilever's cross-section is the same, regardless whether the measuring units are meters or inches.

The scaling laws, as mentioned by Spearing [4], can be *fundamental* (or *quasi-fundamental),* which are basically obtained from the theory of similitude and the dimensional analysis, and which consider that material properties and physical quantities such as density, elastic constants, or thermo-electric properties are constant. Another category of scaling laws are the *mechanism-dependent* ones, which take note that under a threshold value of approximately 0.1 μm, certain material and physical properties are no longer constant, and their values will vary according to the mechanisms that dominate their behavior. A third branch of scaling laws, as also mentioned by Spearing [4], form the *extrinsic* or *indirect* category, where restrictions imposed by the peculiarities of a specific microfabrication technology, in relationship with the given set of geometric shapes that can be obtained by that microtechnology, affect scaling properties. Addressed will be here only the fundamental scaling laws.

Among the features that determine the scaling trends of MEMS, the *length* is a key parameter because the length directly reflects the dimensional differences between small- and large-scale, and therefore carries over the amount whose scale-dependence is being studied. As a consequence, the length – denoted by 1 in the following – is the paramount basic variable, and all the derivative amounts of interest are related to it. The length scales to itself, namely to l^1, the area A scales to l^2, the volume V scales to l^3, whereas the moment of inertia scales to l^4.

One important feature in scaling properties is the *surface-to-volume ratio* (SVR) of a body, which is:

$$SVR = A / V \tag{6.57}$$

Example 6.10

Compare the surface-to-volume ratio of a cube to that of a sphere.

Solution:

For a cube, the surface-to-volume ratio of Eq. (6.57) is simply the inverse of the length (or l^{-1}), where l is the cube's side. For a sphere of radius R, this ratio becomes:

$$SVR = (\pi R^2)/(4\pi R^3/3) = 0.75/R \tag{6.58}$$

and Fig. 6.31 plots this ratio when the radius ranges from 0.01 μm to 10 μm and it can be seen that for small geometric features, this ratio becomes very large.

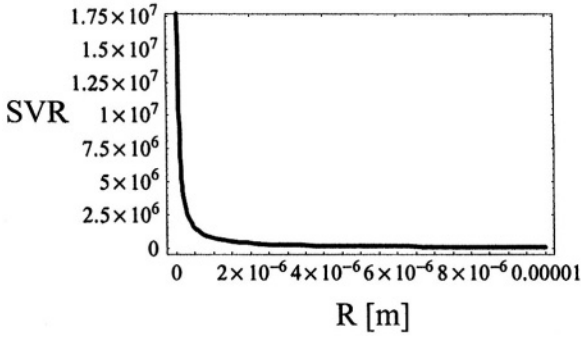

Figure 6.31 Surface-to-volume ratio for a sphere

It is interesting to mention that when the cube and the sphere have the same volume, the surface-to-volume ratio of the sphere is approximately 1.21 larger than the cube's ratio, whereas when the cube and the sphere have the same area, the $r_{s\text{-}v}$ of the sphere is approximately 1.34 larger than the $r_{s\text{-}v}$ of the cube. In other words, forces that are proportional to the area (such as external friction or superficial tension) become more important than forces that are proportional to the volume (such as gravity, for instance) at small scale, and the forces that are proportional to surface-to-volume are always larger for sphere-like microcomponents than those of equivalent cube-like ones.

Another amount which is of interest in qualifying the specific resistance of a mechanical component is the *strength-to-weight ratio,* which is defined as the maximum load over the mass. For a strut that is compressed by an axial load F, the strength-to-weight ratio, SWR, is:

$$SWR = F_{max} /(\rho V) = (\sigma_Y / \rho)(A/V) \tag{6.59}$$

When the yield stress σ_Y and the density ρ are constant, SWR scales (is proportional) to the surface-to-volume ratio SVR, which was shown previously to scale to l^{-1}.

Stiffness is another feature which is of particular interest to this book, as the main objective here was to qualify MEMS quasi-statically and therefore to define/determine relationships between load and displacement/deformation by means of stiffness.

Example 6.11

Determine the stiffness scaling for a fixed-free microcantilever of constant rectangular cross-section.

Solution:

A constant cross-section microcantilever can be defined in bending by three stiffnesses, namely the direct linear stiffness, $K_{Fz\text{-}uz}$, the direct rotary stiffness $K_{My\text{-}\theta y}$, and the cross stiffness, $K_{Fz\text{-}\theta y}$:

$$\begin{cases} K_{Fz-uz} = 3EI_y / l^3 \\ K_{My-\theta y} = EI_y / l \\ K_{Fz-\theta y} = 2EI_y / l^2 \end{cases} \tag{6.60}$$

By taking into account that E is considered constant and I_y scales to l^4, it follows that $K_{Fz\text{-}uz}$ scales to l^1, $K_{My\text{-}\theta y}$ scales to l^3 and $K_{Fz\text{-}\theta y}$ scales to l^2. The torsional stiffness $K_{Mx\text{-}\theta x}$ is similar to the direct rotary bending stiffness and consequently scales to l^3. Because of the linear relationships between force and deflection, on one hand, and moment and slope (rotation angle), on the other hand, which are:

$$\begin{cases} F_z = K_{Fz-uz} u_z \\ M_y = K_{My-\theta y} \theta_y \end{cases} \tag{6.61}$$

the force F_z will also scale to l^1, as $K_{Fz\text{-}uz}$ does, and M_y scales to l^3, similarto $K_{My\text{-}\theta y}$.

Trimmer [18] and [19] introduced the so-called *vertical Trimmer bracket* symbolism as a way of determining the scaling proprieties of amounts that result from forces/moments (which will be discussed shortly) and other amounts, whose scalability is known. The load (composed of forces and/or moments), depending on the specific character of the actuation – as detailed in Chapter 4 –, can scale with different powers (exponents) of 1, and the following formalism can be used to illustrate this connection:

$$F = \begin{bmatrix} l^{f1} \\ l^{f2} \\ . \\ l^{fn} \end{bmatrix} \tag{6.62}$$

which simply indicates that one specific load can scale to either of the components l^{f1}, l^{f2} to l^{fn} (f1 < f2 < … < fn). If another amount A, formally defined as:

$$A = \begin{bmatrix} l^{a} \\ l^{a} \\ . \\ l^{a} \end{bmatrix} \tag{6.63}$$

combines to F in a way that produces another amount X, in the form:

$$X = FA \tag{6.64}$$

then the scale definition of the new amount X is:

$$X = \begin{bmatrix} l^{f1} \\ l^{f2} \\ . \\ l^{fn} \end{bmatrix} \begin{bmatrix} l^{a} \\ l^{a} \\ . \\ l^{a} \end{bmatrix} = \begin{bmatrix} l^{f1+a} \\ l^{f2+a} \\ . \\ l^{fn+a} \end{bmatrix} \tag{6.65}$$

Equation (6.65) shows that when the force scales with l^{f2} for instance, the derivative amount X will scale to l^{f2+a}.

A direct application of the Trimmer symbolism is calculating linear/angular displacements by utilizing corresponding forces/moments and stiffnesses.

Example 6.12

Establish the scaling properties of linear and angular displacements of a microcomponent by utilizing the vertical Trimmer bracket symbolism.

Solution:

A linear displacement is calculated as the ratio between the generating force and the corresponding stiffness and it scales as:

$$u = F / K_l = \begin{bmatrix} l^{f1} \\ l^{f2} \\ . \\ l^{fn} \end{bmatrix} \begin{bmatrix} l^{-1} \\ l^{-1} \\ . \\ l^{-1} \end{bmatrix} = \begin{bmatrix} l^{f1-1} \\ l^{f2-1} \\ . \\ l^{fn-1} \end{bmatrix} \tag{6.66}$$

Similarly, a rotary displacement which is produced by a moment is the ratio between the moment and the corresponding stiffness and it scales as:

$$\theta = F / K_r = \begin{bmatrix} l^{f1} \\ l^{f2} \\ . \\ l^{fn} \end{bmatrix} \begin{bmatrix} l^{-3} \\ l^{-3} \\ . \\ l^{-3} \end{bmatrix} = \begin{bmatrix} l^{f1-3} \\ l^{f2-3} \\ . \\ l^{fn-3} \end{bmatrix} \tag{6.67}$$

Eventually, a rotary displacement which is produced by a force is the ratio of the force to the corresponding cross stiffness and scales as:

$$\theta = F / K_c = \begin{bmatrix} l^{f1} \\ l^{f2} \\ . \\ l^{fn} \end{bmatrix} \begin{bmatrix} l^{-2} \\ l^{-2} \\ . \\ l^{-2} \end{bmatrix} = \begin{bmatrix} l^{f1-2} \\ l^{f2-2} \\ . \\ l^{fn-2} \end{bmatrix} \tag{6.68}$$

The static work can also be scale-evaluated by using the vertical Trimmer bracket method, as shown in the next example.

Example 6.13

Determine the scaling laws corresponding to linear and rotary work by applying the vertical Trimmer bracket notation.

Solution:

The linear work produced by a force over a distance is proportional to the force-distance product and scales as:

$$W_l = 1/2Fu = \begin{bmatrix} l^{f1} \\ l^{f2} \\ . \\ l^{fn} \end{bmatrix} \begin{bmatrix} l^{1} \\ l^{1} \\ . \\ l^{1} \end{bmatrix} = \begin{bmatrix} l^{f1+1} \\ l^{f2+1} \\ . \\ l^{fn+1} \end{bmatrix} \tag{6.69}$$

Similarly, the rotary work produced by a moment is proportional to the product between the moment and the resulting rotation angle, and it scales as:

$$W_r = 1/2M\theta = \begin{bmatrix} l^{m1} \\ l^{m2} \\ . \\ l^{mn} \end{bmatrix} \begin{bmatrix} l^0 \\ l^0 \\ . \\ l^0 \end{bmatrix} = \begin{bmatrix} l^{m1} \\ l^{m2} \\ . \\ l^{m3} \end{bmatrix} \tag{6.70}$$

where ml, m2, ..., mn represent the (potential) scaling laws of the moment.

Analyzed will be next the scaling of the various forces introduced in Chapter 4.

The *thermal force* that is developed by a fixed-free bar under a temperature increase of ΔT has been evaluated in Chapter 4 as:

$$F = \alpha EA\Delta T \tag{6.71}$$

and therefore, the force scales with the cross-sectional area, $F \sim l^2$ when Young's modulus E and the coefficient of thermal expansion α are constant.

Forces such as *piezoelectric* or produced by *shape-memory alloys* also do scale to l^2, and this can simply be shown by considering again a fixed-free bar whose expansion/contraction needs to be prevented by an axial force, which is proportional to the product between the maximum stress (which is a constant material-dependent feature) and the cross-sectional area. As a result, the respective force scales with A and consequently to l^2.

Similarly, electrostatic forces scale to l^2. In a transverse (plate-type) actuation for instance, the electrostatic force has been defined in Chapter 4 as:

$$F = \varepsilon_0 E^2 A/2 \tag{6.72}$$

and therefore for constant electric permittivity and constant electric field, the electrostatic force scales proportionally to the plate area and therefore to l^2. For longitudinal (comb-finger) actuation, the electrostatic force has been found to be:

$$F = \varepsilon_0 l_z V^2/(2g) = \varepsilon_0 l_z E^2 g/2 \tag{6.73}$$

and again for constant values of ϵ_0 and E, the electrostatic force scales to l^2.

The attraction *magnetic force* developed between a permanent magnet and a mating ferroelectric surface was found to be in Chapter 4:

$$F = B_m A^2 / (2\mu_0) \tag{6.74}$$

which indicates that, being proportional to the square of the cross-section, the magnetic force will scale to l^4.

The Lorentz electromagnetic force that acts on a conductor of length l carrying a current I when placed in an external magnetic field B was defined as:

$$F = IlB \tag{6.75}$$

in the case where the magnetic field B is perpendicular to the linear conductor. The current is defined as:

$$I = \int_A j dA \tag{6.76}$$

where j is the current density and A is the cross-sectional area of the conductor. In the case where the current density is a constant, the current I is proportional to A, and therefore scales to l^2, as suggested by Eq. (6.76), which means that the electromagnetic force will scale to l^3 for constant B.

Example 6.14

Determine the scaling with respect to length of the electromagnetic force acting between two parallel conductors of lengths l_1 and l_2 (as shown in Fig. 6.32) that are placed at a distance d in vacuum and carry the currents I_1 and I_2, respectively.

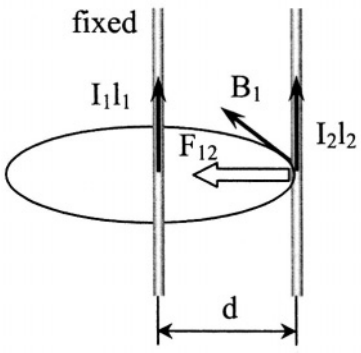

Figure 6.32 Electromagnetic force between two conductors

Solution:

The electromagnetic force that will act on the mobile conductor is:

$$F_{12} = I_2 l_2 B_1 \tag{6.77}$$

It is known that the magnetic field generated by the left conductor is:

$$B_1 = \mu_0 I_1 /(2\pi d) \tag{6.78}$$

and therefore the attraction force of Eq. (6.77) becomes:

$$F_{12} = \mu_0 I_1 I_2 l_2 /(2\pi d) \tag{6.79}$$

It has been shown previously that the current is proportional to the cross-sectional area for constant current densities, and therefore Eq. (6.79) indicates that the Lorentz force is proportional to the square of the current and therefore scales to l^4.

Example 6.15

Establish the length-related scaling law of the force generated between a magnet and an electromagnet, as shown in Fig. 4.38.

Solution:

It has been shown that the magnet of Fig. 4.38 (a) can be substituted by an equivalent coil, as sketched in Fig. 4.38 (b) and the corresponding force generated between the two coils (the real one and the equivalent one) is re-written here for convenience:

$$F = 3\mu_0 A_1 A_2 I_1 I_2 n_1 t_g /[2\pi(R_1^2 + t_g^2)^{5/2}] \tag{6.80}$$

where t_g is the distance between the two coils and n_1 is the number of windings of the real coil. If one carries a dimensional analysis in terms of length, it is apparent that the force is proportional to l^1 (from strictly looking at the relationship between A_1, A_2, R_1 and t_g) and to the square of the current (because of the product $I_1 I_2$), and therefore, because the current itself is proportional to l^2, as shown in the previous problem, the force will scale to l^1 times l^4, which is l^5.

Two other possibilities that can occur and are connected to the current density are analyzed by Trimmer [18] and the conclusions are briefly mentioned here. In the case where there is a constant heat flow generated in the conductor, the electromagnetic force scales to l^3, whereas in the situation where a constant temperature increase is applied to the conductor, the electromagnetic force will scale to l^2.

Problems

Problem 6.1

A thermal bimorph, which is composed of two materials with $E_1 = 100$ GPa, $E_2 = 150$ GPa, $\alpha_1 = 1.6 \times 10^{-6}$ 1/°, $\alpha_2 = 2.2 \times 10^{-6}$ 1/° and having identical cross-sections with $w = 10$ μm and $t = 2$ μm, is subject to a temperature increase of $\Delta T = 100°$ C. Young's modulii are only known approximately, namely E_1 ranging in a $[E_1 - pE_1, E_1 + pE_1]$ interval and E_2 in a $[E_2 - pE_2, E_2 + pE_2]$ interval. Calculate the minimum and the maximum curvature radii that can be produced when p varies from – 0.2 to + 0.2.

Answer:

$R_{min} = 0.043$ m, $R_{max} = 0.048$ m

Problem 6.2

A bent beam thermal actuator, as the one shown in Fig. 4.3 is microfabricated with the following nominal dimensions: cross-sectional width $w = 2$ μm, thickness $t = 2$ μm, leg length $l = 100$ μm and inclination angle $\beta = 5°$. Young's modulus is $E = 160$ GPa and the temperature increase is $\Delta T = 50°$ C. The microfabrication process ensures that β is realized with a precision of +/- $\Delta\beta$ around the nominal value. Also the precision of measuring temperature variations is within a tolerance of +/- $\Delta(\Delta T)$. Considering that $\Delta\beta = p\beta$ and $\Delta(\Delta T) = p\Delta T$ (where p is a tolerance fraction that can vary between - 0.2 and + 0.2) determine the maximum and minimum values of the output displacement u_{1y}.

Answer:

$u_{1y, min} = 0.517$ μm for p = - 0.2;

$u_{1y, max} = 0.523$ μm for p = + 0.2; (because the function u_{1y} (p) is increasing monothonically

Problem 6.3

In a transverse (parallel-plate) electrostatic actuator, as the one pictured in Fig. 4.19, the microfabrication technology produces linear dimensions within a tolerance field of $(l - p) \rightarrow (l + p)$, such that the dimension l_y for instance is located anywhere un the interval $(l_y - p) \rightarrow (l_y + p)$. Calculate the percent relative error between the maximum and minimum initial force in terms of the minimum initial force (x = 0), namely $100\ (F_{max} - F_{min})/F_{min}$. Numerical application: p = 0.1.

Answer:

$error = 2p(3 + p^2)/(1 - p)^3$

Numerical percentage error: 82.58%

Problem 6.4

A microcantilever of the type shown in Fig. 6.29 of Example 6.9 is realized through wet etching and therefore the cross-section, instead of being rectangular, is trapezoid with the dimensions $w = 10\ \mu m$, $w_{max} = 16\ \mu m$ and $t = 2\ \mu m$ (as shown in Fig. 6.19). The microcantilever is used in a reading AFM application, which gives a tip deflection of $3\ \mu m$ and a slope of 1°. Find the force F_z producing these deformations and determine the error on this force when the cross-section is considered rectangular (w x t). The length is $l = 100\ \mu m$ and $E = 160$ GPa. Consider that the anchor leg is rigid and that there are no other forces acting on the microcantilever,

Answer:

$F_{z,trapeze} = 20.5\ \mu N$, $F_{z,rectangular} = 16.06\ \mu N$, $100\ (F_{z,trapeze} - F_{z,rectangular})/F_{z,rectangular} = 27.69\ \%$.

Problem 6.5

The vertical microcantilever in Fig. 6.33 is microfabricated by DRIE in order to be utilized in a vibration detection application. The dimensions of the microcantilever are: $l = 100\ \mu m$, $w = 10\ \mu m$ and $t = 1.5\ \mu m$. A runout of $\alpha = 0.4°$ results through microfabrication. Find the difference in the tip deflection between the real microcantilever and the ideal one (with no runout) when a force $F_{1y} = 15\ \mu N$ is applied. Young's modulus is E = 150 GPa.

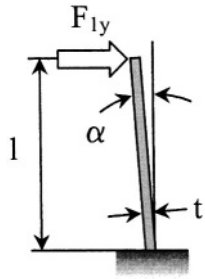

Figure 6.33 Microcantilever for vibration monitoring

Answer:

$\Delta u_{1y} = 7.23 \times 10^{-3}\ \mu m$

Problem 6.6

Determine the deflection at the midpoint of the microbridge shown in Fig. 6.34 when considering the flexibility of all three segments. Find the error in deflection when only the flexibility of the middle (horizontal) link is taken into account. Known are: $t_1 = 1\ \mu m$, $t_2 = 5\ \mu m$, $w = 20\ \mu m$ (w is the width of the microdevice), $l = 200\ \mu m$, $h = 50\ \mu m$, $F_{1z} = 30\ \mu N$ and E = 150 GPa.

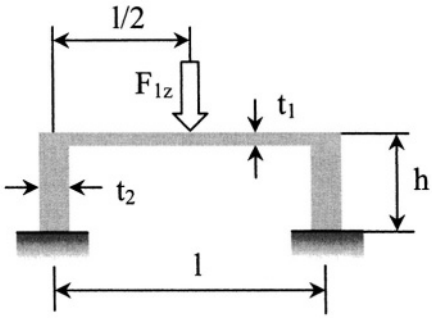

Figure 6.34 Microbridge with force applied at midspan

Answer:

$u_{1z} = 10.03\ \mu m$ for fully-flexible microbridge;
$u_{1z} = 9.97\ \mu m$ for partially-flexible microbridge;
Relative error is 0.6 %.

Problem 6.7

A constant rectangular cross-section microcantilever has a length l =100 μm, cross-sectional dimensions w = 20 μm and t = 2 μm, Young's modulus E = 135 GPa and Poisson's ratio of 0.25. Calculate its main stiffness $K_{Fz\text{-}uz}$ according to the long beam theory and compare it to the similar stiffness which is obtained by the short beam theory.

Answer:

$K_{Fz\text{-}uz} = 21.6$ N/m (long-beam theory); $K_{Fz\text{-}uz} = 21.574$ N/m (short-beam theory)

Problem 6.8

A hollow rectangular microcantilever as the one sketched in Fig. 2.17 is acted upon by a force of 300 μN at point 3, about a direction perpendicular to its plane. Given are $l_1 = 150\ \mu m$, the cross-sectional dimensions w = 8 μm and t = 1 μm, and Young's modulus, E = 130 GPa. Determine the deflection at point 3 by means of the small-deformation theory and compare it to the result obtained by using the large displacement theory, Consider the short segment of length l_2 is rigid. (Hint: The two flexible links act as two beams in parallel).

Answer:

$u_{3z} = 168.75\ \mu m$ (small-deformations);
$u_{3z} = 95.4\ \mu m$ (large-deformations)

Problem 6.9

The residual stress of a thin-film material is known to be $\sigma_r = 55$ MPa. By using the disc method experiment, the center deflection is found to be $u_{1z} = 2$ μm. Determine the material's Poisson's ratio μ_f when the following amounts are given: $E_f = 120$ GPa, $R = 150$ μm, and $t_f = t_s = 0.5$ μm.

Answer:

$\mu_f = 0.21$

Problem 6.10

A thick-film microcantilever has residual stresses in it after microfabrication, and it bends downwards, as shown in Fig. 6.27 (a). The tip slope θ_y is available experimentally and has a value of 1°. Determine the maximum residual stress in the microcantilever, knowing that $l = 200$ μm, $w = 20$ μm, $t = 15$ μm and E= 150GPa.

Answer:

$\sigma_r = 98.17$ MPa

Problem 6.11

A constant rectangular cross-section microcantilever is acted upon by a transverse force F_{1z} at its free tip. Determine the scaling law of the corresponding strength-to-weight ratio when known are the microcantilever's geometry (l, w and t), as well as the material's density ρ. (Hint: SWR = Maximum bending moment / Mass).

Answer:

$SWR \sim l^0$

Problem 6.12

Determine the stiffness scaling for a fixed-free thin-film microbar of constant rectangular cross-section, which is used to evaluate its tensile residual stresses.

Answer:

$Stiffness \sim l^1$

Problem 6.13

Establish the scaling for the tip deflection of a microcantilever that can deflect when placed in an external magnetic field.

Answer:

$Deflection \sim l^3$

Problem 6.14

Derive the scaling for the torque generated in rotary electrostatic actuation.

Answer:

$M_t \sim l^3$

References

1. M. J. Madou, *Fundamentals of Microfabrication. The Science of Miniaturization,* Second Edition, CRC Press, Boca Raton, 2002.
2. M. Gad-el-Hak – Editor, *The MEMS Handbook,* CRC Press, Boca Raton, 2002.
3. Y. Xia, J.A. Rogers, K.E. Paul, G.M. Whitesides, Unconventional methods for fabricating and patterning nanostructures, *Chemical Reviews,* 99, 1999, pp. 1823-1848.
4. S.M. Spearing, Materials issues in microelectromechanical systems (MEMS), *Acta Materialia,* Vol. 48, 2000, pp. 179-196.
5. J.M. Bustillo, R.T. Howe, R.S. Muller, Surface micromachining for microelectromechanical systems, *Proceedings of the IEEE,* Vol. 86, No. 8, 1998, pp. 1552-1574.
6. G.T.A Kovacs, N.I. Malouf, K.E. Petersen, Bulk micromachining of silicon, *Proceedings of the IEEE,* Vol. 86, No. 8, 1998, pp. 1536-1551.
7. H. Guckel, High-aspect-ratio micromachining via deep X-Ray lithography, *Proceedings of the IEEE,* Vol. 86, No. 8, 1998, pp. 1586-1593.
8. C.K. Malek, V. Saile, Applications of LIGA technology to precision manufacturing of high-aspect-ratio micro-components and – systems: a review, *Microelectronics Journal,* 35, 2004, pp. 131-143.
9. A. Bertsch, P. Bernhard, P. Renaud, Microstereolithography: Concepts and applications, *8th IEEE International Conference on Emerging Technologies and Factory Automation,* 2, 2001, pp. 289-298.
10. W.N. Sharpe, Jr., *Mechanical Properties of MEMS Materials,* in *The MEMS Handbook,* edited by M. Gad-el-Hak , CRC Press, Boca Raton, 2002.
11. T. Yi, C.-J. Kim, Measurement of mechanical properties for MEMS materials, *Journal of Measurement Science Technology,* 10, 1999, pp. 706-716.
12. C.A. Zorman, M. Mehregany, *Materials for Microelectromechanical Systems,* in *The MEMS Handbook,* edited by M. Gad-el-Hak, CRC Press, Boca Raton, 2002.
13. X. Li, B. Bhushan, Fatigue studies for nanoscale structures for MEMS/NEMS applications using nanoindentation techniques, *Surface and Coatings Technology,* 163-164, 2003, pp. 521-526.
14. W.C. Young, R.G. Budynas, *Roark's Formulas for Stress and Strain,* Seventh Edition, McGraw Hill, New York, 2002.
15. C.H. Mastrangelo, C.H. Hsu, Mechanical stability and adhesion in microstructures under capillary forces – part II: experiments, *Journal of Microelectromechanical Systems,* 2 (1), 1993, pp. 44-55.
16. G. Murphy, *Similitude in Engineering,* The Ronald Press Company, New York, 1950.
17. E.S. Taylor, *Dimensional Analysis for Engineers,* Clarendon Press, Oxford, 1974.
18. W.S.N. Trimmer, Microrobots and micromechanical systems, *Sensors and Actuators,* 19, 1989, pp. 267-287.
19. W.S.N. Trimmer, *Scaling of Micromechanical Devices,* in *The MEMS Handbook,* M. Gad-el-Hak – Editor, CRC Press, Boca Raton, 2002.

Index

active force, 297
actuation, 43, 66, 68, 98, 115, 183, 184, 185, 186, 195, 198, 200, 202, 204, 209, 210, 211, 212, 215, 216, 224, 232, 236, 237, 245, 250, 253, 254, 255, 256, 259, 262, 263, 264, 266, 269, 270, 271, 273, 274, 275, 276, 277, 278, 279, 280, 281, 283, 286, 298, 299, 304, 305, 306, 326, 328, 330, 335, 336, 337, 338, 340, 384, 387, 394
additive, 344, 349
adhesion, 66, 378, 394
aluminum, 323, 350, 355, 364
anisotropic etching, 354, 356
area, 7, 14, 15, 18, 21, 35, 66, 68, 86, 98, 128, 161, 169, 177, 181, 184, 187, 200, 204, 207, 215, 219, 220, 227, 237, 257, 258, 260, 273, 283, 308, 336, 337, 341, 348, 355, 362, 368, 382, 383, 387, 388, 389
aspect ratio, 66, 346, 347, 348, 351, 356, 358, 359, 360, 361
atomic force microscopy, 67, 80
austenite, 233, 234, 235, 236, 237, 238, 247, 248, 255, 260
axial loading, 18, 21, 30, 32, 43, 47, 49, 52, 98, 99, 139, 324, 326, 330
axial rigidity, 47, 48
beam suspensions, 336, 337, 338
beam-columns, 318, 319, 321
beams, 1, 3, 11, 14, 33, 49, 53, 55, 56, 58, 62, 63, 111, 112, 131, 132, 147, 163, 166, 170, 175, 186, 192, 194, 250, 257, 262, 278, 280, 326, 348, 375, 392
beams in parallel, 63, 166, 250, 392
bending, 1, 3, 4, 5, 6, 14, 16, 17, 18, 19, 20, 21, 23, 24, 25, 27, 28, 29, 34, 35, 36, 37, 40, 41, 43, 44, 45, 46, 47, 48, 49, 50, 53, 55, 56, 57, 58, 59, 60, 62, 63, 64, 65, 67, 69, 72, 73, 74, 75, 80, 82, 83, 85, 86, 87, 88, 89, 91, 92, 93, 95, 97, 98, 100, 101, 102, 103, 106, 108, 109, 110, 111, 113, 114, 115, 116, 118, 119, 120, 121, 124, 125, 126, 127, 129, 132, 133, 134, 135, 136, 137, 138, 139, 141, 143, 145, 146, 147, 348, 156, 157, 159, 160, 161, 163, 164, 165, 167, 168, 174, 175, 178, 186, 187, 192, 194, 209, 210, 215, 222, 223, 240, 241, 242, 243, 244, 245, 246, 247, 248, 250, 252, 253, 254, 255, 260, 263, 287, 288, 289, 290, 298, 304, 310, 314, 317, 318, 320, 324, 325, 326, 327, 330, 333, 334, 335, 366, 367, 369, 372, 373, 377, 393
bending rigidity, 46, 48, 62, 64, 241, 248
bent beam serpentine spring, 131, 160, 161, 181
bent beams, 131, 187, 278
bifurcation buckling, 317
bi-metal thermostat, 242, 262
bimorph, 195, 229, 239, 241, 242, 244, 245, 247, 248, 249, 261, 340, 372, 373
bloc force, 185, 186, 187, 189, 190, 191, 192, 193, 194, 241, 248, 257, 258, 260, 261, 277, 278, 279, 281, 293, 305, 340

boundary conditions, 14, 20, 21, 28, 30, 32, 53, 55, 57, 65, 113, 122, 133, 138, 143, 156, 181, 186, 207, 320, 321, 324, 326, 327, 328, 379, 380
brittle, 330, 350, 363, 364
buckling, 133, 159, 186, 263, 316, 317, 318, 319, 320, 321, 322, 323, 326, 328, 329, 330, 341, 342, 375, 376
bulk micromachining, 343, 344, 352, 354, 360, 364
capacitive change, 196
Castigliano's first theorem, 22, 26, 27, 29, 31, 71, 298
Castigliano's second theorem, 22, 38
Castigliano's theorems, 1, 21
charge constant matrix, 226
chemical vapor deposition, 344
circular loop, 214, 215, 216, 284
circularly-filleted microcantilever, 66, 86, 87, 90, 91, 126
coefficient of linear thermal expansion, 184, 245
columns, 14, 318, 322
comb-finger, 197, 198, 387
complementary energy, 21, 22, 23
compliance, 1, 2, 3, 4, 5, 14, 20, 29, 37, 39, 41, 42, 43, 50, 51, 55, 62, 68, 69, 70, 71, 72, 73, 79, 82, 83, 85, 86, 87, 88, 89, 94, 102, 105, 106, 110, 112, 118, 120, 128, 139, 140, 141, 143, 144, 145, 146, 148, 151, 156, 158, 165, 171, 172, 174, 175, 177, 178, 180, 181, 182, 226, 229, 231, 260, 268, 271, 273, 303, 366, 367, 379, 381
compound microbridge, 121
continuous stiffness measurement, 368
control, 232, 256, 267, 283, 284, 376
copper, 350, 361, 362, 364
corner spring, 138
corner-filleted microhinge, 98, 99, 100, 129, 135, 284, 285
coupling factor, 229, 232
critical load, 317, 319, 321, 324, 325, 326, 328, 329
critical stress, 321, 322
cross-section, 1, 5, 11, 14, 15, 16, 17, 18, 23, 26, 31, 33, 34, 35, 42, 43, 44, 45, 46, 47, 48, 54, 60, 61, 62, 63, 64, 68, 70, 71, 72, 73, 74, 75, 76, 79, 80, 82, 84, 88, 90, 98, 104, 106, 110, 111, 114, 115, 116, 119, 120, 121, 123, 124, 125, 126, 127, 128, 129, 130, 133, 134, 135, 136, 141, 143, 145, 146, 147, 148, 149, 151, 156, 157, 158, 159, 161, 163, 164, 165, 166, 167, 168, 169, 171, 172, 174, 175, 177, 179, 180, 181, 182, 184, 187, 188, 189, 190, 191, 194, 216, 222, 227, 237, 241, 257, 259, 260, 270, 273, 279, 280, 287, 289, 290, 308, 312, 318, 323, 324, 330, 332, 333, 334, 335, 336, 338, 341, 342, 347, 361, 365, 366, 367, 368, 369, 370, 371, 374, 375, 382, 384, 387, 388, 389, 390, 391, 392, 393
cross-stiffness, 3, 6, 29, 75
curvature, 240, 241, 242, 245, 246, 247, 248, 252, 253, 255, 302, 310, 314, 325, 326, 372, 373, 374, 390

curved beams, 34, 147, 170
curved-beam springs, 131
deep reaction ion-enhanced etching, 351, 356
definition stiffness, 141, 144, 146, 148, 149, 156, 157, 161, 162, 178
deflection, 2, 3, 4, 5, 6, 16, 21, 24, 25, 27, 28, 29, 42, 43, 50, 52, 53, 54, 55, 59, 60, 61, 63, 68, 72, 73, 74, 77, 79, 82, 92, 103, 104, 113, 116, 118, 122, 124, 125, 126, 130, 133, 149, 181, 187, 210, 211, 221, 238, 241, 258, 259, 260, 261, 268, 310, 311, 312, 313, 317, 319, 320, 329, 365, 366, 368, 372, 373, 374, 375, 377, 379, 384, 391, 392, 393
deformation, 1, 2, 3, 4, 6, 7, 12, 14, 21, 22, 23, 26, 29, 32, 34, 42, 58, 59, 61, 69, 80, 82, 91, 93, 97, 106, 108, 113, 130, 146, 159, 160, 171, 191, 195, 223, 225, 226, 230, 232, 233, 234, 235, 238, 239, 245, 246, 249, 250, 255, 256, 263, 278, 287, 289, 290, 293, 309, 313, 314, 317, 324, 327, 328, 330, 331, 341, 345, 350, 363, 368, 379, 384, 392
degrees of freedom, 69, 91, 131, 143
deposition, 77, 107, 126, 129, 130, 230, 344, 345, 349, 350, 351, 353, 356, 357, 359, 371, 376
diamond-like carbon, 364
dielectrophoresis, 257
dimensional analysis, 382, 389
direct compliance, 51
direct stiffness, 4, 6, 52, 54, 68, 123
disc method, 373, 393
displacement, 9, 13, 21, 22, 23, 24, 26, 27, 34, 35, 50, 51, 52, 53, 56, 57, 59, 69, 77, 79, 82, 92, 102, 104, 113, 116, 120, 122, 125, 133, 135, 137, 139, 141, 143, 144, 146, 148, 156, 157, 162, 163, 164, 168, 174, 175, 176, 178, 183, 184, 185, 187, 188, 189, 190, 191, 194, 195, 200, 201, 206, 210, 212, 226, 228, 232, 237, 241, 249, 256, 264, 265, 266, 267, 275, 276, 277, 278, 279, 280, 281, 283, 285, 286, 287, 288, 289, 292, 293, 294, 295, 296, 297, 298, 299, 300, 301, 302, 303, 304, 305, 306, 307, 308, 309, 310, 311, 312, 313, 314, 315, 328, 335, 337, 338, 339, 340, 341, 384, 385, 386, 390, 392
displacement amplification, 162, 286, 287, 288, 289, 294, 295, 296, 297, 299, 300, 301, 302, 304, 305, 306
displacement vector, 228, 232
distributed load, 7, 16, 17, 124, 125, 130
ductile, 318, 319, 330, 332, 334, 363
eccentricity, 34, 35, 61, 148, 175
effective length, 321
electric permittivity, 200, 387
electric permittivity matrix, 228, 232
electromagnetic energy, 219, 220
electron-beam lithography, 348
electrostatic, 98, 115, 183, 195, 196, 198, 200, 201, 204, 205, 206, 208, 209, 210, 212, 258, 263, 264, 266, 267, 268, 269, 270, 273, 283, 335, 336, 337, 338, 339, 342, 377, 387, 390, 394

electrostatic force, 196, 200, 204, 210, 264, 266, 267, 268, 269, 283, 387
electrostatic transduction, 195, 209, 210, 264, 269, 270
elliptic integral, 311
energy, 13, 21, 22, 30, 148, 174, 183, 184, 200, 208, 223, 228, 229, 238, 296, 324, 325, 326, 327, 331, 344, 347, 348
etching, 343, 344, 346, 349, 350, 351, 352, 353, 354, 355, 356, 357, 359, 362, 364, 368, 378, 391
Euler-Bernoulli beam model, 17
fiber, 19, 26, 239, 240, 250, 255, 369, 370, 376, 377
fillet, 68, 86, 98, 129, 135
filleted microcantilever, 66, 86, 88, 89
fixed, 1, 3, 5, 6, 7, 14, 15, 18, 19, 20, 21, 26, 28, 33, 34, 39, 42, 46, 49, 53, 54, 55, 56, 59, 60, 61, 62, 63, 65, 68, 75, 79, 92, 98, 100, 105, 113, 114, 116, 117, 118, 119, 120, 129, 132, 134, 138, 140, 163, 171, 173, 174, 178, 179, 184, 186, 187, 190, 191, 192, 193, 196, 198, 200, 201, 202, 204, 205, 206, 207, 209, 211, 220, 227, 241, 259, 264, 266, 269, 270, 273, 279, 281, 308, 309, 321, 323, 324, 328, 329, 332, 334, 341, 342, 358, 360, 368, 369, 374, 375, 376, 379, 384, 387, 393
fixed-guided beam, 53, 134, 179, 281
flexure microhinges, 268, 337, 339
focused ion-beam lithography, 348
folded beams, 131, 166
folded microcantilever, 108, 109, 110, 111, 112, 113, 129
force, 1, 2, 3, 4, 5, 6, 7, 9, 11, 12, 14, 16, 17, 18, 19, 20, 21, 23, 25, 26, 27, 28, 29, 30, 35, 36, 37, 42, 45, 46, 51, 52, 53, 55, 58, 59, 60, 63, 66, 72, 73, 76, 80, 81, 82, 86, 90, 91, 92, 96, 97, 103, 104, 107, 113, 116, 121, 125, 126, 127, 130, 133, 135, 137, 141, 143, 144, 146, 149, 157, 161, 163, 164, 167, 168, 179, 181, 183, 184, 185, 186, 187, 189, 190, 191, 192, 194, 195, 196, 198, 200, 201, 202, 204, 205, 208, 210, 211, 213, 214, 217, 218, 219, 220, 221, 222, 227, 232, 236, 237, 238, 239, 240, 241, 248, 251, 254, 255, 256, 257, 258, 263, 264, 265, 266, 267, 268, 269, 273, 274, 275, 276, 277, 278, 279, 280, 281, 283, 286, 287, 288, 291, 292, 293, 296, 298, 299, 300, 302, 303, 304, 305, 306, 307, 308, 309, 311, 312, 313, 314, 315, 317, 319, 325, 326, 327, 328, 329, 334, 340, 341, 348, 352, 365, 366, 367, 368, 375, 384, 385, 386, 387, 388, 389, 390, 391, 392, 393
force detection, 127
forcing vector, 69
fracture strength, 363, 364, 368, 370
free displacement, 185, 186, 187, 188, 190, 191, 192, 193, 194, 195, 241,248, 249, 257, 277, 278, 279, 281, 293
gallium arsenide, 365
gap, 196, 198, 200, 201, 202, 203, 204, 205, 206, 207, 208, 209, 210, 211, 220, 258, 264, 266, 268, 283, 336, 352, 377

geometry, 11, 28, 34, 44, 53, 75, 80, 83, 85, 86, 92, 94, 104, 107, 134, 138, 155, 171, 176, 180, 187, 188, 194, 208, 210, 215, 219, 241, 250, 251, 259, 276, 279, 280, 302, 335, 363, 377, 393
germanium, 353, 364
gold, 233, 347, 348, 350, 357, 364
growth, 66, 344
Guckel ring, 376
guided, 20, 24, 60, 134, 198, 321, 323, 328, 329, 342
hollow microcantilever, 91, 94, 127, 128
hydraulic, 256
inclined beams, 136, 278, 340
indium phosphide, 365
induced-strain, 241
in-plane compliance, 36, 39, 93, 143, 147, 149, 150, 156, 159, 160, 174, 175, 181
input stiffness, 296, 297, 298, 300, 301, 302, 303, 304, 306, 307
ion-beam lithography, 348
isolated magnetic charge, 217
isotropic etching, 354
large curvature, 33
large deformations, 58, 263, 307, 309, 315, 328
laser machining, 344
layer, 43, 52, 64, 76, 218, 238, 239, 240, 241, 242, 243, 244, 245, 246, 247, 248, 249, 250, 251, 252, 253, 254, 255, 256, 261, 262, 346, 349, 351, 352, 356, 357, 358, 359, 360, 361, 362, 364, 372, 373
lead zirconate titanate, 223, 365
leg, 94, 112, 113, 129, 138, 146, 157, 159, 168, 169, 170, 180, 181, 191, 258, 381, 390, 391
length, 7, 13, 15, 17, 26, 31, 46, 47, 49, 52, 60, 61, 62, 63, 71, 74, 75, 76, 84, 86, 88, 90, 92, 93, 98, 99, 102, 104, 111, 119, 121, 122, 124, 127, 128, 129, 135, 136, 138, 146, 157, 158, 159, 163, 168, 169, 170, 179, 180, 181, 184, 188, 189, 190, 192, 194, 195, 205, 206, 209, 210, 211, 212, 213, 214, 216, 221, 222, 237, 241, 244, 248, 249, 252, 254, 257, 258, 261, 268, 269, 283, 287, 291, 292, 295, 307, 308, 310, 311, 312, 319, 321, 323, 328, 329, 332, 336, 341, 342, 343, 347, 365, 366, 372, 374, 375, 376, 382, 383, 388, 389, 390, 391, 392
LIGA, 357, 358, 359, 394
linear compliance, 2, 51, 105
linear motion, 170, 186, 272, 273, 286
linear spring, 1, 2, 3, 6, 131, 271
linear stiffness, 2, 6, 54, 56, 124, 127, 128, 142, 146, 171, 172, 384
linear transduction, 198
link, 143, 147, 192, 195, 272, 273, 292, 295, 296, 298, 302, 391
liquid-vapor phase change, 257
lithography, 344, 345, 346, 347, 348, 349, 357, 394

loading, 1, 8, 11, 14, 15, 16, 18, 23, 27, 34, 36, 38, 47, 54, 109, 139, 181,210, 226, 234, 236, 282, 307, 326, 327, 330, 331, 332, 334, 335, 369, 379
long beams, 17, 111, 113
longitudinal transduction, 198, 199, 206
Lorentz force, 212, 213, 214, 389
lumped-parameter model, 55, 69, 72, 130
magnet, 216, 217, 218, 219, 220, 221, 259, 260, 262, 387, 389
magnetic, 126, 183, 212, 213, 214, 215, 216, 217, 218, 219, 220, 221, 222, 230, 231, 232, 244, 245, 259, 260, 262, 284, 338, 342, 387, 388, 389, 393
magnetic charge constant matrix, 231
magnetic dipole moment, 215, 216, 218
magnetic energy, 219, 232
magnetic field, 212, 213, 214, 215, 216, 217, 219, 222, 230, 231, 232, 244, 245, 259, 260, 262, 284, 338, 342, 388, 389, 393
magnetic permeability matrix, 232
magnetic reluctance, 220
magnetic transduction, 212, 218
magnetization, 218, 222, 230, 260
magnetostrictive, 230, 231
martensite, 233, 234, 235, 236, 237, 238, 246, 247, 248, 255, 260
mass, 67, 68, 76, 77, 78, 79, 86, 97, 103, 107, 108, 126, 129, 132, 133, 134, 135, 136, 138, 142, 154, 159, 162, 166, 168, 267, 269, 272, 273, 274, 281, 282, 285, 336, 337, 338, 339, 383
mass detection, 67, 78, 86
material, 2, 7, 8, 21, 23, 34, 42, 43, 47, 51, 61, 62, 63, 64, 66, 85, 96, 107, 111, 113, 119, 127, 129, 158, 161, 168, 172, 175, 176, 177, 180, 181, 184, 188, 190, 194, 211, 215, 218, 224, 225, 227, 230, 231, 241, 242, 243, 244, 245, 249, 250, 253, 258, 260, 279, 280, 318, 319, 322, 323, 334, 336, 340, 343, 344, 347, 348, 349, 350, 351, 352, 353, 355, 356, 357, 361, 362, 363, 364, 365, 369, 371, 372, 373, 374, 375, 377, 382, 387, 393
mechanical advantage, 287
mechanical energy, 183, 228, 229
mechanical motion, 183, 196, 241
membranes, 1, 14, 318, 348, 378
MEMS, 1,6, 10, 11, 14, 15,46, 58, 65, 68, 97, 130, 131, 183, 195, 196, 198, 213, 215, 219, 230, 232, 234, 244, 256, 263, 271, 272, 273, 285, 287, 307, 309, 317, 318, 323, 328, 330, 331, 342, 343, 344, 346, 350, 351, 352, 353, 355, 357, 358, 360, 362, 363, 364, 365, 368, 371, 379, 382, 384, 394
microaccelerometer, 132, 180, 267, 268, 272, 285, 286, 336, 337, 339
microactuator, 323, 324, 337
microbridge, 63, 115, 116, 117, 118, 119, 120, 121, 122, 124, 125, 129, 130, 259, 375, 391, 392
microbubbles, 257
microcantilever-in- microcantilever, 108

microcantilevers, 5, 51, 65, 66, 67, 68, 75, 77, 85, 90, 91, 92, 98, 103, 105, 108, 110, 114, 198, 209, 210, 221, 229, 232, 376, 378
microelectromechanical systems, 394
microfabrication, 12, 15, 86, 127, 287, 343, 344, 345, 352, 357, 358, 360, 362, 363, 364, 365, 368, 371, 377, 378, 382, 390, 391, 393
microgyroscope, 269
microhinge, 98, 100, 113, 117, 128, 129, 135, 164, 263
micromachining, 349, 350, 351, 352, 353, 394
micromirror, 97, 98, 281, 282, 360
micromolding, 343, 357
microscopy, 348
microspring, 159, 164, 165, 168, 170, 266
microsuspension, 131, 139, 141, 143, 159, 162, 168, 170, 173, 180, 263, 264, 269, 270, 285, 334
microswitch, 273
Miller-indices, 353
moment, 1, 3, 4, 5, 6, 16, 17, 18, 19, 20, 21, 23, 24, 25, 26, 27, 29, 31, 32, 33, 34, 35, 36, 37, 40, 41, 44, 45, 46, 57, 58, 72, 78, 93, 104, 111, 113, 114, 116, 124, 125, 133, 135, 137, 157, 164, 169, 174, 175, 178, 183, 187, 208, 214, 215, 216, 217, 219, 222, 241, 245, 246, 247, 248, 252, 253, 254, 255, 257, 259, 263, 268, 283, 284, 286, 302, 303, 304, 307, 310, 320, 325, 326, 332, 333, 335, 366, 369, 370, 372, 373, 377, 382, 384, 386, 387, 393
moment of inertia, 16, 32, 35, 45, 111, 114, 124, 135, 169, 187, 247, 257, 366, 369, 370, 377, 382
motion, 23, 67, 91, 97, 98, 114, 115, 131, 133, 138, 139, 142, 151, 154, 162, 163, 165, 166, 167, 168, 169, 170, 179, 180, 183, 196, 197, 198, 199, 203, 204, 205, 206, 208, 209, 230, 241, 273, 274, 275, 276, 277, 280, 285, 287, 305, 340, 381
multimorph, 195, 229, 249, 250, 251, 252, 253, 254, 255, 256, 261
negative magnetostrictive, 230, 262
neutral axis, 16, 17, 34, 44, 45, 48, 61, 240, 247, 254, 370
nickel, 230, 233, 350, 361, 362, 364
nickel-iron, 364
node, 303, 304
normal strain, 8, 9
notched microcantilever, 103, 104, 129
one-way, 234
optical chopper, 278, 340
out-of-the-plane compliance, 38, 39, 40, 41, 96, 172
output stiffness, 296, 297, 299, 300, 301, 302, 303, 304, 305, 306
packaging, 362, 363
parallel-plate, 197, 198, 390
permeability, 218, 219, 260
physical vapor deposition, 344

piezoelectric, 43, 183, 223, 224, 225, 226, 227, 228, 229, 231, 232, 242, 243, 244, 254, 260, 261, 365, 387
piezoelectric bimorph, 243, 244
piezoelectric effect, 223, 224, 225, 227, 231, 232
piezoelectric energy, 228, 229
piezomagnetic bimorph, 245
piezomagnetic energy, 232
pinned, 20, 60, 307, 319, 321, 324, 326, 327
pneumatic, 256
Poisson's ratio, 8, 60, 113, 114, 128, 129, 157, 260, 363, 364, 365, 366, 367, 392, 393
polysilicon, 26, 66, 127, 179, 181, 188, 245, 247, 253, 254, 257, 261, 262, 350,351, 352, 357, 363, 364
positive magnetostrictive, 230, 231
post-buckling, 263, 328
proof mass, 132, 134, 142, 154, 165, 166, 268, 269, 285, 286
properties, 2, 14, 21, 23, 43, 47, 49, 66, 68, 71, 75, 92, 96, 104, 119, 135, 142, 157, 168, 172, 176, 180, 181, 190, 209, 218, 232, 233, 238, 241, 243, 245, 249, 250, 253, 258, 264, 265, 279, 280, 281, 292, 305, 306, 347, 350, 363, 364, 365, 368, 369, 372, 373, 377, 382, 385, 394
pull-in, 266, 267, 282, 284, 336
radius, 34, 42, 58, 61, 86, 98, 104, 128, 129, 135, 147, 149, 150, 151, 153, 171, 172, 173, 174, 175, 177, 182, 207, 208, 214, 220, 238, 240, 241, 242, 244, 245, 246, 252, 253, 255, 284, 302, 314, 321, 338, 342, 372, 373, 374, 383
radius of gyration, 321
reaction ion-enhanced etching, 356
reactions, 19, 20, 21, 23, 57, 58, 92, 113, 116, 118, 120, 122, 125, 137, 163, 176, 186, 193, 346, 355, 356, 363
rectangular, 1, 15, 16, 31, 33, 34, 42, 51, 59, 61, 62, 63, 68, 70, 72, 73, 74, 76, 80, 84, 85, 92, 93, 94, 95, 96, 97, 98, 104, 105, 106, 108, 110, 114, 115, 119, 120, 123, 124, 125, 126, 127, 128, 129, 130, 133, 136, 141, 145, 148, 151, 157, 158, 165, 168, 169, 171, 172, 177, 179, 181, 188, 213, 215, 257, 273, 287, 289, 323, 332, 336, 365, 367, 368, 369, 370, 371, 375, 384, 391, 392, 393
rectangular loop, 213
residual stresses, 12, 371, 372, 373, 374, 376, 393
resistance force, 296, 297
right circular microhinge, 101, 103
right elliptic microhinge, 102, 136
rigid link, 53, 56, 97, 192, 274, 292, 294, 296, 297, 302
rigidity, 47, 48, 49, 52, 59, 62, 241, 248
root, 79, 86, 98, 105, 106, 108, 109, 136, 232, 249, 332
rotary compliance, 3
rotary motion, 131, 132, 170, 173, 206, 207, 208, 263

rotary spring, 3, 55, 271
rotary stiffness, 3, 4, 6, 75, 384
rotary transduction, 207
sacrificial layer, 349, 350, 351, 352, 358, 359, 362, 364, 378
sagittal displacement-amplification microdevices, 286
sagittal springs, 131, 162
scale, 97, 154, 225, 232, 238, 256, 343, 349, 358, 360, 377, 382, 383, 384, 385, 386, 387, 388, 389
scaling, 154, 159, 343, 382, 384, 385, 386, 387, 388, 389, 393, 394
scaling laws, 343, 382, 386, 387
scanning tunneling microscopy, 348
sensitivity, 91, 195, 203, 205, 230, 258, 286, 348, 377, 378
serially-connected members, 49
serpentine springs, 131, 154, 156
shape memory alloys, 183, 232, 233, 234, 236
shape memory effect, 232, 233, 254
shear modulus, 8, 60, 114, 129, 284, 342
shear strain, 7, 8,9, 15, 16, 18
shearing effects, 17, 18, 26, 40, 41, 60, 146, 147, 334, 367, 379
short beams, 17, 18, 367, 379
silicon, 254, 343, 344, 347, 350, 351, 352, 353, 354, 355, 356, 364, 366, 368, 394
silicon carbide, 350, 364
silicon dioxide, 355, 364
silicon nitride, 254, 347, 350, 355, 364, 366
silver, 364
simply-supported, 20, 21
single-crystal silicon, 350, 364, 365
single-profile, 121
slenderness ratio, 322, 323
slope, 3, 4, 16, 21, 23, 24, 25, 26, 27, 28, 29, 54, 55, 56, 58, 63, 68, 72, 73, 74, 76, 77, 79, 80, 82, 90, 103, 104, 107, 113, 116, 122, 126, 128, 215, 216, 222, 235, 253, 261, 262, 264, 266, 268, 288, 289, 292, 298, 310, 311, 314, 329, 365, 366, 379, 384, 391, 393
SMA, 232, 233, 234, 235, 236, 237, 238, 245, 246, 247, 248, 254, 255, 260
SMA bimorph, 245, 247
small curvature, 34, 324
small deformations, 7, 58, 239
snap-through buckling, 317, 318
soft lithography, 349
solid microcantilevers, 103
solid trapezoid microcantilever, 83
spiral spring with large number of turns, 173
spiral spring with small number of turns, 173
spiral springs, 131, 157

springs, 2, 6, 47, 50, 52, 55, 56, 58, 72, 73, 131, 138, 139, 154, 159, 161, 166, 170, 180, 182, 271, 272, 274, 277, 278, 280, 281, 285, 296, 300
state of plane strain, 11
state of plane stress, 11, 12, 331
state of uniaxial stresses, 12
static equilibrium, 1, 8, 13, 23, 113, 263, 264, 267, 280
static response, 1, 68, 69, 131, 263, 273
statically-indeterminate, 23
stereolithography, 343, 361
stiction, 378
stiffness, 1, 2, 3, 4, 5, 6, 14, 21, 29, 30, 31, 32, 33, 43, 47, 49, 50, 52, 53, 54, 55, 56, 57, 58, 60, 61, 62, 68, 71, 72, 74, 75, 84, 85, 86, 90, 91, 93, 100, 101, 102, 103, 104, 106, 107, 110, 111, 112, 114, 116, 118, 119, 120, 121, 124, 125, 126, 127, 129, 131, 133, 134, 135, 136, 137, 138, 139, 140, 141, 142, 144, 146, 148, 149, 151, 153, 154, 156, 157, 158, 159, 161, 162, 163, 164, 165, 166, 167, 168, 169, 170, 171, 172, 173, 175, 176, 178, 179, 180, 182, 237, 238, 250, 266, 271, 273, 274, 275, 277, 278, 279, 281, 284, 285, 286, 296, 298, 299, 300, 301, 305, 306, 340, 363, 366, 367, 368, 379, 381, 384, 385, 386, 392, 393
stiffness matrix, 4, 5, 6, 71, 72, 85, 106, 110, 140, 144, 148, 156, 171, 367
strain, 1, 7, 8, 9, 11, 13, 14, 15, 16, 17, 18, 21, 22, 23, 25, 27, 30, 31, 35, 38, 40, 41, 43, 44, 45, 60, 139, 143, 145, 187, 194, 210, 223, 226, 227, 229, 234, 239, 240, 241, 242, 243, 244, 245, 250, 253, 254, 255, 260, 261, 262, 308, 314, 315, 318, 319, 322, 325, 327, 331, 340, 363, 372, 373, 376
strain energy, 1, 13, 14, 15, 16, 17, 18, 21, 22, 23, 25, 27, 30, 31, 35, 38, 40, 41, 60, 139, 143, 145, 187, 194, 210, 325, 327, 331
strength-to-weight ratio, 383, 393
stress, 1, 7, 8, 9, 11, 12, 13, 14, 15, 16, 43, 44, 45, 60, 63, 86, 180, 226, 227, 228, 229, 232, 234, 236, 315, 318, 322, 330, 331, 332, 334, 335, 345, 363, 369, 370, 371, 372, 373, 374, 375, 376, 377, 384, 387, 393
stress concentrations, 86
structural instability, 315
structural layer, 43, 52, 229, 244, 249, 253, 254, 349, 350
subtractive, 343, 344
superelasticity, 232, 236
surface micromachining, 66, 343, 344, 350, 351, 352, 357, 362, 364, 377
surface-to-volume ratio, 232, 382, 383, 384
suspension, 133, 138, 159, 168, 169, 170, 171, 172, 198, 263, 269, 270, 275, 280, 293
theory of similitude, 381, 382
thermal actuation, 184, 193, 279, 292, 341
thermal bimorph, 241, 242, 243, 244, 390
thermal expansion, 184, 185, 186, 192, 257, 261, 278, 279, 371, 387
thick spiral spring, 174, 175
thin films, 232, 372, 374

thin members, 32
thin plates, 1
thin spiral spring, 176, 177, 182, 271
Timoshenko's beam model, 17
tip, 4, 5, 6, 12, 19, 28, 30, 31, 52, 56, 60, 63, 67, 68, 72, 73, 74, 76, 77, 78, 79, 80, 82, 85, 86, 90, 91, 92, 96, 97, 103, 104, 105, 107, 126, 127, 128, 135, 139, 148, 172, 185, 210, 211, 215, 216, 222, 223, 241, 245, 253, 254, 255, 257, 258, 261, 262, 267, 268, 287, 288, 289, 292, 309, 311, 312, 313, 314, 315, 329, 332, 333, 336, 340, 341, 365, 366, 367, 372, 373, 377, 391, 393
titanium, 233, 347, 364
torque, 2, 3, 15, 120, 121, 125, 130, 135, 171, 172, 178, 182, 208, 258, 270, 271, 281, 283, 284, 394
torsion, 1, 2, 11, 14, 15, 18, 19, 20, 23, 26, 31, 32, 33, 37, 41, 43, 47, 49, 52, 62, 65, 67, 69, 70, 74, 75, 77, 78, 79, 80, 82, 85, 91, 92, 93, 97, 98, 99, 101, 106, 107, 112, 115, 120, 121, 126, 128, 132, 133, 134, 135, 136, 141, 157, 161, 165, 168, 171, 177, 178, 181, 222, 223, 281, 282, 284, 318, 330, 332, 334, 335, 338, 339, 340, 342
torsion beams, 135
torsion microhinges, 136, 338, 339, 340
torsion moment of inertia, 15, 32, 33, 70
torsional rigidity, 47, 223
transduction, 43, 183, 195, 196, 199, 206, 209, 219, 225, 229, 241, 256, 257, 263, 270, 343, 372
transverse transduction, 199
Tresca criterion, 331, 335
triangular, 94, 95, 96, 97, 127
two-beam thermal actuator, 192, 193, 194, 195, 258
two-spring linear-motion mircodevices, 273
two-way, 234
ultimate strength, 363
U-springs, 131, 142
vertical Trimmer bracket, 384, 385, 386
voltage, 195, 200, 203, 205, 206, 208, 209, 211, 243, 244, 253, 254, 255, 258, 260, 265, 266, 267, 270, 273, 283, 284, 336, 337, 338, 339
voltage control, 283
von Mises theory, 331, 335
work, 13, 21, 65, 277, 296, 325, 327, 386, 387
X-ray lithography, 346, 347, 357, 358
yield strength, 363
yielding, 330, 331,332
yielding criteria, 332
Young's modulus, 7, 8, 47, 60, 63, 64, 111, 114, 128, 169, 179, 180, 184, 211, 227, 229, 237, 248, 260, 270, 273, 279, 280, 308, 312, 315, 322, 341, 363, 364, 365, 366, 368, 369, 370, 371, 375, 387, 390, 391, 392
zinc oxide, 365